



DOCTORAL DISSERTATION

Modeling of moisture transport associated with tropical cyclones

Albenis Pérez Alarcón

2022
“International Mention”

Universidade de Vigo

Escola Internacional de Doutoramento

Albenis PÉREZ ALARCÓN

DOCTORAL DISSERTATION

Modeling of moisture transport associated
with tropical cyclones

Supervised by:

Luis GIMENO PRESA, PhD

Raquel Olalla NIETO MUÑOZ, PhD

2022

“International Mention”

Universidade de Vigo

Escola Internacional de Doutoramento

Luis GIMENO PRESA, PhD and Raquel Olalla NIETO MUÑIZ, PhD

DECLARE that the present PhD Thesis, entitled “**Modeling of moisture transport associated with tropical cyclones**”, submitted by **Albenis PÉREZ ALARCÓN** to obtain the title of Doctor with “International Mention” by the Universidade de Vigo, was carried out under our supervision in the PhD Program “Auga, Sustentabilidade e Desenvolvemento”, and it is presented under the modality of compendium of research articles.

Ourense, 9th December, 2022

The supervisors:

Luis GIMENO PRESA, PhD

Raquel Olalla NIETO MUÑIZ, PhD

Campus Universitario de Ourense, Universidade de Vigo
Departamento de Física Aplicada | Environmental Physics Laboratory (EPhysLab)
Albenis PÉREZ ALARCÓN (albenis.perez.alarcon@uvigo.es)

To my Mom

*who is always there for me.
Thanks for your love and understanding.*

Acknowledgements

Many people have contributed to the successful development of my PhD. I would especially like to thank:

- My supervisors, **Luis GIMENO PRESA, PhD** and **Raquel Olalla NIETO MUÑIZ, PhD**. Thank you for trusting me and allowing me to start this PhD project. Without your mentorship and patience, research would be nothing more than a project yet to be performed. Thank you for reviewing each paper in detail and for your valuable comments to improve the work. Thanks very much for the scientific discussions that contributed to the development of this thesis.
- **Rogert**. Thank you for introducing me to research about moisture transport, a fascinating field of atmospheric sciences, for your concern and for being aware of all my documentation when I was in Cuba. Thank you for your advice, the review of the papers, and all the moments shared during this period. Above all, thank you for becoming a great Friend.
- **Patricia**. Despite the distance, thank you for staying with me in this process, motivating me to improve myself at all times and loving me.
- **José Carlos**, who is a friend more than my colleague and co-worker. Thank you for collaborating with the development of numerical algorithms to process data and obtain graphics. Thank you for the ideas and inventions that occur to us from time to time because we are a great team.
- My family in Cuba, especially my mom, my sister (Rosana), my uncle (Alarcón) and my brother-in-law (Edel). I appreciate your support from the other side of the Atlantic Ocean.
- Jose, Miguel and Gleisis for being part of the Cuban family in Ourense and for all the moments we have enjoyed together.
- The EPhysLab group for their welcome from the first day, making me feel like part of the family as soon as I arrived, especially Iago, Milica, Coral, Marta, Luis, Susana and Angel. Thanks to all the professors of the EPhysLab for their teachings.
- My professors at the Higher Institute of Technologies and Applied Sciences, University of Havana, Cuba, for their teachings that have contributed to the development of this thesis. I thank Maykel, Abel and Santana for their support during the PhD.

I have probably forgotten names on this list. To all those people: **THANK YOU!**

I would like to acknowledge the PhD grant from the Universidade de Vigo (“Axudas para contratos predoutorais da Universidade de Vigo”). This work was also supported by the LAGRIMA project (grant no. RTI2018-095772-B-I00) funded by the Ministerio de Ciencia, Innovación y Universidades, Spain, and the partial support from the Xunta de Galicia under the Project ED431C 2021/44 (Programa de Consolidación e Estructuración de Unidades de Investigación Competitivas (Grupos de Referencia Competitiva) and Consellería de Cultura, Educación e Universidade). This PhD Thesis was also thank to the computing resources and technical support provided by the Centro de Supercomputación de Galicia (CESGA).



Albenis PÉREZ ALARCÓN
albenis.perez.alarcon@uvigo.es
Environmental Physics Laboratory (EPhysLab)
Universidade de Vigo
9th December, 2022

Contents

Abstract	v
Resumen	x
List of Figures	xvi
List of Tables	xvii
List of Acronyms	xviii
1 Introduction	1
1.1 Atmospheric branch of the hydrological cycle	1
1.2 Brief description of tropical cyclone structure	3
1.3 Role of water vapour in tropical cyclones	6
1.4 Scope of this thesis	7
2 Objectives	8
2.1 Specific objectives	8
3 Data and Methodology	11
3.1 Datasets	11
3.1.1 Tropical cyclone best-track archives	11
3.1.2 ECMWF ERA-Interim reanalysis	12
3.1.3 Sea surface temperature	12
3.1.4 Precipitation data	12
3.2 Methodology	13
3.2.1 Outer radius of tropical cyclones	13
3.2.2 Cluster analysis	14
3.2.3 Identification of the onset and demise of the monsoon season	15
3.2.4 FLEXPART model simulations	16
3.2.5 Lagrangian moisture source diagnostic method	17
3.2.6 Lagrangian estimation of the mean water vapour residence time	19
3.2.7 Determination of the mean position of the moisture sources	19
4 Set of publications	21

4.1	List of publications	21
4.2	Comparative climatology of outer tropical cyclone size using radial wind profiles	24
4.3	Dataset of outer tropical cyclone size from a radial wind profile	43
4.4	Where does the moisture for North Atlantic tropical cyclones come from?	51
4.5	Moisture source identification for precipitation associated with tropical cyclone development over the Indian Ocean: a Lagrangian approach	68
4.6	Moisture source for the precipitation of tropical cyclones over the Pacific Ocean through a Lagrangian approach	93
4.7	Estimation of mean water vapour residence time during tropical cyclones using a Lagrangian approach	119
4.8	Moisture sources for precipitation associated with major hurricanes during 2017 in the North Atlantic basin	132
5	Summary and Conclusions	150
5.1	Main results	150
5.2	General conclusions	155
5.3	Future works	156
A	Supplementary Material	160
	References	221

Abstract

Tropical cyclones (TCs) are major natural hazards that cause adverse impacts on ecosystems and society, including the destruction of infrastructure and loss of human lives, in coastal regions at tropical and subtropical latitudes. The principal impacts of TCs are caused by strong winds, intense precipitation, associated tornadoes, storm surge, and coastal flooding. Nevertheless, despite their destructive power, TCs act as a source of freshwater by transporting water from oceans to land, which contributes to the attenuation of drought episodes. Therefore, they play an important role in the hydrological cycles in the tropics and subtropics.

The main source of energy for TCs is the release of latent heat from the condensation of water vapour from evaporation on the ocean surface. However, previous studies have not established which oceanic regions are the predominant contributors of moisture according to the TC trajectory. Other authors have pointed out that TCs can extract moisture from soil after crossing the coastline because of the “brown ocean” effect, which is when a TC maintains or even intensifies in strength as it moves inland. This thesis aims to analyse multiple parameters through modelling to objectively identify and characterise the areas that contribute to the evolution of precipitation (moisture sources) during the genesis and development of TCs formed from 1980 to 2018 in the six basins with tropical cyclogenesis: North Atlantic (NATL), Central and East North Pacific (NEPAC), North Indian Ocean (NIO), South Indian Ocean (SIO), South Pacific Ocean (SPO), and Western North Pacific (WNP). To address these objectives, cluster analysis was applied to identify the regions where TCs frequently formed, reached maximum intensity during their life cycle, and dissipated in each basin. The mean water vapour residence time (MWVRT) before precipitation was also estimated, and the moisture sources for precipitation along the pathways of the major hurricanes (Category 3+ on the Saffir-Simpson wind scale) Harvey, Irma, Jose, Lee, Maria, and Ophelia that formed in the NATL basin in the 2017 TC season were analysed.

Information on TCs in the NATL and NEPAC basins was obtained from the HURDAT2 databases provided by the United States (US) National Hurricane Center (NHC) and historical records from the US Joint Typhoon Warning Center (JTWC) for the remaining basins. These databases contain the position, maximum wind, and minimum pressure of all TCs every 6 hours. The first and last entries in the historical records of a TC were assumed to be the genesis and dissipation times, whereas the lifetime maximum intensity (LMI) represented the entry where the TC reached its maximum strength. Using a Lagrangian moisture source diagnostic method applied to the global outputs of the Lagrangian FLEXible PARTicle dispersion model (FLEXPART) v9.0, precipitating air parcels over the area enclosed by the outer radius of the TCs were tracked for up to 10 days to identify the origin of the

humidity that caused the associated precipitation. FLEXPART was forced with meteorological fields every 6 hours of the ERA-Interim reanalysis of the European Centre for Medium-Range Weather Forecasts (ECMWF), with a horizontal and vertical resolution of 1° in latitude and longitude and 61 levels from 1000 to 0.1 hPa. In the simulations, the atmosphere was homogeneously divided into approximately two million air parcels of equal mass. Parcels were transported throughout the atmosphere using a three-dimensional wind field. In addition, the moisture source tracking method has the advantage of providing an objective view of the origin of the moisture that finally precipitated in the region delimited by the outer radius of the TC (the target region) because it proportionally discounts the precipitation en route to all previous moisture uptakes along the trajectory of the air parcels. Therefore, more distant sources contributed less to the final precipitation within the target region.

TC size is an important metric that specifies the extent of the damage to the wind area and precipitation associated with the system. As noted above, the target region was defined as the area enclosed by the outer radius of the TC. Both the tropical storm force radius and the outermost closed isobar have been widely used as measures of the size of TCs; however, in historical records, these parameters are not available for all cases, especially during the genesis and dissipation stages. Therefore, a comparative climatology of TCs based on size was performed using five radial wind profiles. In this analysis, a tangential wind speed threshold of 2 m/s was used to estimate the outer radius of TCs. During the evaluation, the method proposed by Willoughby et al. (2006) was better adjusted to the radial structure of the TC wind field and used to develop a climatological database based on TC size (TCSize). According to this analysis, the largest and smallest TCs occurred over the NATL (~ 804.3 km) and NIO (~ 696.6 km) basins, respectively. The global mean TC size is estimated at 748.7 km. TCSize can also be used for analysing storm surge risk, predicting radial precipitation intensity distribution, and benchmarking different methodologies in terms of performance to obtain TC sizes using artificial intelligence.

By applying the K-means cluster analysis technique, seven different regions where TCs generally formed and reached maximum intensity were identified in the NATL basin (NATL area near the coast of West Africa, seas around the Lesser Antilles arc, Caribbean Sea, Gulf of Mexico, and western and central NATL) and six regions for the dissipation stage (Lesser Antilles arc, Central America and the Caribbean, southern and eastern coasts of the United States, southeastern Labrador Peninsula, NATL open waters around the Azores Islands, and shores of Western Europe). The application of the Lagrangian method of humidity monitoring revealed that the Atlantic Ocean north of the mean position of the Intertropical Convergence Zone (ITCZ) during boreal summer ($\sim 10^\circ\text{N}$), including the Caribbean Sea and Gulf of Mexico, acted as the principal source of moisture for TCs formed in the NATL and contributed approximately 87% of the total moisture uptake. The Atlantic Ocean south of the ITCZ contributed $\sim 11\%$, and its contribution was more significant during the genesis phase. Overall, the contribution from the eastern region of the tropical North Pacific Ocean was small ($\sim 2\%$) but not negligible. In general, the easterly winds and circulation associated with the North Atlantic Subtropical High were the main mechanisms underlying moisture transport toward TC locations.

The origin of precipitation for TCs over the Indian Ocean was studied separately for cyclones over the NIO and SIO basins. Cluster analysis revealed two regions for genesis and LMI (Arabian Sea and

Bay of Bengal) and three for the dissipation phase (Arabian Sea, Bay of Bengal, including coastal areas, and Indian Peninsula) in the NIO. The combined contribution from the Arabian Sea, Bay of Bengal, Indian Peninsula, and Ganges basin accounted for $\sim 70\%$ of the total amount of moisture, followed by the Indochina Peninsula and South China Sea with $\sim 20\%$ and Western Indian Ocean with $\sim 10\%$. The wind flow linked to the Somali low-level jet acted as the principal moisture transport mechanism in the NIO basin, while the Indian Summer Monsoon and East Asian Summer Monsoon highly modulated the intensity and extent of the sources. By applying the K-means clustering technique to the positions of TCs at different phases of development in the SIO, northwestern Australia and central and western SIO were identified as regions where TCs often formed, reached the LMI, and dissipated. The highest moisture contribution ($\sim 65\%$) came from the central Indian Ocean and Wharton and Perth basins (located in western Australia), whereas $\sim 22\%$ of the moisture was supplied by the western Indian Ocean. Similarly, the remaining $\sim 13\%$ was supported by northern Australia and the Coral Sea. The circulation of the Mascarene High and westerly monsoon winds over northern Australia were the main drivers of moisture for TCs in the SIO. In addition, southeastern African and northern Australian monsoons weakly influenced the intensity and extent of moisture sources for TC precipitation in the SIO basin.

The Pacific Ocean is divided into the NEPAC, WNP and SPO cyclogenetic basins; thus, the moisture sources for TC precipitation were investigated. Approximately 62% of annual TCs formed in these three basins on a global scale. Cluster analysis revealed that NEPAC genesis and dissipation occurred in four regions, whereas TCs reached the LMI in the three groups. The regions of genesis in the NEPAC included the Mesoamerican Trench, the area which centroid is located at approximately 12°N and 128°W , the southwestern Pacific coast of Mexico, and the central Pacific Ocean south of the Hawaiian Islands. Likewise, TCs dissipated over the Mexican Pacific coast, western Pacific Ocean, eastern tropical North Pacific Ocean, and Hawaiian Islands and surrounding seas. The maximum intensification of TCs in the NEPAC occurred in the oceanic area near the coast of Central America, the region bounded by 10° to 20°N and 116° to 143°W , and southern Hawaiian Islands. In general, the moisture sources exhibited a north-south split at 10°N , which coincided with the mean position of the ITCZ during boreal summer. Moisture underlying TC precipitation in the NEPAC was mainly contributed from the eastern tropical North Pacific Ocean, including Central America ($\sim 65\%$), eastern tropical South Pacific Ocean ($\sim 20\%$), and Caribbean Sea ($\sim 15\%$). The trade winds from both hemispheres and easterly winds that cross over the tropical North Atlantic Ocean and the Caribbean Sea were the main moisture transport mechanisms.

Using the cluster analysis technique, four regions for the genesis and dissipation phases and three regions for the LMI stage were found in the WNP basin. While genesis generally occurred in the Philippine Sea, South China Sea, seas around the Mariana Islands, and central Pacific Ocean between the Marshall Islands and Hawaii, peak intensity was reached in the South China Sea, from the East China Sea to the western Philippine Sea, and from the central Philippine Sea to the central North Pacific Ocean. Dissipation occurred in the band between $0\text{--}55^\circ\text{N}$ and $150^\circ\text{--}180^\circ\text{E}$, in a small group over the Bering Sea, South China Sea, and the region extended from the Korean Peninsula to the Philippine Sea, including the East China Sea, and Japan Sea. Analysis of moisture sources revealed that during the genesis and peak of maximum intensity, moisture sources for TCs formed over the WNP extended eastward with the highest contribution ($\sim 60\%$) from the Western Tropical

North Pacific Ocean (WTNPac) and Philippine Sea, followed by the contribution ($\sim 25\%$) from the China Seas. Meanwhile, the Bay of Bengal, South Asia, and central Pacific Ocean near southwestern Hawaiian Islands supplied the remaining $\sim 15\%$. However, during the dissipation stage, moisture sources shifted northward, with the largest contributions ($\sim 85\%$) coming from the WTNPac, East China Sea, Japan Sea, East China, and Korean Peninsula. The moisture that precipitated in the area enclosed by the outer radius of the TCs was mostly transported by the circulation of winds associated with the western North Pacific Subtropical High and westerly winds associated with the South Asian monsoon.

In the SPO basin, three groups for the genesis and LMI stages and four groups for the dissipation stage were identified. TCs generally formed in northern Australia, the central South Pacific Ocean, and the Coral Sea. The LMI occurred over the seas north of Australia and the western Coral Sea, the region extending from the Fiji Islands to the central South Pacific Ocean, and the Melanesian archipelago and the surrounding seas. In contrast, the K-means technique revealed that the dissipation of TCs in the SPO occurred in the western South Pacific Ocean, Coral Sea, central South Pacific Ocean, and region consisting of mainland Australia and the eastern Indian Ocean. The moisture for TC precipitation in the SPO was mainly contributed by the Coral Sea ($\sim 40\text{-}50\%$), western tropical South Pacific Ocean ($\sim 20\text{-}35\%$), and northern Australia ($\sim 20\text{-}30\%$). The central South Pacific Ocean also contributed approximately $\sim 10\text{-}15\%$ of the moisture. The convergence of westerly and easterly winds that form the South Pacific Convergence Zone was identified as the main driver of moisture in each cluster.

The findings also revealed that the moisture uptake in all basins was higher during the hurricane category (Saffir-Simpson Wind Scale Category 1 and 2 hurricanes) than at any other stage. The pattern of moisture sources showed that TCs gained more moisture from oceanic sources than from terrestrial sources, thus confirming previous findings of the ocean's role as a source of energy and moisture for the genesis and development of TCs. Furthermore, analysis of the origin of precipitation associated with the major hurricanes (Saffir Category 3+ hurricane-Simpson wind scale) formed in 2017 in the NATL basin suggests that the highest moisture uptake generally occurred within approximately 3° to 5° of their trajectories. This thesis also shows that evaporation from local sources cannot fully explain the TC precipitation, thus highlighting the role of low-level convergence associated with secondary circulation in transporting moisture to the eyewall. This study also confirmed the ability of the Lagrangian moisture tracking method to estimate precipitation associated with TCs.

TC-related precipitation depends on the availability of atmospheric moisture and moisture transport mechanisms, which are strongly modulated by the MWVRT in the atmosphere from evaporation to precipitation. The Lagrangian method of diagnosis of moisture sources applied in this thesis also allows the evaluation of the MWVRT for precipitation associated with TCs. The highest MWVRT was found in the SIO and SPO basins at approximately 3.08 days, followed by the WNP (~ 2.98 days), NEPAC (~ 2.94 days), NIO (~ 2.85 days), and NATL (~ 2.72 days). The overall MWVRT was estimated as $\sim 2.96 \pm 0.4$ days. In general, the MWVRT exhibited the highest values towards the equator, probably due to vertical movements in the ITCZ, which induced a generalised convergence of moisture from the subtropical regions in the equatorial zone through trade winds. Similarly, a poleward decrease in the MWVRT was detected, which was more noticeable in the NATL basin. During

El Niño, the MWVRT values were higher than the mean values in each basin, and the opposite pattern was observed during La Niña years. The analysis also shows a statistically significant ($p < 0.05$) decrease in the MVWRT at a rate of ~ 2.4 hours/decade in the NIO and ~ 1.0 hour/decade in the remaining basins. The relationship between the MWVRT and TC precipitation is complex because of the thermodynamic and dynamic processes involved. The decrease in the MWVRT can be associated with the increase in the rainfall rate of TCs due to higher water vapour availability in the atmosphere, which is associated with rising sea surface temperatures. Additionally, the time spent by the water vapour in the atmosphere after evaporation decreased 24 hours before TCs landfall. Water vapour also precipitated faster when TCs moved over land than over the ocean.

This thesis shows that the Lagrangian moisture source diagnostic method is a suitable tool for providing useful information on the geographic position of moisture sources for precipitation associated with TCs and quantifying precipitation. The results can support the forecasting of rainfall associated with TCs and, in turn, the possible negative (floods) and positive (drought period attenuation) impacts on the continental hydrological cycle and associated socioeconomic effects. Identifying the regions where moisture-producing precipitation accompanies TCs and where TCs originated can help improve seasonal predictions of TC activity and related precipitation. Therefore, in the context of global warming and the projected increase in low-level moisture content at a rate of 6-7% per degree of sea surface temperature warming, these results could be used as a reference to identify changes in moisture sources for TC precipitation under a warmer climate.

Resumen

Los ciclones tropicales (CTs) son uno de los fenómenos naturales que provocan impactos adversos en los ecosistemas y en la sociedad en las regiones costeras de latitudes tropicales y subtropicales, incluyendo la destrucción de infraestructuras y pérdida de vidas humanas. Los principales impactos asociados a los CTs son consecuencia de la acción de los fuertes vientos, precipitaciones intensas, tornados asociados, marejadas ciclónicas e inundaciones costeras. Sin embargo, a pesar de su poder destructivo, los CTs actúan como una fuente de agua dulce mediante el transporte agua desde los océanos a tierra, lo que contribuye a la atenuación de episodios de sequía. Por lo tanto, juegan un papel esencial en el ciclo hidrológico en los trópicos y subtrópicos.

Es bien conocido que la principal fuente de energía para los CTs es la liberación de calor latente de la condensación del vapor de agua proveniente de la evaporación sobre la superficie oceánica. Sin embargo, los estudios previos existentes en la literatura no establecen qué regiones oceánicas son predominantes en el aporte de humedad en función de la posición y trayectoria de los CTs. Así pues, esta tesis está dirigida a analizar múltiples parámetros, a través de la modelización, que permiten identificar y caracterizar de forma objetiva las áreas oceánicas (fuentes de humedad) que contribuyen a la precipitación durante la génesis e intensificación de los CTs en las diferentes cuencas oceánicas en las que se produce ciclogénesis tropical. El estudio se realiza para todos los CTs formados en el período 1980-2018 en las cuencas del Atlántico Norte, Pacífico Central y Oriental, Océano Índico Norte, Océano Índico Sur, Océano Pacífico Sur y Pacífico Norte Occidental (NATL, NEPAC, NIO, SIO, SPO y WNP, por sus siglas en inglés, respectivamente). Para cumplir con el objetivo propuesto, se aplica un análisis cluster para identificar en cada cuenca las regiones donde se forman frecuentemente los CTs, alcanzan su máxima intensidad (LMI, por las siglas en inglés de *lifetime maximum intensity*) y se disipan. Asimismo, se estima el tiempo medio de residencia del vapor de agua en la atmósfera (MWVRT, por sus siglas en inglés) antes de que se genere la precipitación. Por otro lado, para obtener una visión de los cambios en las fuentes de humedad para la precipitación a lo largo de la trayectoria de los CTs, se seleccionaron como casos de estudio los huracanes intensos (Categoría 3+ en la escala de vientos Saffir-Simpson) Harvey, Irma, Jose, Lee, Maria y Ophelia, formados en la cuenca NATL en la temporada ciclónica del año 2017.

La información de los CTs para las cuencas NATL y NEPAC se extrajo de la base de datos HURDAT2 del Centro Nacional de Huracanes (NHC, por sus siglas en inglés) de los Estados Unidos, y para las cuencas restantes de los registros históricos del Centro Conjunto de Alerta de Tifones (JTWC, por sus siglas en inglés). Estas bases de datos contienen la posición, viento máximo y presión mínima de todos los CTs cada 6 horas. Como fecha de génesis y disipación del CT se consideró

la primera y última entrada en el registro histórico correspondiente a ese CT en la base de datos, mientras que el momento de máxima intensificación se asumió como aquel en el que el CT alcanzó por primera vez su máximo de intensidad.

Mediante el empleo de un método lagrangiano de diagnóstico de fuentes de humedad, aplicado a las salidas globales del modelo de transporte lagrangiano FLEXPART v9.0 (FLEXible PARTicle dispersion model), las parcelas de aire precipitantes sobre el área encerrada por el radio exterior de los CTs se rastrean temporalmente hacia atrás durante 10 días, para así identificar el origen de la humedad que originó la precipitación asociada a los mismos. El modelo FLEXPART fue forzado con los campos meteorológicos (campo de viento, humedad específica, temperatura, precipitación, presión en superficie, flujo de calor sensible y de humedad) cada 6 horas del reanálisis ERA-Interim del Centro Europeo de Previsiones Meteorológicas a Plazo Medio (ECMWF, de sus siglas en inglés), con una resolución horizontal de 1° en latitud y longitud y 61 niveles en la vertical, desde 1000 hasta 0.1 hPa. En estas simulaciones, la atmósfera es dividida homogéneamente en aproximadamente 2 millones de parcelas de aire de igual masa que son transportadas a través de la atmósfera por el campo tridimensional de viento. Por otro lado, el método utilizado en esta tesis para el seguimiento de las parcelas de aire y la determinación de sus cambios de humedad específica (q) para localizar las fuentes de la humedad que finalmente precipitó en la región delimitada por el radio exterior del CT (la región de interés) tiene la ventaja de brindar una visión objetiva del origen de la misma. El método descuenta proporcionalmente la precipitación en ruta a las ganancias previas de humedad a lo largo de las trayectorias de las parcelas, y así, de esta forma, las fuentes más lejanas contribuyen cada vez menos a la precipitación final en la región objetivo.

Como se comentó anteriormente, en este trabajo se determinan las fuentes de humedad que generan la precipitación en los CTs, y por tanto es esencial definir de forma precisa el área influenciada por el CT. El tamaño del CT es una métrica importante que especifica la extensión del área de viento dañino y de la precipitación asociada con el sistema. Tanto el radio de fuerza de tormenta tropical como el radio de la última isobara cerrada han sido ampliamente utilizados como una medida del tamaño de los CTs. Sin embargo, en los registros históricos no están disponibles estas variables para todos los casos, especialmente durante las etapas de génesis y disipación. Por lo tanto, se realiza en este trabajo una climatología comparativa del tamaño de los CTs utilizando cinco perfiles radiales de viento. En este análisis se asumió 2 m/s como umbral de velocidad del viento tangencial para estimar el radio exterior de los CTs. En la evaluación realizada, el método propuesto por Willoughby et al. (2006) se ajustó mejor a la estructura radial del campo de viento de los CTs, por lo que se utilizó para desarrollar una base de datos climatológica del tamaño de los mismos (TCSIZE database). Según los resultados, los CTs más grandes ocurrieron sobre la cuenca NATL (~ 804.3 km) y los más pequeños sobre la cuenca NIO (~ 696.6 km). El tamaño medio global de los CTs se estimó en 748.7 km. La base de datos TCSIZE se encuentra disponible en abierto y puede ser utilizada adicionalmente para otros estudios interesantes como pueden ser por ejemplo el análisis de riesgo de marea de tormenta, estudiar la distribución radial de la intensidad de la precipitación o para evaluar comparativamente el rendimiento de diferentes metodologías para obtener tamaños de CTs a partir del uso de la inteligencia artificial.

Mediante la aplicación de la técnica de análisis de clúster K-means, se identificaron siete regiones

diferentes en la cuenca NATL donde generalmente los CTs se formaron y alcanzaron su máxima intensidad: cerca de las costas de África Occidental, en los mares alrededor del Arco de las Antillas Menores, el Mar Caribe, el Golfo de México y el NATL occidental y central. Otras seis regiones fueron identificadas para la etapa de disipación: el arco de las Antillas Menores, Centroamérica y El Caribe, las costas sur y este de los Estados Unidos, la zona al sudeste de la Península del Labrador, las aguas abiertas del NATL alrededor de las Islas Azores y las costas de Europa Occidental. La aplicación del método Lagrangiano para determinar las fuentes de humedad reveló que el Océano Atlántico al norte de la posición media de la Zona de Convergencia Intertropical (ITCZ, de sus siglas en inglés) durante el verano boreal ($\sim 10^\circ\text{N}$), incluyendo el Mar Caribe y el Golfo de México, actuó como la principal fuente para la precipitación de los CTs formados en NATL, aportando aproximadamente el 87% de la humedad. Por su parte, el Océano Atlántico, al sur de la ITCZ, aportó $\sim 11\%$, siendo más relevante su contribución durante la fase de génesis. Además, resultó interesante el aporte ($\sim 2\%$) desde la región oriental del Océano Pacífico Norte tropical. En general, los vientos del este y la circulación de la Alta Subtropical del Atlántico Norte fueron identificados como los mecanismos principales del transporte de humedad hacia las ubicaciones de los CTs.

El origen de la precipitación de los CTs que tienen lugar sobre el Océano Índico se estudió por separado para sus dos subcuencas, el NIO y el SIO. El análisis clúster sobre NIO reveló dos regiones habituales para la génesis y LMI (el Mar Árabe y la Bahía de Bengala) y tres para la fase de disipación (de nuevo el Mar Árabe y la Bahía de Bengala -incluyendo las regiones costeras- y la Península de la India). La contribución combinada de cuatro regiones fuente compuesta por el Mar Árabe, la Bahía de Bengala, la Península India y la cuenca del Ganges representó el $\sim 70\%$ de la cantidad total de humedad para la precipitación de los CTs, seguida por la Península de Indochina y el Mar de China Meridional con un $\sim 20\%$, y el Océano Índico Occidental con un $\sim 10\%$. En la cuenca NIO, el flujo de viento vinculado al chorro de bajo nivel somalí actuó como el mecanismo principal de transporte de humedad, mientras que la intensidad y la extensión de las fuentes fueron moduladas en gran medida por el monzón de verano de la India y el monzón de verano de Asia oriental. Al aplicar la técnica de agrupamiento K-means a las posiciones de los CTs en sus diferentes fases de desarrollo sobre la subcuenca SIO, fueron identificadas tres regiones diferentes, pero comunes, donde a menudo los CT se formaron, alcanzaron la máxima intensidad y se disiparon: el noroeste de Australia y las zonas central y occidental de SIO. La mayor contribución de humedad ($\sim 65\%$) para la precipitación de los CTs provino del Océano Índico central y las cuencas Wharton y Perth (localizadas al oeste de Australia), mientras que el Océano Índico occidental suministró un $\sim 22\%$ de la humedad. El $\sim 13\%$ restante fue aportado desde el norte de Australia y por el Mar del Coral. La circulación de la alta presión de Mascarene y los vientos monzónicos del oeste sobre el norte de Australia fueron los principales impulsores de la humedad para los CTs en esta subcuenca. Además, se encontró que el monzón del sureste de África y el monzón del norte de Australia influyeron débilmente en la intensidad y extensión de las fuentes de humedad.

El Océano Pacífico se divide en tres cuencas ciclogénicas -NEPAC, WNP y SPO-, y por lo tanto las fuentes de humedad para la precipitación de los CTs se investigaron para cada una de ellas por separado. En estas tres cuencas se forma aproximadamente el 62% de los CTs anuales a escala global. El análisis de clúster reveló que la génesis y disipación en NEPAC ocurrieron en cuatro regiones, mientras que los CTs alcanzaron el LMI en tres regiones. Para la génesis las cuatro regiones

se identificaron en el área oceánica de la Fosa Mesoamericana, una segunda zona centrada en 12°N y 128°W, la costa suroeste del Pacífico de México y finalmente en el Océano Pacífico central al sur de las Islas Hawái. La máxima intensificación de los CTs en NEPAC ocurrió en el área oceánica cercana a la costa de América Central, la región limitada por 10–20°N y 116–143°W y al sur de las Islas Hawái; mientras que su disipación tuvo lugar principalmente sobre la costa del Pacífico mexicano, el océano Pacífico occidental, el océano Pacífico norte tropical oriental y sobre las Islas de Hawái y mares circundantes a ellas. En general, el patrón global de las fuentes de humedad para la precipitación asociada a los CTs en NEPAC exhibió una división norte-sur entorno a 10°N, coincidiendo con la posición media de la ITCZ durante el verano boreal; con un aporte mayoritario desde el Océano Pacífico Norte tropical oriental y Centro América (~65%), seguido del Océano Pacífico Sur tropical oriental (~20%) y el Mar Caribe (~15%). Los vientos alisios de ambos hemisferios y los vientos del este que cruzan sobre el Océano Atlántico Norte tropical y el Mar Caribe fueron los principales mecanismos de transporte de humedad.

Para la cuenca WNP se encontraron cuatro regiones habituales para las fases de génesis y disipación de los CTs y tres para la etapa de máxima intensidad. Mientras la génesis generalmente ocurrió en el Mar de Filipinas, Mar de China Meridional, mares circundantes a las Islas Marianas y el Océano Pacífico central entre las Islas Marshall y Hawái, el pico de máxima intensidad fue alcanzado en las regiones del Mar de China Meridional, la zona que comprende desde el Mar de China Oriental hasta el Mar de Filipinas occidental y otra desde el centro del Mar de Filipinas hasta el centro del Océano Pacífico Norte. La disipación ocurrió en la banda entre 0–55°N y 150°–180°E, sobre el mar de Bering, el mar de China Meridional y una región que cubre desde la Península de Corea hasta el mar de Filipinas, incluido el mar de China Oriental y el mar de Japón. El análisis de las fuentes de humedad reveló que durante la génesis y pico de máxima intensidad las fuentes de humedad para los CTs formados sobre WNP se extendieron hacia el este con la mayor contribución (~60%) desde el Océano Pacífico Norte tropical occidental (WTNPac, por sus siglas en inglés) y el Mar de Filipinas, seguido por un (~25%) proveniente de los Mares de China. Mientras tanto, la Bahía de Bengala, el sur de Asia y el Océano Pacífico central al suroeste de las Islas Hawái suministraron el ~15% restante. Sin embargo, durante la etapa de disipación, las fuentes de humedad se desplazaron hacia el norte, con la mayor contribución (~85%) desde el WTNPac, los mares de China oriental, el mar de Japón, China oriental y la península de Corea. La humedad que precipitó en el área encerrada por el radio exterior de los CTs fue mayormente transportada por la circulación de los vientos asociados al alta subtropical del Pacífico Norte occidental y los vientos del oeste vinculados al monzón del sur de Asia.

En la cuenca SPO se encontraron tres regiones para la génesis y máxima intensidad de los CTs, y cuatro para su etapa de disipación. La génesis de los CTs ocurrió en el norte de Australia, el Océano Pacífico Sur central y el Mar del Coral, mientras que alcanzaron el máximo de intensificación en los mares al norte de Australia y el Mar de Coral occidental, la región extendida desde las Islas Fiji hasta el Océano Pacífico Sur central y el archipiélago de Melanesia y mares circundantes. Por otro lado, la disipación de los CTs en SPO ocurrió en el Océano Pacífico Sur occidental, el Mar del Coral, el Océano Pacífico Sur central y la región comprendida por Australia continental y el Océano Índico oriental. La humedad para la precipitación de los CTs en SPO provino principalmente del Mar de Coral (~40-50%), del Océano Pacífico Sur tropical occidental (~20-35%) y del norte de Australia (~20-30%). El Océano Pacífico Sur central también aportó aproximadamente un ~10-15% de la humedad. La

convergencia de los vientos del oeste y del este que forman la Zona de Convergencia del Pacífico Sur se identificó como el principal impulsor de la humedad hacia cada grupo.

En general, y como resumen, se puede concluir que el análisis individual en cada cuenca muestra diferencias en la distribución espacial de las fuentes de humedad, las cuales están relacionadas con las particularidades de la actividad ciclónica en cada una de ellas. El origen del vapor de agua para la precipitación generada por los CTs en NIO proviene fundamentalmente de la Bahía de Bengala y el Mar Árabe, las dos regiones de máxima actividad de CTs, mientras que en SIO las fuentes de humedad se extienden zonalmente hacia el oeste. En NATL y NEPAC es notable la división norte-sur causada por la posición de la ITCZ, mientras que en WNP y SPO, la región con el mayor aporte de humedad coincide con la posición media de la vaguada monzónica y la Zona de Convergencia del Pacífico Sur, respectivamente. Además, como los CTs tienden a disiparse en altas latitudes en NATL y WNP, las fuentes de humedad se desplazan ligeramente hacia el norte en estas cuencas durante la etapa de disipación.

Como característica común, los hallazgos también revelan que la absorción de humedad para los CTs en todas las cuencas fue mayor durante la categoría de huracán (huracán de categoría 1 y 2 de la escala de vientos Saffir-Simpson) que en cualquier otra etapa. Además, el patrón de fuentes de humedad mostró que los CTs obtuvieron más humedad proveniente de fuentes oceánicas que de fuentes terrestres, lo que confirma hallazgos anteriores del papel del océano como la mayor fuente de energía y humedad para la génesis y desarrollo de los CTs. Por otro lado, el análisis de las fuentes de humedad para la precipitación de los huracanes intensos (huracán de categoría 3+ en la escala de vientos de Saffir-Simpson) formados en 2017 en la cuenca NATL sugiere que la mayor absorción de humedad ocurre generalmente dentro un área posicionada aproximadamente de 3° a 5° respecto de las trayectorias de los mismos. Además, muestra que la evaporación de fuentes locales no puede explicar completamente la precipitación de los CTs, destacando el papel de la convergencia de bajo nivel asociada con la circulación secundaria en el transporte de humedad hacia la pared del ojo. Este estudio también confirmó la capacidad del método Lagrangiano de seguimiento de la humedad para estimar la precipitación asociada con los CTs.

Es importante destacar que la precipitación relacionada con los CTs depende de la disponibilidad de humedad atmosférica y de los mecanismos de transporte de humedad, los cuales son fuertemente modulados por el tiempo medio de residencia del vapor de agua (MWVRT, por sus siglas en inglés) en la atmósfera desde que esta se evapora hasta que se produce la precipitación. El método Lagrangiano de diagnóstico de fuentes de humedad aplicado en esta tesis también permitió evaluar el MWVRT para el agua que precipita asociada a los CTs. El MWVRT más grande se encontró en las dos cuencas del Hemisferio Sur (SIO y SPO), siendo aproximadamente de 3.08 días, seguido por WNP (~2.98 días), NEPAC (~2.94 días), NIO (~2.85 días) y NATL (~2.72 días). El MWVRT global durante la ocurrencia de CTs se estimó en $\sim 2.96 \pm 0.4$ días. En general, el MWVRT exhibió los valores más elevados hacia el Ecuador, posiblemente debido a los movimientos verticales en la ITCZ que inducen una convergencia generalizada de la humedad de las regiones subtropicales en la zona ecuatorial mediante los vientos alisios. Por otro lado, se observó una disminución del MWVRT hacia ambos polos, siendo esta más notable en la cuenca NATL. Además, se encontró que el MWVRT está influenciado por el fenómeno de El Niño-Oscilación del Sur (ENSO). Así, durante la fase cálida

de ENSO se encontraron valores de MWVRT superiores a los valores medios en todas las cuencas, mientras que se detectó un patrón opuesto durante la fase fría. El análisis realizado también encontró que existen tendencias en el MWVRT, ocurriendo una disminución estadísticamente significativa ($p < 0.05$) del MWVRT a razón de ~ 2.4 horas/década en NIO y ~ 1.0 hora/década en el resto de las cuencas. Aunque la relación entre el MWVRT y la precipitación de los CTs es compleja debido a los procesos termodinámicos y dinámicos que intervienen en la generación de la precipitación, la disminución del MWVRT puede estar asociada al aumento de la tasa de lluvia de los CTs como consecuencia de una mayor disponibilidad de vapor de agua en la atmósfera debido al aumento de la temperatura superficial del mar. Otro resultado importante encontrado durante el desarrollo de esta tesis doctoral es que el tiempo que pasa el vapor de agua en la atmósfera después de la evaporación disminuyó en las 24 horas anteriores a la llegada a tierra de los CTs, y es además más rápido cuando los sistemas se movieron sobre tierra que sobre el océano.

Los hallazgos presentados en esta tesis muestran que el método Lagrangiano de diagnóstico de fuentes de humedad es una herramienta adecuada para proporcionar información útil sobre la posición geográfica de las fuentes de humedad para la precipitación asociada con los CTs y para cuantificar esa precipitación. Los resultados pueden respaldar el pronóstico de lluvia asociado con los CTs y, a su vez, los posibles impactos negativos (inundaciones) y positivos (atenuación de período de sequía) en el ciclo hidrológico continental y los efectos socioeconómicos asociados. La identificación de las regiones donde la humedad que produce la precipitación que acompaña a los CTs y dónde se originó puede ayudar a mejorar la predicción estacional de la actividad de los CTs y la precipitación relacionada. Por lo tanto, en un contexto de calentamiento global y el aumento proyectado en el contenido de humedad a una tasa de 6-7% por grado de calentamiento de la temperatura de la superficie del mar, los resultados podrían usarse como referencia para identificar los cambios en las fuentes de humedad para la precipitación de los CTs en un clima más cálido.

List of Figures

1.1	Schematic diagram of the water cycle	2
1.2	Schematic representation of the intensification of the hydrological cycle	3
1.3	Boundaries of tropical cyclone basins	4
1.4	Schematic cross-section of the structure of a typical tropical cyclone	5
1.5	Schematic representation of the primary and secondary circulations of a tropical cyclone	5
3.1	Schematic representation of an air parcel trajectory	18

List of Tables

1.1	Saffir-Simpson tropical cyclones wind scale	4
4.1	List of publications.	23
4.2	Summary of the impact and quality of the journal where the first paper that conformed to this thesis was published	24
4.3	Summary of the impact and quality of the journal where the second paper that conformed to this thesis was published	43
4.4	Summary of the impact and quality of the journal where the third paper that conformed to this thesis was published	51
4.5	Summary of the impact and quality of the journal where the fourth paper that conformed to this thesis was published	68
4.6	Summary of the impact and quality of the journal where the fifth paper that conformed to this thesis was published	93
4.7	Summary of the impact and quality of the journal where the sixth paper that conformed to this thesis was published	119
4.8	Summary of the impact and quality of the journal where the seventh paper that conformed to this thesis was published	132

List of Acronyms

- **BTT**: Backward transit time
- **EASM**: East Asian Summer monsoon
- **ECMWF**: European Centre for Medium–Range Weather Forecast
- **ENSO**: El Niño–Southern Oscillation
- **EPhysLab**: Environmental Physical Laboratory
- **FLEXPART**: FLEXible PARTicle dispersion model
- **HURDAT2**: Atlantic hurricane database 2nd generation
- **IBTrACS**: International Best Track Archive for Climate Stewardship
- **ISM**: Indian Summer Monsoon
- **IOD**: Indian Ocean Dipole
- **JTWC**: Joint Typhoon Warning Center
- **LMI**: Lifetime Maximum Intensity
- **NAM**: North Australia Monsoon
- **NAO**: North Atlantic Oscillation
- **NATL**: North Atlantic basin
- **MH**: Major Hurricane
- **MSWEP**: Multi–Source Weighted–Ensemble Precipitation
- **MU**: Moisture uptake
- **MWVRT**: Mean water vapour residence time
- **NASH**: North Atlantic Subtropical High
- **NEPAC**: Central and East North Pacific Ocean basin
- **NHC**: US National Hurricane Center
- **NIO**: North Indian Ocean basin
- **OISST**: Optimum Interpolation Sea Surface Temperature

- **QuikSCAT**: Quick Scatterometer Satellite
- **PDO**: Pacific Decadal Oscillation
- **ROCI**: Radius of the outermost closed isobar
- **SC**: Sources Contributions
- **SEAM**: Southeastern African Monsoon
- **SIO**: South Indian Ocean basin
- **SPO**: South Pacific Ocean basin
- **SST**: Sea Surface Temperature
- **TC**: Tropical cyclone
- **US**: United States
- **UTC**: Universal Time Coordinated
- **WMO**: World Meteorological Organization
- **WNP**: Western North Pacific Ocean basin
- **WNPMT**: Western North Pacific monsoon trough
- **WRF**: Weather Research and Forecasting
- **WVRT**: Water vapour residence time

Introduction

1.1 Atmospheric branch of the hydrological cycle

The hydrological or water cycle is a complex scheme that depicts the transport of water and its conversion under different statuses as it circulates through both local and global systems (WMO, 2012). In essence, it is an extremely complicated dynamic phenomenon because it occurs through a wide range of Earth processes associated with the atmosphere, land, oceans, and life on Earth (Chen and Wang, 2018), such as evaporation from the land, sea, or inland water, cloud-forming condensation, precipitation, interception, infiltration, percolation, runoff, soil water accumulation, or water body accumulation, and re-evaporation (Peixoto and Oort, 1992; Palazzi and Provenzale, 2016), as shown in Figure 1.1.

The atmospheric branch of this cycle plays a key role as a natural conveyor of water bodies (oceans, rivers, and lakes), evaporation, and continental precipitation (Gimeno et al., 2020). Water that falls on a specific area as precipitation can be the result of local evaporation or transpiration or driven by atmospheric winds from remote oceanic or terrestrial sources (Dirmeyer and Brubaker, 1999). Early studies (for example, Baumgartner and Reichel., 1975) found that oceans hold $\sim 97\%$ of the global water resources, and evaporation over oceans is greater than precipitation over oceans, which leads to oceans playing an important role in moisture supply for precipitation over the continents (Gimeno et al., 2010). According to VanDerEnt et al. (2010) and VanDerEnt and Savenije (2011), water vapour from ocean regions accounts for $\sim 60\%$ of the moisture that precipitates over land, while the remaining $\sim 40\%$ comes from terrestrial evaporation and regional recycling processes.

Several authors have investigated the source-sink relationship (for example, Gimeno et al., 2010; VanDerEnt et al., 2014; Keys et al., 2016; Sorí et al., 2017; Gimeno et al., 2020; Vázquez et al., 2020), identified geographical regions that act as moisture sources for precipitation over specific areas, and established the main mechanisms for moisture transport (for example, Gimeno et al., 2016, 2020).

To identify the origin of moisture that produces precipitation over a specific region and moisture transport patterns, authors have commonly applied Eulerian and Lagrangian approaches (Gimeno et al., 2012, 2020, and references therein) or stable water isotopes (Gedzelman et al., 2003; Jouzel et al., 2013; Allen et al., 2017). Lagrangian frameworks have been widely used because of their ability to determine long-term moisture sources (Gimeno et al., 2010, 2020). Previously, Gimeno et al. (2012) noted that Lagrangian techniques are the most suitable for evaluating the origin of precipitation over land.

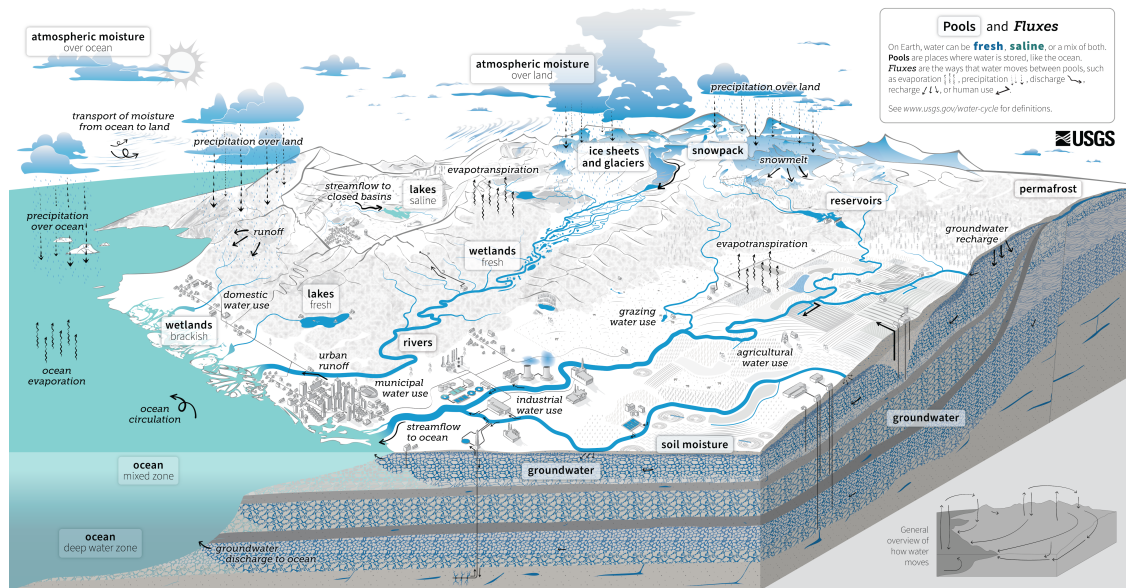


Figure 1.1: Schematic diagram of the water cycle from the United States Geological Survey (USGS; <https://www.usgs.gov/media/images/water-cycle-png>).

The hydrological cycle in tropical regions differs from that in other geographical areas, and it is characterised by the highest energy inputs and faster rates of change (Wohl et al., 2012). Tropical cyclones (TCs) are one of the most relevant elements of the hydrological cycle in tropical and subtropical latitudes (Dominguez and Magaña, 2018) because they cool the ocean and act as drought busters over continents (Maxwell et al., 2012; Brun and Barros, 2014). The role of TCs in the hydrological cycle has been investigated in several studies (for example, Prat and Nelson, 2016; Xu et al., 2017; Franco-Díaz et al., 2019; Fernández-Alvarez et al., 2020), and the findings indicated that TCs contribute ~ 6 to 9% of the annual amount of precipitation over the affected regions.

Understanding the processes that modulate the evaporation of water and moisture transport throughout the atmosphere is a challenge for atmospheric sciences, particularly under global warming (Gimeno, 2013). The relationship between the moisture distribution and surface energy balance implies a link between moisture and temperature. Recent studies have shown that rising sea surface temperature (SST) due to global warming leads to areas of intensified evaporation around the world, thus producing and affecting moisture transport and total precipitation over continents (Shi and Durran, 2015; Giorgi et al., 2019). According to the Clausius–Clapeyron relationship (O’Gorman and Muller, 2010), atmospheric water vapour will increase by 6–7% per degree of SST warming,

thereby strengthening horizontal moisture transport (Held and Soden, 2006; Allan et al., 2020) and the contribution of oceanic evaporation to continental precipitation (Findell et al., 2019), as illustrated in Figure 1.2. In addition, upward global trends in TC-associated rainfall have been projected (Kossin, 2018).

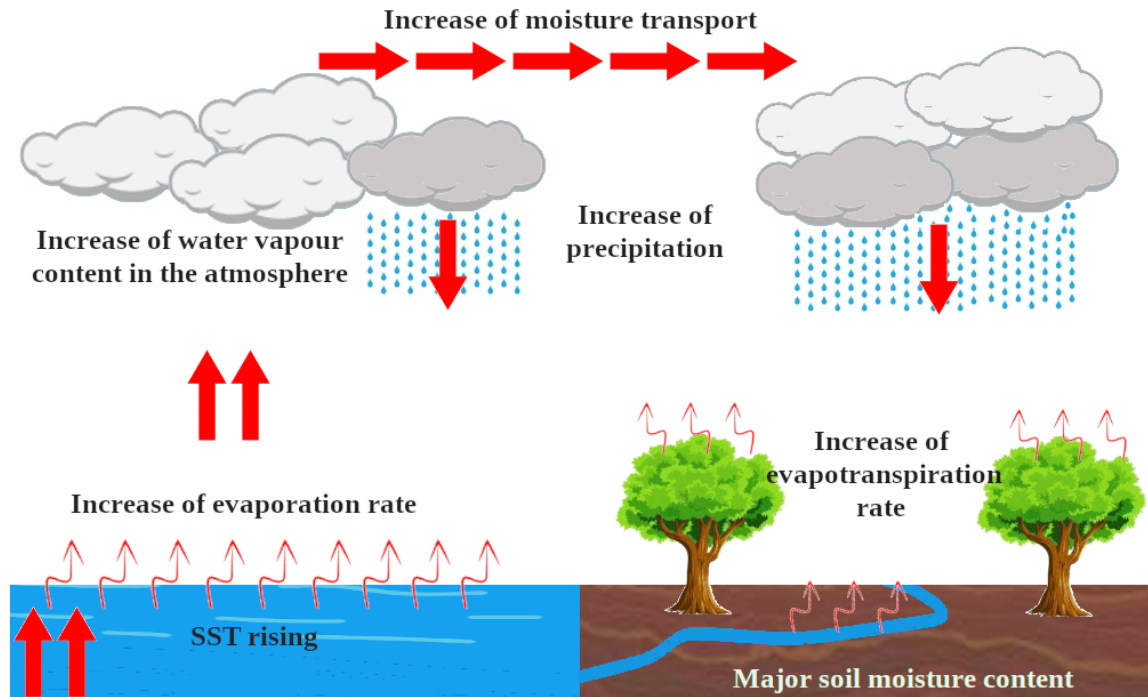


Figure 1.2: Schematic representation of the intensification of the hydrological cycle. Increasing sea surface temperatures (SSTs) under global warming suggest an increase in evaporation rates, thus favouring an increase in the moisture content in the atmosphere and precipitation.

1.2 Brief description of tropical cyclone structure

TCs are intense rotating vortices and low-pressure atmospheric systems with warm cores, organised deep convection, and closed low-level circulation that form over the tropical and subtropical North Atlantic Ocean (NATL), Central and East North Pacific Ocean (NEPAC), western North Pacific Ocean (WNP), North Indian Ocean (NIO), South Indian Ocean (SIO), and South Pacific Ocean (SPO). Figure 1.3 shows the boundaries for each basin.

Approximately 80 to 90 TCs form globally every year, and the annual global rate has been remarkably steady since reliable global best-track data have been recorded (Frank and Young, 2007; Schreck III et al., 2014; Walsh et al., 2015). The WNP basin accounts for $\sim 31\%$ of the global annual TCs, followed by the NEPAC ($\sim 20\%$), SIO ($\sim 17\%$), NATL ($\sim 16\%$), SPO ($\sim 11\%$), and NIO ($\sim 5\%$) (Schreck III et al., 2014). Overall, the Northern Hemisphere hosts approximately 70% of the total global TCs, whereas the Southern Hemisphere accounts for the remaining $\sim 30\%$ (Ramsay, 2017).

According to Gray (1968), TC genesis depends on several large-scale features of the atmosphere and ocean, such as a pre-existing low-level cyclonic disturbance with at least 5° of latitude from the Equator, conditional instability, high water vapour content in the low- and mid-troposphere, weak vertical wind shear, and SSTs higher than 26.5°C to a depth of approximately 40 to 60 m. These factors are necessary but not sufficient for cyclogenesis (Wang, 2015).

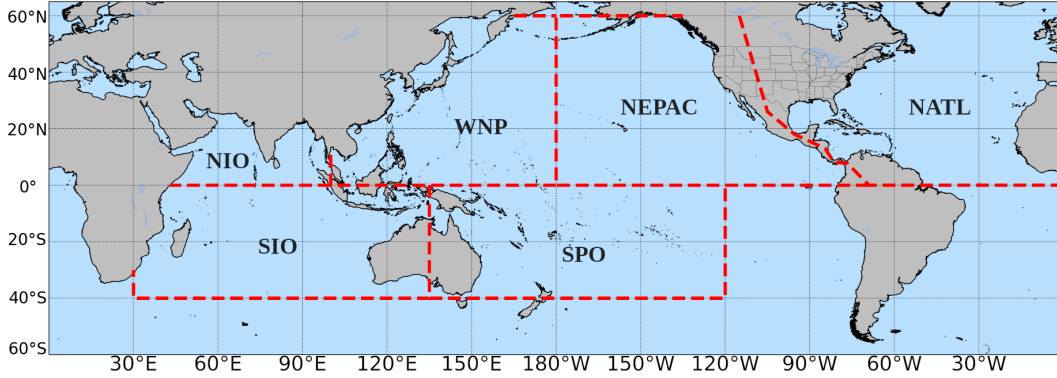


Figure 1.3: Boundaries of tropical cyclone basins. NATL: North Atlantic Ocean, NEPAC: Central and East North Pacific Ocean, WNP: western North Pacific Ocean, NIO: North Indian Ocean, and SIO: South Pacific Ocean.

Based on the Saffir-Simpson wind scale, TCs are classified into tropical depressions, tropical storms, and Category 1 to Category 5 hurricanes, as shown in Table 1.1. TCs categorised as Category 3 hurricanes or higher are also known as major hurricanes (MHs).

Table 1.1: Saffir-Simpson tropical cyclones wind scale adapted from the United States National Hurricane Center (<https://www.nhc.noaa.gov/aboutsshws.php>). The maximum sustained surface wind speed (V_{max}) is the average wind within 1-minute at the standard meteorological observation height of 10 m. TD: Tropical Depression, TS: Tropical Storm, H_N , $N=1,2,3,4,5$: Category 1 to Category 5 hurricanes.

Category	V_{max}	Types of Damage
TD	< 17 m/s	-
TS	$17 \leq V_{max} < 33$ m/s	-
H_1	$33 \leq V_{max} < 43$ m/s	Very dangerous winds will produce some damage
H_2	$43 \leq V_{max} < 50$ m/s	Extremely dangerous winds will cause extensive damage
H_3	$50 \leq V_{max} < 58$ m/s	Devastating damage will occur
H_4	$58 \leq V_{max} < 70$ m/s	Catastrophic damage will occur
H_5	≥ 70 m/s	Catastrophic damage will occur

Figure 1.4 shows a schematic representation of the mature TC structure. As shown, TCs are formed by eyewall clouds that surround the largely cloud-free eye at the centre of the storm, spiral bands of deep convection outside the eyewall, and dense cirrus overcast in the upper troposphere (Vogl, 2009). Overall, a TC can be considered a giant vertical heat engine supported by mechanisms driven by physical forces, such as Earth's rotation and gravity. The flow in a TC is separated into two circulations

(Figure 1.5). Primary circulation is a horizontal quasi-symmetric circulation superposed by thermally direct vertical circulation (secondary circulation). The combination of these two circulations leads to spiralling motion of TCs, which is often notable in cloud patterns from satellite and radar products.

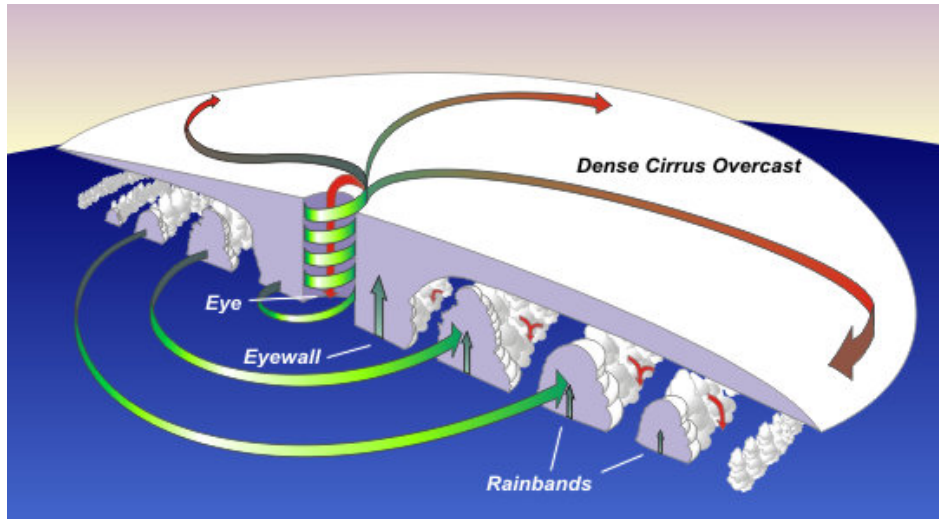


Figure 1.4: Schematic cross-section of the structure of a typical tropical cyclone from the United States National Weather Service (https://www.weather.gov/jetstream/tc_structure).

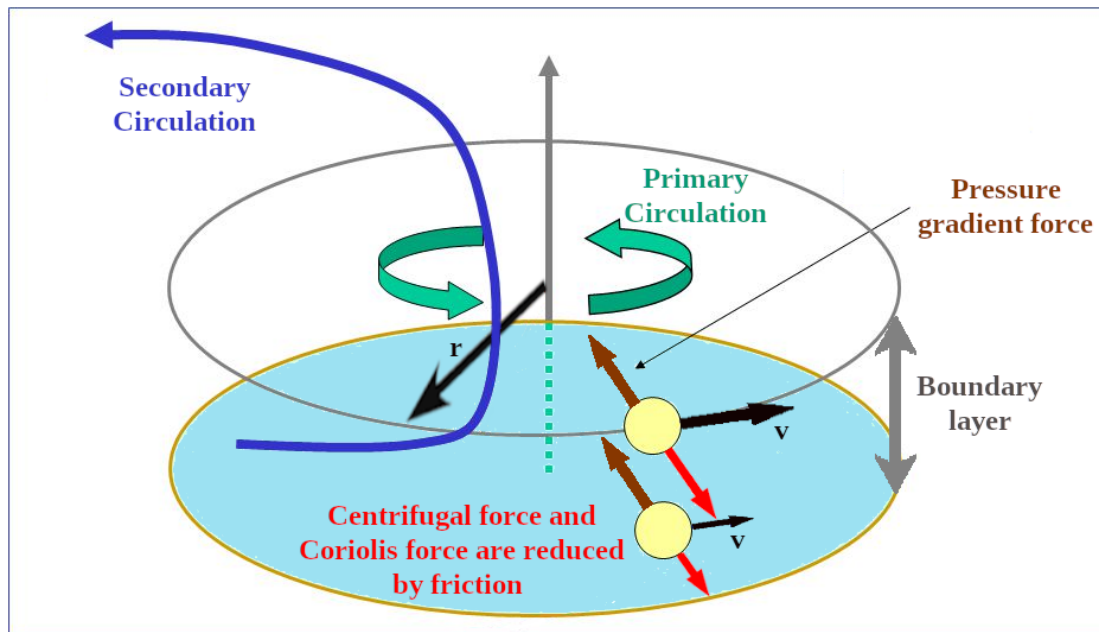


Figure 1.5: Schematic representation of the primary and secondary circulations of a tropical cyclone. Figure adapted from Smith and Montgomery (2016).

Mature TCs are known to be stable. Therefore, by considering a stationary system ($\frac{\partial v}{\partial t} = 0$) and neglecting the radial velocity ($u=0$), the gradient wind balance (Eq. 1.1) is assumed, establishing the primary circulation.

$$\frac{v^2}{r} + fv = \frac{1}{\rho} \frac{\partial P}{\partial r} \quad (1.1)$$

where v is the tangential wind speed, r is the radial distance from the TC centre, P is the pressure, and f is the Coriolis parameter. Willoughby (1990) demonstrated that considering the tangential circulation of the TC in gradient wind balance in the free atmosphere is a good approximation strategy.

Nevertheless, Figure 1.5 shows that a reduction in the tangential wind speed due to surface friction causes a reduction in the centrifugal and Coriolis forces. Therefore, the pressure gradient force is higher than the sum of the two outwards pointing forces, and the parcel of air moves inward towards the eyewall, resulting in convergence of the cyclonic boundary layer flow. This process favours the formation of secondary circulation, in which the air moves from the periphery towards the TC core and ascends in the eyewall. The angular momentum and equivalent potential temperature are conserved during the upward motion of the air parcel. This strong upflow transports moist air to the upper levels. Despite losses due to surface friction and radiative cooling, secondary circulation supplies the storm of angular momentum and heat energy needed to maintain and intensify the primary circulation (Malkus and Riehl, 1960).

1.3 Role of water vapour in tropical cyclones

Early studies highlighted the role played by atmospheric moisture availability in the genesis and intensification of TCs (for example, Gray, 1968; Anthes, 1982; Emanuel, 1987; Gray, 1998; Montgomery and Farrell, 1993; Hendricks et al., 2004). According to Montgomery et al. (2006) and Wang (2014), moist convection is the primary factor driving TC formation and development. Low water vapour content inhibits medium and low-level vortices from becoming TCs, as revealed in the sensitive experiments performed by Yoshida et al. (2017).

Braun (2006) noted that the water budget of a mature TC is mainly controlled by the advection of water vapour and net condensation. Based on high-resolution numerical simulations, the vertically integrated inward moisture flux supplies substantial moisture for total condensation, increasing from tropical wave stage to mature TC, while local evaporation exhibits an opposite pattern (Fritz and Wang, 2014). Similarly, theoretical studies (for example, Emanuel et al., 2004; Kimball, 2006; Ge et al., 2013) have demonstrated that high environmental moisture favour TC intensification. Nevertheless, several research studies (Tao and Zhang, 2014; Wang et al., 2009; Ying and Zhang, 2012) have shown that excess moisture may also limit TC strength owing to the formation of outer rain bands.

TCs induce heavy precipitation, which mostly depends on atmospheric moisture content, and this process has received attention from researchers as a key component of the TC water budget. Previously, Wei and Ji-Long (2012) pointed out that a reduction in atmospheric moisture causes a dramatic reduction in TC precipitation owing to a decrease in moisture convergence. A recent study performed by Makarieva et al. (2017) revealed that TC precipitation could not be fully explained by local evaporation, which is consistent with Montgomery and Smith (2017), who showed that TC precipitation is mainly favoured by secondary circulation transporting moisture inward. Moreover,

the TC rainfall area is closely related to the TC wind field, with heavy precipitation generally confined to the area within the outermost closed isobar (Matyas, 2010).

1.4 Scope of this thesis

As noted above and confirmed by Fujiwara et al. (2017) using a cloud-resolving regional model and Lagrangian diagnostics, the main fuel for TCs is latent heat released from the condensation of water vapour. Although the ocean is the primary source of water vapour for TCs through evaporation, TCs can also gain moisture from terrestrial regions, especially from those located in the western or southern branches of TC spiral bands, as shown in Xu et al. (2017).

The role of secondary circulation of TCs, which transport moisture from the periphery towards the eyewall, suggests that specific oceanic or terrestrial regions act as the main moisture sources for a TC, depending on its location. While several studies (for example, Braun, 2006; Ge et al., 2013; Wang, 2014; Huang et al., 2014; Makarieva et al., 2017; Xu et al., 2017) have focused on the water budget of TCs, methods of identifying the origin of moisture for TCs genesis and development have been poorly studied. For example, Schumacher and Galarneau Jr (2012) quantified the moisture transported by two TCs formed in the NATL basin; Kudo et al. (2014) highlighted that the water vapour contributed from remote oceans accounted for a large fraction of the total precipitable water of TC Man-yi, which formed in 2007 over the WNP, and Pazos and Gimeno (2017) applied a Lagrangian approach to identify the origin of moisture for TCs formed in the NATL between the Lesser Antilles arc and the western coast of Africa.

Although previous studies that investigated the moisture sources for TCs addressed the contribution of atmospheric moisture to TCs, they did not provide a complete overview of the different phases of TC development over each basin. Therefore, this PhD thesis aims to identify the moisture sources for precipitation associated with tropical cyclones during the genesis, lifetime maximum intensity, and dissipation stages over each basin from 1980 to 2018 by applying a Lagrangian moisture source diagnostic method.

Following Gimeno (2013) and Gimeno et al. (2012), the diagnosis of TC sources and transport could provide a better understanding of future changes in precipitation associated with TCs due to global warming. Furthermore, identifying the origin of moisture during the different life stages of TCs is necessary to improve numerical TC prediction models and provide a better understanding of the global hydrological cycle.

Objectives

This chapter presents the objectives to be achieved in this work. The main objective of the current study is to **model moisture transport associated with tropical cyclones**.

This thesis focuses on the identification of source regions of moisture for precipitation associated with TCs during the genesis, lifetime maximum intensity (LMI), and dissipation stages. The intensity and spatial location of these moisture source regions are particularly relevant because an increase (or decrease) in moisture availability can lead to higher (or lower) moisture transport and, therefore, a higher (or lower) total amount of precipitations produced by TCs, which could be useful for forecasters for warning outlooks.

2.1 Specific objectives

To drive the study, a set of specific objectives were followed, as listed below:

1. **Developing a climatology of the outer radius of tropical cyclones.**

Determining the target region is a critical step for investigating the moisture sources for weather systems, such as TCs, and in this work, the area enclosed by the TC size was assumed as the region of interest. Although several metrics (e.g., radius of gale force or radius of the outermost closed isobar) have been used as a measurement for TC size, they are generally missing in historical records during the genesis and dissipation stages of TCs. Therefore, a climatology of the outer radius of TCs was performed. This objective is addressed in articles titled “Comparative climatology of outer tropical cyclone size using radial wind profiles” (Pérez-Alarcón et al., 2021c) and “Dataset of outer tropical cyclone size from a radial wind profile” (Pérez-Alarcón et al., 2022d) published in *Weather and Climate Extremes* and *Data in Brief*, respectively.

2. Performing a cluster analysis to determine the main zones where the genesis, intensification and dissipation of tropical cyclones occur.

Because TCs can form in a wide area across tropical oceans and present long trajectories, i.e., in the NATL and WNP basins, the genesis, LMI, and dissipation locations of TCs were grouped in each basin by applying the K-means clustering technique. Therefore, a moisture source analysis was performed for each cluster in each basin.

3. Identifying the moisture sources in each basin for the precipitation associated with tropical cyclones during their different phases of development.

The relative importance of environmental parameters for TC activity and the spatial distributions of TCs locations during the genesis, LMI, and dissipation stages can be very different in each ocean basin or even in different regions of the same basin (for example, Zhao et al., 2018; Shan and Yu, 2020). Therefore, we separately performed the Lagrangian moisture source analysis for each cluster, phase, and basin.

These last two specific objectives (2 and 3) are addressed in three papers titled “Where does the moisture for North Atlantic tropical cyclones come from?” (Pérez-Alarcón et al., 2022e) for the North Atlantic basin published in *Journal of Hydrometeorology*, “Moisture source identification for precipitation associated with tropical cyclone development over the Indian Ocean: a Lagrangian approach” (Pérez-Alarcón et al., 2022c) for the Indian Ocean basins published in *Climate Dynamics*; and “Moisture source for the precipitation of tropical cyclones over the Pacific Ocean through a Lagrangian approach” (Pérez-Alarcón et al., 2023) for Pacific Ocean basins published in *Journal of Climate*.

4. Estimating the mean water vapour residence time for the precipitation associated with tropical cyclones.

The time taken by water vapour from evaporation to precipitation is a relevant characteristic of the hydrological cycle (VanDerEnt and Tuinenburg, 2017; Gimeno et al., 2021). As TCs play a crucial role in the water cycle in tropical and subtropical regions, the mean water vapour residence time (MWVRT) for the precipitation associated with TCs in each basin was also estimated to have new insights into the origin of moisture for TC-related rainfall. This objective was attended in the paper titled “Estimation of mean water vapour residence time during tropical cyclones using a Lagrangian approach” (Pérez-Alarcón et al., 2022a) published in *Tropical Cyclone Research and Review*.

5. Identifying the moisture sources for the precipitation during the genesis and intensification of individual cases of tropical cyclones.

The genesis and evolution of individual TCs differ (Ren et al., 2014). Thus, the relationship between the TC trajectory and precipitation moisture sources must be better understood to improve the knowledge about the mechanism governing the moisture transport of individual TCs. This objective is addressed by investigating the moisture sources for six TCs formed in the NATL basin in the article titled “Moisture sources for precipitation associated with major

hurricanes during 2017 in the North Atlantic basin” (Pérez-Alarcón et al., 2022b) published in *Journal of Geophysical Research: Atmospheres*.

Data and Methodology

3.1 Datasets

3.1.1 Tropical cyclone best-track archives

The position and intensity of each TC were extracted from best-track archives. The United States (US) National Hurricane Centre (NHC) provided the HURDAT2 database (Landsea and Franklin, 2013) for the NATL and NEPAC basins, while the US Joint Typhoon Warning Center (JTWC) provided historical records of TCs for the remaining basins (Chu et al., 2002). These databases include the position of TCs in latitude and longitude, maximum sustained wind speed, and minimum sea level central pressure during synoptic times (00, 06, 12, and 18 UTC). Non-synoptic time records are also available in the HURDAT2 dataset to indicate landfall and intensity maxima (Landsea and Franklin, 2013). Both the NHC and JTWC registered the intensity of TCs based on the average wind for 1-minute instead of 10- or 3-minutes. The HURDAT2 and JTWC archives are freely available at <https://www.nhc.noaa.gov/data/#hurdat> and https://www.usno.navy.mil/NOOC/nmfc-ph/RSS/jtwc/best_tracks/TC_bt_report.html. Furthermore, these datasets are hosted in the International Best Track Archive for Climate Stewardship (IBTrACS) project (Knapp et al., 2010, 2018). Although other agencies provide historical records of the activity of TCs in the WNP, NIO, SIO, and SPO basins, that is, the China Meteorological Administration, the Regional Specialised Meteorological Centre of Tokyo, the Indian Meteorological Department, and the Bureau of Meteorology, the usage of records from US agencies ensures homogeneity in the maximum wind speed records.

Despite long-term datasets of TC records, changes in observational methods have limited the reliable detection of climatic signals in TC activity (Emanuel, 2021). Several authors noted that after the beginning of the meteorological satellite era in the 1970s, TC records were of high quality for climatic studies (for example, Vecchi and Knutson, 2008; Kossin et al., 2013; Bhatia et al., 2019). Although the climatological analysis of TC size based on radial wind profiles was performed since

records began in each basin, the study period for the Lagrangian analysis of moisture sources was from 1980 to 2018 because data from ERA-Interim were only available until August 2019.

3.1.2 ECMWF ERA-Interim reanalysis

The ERA-Interim dataset is a global reanalysis generated by the European Centre for Medium-Range Weather Forecasts (ECMWF) (Dee et al., 2011). This reanalysis was performed using a data assimilation system based on the Integrated Forecast System (IFS) released in 2006, and it includes a 4-dimensional variational analysis with a 12-hour analysis window. ERA-Interim reanalysis data can be obtained from <https://www.ecmwf.int/en/forecasts/datasets/reanalysis-datasets/era-interim>.

Data from the ERA-Interim reanalysis from 1980 to 2018, which were recorded every 6 hours with $1^\circ \times 1^\circ$ horizontal resolution and 61 vertical levels from 0.1 to 1000 hPa, were used to feed the FLEXPART model. The three-dimensional wind field, specific humidity and temperature, two-dimensional total cloud cover, eastern/western and northern/southern surface stress, 10 m horizontal wind components, large-scale and convective precipitation, 2 m temperature, dew point temperature, surface pressure, sub-grid standard topography deviation, topography, sensible heat flux, land-sea mask, and eastward/northward vertically integrated moisture flux were used.

3.1.3 Sea surface temperature

The US National Oceanic and Atmospheric Administration provided the Daily Optimum Interpolation Sea Surface Temperature (OISST) dataset v2.1 (Banzon et al., 2020; Huang et al., 2021). This dataset combines daily data from different platforms, namely, satellites (from the Advanced Very High Resolution Radiometer), ships, buoys, and Argo floats, into a regular global grid of $0.25^\circ \times 0.25^\circ$ spatial resolution. This is available at <https://www.ncei.noaa.gov/products/optimum-interpolation-sst>.

3.1.4 Precipitation data

Daily precipitation data were extracted from the Multi-Source Weighted-Ensemble Precipitation (MSWEP) database with a grid spacing of $0.1^\circ \times 0.1^\circ$ and temporal resolution of three hours, and it covered the temporal period from 1979 to seven months from the present (Beck et al., 2017, 2019). The MSWEP merges observations from a wide range of data sources, namely, ~ 13762 gauges across the globe, satellite, and reanalysis data, to eliminate systematic biases. Therefore, this is a high-quality precipitation estimate. Precipitation from this dataset was used to determine the onset and demise of the Indian Summer Monsoon (ISM), East Asian Summer Monsoon (EASM), North Australian monsoon (NAM), and Southeastern African Monsoon (SEAM). The MSWEP database is available upon request in <http://www.gloh2o.org/>

3.2 Methodology

3.2.1 Outer radius of tropical cyclones

The size of TCs is an important structural parameter (Jaiswal et al., 2019), and its estimation is crucial for identifying the origin of moisture for precipitation. Several metrics have been defined to estimate the size of TCs; however, the radius of the gale force (R_{34} , radius at which the maximum wind speed is equal to 34 kt (~ 17.5 m/s)) (Dean et al., 2009; Wu et al., 2015), and radius of the outermost closed isobar (ROCI) (Lu et al., 2011; Kilroy and Smith, 2017) have been widely used to achieve this goal. However, by definition, R_{34} is frequently missing during the genesis and dissipation stages of TCs. Likewise, the ROCI is generally missing in the first and last times of TC development or during a marked weakness of TC. Other authors have assumed that the TC outer radius is the radial distance from the TC centre at which the tangential wind speed is equal to 15 m/s (Cocks and Gray, 2002), 12 m/s (Chavas and Emanuel, 2014) or 2.5 m/s (Knaff et al., 2014). The latter approaches are based on the QuikSCAT global near-surface wind vector database, which has been available only since 1999.

To fill these gaps and use a homogeneous TC size approach across the study period, many radial wind profiles were applied to define the TC outer radius, which followed the definition of TC size by Knaff et al. (2014). Several radial wind profiles (for example, Holland, 1980; DeMaria, 1987; Willoughby et al., 2006; Emanuel and Rotunno, 2011; Frisius et al., 2013; Holland et al., 2010; Wood and White, 2011; Wood et al., 2013) have been developed to depict the radial distribution of tangential wind speed of TCs. The first approximations were based on the Rankine combined vortex (for example, Deppermann, 1947) and rectangular hyperbolas (Schloemer, 1954; Holland, 1980), whereas the most recent approach involved many parameters, namely, scaling and statistical parameters (for example, Willoughby et al., 2006; Emanuel and Rotunno, 2011; Frisius et al., 2013).

Holland (1980) improved the relationship of Schloemer (1954) and proposed one of the most widely used radial wind profiles of TCs:

$$v = V_{max} \left[\left(\frac{r_m}{r} \right)^b e^{1 - \left(\frac{r}{r_m} \right)^{-b}} \right]^{0.5} \quad (3.1)$$

where v is the wind speed at a distance r from the centre, r_m is the radius of the maximum winds, V_{max} is the maximum wind speed, and b is a parameter that ranges between 1 and 2.5. The r_m in the NATL and NEPAC was computed using the empirical formula proposed by Willoughby et al. (2006). In the other basins, it was estimated following Tan and Fang (2018). Following Kowaleski and Evans (2016), $b = 2$. Meanwhile, DeMaria (1987) developed a radial wind profile given by

$$v = V_{max} \left(\frac{r}{r_m} \right) e^{\left(\frac{\frac{1}{c} - \frac{1}{c} \left(\frac{r}{r_m} \right)^c}{d} \right)} \quad (3.2)$$

where $c = 0.63$ and $d = 1$ according to Kowaleski and Evans (2016).

The main limitations of the Holland (1980) wind profile are the (i) unrealistically strong winds in the eyewall compared to observations and (ii) rapid decay of the tangential wind with increasing radial distance from the TC centre (Wood et al., 2013). Willoughby et al. (2006) addressed the shortcomings of Holland (1980) and proposed a parametric radial wind profile designed to fit observational data from reconnaissance aircraft. This profile is given by

$$v = \begin{cases} V_{max} \left(\frac{r}{r_m} \right)^n & r < r_1 \\ V_i(1-w) + V_0w & r_1 \leq r \leq r_2 \\ V_{max} \left[(1-A)e^{-\frac{r-r_m}{X_1}} + Ae^{-\frac{r-r_m}{X_2}} \right] & r > r_2 \end{cases} \quad (3.3)$$

where n , A , X_1 , and X_2 are parameters associated with TC intensity, V_i and V_0 are the tangential wind speeds at r_1 and r_2 radii, respectively, and w is a weight function. Holland et al. (2010) highlighted that the Willoughby et al. (2006) profile accurately fits known profiles.

In addition, this thesis includes the wind profiles developed by Emanuel and Rotunno (2011) and Frisius et al. (2013). The parametric wind profile proposed by Emanuel and Rotunno (2011) is as follows.

$$v = \frac{2r(r_m V_{max} + 0.5fr_m^2)}{r_m^2 + r^2} - \frac{fr}{2} \quad (3.4)$$

where f denotes the Coriolis parameter. Frisius et al. (2013) developed another radial wind profile:

$$v = V_{max} \frac{r_m}{r} \cdot \left[\frac{2 \left(\frac{r_m}{r} \right)^2}{2 - \left(\frac{C_H}{C_d} \right) \left[1 - \left(\frac{r}{r_m} \right)^2 \right]} \right]^{\frac{1}{2} - \frac{C_H}{C_d}} - \frac{fr}{2} \quad (3.5)$$

where C_d is the surface drag coefficient and C_H is the surface transfer coefficient for enthalpy.

Using five previously described radial wind profiles (Holland, 1980; DeMaria, 1987; Willoughby et al., 2006; Emanuel and Rotunno, 2011; Frisius et al., 2013), a climatology analysis was performed to determine the outer radius of each TCs at 6-hour interval. This outer radius was then used to delimit the target region during Lagrangian identification of the moisture sources.

3.2.2 Cluster analysis

To gain a complete overview of the moisture sources for the TC precipitation during the genesis, LMI, and dissipation stages, TCs were grouped during each stage by applying the K-mean cluster analysis technique (MacQueen et al., 1967; Jain and Dubes, 1988; Jain, 2010). This method is one of the simplest and most extensively used unsupervised machine learning algorithms (Kim and Seo, 2016). K-means proceeds as follows: (i) K centroids are randomly selected to group each sample into different classes, (ii) the Euclidian distance is computed between each sample in the dataset and the

centroids, and (iii) each sample is assigned to the closest centroid based on the minimum distance from the centroids. This process is iterative until the squared error between the empirical centroid of a cluster and points in the cluster is minimised.

As input parameters, the K-means algorithm requires a cluster number K and data points. According to Jain (2010), the selection of K is the most critical choice because an increase in the number of clusters leads to a decrease in squared error. Therefore, K is objectively selected based on the geographical distribution of clusters and by applying the Silhouette coefficient (Sinnott et al., 2016; Belyadi and Haghighat, 2021). The Silhouette coefficient for a single sample (X_i) is computed using Eq. 3.6

$$S(i) = \frac{b(i) - a(i)}{\max\{a, b\}} \quad (3.6)$$

where $a(i)$ denotes cluster cohesion, which is defined as the average distance from X_i to other data points within the same cluster, and $b(i)$ is the cluster separation, which is defined as the mean distance between X_i and all data points within the nearest cluster. The Silhouette coefficient ranges between -1 and 1. When $S(i) \rightarrow 1$, X_i is correctly assigned to a cluster; $S(i) = 0$, X_i is on or very close to the decision boundary between two neighbouring clusters; and $S(i) \rightarrow -1$, X_i is assigned to an incorrect cluster.

This cluster technique has been previously applied to TCs for classifying their genesis, track, and decay locations in the NATL basin (Corporal-Lodangco et al., 2014), identifying the landfall regions of TCs in the whole NATL (Pérez-Alarcón et al., 2021b) and for Cuba (Coll-Hidalgo and Pérez-Alarcón, 2021), detecting interdecadal changes in the genesis of TCs over WNP (Ye et al., 2022), and grouping TC trajectories in the WNP (Yu et al., 2016) and NIO (Rahman et al., 2018) basins.

3.2.3 Identification of the onset and demise of the monsoon season

Several regions of TC activity (e.g., NIO, SIO, and WNP) are influenced by monsoon systems; therefore, it is important to investigate how the changes in the atmospheric circulation induced by the monsoon systems influence the moisture sources for TC precipitation. The Indian Summer Monsoon (ISM) is part of the Asia Summer Monsoon, which is the most important monsoon system in the world (Liu et al., 2019b), and causes changes in atmospheric circulation patterns over the NIO basin. TC activity over the NIO basin has a bimodal distribution, with peaks of activity during the pre-monsoon (May-June) and post-monsoon (October-November) seasons (Krishna, 2009; Yanase et al., 2012; Li et al., 2013).

According to Misra et al. (2018), the onset and demise of the ISM vary annually. Therefore, to objectively identify the linkages between the monsoon season and the intensity and spatial pattern of moisture sources for TC precipitation, the onset and demise of the monsoon system were computed following Noska and Misra (2016). Monsoon onset (demise) is defined as the first day of the year after the minimum (maximum) daily cumulative anomaly (C'_m) of the average rainfall over a specific area (A). The C'_m for day i of year m is given by

$$C'_m(i) = \sum_{n=1}^i [D_m(n) - R_c] \quad (3.7)$$

where,

$$R_c = \frac{1}{MN} \sum_{m=1}^M \sum_{n=1}^N D(m, n) \quad (3.8)$$

R_c is the climatology of the annual mean rainfall over A for N days for M years and $D_m(n)$ is the daily rainfall over A for day n of year m .

Here, the onset and demise of the East Asian Summer monsoon (EASM), Southeastern African Monsoon (SEAM), and North Australian Monsoon (NAM) were also estimated. The area A corresponds to the limited regions (7° to 22° N, 73° to 90° E), (5° to 45° N, 90° to 125° E), (0° to 40° S, 25° to 50° E) and (10° to 22° S, 110° to 140° E) for the ISM, EASM, SEAM, and NAM, respectively.

3.2.4 FLEXPART model simulations

The FLEXible PARTicle dispersion model (FLEXPART) is a Lagrangian transport and particle dispersion model that was first developed in the 1990s (Stohl et al., 1998; Stohl and Thomson, 1999) to investigate the long-range and mesoscale dispersion of hazardous substances from point sources. The FLEXPART model is also a useful tool for atmospheric transport modelling and analysis (Stohl et al., 2005), that is, for investigating the global or regional water cycle (Gimeno et al., 2012, 2020). Moreover, this model includes a set of parameterisations but the parameterisation of turbulence and convection are particularly relevant in the simulation of the effects of humidity.

In this thesis, global simulations of FLEXPART v9.0 developed by the Environmental Physical Laboratory (EPHysLab) research group of the University of Vigo (Spain) were used. The outputs of this Lagrangian model have been used in several studies to investigate the moisture source-sink relationships. For example, the outputs have been used to investigate moisture sources for extreme precipitation events (Liberato et al., 2012; Vázquez et al., 2020; Sun and Wang, 2014), moisture transport from oceans to continents (Gimeno et al., 2010; Gimeno, 2013, 2014; Gimeno et al., 2015; Drumond et al., 2014; Ciric et al., 2018; Gimeno et al., 2020), low-level jets (Algarra et al., 2019a,b), and the origin of atmospheric humidity for atmospheric rivers (Algarra et al., 2020; Ramos et al., 2016). The full list of studies of the EPysLab group that have used the global outputs of FLEXPART v9.0 can be found at <https://ephyslab.uvigo.es/moisturetransport/index.php/Publications>. The model source code is available at <https://flexpart.eu/>. Recently, Pisso et al. (2019) launched FLEXPART v10.4, which is forced with the ECMWF fifth-generation reanalysis product (ERA-5; Hersbach et al., 2020); however, it requires a long computing time to perform global simulations for the entire study period. Nonetheless, the EPHysLab research group is now performing FLEXPART v10.4 simulations forced with the ERA-5 reanalysis.

For this thesis, FLEXPART v9.0 was fed by the ECMWF ERA-Interim reanalysis; however, it can also be forced with data from the US National Centers of Environmental Prediction Global Forecast

System. For the global simulations performed in EPhysLab, the atmosphere was homogeneously divided into approximately 2 million air parcels with a constant mass. The model requires three-dimensional wind temperature and specific humidity fields as inputs to the ECMWF vertical hybrid coordinate system. It also requires several two-dimensional variables, such as surface pressure, total cloud cover, 10 m horizontal wind components, 2 m temperature, and dew point temperature. The model outputs were recorded at 6-hour intervals containing the information of each parcel, that is, position in latitude and longitude, height, topography, and specific humidity.

3.2.5 Lagrangian moisture source diagnostic method

According to the Lagrangian approach, the atmosphere is divided into a finite number of homogeneously distributed parcels, for which the position and properties are known at every time step (Stohl and James, 2004, 2005). Therefore, an air parcel was advected by the 3D wind field according to the trajectory equation (Eq. 3.9).

$$\frac{\partial \vec{x}}{\partial t} = \vec{v}[\vec{x}(t)] \quad (3.9)$$

where \vec{x} is the parcel's position and $\vec{v}[\vec{x}(t)]$ is the wind velocity interpolated in space and time from the analysis grid to $\vec{x}(t)$. By interpolating the specific humidity (q) to $\vec{x}(t)$ and assuming that the specific humidity changes only occur by evaporation (e) or precipitation (p) along the parcel trajectory, the net rate of change of the water vapour content of a parcel is given by

$$e - p = m \frac{dq}{dt} \quad (3.10)$$

where m is the mass and $(e - p)$ is the freshwater flux of the parcel. In this approach, the presence of liquid water and ice in the atmosphere was neglected.

By applying Eq. 3.10, the precipitant parcels over a target region were followed every 6 hours backward in time. The parcel trajectories were extracted from the global outputs of the FLEXPART model, the target region was defined at each TC position as the area enclosed by the outer radius of the TC, and the precipitant parcels were those in which the specific humidity decreased more than 0.1 g/kg in the 6 hours before until the arrival at the area of interest following Läderach and Sodemann (2016). In addition, every parcel was backtracked for up to 10 days (240 hours), which is considered the mean residence time of water vapour in the atmosphere (Numaguti, 1999; VanDerEnt and Tuinenburg, 2017; Gimeno et al., 2021).

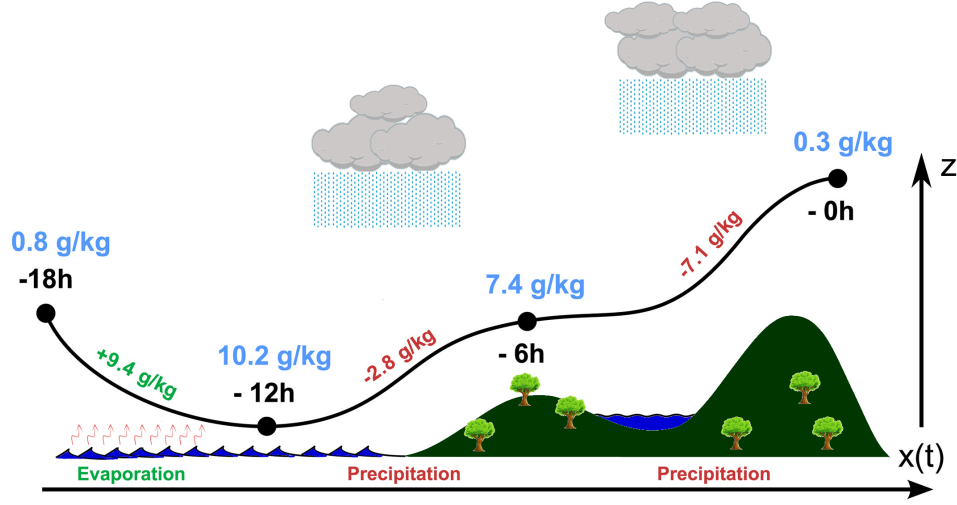


Figure 3.1: Schematic representation of an air parcel trajectory. Along the trajectory, the parcel can gain or lose moisture by evaporation or precipitation, respectively. Figure adapted from Läderach and Sodemann (2016).

The Stohl and James (2004, 2005) approach has been widely used to identify moisture sources and investigate the source–sink relationship (for example, Gimeno et al., 2016; Algarra et al., 2019a; Nieto et al., 2019; Gimeno et al., 2020; Vázquez et al., 2020; Sorí et al., 2021). Cloux et al. (2021) and Keune et al. (2022) noted that this approach could overestimate the moisture sources in some cases because the moisture gained by a parcel over an specific area could precipitate before it reaches the target region (Figure 3.1). To avoid this issue, Sodemann et al. (2008) quantified the relative contribution of the sources by proportionally discounting the precipitation along the route to all previous moisture uptakes, and this approximation was used in Cloux et al. (2021) and Keune et al. (2022).

As previously noted, an air parcel can precipitate before reaching the target region, as illustrated in the schematic trajectory of the parcel shown in Figure 3.1. Then, starting at the end of the trajectory (240-hour before) and assuming that evaporation or precipitation dominates in a particular 6-hour interval following Sodemann et al. (2008), the adjusted moisture of the parcel ($\Delta q'_j$) at time t_j after discounting the precipitation in route (Δq_i) at time t_i is given by

$$\Delta q'_j = \Delta q_j + \Delta q_i \frac{\Delta q_j}{\sum_{k=i}^j \Delta q_k} \quad (3.11)$$

where i denotes the parcel position at time t_i and j represents the parcel position at time t_{i-6} , t_{i-12} , ..., t_{i-240} . By amassing the final moisture changes ($\Delta q'_j$) of all the parcels over area A , the total moisture uptake (MU) was estimated as follows:

$$MU = \frac{m \sum_{k=1}^N \Delta q'_k}{A} \quad (3.12)$$

where N denotes the number of parcels residing over A .

The moisture source diagnostic method proposed by Sodemann et al. (2008) also provides the fractional contribution (fc) of each evaporation location along the parcel trajectory to the final precipitation over the target region, which can be estimated by applying Eq. 3.13:

$$fc_i = \frac{\Delta q_i}{Q} \quad (3.13)$$

where i denotes the parcel position at time t_i and Q is the total specific humidity of the parcel that precipitates over the target region. By averaging all the fractional contributions over area A , the moisture source contributions (SC) was computed.

$$SC = \frac{\sum_{k=1}^M fc_k}{A} \quad (3.14)$$

where M denotes the number of fractional contributions over A .

3.2.6 Lagrangian estimation of the mean water vapour residence time

The time spent by water vapour in the atmosphere from evaporation to precipitation is called the backward transit time (BTT) or water vapour residence time (WVRT) (Gimeno et al., 2021). Several metrics have been used to estimate the WVRT, such as turnover time, which is defined as the ratio of the global average of water vapour and precipitation; depletion time constant, which is defined as the local ratio of water vapour and precipitation; and metrics that require Eulerian, Lagrangian, or tracer moisture tracking models (Gimeno et al., 2021). Based on all metrics, the mean WVRT (MWVRT) globally ranged from 4-5 to 8-10 days (Trenberth, 1998; Numaguti, 1999; Läderach and Sodemann, 2016; VanDerEnt and Tuinenburg, 2017; Sodemann, 2020). The review paper by Gimeno et al. (2021) provides a description of all the methods for estimating the MWVRT.

In this thesis, the MWVRT for precipitation associated with TC was estimated following the Lagrangian approach proposed by Läderach and Sodemann (2016). That is, the WVRT for each particle was computed by weighting the time between evaporation and final precipitation according to Eq. 3.15.

$$WVRT = \sum_{i=1}^T fc_i \cdot t_i \quad (3.15)$$

where t ranges from $t = 6$ to $t = 240$ at 6-hour intervals and fc_i is the fractional contribution at time t_i (Eq. 3.13). Then, by averaging the WVRT of all parcels, we estimated the MWVRT for precipitation at each TC location.

3.2.7 Determination of the mean position of the moisture sources

The annual mean position of the moisture sources for each TC development stage in each cluster was determined by computing the weighted centroids (lat_c and lon_c), as described in Nishikawa (2020):

$$(lat_c, lon_c) = \frac{\sum_{k=1}^N w_k (lat_k, lon_k)}{\sum_{k=1}^N w_k} \quad (3.16)$$

where N is the number of grid points where moisture uptake (MU) occurs and w is the weighted vector.

$$w = \frac{MU}{max\{MU\}} \quad (3.17)$$

Set of publications

4.1 List of publications

This chapter includes a total of **7** publications, with two addressing the global climatology of TC size based on radial wind profiles; three addressing the identification of moisture sources for the precipitation associated with TCs during their three well-known stages: genesis, lifetime maximum intensity, and dissipation; one investigating the MWVRT for the precipitation produced by TCs; and one studying the moisture sources along the trajectory of six particular TCs formed in the NATL basin. Table 4.1 provides a summary of each paper and the title, authors, year of publication and journal where the articles have been published. The articles were not listed in the order of publication, but in a coherent sequence. Moreover, the supplementary material linked to each article is presented in Appendix A.

The first article is titled “Comparative climatology of outer tropical cyclone size using radial wind profiles” by **A. Pérez-Alarcón**, R. Sorí, J.C. Fernández-Alvarez, R. Nieto, R. and L. Gimeno, published in 2021 in *Weather and Climate Extremes* (Pérez-Alarcón et al., 2021c). This study performed a global climatology of TC size based on five radial wind profiles to identify the radial wind profile that better fits the TC radial structure using observations from the best track archives. From the analysis, the radial wind profile by Willoughby et al. (2006) was the most skilful for reproducing the tangential velocity of TCs and, therefore, for estimating the outer radius.

Based on the results of this first article, a dataset of the TC outer radius was generated, which was published in a second article titled “Dataset of outer tropical cyclone size from a radial wind profile” by **A. Pérez-Alarcón**, R. Sorí, J.C. Fernández-Alvarez, R. Nieto, R. and L. Gimeno, and published in 2022 in *Data in Brief* (Pérez-Alarcón et al., 2022d). Statistical analysis of this database revealed that the largest TCs occurred in the NATL basin and the smallest occurred in the NIO.

Furthermore, this dataset was used to determine the target region corresponding to each TC for a Lagrangian analysis for moisture source determination.

For each oceanic basin, by applying the K-mean cluster analysis technique (as explained in Section 3.2.2), the areas for genesis, lifetime maximum intensity (LMI), and dissipation of TCs were identified. The third article that forms part of this thesis is titled “Where does the moisture for North Atlantic tropical cyclones come from?”, by **A. Pérez-Alarcón**, R. Sorí, J.C. Fernández-Alvarez, R. Nieto, R. and L. Gimeno; published in 2022 in *Journal of Hydrometeorology* (Pérez-Alarcón et al., 2022e). In this study, by applying the Lagrangian moisture source diagnostic method, the main moisture sources for the precipitation of TC formed over the NATL basin during the genesis, LMI, and dissipation stages were identified. Although previous studies have performed several analyses of the water budget of specific TCs, this study is the first to investigate the climatological moisture sources for TC precipitation. Additionally, this study determined the main moisture drivers of TCs during each stage.

The fourth article in this thesis is titled “Moisture source identification for precipitation associated with tropical cyclone development over the Indian Ocean: a Lagrangian approach”, by **A. Pérez-Alarcón**, J.C. Fernández-Alvarez, R. Sorí, R. Nieto, R. and L. Gimeno; published in 2022 in *Climate Dynamics* (Pérez-Alarcón et al., 2022c). By applying a methodology similar to that in the third paper, this study focuses on determining the origin of moisture that precipitated over the location of TCs formed over the NIO and SIO basins. In addition, the relationship between moisture sources and the TC precipitation during monsoon seasons is presented. This study revealed that the moisture sources for TCs that formed over the NIO were mainly modulated by the monsoon seasons than in the SIO basin.

The fifth article that forms this thesis is focused on the moisture sources for the TC precipitation over the Pacific Ocean in the NEPAC, WNP and SPO basins and follows the same methodology as in the previous papers for other basins. It is titled “Moisture source for the precipitation of tropical cyclones over the Pacific Ocean through a Lagrangian approach”, by **A. Pérez-Alarcón**, R. Sorí, J.C. Fernández-Alvarez, R. Nieto, R. and L. Gimeno; published in 2023 in *Journal of Climate* (Pérez-Alarcón et al., 2023). This study also presents how large-scale and local conditions that favoured cyclogenesis modulate moisture transport during TC genesis. Likewise, the role played by seasonal variations in the subtropical pressure highs in the seasonal variation of moisture contributions is also discussed.

The sixth paper provides a climatological overview of the mean water vapour residence time (MWVRT) for precipitation associated with TCs in each basin. It is titled “Estimation of mean water vapour residence time during tropical cyclones using a Lagrangian approach” by **A. Pérez-Alarcón**, P. Coll-Hidalgo, J.C. Fernández-Alvarez, R. Nieto and L. Gimeno; published in 2022 in *Tropical Cyclone Research and Review* (Pérez-Alarcón et al., 2022a). This study examined the interbasin differences in the MWVRT, its annual trend, spatial distribution, and changes 24 hours before and after TCs made landfall.

The seventh article titled “Moisture sources for precipitation associated with major hurricanes during 2017 in the North Atlantic basin”, by **A. Pérez-Alarcón**, P. Coll-Hidalgo, J.C. Fernández-Alvarez, R. Sorí, R. Nieto, R. and L. Gimeno, was published in 2022 in *Journal of Geophysical*

Research: Atmospheres (Pérez-Alarcón et al., 2022b). The major hurricanes that formed in the NATL basin in 2017 were particularly interesting. Harvey caused extreme rainfall amounts in metropolitan areas of Texas (Emanuel, 2017), Irma was the strongest and costliest hurricane on record in the NATL basin (Cangialosi et al., 2021), Ophelia formed and intensified in the central North Atlantic Ocean under relatively cold SSTs (Stewart, 2018), and Jose, Maria, and Lee reached Category 3 on the Saffir-Simpson wind scale. This study examines the SST anomalies that favoured the development of these MHs and precipitation along their trajectories. In addition, this study confirms the ability of the Lagrangian methodology to estimate the precipitation associated with individual TCs because it fits very well with the rainfall measured from the Global Precipitation Measurement mission (Huffman et al., 2019).

Table 4.1: List of publications.

Title	Authors	Year	Journal
Comparative climatology of outer tropical cyclone size using radial wind profiles	Pérez-Alarcón, A.; Sorí, R.;; Fernández-Alvarez, J.C. Nieto, R.; Gimeno, L.	2021	Weather and Climate Extremes
Dataset of outer tropical cyclone size from a radial wind profile	Pérez-Alarcón, A.; Sorí, R.;; Fernández-Alvarez, J.C.;; Nieto, R.; Gimeno, L.	2022	Data in Brief
Where does the moisture for North Atlantic tropical cyclones come from?	Pérez-Alarcón, A.; Sorí, R.;; Fernández-Alvarez, J.C.;; Nieto, R.; Gimeno, L.	2022	Journal of Hydrometeorology
Moisture source identification for precipitation associated with tropical cyclone development over the Indian Ocean: a Lagrangian approach	Pérez-Alarcón, A.; Fernández-Alvarez, J.C.;; Sorí, R.;; Nieto, R.; Gimeno, L.	2022	Climate Dynamics
Moisture source for the precipitation of tropical cyclones over the Pacific Ocean through a Lagrangian approach	Pérez-Alarcón, A.; Sorí, R.;; Fernández-Alvarez, J.C.;; Nieto, R.; Gimeno, L.	2023	Journal of Climate
Estimation of mean water vapour residence time during tropical cyclones	Pérez-Alarcón, A.; Coll-Hidalgo, P.;; Fernández-Alvarez, J.C.;;	2022	Tropical Cyclone Research

using a Lagrangian approach	Nieto, R.; Gimeno, L.	and Review
Moisture sources for precipitation associated with major hurricanes during 2017 in the North Atlantic basin	Pérez-Alarcón, A. ; Coll-Hidalgo, P.; Fernández-Alvarez, J.C.; Sorí, R.; Nieto, R.; Gimeno, L.	2022 Journal of Geophysical Research: Atmospheres

4.2 Comparative climatology of outer tropical cyclone size using radial wind profiles

Pérez-Alarcón, A., Sorí, R., Fernández-Alvarez, J.C., Nieto, R., Gimeno, L., 2021. Comparative climatology of outer tropical cyclone size using radial wind profiles. *Weather and Climate Extremes* 33, 100366. doi:10.1016/j.wace.2021.100366.

Table 4.2: Summary of the impact and quality of the journal where the first paper that conformed to this thesis was published. The data correspond to the year 2021 (last year available at the date of preparation of this document) in the Web of Science (JCR). **IF:** Impact Factor

Journal	Description	Journal Metrics
Weather and Climate Extremes	It is published by Elsevier and provides publications on different aspects of research in weather and climate extremes.	IF: 7.761, 5-year IF: 8.757 Ranking: 10 out of 108 (Q1) in Meteorology & Atmospheric Sciences



Contents lists available at ScienceDirect

Weather and Climate Extremes

journal homepage: www.elsevier.com/locate/wace

Comparative climatology of outer tropical cyclone size using radial wind profiles[☆]

Albenis Pérez-Alarcón^{a,b,*}, Rogert Sorí^{a,c}, José C. Fernández-Alvarez^{a,b}, Raquel Nieto^a, Luis Gimeno^a

^a Centro de Investigación Mariña, Universidade de Vigo, Environmental Physics Laboratory (EPhysLab), Campus As Lagoas s/n, Ourense, 32004, Spain

^b Departamento de Meteorología, Instituto Superior de Tecnologías y Ciencias Aplicadas, Universidad de La Habana, 10400 La Habana, Cuba

^c Instituto Dom Luiz, Faculdade de Ciências da Universidade de Lisboa, 1749-016 Campo Grande, Portugal

ARTICLE INFO

Keywords:

Tropical cyclone size
Radial wind profiles
Tropical cyclones database
Tropical cyclones climatology

ABSTRACT

In this study was performed a comparative climatology of outer tropical cyclone (TCs) size using radial wind profiles. A wind speed of 2 ms^{-1} ($\sim 4 \text{ kt}$) was taken as the threshold to define the TC size. The method proposed by Willoughby et al. (2006) (W06) to determine the wind profile showed the least variance and the smallest coefficient of variation of all profiles. W06 correctly described the radial wind structure of storms such as Hurricane Irma (2017) and Cyclone Giri (2010), compared with the European Centre for Medium-Range Weather Forecasts ERA-5 reanalysis data. Thus, W06 was used to develop the climatological TC size (TCSize) database. It was found that the tropical cyclones are largest when the maximum wind speed ranges between 20 and 40 ms^{-1} and they most frequently reach a size between 700 and 800 km . The TCs exhibit their maximum size when they are in extratropical latitudes, while the smallest are observed in the low latitudes of both hemispheres. The global mean size is 748.7 km with a 95% confidence interval of $[748.2, 749.2] \text{ km}$. Median storm size is largest in the North Atlantic basin and smallest in the North Indian Ocean. The method proposed here is designed to be an objective metric that can be quickly applied to any TC when its position, maximum wind speed, and minimum central pressure are known. As a result, a TCSize database was created for all ocean basins, which could be useful for many applications, including different risk analyses.

1. Introduction

The need for a better understanding of the structure of tropical cyclones (TCs) to improve prediction, dynamics and climatological studies makes the determination of the size of TCs increasingly important. The parameters referring to the TC structure (maximum wind speed, minimum central pressure and size metrics) should be estimated as realistic as possible to guarantee forecasts of acceptable quality (Weber et al., 2014). Therefore, the size of a TC greatly affects the way that forecasters issue warnings and alerts to the public. If the estimated affected area by the TC is unreliable due to the size of the TC, the forecasts may potentially be incomplete, and livelihoods can therefore be impacted without sufficient warning (McKenzie, 2017). However, the

time constraints under which forecasters operate and the subjectivity and complexity of the methods make it challenging to issue accurate storm size warnings.

Several metrics have been defined to estimate the size of TCs. One of the most recognized is the R_{34} radius, defined as the radial distance from the centre to the four quadrants (NE: northeast, SE: southeast, SW: southwest and NW: northwest), where sustained winds of 34 kt (approximately 17 ms^{-1}) are observed on the surface (Sampson and Knaff, 2015). This wind radius is taken as the extent of tropical storm force winds. The R_{50} and R_{64} radii are also commonly used. These are defined in a similar way to R_{34} , considering the radial distance in direction of the four quadrants, where the sustained wind

[☆] This work is supported by the LAGRIMA project (grant no. RTI2018-095772-B-I00) funded by the Ministerio de Ciencia, Innovación y Universidades, Spain. Partial support was also obtained from from the Xunta de Galicia under the Project ED431C 2021/44 (Programa de Consolidación e Estructuración de Unidades de Investigación Competitivas (Grupos de Referencia Competitiva) and Consellería de Cultura, Educación e Universidade).

* Corresponding author at: Centro de Investigación Mariña, Universidade de Vigo, Environmental Physics Laboratory (EPhysLab), Campus As Lagoas s/n, Ourense, 32004, Spain.

E-mail addresses: albenis.perez.alarcon@uvigo.es (A. Pérez-Alarcón), rogert.sori@uvigo.es (R. Sorí), jose.carlos.fernandez.alvarez@uvigo.es (J.C. Fernández-Alvarez), rnieto@uvigo.es (R. Nieto), lgimeno@uvigo.es (L. Gimeno).

URLs: <http://ephyslab.uvigo.es>, <http://www.instec.uvigo.es> (A. Pérez-Alarcón), <http://ephyslab.uvigo.es> (R. Sorí), <http://ephyslab.uvigo.es>, <http://www.instec.uvigo.es> (J.C. Fernández-Alvarez), <http://ephyslab.uvigo.es> (R. Nieto), <http://ephyslab.uvigo.es> (L. Gimeno).

<https://doi.org/10.1016/j.wace.2021.100366>

Received 9 January 2021; Received in revised form 10 July 2021; Accepted 5 August 2021

Available online 11 August 2021

2212-0947/© 2021 The Author(s).

Published by Elsevier B.V. This is an open access article under the CC BY-NC-ND license

(<http://creativecommons.org/licenses/by-nc-nd/4.0/>).

on surface reaches speeds of 26 ms^{-1} ($\sim 50 \text{ kt}$) and 33 ms^{-1} ($\sim 64 \text{ kt}$) respectively. However, the R_{64} wind radius is reserved for TCs of hurricane strength. The combination of R_{34} , R_{50} , and R_{64} are known as the TC critical wind radii and are used to approximate the TC wind field structure (McKenzie, 2017). It is remarkable that, starting in 2004, the National Hurricane Center (NHC) began to provide poststorm analyses of the R_{34} , R_{50} , and R_{64} wind radii (Carrasco et al., 2014).

The radius of outermost closed isobar (ROCI) is another metric used to estimate the size of TCs. The method for calculating ROCI was proposed by Merrill (1984) and since then, many researchers have used ROCI as the first metric of TC size. The ROCI values have also been recorded by many agencies, such as the JTWC (Joint Typhoon Warning Center) (Chu et al., 2002), while the NHC records ROCI in the TCvitals (Tropical Cyclone Vitals Database) database. However, the ROCI has a number of shortcomings that make difficult climatological studies and interbasin comparisons. Generally, it is subjective estimated from the available data, and it is method dependent (Knaff et al., 2014). Moreover, the specific methods used to estimate the ROCI have changed throughout the years, and such changes are not well documented. According to Knaff et al. (2014), the ROCI also depends on the pressure field and the environment where the TC is developed. For example, the ROCI would be infinity for a vortex with no ambient flow. Additionally, it is worth noting that the ROCI is only operationally estimated and not quality controlled after the TC season.

Climatological studies and model simulations (e.g. Cocks and Gray, 2002; Kimball and Mulekar, 2004; Willoughby and Rahan, 2004; Knaff and Zehr, 2007) have motivated researchers to understand important details linked to TC size, such as seasonal and large-scale atmospheric preferences for various-sized storms. Surface wind observations from scatterometers available on several satellites have led many authors to analyse the wind structure of TCs (Jaiswal and Kishtawal, 2019). Chavas and Emanuel (2010) employed version 3 of the Quick Scatterometer (QuikSCAT) database (1999–2008) to analyse the global climatic features of TC size, defined by these authors as the radius where the winds disappear. Knaff et al. (2014) estimated the radius of 2.5 ms^{-1} ($\sim 5 \text{ kt}$) from a combination of satellite infrared data and a climatological linear model of the outer wind field. More recently, Chavas et al. (2016) created a new dataset of the radius of 12 ms^{-1} winds based on a recently updated version of the QuikSCAT ocean wind vector database. These authors applied an improved analytical outer wind model (Emanuel, 2004) to estimate the outer radius of vanishing wind. This model has been shown to fit very well with observations (Chavas et al., 2015). On the other hand, Jaiswal and Kishtawal (2019) used the wind data observed by a scatterometer onboard Oceansat-2 satellite (OSCAT) to estimate the size of the cyclones formed from 2010–2013 in the North Indian Ocean (NIO).

All of the above mentioned methods provide an estimate of the size of the TC; however, they depend on observations from satellites, which hinders the analysis of TCs formed before the start of these measurements. Unfortunately, the size of a TC is very difficult to estimate directly from observations or numerical models due to the interaction between the TC circulation and the variability of background flow over large radii (McKenzie, 2017). Additionally, neglecting the shortcomings of the ROCI, the data records of R_{34} and ROCI are too short to create a TC size climatology. For this reason, in this study, we developed a database of the size of TCs in every cyclogenetic basin of the planet, applying an uniform method since records began. This database was developed based on comparative climatology of the size of TCs estimated from radial wind profiles that are presented in Section 2.

2. TC radial wind profiles

Several radial wind profiles have been developed to estimate the TC wind structure. Some of these profiles are relatively simple requiring two to four parameters (Depperman, 1947; Jelesnianski, 1965; Holland, 1980; DeMaria, 1987; Frisius and Scgöemann, 2013). Recent models

appear to be more complex but more accurately represent the structure of a TC (Emanuel, 2004; Willoughby et al., 2006; Chavas et al., 2015; Olfateh et al., 2017). Here, five radial wind profiles (Holland, 1980; DeMaria, 1987; Willoughby et al., 2006; Emanuel and Rotunno, 2011; Frisius and Scgöemann, 2013) are evaluated to calculate the TC size. A brief description of each profile is provided below.

Holland (1980) (hereafter H80) developed a universal model to determine the wind profiles for all TCs, given by:

$$v = V_{max} \left[\left(\frac{r_m}{r} \right)^b e^{1 - \left(\frac{r}{r_m} \right)^{-b}} \right]^{0.5} \quad (1)$$

where v is the wind speed at a distance r from the centre, V_{max} is the maximum wind speed, r_m is the radius of maximum winds and b is a parameter ranging between 1 and 2.5. For this study it is assumed $b = 2$ following Kowaleski and Evans (2016). According to Kepert (2010), the H80 radial wind profile continues to be one of the most widely used by forecasters and researchers due to its simplicity and somewhat accurate representation of the wind structure of a TC.

DeMaria (1987) (hereafter D87) developed the following radial wind profile:

$$v = V_{max} \left(\frac{r}{r_m} \right) e^{\left(\frac{\frac{1}{c} - \frac{1}{c} \left(\frac{r}{r_m} \right)^c}{d} \right)} \quad (2)$$

where $c = 0.63$ and $d = 1$ according to Kowaleski and Evans (2016). Willoughby et al. (2006) (hereafter W06) demonstrated that on the eyewall, the wind increases in proportion to the decrease the radius until the radius of maximum winds, while in the outer region, the wind decreases exponentially with the distance to the centre of the storm. The tangential wind profile is given by:

$$v = \begin{cases} V_{max} \left(\frac{r}{r_m} \right)^n & r \leq r_1 \\ V_i(1-w) + V_0 w & r_1 \leq r \leq r_2 \\ V_{max} \left[(1-A)e^{-\frac{r-r_m}{X_1}} + Ae^{-\frac{r-r_m}{X_2}} \right] & r > r_2 \end{cases} \quad (3)$$

where n , A , X_1 , and X_2 are parameters that are associated with the TC intensity, V_i and V_0 are the tangential wind speeds at r_1 and r_2 radius, respectively, and w is a weight function (see Willoughby et al., 2006).

In Emanuel and Rotunno (2011) (hereafter E11), the parametric wind profile is given by:

$$v = \frac{2r(r_m V_{max} + 0.5 f r_m^2)}{r_m^2 + r^2} - \frac{f r}{2} \quad (4)$$

where f is the Coriolis parameter. This profile is most applicable to the region inside of approximately $2.5 r_m$ (Morris and Ruf, 2017). Moreover, Chavas et al. (2015) showed that the outer wind radii tend to be underestimated by this profile. Despite this fact, E11 was tested in this research.

Frisius and Scgöemann (2013) (hereafter F13) developed another radial wind profile:

$$v = V_{max} \frac{r_m}{r} \cdot \left[\frac{2 \left(\frac{r_m}{r} \right)^2}{2 - \left(\frac{C_H}{C_d} \right) \left[1 - \left(\frac{r}{r_m} \right)^2 \right]} \right]^{\frac{1}{2} - \frac{C_H}{C_d}} - \frac{f r}{2} \quad (5)$$

where C_d is the surface drag coefficient and C_H is the surface transfer coefficient for enthalpy. The separation between the inner and outer region is not necessary because the solution satisfies the entire vortex, following F13 $C_H/C_d = 1$.

In all cases, the Coriolis parameter is determined by the storm centre location coordinates. These radial wind profiles all depend on parameters such as the position and maximum wind speed of TCs, which generally are included in the best-track records of many agencies, such as the NHC and JTWC, but also depend on the radius of maximum winds. For North Atlantic (NATL) and Central & East Pacific (NEPAC)

basins, [Vickery and Wadhera \(2008\)](#) proposed an empirical formula for r_m as a function of the minimum central pressure (P_c); however, there is a high percentage of missing P_c values in the NATL best-track records caused by a lack of measurements before the 1950s ([Tan and Fang, 2018](#)). For that, r_m will be calculated following the expression proposed by [Willoughby et al. \(2006\)](#) in these basins :

$$r_m = 46.6e^{(-0.015V_{max}+0.0169\varphi)} \quad (6)$$

where φ is the latitude. Additionally, for the North Western Pacific (WNP, Eq. (7)), NIO (Eq. (8)), South Indian Ocean (SIO, Eq. (9)) and South Pacific Ocean (SPO, Eq. (10)) the empirical functions of r_m by [Tan and Fang \(2018\)](#) are used.

$$r_m = -18.29 \cdot \ln(1010 - P_c) + 113.23 \quad (7)$$

$$r_m = -26.73 \cdot \ln(1013.25 - P_c) + 142.41 \quad (8)$$

$$r_m = -18.82 \cdot \ln(1010 - P_c) + 111.95 \quad (9)$$

$$r_m = -22.31 \cdot \ln(1010 - P_c) + 126.50 \quad (10)$$

These expressions for the r_m are also a function of P_c . Where there are missing values in the best-track database, Eq. (6) will be used.

3. Data and methodology

3.1. Data availability

To calculate the radial wind profiles of the TCs in the NATL and NEPAC basins, the NHC HURDAT2 (<https://www.nhc.noaa.gov/data/#hurdat>) database ([Landsea and Franklin, 2013](#)) was used, while for the systems formed on the WNP, NIO, SIO and SPO the best-track of the JTWC (<https://www.metoc.navy.mil/jtwc/jtwc.html?best-tracks>) was used. These datasets have a text format which contains the location, maximum winds, and minimum central pressure of all known tropical and subtropical cyclones at every six hours. The NATL best-track contains information from 1851 to 2020, the NEPAC one from 1949 to 2020 and the rest of the basins from 1945 to 2019. Furthermore, to verify the maximum wind radius estimations made in this study using the Eqs. (6) to (10), we use the maximum wind radius operationally estimated (hereafter R_m) by the NHC for the NATL and NEPAC basins from the TCvitals database (free available at <https://ftp.nhc.noaa.gov/atcf/archive/>), and by the JTWC for the remaining basins. However, like the ROCI, R_m is not poststorm quality controlled.

In addition, the European Centre for Medium-Range Weather Forecasts (ECMWF) ERA-5 reanalysis data ([Hersbach et al., 2020](#)) were used for the structure of TC case studies. This reanalysis covers the period from 1979 to the present and contains data at six-hourly intervals with a spatial resolution of $0.25^\circ \times 0.25^\circ$ in latitude and longitude. This dataset is freely available at <https://cds.climate.copernicus.eu/cdsapp#!/home>. The TC structure observed in the reanalysis data was compared with TC size calculated from each radial wind profile. Moreover, the mean TC size in each basin obtained by [Chavas et al. \(2016\)](#) (hereafter C16), was used as a baseline.

To analyse the radial profile of the rain rate of TCs, the GPM (Global Precipitation Measurement) database ([Huffman et al., 2019](#)) was used. In this dataset, the precipitation is estimated every 30 min from the various precipitation—relevant satellite passive microwave sensors comprising the GPM constellation, computed using the Goddard Profiling Algorithm ([Kummerow et al., 2015](#); [Randel et al., 2020](#)), then gridded and intercalibrated to the GPM Combined Ku Radar-Radiometer Algorithm (CORRA, [Greco et al., 2016](#)) product, and merged into half-hourly $0.1^\circ \times 0.1^\circ$ (approximately 10×10 km) fields. The CORRA is adjusted to the monthly Global Precipitation Climatology Project ([Adler et al., 2003, 2018](#)) Satellite-Gauge ([Behrangi et al., 2014](#)) product over high-latitude ocean and tropical land to correct known biases. This database is publicly available from June 2000 to present at <https://gpm.nasa.gov/data-access/downloads/gpm>.

3.2. Determination of TC size

Similar to [Knaff et al. \(2014\)](#), the radial distance from the centre to where the wind speed of each radial wind profile is equal or less than 2 ms^{-1} ($\sim 4 \text{ kt}$) was selected as the metric of TC size. In addition, the ability of each profile to estimate the critical wind radii of R_{34} , R_{50} , and R_{64} was evaluated by comparison with those recorded in the best-track database. A similar procedure was performed to assess the ability to estimate the radius of maximum winds. To understand the relationship of TC size and intensity (the TC intensity is defined as the maximum wind speed in each record of the best-track database), Spearman's correlation between these TC metrics as well as the correlation between TC size and latitude were calculated. In order to verify the ability to estimate the size of TCs, twelve TCs evenly distributed in each basin were used, as shown in [Fig. 1](#). These systems were chosen because of the intensity they reached, the socioeconomic damage caused, and the loss of human lives.

For example, Hurricane Irma, which formed in the NATL in 2017, damaged more than 150,000 homes and completely destroyed nearly 15,000 homes in Cuba. Across the island, losses from damage caused by Irma were estimated to be close to 200 million USD, which was the greatest economic loss in Cuba in the 55-year period preceding the event ([Cangialosi et al., 2018](#)). Hurricane Harvey (developed in the NATL in 2017) was the most significant tropical cyclone precipitation event in United States history, both in range and in maximum rainfall amount. Harvey's highest total storm rainfall was reported to be 1538.72 mm (60.58 inches) in Nederland, near Texas. Although maximum rainfall amounts were exceptional in Texas, the observed extent of heavy rainfall was exceptionally large ([Blake and Zelinsky, 2018](#)).

Hurricane Patricia was a historic tropical cyclone that broke many records, such as the intensification rate, peak intensity, and overwater weakening rate, during a life cycle of just four days in late October 2015 in the NEPAC basin ([Rogers et al., 2017](#)). On 8 November 2013, cyclone Haiyan over the WNP basin made landfall in the islands of the central Philippines. It is considered one of the most powerful typhoons to make landfall. By crossing the Philippines archipelago, it caused extreme loss of life and widespread property damage due to strong winds, heavy rain, and storm surges ([Lagmay et al., 2015](#)). Cyclone Chapala (from 28 October to 4 November 2015) is the second strongest cyclone event since 1945 (the strongest being Cyclone Gonu in 2007) in the Arabian Sea (NIO basin) ([Sarker, 2018](#)). Cyclone Winston caused heavy rains in Fiji (SPO basin), with the cumulative rainfall on 20 and 21 February 2016 reaching 479 mm in Nadarivatu, compared to the long-term average rainfall for February based on the period 1971–2000, which is less than 300 mm. This intense precipitation over a short duration generated flooding in various locations in Fiji ([Jacot, 2020](#)).

To analyse the geographical distribution of the size of TCs, a segmentation of the dataset was performed considering the maximum wind speed and the position of the TC in each best-track record. Thus, the dataset was subdivided into Tropical depression (TD, $V_{max} < 17 \text{ ms}^{-1}$), Tropical storm (TS, $17 \leq V_{max} \leq 33 \text{ ms}^{-1}$), Hurricane (H, $33 < V_{max} < 49 \text{ ms}^{-1}$), Major Hurricane (MH, $V_{max} \geq 49 \text{ ms}^{-1}$), TC in a tropical zone (Trop, $|\text{latitude}| \leq 30^\circ$), TC in an extratropical zone (ExTrop, $|\text{latitude}| > 30^\circ$), and Hurricane in tropical areas (HTrop, $|\text{latitude}| \leq 30^\circ$ and $V_{max} \geq 33 \text{ ms}^{-1}$). The last classification is similar to a classification made by C16, making them statistically comparable. Moreover, in this study, the TC extratropical stage records were neglected.

Additionally, with the goal to evaluate the ability of each radial wind profile to estimate the TC outer radius, the TC size was also estimated using the ERA-5 reanalysis by averaging the radial distance to the TC centre of grid points in all directions where the wind speed was equal to or less than 2 m/s .

Statistical analysis was performed to develop a TC size database in each basin. The data acquired from the methods already described were compiled to produce the new database of TC size. The interpercentile range used in this research denotes the 25th–95th percentile.

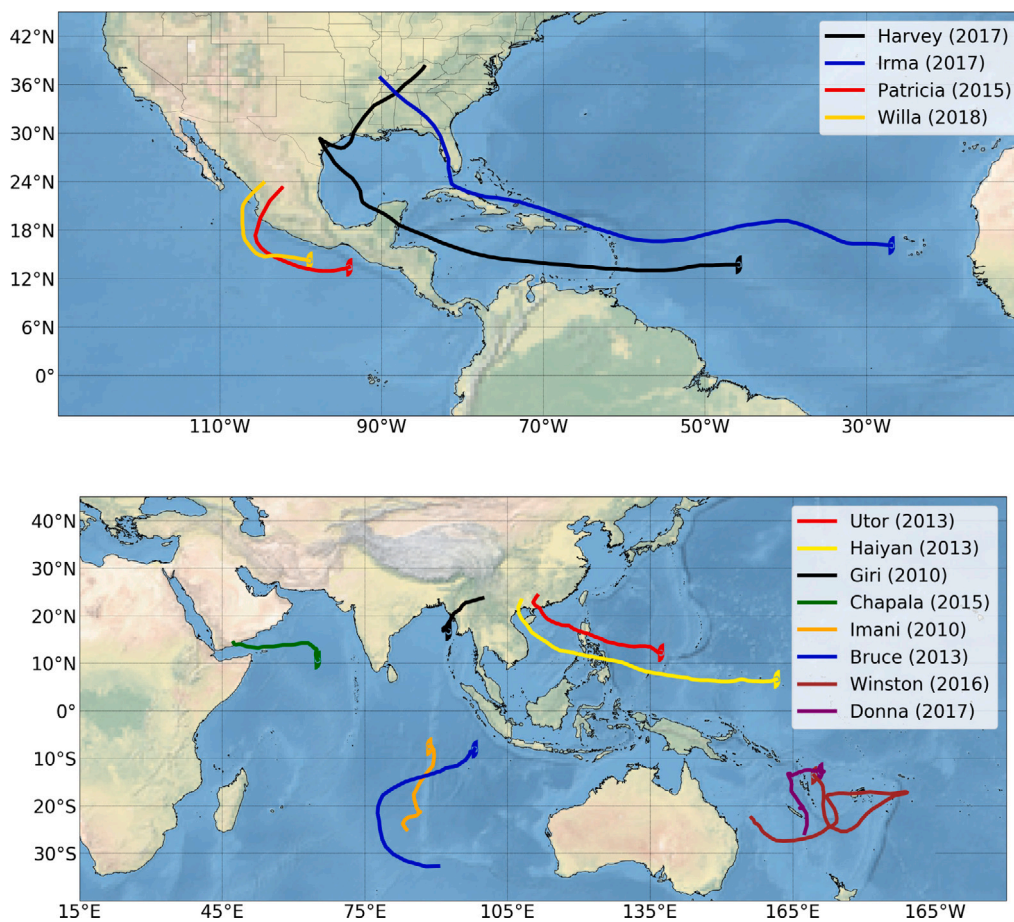


Fig. 1. Trajectories of all TCs taken as case studies: NATL y NEPAC (top), WNP, NIO, SIO, and SPO (bottom). The marker represents the genesis point.

4. Results

4.1. North Atlantic basin

According to Hart and Evans (2001) and Chavas et al. (2016), in the NATL the smallest storms are developed at low latitudes in the central and eastern Atlantic. Additionally, a mix of sizes are observed at intermediate latitudes while the largest TCs are observed at high latitudes. In this study, reports every 6 h for all TCs formed in the NATL basin from 1851 to 2020 were analysed.

The estimated r_m for a Tropical storms using Eq. (6) is 50.1 km, while the mean R_m from the TCVitals database records is 87.6 km. Therefore, r_m was underestimated by 37.1 km. During TS intensity category of TCs, W06 performs best estimating R_{34} , although its estimation is lower than the mean value of R_{34} from the best-track records. Moreover, D87 and W06 have greater ability to estimate R_{50} , however, they both underestimate it at 11 km and 13 km, respectively, as shown in supplementary Table S1. The estimated mean r_m [by Eq. (6)] for Hurricanes is 40.1 km, close to the 47.2 km obtained from the TCVitals records. W06 most accurately estimates the R_{34} and R_{50} wind radius, while E11 and H80 are better to calculated R_{64} .

For Major Hurricanes, the estimated r_m from Eq. (6) is almost equal to the mean maximum wind radius obtained from the TCVitals database. Again, W06 most accurately estimates the R_{34} and R_{50} , with mean absolute error of 68.0 km and 42.1 km, respectively, while D87, E11 and H80 most accurately estimate R_{64} . Furthermore, H80, W06, E11 and F13 estimated an R_{100} of approximately 43 km. W06 yields the most accurate estimate of R_{34} and R_{50} for TC over the tropical NATL (see Table S1); however, it was the least accurate at estimating R_{64} , which is best estimated by E11 and H80. For R_{100} , all profiles estimate

an outer radius ranging from 40 to 46 km. The estimated r_m in this study for Trop TCs was 44.5 km, lower than the R_m operationally estimated by NHC.

Moreover, as shown in supplementary Table S1, the estimated r_m from Eq. (6) for the TCs that reach the Hurricane category on the Saffir–Simpson scale and move over tropical waters in NATL basin is very similar to the maximum wind radius operationally estimated by NHC. As in previous classifications, W06 estimated R_{34} and R_{50} somewhat accurately, while E11 and H80 have better ability to estimate R_{64} . In this work, the estimated maximum wind radius for TCs that move over extratropical waters (ExTrop) is underestimated by approximately 29 km. Additionally, the critical wind radii of R_{34} , R_{50} and R_{64} are more accurately estimated by W06, and all profiles have a similar behaviour for the R_{100} estimation. By analysing all TCs classifications, the maximum wind radius is underestimated (see Table S1). Similar to previous analysis, W06 most accurately estimates R_{34} and R_{50} , while D87 and E11 are better to estimate R_{64} in the whole basin.

The largest TD are estimated by W06 and H80, while from F13 is computed the smallest. Moreover, H80 estimates a TS size of 962.21 km, higher than the 821.21 km estimated by W06. E11 and F11 similarly estimate an outer radius of TS less than 255 km. W06 has a lower coefficient of variation, while H80 has the highest standard deviation (see Table S2). In Addition, H80 estimates the largest Hurricanes with 1319.3 km of outer radius, while W06 estimates a mean Hs size of 876.8 km. E11, F13, and W06 have the lowest coefficients of variation; and H80, W06, and D87 have the highest standard deviation, as shown in supplementary Table S2. H80 estimated a MH mean size of 1368.2 km while W06 calculated a MH outer radius of 800.93 km. D87, E11, and F13 estimated an outer radius less than 350 km. The mean outer radius estimated by W06 (H80) for tropical cyclones moving over the tropical

NATL is 768.11 km (914.07 km). As shown in Table S2, the outer radius estimated by the rest of the remaining profiles is less than 400 km. Moreover, W06 has the lowest coefficient of variation and H80 has the largest variance.

The mean TC size estimated for HTrop by H80 is 1234.9 km and W06 estimated a size of 818.42 km, comparable to the mean size estimated by C16 of 795.9 km. Additionally, H80 estimates an exterior radius of 1200.4 km for TCs classified as ExTrop, comparable to the outer radius proposed by Emanuel (2004), while the size estimated by W06 is 889.77 km. The remaining profiles estimate the smallest outer radius and W06 shows the lowest coefficient of variation of all (see Table S2).

In the entire NATL basin, as indicates in Table 1, H80 calculated the largest outer radius, with an average value of 999.17 km, slightly lower than the 1200 km proposed by Emanuel (2004). Nevertheless, H80 has the highest variance of all, while W06 calculated 804.3 km, and shows the lowest coefficient of variation. D87, E11, and F13 calculate an outer radius significantly smaller than previous works (Emanuel, 2004; Kimball and Mulekar, 2004; Knaff et al., 2014; Chavas et al., 2016).

In addition, in order to have a robust criterion to determine which radial wind profile estimate better the TC outer radius, we calculated the TC size using ERA-5 reanalysis data from 1980 to 2020 and recalculated the outer radius of the TC using each radial wind profile for the same period. By comparing both estimates, H80 and W06 show the lowest mean absolute error (MAE) in all classes, but W06 is the most skillful, as shown in Supplementary Table S3. It is worth noting that there are no noticeable differences between the estimated TC sizes for the periods 1851–2020 and 1980–2020 (see Table 1 and Tables S2 and S3).

The largest TCs according to W06 estimations have maximum wind speeds between 20 and 40 ms^{-1} when the system is in an intensification or weakening process. However, it is more likely to be dissipating when they move over extratropical latitudes, as revealed by previous studies (e.g., Hart and Evans, 2001; Knaff et al., 2014). For intense TCs, W06 estimates a size ranging between 650 and 850 km (supplementary Fig. S1). Besides, the frequency distribution of TCs is greater than 400 km. In the NATL basin, TCs that reach a size between 700 and 900 km during their life cycles are more frequent. The frequency distribution of the TC size in the NATL is similar to a Gaussian distribution.

As an example, for Hurricane Irma, on 9 September 2017 at 0600 UTC each radial wind profile shows a similar behaviour in the inner region ($r < r_m$); however, in the outer region a rapid decrease in azimuthal velocity is observed in E11 and F13, while W06 described a similar behaviour in the tangential velocity for distances $r > r_m$. In the case of D87, the change in tangential velocity with the radius was less than E11 and F13 (Fig. 2a). The maximum wind radius operationally estimated by NHC for Hurricane Irma on this date was 28 km, while the r_m estimated by Eq. (6) was 24 km. The estimated critical wind radii for each profile are underestimated in all cases, although W06 showed the smallest errors.

The NHC reports that Hurricane Irma recorded an R_{34} of 315 km and ROCI of 445 km. Fig. 2b shows that the outer radius estimated by F13 is similar to the R_{34} wind radii, while W06 calculated an outer radius of 745 km, comparable with the C16 mean TC size and H80 estimates of 1376 km. Analysing the wind field (Fig. 2c), it is easy to see that H80 overestimates the size of Hurricane Irma, while W06 makes a more realistic representation of the TC circulation. On the other hand, the rain rate associated with Irma is represented within the size described by W06.

Fig. 3 shows the radial distribution of the rain rate for Hurricanes Harvey and Irma every 24 h throughout their life cycles. As shown in Fig. 3a, the size of Harvey at 20170823 0000 UTC estimated using ROCI would not include the area between 350 and 400 km from the centre, with a maximum rain rate close to 25 mmh^{-1} . This could have serious consequences for the spatial public warning coverage. A similar behaviour is observed for Hurricane Irma (Fig. 4b) at 20170831 0000

UTC where a maximum rain rate is observed between 400 and 550 km from the centre, beyond the size estimated by the ROCI. In both cases, the size estimated by W06 includes all areas with precipitation intensities greater than 10 mmh^{-1} . However, the area observed in Hurricane Irma at 20170910 0000 UTC 950 km from the centre, where a rain rate close to 30 mmh^{-1} is observed, is not taken into account.

In summary, W06 most accurately estimates the TC critical wind radii in the NATL basin and exhibits the smallest errors when its TC outer radius estimation is compared with the estimated TC size from the ERA-5 reanalysis. It is also capable of giving a more accurate representation of the radial wind profile of the TC while the heaviest precipitation is included in the area enclosed by the TC size estimated by W06. H80 estimates the largest TC size, and E11 and F13 showed a similar behaviour in all cases. The largest TCs in the NATL are observed in extratropical latitudes, while the smallest are close to the equator. It was observed that category 1 and 2 hurricanes on the Saffir Simpson scale reach the largest size over all intensities. In addition, in the NATL a significant correlation is observed between the TC size estimated by W06 and the latitude (0.77, $p < 0.05$), higher than the correlation between the TC intensity and size (0.62, $p < 0.05$). This result agrees with Merrill (1984), Chan and Chan (2012) and Knaff et al. (2014). H80 yields coefficients of correlation of 0.56 and 0.90 ($p < 0.05$), suggest a statistically significant relationship between TC size and latitude and intensity, respectively.

4.2. Central and East Pacific basin

Small TCs frequently occur in the NEPAC (Hart and Evans, 2001; Chavas et al., 2016). The NEPAC HURDAT2 database contains information for every six hours since 1949. Only 1.2% of the analysed reports in the study period were found in extratropical latitudes. Thus, we remove them for the statistical analysis.

W06 yields the best estimates of R_{34} and R_{50} critical wind radii of tropical storms. Moreover, the maximum wind radius of TS is underestimated by approximately 17 km respect to the R_m operationally estimated by the NHC agency. The mean r_m estimated by Eq. (6) for Hurricanes was 34.3 km, which is similar to that obtained from the TCVitals database. Again W06 more accurately estimates R_{34} for hurricanes, E11 and D87 best estimate R_{50} , while H80 and F13 calculate the most accurate R_{64} . Furthermore, the mean r_m of Major Hurricanes estimated by Eq. (6) underestimates by ~ 5 km the R_m operationally estimated by NHC. The R_{34} and R_{50} critical wind radii are most accurately estimated by W06 and E11, respectively, while H80 and E11 most accurately estimate the R_{64} . D87, W06, and E11 estimated R_{100} to be slightly higher than 40 km.

The TCs that move over the tropical waters in the NEPAC have an mean estimated r_m from Eq. (6) of 42.9 km, similar to the R_m operationally estimated by NHC. W06 accurately estimates R_{34} but least accurately estimates R_{50} and R_{64} . D87 is most able to calculate R_{50} , while H80 is better to estimate R_{64} . Additionally, F13 estimated a lower R_{100} than the other radial wind profiles. For HTrop, the estimated r_m [by Eq. (6)] of approximately 31.9 km is similar to the R_m operationally estimated by NHC for these systems. Again, W06 is able to estimate R_{34} , D87 most accurately calculates R_{50} , and H80 calculates R_{64} better. The mean maximum wind radius (43.2 km) estimated in this study using Eq. (6) for the NEPAC underestimates the r_m operationally estimated by NHC. As previously discussed, R_{34} , R_{50} , and R_{64} are more accurately estimated by W06, D87, and H80, respectively. This statistics are shown in supplementary Table S4

In the NEPAC basin, the TD outer radius estimated by W06 is higher than that estimated by the remaining radial wind profiles. For TS, W06 estimated an outer radius of 758.4 km the smallest coefficient of variation of all, while H80 estimated an outer radius higher than that estimated by W06, with the greater standard deviation and coefficient of variation than all methods. The remaining profiles estimated a TS size less than 400 km. Moreover, W06 estimates an average hurricane

Table 1

NATL statistics for TC outer radius from 1851 to 2020: including the mean (μ), median, standard deviation (σ), coefficient of variation (CV), 25th percentile (P_{25}), 75th percentile (P_{75}), 95th percentile (P_{95}) and the 95% confidence interval (CI). N represents the total data analysed and the outer radius is given in km.

Wind profile	N	μ	Median	σ	CV	P_{25}	P_{75}	P_{95}	CI
H80	46847	999.17	980.00	314.2	0.3145	732.50	1244.0	1524.5	996.32, 1002.0
D87	46847	414.61	408.50	64.99	0.1567	364.50	458.50	528.00	414.02, 415.20
W06	46847	804.30	803.50	94.69	0.1177	739.00	872.50	958.50	803.44, 805.16
E11	46847	253.96	255.50	36.81	0.1449	227.50	281.00	312.00	253.63, 254.29
F13	46847	244.72	247.00	41.77	0.1707	215.00	275.50	309.50	244.34, 245.10

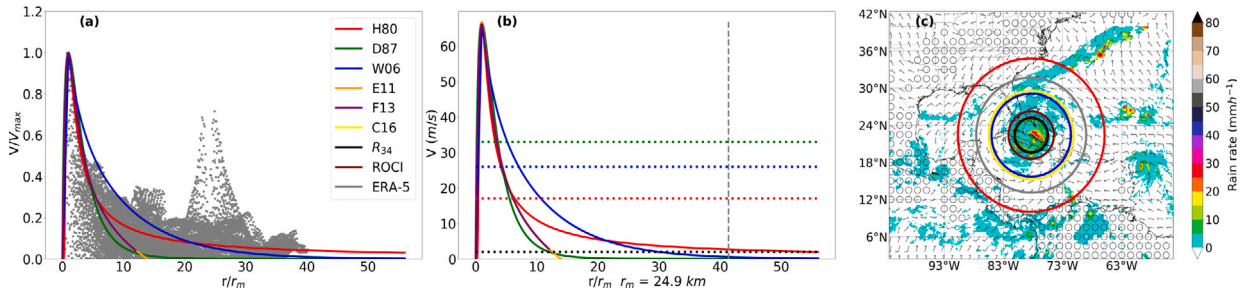


Fig. 2. Hurricane Irma on 9 September 2017 at 0600 UTC. (a) Radial wind profiles. (b) Radial wind profiles and the wind speed threshold for TC size (2 m/s, dotted black line), R_{34} (17 m/s, dotted red line), R_{50} (26 m/s, dotted blue line), R_{64} (33 m/s, dotted green line) and the TC size estimated from the ERA-5 reanalysis (vertical dashed grey line). (c) Estimated TC size from each radial wind profile. R_{34} , C16, ROCI radius, the surface wind obtained and TC size from the ERA-5 reanalysis, and the GPM rain rate have also been plotted. (For interpretation of the references to colour in this figure legend, the reader is referred to the web version of this article.)

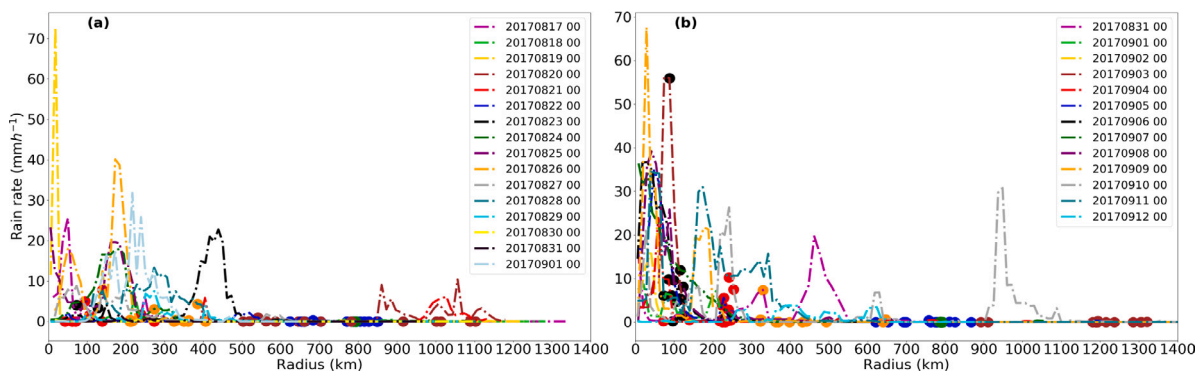


Fig. 3. Radial rain rate profile taken from the GPM (Northeast quadrant) (a) Hurricane Harvey. (b) Hurricane Irma. The critical wind radii estimated by W06 are plotted: R_{34} (red point), R_{64} (black point), outer radius (blue point). The C16 mean TC size (green point), the outer radius estimated by H80 (brown point) and the ROCI (orange point) recorded in the TCVitals database are also plotted. (For interpretation of the references to colour in this figure legend, the reader is referred to the web version of this article.)

size of 794.9 km and H80 calculates hurricanes with an outer radius of 1104.3 km. For major hurricanes, H80 estimates a larger size than W06; the remaining profiles estimated a small MHs. Additionally, TCs over tropical waters have a mean size of 804.65 km estimated by H80 and 725.45 km by W06. The remaining profiles considerably underestimate the TC size. For HTrop, W06 estimated a mean TC size of 777.55 km, similar to the 759.3 km estimated by C16, while H80 estimated a size greater than 1100.0 km. Similar to the behaviour observed in the NATL, both H80 and W06 estimate the largest TCs in the extratropical zone. Supplementary Table S5 summarizes these results.

In the whole basin, the outer radius calculated using the H80 radial wind profile has the greatest variance of all, while the mean outer radius computed using W06 is 726.93 km. The smallest outer radii are obtained using D87, E11, and F13. Moreover, W06 yields the lowest coefficient of variation and H80 yields the greatest, as shown in Table 2. By comparing the estimated TC size using each radial wind profile with the TC outer radius computed from the ERA-5 reanalysis, it is verified that H80 and W06 have a similar behaviour, although W06 is most able to compute TC size, as shown in supplementary Table S6. The estimation of the TC outer radius by E11 and F13 is similar too, however, it exhibits the largest mean absolute error.

In the NEPAC basin, the TCs are largest when the wind speed ranges between 25 and 40 ms^{-1} , while the most intense TCs are generally between 600 and 700 km. Supplementary Fig. S2 shows this distribution for W06. Besides, TCs size is most frequently between 650 and 800 km.

On 24 October 2018 at 0000 UTC, Hurricane Willa had a maximum wind speed of 50.0 ms^{-1} and was a category 3 hurricane on the Saffir-Simpson scale. Fig. 4a shows the radial structure of the azimuthal velocity estimated by each profile. F13 decreases rapidly while W06 and H80 have a slower decrease in tangential velocity. Therefore they are a better representation of the storm wind structure. The estimated maximum wind radius from Eq. (6) for Willa was 31.0 km, similar to the 28.0 km operationally estimated by NHC. H80 more accurately estimated R_{34} , although it underestimated wind radii and accurately estimated R_{50} and R_{64} . The TCVitals database, recorded a R_{34} wind radii of 185.0 km and an outermost closed isobar of 318.0 km. D87, E11 and F13, calculated the size of Willa similar to the ROCI.

W06 estimated an outer radius of 812.0 km, slightly higher than the size computed from ERA-5 reanalysis (736.6 km), and more than the TC size estimated by C16 and the mean MH size estimated by it for the NEPAC basin. Fig. 4b shows that the estimated size by H80 of 1336.0 km is significantly more than the rest of the profiles. W06 best satisfies the condition imposed in this study, to determine the outer radius of

Table 2

NEPAC statistics for TC outer radius from 1949 to 2020: including the mean (μ), median, standard deviation (σ), coefficient of variation (CV), 25th percentile (P_{25}), 75th percentile (P_{75}), 95th percentile (P_{95}) and the 95% confidence interval (CI). N represents the total data analysed and the outer radius is given in km.

Wind profile	N	μ	Median	σ	CV	P_{25}	P_{75}	P_{95}	CI
H80	29435	806.99	787.00	238.7	0.2958	595.50	1010.5	1200.0	804.26, 809.72
D87	29435	359.62	358.50	36.99	0.1028	338.50	380.50	418.50	359.19, 360.04
W06	29435	726.93	738.00	69.47	0.0955	674.50	778.50	825.00	726.14, 727.72
E11	29435	261.45	259.00	43.70	0.1671	227.00	296.00	332.00	260.95, 261.95
F13	29435	254.51	252.50	47.26	0.1857	218.50	292.00	330.00	253.97, 255.05

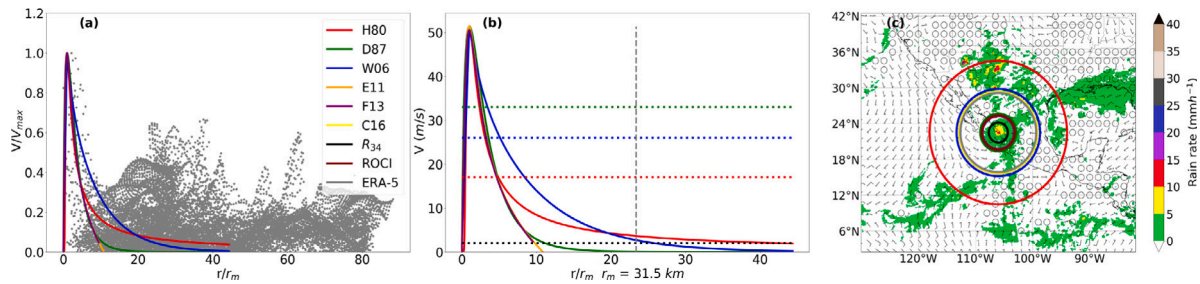


Fig. 4. Hurricane Willa on 24 October 2018 at 0000. (a) Radial wind profiles. (b) Radial wind profiles and the wind speed threshold for TC size (2 m/s, dotted black line), R_{34} (17 m/s, dotted red line), R_{50} (26 m/s, dotted blue line), R_{64} (33 m/s, dotted green line) and the TC size estimated from the ERA-5 reanalysis (vertical dashed grey line). (c) Estimated TC size from each radial wind profile. R_{34} , C16, ROCI radius, the surface wind obtained and TC size from the ERA-5 reanalysis, and the GPM rain rate have also been plotted. (For interpretation of the references to colour in this figure legend, the reader is referred to the web version of this article.)

TCs; however, it does not include the north of Mexico with a rain rate greater than 15.0 mmh^{-1} , in the area enclosed by the outer radius, as shown in Fig. 4c.

Fig. 5 shows the radial rain rate profile for Hurricanes Patricia and Willa throughout their life cycles. As can be seen, taking a TC size greater than the ROCI allows consideration of the areas of intense precipitation associated with the outermost spiral bands. Thus, issuing alerts to the areas affected by heaviest rain is guaranteed assuming there is a TC with an outer radius similar to that determined by W06.

To summarize, W06 more accurately estimated the TC outer radius by comparing it with the size estimation from ERA-5 reanalysis. Furthermore, similar correlations were observed between the size of the TC estimated by W06 and latitude, as well as the intensity. The correlation coefficients were 0.59 and 0.67 ($p < 0.05$), respectively. However, the strong correlation of 0.96 observed between the TC size estimated by H80 and the intensity contradicts previous work. This behaviour can be explained by the formulations of both profiles.

4.3. Western North Pacific basin

Kimball and Mulekar (2004) suggested that TC eyes are slightly smaller in the WNP than in the NATL, thus resulting in a smaller r_m in the WNP. All wind profiles studied to determine the TC size depend on the r_m which has an impact on the expected TC size in the WNP.

The estimated r_m using Eq. (7) for TS is less than the R_m operationally estimated by the JTWC and is similar to the maximum wind radius observed for TCs with wind speeds higher than 33 ms^{-1} over the entire basin. Furthermore, the calculated r_m has a similar behaviour to that operationally estimated for all systems moving over tropical and extratropical waters, while for TCs with $V_{max} > 33 \text{ ms}^{-1}$ in the tropical latitudes (HTrop), the estimated r_m from Eq. (7) is quite similar to that operationally estimated by JTWC. For the entire basin, the estimated maximum wind radius applying Eq. (7) was 47.6 km, slightly less than the mean R_m operationally estimated by JTWC. Moreover, W06 most accurately estimates R_{34} in all TC segmentations, showing the least errors, while H80 accurately estimates R_{64} . E11 calculates better R_{50} for TS, while D87 yield better estimations of R_{50} for the remaining classes. With the exception of F13, all profiles yield similar estimations of R_{100} . As previously shown, for the whole basin, W06 more accurately calculates R_{34} , while D87 and H80 more accurately

estimate R_{50} and R_{64} , respectively. For R_{100} , the behaviour discussed previously was observed; however, it is not possible to assess the skill of each profile because the used database does not contain R_{100} records. Supplementary Table S7 shows these statistics.

The largest TCs observed in the WNP are found in extratropical latitudes where the estimated mean size using W06 is 886.33 km, while H80 estimates an outer radius of 1150.0 km. Tropical depressions exhibit the smallest size in the entire basin of approximately 580.07 km and 632.28 km estimated using H80 and W06, respectively. For TS, both, H80 and W06 estimate the largest size. In TCs moving over tropical waters, the outer radius estimated using W06 is 724.23 km from the centre, while H80 estimates a slightly bigger size than W06. The most intense TCs (MHs) reach an average size of 748.51 km using W06 and 1359.2 km using H80. Furthermore, the size estimation for HTrop using W06 is lower than those of C16 (993.5 km), while H80 estimates a significantly bigger TC. The smallest TCs are obtained using D87, E11, and F13. In all cases, W06 yields a smaller variance and coefficient of variation than H80. These results are summarized in supplementary Table S8.

In the whole basin, H80 calculates a mean TC size of 932.8 km; however, the variance is considerably high. W06 yields an outer radius of 741.66 km. D87, E11, and F13 show similar results to those observed in the NATL and NEPAC, with the lowest outer radius, as shown in Table 3. The largest coefficient of variation is found using H80, while W06 yields the smallest.

When comparing the estimated TC size using each radial wind profile with the estimated TC outer radius from the ERA-5 reanalysis, again W06 shows the smallest mean absolute error for all classes, as it is revealed by supplementary Table S9. In contrast to previous research (Chan and Chan, 2015; Chavas et al., 2016), the mean size of TCs in the WNP calculated by each profile is less than the respective mean outer radius in the NATL. Nevertheless, the mean TC size from ERA-5 reanalysis is slightly higher to that in the NATL and NEPAC basins, which confirms previous research findings (Chan and Chan, 2015; Chavas et al., 2016).

In the WNP basin, following W06, TCs reach the largest size when the wind speed is between 20 and 45 ms^{-1} . A major contribution to this behaviour corresponds to systems that move in extratropical latitudes, in correspondence with the results of (Merrill, 1984; Kimball and Mulekar, 2004; Knaff et al., 2014). In addition, intense TCs

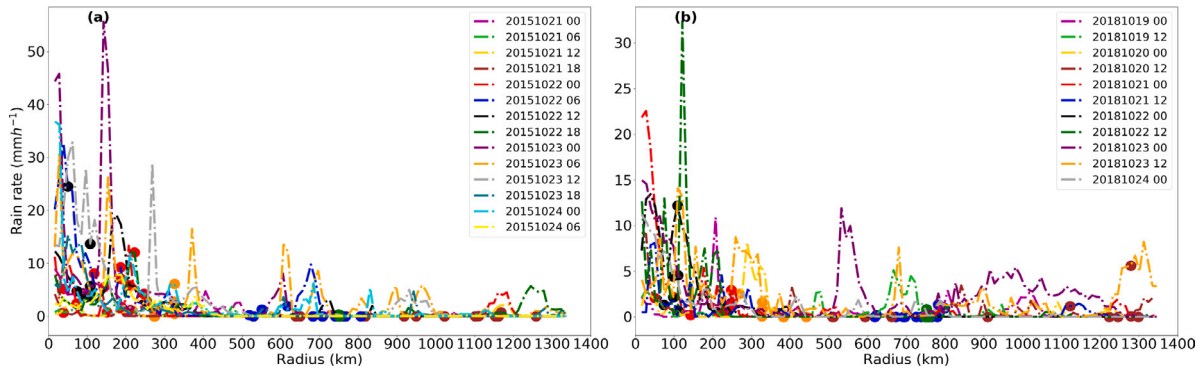


Fig. 5. Radial rain rate profile taken from the GPM (Northeast quadrant) (a) Hurricane Patricia. (b) Hurricane Willa. The critical wind radii estimated by W06 are plotted: R_{34} (red point), R_{64} (black point), outer radius (blue point). The C16 mean TC size (green point), the outer radius estimated by H80 (brown point) and the ROCI (orange point) recorded in the TCvitals database are also plotted. (For interpretation of the references to colour in this figure legend, the reader is referred to the web version of this article.)

Table 3

WNP statistics for TC outer radius from 1945 to 2019: including the mean (μ), median, standard deviation (σ), coefficient of variation (CV), 25th percentile (P_{25}), 75th percentile (P_{75}), 95th percentile (P_{95}) and the 95% confidence interval (CI). N represents the total data analysed and the outer radii are given in km.

Wind profile	N	μ	Median	σ	CV	P_{25}	P_{75}	P_{95}	CI
H80	61711	932.80	935.00	344.1	0.3689	660.00	1190.0	1510.0	930.09, 935.52
D87	61711	396.33	378.50	87.20	0.2200	332.50	459.00	555.00	395.64, 397.02
W06	61711	741.66	755.00	111.2	0.1500	675.00	816.50	906.00	740.78, 742.54
E11	61711	275.28	274.00	58.49	0.2125	233.50	310.00	374.50	274.82, 275.74
F13	61711	266.69	266.00	62.09	0.2328	222.00	305.50	369.50	266.20, 267.18

are frequently close to 600 ± 100 km (supplementary Fig. S3). The frequency of TCs between 700 and 850 km estimated using W06 is greater than those of smaller size. In the WNP basin, smaller TCs are typically associated with a strong subtropical ridge and monsoon depression and their trajectory is strongly influenced by environmental or topographic characteristics, while larger TCs frequently form within a south-westerly surge or late-season synoptic pattern (McKenzie, 2017).

A maximum wind radius of 29.0 km was estimated using Eq. (7) for Cyclone Utor on 11 August 2013 at 0000 UTC. This r_m is similar to the maximum wind radius operationally estimated by JTWC. W06 overestimated R_{34} but gave the most accurate estimation of all. Nevertheless, D87 almost matched the R_{50} , while the R_{64} estimated using H80 is similar to that recorded in the best-track database. The radial wind profiles described the wind structure for Cyclone Utor using E11 and F13 showed a rapid decrease in tangential velocity from the eyewall towards the undisturbed environment, as shown in Fig. 6a. W06 most accurately fits the radial wind profile obtained from the ERA-5 reanalysis.

The JTWC recorded a ROCI of 370 km. On the abovementioned date, Utor had a maximum wind speed of 48.6 ms^{-1} and a minimum central pressure of 952 hPa. D87, E11, and F13 estimated a TC size bigger than the R_{34} , but similar to the ROCI. W06 estimated an outer radius of 783.5 km and H80 estimated 1568.0 km (Fig. 6b). The analysis of the wind field associated with Utor confirms that W06 provides a good estimation of the TC size, being quite similar to the TC size (783.68 km) estimated using the ERA-5 reanalysis, while H80 overestimates it. Moreover, the areas with the highest rain rate are enclosed in the area determined by W06, as shown in Fig. 6c. However towards the southeast on the periphery of the outer radius estimated by W06, a maximum rain rate over 30.0 mmh^{-1} is observed, which is in the outermost spiral bands associated with the Utor external circulation. A somewhat accurate estimation of the TC size over the WNP using W06 is observed in Fig. 7 where the rain rate radial profile is shown for cyclones Utor and Haiyan during their life cycles. As can be seen, the rain rate does not exceed 5 mmh^{-1} at any distance more than the outer radius calculated by W06.

The latitude and TC size estimated using W06 in the WNP has a strong correlation coefficient ($0.75, p < 0.05$), likewise the maximum

wind speed and the outer radius has a higher correlation ($0.63, p < 0.05$). The former can be easily explained by the dependency between the latitude and the parameters of the W06 radial wind profile and is in agreement with previous work (Knaff et al., 2014). Additionally, all profiles studied in this work depend on the maximum wind speed. This would explain why when using H80, the highest correlation ($0.88, p < 0.05$) is observed between the TC size and intensity. The remaining profiles behave similar to W06.

4.4. North Indian Ocean basin

Chavas et al. (2016) showed that the NIO basin is characterized by small and medium storms, although this may be a consequence of the geometry of the confined coastline of South Asia. Owing to these conditions, none of the analysed samples moved over extratropical latitudes.

The NIO gave one the most accurate estimation using Eq. (8) of the maximum wind radius of any basins. Furthermore, W06 yields the most accurate R_{34} estimation in all cases, although D87 accurately estimated the R_{34} of TS. H80 and W06 accurately estimate R_{50} in TS, while D87 most accurately estimate this critical wind radii in MHs. Moreover, H80 accurately estimated R_{64} in all TCs and R_{50} in HTrops and hurricane systems. The estimated R_{100} has a similar behaviour to that discussed in Section 4.3. The mean radius of maximum winds for the entire basin is overestimated by approximately 1.5 km. As previously discussed, W06, E11, and H80 most accurately estimate the R_{34} , R_{50} , and R_{64} critical wind radii, respectively. Supplementary Table S10 exhibits a more complete overview of these statistics.

The smallest TCs in the NIO are tropical depressions, with a mean size of 628.36 km estimated using H80 and 632.55 km using W06. The largest TCs estimated by H80 are those that exhibit $V_{max} > 49 \text{ ms}^{-1}$ (MH) with an outer radius of 1256.7 km. However, W06 estimates an outer radius of the largest TCs of 784.5 km for systems where the maximum wind speed ranges from 33 to 49 ms^{-1} (H). For TCs with $V_{max} > 33 \text{ ms}^{-1}$ that move over the tropics (HTrop), C16 estimated an outer radius of 880.5 km. Therefore, this metric is underestimated by W06 and overestimated by H80, as indicated supplementary Table S11.

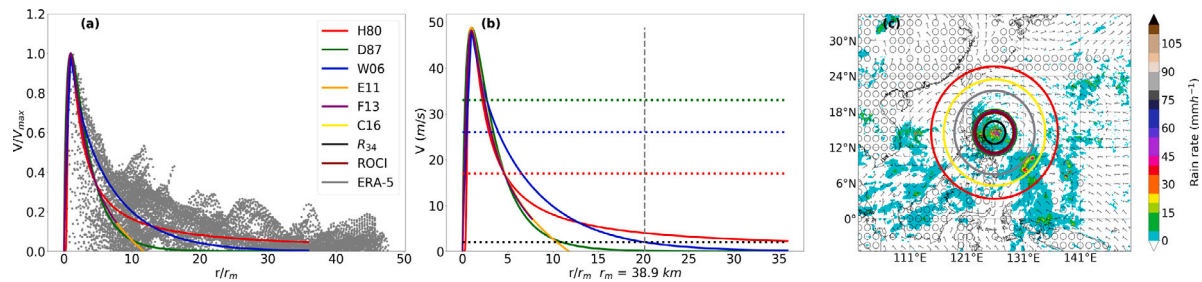


Fig. 6. Cyclone Utor on 11 August 2013 at 0000 UTC. (a) Radial wind profiles. (b) Radial wind profiles and the wind speed threshold for TC size (2 m/s, dotted black line), R_{34} (17 m/s, dotted red line), R_{50} (26 m/s, dotted blue line), R_{64} (33 m/s, dotted green line) and the TC size estimated from the ERA-5 reanalysis (vertical dashed grey line). (c) Estimated TC size from each radial wind profile. R_{34} , C16, ROCI radius, the surface wind obtained and TC size from the ERA-5 reanalysis, and the GPM rain rate have also been plotted. (For interpretation of the references to colour in this figure legend, the reader is referred to the web version of this article.)

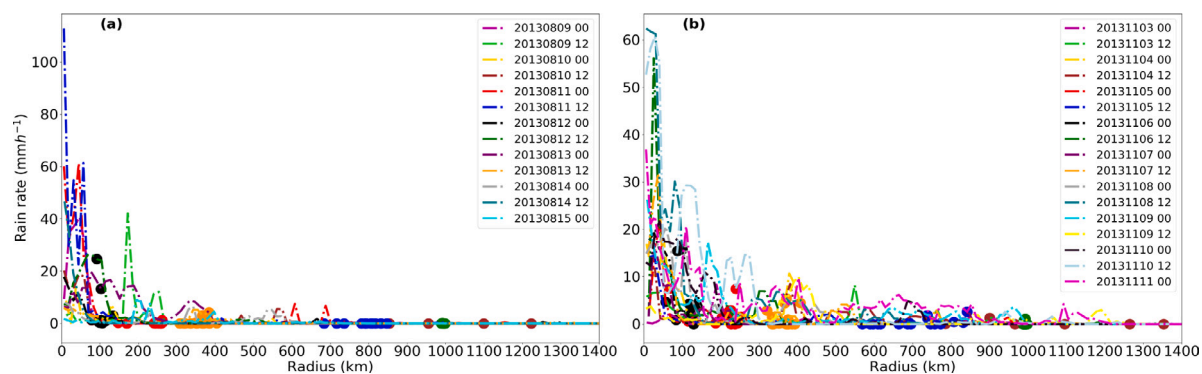


Fig. 7. Radial rain rate profile taken from the GPM (Northeast quadrant) (a) Cyclone Utor. (b) Cyclone Haiyan. The critical wind radii estimated by W06 are plotted: R_{34} (red point) R_{64} (black point), outer radius (blue point), C16 mean TC size (green point), the outer radius estimated by H80 (brown point), and the ROCI (orange point) recorded by JTWC have also been plotted. (For interpretation of the references to colour in this figure legend, the reader is referred to the web version of this article.)

In all cases, H80 has the highest variance, while W06 has the lowest coefficient of variation.

The largest outer radius was calculated in the NIO using the H80 wind profile; however, it presents the highest variance and largest coefficient of variation. The mean outer radius obtained from W06 is 696.62 km, as shown in Table 4. D87 exhibits a coefficient of variation slightly lower than that of H80, but the mean value of the outer radius is noticeably lower than the outer radius recorded in previous work (Chavas et al., 2016). Nevertheless, the TC sizes calculated using E11 and F13 are similar to the TC size obtained by Jaiswal and Kishtawal (2019).

Furthermore, the mean outer radius estimated by H80 using the TC records from 1980 to 2019 is almost similar to that estimated using the ERA-5 reanalysis for the same period. Again, W06 exhibits the smallest mean absolute error for all classes (see supplementary Table S12). This behaviour and the previously discussed findings allow us to affirm that W06 is the most able to estimate the size of TCs formed over the NIO basin.

As in the NATL, NEPAC, and WNP basins, in the NIO the TCs are larger when the maximum wind speed ranges between 25 and 35 ms^{-1} and the size of the most intense TCs is more than 650.0 km (supplementary Fig. S4). Tropical cyclones greater than 650.0 km are most frequency in the North Indian Ocean basin. The most frequent TC size ranges from 650.0 to 800.0 km. Only 5.8% of the best-track records analysed reached a size greater than 800.0 km (supplementary Fig. S4).

As an example, the maximum wind radius estimated using Eq. (8) for the Cyclone Giri on 22 October 2010 at 1200 UTC was 21.8 km, somewhat close to the R_m operationally estimated by the JTWC agency. W06 estimated R_{34} better than all other profiles, while the R_{50} estimated by the remaining profiles was comparable with the recorded wind radii. Furthermore, all profiles overestimated R_{64} , but H80 showed the least errors. Fig. 8a shows the radial wind profiles for the Cyclone Giri and Fig. 8b exhibits the wind speed threshold for TC

size metrics. There is a rapid decrease in tangential wind speed in the outer region ($r > r_m$), although W06 overestimates tangential speed up to a distance of $10r_m$ from the centre. At the abovementioned time, Giri had a maximum wind speed of 69.5 ms^{-1} and a minimum central pressure of 922 hPa.

The ROCI and R_{34} estimated by JTWC are 222.0 km and 175.0 km, respectively. Fig. 8c shows that both metrics are lower than the values obtained by each profile. The NIO TC size obtained by Jaiswal and Kishtawal (2019) ranged from 196.3 to 480.6 km from OSCAT data and from 217.2 to 452.5 km using the ROCI recorded by JTWC. For the Cyclone Giri specifically, Jaiswal and Kishtawal (2019) obtained a mean TC size of 262.45 km, similar to the value obtained by D87. The spatial distribution of the precipitation rate around the centre of Giri (Fig. 8c) shows that H80 (1245.0 km) overestimates the outer radius, while W06 (704 km) yields a more realistic TC size estimation, which is also verified by analysing the wind circulation associated with Giri and the TC size (681.55 km) estimated from the ERA-5 reanalysis.

Countries that have their coastlines in the North Indian Ocean are vulnerable to destruction by strong winds, storm surge, and heavy rainfall associated with landfalling TCs that form in this cyclogenetic basin. Understanding the radial rainfall distribution of a TC allows us make more reliable forecasts (Balachandran et al., 2014). It has been shown that the rain rate distribution around a TC is highly complex and is determined by several factors (Chen et al., 2006; Yu et al., 2010). Therefore, an outer radius of a TC that considers the maximum areas of precipitation contributes to the issuance of public advisories to reduce possible damage by the TC. The outer radius obtained using W06 is a good approximation for the TC size in the NIO, as shown in Fig. 9, in which the radial profiles of rain rate for the cyclones Giri and Chapala during their life cycles are shown. It is clear that the precipitation rate can be neglected at distances more than the outer radius estimated by W06.

Table 4

NIO statistics for TC outer radius from 1945 to 2019: including the mean (μ), median, standard deviation (σ), coefficient of variation (CV), 25th percentile (P_{25}), 75th percentile (P_{75}), 95th percentile (P_{95}) and the 95% confidence interval (CI). N represent the total data analysed and the outer radius are given in km.

Wind profile	N	μ	Median	σ	CV	P_{25}	P_{75}	P_{95}	CI
H80	5393	813.06	819.50	278.4	0.3424	579.50	1004.5	1272.0	805.63, 820.50
D87	5393	414.35	376.50	102.9	0.2485	330.50	523.50	577.00	411.60, 417.10
W06	5393	696.62	712.50	86.62	0.1243	647.00	762.50	809.00	694.31, 698.93
E11	5393	288.98	282.00	70.42	0.2436	238.00	331.00	401.40	287.10, 290.86
F13	5393	279.54	271.50	71.82	0.2569	228.50	324.50	393.20	277.62, 281.45

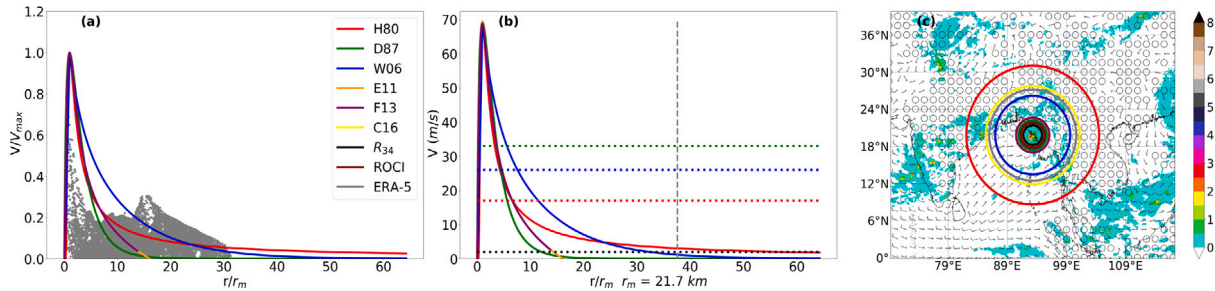


Fig. 8. Cyclone Giri on 22 October 2010 at 1200 UTC. (a) Radial wind profiles. (b) Radial wind profiles and the wind speed threshold for TC size (2 m/s, dotted black line), R_{34} (17 m/s, dotted red line), R_{50} (26 m/s, dotted blue line), R_{64} (33 m/s, dotted green line) and the TC size estimated from the ERA-5 reanalysis (vertical dashed grey line). (c) Estimated TC size from each radial wind profile. R_{34} , C16, ROCI radius, the surface wind obtained and TC size from the ERA-5 reanalysis, and the GPM rain rate have also been plotted. (For interpretation of the references to colour in this figure legend, the reader is referred to the web version of this article.)

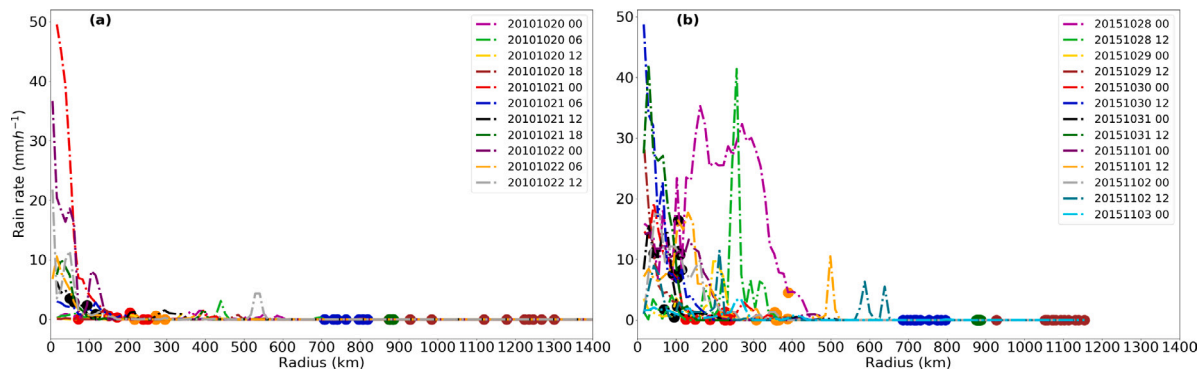


Fig. 9. Radial rain rate profile taken from the GPM (Northeast quadrant) (a) Cyclone Giri. (b) Cyclone Chapala. The critical wind radii estimated by W06 are plotted: R_{34} (red point), R_{64} (black point), and outer radius (blue point). The C16 mean TC size (green point), the outer radius estimated by H80 (brown point), and the ROCI (orange point) recorded in the JTWC best-track database have also been plotted. (For interpretation of the references to colour in this figure legend, the reader is referred to the web version of this article.)

Balachandran et al. (2014) studied the climatological rainfall characteristics of 43 TCs formed over the NIO from 2000–2010. They demonstrated that the most frequent rain rate of TCs in the NIO is in the range of 1–2.5 mmh⁻¹ which occur over an area of approximately 10%–14% within 5° (~ 555.0 km) radial distance during the intensification stages. The mean TC size over the NIO determined in this research using the W06 radial wind profile is greater than the TC size assumed by Balachandran et al. (2014). Thus, it also demonstrates that the W06 accurately estimates the TC size in this basin.

To summarize, over the NIO basin, W06 accurately estimates the TC outer radius and D87, E11, and F13 estimate small TCs. Moreover, the correlation between the intensity and the TC size (0.84, $p < 0.05$) is notably higher than the correlation between latitude and TC size (0.5, $p < 0.05$). This can be explained by the fact that the TCs in this basin have limited latitudinal movement over ocean water before landfall. In addition, the estimations yielded by H80 are similar to those of W06.

4.5. Southern Indian Ocean basin

The expression (Eq. (9)) used to determine the maximum wind radius in the SIO was a good fit. The maximum absolute error observed is 15.1 km for tropical storms. Additionally, W06, E11, and

H80 most accurately estimate the R_{34} , R_{50} , and R_{64} critical wind radii, respectively. H80 also accurately estimated R_{50} in all cases. For the entire basin, the mean radius of maximum winds was underestimated by approximately 0.8 km. As previously analysed, W06 accurately estimates R_{34} , and E11 and H80 more accurately calculate R_{50} and R_{64} , respectively. See supplementary Table S13 for further details.

Following the W06 estimation, the largest TCs are found in the extratropical zone of the South Indian Ocean, similar to observations in the NATL, NEPAC, and WNP basins. For these systems, the W06 radial wind profile estimates an outer radius of 842.96 km. However, for H80 the largest TCs are those that reach a maximum wind speed greater than 49 ms⁻¹ (MH), with an average size of 1337.7 km. For tropical depressions and tropical storms, W06 estimates a size of 633.26 km and 764.73 km, respectively. The W06 TD outer radius estimations is very close to the average size estimated by H80, however, H80 estimates the higher TS than all radial wind profiles. Over tropical waters, the average size of the TCs is 710.47 km and 841.32 km estimated by W06 and H80, respectively. Moreover, TCs with $V_{max} > 33$ ms⁻¹ over tropical waters (HTrop) have an average size of 781.9 km estimated by W06 and 1234.9 km by H80. The size of W06 TCs is lower than the mean outer radius obtained by C16 (871.9 km), while H80 obtains a much larger

value. The mean sizes estimated by D87, E11, and F13 are not discussed here as they estimate small TCs, similar to observations in other basins. These statistics are summarized in Table S14.

The Southern Indian Ocean basin does not present a characteristic pattern in TC size (Chavas et al., 2016). As previously shown, the highest outer radius was obtained using H80 at 843.4 km; however, it exhibits the biggest variation coefficient and the greatest variance. Furthermore, W06 has the lowest coefficient of variation with a mean outer radius of 712.4 km. D87, E11, and F13 exhibit coefficients of variation and variances less than H80, but the outer radius obtained using them are very small compared to H80 and W06, as shown in Table 5. Furthermore, W06 has the lowest mean absolute error when comparing the estimated TC outer radius by each radial wind profile with that estimated using the ERA-5 reanalysis from 1980 to 2019. As we found for the basins previously presented, W06 is the most skillful to estimate the TC size (see supplementary Table S15).

In the South Indian Ocean, tropical cyclones generally reach their greatest size when maximum wind speeds range between 20 and 35 ms^{-1} , similar to the North Indian Ocean, while the most intense TCs reach a size estimated using W06 between 600.0 and 750.0 km (supplementary Fig. S5). In addition, the most frequent size of TCs in this basin ranges between 700.0 and 800.0 km, although TCs of 650.0 to 700.0 km of size are very common.

The maximum wind radius estimated using Eq. (9) for Cyclone Imani on 25 March 2010 at 1200 UTC is 39.4 km. This is less than the maximum wind radius (46 km) operationally recorded by JTWC. W06 overestimates R_{34} , but is the most accurate. The R_{50} wind radii estimated by D87 and E11 is similar to the recorded value, while H80 and F13 estimates R_{64} similar to the recorded value. Through analysis of the radial velocity distribution in Cyclone Imani obtained from the ERA-5 reanalysis, we can see that W06 accurately estimates the TC outer wind structure (Fig. 10a), while D87, E11, and F13 show a rapid decrease in tangential velocity.

The JTWC reports show that E11 and F13 estimates an external TC size similar to ROCI (305.0 km), while W06 estimates an outer radius of 728.0 km, lower than the 986.96 km estimated using the ERA-5 reanalysis. Moreover, H80 calculates an outer radius of 1229.0 km, the largest of all profiles, as shown in Fig. 10b. The wind field associated with Imani shows that the estimation of the TC size by W06 is accurate. Additionally, from Fig. 10c, the analysis of the rain rate obtained from the GPM shows that the maximum rainfall intensities are in the area enclosed by W06.

Fig. 11 shows the radial distribution of rainfall intensity for cyclones Imani and Bruce throughout their life cycles. As can be seen in the case of Imani (Fig. 11a), W06 did not consider the maximum rain rate of approximately 27.0 mmh^{-1} and 23.0 mmh^{-1} observed at 20100327 0000 UTC and 20100329 0000 UTC, respectively. Nevertheless, for Bruce, the size estimated by W06 is reasonable. In both cases, assuming the ROCI outer radius value would cause areas located more than 500.0 km from the centre to be affected by heavy rains without prior warning. However, it has been demonstrated in previous studies that the distribution of the rain rate associated with the TCs is affected by several factors such as wind shear, TC intensity, sea surface temperature, and moisture distribution. Consequently, the TCs rainfall characteristics can vary significantly from one TC to another, and even sometimes for a singular TC (Balachandran et al., 2014).

In the SIO, a correlation of 0.80 ($p < 0.05$) is observed between the TC intensity and size, and 0.60 ($p < 0.05$) between the latitude and the TC size. This result agrees with Chan and Chan (2015), who suggests that the outer radius does not necessarily increase with latitude monotonically. Moreover, H80 exhibits a strong correlation of 0.87 ($p < 0.05$) between TC size and intensity. As it was demonstrated for each group into which the sample was divided, W06 is the radial wind profile that most accurately describes the R_{34} and the TC size. Thus, W06 is useful to use in different applications that require the TC size.

4.6. South Pacific Ocean basin

According to Chavas et al. (2016), the South Pacific Ocean basin has similar trends to the Southern Indian Ocean. The estimated maximum wind radius using Eq. (10) is similar to the mean R_m operationally estimated by the JTWC agency for all cases, except for tropical storms which has the greatest mean absolute error of 16.5 km. As previously shown for the other basins, W06, E11, and H80 most accurately estimate the R_{34} , R_{50} , and R_{64} , respectively. For the entire basin, the average radius of maximum winds is similar to the mean R_m operationally estimated by the JTWC agency. More details of these statistics are presented in the supplementary Table S16.

Both W06 and H80 estimate that the smallest TCs developed in the South Pacific Ocean are tropical depressions at 635.89 km and 605.96 km, respectively, while the largest TCs determined by W06 are found in extratropical latitudes at 841.38 km. However, similar to observations in the SIO basin, the largest TCs estimated by H80 with an outer radius of 1320.8 km are the TCs that reach a maximum wind speed higher than 49 ms^{-1} (MH). For this basin, only 2.95% of the analysed best-track reports were found in the extratropics, while 5.24% of all TCs records can be classified as MH. C16 estimated an outer radius of 948.0 km for TCs classified as HTrop at any time of their trajectories. This metric is underestimated by W06 and overestimated by H80. The TCs in the first intensification stages of the hurricane category of the Saffir Simpson scale (categories 1 and 2) reach a mean size of 803.33 km estimated by W06 and 1198.6 km calculated by H80. E11, D87 and F13 underestimates the size of the TCs in the SIO as well as in the other basins, as it was discussed in Chavas et al. (2015). Supplementary Table S17 summarizes these findings.

For the whole basin, H80 calculates an outer radius of 843.96 km. Nevertheless, as it was previously found, H80 has the highest variance and the highest coefficient of variation of all. Moreover, W06 estimates an outer radius of 717.27 km, as shown in Table 6. These values are very similar to those obtained for the SIO. D87, E11, and F13 also present similar values to those of the SIO basin. Furthermore, similar to what was observed in NIO and SIO basins, the mean TC outer radius estimated by H80 is almost similar to that calculated using the ERA-5 reanalysis from 1980 to 2019, however, W06 has the least mean absolute error of all, which suggests that W06 is the most skilled to estimate the TC size, as indicated in supplementary Table S18.

There are no significant differences in the distribution of TC size and intensity compared to observations in the Southern Indian Ocean basin, these results are similar to those of Chavas et al. (2016). The largest TCs according to W06 have a maximum wind speed of approximately 20–30 ms^{-1} , while TCs with a size between 700.0 and 800.0 km are more frequent (supplementary Fig. S6). Only 5% of the analysed reports were less than 450.0 km and 0.08% were more than 900.0 km.

The maximum wind radius operationally estimated by JTWC for Cyclone Donna on 8 May 2017 at 0000 UTC, is 23 km. This is slightly overestimated by the r_m calculated in this study (28.0 km). All profiles showed the least accurate performance in the R_{34} estimation, however W06 had the least amount of errors. F13 accurately estimated R_{50} , while E11 and F13 were similar to the recorded R_{64} . W06 accurately reproduces the radial wind structure of Cyclone Donna when compared with the radial velocity obtained from the ERA-5 reanalysis. H80, D87, E11, and F13 show a rapid decrease in the tangential wind speed from r_m towards the periphery, although H80 at a distance of $15r_m$ from the centre showed a slower change in azimuthal velocity (Fig. 12a).

D87 estimated a size of 280.0 km less than the R_{34} recorded by the JTWC agency, while E11 calculated a size of 368.0 km, comparable to the ROCI of 388.0 km. However, as shown in Fig. 12b, these metrics should not be assumed as the size of Cyclone Donna as on the abovementioned date, due to the TC had a maximum wind speed of 64.0 ms^{-1} and a minimum central pressure of 929 hPa. This intensity suggests a circulation of the winds beyond the 368.0 km estimated by E11. W06 estimated a radius of 728.0 km, close to the estimated

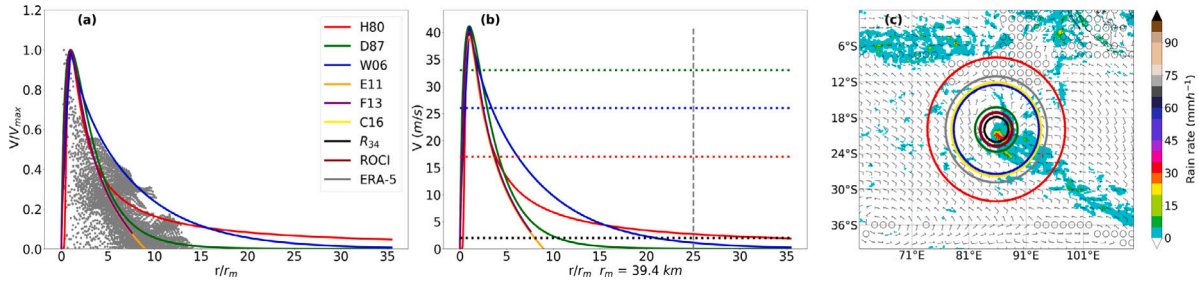


Fig. 10. Cyclone Imani on 25 March 2010 at 1200 UTC. (a) Radial wind profiles. (b) Radial wind profiles and the wind speed threshold for TC size (2 m/s, dotted black line), R_{34} (17 m/s, dotted red line), R_{50} (26 m/s, dotted blue line), R_{64} (33 m/s, dotted green line) and the TC size estimated from the ERA-5 reanalysis (vertical dashed grey line). (c) Estimated TC size from each radial wind profile. R_{34} , C16, ROCI radius, the surface wind obtained and TC size from the ERA-5 reanalysis, and the GPM rain rate have also been plotted. (For interpretation of the references to colour in this figure legend, the reader is referred to the web version of this article.)

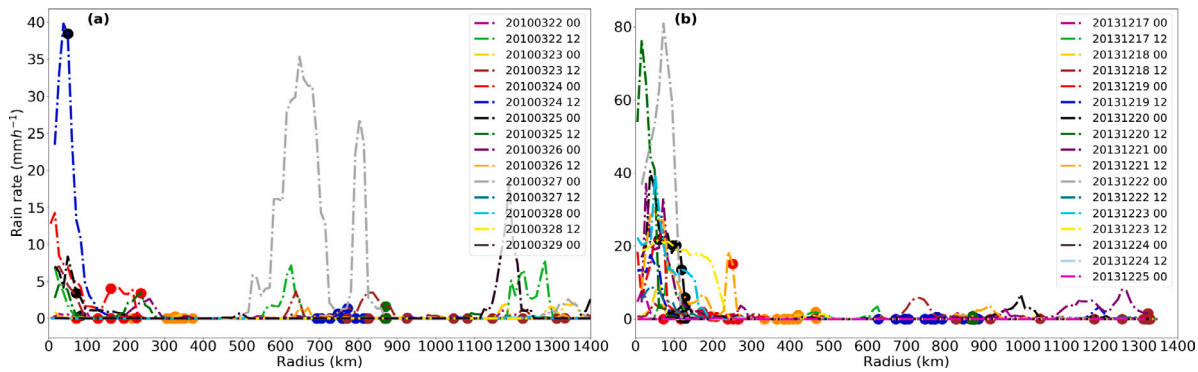


Fig. 11. Radial rain rate profile taken from the GPM (Northeast quadrant) (a) Cyclone Imani. (b) Cyclone Bruce. The critical wind radii estimated by W06 are plotted: R_{34} (red point), R_{64} (black point), and outer radius (blue point). The C16 mean TC size (green point), outer radius estimated by H80 (brown point), and ROCI (orange point) recorded in the JTWC best-track database are also plotted. (For interpretation of the references to colour in this figure legend, the reader is referred to the web version of this article.)

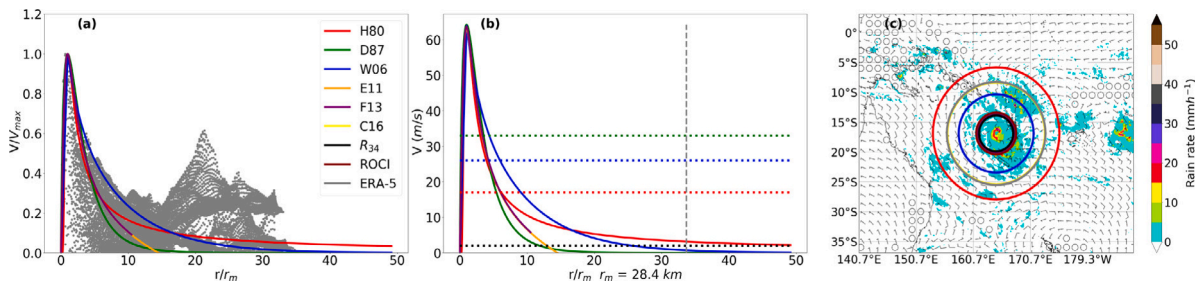


Fig. 12. Cyclone Donna on 8 May 2017 at 0000 UTC. (a) Radial wind profiles. (b) Radial wind profiles and the wind speed threshold for TC size (2 m/s, dotted black line), R_{34} (17 m/s, dotted red line), R_{50} (26 m/s, dotted blue line), R_{64} (33 m/s, dotted green line) and the TC size estimated from the ERA-5 reanalysis (vertical dashed grey line). (c) Estimated TC size from each radial wind profile. R_{34} , C16, ROCI radius, the surface wind obtained and TC size from the ERA-5 reanalysis, and the GPM rain rate have also been plotted. (For interpretation of the references to colour in this figure legend, the reader is referred to the web version of this article.)

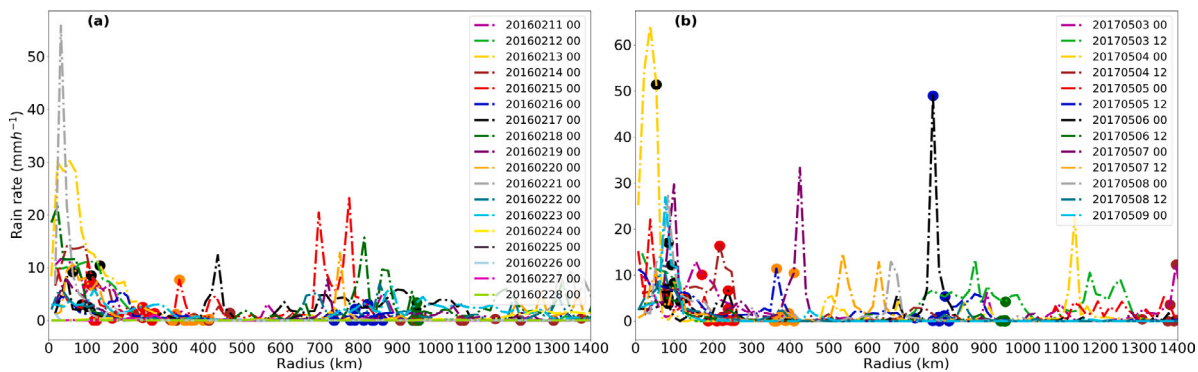


Fig. 13. Radial rain rate profile taken from the GPM (Northeast quadrant) (a) Cyclone Winston. (b) Cyclone Donna. The critical wind radii estimated by W06 are plotted: R_{34} (red point), R_{64} (black point), and outer radius (blue point). The C16 mean TC size (green point), the outer radius estimated by H80 (brown point), and the ROCI (orange point) recorded in the JTWC best-track database are also plotted. (For interpretation of the references to colour in this figure legend, the reader is referred to the web version of this article.)

Table 5

SIO statistics for TC outer radius from 1945 to 2019: including the mean (μ), median, standard deviation (σ), coefficient of variation (CV), 25th percentile (P_{25}), 75th percentile (P_{75}), 95th percentile (P_{95}) and the 95% confidence interval (CI). N represents the total data analysed and the outer radii are given in km.

Wind profile	N	μ	Median	σ	CV	P_{25}	P_{75}	P_{95}	CI
H80	22758	843.40	828.00	297.7	0.3530	608.50	1053.8	1379.5	839.53, 847.27
D87	22758	398.97	374.50	83.44	0.2091	336.00	475.00	544.50	397.89, 400.06
W06	22758	712.40	728.00	94.41	0.1325	659.50	780.00	836.50	711.17, 713.63
E11	22758	258.33	256.50	64.52	0.2497	212.12	303.50	365.00	257.49, 259.17
F13	22758	267.62	265.50	61.10	0.2283	223.50	309.00	370.50	266.83, 268.42

Table 6

SPO statistics for TC outer radius from 1945 to 2019: including the mean (μ), median, standard deviation (σ), coefficient of variation (CV), 25th percentile (P_{25}), 75th percentile (P_{75}), 95th percentile (P_{95}) and the 95% confidence interval (CI). N represents the total data analysed and the outer radii are given in km.

Wind profile	N	μ	Median	σ	CV	P_{25}	P_{75}	P_{95}	CI
H80	13380	843.96	855.00	304.5	0.3608	592.00	1071.0	1359.5	838.80, 849.12
D87	13380	404.94	373.50	97.70	0.2412	338.00	467.50	600.00	403.29, 406.60
W06	13380	717.27	735.50	100.8	0.1405	663.00	787.50	847.02	715.57, 718.98
E11	13380	249.18	245.50	63.76	0.2558	205.50	293.00	355.52	248.10, 250.26
F13	13380	259.40	255.50	60.53	0.2333	217.00	300.50	362.50	258.38, 260.43

average size for this basin, but lower than the 957.9 km estimated using the ERA-5 reanalysis. Moreover, H80 calculated a size of 1229.0 km, approximately 300.0 km higher than the mean value estimated by C16.

Fig. 12c shows that the most intense rain rate areas are within the circulation associated with the TC estimated by W06, determined from the outer radius. Fig. 13 shows the rain rate radial profile for cyclones Winston and Donna throughout their life cycles. For Winston (Fig. 13a), the most intense rainfall is observed by the size estimated by W06; however, at 20170803 1200 UTC and 20170504 0000 UTC in the radial distribution of the precipitation rate of Cyclone Donna (Fig. 13b), a maximum rain rate as much as 1000 km from the centre is observed. Therefore, these intensities were not considered in the TC size determined by W06, but they are included in the area enclosed by outer radius calculated by H80.

In the SPO, correlations similar to the SIO are observed between the TC intensity and size (0.78, $p < 0.05$) as well as between the latitude and the TC size (0.62, $p < 0.05$). However, a strong correlation (0.84, $p < 0.05$) is found between the intensity and size in the outer radius estimated by H80.

5. Discussion

Fig. 14 displays the plot of the estimated r_m (by Eqs. (6)–(10)) globally and within each ocean basin. The statistics for these distributions are shown in Table 7. The mean value of the estimated r_m in the tropics ranges between 20.0 and 55.0 km. The radius of maximum wind speed of the TCs can reach extreme values, with a greater incidence in the WNP basin. The global mean value of r_m is 47.67 km, in agreement with previous works (Smith, 2003; Willoughby et al., 2006; Takagi and Wu, 2016; Morris and Ruf, 2017).

On average, the TCs of the NIO had a larger mean r_m and variance than in any basin and the NEPAC presents the lowest variance of all. Furthermore, there is a significant correlation between the latitude and radius of maximum winds in the NATL (0.53, $p < 0.05$) and NEPAC (0.48, $p < 0.05$), not observed for the remaining cyclogenetic basins. This can be explained by the empirical expression used to determine r_m in these basins. Overall, W06, and H80 more accurately estimate the R_{34} and R_{64} critical wind radii, respectively, as previously was discussed; while, D87 and E11 are able to estimate R_{50} .

Globally, W06 estimate the largest tropical depression, as we found in each basin. Moreover, tropical storms have a mean size of 789.99 km and 923.72 km estimated by W06 and H80, respectively. For the remaining classes, the mean size estimated by W06 is lower than that estimated by H80. From Table 8 is also observed that H80 calculates a mean global outer radius similar to that obtained by C16, however, H80

exhibits the highest variance and the highest coefficient of variation, as it was demonstrated in the individual analysis of each basin. Furthermore, W06 estimates a mean global TC size of 748.71 km, while the remaining radial wind profiles estimate smaller TCs than W06 and H80. Additionally, W06 shows the most accurate statistics in each basin, as it was discussed in previous sections. More details of these statistics are presented in supplementary Table S19.

Table 9 show the mean values of the TC size obtained for each radial wind profile in each basin. As can be seen, with 60% of the profiles the largest TCs are formed and developed over the NATL ocean, in contradiction with the results obtained by Chan and Chan (2015) and Chavas et al. (2016), where they state that the largest TCs are formed in the WNP. Overall, following W06 and H80, TCs are larger in the NATL than in any basin (see supplementary Table S20 for further information). Nevertheless, according to Chan and Chan (2013, 2015), the TCs in the WNP are the largest most likely because they are mostly embedded monsoon channels and are more likely to move poleward so that they can grow through the angular momentum import mechanisms; however, in the climatology presented in this research, those characteristics are not taken into account. Here, the latitudinal dependence has a strong impact on the calculation of r_m and the tangential velocity by each radial wind profile. In addition, the results show that the smallest TCs are observed over the NIO basin.

In addition, as discussed in the assessment of the ability of radial wind profile to estimate the TCs outer radius, the ROCI underestimates the TC size. Table 9 shows that the mean TC size estimated using W06, H80 and the ERA-5 reanalysis is at least two times higher than the TC size estimated using ROCI. This result confirms previous research findings (e.g. Dean et al., 2009). Conversely, D87 estimated a mean TC outer radius quite similar to the ROCI, while the E11 and F13 estimations are lower than ROCI, as previously was discussed. However, it should be noted that according to our findings the ROCI underestimates the size of TCs.

Based on the statistical analysis performed for each basin, on the error analysis between the estimated outer radius by each radial wind profile and the mean TC size estimated from the ERA-5 reanalysis, and on the ability to estimate R_{34} , W06 is determined to more accurately estimate the TC outer radius. Fig. 15 shows the geographic distribution of the TC size obtained from W06 over each ocean basin. It is worth noting that TC size is smaller when TCs are relatively close to the Equator. This behaviour shows the same pattern in each basin. Following this findings, Fig. 16 displays box-and-whisker plots of TC size globally and within each ocean basin, confirming the results previously discussed.

Furthermore, the TCs increase in size as they move towards extratropical latitudes, coinciding with the results of Hart and Evans

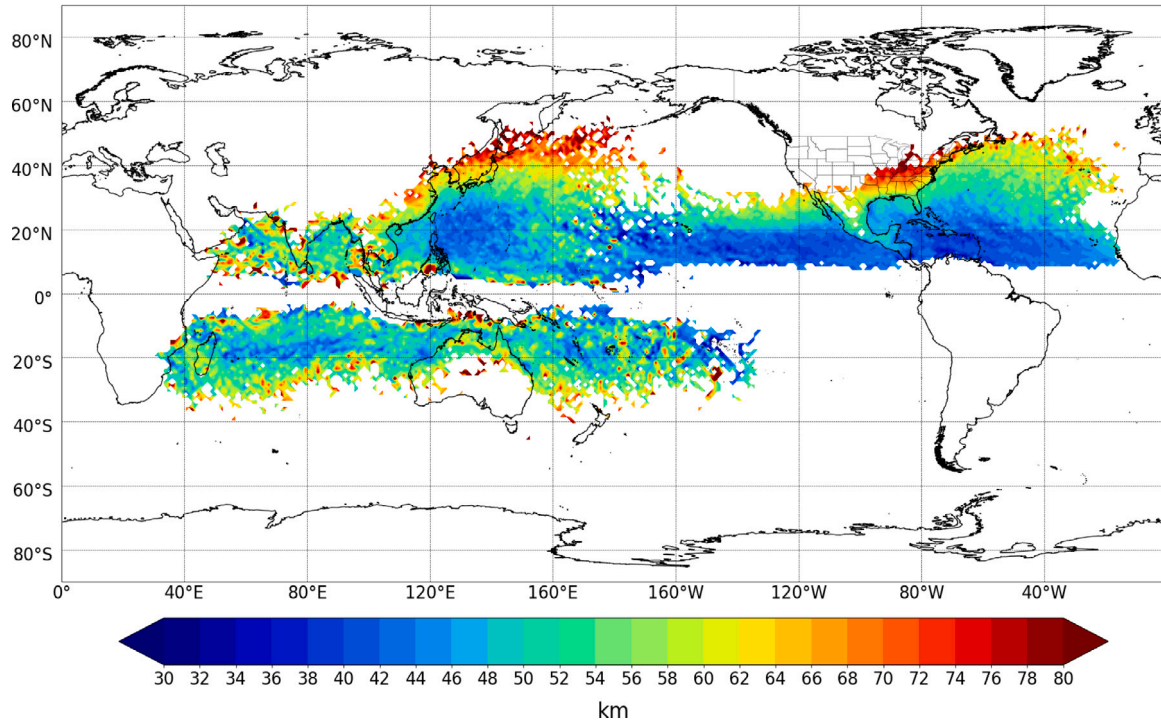


Fig. 14. Global spatial distribution of the r_m estimated by Eqs. (6) to (10) smoothed by averaging the r_m in a grid cell of $1^\circ \times 1^\circ$ of horizontal resolution for each TC position along their trajectory from the best-track records. The extratropical stage of tropical cyclones was neglected. (For interpretation of the references to colour in this figure legend, the reader is referred to the web version of this article.)

Table 7

Statistics for the r_m estimated in this study using Eqs. (6)–(10) in each basin as appropriate: including the mean (μ), median, standard deviation (σ), coefficient of variation (CV), 25th percentile (P_{25}), 75th percentile (P_{75}), 95th percentile (P_{95}) and the 95% confidence interval (CI). N represents the total data analysed and the radius of maximum winds are given in km.

Basin	N	μ	Median	σ	CV	P_{25}	P_{75}	P_{95}	CI
NATL	46847	47.746	47.470	10.55	0.2210	40.831	54.602	65.642	47.650, 47.84
NEPAC	29435	43.163	44.289	8.597	0.1991	37.663	48.614	56.326	43.06, 43.26
WNP	61711	47.610	45.721	14.91	0.3131	37.867	54.356	77.639	47.49, 47.72
NIO	5393	53.547	48.368	16.39	0.3062	42.848	66.287	82.945	53.10, 53.98
SIO	22758	50.130	47.552	14.30	0.2854	41.164	56.667	78.229	49.94, 50.32
SPO	13380	51.163	47.855	15.69	0.3068	42.344	55.664	86.525	50.89, 51.42
Global	179524	47.674	46.32	13.26	0.2783	39.54	53.63	73.04	47.61, 47.73

Table 8

Global statistics for TC outer radius: including the mean (μ), median, standard deviation (σ), coefficient of variation (CV), 25th percentile (P_{25}), 75th percentile (P_{75}), 95th percentile (P_{95}) and the 95% confidence interval (CI). N represents the total data analysed and the outer radii are given in km.

Wind profile	N	μ	Median	σ	CV	P_{25}	P_{75}	P_{95}	CI
H80	179524	907.93	888.5	318.5	0.3508	652.0	1143.0	1450.5	906.46, 909.40
D87	179524	396.60	378.5	78.59	0.1981	342.5	446.5	543.5	396.23, 396.96
W06	179524	748.71	756.5	103.5	0.1383	686.0	813.0	913.0	748.23, 749.19
E11	179524	263.77	262.0	54.15	0.2053	226.5	297.5	352.5	263.52, 264.02
F13	179524	258.92	257.0	56.10	0.2166	219.0	294.5	351.0	258.66, 259.18
C16	578	909.4	881.0	248.5	0.27	740.7	1054.4	–	–

Table 9

Mean outer radius (km) estimated using each radial wind profile in each basin.

Wind profile	NATL	NEPAC	WNP	NIO	SIO	SPO	Global
H80	999.17	806.99	932.80	813.06	843.30	843.96	907.93
D87	414.61	359.62	396.33	414.35	398.97	404.94	396.60
W06	804.30	726.93	741.66	696.61	712.40	717.27	748.71
E11	253.96	261.25	275.28	288.98	258.33	249.18	263.77
F13	244.72	254.52	266.69	279.54	267.62	259.40	258.92
ERA-5	808.25	789.50	824.62	688.75	780.41	776.20	796.86
ROCI	342.17	322.06	336.18	314.69	323.55	323.11	329.72
C16	795.90	759.30	993.50	880.50	871.00	948.10	909.40

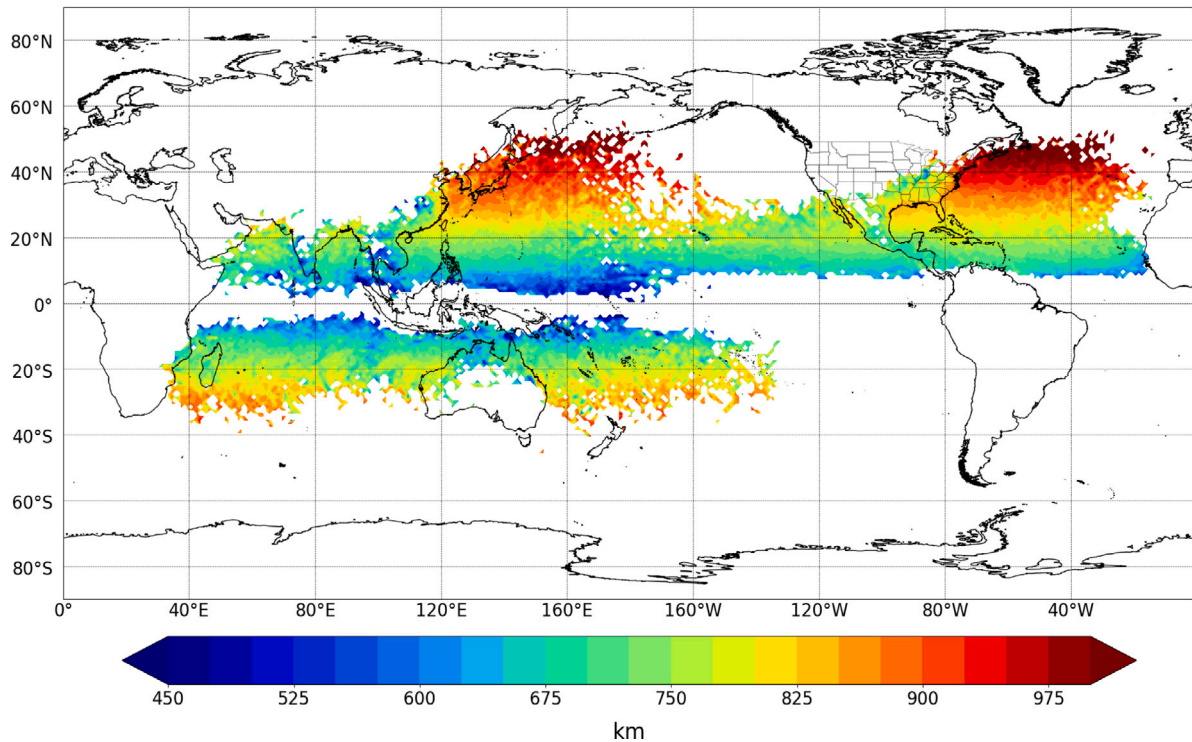


Fig. 15. Global spatial distribution of storm size estimated using W06 smoothed by averaging in a grid cell of $1^\circ \times 1^\circ$ of horizontal resolution the TC outer radius for each position along the trajectory from the best-track records for each basin (NATL from 1851 to 2020, NEPAC from 1949 to 2020, and the NIO, SIO, WNP and SPO basins from 1945 to 2019). The extratropical stage of tropical cyclones was neglected. (For interpretation of the references to colour in this figure legend, the reader is referred to the web version of this article.)

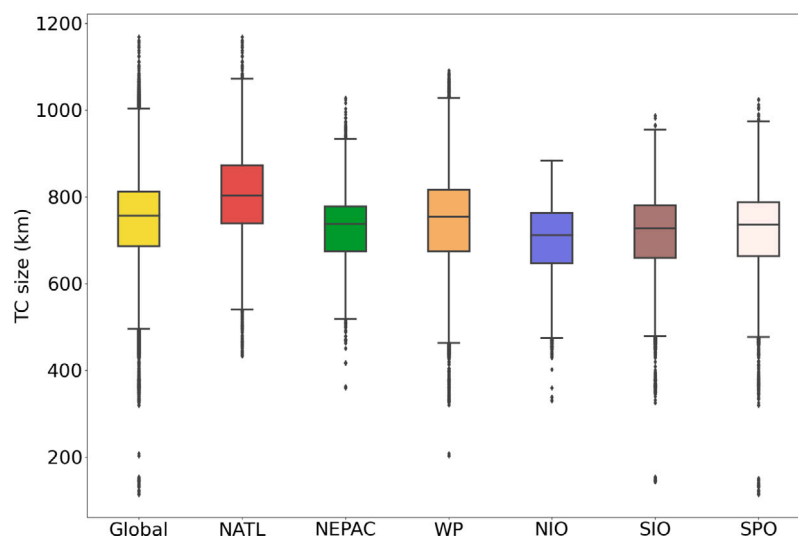


Fig. 16. Box-and-whisker plot of the distributions estimated by W06 globally and by basin. The box plot displays median and interquartile range [q1, q3], whiskers (black line) and outliers (grey markers outside the range $[q1 - 1.5(q3 - q1), q3 + 1.5(q3 - q1)]$). q1 and q3 represent the 25th and 75th percentile respectively. Corresponding statistics and basin expansions are displayed in Table 8.

(2001). Knaff et al. (2014) suggested that the smallest TCs are generally located at the lowest latitudes associated with the westward steering flow, while the largest TCs are located at the high latitudes on their poleward movement. Kimball and Mulekar (2004) demonstrated that the critical wind radii of TCs generally increase as storms move poleward and westward, which may be due to increased angular momentum in response to changes in the synoptic environment. A similar trend is expected to happen with TC size, as shown in Fig. 15.

Moreover, supplementary Fig. S7 shows the frequency distribution for the TC size estimated by W06. Globally, systems with sizes between

700.0 and 800.0 km are more frequent. This distribution is similar to that obtained by Chavas and Emanuel (2010), although their mean outer radius is lower than that obtained here. Additionally, as it was observed in previous sections, tropical cyclones in all basins reach their greatest size when the maximum wind speed ranges between 20 and 40 ms^{-1} , associated with the intensification and weakening processes. It is assumed that the greatest impact on this behaviour is movement of TCs over extratropical latitudes, where they are generally in dissipation processes.

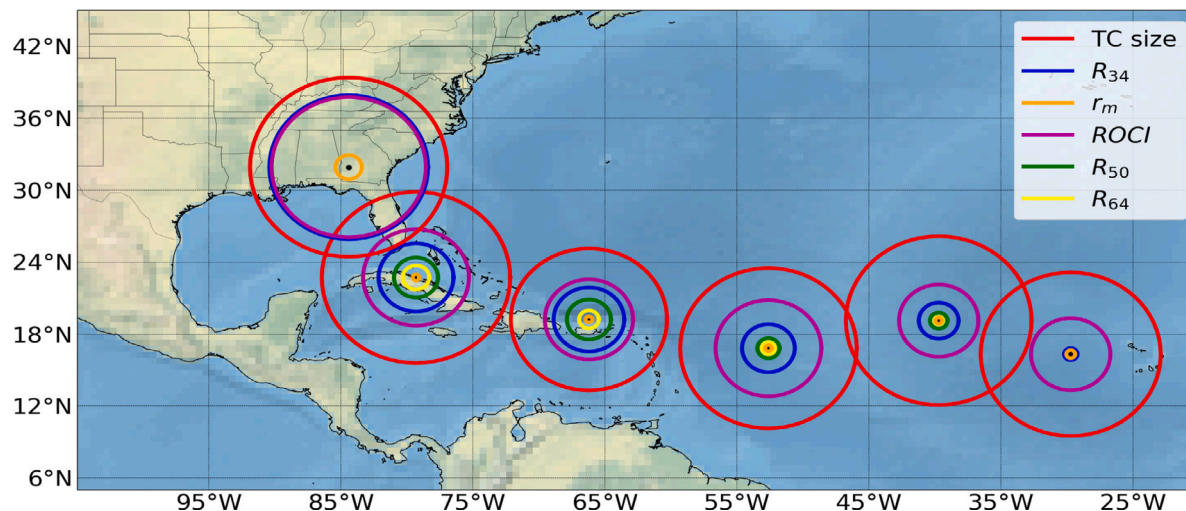


Fig. 17. Representation of various positions of the Hurricane Irma track and the area enclosed by the different TC metrics. R_{34} , R_{50} , R_{64} , r_m and ROCI are taken from the TCvitals database and the TC size is estimated by W06. (For interpretation of the references to colour in this figure legend, the reader is referred to the web version of this article.)

Previous research (e.g. Merrill, 1984; Weatherford and Gray, 1988; Chavas and Emanuel, 2010; Chan and Chan, 2012) suggests that the correlation between TC size and intensity is low. In this study, the Spearman's correlation coefficients ($p < 0.05$) obtained are 0.84 for the NIO, 0.80 for the SIO, 0.78 for the SPO, 0.76 for the NEPAC, 0.63 for the WNP and 0.62 for the NATL. Therefore, it is possible to confirm that exists some direct relationship between the TC size and intensity. Nevertheless, these high correlations may be the result of the dependence of the expressions of maximum wind radius and radial wind profiles on intensity and position.

Supplementary Fig. S8 shows the scatter diagram for TC size as a function of the maximum wind speed. The shape observed here is similar to the mean size distribution produced from the datasets of Knaff et al. (2014) and Wu et al. (2015). The TC mean size generally increases with increasing TC intensity before reaching the maximum and slightly decreases with further intensity increase. Tsuji et al. (2016) showed that TC size is influenced more by external factors than the intensity. Carrasco et al. (2014) studied the relationship between TC size and the potential to undergo rapid intensification processes; however, they did not find a relationship between the TC intensity and the ROCI.

In addition to the subjectivity in outer radius determination, the low correlation may also be due to the nonlinear relationship between the TC size and intensity, in agreement with Wu et al. (2015), who calculated the correlations between the TC intensity for the samples with intensity less than 48 ms^{-1} ($\sim 93 \text{ kt}$) and R_{34} less than 427.0 km (3.85° of latitude). They found a correlation of 0.64 in the MTCSSWA (Multiplatform Tropical Cyclone Surface Wind Analysis, Knaff et al. (2011)) data for the WNP basin, suggesting a statistically significant relationship between TC intensity and size.

6. Applicability of the TCSize database and implications for future studies

TC size has a direct impact on weather and climate, and corresponding effects on the ocean (Li et al., 2019). In recent years, it has been assumed that hurricane storm surge depends primarily of the TC intensity. However, Irish et al. (2008) showed that using only the maximum wind speed of Hurricane Katrina was insufficient to describe the surge behaviour. In fact, the size of the storm plays an important role in the generation of storm surges, particularly for very intense storms (Irish et al., 2008; Needham and Keim, 2014), and must be considered when predicting the socioeconomic impacts and flood risk (Irish et al., 2008; Li et al., 2019). Therefore, the TC size database generated for each cyclogenetic basin will allow further studies on

the relationship between size and storm surge, but also support the assessment and mapping of potential storm surge impacts on global population, ecosystems, and economies.

As the size attribute of hurricanes is operationally difficult to estimate and predict (Knaff and Zehr, 2007), one of the most important uses of the methodology developed in this research is its ability to determine the TC size from the output of the numerical weather prediction models, and thus, forecasters can prepare special warnings for the possible affected areas before the storm landfalls. Fig. 17 shows the different metrics for Hurricane Irma throughout its trajectory. As can be seen, a greater area is considered for the emission of warnings if the outer radius estimated by W06 is taken as the TC size instead of the ROCI. Therefore, more people can take actions to minimize the damage produced by TC heavy rain, strong winds, or storm surges.

The analysis of the TC rainfall characteristics helps to understand and improve quantitative precipitation forecasts of TCs. This is another important application in which the database presented here would be useful. For analysis of the rain rate, radial distribution around the TC centre is needed to approximate the TC outer radius, as shown by Balachandran et al. (2014).

Chavas et al. (2016) noted that the outer radius translates to the surface area occupied by a storm, and thus its dynamics may impose limits on the number of storms that can form in a limited area at a given time. The database of TC sizes developed in this research contains information for each basin since records began. Therefore, it could be also used for statistical analysis of tropical cyclogenesis, as suggested by Chavas et al. (2016). Moreover, this dataset could be employed to represent the area occupied by a TC in climatological studies, related to the influence of some atmospheric variables on the TC genesis and development, in any of the cyclogenetic basins.

The TCsize database generated in this research is freely available at Mendeley Data (<http://dx.doi.org/10.17632/8997r89fbf.1>).

7. Conclusions

This study provides a new climatology of the tropical cyclones' (TCs) size in every cyclogenetic basin. The proposed method is designed to be a more objective metric that can be quickly applied to any TC, knowing its position and maximum wind speed. These parameters are registered in the best-track databases of agencies such as National Hurricane Center (NHC) and Joint Typhoon Warning Center (JTWC). Moreover, the geographic variation in size was analysed and the statistical distributions of each size metric were calculated globally and for each basin separately. The results reveal that the largest TCs exists

in extratropical zones, while the smallest storms are found close to equatorial line. Contrary to previous work, the largest TCs are found in the North Atlantic (NATL), while the smallest are in the North Indian Ocean basins. Furthermore, a significant correlation between TC size and latitude was found in the NATL and the Central & East Pacific. Moreover, the TC increase in size as they intensify before reaching their maximum size; thereafter, the outer radius slightly decreases as the wind speed increases. Despite the limitations and contradictions found here with other research, the database presented could be useful for many applications, including different risk analysis. Furthermore, it could be used to determine sources and sinks of atmospheric moisture associated with the genesis, intensification, and weakening of TCs.

CRedit authorship contribution statement

Albenis Pérez-Alarcón: Conceptualization, Data curation, Methodology, Formal analysis, Software, Investigation, Validation, Visualization, Writing – original draft, Writing – review & editing. **Rogert Sorí:** Conceptualization, Methodology, Formal analysis, Investigation, Validation, Writing – review & editing. **José C. Fernández-Alvarez:** Conceptualization, Data Curation, Methodology, Investigation, Validation, Visualization, Writing – review & editing. **Raquel Nieto:** Methodology, Validation, Writing – review & editing, Supervision. **Luis Gimeno:** Methodology, Validation, Writing – review & editing, Supervision.

Declaration of competing interest

The authors declare that they have no known competing financial interests or personal relationships that could have appeared to influence the work reported in this paper.

Acknowledgments

A.P-A acknowledges a PhD grant from the Universidade de Vigo. J.C.F-A and R.S acknowledge the support from the Xunta de Galicia (Galician Regional Government) under the grants no. ED481A-2020/193 and ED481B 2019/070, respectively. The authors acknowledge NHC and JTWC for freely provide the best track archive and Copernicus Climate Change Service for the ERA-5 reanalysis database. We acknowledge the funding for open access from the Universidade de Vigo/Consortio Interuniversitario do Sistema Universitario de Galicia (CISUG) and the partial support from the Xunta de Galicia under the Project ED431C 2021/44. The authors also thank to Christopher W. Landsea and one anonymous reviewer for their comments and suggestions to improve the manuscript.

Appendix A. Supplementary data

Supplementary material related to this article can be found online at <https://doi.org/10.1016/j.wace.2021.100366>.

References

- Adler, R., Huffman, G., Chang, A., Ferraro, R., Xie, P., Janowiak, J., Rudolf, B., Schneider, U., Curtis, S., Bolvin, D., Gruber, A., Susskind, J., Arkin, P., Nelkin, E., 2003. The version 2 global precipitation climatology project (GPCP) monthly precipitation analysis (1979-present). *J. Hydrometeorol.* 4 (6), 1147–1167.
- Adler, R., Sapiiano, M., Huffman, G., Wang, J.J., Gu, G., Bolvin, D., Chiu, L., Schneider, U., Becker, A., Nelkin, E., Xie, P., Ferraro, R., Shin, D.B., 2018. The global precipitation climatology project (GPCP) monthly analysis (new version 2.3) and a review of 2017 global precipitation. *Atmosphere* 9 (4), 138. <http://dx.doi.org/10.3390/atmos9040138>.
- Balachandran, S., Geetha, B., Ramesh, K., Selvam, N., 2014. Tcrain – A database of tropical cyclone rainfall products for north Indian ocean. *Trop. Cyclone Res. Rev.* 3 (2), 122–129. <http://dx.doi.org/10.6057/2014TCRR02.05>.
- Behrangi, A., Stephens, G., Adler, R., Huffman, G., Lambrihtsen, B., Lebsock, M., 2014. An update on oceanic precipitation rate and its zonal distribution in light of advanced observations from space. *J. Clim.* 27, 3957–3965. <http://dx.doi.org/10.1175/JCLI-D-13-00679.1>.
- Blake, E.S., Zelinsky, D.A., 2018. National Hurricane Center Tropical Cyclone Report. Hurricane Harvey. Technical Report, National Hurricane Center, https://www.nhc.noaa.gov/data/tcr/AL092017_Harvey.pdf, retrieved: May 12, 2020.
- Cangialosi, P.J., Latto, A.S., Berg, R., 2018. National Hurricane Center Tropical Cyclone Report. Hurricane Irma. Technical Report, National Hurricane Center, https://www.nhc.noaa.gov/data/tcr/AL112017_Irma.pdf, retrieved: June 14, 2019.
- Carrasco, C.A., Landsea, C.W., Lin, Y.L., 2014. The influence of tropical cyclone size on its intensification. *Weather Forecast.* 29 (3), 582–590. <http://dx.doi.org/10.1175/WAF-D-13-00092.1>.
- Chan, K.T.F., Chan, J.C.L., 2012. Size and strength of tropical cyclones as inferred from QuikSCAT data. *Mon. Wea. Rev.* 140, 811–824. <http://dx.doi.org/10.1175/MWR-D-10-05062.1>.
- Chan, K.T.F., Chan, J.C.L., 2013. Angular momentum transports and synoptic flow patterns associated with tropical cyclone size change. *Mon. Wea. Rev.* 141, 3985–4007. <http://dx.doi.org/10.1175/MWR-D-12-00204.1>.
- Chan, K.T.F., Chan, J.C.L., 2015. Global climatology of tropical cyclone size as inferred from QuikSCAT data. *Int. J. Climatol.* 35 (15), 4843–4848. <http://dx.doi.org/10.1002/joc.4307>.
- Chavas, D.R., Emanuel, K.A., 2010. A QuikSCAT climatology of tropical cyclone size. *Geophys. Res. Lett.* 37 (L18816), 45–53. <http://dx.doi.org/10.1029/2010GL044558>.
- Chavas, D.R., Lin, N., Dong, W., Lin, Y., 2016. Observed tropical cyclone size revisited. *J. Clim.* 29 (8), 2923–2939. <http://dx.doi.org/10.1175/JCLI-D-15-0731.1>.
- Chavas, D.R., Lin, N., Emanuel, K.A., 2015. A model for the complete radial structure of the tropical cyclone wind field. Part I: Comparison with observed structure. *J. Atmos. Sci.* 72, 3647–3662. <http://dx.doi.org/10.1175/JAS-D-15-0014.1>.
- Chen, S., Knaff, J., Marks, F., 2006. Effects of vertical wind shear and storm motion on tropical cyclone rainfall asymmetries deduced from TRMM. *Mon. Wea. Rev.* 134, 3190–3208.
- Chu, J.H., Sampson, C.R., Levine, A.S., Fukada, E., 2002. The joint typhoon warning center tropical cyclone best-tracks, 1945–2000. URL: http://www.usno.navy.mil/NOOC/nmfc-ph/RSS/jtbc/best_tracks/TC_bt_report.html.
- Cocks, S.B., Gray, W.M., 2002. Variability of the outer wind profiles of western north Pacific typhoons: Classifications and techniques for analysis and forecasting. *Mon. Wea. Rev.* 130 (8), 1989–2005. [http://dx.doi.org/10.1175/1520-0493\(2002\)130%3C1989:VOTOWP%3E2.0.CO;2](http://dx.doi.org/10.1175/1520-0493(2002)130%3C1989:VOTOWP%3E2.0.CO;2).
- Dean, L., Emanuel, K.A., Chavas, D.R., 2009. On the size distribution of atlantic tropical cyclones. *Geophys. Res. Lett.* 36 (14), L14803. <http://dx.doi.org/10.1029/2009GL039051>.
- DeMaria, M., 1987. Tropical cyclone track prediction with a barotropic spectral model. *Mon. Wea. Rev.* 115, 2346–2357. [http://dx.doi.org/10.1175/1520-0493\(1987\)115,2346:TCTPWA.2.0.CO;2](http://dx.doi.org/10.1175/1520-0493(1987)115,2346:TCTPWA.2.0.CO;2).
- Depperman, C.E., 1947. Notes on the origin and structure of Philippine typhoons. *Bull. Am. Meteorol. Soc.* 28, 399–404.
- Emanuel, K.A., 2004. Tropical cyclones energetics and structure. In: Fedorovich, E., Rotunno, R., Stevens, B. (Eds.), *Atmospheric Turbulence and Mesoscale Meteorology*. Cambridge University Press, pp. 165–192.
- Emanuel, K., Rotunno, R., 2011. Self-stratification of tropical cyclone outflow. Part I: Implications for storm structure. *J. Atmos. Sci.* 68, 2236–2249. <http://dx.doi.org/10.1175/JAS-D-10-05024.1>.
- Frisius, T., Scgönemann, D., 2013. The impact of gradient wind imbalance on potential intensity of tropical cyclones in an unbalanced slab boundary layer model. *J. Atmos. Sci.* 70, 1874–1890. <http://dx.doi.org/10.1175/JAS-D-12-0160.1>.
- Greco, M., Olson, W.S., Munchak, S.J., Ringerud, S., Liao, L., Haddad, Z., Kelley, B.L., McLaughlin, S.F., 2016. The GPM combined algorithm. *J. Atmos. Ocean. Technol.* 33 (10), 2225–2245. <http://dx.doi.org/10.1175/JTECH-D-16-0019.1>.
- Hart, R.E., Evans, J.L., 2001. A climatology of the extratropical transition of atlantic tropical cyclones. *J. Clim.* 14, 546–564. [http://dx.doi.org/10.1175/1520-0442\(2001\)014,0546:ACOTET.2.0.CO;2](http://dx.doi.org/10.1175/1520-0442(2001)014,0546:ACOTET.2.0.CO;2).
- Hersbach, H., Bell, B., Berrisford, P., Hirahara, S., Horányi, A., Muñoz Sabater, J., Nicolas, J., Peubey, C., Radu, R., Schepers, D., Simmons, A., Soci, C., Abdalla, S., Abellan, X., Balsamo, G., Bechtold, P., Biavati, G., Bidlot, J., Bonavita, M., De Chiara, G., Dahlgren, P., Dee, D., Diamantakis, M., Dragani, R., Flemming, J., Forbes, R., Fuentes, M., Geer, A., Haimberger, L., Healy, S., Hogan, R.J., Hólm, E., Janisková, M., Keeley, S., Laloyaux, P., Lopez, P., Lupu, C., Radnoti, G., de Rosnay, P., Rozum, I., Vamborg, F., Villaume, S., Thépaut, J.N., 2020. The ERA5 global reanalysis. *Q. J. R. Meteorol. Soc.* 146 (730), 1999–2049. <http://dx.doi.org/10.1002/qj.3803>.
- Holland, G.J., 1980. An analytic model of the wind and pressure profiles in hurricanes. *Mon. Wea. Rev.* 108, 1212–1218. [http://dx.doi.org/10.1175/1520-0493\(1980\)108,1212:AAMOTW.2.0.CO;2](http://dx.doi.org/10.1175/1520-0493(1980)108,1212:AAMOTW.2.0.CO;2).
- Huffman, G., Stocker, E., Bolvin, D., Nelkin, E., Tan, J., 2019. GPM IMERG early precipitation L3 half hourly 0.1 degree x 0.1 degree V06, greenbelt, MD, goddard earth sciences data and information services center (GES DISC). <http://dx.doi.org/10.5067/GPM/IMERG/3B-HH-E/06>, Accessed: May 20, 2020.
- Irish, J.L., Resio, D.T., Ratcliff, J.J., 2008. The influence of storm size on hurricane surge. *J. Phys. Oceanogr.* 38 (9), 2003–2013. <http://dx.doi.org/10.1175/2008JPO3727.1>.

- Jacot, D.C.H., 2020. Storm surges, heavy rain and strong wind: Impacts of tropical cyclone winston in Fiji-focus on health. In: R., A. (Ed.), *Extreme Weather Events and Human Health*. Springer, Cham, pp. 185–196. http://dx.doi.org/10.1007/978-3-030-23773-8_13.
- Jaiswal, D., Kishtawal, C., 2019. Estimation of size of tropical cyclones in the north Indian ocean using oceansat-2 scatterometer high-resolution wind products. *Theor. Appl. Climatol.* 136, 45–53. <http://dx.doi.org/10.1007/s00704-018-2464-y>.
- Jelesnianski, C.P., 1965. A numerical calculation of storm tides induced by a tropical storm impinging on a continental shelf. *Mon. Wea. Rev.* 93 (6), 343–358.
- Kepert, J.D., 2010. Tropical cyclone structure and dynamics. In: *Global Perspectives on Tropical Cyclones*. World Scientific Series on Asia-Pacific Weather and Climate, pp. 3–53. http://dx.doi.org/10.1142/9789814293488_0001.
- Kimball, S.K., Mulekar, M.S., 2004. A 15-year climatology of north atlantic tropical cyclones. Part I: Size parameters. *J. Clim.* 17 (18), 3555–3575. [http://dx.doi.org/10.1175/1520-0442\(2004\)017<3555:AYCONA>2.0.CO;2](http://dx.doi.org/10.1175/1520-0442(2004)017<3555:AYCONA>2.0.CO;2).
- Knaff, J.A., DeMaria, M., Molenaar, D.A., Sampson, C.R., Seybold, M.G., 2011. An automated, objective, multiple-satellite-platform tropical cyclone surface wind analysis. *J. Appl. Meteorol. Climatol.* 50, 2149–2166. <http://dx.doi.org/10.1175/2011JAMC2673.1>.
- Knaff, J.A., Longmore, S.P., Molenaar, D.A., 2014. An objective satellite-based tropical cyclone size climatology. *J. Clim.* 27 (L18816), 455–476. <http://dx.doi.org/10.1175/JCLI-D-15-0610.1>.
- Knaff, J.A., Zehr, R.M., 2007. Reexamination of tropical cyclone wind-pressure relationships. *Weather Forecast.* 22 (1), 71–88. <http://dx.doi.org/10.1175/WAF965.1>.
- Kowaleski, A.M., Evans, J.L., 2016. A reformulation of tropical cyclone potential intensity theory incorporating energy production along a radial trajectory. *Mon. Wea. Rev.* 144 (10), 3569–3578. <http://dx.doi.org/10.1175/MWR-D-15-0383.1>.
- Kummerow, C.D., Randel, D.L., Kulie, M., Wang, N.Y., Ferraro, R., Joseph Munchak, S., Petkovic, V., 2015. The evolution of the goddard profiling algorithm to a fully parametric scheme. *J. Atmos. Ocean. Technol.* 32 (12), 2265–2280. <http://dx.doi.org/10.1175/JTECH-D-15-0039.1>.
- Lagmay, A.M.F., Agaton, R.P., Bahala, M.A.C., Briones, J.B.L.T., Cabacaba, K.M.C., Caro, C.V.C., Dasallas, L.L., Gonzalo, L.A.L., Ladiero, C.N., Lapidez, J.P., Mungcal, M.T.F., Puno, J.V.R., Ramos, M.M.A.C., Santiago, J., Kenneth, S.J., Tablazon, J.P., 2015. Devastating storm surges of typhoon haiyan. *Int. J. Disaster Risk Sci.* 11, 1–12. <http://dx.doi.org/10.1016/j.ijdr.2014.10.006>.
- Landsea, C.W., Franklin, J.L., 2013. Atlantic hurricane database uncertainty and presentation of a new database format. *Mon. Wea. Rev.* 141 (10), 3576–3592. <http://dx.doi.org/10.1175/MWR-D-12-00254.1>.
- Li, J., Hou, D., Liu, Q., Zhang, Y., 2019. Influence of tropical cyclone intensity and size on storm surge in the northern east China sea. *Remote Sens.* 11 (24), 3033. <http://dx.doi.org/10.3390/rs11243033>.
- McKenzie, T.B., 2017. A Climatology of Tropical Cyclone Size in the Western North Pacific Using an Alternative Metric (Master's thesis). Florida State University, Electronic Theses, Treatises and Dissertations, URL: <http://fsu.digital.flvc.org/islandora/object/fsu%3A507708>.
- Merrill, R.T., 1984. A comparison of large and small tropical cyclones. *Mon. Wea. Rev.* 112 (7), 1408–1418. [http://dx.doi.org/10.1175/1520-0493\(1984\)112<1408:ACOLAS>2.0.CO;2](http://dx.doi.org/10.1175/1520-0493(1984)112<1408:ACOLAS>2.0.CO;2).
- Morris, M., Ruf, C.S., 2017. Determining tropical cyclone surface wind speed structure and intensity with the CYGNSS satellite constellation. *J. Appl. Meteorol. Climatol.* 56 (7), 1847–1865. <http://dx.doi.org/10.1175/JAMC-D-16-0375.1>.
- Needham, H., Keim, B., 2014. An empirical analysis on the relationship between tropical cyclone size and storm surge heights along the U.S. Gulf Coast. *Earth Interact.* 18, 1–15. <http://dx.doi.org/10.1175/2013EI000558.1>.
- Olfateh, M., Callaghan, D.P., Nielsen, P., Baldock, T.E., 2017. Tropical cyclone wind field asymmetry-development and evaluation of a new parametric model. *J. Geophys. Res. Oceans* 122, 458–469. <http://dx.doi.org/10.1002/2016JC012237>.
- Randel, D., Kummerow, C., Ringerud, S., 2020. The goddard profiling (gprof) precipitation retrieval algorithm. In: Levizzani, V., Kidd, C., Kirschbaum, D., Kummerow, C., Nakamura, K., Turk, F. (Eds.), *Satellite Precipitation Measurement*. In: *Advances in Global Change Research*, Springer, Cham, pp. 141–152. http://dx.doi.org/10.1007/978-3-030-24568-9_8.
- Rogers, R.F., Aberson, S., Bell, M.M., Cecil, D.J., Doyle, J.D., Kimberlain, T.B., Morgerman, J., Shay, L.K., Velden, C., 2017. Rewriting the tropical record books: The extraordinary intensification of hurricane patricia (2015). *Bull. Am. Meteorol. Soc.* 98 (10), 2091–2112. <http://dx.doi.org/10.1175/BAMS-D-16-0039.1>.
- Sampson, C.R., Knaff, J.A., 2015. A consensus forecast for tropical cyclone gale wind radii. *Weather Forecast.* 30 (5), 1397–1403. <http://dx.doi.org/10.1175/WAF-D-15-0009.1>.
- Sarker, M.A., 2018. Numerical modelling of waves and surge from cyclone chapala (2015) in the arabian sea. *Ocean Eng.* 158, 299–310. <http://dx.doi.org/10.1016/j.oceaneng.2018.04.014>.
- Smith, R., 2003. A simple model of the hurricane boundary layer. *Q. J. R. Meteorol. Soc.* 128, 1–20. <http://dx.doi.org/10.1256/qj.01.197>.
- Takagi, H., Wu, W., 2016. Maximum wind radius estimated by the 50kt radius: improvement of storm surge forecasting over the western north Pacific. *Nat. Hazards Earth Syst. Sci.* 16 (3), 705–717. <http://dx.doi.org/10.5194/nhess-16-705-2016>.
- Tan, C., Fang, W., 2018. Mapping the wind hazard of global tropical cyclones with parametric wind field models by considering the effects of local factors. *Int. J. Disaster Risk Sci.* 9, 86–99. <http://dx.doi.org/10.1007/s13753-018-0161-1>.
- Tsuji, H., Itoh, H., Nakajima, K., 2016. Mechanism governing the size change of tropical cyclone-like vortices. *J. Meteorol. Soc. Jpn. Ser. II* 94 (3), 219–236. <http://dx.doi.org/10.2151/jmsj.2016-012>.
- Vickery, P., Wadhwa, D., 2008. Statistical models of holland pressure profile parameter and radius to maximum winds of hurricanes from flight-level pressure and H* wind data. *J. Appl. Meteorol. Climatol.* 47 (10), 2497–2517.
- Weatherford, C.L., Gray, W.M., 1988. Typhoon structure as revealed by aircraft reconnaissance. Part I: Data analysis and climatology. *Mon. Wea. Rev.* 116, 1032–1043. [http://dx.doi.org/10.1175/1520-0493\(1988\)116,1032:TSARBA.2.0.CO;2](http://dx.doi.org/10.1175/1520-0493(1988)116,1032:TSARBA.2.0.CO;2).
- Weber, H.C., Lok, C.C., Davidson, N.E., Xiao, Y., 2014. Objective estimation of the radius of the outermost closed isobar in tropical cyclones. *Trop. Cyclone Res. Rev.* 3 (1), 1–21. <http://dx.doi.org/10.6057/2014TCRR01.01>.
- Willoughby, H.E., Darling, R.W.R., Rahn, M., 2006. Parametric representation of the primary hurricane vortex. Part II: A new family of sectionally continuous profiles. *Mon. Wea. Rev.* 134, 1102–1120. <http://dx.doi.org/10.1175/MWR3106.1>.
- Willoughby, H.E., Rahan, M.E., 2004. Parametric representation of the primary hurricane vortex. Part I: Observations and evaluation of the Holland (1980) model. *Mon. Wea. Rev.* 132 (12), 3033–3048. <http://dx.doi.org/10.1175/MWR2831.1>.
- Wu, L., Tian, W., Liu, Q., Cao, J., Knaff, J.A., 2015. Implications of the observed relationship between tropical cyclone size and intensity over the western north Pacific. *J. Clim.* 28 (24), 9501–9506. <http://dx.doi.org/10.1175/JCLI-D-15-0628.1>.
- Yu, J., Tan, Z., Wang, Y., 2010. Effects of vertical wind shear on intensity and rainfall asymmetries of strong tropical storm bilis (2006). *Adv. Atmos. Sci.* 27, 552–561. <http://dx.doi.org/10.1007/s00376-009-9030-6>.

4.3 Dataset of outer tropical cyclone size from a radial wind profile

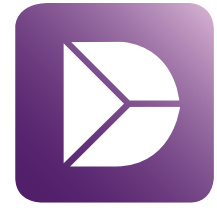
Pérez-Alarcón, A., Sorí, R., Fernández-Alvarez, J.C., Nieto, R., Gimeno, L., 2022. Dataset of outer tropical cyclone size from a radial wind profile. Data in Brief 40, 107825. doi:10.1016/j.dib.2022.107825.

Table 4.3: Summary of the impact and quality of the journal where the second paper that conformed to this thesis was published. The data correspond to the year 2021 (last year available at the date of preparation of this document) in the Web of Science (JCR). **IF:** Impact Factor

Journal	Description	Journal Metrics
Data in Brief	It is a multidisciplinary, open access, and peer-reviewed journal, which publishes short articles that describe and provide access to research data.	IF: -, 5-year IF: - Ranking: 70 out of 135 (Q3) Multidisciplinary

Contents lists available at [ScienceDirect](https://www.sciencedirect.com)

Data in Brief

journal homepage: www.elsevier.com/locate/dib

Data Article

Dataset of outer tropical cyclone size from a radial wind profile



Albenis Pérez-Alarcón^{a,b,*}, Rogert Sorí^{a,c},
 José C. Fernández-Alvarez^{a,b}, Raquel Nieto^a, Luis Gimeno^a

^a Centro de Investigación Mariña, Environmental Physics Laboratory (EPhysLab), Universidade de Vigo, Campus As Lagoas s/n, Ourense 32004, Spain

^b Departamento de Meteorología, Instituto Superior de Tecnologías y Ciencias Aplicadas, Universidad de La Habana, La Habana 10400, Cuba.

^c Instituto Dom Luiz, Faculdade de Ciências da Universidade de Lisboa, Campo Grande 1749-016, Portugal

ARTICLE INFO

Article history:

Received 25 August 2021

Accepted 10 January 2022

Available online 13 January 2022

Keywords:

Tropical cyclone

Tropical cyclones database

Tropical cyclone climatology

Tropical cyclones size

ABSTRACT

Pérez-Alarcón et al. [1] developed a comparative climatology of the outer radius of tropical cyclones (TCs) from several radial wind profiles. They showed that the Willoughby et al. (2006) (W06) profile can be used to reproduce the TC tangential wind speed; thus, this profile is skilful for estimating the TC outer radius. Here, we present a database of TC sizes estimated from the W06 radial wind profile in each cyclogenetic basin worldwide. The database incorporates the critical wind radii, where the tangential wind speed is approximately 17.5 ms^{-1} (R_{34}), 26 ms^{-1} (R_{50}), 33 ms^{-1} (R_{64}), and 51 ms^{-1} (R_{100}), estimated by the W06 profile. The database has a comma-delimited text format with six-hour information on the location, maximum wind speed, central pressure, and the different TC metrics mentioned above. This database has a similar structure to that of the Atlantic Hurricane Database (HURDAT2) of the National Hurricane Center. The database presented here is applicable to studies on TC storm surge risks as well as to the determination of the sources and sinks of atmospheric moisture related to tropical cyclogenesis processes.

DOI of original article: [10.1016/j.wace.2021.100366](https://doi.org/10.1016/j.wace.2021.100366)

* Corresponding author at: Centro de Investigación Mariña, Environmental Physics Laboratory (EPhysLab), Universidade de Vigo, Campus As Lagoas s/n, Ourense 32004, Spain.

E-mail address: albenis.perez.alarcon@uvigo.es (A. Pérez-Alarcón).

Social media: (A. Pérez-Alarcón), (J.C. Fernández-Alvarez), (R. Nieto)

<https://doi.org/10.1016/j.dib.2022.107825>

2352-3409/© 2022 The Author(s). Published by Elsevier Inc. This is an open access article under the CC BY-NC-ND license (<http://creativecommons.org/licenses/by-nc-nd/4.0/>)

Specifications Table

Subject	Climatology
Specific subject area	Tropical cyclones size climatology
Type of data	Text
How data were acquired	The data were acquired by processing the best-track databases of the National Hurricane Center and the Joint Typhoon Warning Center, which are freely available.
Data format	Secondary Data (Analyzed)
Parameters for data collection	For database preparation, the entries with missing maximum wind speed values in the best-track database records were excluded.
Description of data collection	The database was created from the Willoughby et al. [2] radial wind profile with known tropical cyclone position and intensity in each best-track record.
Data source location	Institution: Environmental Physics Laboratory, Faculty of Science, University of Vigo, City/Town/Region: Ourense Country: Spain Primary data sources: The National Hurricane Center tropical cyclones best track archive (HURDAT2, https://www.nhc.noaa.gov/data/#hurdat) and the Joint Typhoon Warning Center best track tropical cyclones records (https://www.metoc.navy.mil/jtwc/jtwc.html?best-tracks)
Data accessibility	With the article and at http://doi.org/10.17632/8997r89fbf.1
Related research article	A. Pérez-Alarcón, R. Sorí, J. C. Fernández-Alvarez, R. Nieto, L. Gimeno, Comparative climatology of outer tropical cyclone size using radial wind profiles. <i>Weather and Climate Extremes</i> . 33 (2021), 100366. 10.1016/j.wace.2021.100366

Value of the Data

- This dataset provides climatology information on the tropical cyclone sizes over each cyclogenetic basin worldwide since the beginning of cyclone records, and this information is useful for different applications.
- Researchers could use this dataset for many applications, including different risk analyses.
- Researchers could use this dataset to analyse the rain rate radial distribution around the TC centre to map potential storm surge risk impacts on the global population and to determine sources and sinks of atmospheric moisture related to tropical cyclone genesis as well as to intensification and weakening mechanisms.
- Tropical cyclone forecasters could use the methodology used to generate this database to quickly determine the TC size using the position and intensity predicted by numerical weather forecast models and thus make their tropical cyclone warnings applicable to a larger population exposed to the possible impact of the storm.
- Machine learning researchers can use the dataset for benchmarking the performance of different methodologies to obtain tropical cyclone sizes.

1. Data Description

The size of tropical cyclones (TCs), as well as the TC intensity, is a very important structural parameter. Determining the TC size climatology is essential for adopting strategies that minimize the damage caused by these storms.

The TC size database presented here has a comma-delimited text format with six-hourly information on the date, location, maximum wind speed (kmh^{-1}), minimum central pressure (hPa), estimated radius of maximum wind speed (km), estimated R_{34} , R_{50} , R_{64} , and R_{199} critical wind radii, and outer radius (km) calculated by the Willoughby et al. [2] radial wind profile of all known TCs and subtropical cyclones. The TCSIZE database format is similar to that described by Landsea and Franklin [3] for the HURDAT2 database. The supplementary files contain the full TCSIZE database for each TC basin, which also can be download from the Mendeley Data repository [4]. Below is an example of the TCSIZE database entries, with each part defined.

```
AL112017, IRMA, 66,
20170902, 1800, 18.7N, 44.1W, 175.7, 973, 29.99, 237.0, 145.5, 93.00, -9999, 786.00
20170903, 0000, 18.5N, 45.5W, 175.7, 973, 29.89, 236.5, 145.0, 93.00, -9999, 784.00
20170903, 0600, 18.2N, 46.7W, 175.7, 973, 29.73, 235.0, 144.0, 92.50, -9999, 781.50
20170903, 1200, 17.9N, 47.9W, 185.0, 969, 28.43, 237.0, 148.5, 97.50, -9999, 771.00
20170903, 1800, 17.6N, 49.2W, 185.0, 965, 28.29, 236.0, 147.5, 97.00, -9999, 768.50
20170904, 0000, 17.3N, 50.4W, 185.0, 959, 28.14, 235.0, 146.5, 96.00, -9999, 766.00
20170904, 0600, 17.0N, 51.5W, 194.2, 952, 26.91, 236.0, 150.0, 100.5, 32.50, 754.00
20170904, 1200, 16.8N, 52.6W, 203.5, 945, 25.77, 236.5, 152.5, 104.0, 37.00, 742.00
20170904, 1800, 16.7N, 53.9W, 212.7, 944, 24.72, 236.5, 154.5, 107.0, 41.00, 730.50
20170905, 0000, 16.6N, 55.1W, 231.2, 943, 22.79, 235.0, 157.5, 112.0, 48.00, 705.50
20170905, 0600, 16.6N, 56.4W, 249.7, 933, 21.04, 232.0, 158.5, 115.5, 53.50, 678.50
20170905, 1200, 16.7N, 57.8W, 277.5, 929, 18.70, 223.5, 156.5, 117.5, 59.50, 635.50
20170905, 1800, 16.9N, 59.2W, 286.7, 926, 18.04, 221.0, 156.0, 118.0, 61.00, 622.00
20170906, 0000, 17.3N, 60.6W, 286.7, 915, 18.16, 222.5, 157.0, 118.5, 61.50, 625.50
20170906, 0545, 17.7N, 61.8W, 286.7, 914, 18.28, 224.0, 158.0, 119.5, 62.00, 629.00
...
```

The TCSIZE database contains two line types. The first type is the heading with information about the basin, the number, and the year of TC genesis, and the second type contains information on the different parameters of the TC. The first line has the following format:

```
AL112017, IRMA, 66,
```

The first two spaces correspond to the basin identifier (**AL**: North Atlantic, **EP**: East Pacific, **CP**: Central Pacific, **WP**: Western North Pacific, **IO**: North Indian Ocean, **SI**: South Indian Ocean, and **SP**: South Pacific Ocean). The third and fourth characters refer to the Automated Tropical Cyclone Forecast (ATCF, Sampson and Schrader [5]) TC number. Characters 5-8 before the first comma represent the year. The characters between the first and the second commas refer to the TC name. The TC entry number in the database appears after the second comma. The rest of the lines contain the data information for each TC. These have the following format:

```
20170905, 0000, 16.6N, 55.1W, 231.2, 943, 22.79, 235.0, 157.5, 112.0, 48.00, 705.50
```

The element in the first column represents the date in the yyyyddmm (20170905) format. In the second column, the UTC time of the report appears in the hhmm (0000) format, generally coinciding with the synoptic time, although non-synoptic times are found that indicate either TC landfall or the peak maximum intensity. The third column contains the latitude (16.6N), specifying the hemisphere (**N**: Northern Hemisphere and **S**: Southern Hemisphere), and similarly, the fourth column represents the longitude (55.1W) (**W**: Western Hemisphere and **E**: Eastern Hemisphere). The fifth and sixth columns contain the maximum wind speed in kmh^{-1} (231.1 kmh^{-1}) and the minimum central pressure in hPa (943 hPa), respectively, while the seventh column records the estimated radius of maximum wind speed in km (26.91 km). The eighth to the twelfth columns contain the estimated R_{34} , R_{50} , R_{64} , and R_{100} critical wind radii (in km), respectively. The last column contains the TC outer radius in km (754.00 km) estimated from the radial wind profile of Willoughby et al. [2]. Missing values are given by -9999.

The global mean size of tropical cyclones from the database presented in this article is 755.2 km with a standard deviation of 109.5 km and a 95% confidence interval of [754.4, 755.7] km. The interpercentile range (25th–95th percentiles) is from 689.0 to 933.0 km. The median storm size is largest in the North Atlantic and smallest in the North Indian Ocean basins. The

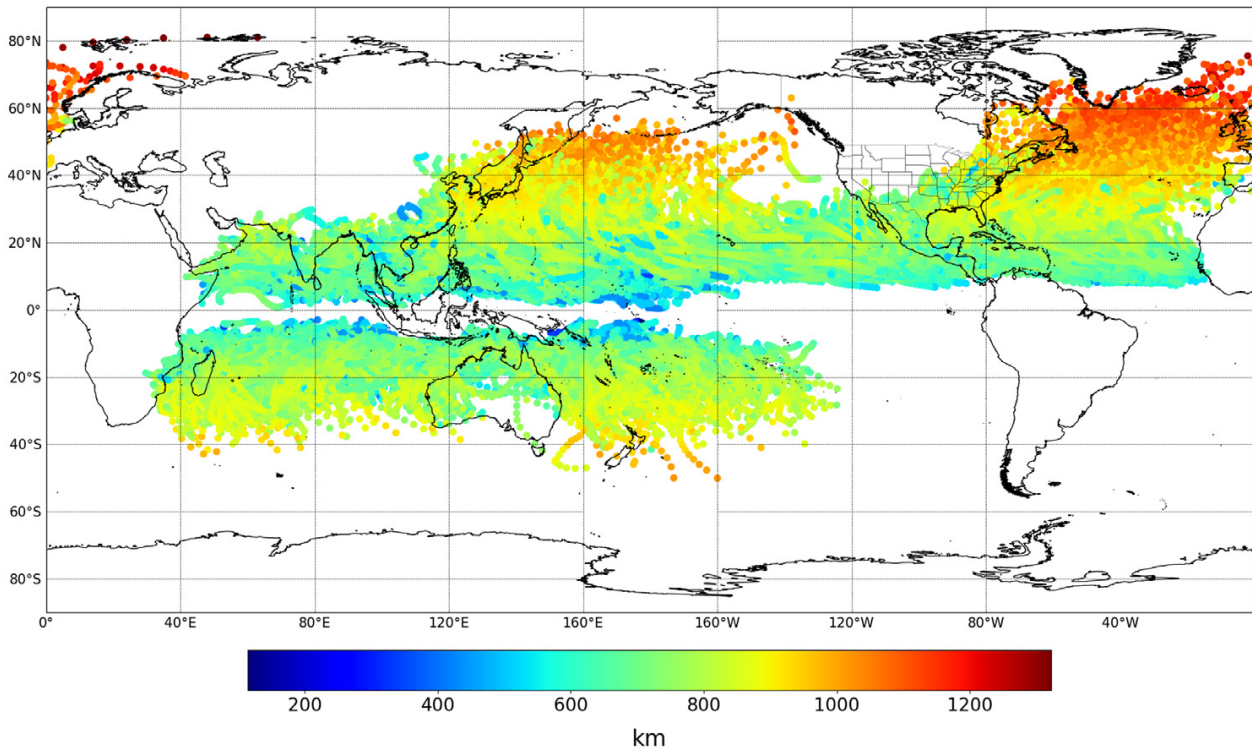


Fig. 1. Spatial distribution map of the outer tropical cyclone sizes estimated using the Willoughby et al. [2] radial wind profile.

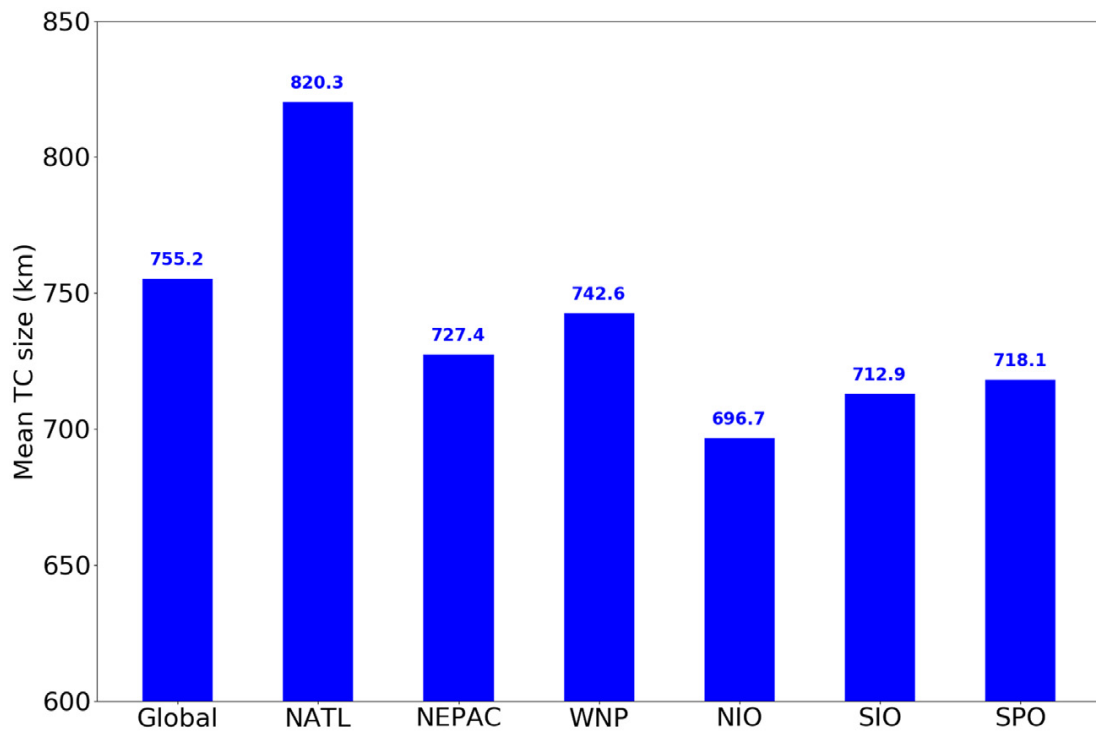


Fig. 2. Mean outer TC size (km) in each basin: North Atlantic (NATL), Central and East Pacific (NEPAC) Western North Pacific (WNP), North Indian Ocean (NIO), South Indian Ocean (SIO), and South Pacific Ocean (SPO).

Western North Pacific exhibits the largest variance in size of any basin, while the largest coefficients of variation are found in the basins of the Southern Hemisphere. Fig. 1 shows the global distribution of the TC sizes, whereas Fig. 2 shows a comparison of the mean TC size in each basin.

2. Experimental Design, Materials and Methods

The database of the TC sizes in each cyclogenetic basin worldwide was obtained from the Willoughby et al. [2] radial wind profile. This wind profile is given as follows:

$$V = \begin{cases} V_{max} \left(\frac{r}{r_m} \right)^n & r \leq R_1 \\ V_i (1 - w_1) + V_0 w_1 & R_1 \leq r \leq R_2 \\ V_{max} \left[(1 - A) e^{-\frac{(r-r_m)}{X_1}} + A e^{-\frac{(r-r_m)}{X_2}} \right] & r > R_2 \end{cases} \quad (1)$$

where V is the tangential wind speed at a distance r from the centre, V_{max} is the maximum wind speed, r_m is the radius of maximum wind speed, A , X_1 , and X_2 are parameters associated with the TC intensity, V_i and V_0 are the tangential wind speeds at radii of R_1 and R_2 , respectively, and w is a weight function (see Willoughby et al. [2]). The radius of maximum wind speed was estimated following Willoughby et al. [2] for the North Atlantic (NATL) and Central and East Pacific (NEPAC) basins, whereas for the Western North Pacific (WNP), North Indian Ocean (NIO), South Indian Ocean (SIO), and South Pacific Ocean (SPO) basins, it was estimated following Tan and Fang [6].

Determination of the radial wind profile requires the position and intensity of the storm. This information, for the NATL and NEPAC basins, was extracted from the National Hurricane Center (NHC) HURDAT2 database [2], which is freely available at <https://www.nhc.noaa.gov/data/#hurdat>, whereas for the rest of the cyclogenetic basins, this information was taken from the Joint Typhoon Warning Center (JTWC) best-track databases available at <https://www.metoc.navy.mil/jtwc/jtwc.html?best-tracks>. The NATL best-track contains information from 1851 to 2020; NEPAC, from 1949 to 2020; and the rest of the basins, from 1945 to 2019.

Similar to the procedure described by Knaff et al. [7], a tangential wind speed of 2 ms^{-1} was assumed as the threshold to define the TC size. Thus, from the Willoughby et al. [2] radial wind profile, the radial distance from the centre where the tangential wind speed was equal to or less than 2 ms^{-1} was considered as the tropical cyclone outer radius. A similar procedure was applied to determine the R_{34} , R_{50} , R_{64} , and R_{100} critical wind radii.

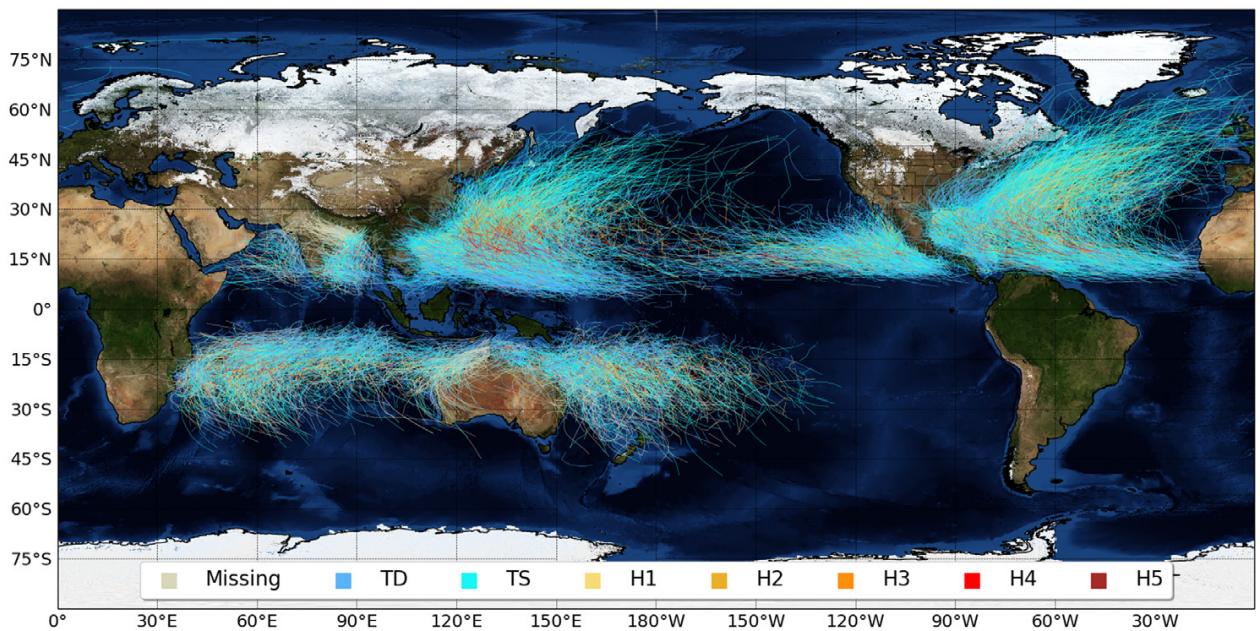


Fig. 3. Global tropical cyclone tracks by ocean basin based on historical TC best track datasets. Tropical cyclone intensities are displayed with seven scales according to the Saffir-Simpson scale: TD - Tropical Depression, TS - Tropical Storm, H1 - Hurricane category 1, H2 - Hurricane category 2, H3 - Hurricane category 3, H4 - Hurricane category 4, and H5 - Hurricane category 5.

During processing of the best-track database records, missing values of the maximum wind speed were disregarded; however, the records encoded with -9999 were incorporated into the TC size database presented in this article, with the intention of keeping all records of each tropical cyclone in each basin.

Fig. 3 shows the trajectories of all tropical and subtropical cyclones in each basin since the beginning of the records.

Ethics Statements

Not applicable

Declaration of Competing Interest

The authors declare that they have no known competing financial interests or personal relationships which have, or could be perceived to have, influenced the work reported in this article.

CRediT Author Statement

Albenis Pérez-Alarcón: Conceptualization, Data curation, Methodology, Formal analysis, Software, Investigation, Validation, Visualization, Writing – original draft, Writing – review & editing; **Rogert Sorí:** Conceptualization, Methodology, Formal analysis, Investigation, Validation, Writing – review & editing; **José C. Fernández-Alvarez:** Conceptualization, Data curation, Methodology, Investigation, Validation, Visualization, Writing – review & editing; **Raquel Nieto:** Methodology, Validation, Writing – review & editing, Supervision; **Luis Gimeno:** Methodology, Validation, Writing – review & editing, Supervision.

Acknowledgments

A.P-A acknowledges a PhD grant from the Universidade de Vigo. J.C.F-A and R.S acknowledge the support from the Xunta de Galicia (Galician Regional Government) under the Grants no. ED481A-2020/193 and ED481B 2019/070, respectively. The authors acknowledge NHC and JTWC for freely provide the best track archives. We acknowledge the funding for open access from the Universidade de Vigo/Consortio Interuniversitario do Sistema Universitario de Galicia (CISUG) and the partial support from the Xunta de Galicia under the Project ED431C 2021/44. The authors also thank to anonymous reviewers for their comments and suggestions to improve the manuscript.

Funding

This work is supported by the LAGRIMA project (Grant no. RTI2018-095772-B-I00) funded by the Ministerio de Ciencia, Innovación y Universidades, Spain. Partial support was also obtained from the Xunta de Galicia under the Project ED431C 2021/44 (Programa de Consolidación e Estructuración de Unidades de Investigación Competitivas (Grupos de Referencia Competitiva) and Consellería de Cultura, Educación e Universidade).

Supplementary Materials

Supplementary material associated with this article can be found in the online version at doi:[10.1016/j.dib.2022.107825](https://doi.org/10.1016/j.dib.2022.107825).

References

- [1] A. Pérez-Alarcón, R. Sorí, J.C. Fernández-Alvarez, R. Nieto, L. Gimeno, Comparative climatology of outer tropical cyclone size using radial wind profiles, *Weather Clim. Extrem.* 33 (2021) 100366, doi:[10.1016/j.wace.2021.100366](https://doi.org/10.1016/j.wace.2021.100366).
- [2] H.E. Willoughby, R.W.R. Darling, M. Rahn, Parametric representation of the primary hurricane vortex. Part II: A new family of sectionally continuous profiles, *Mon. Weather Rev.* 134 (2006) 1102–1120, doi:[10.1175/MWR3106.1](https://doi.org/10.1175/MWR3106.1).
- [3] C.W. Landsea, J.L. Franklin, Atlantic hurricane database uncertainty and presentation of a new database format, *Mon. Weather Rev.* 141 (2013) 3576–3592, doi:[10.1175/MWR-D-12-00254.1](https://doi.org/10.1175/MWR-D-12-00254.1).
- [4] A. Pérez-Alarcón, R. Sorí, J.C. Fernández-Alvarez, R. Nieto, L. Gimeno, Dataset of outer radius of tropical cyclone from a radial wind profile, *Mendeley Data V1* (2021), doi:[10.17632/8997r89fbf.1](https://doi.org/10.17632/8997r89fbf.1).
- [5] C.R. Sampson, A.J. Schrader, The automated tropical cyclone forecasting system (version 3.2), *Bull. Am. Meteorol. Soc.* 81 (2000) 1231–1240, doi:[10.1175/1520-0477\(2000\)081\(1231:TATCFS\)2.3.CO;2](https://doi.org/10.1175/1520-0477(2000)081(1231:TATCFS)2.3.CO;2).
- [6] C. Tan, W. Fang, Mapping the wind hazard of global tropical cyclones with parametric wind field models by considering the effects of local factors, *Int. J. Disaster Risk Sci.* 9 (2018) 86–99, doi:[10.1007/s13753-018-0161-1](https://doi.org/10.1007/s13753-018-0161-1).
- [7] J. Knaff, S.P. Longmore, D.A. Molenaar, An objective satellite-based tropical cyclone size climatology, *J. Clim.* 27 (2014) 455–476, doi:[10.1175/JCLI-D-15-0610.1](https://doi.org/10.1175/JCLI-D-15-0610.1).

4.4 Where does the moisture for North Atlantic tropical cyclones come from?

Pérez-Alarcón, A., Sorí, R., Fernández-Alvarez, J.C., Nieto, R., Gimeno, L., 2022. Where does the moisture for North Atlantic tropical cyclones come from? *Journal of Hydrometeorology* 23(3), 457–472. doi:10.1175/JHM-D-21-0117.1. ©American Meteorological Society. Used with permission.

Table 4.4: Summary of the impact and quality of the journal where the third paper that conformed to this thesis was published. The data correspond to the year 2021 (last year available at the date of preparation of this document) in the Web of Science (JCR). **IF:** Impact Factor

Journal	Description	Journal Metrics
Journal of Hydrometeorology	It publishes research on modelling, observing and forecasting processes related to fluxes and storage of water and energy including interactions with the boundary layer.	IF: 4.871, 5-year IF: 5.376 Ranking: 30 out of 108 (Q2) in Meteorology & Atmospheric Sciences

Where Does the Moisture for North Atlantic Tropical Cyclones Come From?

ALBENIS PÉREZ-ALARCÓN,^{a,b} ROBERT SORÍ,^{a,c} JOSÉ C. FERNÁNDEZ-ALVAREZ,^{a,b} RAQUEL NIETO,^a
AND LUIS GIMENO^a

^a *Environmental Physics Laboratory, Centro de Investigación Mariña, Universidade de Vigo, Ourense, Spain*

^b *Departamento de Meteorología, Instituto Superior de Tecnologías y Ciencias Aplicadas, Universidad de La Habana, Havana, Cuba*

^c *Instituto Dom Luiz, Faculdade de Ciências, Universidade de Lisboa, Campo Grande, Portugal*

(Manuscript received 17 June 2021, in final form 27 November 2021)

ABSTRACT: In this study, we identified the origin of the moisture associated with the tropical cyclones' (TCs) precipitation in the North Atlantic Ocean basin during their three well-differentiated life stages between 1980 and 2018. The HURDAT2 database was used to detect the location of 598 TCs during their genesis, maximum intensification peak, and dissipation phases. The global outputs of the Lagrangian FLEXPART model were then used to determine the moisture sources. Using a *k*-means cluster analysis technique, seven different regions were identified as the most common locations for the genesis and maximum intensity of the TC phases, while six regions were found for the dissipation points. Our results showed that the origin of moisture precipitating was not entirely local over the areas of TC occurrence. The North Atlantic Ocean to the north of the intertropical convergence zone at 10°N (NATL)—especially from tropical latitudes, the Caribbean Sea, and the Gulf of Mexico—provides most of the moisture for TCs (~87%). The Atlantic Ocean basin southward of the ITCZ (SATL) played a nonnegligible role (~11%), with its contribution being most pronounced during the TC genesis phase, while the eastern tropical Pacific Ocean made the smallest contribution (~2%). The moisture supported by TCs varied depending on their category, being higher for hurricanes than for major hurricanes or tropical storms. Additionally, the approach permitted the estimation of the mean residence time of the water vapor uptake that produces the precipitation during TC activity, which ranged between 2.6 and 2.9 days.

SIGNIFICANCE STATEMENT: Atmospheric moisture transport plays an important role in the genesis and intensification of tropical cyclones (TCs). In this study, we investigated the moisture source for the genesis, intensification, and dissipation of TCs in the North Atlantic Ocean basin using a Lagrangian approach. This model allowed us to track air masses backward in time from the target area to identify regions where air masses experienced an uptake of moisture prior to reaching the area of interest. The sources were identified individually for each TC, and the results were then combined to provide a broad general picture with some surprising outstanding results, such as the role of the North and South Atlantic and the eastern tropical Pacific as important moisture sources during the different TCs phases and intensities.

KEYWORDS: Tropical cyclones; Climatology; Moisture/moisture budget

1. Introduction

Tropical cyclones (TCs) are atmospheric phenomena that are most likely to cause natural disasters in terms of heavy rainfall, flash flooding, storm surges, and strong winds (Ankur et al. 2020). During the cyclonic season, many disturbances travel over tropical oceans in each cyclogenetic basin; however, very few become TCs. This occurs because TCs form over warm regions in tropical oceans and strengthen when environmental conditions are favorable (Ren et al. 2020). According to Gray (1968), for the formation of a TC, the sea surface temperature (SST) must be higher than 26.5°C at an ocean depth of approximately 50 m (Montgomery 2016). In addition, there must be (i) sufficient atmospheric instability to favor the formation of thunderstorms to release latent heat; (ii) a high water vapor content in the layers of the middle atmosphere; (iii) the presence of an atmospheric disturbance generally above 5° of latitude (north or south), which is

obtained from Earth's spin (a background rotation that can be later amplified); and (iv) low vertical wind shear from the surface to the tropopause.

Gray (1968) defined a TC formation parameter as the product of thermodynamic and dynamic terms. The effects of SSTs and humidity at the upper midlevel were included in the thermodynamic term, while the effects of vertical shear and low-level vorticity were included in the dynamic term. The results of McBride (1995) revealed a significant correlation between the climatological values of this parameter and the global regions of TC formation. Another parameter for estimating the genesis of TCs in the North Atlantic Ocean basin was developed by DeMaria et al. (2001). Similar to the statements by Gray (1968), this genesis parameter combines thermodynamic and dynamic factors using a pentad running mean of the vertical shear, vertical instability, and midlevel moisture available in the atmosphere.

Atmospheric moisture transport and its convergence play an important role in the latent heat distribution of TCs (Huang et al. 2014; Makarieva et al. 2017). Thus, one of the key aspects for understanding the contribution of dynamic mechanisms,

Corresponding author: Albenis Pérez-Alarcón, albenis.perez.alarcon@uvigo.es

DOI: 10.1175/JHM-D-21-0117.1

© 2022 American Meteorological Society. For information regarding reuse of this content and general copyright information, consult the [AMS Copyright Policy](https://www.ametsoc.org/PUBSReuseLicenses) (www.ametsoc.org/PUBSReuseLicenses).

air–sea interactions, and large-scale process interactions in the genesis and development of TCs is the water circulation and budgets inside and outside of a TC system (Fujiwara et al. 2017). Numerical sensitivity experiments performed by Yoshida et al. (2017) showed that despite the existence of medium- and low-level vortices, the disturbance did not become a TC because of the low water vapor content. Furthermore, through a regional cloud resolution model and Lagrange diagnostics, Fujiwara et al. (2017) found a positive feedback between the TC intensity in the western North Pacific basin and the moisture transported from the Indian Ocean, South China Sea, and Philippine Sea. Numerical simulations using the Weather Research and Forecasting (WRF) Model also revealed that environmental moisture modifications had insignificant impacts on a storm unless it changed moisture transport to move into it (Wu et al. 2015). Braun (2006) and Yang et al. (2011) evaluated the water budgets in the inner cores of TCs based on high-resolution simulations with a horizontal grid size of 2 km and concluded that the underlying ocean water vapor was relatively small in the inner core area compared to the humidity gain due to the horizontal convergence of water vapor. Several research studies have been conducted regarding global and regional water vapor transport, as well as the relationship between moisture transport and TCs (DiMego and Bosart 1982; Kung and Zhao 2007; Boutle et al. 2011; Wu et al. 2015).

The main fuel for TCs is the release of latent heat derived from the condensation of water vapor (Fujiwara et al. 2017). Therefore, water vapor from the evaporation of surface ocean water due to high SSTs along with moisture transport via local and global patterns of atmospheric circulation favors the genesis and intensification of TCs. Moisture sources can be identified by analyzing the particle paths through the application of different techniques. Both Lagrangian and Eulerian methods can be used with a good approximation to study the moisture source–sink relationship and its influence on atmospheric processes (Bosilovich and Schubert 2002; de Leeuw et al. 2017; Guo et al. 2018; van der Ent and Tuinenburg 2017). The Lagrangian approach is currently considered to be one of the most suitable methods for the identification and evaluation of moisture sources because it also permits the computation of the amount of moisture uptake (Gimeno et al. 2012).

Climatological statistics show that the highest number of TC genesis in the North Atlantic Ocean basin occurs between mid-August and mid-November, in which TCs generally form from tropical waves between the West Africa coast and the Lesser Antilles Arc (DeMaria et al. 2001; Neumann 1993). According to DeMaria et al. (2001), this region is the source of 40% of TC genesis in the North Atlantic Ocean basin, of which 60% become major hurricanes. Pazos and Gimeno (2017) used a Lagrangian approach to identify the moisture uptake by air masses before reaching the region of the genesis of 110 TCs within a predefined region between 15°–45°W and 8°–20°N from 1979 to 2012. They identified the areas from which the moisture uptake exceeded the climatological average, which were the central and eastern tropical North Atlantic Ocean, the eastern South Atlantic Ocean, and the continental areas of West Africa, and the Sahel. These terrestrial sources involve complex hydroclimatic interactions in

several atmospheric processes at different time scales, such as low-level atmospheric moisture transport and the West African monsoon (Lélé et al. 2015; Redelsperger et al. 2002, 2006). Most recently, Pérez-Alarcón et al. (2021a) improved the findings of Pazos and Gimeno (2017) by considering a variable target region, defined as the area within the TCs outer radius (Pérez-Alarcón et al. 2021b). Although Pazos and Gimeno (2017) and Pérez-Alarcón et al. (2021a) provided new insights into the contribution of atmospheric moisture to the genesis of TCs in the North Atlantic, they did not provide a complete overview of all TC phases over the entire basin. Therefore, no study has identified the source regions of moisture for the different evolution phases of TCs in the North Atlantic Ocean basin. To help fill this knowledge gap, the present study applies a Lagrangian approach to identify the moisture sources precipitating for the area enclosed by the outer radius of the TCs for the three different climatological regions of TC genesis, maximum intensity, and dissipation.

The paper is organized as follows. Section 2 describes the data and methods, including information on the data sources, cluster analysis technique, and moisture uptake for precipitation computation and identification. The results and discussion are presented in section 3, and a summary is provided in section 4.

2. Materials and methods

a. Data

The positions of TCs in the North Atlantic basin from 1980 to 2018 were extracted from the Atlantic hurricane database (HURDAT2), which is freely provided by the National Hurricane Centre and available online at <https://www.nhc.noaa.gov/data/>. This database is a text format with information every 6 h, including the position, intensity, and critical wind radii in the northeast, southeast, southwest, and northwest quadrants of all tropical and subtropical cyclones originating in the Atlantic basin (Landsea and Franklin 2013).

Global outputs every 6 h from the Flexible Particle dispersion model (FLEXPART) v9.0 (Stohl and James 2004; Stohl et al. 2005) were used to investigate the sources of precipitating moisture for TCs. The model is executed for the period from 1980 to 2018 by assuming that the atmosphere was homogeneously divided into approximately 2.0 million uniformly distributed particles of constant mass. The trajectories of these particles are calculated using a 3D wind field (zonal, meridional, and vertical components). In the simulation, FLEXPART model is fed by the global reanalysis ERA-Interim dataset from the European Centre for Medium-Range Weather Forecasts (Dee et al. 2011; ECMWF), using the available data at 6-h intervals with a horizontal resolution of 1° on 60 vertical levels from 0.1 to 1000 hPa. The model implements several parameterizations, such as subgrid-scale atmospheric motions unresolved by meteorological input data (Stohl et al. 2005).

Additionally, ERA-Interim reanalysis was used to compute the vertically integrated moisture flux (VIMF) in a horizontal grid spacing of 1.0° latitude × longitude every 6 h (from the

vertically integrated northward and eastward moisture flux at 0000, 0600, 1200, and 1800 UTC).

b. Methodology

1) CLUSTER ANALYSIS

A k -means (MacQueen 1967) cluster analysis was performed using information from the HURDAT2 database for the genesis, maximum intensity peak, and dissipation point. The k -means technique is a particular case of a normal mixture model with an estimation of the mixtures by maximum likelihood (Morissette and Chartier 2013). To determine the optimum number of clusters, we applied the silhouette coefficient. This technique is based on a full pairwise distance matrix for all data. For a single data point X_i , the silhouette value $s(i)$ is calculated using Eq. (1):

$$s(i) = \frac{b(i) - a(i)}{\max\{a(i), b(i)\}}, \quad (1)$$

where $a(i)$ is the distance of the cluster of X_i , which is defined as the mean distance of X_i from all other data points in its own cluster, and $b(i)$ is the distance between X_i and its closest neighboring cluster, which is defined as the mean distance of X_i from all data points in its closest neighboring cluster (Wang et al. 2017). These techniques were previously applied by Corporal-Lodango et al. (2014) for the classification of TC genesis locations, tracks, and decay locations in the North Atlantic basin.

2) COMPUTATION OF MOISTURE SOURCES

To investigate the moisture sources that contribute precipitation for TC genesis, intensification and dissipation phases, a Lagrangian approach based on the global outputs from FLEX-PART v9.0 (Stohl and James 2004; Stohl et al. 2005) was used. This technique of diagnostic or similar has been successfully used in numerous studies to identify the origin of global or regional continental precipitation (Gimeno et al. 2010, 2012, 2020). In particular, the approach has also been used to identify moisture sources associated with meteorological systems, such as subtropical cyclogenesis over the southwestern Atlantic Ocean (Gozzo et al. 2017) and extratropical cyclones (Brimelow and Reuter 2008; Liberato et al. 2012; Jana et al. 2018; Cloux et al. 2021; Zhao et al. 2021). Further details of the advantages, disadvantages, uncertainties, limitations, and significance of this methodology are discussed in Gimeno et al. (2012).

The humidity budget of an air parcel can be modified by evaporation and precipitation as the air mass moves throughout the atmosphere. According to Stohl and James (2004), along each particle pathway following a Lagrangian approach, the moisture changes in an atmospheric particle are controlled by gains, through evaporation from the environment (e), or losses, through precipitation (p), of specific humidity (q),

$$m \frac{dq}{dt} \approx m \left(\frac{\Delta q}{\Delta t} \right) = (e - p), \quad (2)$$

where m is the mass of each parcel, assumed to be constant. The disadvantage of assuming a constant parcel mass was

eliminated by considering multiple parcels (Stohl and James 2004; Stohl et al. 2005).

To identify the sources of the precipitating moisture for TCs, and to estimate the time interval before the uptake and the final precipitation [the lifetime known as backward transit time (BTT) or the mean water vapor residence time (WVRT); Gimeno et al. 2021], during the genesis, peak of maximum intensification, and dissipation stages we procedure as described below.

In this study, we are interested on the moisture sources associated with TCs precipitation. Therefore, we considered only precipitant particles inside the area enclosed by the outer radius of the TCs. The criteria used is the same as in Läderach and Sodemann (2016), which implies that the specific humidity decreased more than 0.1 g kg^{-1} in the 6 h prior to arrive at the TC radius. These particles were tracked backward in time for a period of up to 10 days, which is considered the mean global residence time of the water vapor in the atmosphere (Numaguti 1999; van der Ent and Tuinenburg 2017). The outer radius for each TC was determined as those where the TC tangential wind speed was less than or equal to 2 m s^{-1} , applying the radial wind profile developed by Willoughby et al. (2006). See Pérez-Alarcón et al. (2021b) for further details on how the TC outer radius was computed.

Along each particle backward trajectory, the moisture changes were estimated using the moisture source diagnostic by Sodemann et al. (2008). By considering that evaporation or precipitation dominates in a particular 6 h interval, the particle can gain moisture in several evaporation locations. Therefore, the moisture loss amount Δq_i due to precipitation in route is proportionally discounted to all previous moisture, according to Eq. (3):

$$\Delta q'_j = \Delta q_j + \Delta q_i \frac{\Delta q_j}{\sum \Delta q_k} \text{ for all } j > i, i \leq k \leq j. \quad (3)$$

Here, i denotes the particle position at time t_i , j represents the position at time $t_{i-6}, t_{i-12}, \dots, t_{\text{end}}$. Note that t_{end} is referred to the particle position 10 days before arrival at the target region. By adding the final moisture changes ($\Delta q'$) of all precipitant particles over the area A , we estimated the total moisture uptake (MU) as

$$\text{MU} = \frac{m \sum_{k=1}^N \Delta q'_k}{A}, \quad (4)$$

where N is the number of particles residing over A .

Due to moisture losses by precipitation along the particle trajectory, the remote moisture sources will contribute less and less to the final precipitation over the target region (Sodemann et al. 2008). Thus, the fractional contribution of each evaporation location to final precipitation can be estimated as

$$f_{c_i} = \frac{\Delta q'_i}{Q}, \quad (5)$$

where i denotes the particle position at time t_i , Q is the specific humidity of the particle when arrival to the target region. By averaging all the fractional contributions over the grid cell

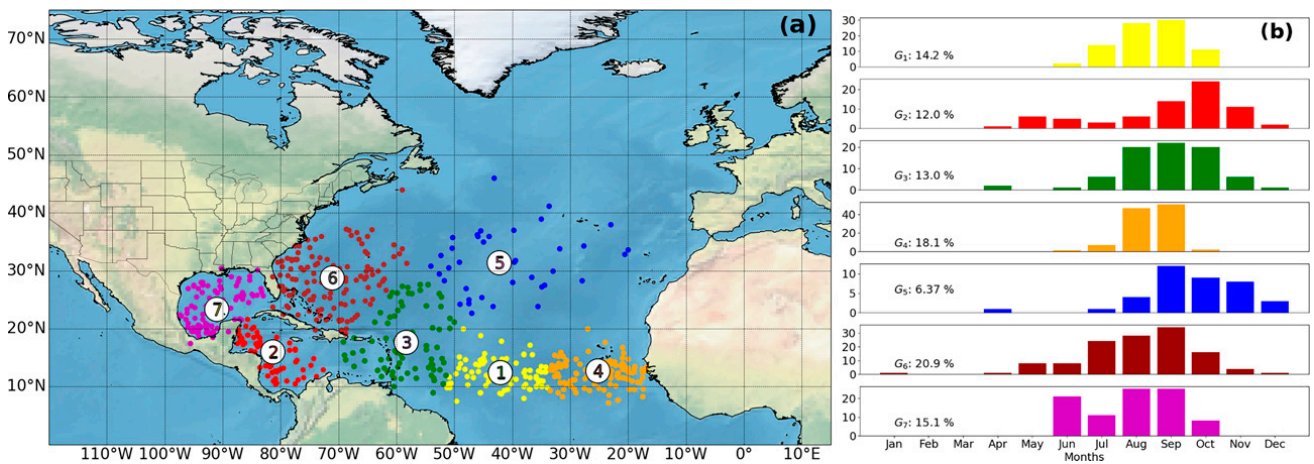


FIG. 1. Genesis of tropical cyclones (TCs) in the North Atlantic Ocean basin during 1980–2018. (a) Each TC genesis position is indicated by a filled point. The colors represent the seven TC genesis clusters calculated by the k -means technique. (b) The number of TCs by month and cluster.

of area A , we computed the moisture source contribution (SC) by grid as follows:

$$SC = \frac{\sum_{k=1}^M fc_k}{M} \times 100, \quad (6)$$

where M represents the number of fractional contributions over the grid cell of area A .

This Lagrangian moisture source diagnostic method provides an estimation of the times and locations where the particles gained moisture. Following Läderach and Sodemann (2016), the WVRT is computed along each particle trajectory from the end to the start point (t_i) according to Eq. (7):

$$WVRT = \sum fc_i \times t_i. \quad (7)$$

The WVRT is given by weighting the time between evaporation and final precipitation; and averaging all the WVRTs estimated the mean is calculated.

3) DETERMINATION OF THE MOISTURE SOURCE WEIGHTED CENTROID

The mean position (latitude and longitude) of each main moisture source for the studied TCs was determined by calculating the weighted centroid coordinates (lat_c , lon_c) of the moisture uptake pattern during TC season, according to Eq. (8):

$$(lat_c, lon_c) = \frac{\sum_{k=1}^N w_k (lat_k, lon_k)}{\sum_{k=1}^N w_k}, \quad \mathbf{w} = \frac{\text{MU}}{\max(\text{MU})}, \quad (8)$$

where N is the number of moisture uptake (MU) grid points, and \mathbf{w} is the weighted vector. As the weights are all positive, the moisture source-weighted centroid is guaranteed to exist inside the moisture uptake pattern.

3. Results and discussion

a. Identification of moisture sources for the TC genesis phase

Seven regions of TC genesis were determined in the North Atlantic basin using the k -means cluster analysis, which agrees with the results of Corporal-Lodangco et al. (2014) and Pérez-Alarcón et al. (2021c). These regions included the tropical central North Atlantic (G1, yellow), the western Caribbean Sea (G2, red), the Lesser Antilles Arc (G3, green), the region near the West Africa coast (G4, orange), the central North Atlantic (G5, blue), the western North Atlantic (G6, brown), and the Gulf of Mexico (G7, purple) (Fig. 1a).

Of the 598 TCs formed in the period 1980–2018, almost 50% (271 TCs) corresponded to clusters 1, 3, and 4, as shown in Fig. 1b. This behavior has been previously attributed to the fact that the TCs that form in these areas originate from tropical waves (DeMaria et al. 2001). In addition, 162 TCs were classified within clusters 2 and 7, which comprised the Caribbean Sea and Gulf of Mexico, respectively, while 163 were observed northward in clusters 5 and 6. Of all the regions, the western North Atlantic (G6) had the highest number of TCs (125, i.e., 20.9% of the total). On a monthly basis for the entire basin, the highest frequency of TC genesis was observed in September (31.5%), followed by August (26.5%). During the remaining months of the hurricane season, the frequency decreased considerably to 15.1% in October, 11.1% in July, 6.4% in June, and 4.9% in November.

Figure 2a shows the climatological pattern of moisture uptake associated with TC genesis in the North Atlantic basin for each cluster. For each TC, the moisture source for precipitation was calculated individually for the area inside the outer radius. In general, easterly winds transport atmospheric humidity along the central Atlantic, and the moisture transport patterns are similar to those of the VIMF. During the most TC active season, the boreal summer, the ITCZ is normally northward positioned over 10°N (Carvalho and Oyama 2013; Pottapinjara et al. 2019), and

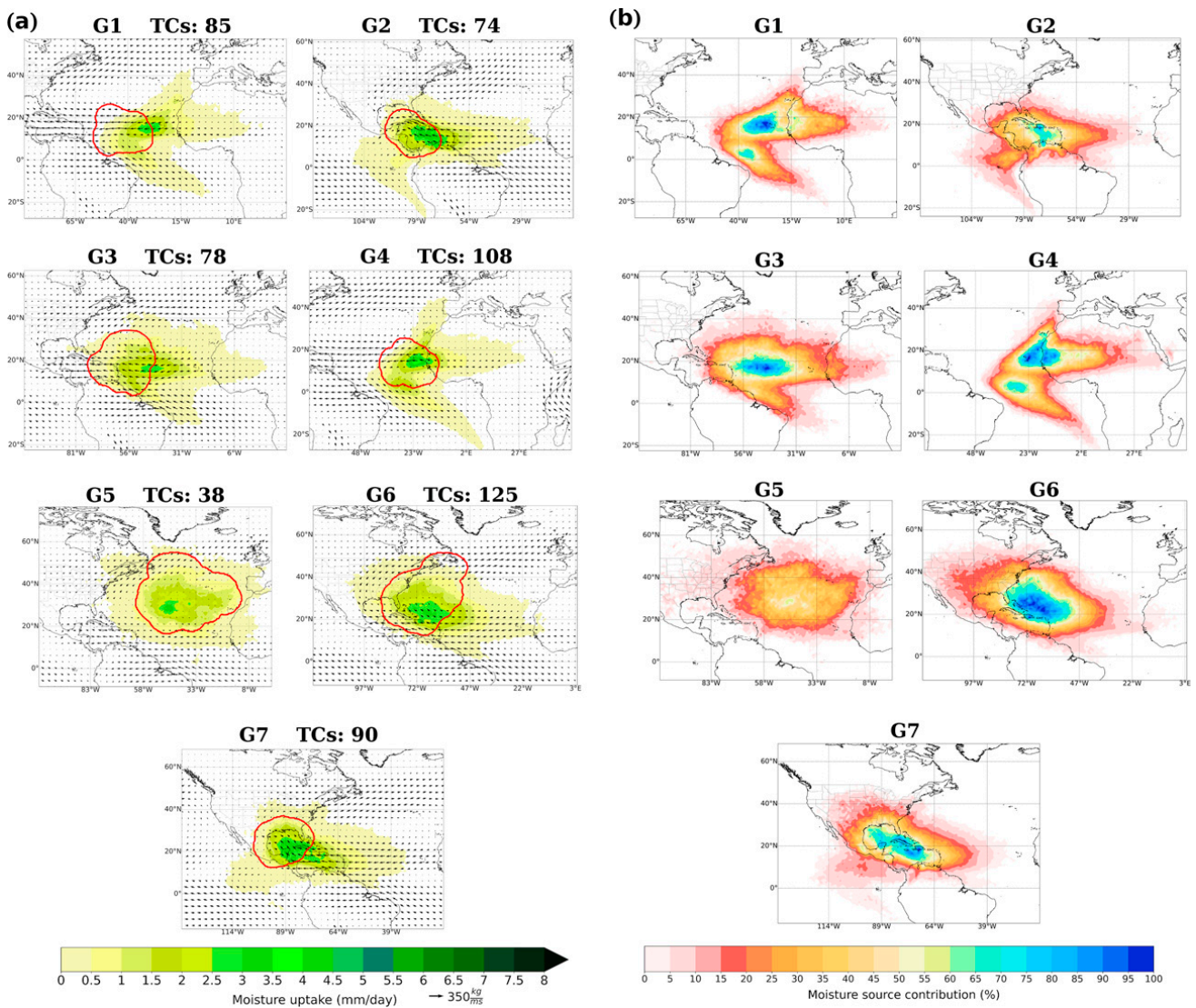


FIG. 2. (a) Climatological patterns of the moisture sources (moisture uptake; greenish colors; mm day^{-1}) for the genesis phase of tropical cyclones (TCs) integrated backward over 10 days, and the vertically integrated moisture flux (VIMF) (arrows; $\text{kg m}^{-2} \text{s}^{-1}$). The red line contours the composite of the outer radius for all TCs in the cluster. (b) Moisture sources contribution composite (percentage). The patterns show the composite for the days of all TCs in each cluster (numbered at the top). Period of study: 1980–2018.

we denote, along the text, the source to the north of the ITCZ as NATL and the source to the south as SATL.

For the TCs positioned over the most southeastward regions (G1 and G4) during their genesis, the moisture came from similar sources. In these two clusters, the moisture uptake pattern showed a north–south spatial configuration on both sides of the intertropical convergence zone (ITCZ), showing a reduction over the ITCZ. The moisture uptake occurred mainly from the NATL source, which extends from the Iberian Peninsula/Atlantic coasts along the West African coast including the band in tropical continental Africa (the Sahel, $\sim 30\%$). The SATL source, from the vicinity of the Gulf of Guinea, supplied up to $\sim 25\%$ – 30% of atmospheric humidity (Fig. 2b). This pattern is similar to that reported by Pazos and Gimeno (2017). Combined with the other preconditions for TC genesis, these areas provide the necessary water vapor to initiate convective activity,

as described by Gray (1968). Furthermore, these results agree with those of Meynadier et al. (2010) and Lélé et al. (2015), who pointed out that West Africa is a moisture source during the summer.

The TCs formed in the G3 region received approximately 75%–80% of moisture from the NATL over the tropical central area, while the remaining amount was supported by the eastern NATL, the Sahel region, and the SALT.

For the TCs formed in the G2 region, the main moisture source was also the NATL, but with its maximum uptake over near the Caribbean Sea, which contributed with $\sim 55\%$ – 70% of moisture; however, TCs in this cluster also took approximately 25% of atmospheric humidity from the eastern tropical Pacific Ocean (ETPac) and northern South America. The area enclosed in the line contouring G2 includes the region of the Central America, for which Durán-Quesada et al. (2017)

found similar sources. In particular, these authors highlighted the role of the ETPac when a reduction in the easterly flow occurs in September–November, which is in concordance with our results showing the maximum activity of TC genesis for G2 (see Fig. 1b).

Moreover, the dominance of the Caribbean Sea region as a source of moisture for G7 was clear, supplying more than ~70% of moist air, whereby the source was induced by the easterlies recurving northward during the summer, accompanied by the Caribbean low-level jet (CLLJ). The climatological moisture uptake pattern suggests that the CLLJ not only acts as a moisture belt, but also acts as a humidity collector that is capable of modulating surface evaporation as a result of its moisture content, which agrees with Wang et al. (2007).

For the TCs located in the large G5 region of TC genesis over the central North Atlantic basin, the moisture mainly came from its own oceanic area (~45%–60%), although some moisture (~10%–15%) was transported along the eastern coast of the United States (see also the pattern of VIMF), possibly modulated by the Gulf Stream, while the coast of West Africa and the Iberian Peninsula provide the remaining ~10%–20%. Furthermore, for G6, the North Atlantic subtropical high (NASH) pressure system circulation acted as the principal mechanism of moisture transport, and the moisture uptake by TCs during genesis phase mainly came from the NATL source (~80%–90%, Fig. 2b), over the northeastern part of the Atlantic warm pool north of the Antilles (Wang et al. 2007).

Figure 3 presents a more complete overview of the moisture sources precipitating for all the clusters, showing the moisture values of the three main moisture sources: two over the Atlantic basin (NATL and SATL) and the ETPac over the Pacific basin. The moisture uptake pattern in the Atlantic Ocean was clearly reduced around at 10°N, where the ITCZ is positioned. Figure 3a clearly shows that the NATL moisture source was the major source of TC genesis. The greatest moisture uptake was found along the belt between 10° and 20°N, stretching from North Africa to Central America, over the main development region (MDR) of the TCs (Gray et al. 1993), indicating the moistening of air parcels by evaporation over the ocean. Therefore, the easterly winds along this same band were the main mechanism of moisture transport for the TC genesis phase in the North Atlantic basin, transporting atmospheric water vapor from the Sahel and eastern tropical North Atlantic basin to the west. Additionally, Fig. 3a reveals the secondary source of moisture to the south of the ITCZ, the SATL, which was associated with the northern branch of the atmospheric circulation corresponding to the South Atlantic subtropical high (SASH) pressure system; the ETPac provided less water vapor to the regions of TC genesis over the region influenced by the Chorro del Occidente Colombiano (“Chocó”) jet (Poveda and Mesa 1999, 2000; Gallego et al. 2019). On average, the NATL source contributed 85.1% of the total moisture that reached the TCs during their genesis phase, in which the major contribution occurred from the tropical North Atlantic, with two marked maximums around 25°W over Madeira archipelago and over the Antilles and the Caribbean Sea, while the SATL and ETPac supplied 12.8% and 2.1%, respectively. Furthermore, the three moisture sources found

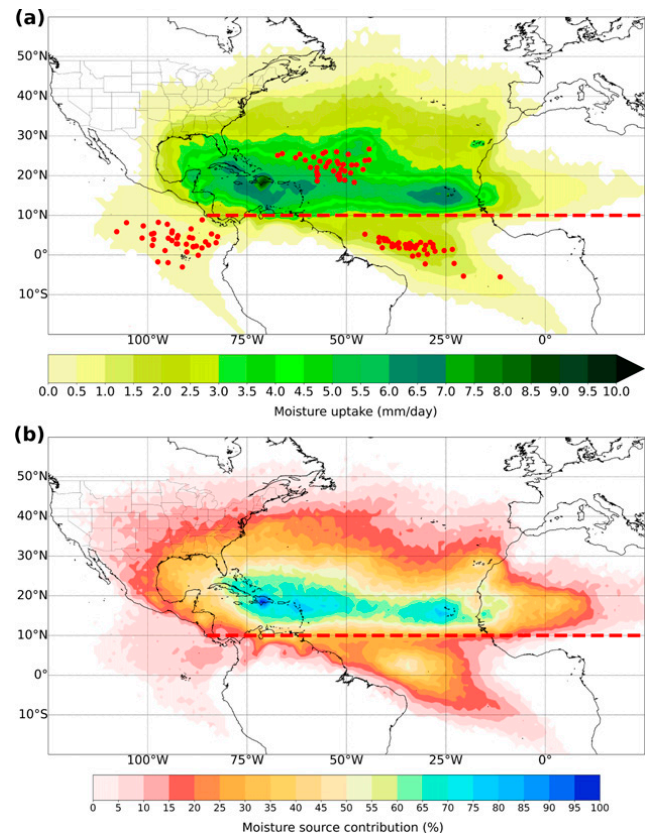


FIG. 3. (a) Climatological pattern of moisture uptake integrated from 1 day to 10 days backward in time from the genesis location of each TC in the entire basin during 1980–2018. The red dots mark the position of the annual moisture source weighted centroid. (b) Moisture sources contribution composite (percentage). The red dashed line indicates the mean annual position of the intertropical convergence zone (ITCZ, ~10°N).

were quasi-permanent in position, as shown the weighted centroids (red dots).

Figure 3b show that the MDR area, as a part of the NATL source, contributed locally with values that reached 60%–80% of the moisture for the TC genesis phase, and that the NATL moisture contribution gradually decreases northward. The SALT moisture contributions reached from 15% to 45%, while the ETPac atmospheric humidity supplied did not exceed 15%.

Our findings also reveal that the mean water vapor residence time (MWVRT) during TC genesis phase ranged from 2.5 to 3.1 days. The highest MWVRT were found over the central tropical North Atlantic (G1) and the lowest value in the cluster positioned over the north-middle Atlantic (G5). Overall, the MWVRT is approximately 2.9 ± 0.4 days (spatial variability indicated by one standard deviation). This result is close but shorter to the findings of Läderach and Sodemann (2016) and Sodemann (2020), who pointed out that the MWVRT in the tropics varies from 4.5 to 5.8 days. Nevertheless, the MWVRT estimation in these previous works was performed for all weather systems, not for specific precipitant phenomena as TCs are.

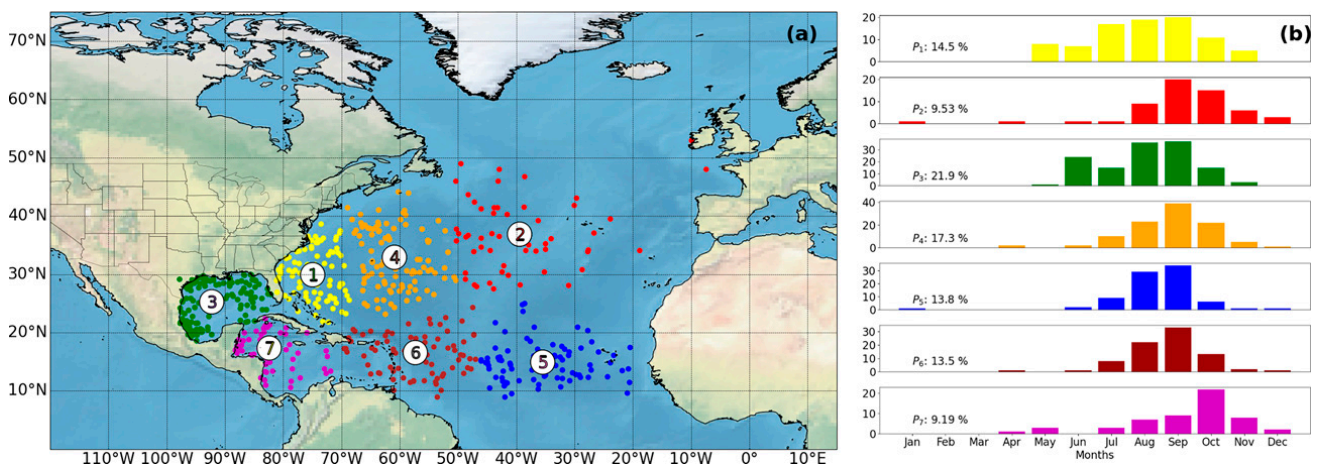


FIG. 4. Maximum intensification peak of tropical cyclones (TCs) in the North Atlantic basin during 1980–2018. (a) The position of each maximum intensification peak is indicated by a filled point. The colors represent the seven maximum intensification peak clusters calculated by the k -means technique. (b) The number of TCs by month and cluster.

b. Identification of the moisture sources for TCs during the maximum intensification phase

A change in the TC intensity is a manifestation of highly complex nonlinear dynamic and thermodynamic processes that interact at and across multiple scales (Ooyama 1982). The intensification processes range from aggregated and organized convective processes to microphysical processes such as evaporation and precipitation (Montgomery and Smith 2017). As suggested by several theoretical and modeling studies (e.g., Emanuel et al. 2004; Kimball 2006; Wu et al. 2015), high environmental moisture may lead to TC intensification. Thus, moisture transport to the regions where a TC intensified probably plays an important role in its development.

By applying cluster analysis, seven regions were identified as those where TCs reached the maximum intensity peak (Fig. 4a). Cluster P1 (yellow) was located northeast of the Bahamas Archipelago and included 14.5% of the TCs at their intensification peak. The Gulf of Mexico (P3, green), the western North Atlantic (P4, orange), the central tropical North Atlantic (P5, blue), the northeast area of the Lesser Antilles Arc (P6, brown), the north-central North Atlantic (P2, red), and the Caribbean Sea (P7) included 21.9%, 17.3%, 13.8%, 13.5%, 9.5%, and 9.2% of the TCs at their intensification peak, respectively. Owing to the close relationship between TC genesis and TC intensification (Ditchek et al. 2017), the monthly distribution of the maximum intensification peak frequency (Fig. 4b) was similar behavior to that observed for genesis. There was a higher number of TCs at the peak intensity in September, except for the Caribbean Sea (P7), which peaked in October.

Figure 5 displays the climatological moisture uptake pattern and VIMF (Fig. 5a), and the moisture contribution (Fig. 5b) for the precipitating air masses inside the outer radius of TC during their intensification peak phase for each cluster. The VIMF revealed strong moisture transport from the central Atlantic to clusters P1, P3, and P4, where easterly winds contributed to the water vapor flux, and the moisture contributions ranged from

35% to 75%. From Fig. 5, it can be seen that the western peripheric circulation around the NASH favored moisture transport from the northwestern Gulf of Mexico, crossing the southeastern United States from clusters P1 and P4. The P2 cluster mainly gained the atmospheric humidity from the subjacent ocean, although a slight moisture contribution ($\sim 15\%$ – 25%) was observed from the eastern coast of United States. Furthermore, in the P5 and P6 clusters, the eastern and southern flanks of the NASH were responsible for moisture transport from the Iberian Peninsula (skirting the West African coast) and the northern flank of the SASH over the South Atlantic Ocean. For these clusters, the NATL provided $\sim 80\%$ of moisture taken by TCs, with a maximum over the central tropic Atlantic for P6 and slightly displaced to the east for P5; the SALT exhibited a smaller contribution, with a local maximum reaching $\sim 60\%$ for the P5 cluster.

The moisture uptake patterns for the Gulf of Mexico (P3) and the Caribbean Sea (P7) clusters were similar, although the VIMF was more intense toward the first. Nevertheless, the moisture source contribution patterns are different within the NATL source. For P3 the maximum moisture contribution ($\sim 50\%$ – 80%) occurred over the Caribbean Sea and Gulf of Mexico, while P7 received the maximum moisture supplied ($\sim 50\%$ – 70%) from the eastern Caribbean Sea. Moreover, a weak contribution from the ETPac ($\sim 15\%$ – 20%) was detected in the Caribbean Sea cluster (P7). This agreed with the VIMF pattern, confirming the important role of the CLLJ in regional moisture transport during the hurricane season. The easterly winds also carried moisture ($\sim 25\%$, see Fig. 5b) from West Africa and the Sahel to P5 and P6. Overall, the source patterns were elongated eastward owing to the prevailing easterly winds, except for cluster P2.

Figure 6a clearly reveals the three sources of moisture that contributed to TCs in the phase of maximum intensification. Again, the most intense moisture source was located over the North Atlantic to the north of 10°N , the NATL, with the core of moisture uptake extended over the western

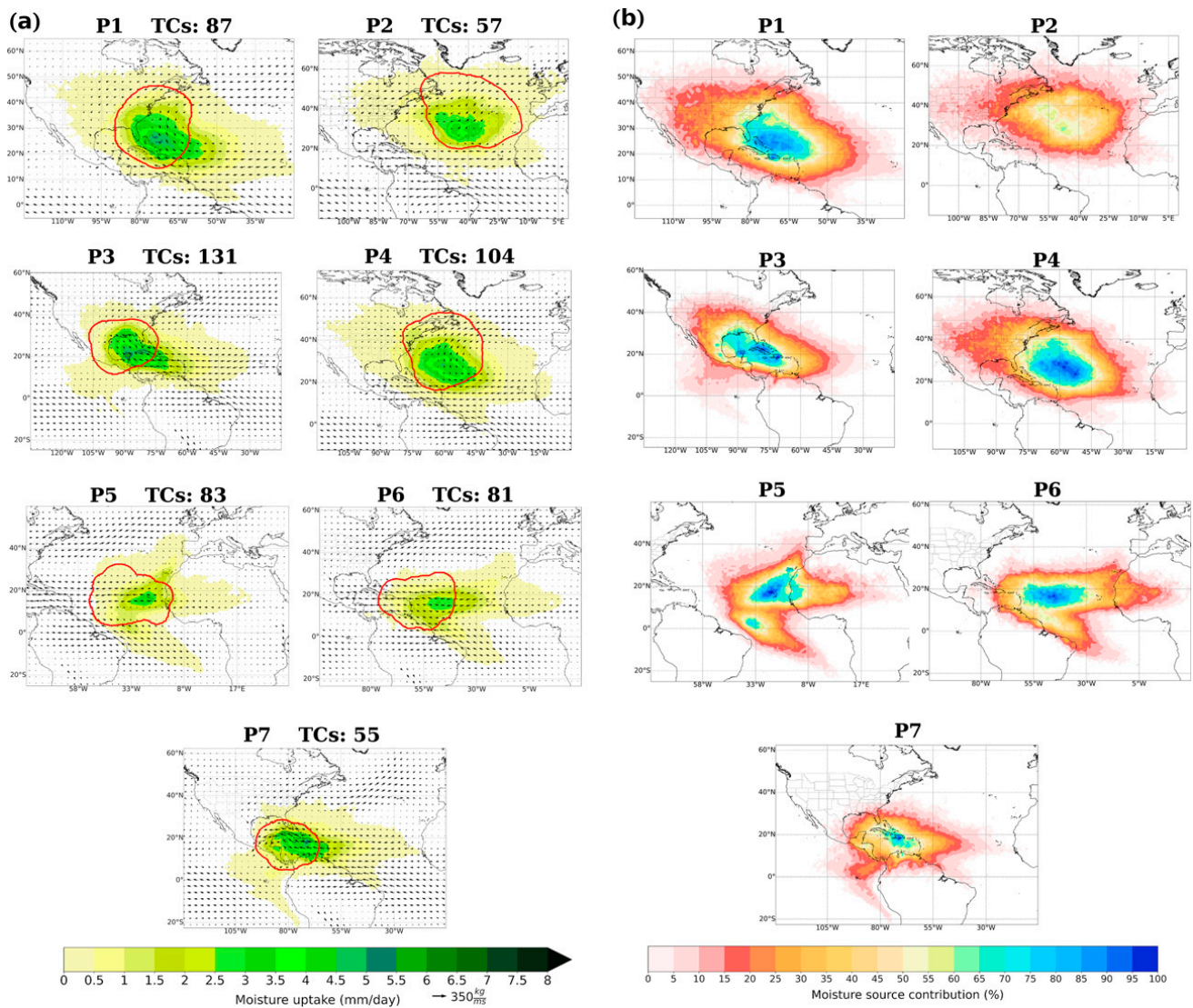


FIG. 5. (a) Climatological patterns of the moisture sources (moisture uptake; greenish colors; mm day^{-1}) for the maximum intensification peak of TCs integrated backward over 10 days, and the vertically integrated moisture flux (VIMF) (arrows; kg m s^{-1}). (b) Moisture sources contribution composite (percentage). The patterns show the composite for the days of all TCs in each cluster (numbered at the top). The red line contours the composite of the outer radius for all TCs in the cluster. Period of study: 1980–2018.

basin. The second was to the south of 10°N , the SATL, and the third was the weak ETPac moisture source. As indicated Fig. 6b, the maximum moisture supplied by NATL came from the western tropical North Atlantic, at northeastern of the Caribbean islands. The pattern of the moisture uptake for the maximum intensification peak indicates that the TCs captured more atmospheric moisture during this phase ($\sim 2323 \text{ mm day}^{-1}$ per TC) than during the genesis phase ($\sim 1560 \text{ mm day}^{-1}$ per TC). On average, the atmospheric moisture contribution from the NATL was approximately 92.6% during the TC maximum intensification stage, while those from the SATL and ETPac were 6.1% and 1.3%, respectively. Similar to TC genesis, the three moisture sources experienced little variation in the mean weighted position during the study period; however, the NATL moisture source shifted northward.

As the intensity of a TC is an important measure, TCs were clustered for the different categories on the Saffir–Simpson wind scale. Six clusters were found for the tropical storm (TS) category, five clusters were found for reached categories 1 and 2 [TCs classified as hurricanes (Hs)], and four clusters were found for categories 3, 4, and 5 [TCs classified as major hurricanes (MHs)]. Figure 7 shows the VIMF and climatological moisture uptake obtained in the backward trajectory of the precipitant air masses residing over the TS, H, and MH clusters. In the TS and H groups, the most intense and widespread pattern was observed in the TS2 and H2 clusters, with the maximum moisture uptake exceeding 10 mm day^{-1} to the northeast of La Española, corresponding to circulation associated with NASH. A nonnegligible contribution of humidity was also observed from the Gulf of Mexico to the southeastern United States. The SASH circulation over the South

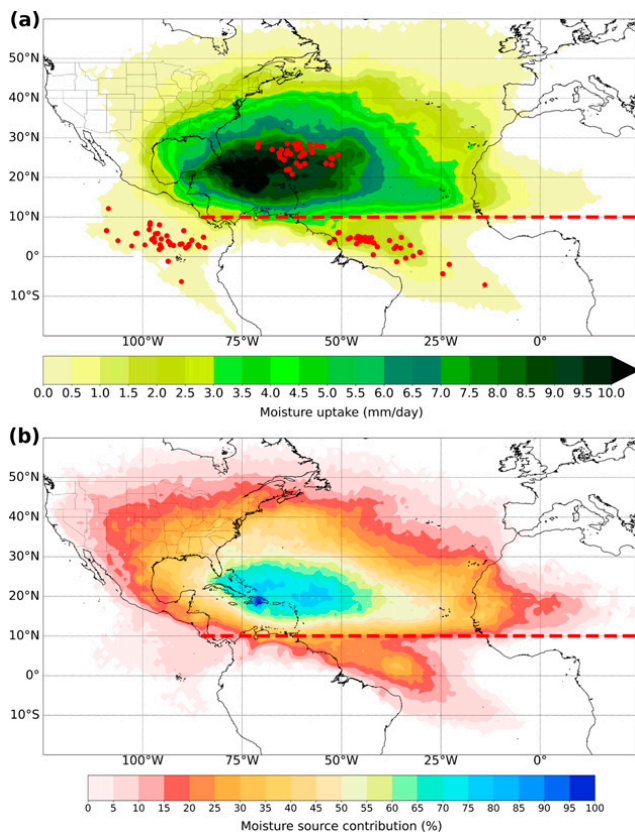


FIG. 6. As in Fig. 3, but for the TCs at their maximum intensification peak phase.

Atlantic basin seemed to be an important mechanism of moisture transport to the TS4, H1, H3, MH2, and MH3 clusters, like that previously discussed for TC genesis and for all TCs together during the maximum intensity peak. In addition, the observed TCs had a drying effect over the continent (southeastern United States), providing moisture to TS2, TS3, H2, H5, and MH4 clusters. This phenomenon usually occurs in the western or southern branches of the TC spiral bands (Xu et al. 2017).

In the clusters including the inter-American seas (TS3, TS6, H4, and MH1), the VIMF was mainly from the east until the eastern Caribbean Sea, largely due to the CLLJ, and then recurved northward to the Gulf of Mexico, being more intense over the Cuba Archipelago. This could have been linked to the excessive latent heat fluxes from the warm pool south of Cuba (Lee et al. 2007). While describing the role of the CLLJ in moisture transport, Bosilovich and Schubert (2002) demonstrated the importance of the Caribbean Sea via the southerly Great Plains low-level jet as a moisture source for the Gulf of Mexico and the southern United States. The Sahel was a weak moisture source for TS1, TS4, H1, and MH2 through easterly flows. Furthermore, the ETPac was a moisture source during the intensification of TCs when the outer radius included the Gulf of Mexico (TS3, TS6, H4, and MH1). In general, the moisture uptake pattern (Fig. 8) for each intensity category (TS, H, and MH) was similar, but for TS and H categories was more extended.

On average, Hs captured more atmospheric humidity (2413 mm day^{-1} per TC) than TSs and MHs (2179 mm day^{-1} and 1964 mm day^{-1} per TC, respectively). Overall, these amounts of moisture were mainly supplied by the NATL moisture source, contributing 88.3%, 89.6%, and 90.3%, for TSs, Hs, and MHs, respectively. Moreover, in all cases, the moisture contribution from the SATL ($\sim 11\%$) was higher than that from the ETPac ($\sim 2.8\%$). Figure 8b also shows that during the TS category the higher contribution occurred in the Caribbean Sea over the Antilles (reaching local values $\sim 65\%$), while during H and MH the maximums were found more eastward over the tropical NATL source (up to $\sim 65\%$ – 70% of moisture). In general, the moisture sources for TSs and Hs exhibited little annual variation in their mean positions, while the positions of the NATL and ETPac moisture sources for MHs showed notable annual variations (red dots in Fig. 8a), which may have been linked to the low frequency of MHs during the study period.

Overall, comparing Figs. 6a and 8a, the moisture uptake pattern during the peak of maximum TC intensification was more intense and more widespread than during each intensity category when studied separately. Furthermore, by intensity category, the core of the moisture uptake pattern appeared zonally stretched between 10° and 30°N in latitude. The latter behavior is more noticeable for MHs, which can be related to the fact that TCs generally reach MH intensity over the tropical band of the North Atlantic, the Caribbean Sea and the Gulf of Mexico (see Fig. 7).

Furthermore, the mean water vapor residence time (MWVRT) during the peak of maximum intensification of TC in the whole basin was estimated in 2.8 ± 0.3 days. No notable differences were observed in the MWVRT when TCs reached each intensity category. However, the MWVRT during TS (2.9 ± 0.3 days) is slightly above the values than during H (2.8 ± 0.3 days) and MH (2.7 ± 0.3 days) intensity categories. Similar to the TC genesis phase, the highest MWVRT values were found in the clusters located over the tropical North Atlantic.

c. Identification of moisture sources for TCs dissipation

The poleward transport of warm and humid air masses from low latitudes is an important part of the atmospheric general circulation and is essential for global energy and water budgets. Because many TCs transit toward poleward latitudes and dissipate above 30°N , they are an important mechanism of moisture transport from tropical to subtropical latitudes (Fig. 9). Some studies (e.g., Konrad and Perry 2009; Dare et al. 2012; Prat and Nelson 2013; Brun and Barros 2014) have found that the contribution of TCs to seasonal or annual rainfall on a regional scale can be up to 50% in some continental regions, depending on the characteristics and evolution of the wind field, topographic effects, atmospheric humidity, and size. Such a contribution is mainly due to the proximity of these systems to the coastline during their movement toward the dissipation areas.

Six broad regions over the North Atlantic basin were identified using the cluster analysis technique as those where the TCs usually dissipated (Fig. 9a), and September was the month with the highest frequency of dissipation processes (Fig. 9b).

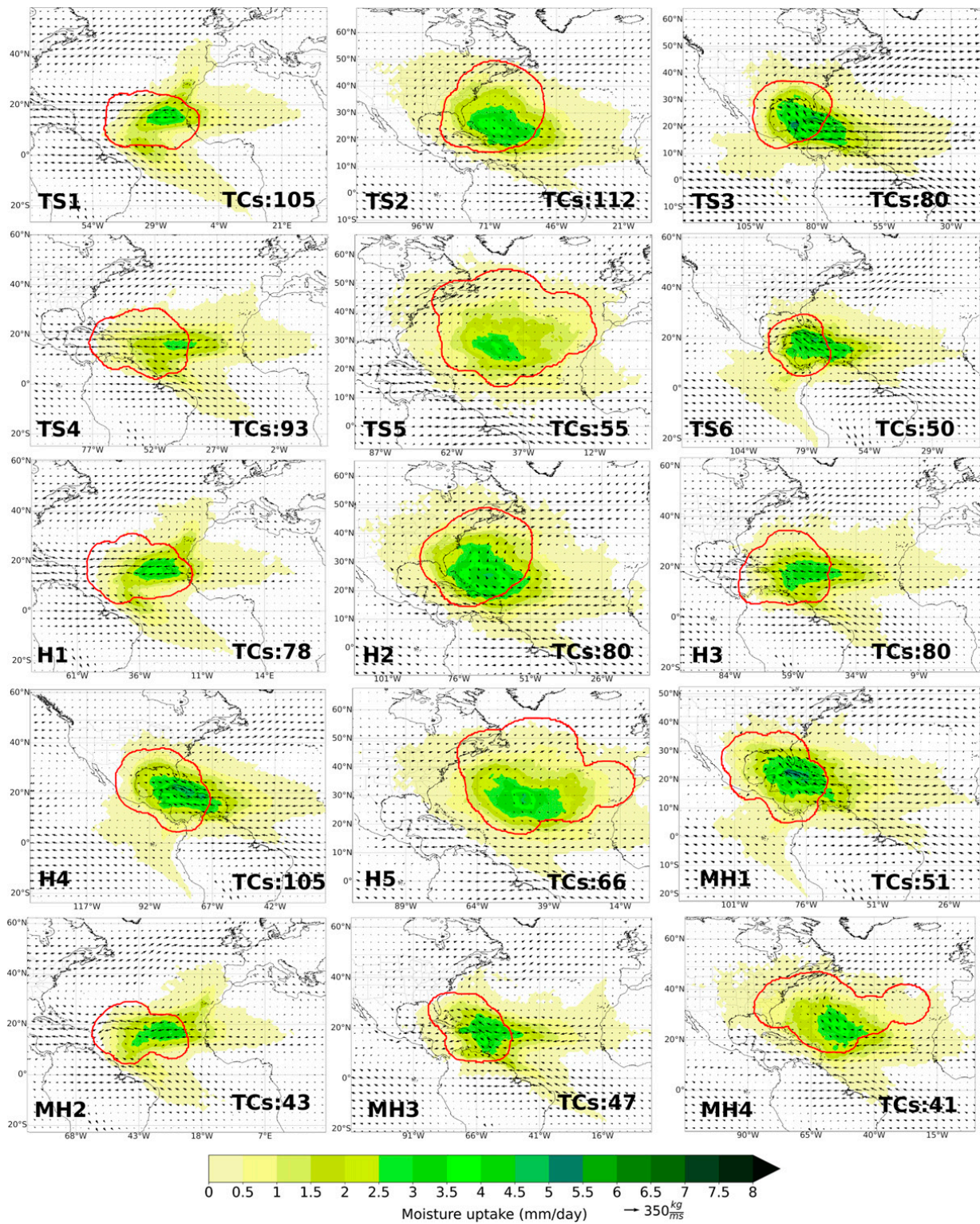


FIG. 7. Climatological patterns of the moisture sources (moisture uptake; greenish colors; mm day^{-1}) for the locations where TCs reached the tropical storm (TS), hurricane (H), and major hurricane (MH) intensity categories integrated backward over 10 days, and the vertically integrated moisture flux (VIMF) (arrows; kg m^{-1}). The patterns show the composite for the days of all TCs in each cluster (numbered at the bottom right). The H groups include TCs that reached hurricane categories 1 and 2 on the Saffir–Simpson wind scale, while the MH groups include categories 3, 4, and 5. Note that the n in TS_n , H_n , and MH_n ($n = 1, 2, \dots, 6$) represents the cluster identification for each category. The red line contours represent the composite of the outer radius for all TCs in the cluster. Period of study: 1980–2018.

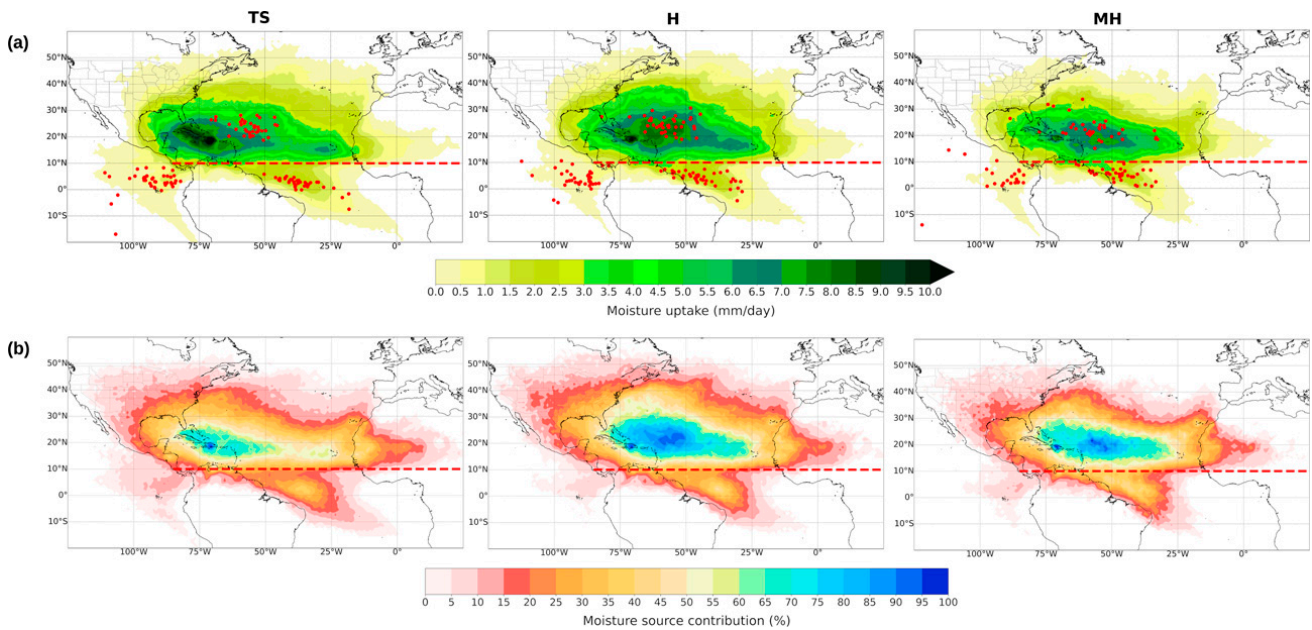


FIG. 8. As in Fig. 3, but for the TCs that reach TS, H, and MH intensity categories. The H groups include TCs that reached categories 1 and 2 on the Saffir–Simpson wind scale, while the MH groups include categories 3, 4, and 5. (a) Moisture sources and (b) moisture source contributions.

The climatological patterns of moisture uptake (Fig. 10a) indicate that the studied TCs transported important amounts of moisture toward high latitudes during their dissipation phase. These high latitudes areas included the Iberian Peninsula and the Atlantic coast of Great Britain and Northern Ireland, when the TCs were located further north and east over the North Atlantic (D1 and D5). The extended moisture uptake patterns (see Fig. 10b) for D1 and D5 revealed a supply of moisture mainly from the central subtropical NATL (higher than 55%), and even from higher latitudes ($\sim 10\%$ – 20%) for D5. It is worth noting the role of continental support over eastern North America ($\sim 10\%$ – 35%) for D1, D4, D5, and D6. For the TCs that dissipated over South, Central, and North America (D2), the air masses that transported moisture come from the Caribbean Sea and Gulf of Mexico (higher than $\sim 65\%$). For example, Fernández-Alvarez et al. (2020) found that the contribution of TCs to the total rainfall over Cuba during the cyclone season was approximately 11%. Khouakhi et al. (2017) showed that the TC-induced total rainfall in the southeastern United States and along the coast of the Gulf of Mexico was approximately 100 – 150 mm yr $^{-1}$. The SATL source only supported moisture to the southernmost part of D3 ($\sim 25\%$), specifically the southern Lesser Antilles Arc.

The intensity and extent of the moisture sources varied for different TC dissipation clusters. In general, TCs move poleward and undergo a transformation process to extratropical cyclones during the dissipation phase (Evans et al. 2017). During this process, the deep warm core associated with TCs becomes shallow and is often replaced by an asymmetric cold core structure (Evans and Hart 2003; Hart et al. 2006), including the development of shallow fronts (Klein et al. 2000). This evolution occurs when TCs move in a baroclinic environment

characterized by large temperature and moisture gradients, as well as a relatively high vertical wind shear, relatively low SST, and increasing Coriolis parameter (Evans et al. 2017). During this process, the storm radius increases (Knaff et al. 2014); therefore, larger moisture air masses from the tropical region are transported by the external circulation of the storm. The size of the impact area of a TC is a critical parameter in the moisture contribution to the dissipation region. Moreover, the distribution of these transport patterns corresponded well with the backward trajectories of TCs.

The results (Fig. 11) showed that the climatological pattern of moisture uptake over the entire North Atlantic basin for TC dissipation was less confined in comparison to the genesis and maximum intensification peak of TCs. Nevertheless, more moisture (2482 mm day $^{-1}$ per TC) was transported to the dissipation regions than for the genesis (1560 mm day $^{-1}$ per TC) and maximum intensification (2323 mm day $^{-1}$ per TC) regions. This may have related to the increased size of TCs at high latitudes (Hart and Evans 2001; Knaff et al. 2014), thus facilitating an increased moisture transport. Overall, the moisture contributions from the NATL source (to the north of 10°N) on average supplied 94.9% of the atmospheric humidity transported to the TC dissipation regions, with an accumulated maximum between 10° and 45°N contributing up to approximately 75%–80% of moisture (as it is shown in Fig. 11b); while the moisture contributions from the SATL (to the south of 10°N) and ETPac sources were negligible during the TC dissipation phase (3.3% and 1.8%, respectively). Furthermore, as can be seen in Fig. 11a, the annual weighted position of the NATL moisture source varied little during the study period, while those of the SATL and ETPac exhibited higher variations.

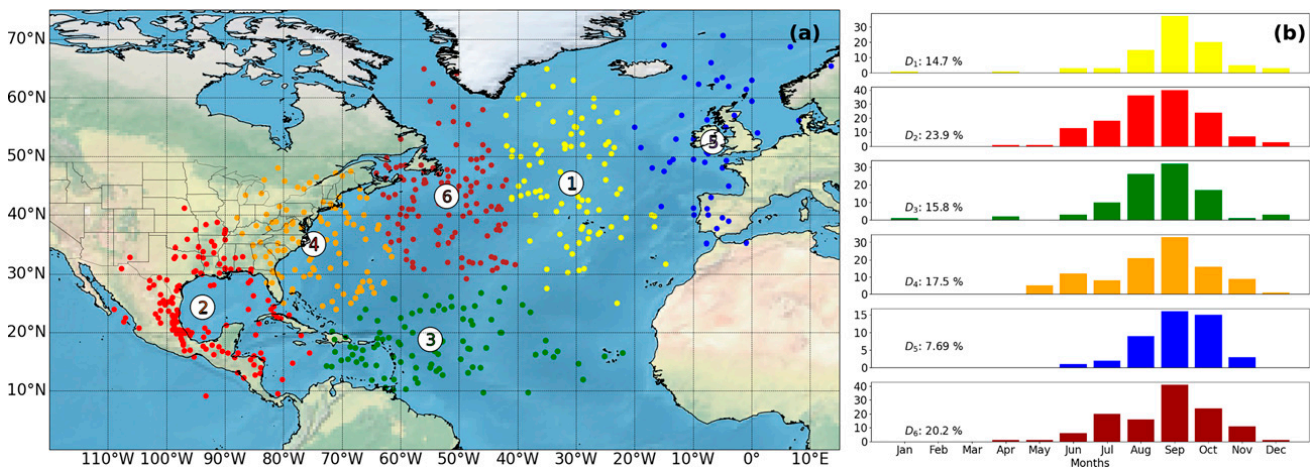


FIG. 9. Dissipation points of tropical cyclones (TCs) in the North Atlantic basin during 1980–2018. (a) Each TC dissipation position is indicated by the filled points. The colors represent the six TC dissipation clusters calculated by the *k*-means technique. (b) The number of TCs by month and cluster.

Moreover, the mean water vapor residence time (MWVRT) during the dissipation phase ranged from 2.4 to 2.7 days. Over the entire basin, the MWVRT (2.6 ± 0.3 days) was slightly lower than those for genesis and peak of maximum intensification.

4. Summary

This study investigated the moisture sources for the precipitation associated to 598 TCs during their genesis, maximum intensity peak, and dissipation phases which formed in the

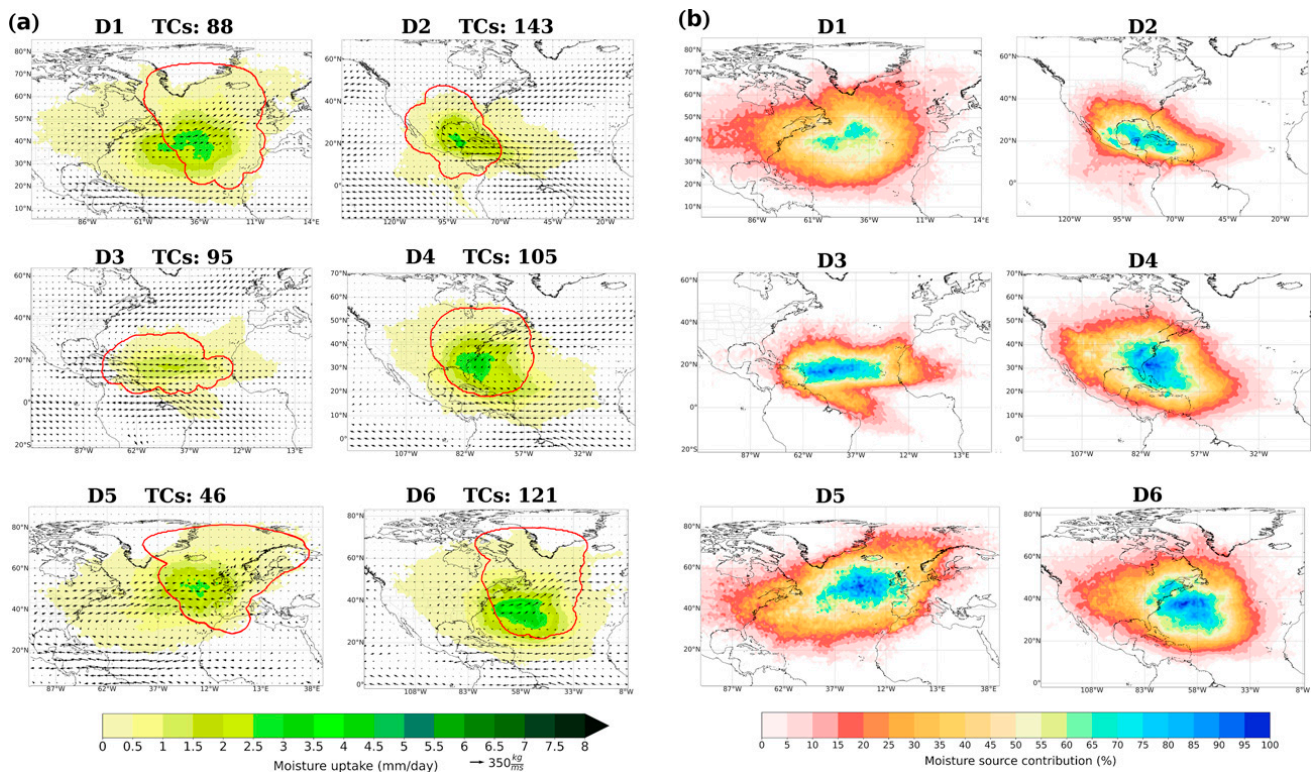


FIG. 10. (a) Climatological patterns of the moisture sources (moisture uptake; greenish colors; mm day^{-1}) for the dissipation phase of TCs integrated backward over 10 days, and the vertically integrated moisture flux (VIMF) (arrows; kg m s^{-1}). (b) Moisture sources contribution composite (percentage). The patterns show the composite for the days of all TCs in each cluster (numbered at the top). The red line contours the composite of the outer radius for all TCs in the cluster. Period of study: 1980–2018.

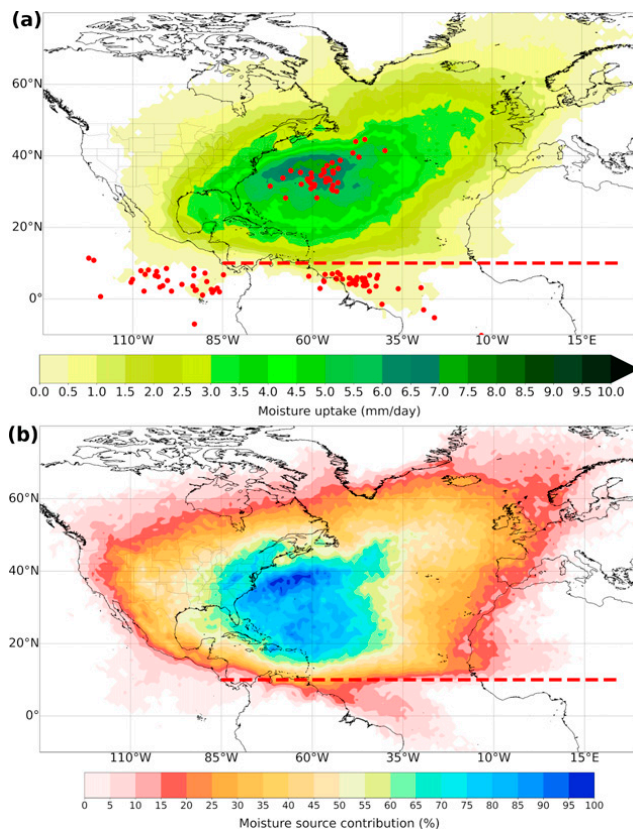


FIG. 11. As in Fig. 3, but for the dissipation phase of TCs.

North Atlantic Ocean basin from 1980 to 2018. With this aim we computed the changes in humidity along the backward trajectories of precipitating air masses (particles) inside each TC outer radius using the global outputs from the Lagrangian model FLEXPART (fed by ERA-Interim data). The characteristics of the TCs during the study period were extracted from the HURDAT2 database of the National Oceanic and Atmospheric Administration/National Hurricane Centre. Based on the k -means cluster analysis technique and silhouette coefficient, seven regions of occurrence were identified for the TC genesis and maximum intensification peak phases, and six regions of TC dissipation. The climatological moisture uptake in each region was characterized.

Our findings show that the North Atlantic Ocean basin to the north of 10°N (NATL) was the main moisture source for all the phases of TC development, supplying $\sim 87\%$ of atmospheric humidity uptakes (playing a special role the tropical part of the source, the Caribbean Sea and the Gulf of Mexico), while the moisture to the south of 10°N (SATL) and the eastern tropical Pacific (ETPac) contributed $\sim 11\%$ and $\sim 2\%$, respectively. Meanwhile, the contributions of the SATL and ETPac were higher for genesis and intensification phases than for the dissipation phase. Furthermore, a slight interannual variation in the position of each moisture source was observed; however, discussion of this aspect is beyond the scope of this studied. Moreover, it is interesting to note that the mean water vapor residence time for the final precipitation during TC activity in the North Atlantic basin ranged from 2.6 to 2.9 days.

The Lagrangian approach used in this investigation was very useful for distinguishing the spatial scale of moisture transport, and for assessing the origin of the precipitated moisture linked to TC genesis, intensification, and dissipation phases. Thus, this approach could support future studies investigating other cyclogenetic basins to assess the role of moisture sources in the variability of TCs, and to determine the contribution of TCs to the hydrological cycle over the continents. Furthermore, in ongoing studies, we will aim to identify the mechanisms that modulate the interannual variation in the position of moisture source regions for TC activity in the North Atlantic basin.

Acknowledgments. A.P-A acknowledges the PhD grant program of the University of Vigo. J.C.F-A and R.S acknowledge the support from the Xunta de Galicia (Galician Regional Government) under Grants ED481A-2020/193 and ED481B 2019/070, respectively. This work is supported by the LAGRIMA project (Grant RTI2018-095772-B-I00) funded by the Ministerio de Ciencia, Innovación y Universidades, Spain. Partial support was also obtained from the Xunta de Galicia under the Project ED431C 2021/44 (Programa de Consolidación e Estructuración de Unidades de Investigación Competitivas (Grupos de Referencia Competitiva) and Consellería de Cultura, Educación e Universidade). This work has been also possible thanks to the computing resources and technical support provided by CESGA (Centro de Supercomputación de Galicia). The authors acknowledge to NHC and Copernicus Climate Change Service for freely provide the HURDAT2 database and ECMWF reanalysis databases, respectively.

Data availability statement. The FLEXPART model is available at <https://www.flexpart.eu/downloads/6>. Several data sources were used in this study: HURDAT2 database from <https://www.nhc.noaa.gov/data/#hurdat>; ERA-Interim from <https://apps.ecmwf.int/datasets/data/interim-full-daily/levtype=sfc/>. The FLEXPART outputs are available upon request.

REFERENCES

- Ankur, K., N. K. R. Busireddy, K. K. Osuri, and D. Niyogi, 2020: On the relationship between intensity changes and rainfall distribution in tropical cyclones over the North Indian Ocean. *Int. J. Climatol.*, **40**, 2015–2025, <https://doi.org/10.1002/joc.6315>.
- Bosilovich, M. G., and S. D. Schubert, 2002: Water vapor tracers as diagnostics of the regional hydrologic cycle. *J. Hydrometeorol.*, **3**, 149–165, [https://doi.org/10.1175/1525-7541\(2002\)003<0149:WVTADO>2.0.CO;2](https://doi.org/10.1175/1525-7541(2002)003<0149:WVTADO>2.0.CO;2).
- Boutle, I. A., S. E. Belcher, and R. S. Plant, 2011: Moisture transport in midlatitude cyclones. *Quart. J. Roy. Meteor. Soc.*, **137**, 360–373, <https://doi.org/10.1002/qj.783>.
- Braun, S. A., 2006: High-resolution simulation of Hurricane Bonnie (1998). Part II: Water budget. *J. Atmos. Sci.*, **63**, 43–64, <https://doi.org/10.1175/JAS3609.1>.
- Brimelow, J. C., and G. W. Reuter, 2008: Moisture Sources for Extreme Rainfall Events over the Mackenzie River Basin. *Cold Region Atmospheric and Hydrologic Studies: The*

- Mackenzie GEWEX Experience, M. Woo, Ed., Springer, 127–136, https://doi.org/10.1007/978-3-540-73936-4_7.
- Brun, J., and A. P. Barros, 2014: Mapping the role of tropical cyclones on the hydroclimate of the southeast United States: 2002–2011. *Int. J. Climatol.*, **34**, 494–517, <https://doi.org/10.1002/joc.3703>.
- Carvalho, M. Â. V., and M. D. Oyama, 2013: Variabilidade da largura e intensidade da Zona de Convergência Intertropical atlântica: aspectos observacionais. *Rev. Bras. Meteor.*, **28**, 305–316, <https://doi.org/10.1590/S0102-77862013000300007>.
- Cloux, S., D. Garaboa-Paz, D. Insua-Costa, G. Miguez-Macho, and V. Pérez-Muñuzuri, 2021: Extreme precipitation events in the Mediterranean area: Contrasting Lagrangian and Eulerian models for moisture sources identification. *Hydrol. Earth Syst. Sci.*, **25**, 6465–6477, <https://doi.org/10.5194/hess-25-6465-2021>.
- Corporal-Lodangco, I., M. B. Richman, L. M. Leslie, and P. J. Lamb, 2014: Cluster analysis of North Atlantic tropical cyclones. *Proc. Comput. Sci.*, **36**, 293–300, <https://doi.org/10.1016/j.procs.2014.09.096>.
- Dare, R. A., N. E. Davidson, and J. L. McBride, 2012: Tropical cyclone contribution to rainfall over Australia. *Mon. Wea. Rev.*, **140**, 3606–3619, <https://doi.org/10.1175/MWR-D-11-00340.1>.
- Dee, D. P., and Coauthors, 2011: The ERA-Interim reanalysis: Configuration and performance of the data assimilation system. *Quart. J. Roy. Meteor. Soc.*, **137**, 553–597, <https://doi.org/10.1002/qj.828>.
- de Leeuw, J., J. Methven, and M. Blackburn, 2017: Physical factors influencing regional precipitation variability attributed using an air mass trajectory method. *J. Climate*, **30**, 7359–7378, <https://doi.org/10.1175/JCLI-D-16-0547.1>.
- DeMaria, M., J. A. Knaff, and B. H. Connell, 2001: A tropical cyclone genesis parameter for the tropical Atlantic. *Wea. Forecasting*, **16**, 219–233, [https://doi.org/10.1175/1520-0434\(2001\)016<0219:ATCGPF>2.0.CO;2](https://doi.org/10.1175/1520-0434(2001)016<0219:ATCGPF>2.0.CO;2).
- DiMego, G. J., and L. F. Bosart, 1982: The transformation of tropical an extratropical cyclone. Part II: Moisture, vorticity and kinetic energy budgets. *Mon. Wea. Rev.*, **110**, 412–433, [https://doi.org/10.1175/1520-0493\(1982\)110<0412:TTOTSA>2.0.CO;2](https://doi.org/10.1175/1520-0493(1982)110<0412:TTOTSA>2.0.CO;2).
- Ditchek, S. D., T. C. Nelson, M. Rosenmayer, and K. L. Corbo-siero, 2017: The relationship between tropical cyclones at genesis and their maximum attained intensity. *J. Climate*, **30**, 4897–4913, <https://doi.org/10.1175/JCLI-D-16-0554.1>.
- Durán-Quesada, A. M., L. Gimeno, and J. Amador, 2017: Role of moisture transport for Central American precipitation. *Earth Syst. Dyn.*, **8**, 147–161, <https://doi.org/10.5194/esd-8-147-2017>.
- Emanuel, K., C. DesAutels, C. Holloway, and R. Korty, 2004: Environmental control of tropical cyclone intensity. *J. Atmos. Sci.*, **61**, 843–858, [https://doi.org/10.1175/1520-0469\(2004\)061<0843:ECOTCI>2.0.CO;2](https://doi.org/10.1175/1520-0469(2004)061<0843:ECOTCI>2.0.CO;2).
- Evans, C., and Coauthors, 2017: The extratropical transition of tropical cyclones. Part I: Cyclone evolution and direct impacts. *Mon. Wea. Rev.*, **145**, 4317–4344, <https://doi.org/10.1175/MWR-D-17-0027.1>.
- Evans, J. L., and R. E. Hart, 2003: Objective indicators of the life cycle evolution of extratropical transition for Atlantic tropical cyclones. *Mon. Wea. Rev.*, **131**, 909–925, [https://doi.org/10.1175/1520-0493\(2003\)131<0909:OIOTLC>2.0.CO;2](https://doi.org/10.1175/1520-0493(2003)131<0909:OIOTLC>2.0.CO;2).
- Fernández-Alvarez, J. C., R. Sorí, A. Pérez-Alarcón, R. Nieto, and L. Gimeno, 2020: The role of tropical cyclones on the total precipitation in Cuba during the Hurricane season from 1980 to 2016. *Atmosphere*, **11**, 1156, <https://doi.org/10.3390/atmos11111156>.
- Fujiwara, K., R. Kawamura, H. Hirata, T. Kawano, M. Kato, and T. Shinoda, 2017: A positive feedback process between tropical cyclone intensity and the moisture conveyor belt assessed with Lagrangian diagnostics. *J. Geophys. Res. Atmos.*, **122**, 12 502–12 521, <https://doi.org/10.1002/2017JD027557>.
- Gallego, D., R. García-Herrera, F. de Paula Gómez-Delgado, P. Ordoñez-Pérez, and P. Ribera, 2019: Tracking the moisture transport from the Pacific towards Central and northern South America since the late 19th century. *Earth Syst. Dyn.*, **10**, 319–331, <https://doi.org/10.5194/esd-10-319-2019>.
- Gimeno, L., A. Drumond, R. Nieto, R. M. Trigo, and A. Stohl, 2010: On the origin of continental precipitation. *Geophys. Res. Lett.*, **37**, L13804, <https://doi.org/10.1029/2010GL043712>.
- , and Coauthors, 2012: Oceanic and terrestrial sources of continental precipitation. *Rev. Geophys.*, **50**, RG4003, <https://doi.org/10.1029/2012RG000389>.
- , and Coauthors, 2020: Recent progress on the sources of continental precipitation as revealed by moisture transport analysis. *Earth-Sci. Rev.*, **201**, 103070, <https://doi.org/10.1016/j.earscirev.2019.103070>.
- , and Coauthors, 2021: The residence time of water vapour in the Atmosphere. *Nat. Rev. Earth Environ.*, **2**, 558–569, <https://doi.org/10.1038/s43017-021-00181-9>.
- Gozzo, L. F., R. P. da Rocha, L. Gimeno, and A. Drumond, 2017: Climatology and numerical case study of moisture sources associated with subtropical cyclogenesis over the southwestern Atlantic Ocean. *J. Geophys. Res. Atmos.*, **122**, 5636–5653, <https://doi.org/10.1002/2016JD025764>.
- Gray, W. M., 1968: Global view of the origin of tropical disturbances and storms. *Mon. Wea. Rev.*, **96**, 669–700, [https://doi.org/10.1175/1520-0493\(1968\)096<0669:GVOTOO>2.0.CO;2](https://doi.org/10.1175/1520-0493(1968)096<0669:GVOTOO>2.0.CO;2).
- , C. W. Landsea, P. W. Mielke Jr., and K. J. Berry, 1993: Predicting Atlantic seasonal tropical cyclone activity by 1 August. *Wea. Forecasting*, **8**, 73–86, [https://doi.org/10.1175/1520-0434\(1993\)008<0073:PABSTC>2.0.CO;2](https://doi.org/10.1175/1520-0434(1993)008<0073:PABSTC>2.0.CO;2).
- Guo, L., N. P. Klingaman, M.-E. Demory, P. L. Vidale, A. G. Turner, and C. C. Stephan, 2018: The contributions of local and remote atmospheric moisture fluxes to East Asian precipitation and its variability. *Climate Dyn.*, **51**, 4139–4156, <https://doi.org/10.1007/s00382-017-4064-4>.
- Hart, R. E., and J. L. Evans, 2001: A climatology of the extratropical transition of Atlantic tropical cyclones. *J. Climate*, **14**, 546–564, [https://doi.org/10.1175/1520-0442\(2001\)014<0546:ACOTET>2.0.CO;2](https://doi.org/10.1175/1520-0442(2001)014<0546:ACOTET>2.0.CO;2).
- , —, and C. Evans, 2006: Synoptic composites of the extratropical transition life cycle of North Atlantic tropical cyclones: Factors determining posttransition evolution. *Mon. Wea. Rev.*, **134**, 553–578, <https://doi.org/10.1175/MWR3082.1>.
- Huang, H. L., M. J. Yang, and C. H. Sui, 2014: Water budget and precipitation efficiency of Typhoon Morakot (2009). *J. Atmos. Sci.*, **71**, 112–129, <https://doi.org/10.1175/JAS-D-13-053.1>.
- Jana, S., B. Rajagopalan, M. A. Alexander, and A. J. Ray, 2018: Understanding the dominant sources and tracks of moisture for summer rainfall in the southwest United States. *J. Geophys. Res. Atmos.*, **123**, 4850–4870, <https://doi.org/10.1029/2017JD027652>.
- Khouakhi, A., G. Villarini, and G. A. Vecchi, 2017: Contribution of tropical cyclones to rainfall at the global scale. *J. Climate*, **30**, 359–372, <https://doi.org/10.1175/JCLI-D-16-0298.1>.
- Kimball, S. K., 2006: A modeling study of hurricane landfall in a dry environment. *Mon. Wea. Rev.*, **134**, 1901–1918, <https://doi.org/10.1175/MWR3155.1>.

- Klein, P. M., P. A. Harr, and R. L. Elsberry, 2000: Extratropical transition of western North Pacific tropical cyclones: An overview and conceptual model of the transformation stage. *Wea. Forecasting*, **15**, 373–395, [https://doi.org/10.1175/1520-0434\(2000\)015<0373:ETOWNP>2.0.CO;2](https://doi.org/10.1175/1520-0434(2000)015<0373:ETOWNP>2.0.CO;2).
- Knaff, J. A., S. P. Longmore, and D. A. Molenaar, 2014: An objective satellite-based tropical cyclone size climatology. *J. Climate*, **27**, 455–476, <https://doi.org/10.1175/JCLI-D-13-00096.1>.
- Konrad, C. E., and L. B. Perry, 2009: Relationships between tropical cyclones and heavy rainfall in the Carolina region of the USA. *Int. J. Climatol.*, **30**, 522–534, <https://doi.org/10.1002/joc.1894>.
- Kung, H., and S. X. Zhao, 2007: Diagnosis on energy budget and moisture supply of Matsa after landfall. *Climatic Environ. Res.*, **12**, 437–452.
- Läderach, A., and H. Sodemann, 2016: A revised picture of the atmospheric moisture residence time. *Geophys. Res. Lett.*, **43**, 924–933, <https://doi.org/10.1002/2015GL067449>.
- Landsea, C. W., and J. L. Franklin, 2013: Atlantic Hurricane database uncertainty and presentation of a new database format. *Mon. Wea. Rev.*, **141**, 3576–3592, <https://doi.org/10.1175/MWR-D-12-00254.1>.
- Lee, S.-K., D. B. Enfield, and C. Wang, 2007: What drives the seasonal onset and decay of the Western Hemisphere warm pool? *J. Climate*, **20**, 2133–2146, <https://doi.org/10.1175/JCLI4113.1>.
- Lélé, M. I., L. M. Leslie, and P. J. Lamb, 2015: Analysis of low-level atmospheric moisture transport associated with the West African monsoon. *J. Climate*, **28**, 4414–4430, <https://doi.org/10.1175/JCLI-D-14-00746.1>.
- Liberato, M. L. R., A. M. Ramos, R. M. Trigo, I. F. Trigo, A. M. Durán-Quesada, R. Nieto, and L. Gimeno, 2012: Moisture sources and large-scale dynamics associated with a flash flood event. *Lagrangian Modeling of the Atmosphere, Geophys. Monogr.*, Vol. 200, Amer. Geophys. Union, 111–126, <https://doi.org/10.1029/2012GM001244>.
- MacQueen, J., 1967: Some methods for classification and analysis of multivariate observations. *Proc. Fifth Berkeley Symp. on Mathematical Statistics and Probability*, Berkeley, CA, University of California, 281–297.
- Makarieva, A. M., V. G. Gorshkov, A. V. Nefiodov, A. V. Chikunov, D. Sheil, A. Donato Nobre, and B. L. Li, 2017: Fuel for cyclones: The water vapor budget of a hurricane as dependent on its movement. *Atmos. Res.*, **193**, 216–230, <https://doi.org/10.1016/j.atmosres.2017.04.006>.
- McBride, J. L., 1995: Tropical cyclone formation. Global perspectives on tropical cyclones, WMO/TD-693, Rep. TCP-38, World Meteorological Organization, 63–105.
- Meynadier, R., O. Bock, F. Guichard, A. Boone, P. Roucou, and J.-L. Redelsperger, 2010: West African monsoon water cycle: 1. A hybrid water budget dataset. *J. Geophys. Res.*, **115**, D19106, <https://doi.org/10.1029/2010JD013917>.
- Montgomery, M. T., 2016: Recent Advances in Tropical Cyclogenesis. *Advanced Numerical Modeling and Data Assimilation Techniques for Tropical Cyclone Prediction*, U.C. Mohanty and S. G. Gopalakrishnan, Eds., Springer, 561–587, https://doi.org/10.5822/978-94-024-0896-6_22.
- , and R. K. Smith, 2017: Recent developments in the fluid dynamics of tropical cyclones. *Annu. Rev. Fluid Mech.*, **49**, 541–574, <https://doi.org/10.1146/annurev-fluid-010816-060022>.
- Morissette, L., and S. Chartier, 2013: The k-means clustering technique: General considerations and implementation in Mathematica. *Tutor. Quant. Methods Psychol.*, **9**, 15–24, <https://doi.org/10.20982/tqmp.09.1.p015>.
- Neumann, C. J., 1993: Global climatology. Global Guide to Tropical Cyclone Forecasting, WMO/TD-560, Rep. TCP-31, World Meteorological Organization, 1.1–1.43.
- Numaguti, A., 1999: Origin and recycling processes of precipitating water over the Eurasian continent: Experiments using an atmospheric general circulation model. *J. Geophys. Res.*, **104**, 1957–1972, <https://doi.org/10.1029/1998JD200026>.
- Ooyama, K. V., 1982: Conceptual evolution of the theory and modeling of the tropical cyclone. *J. Meteor. Soc. Japan Ser. II*, **60**, 369–380, https://doi.org/10.2151/jmsj1965.60.1_369.
- Pazos, M., and L. Gimeno, 2017: Identification of moisture sources in the Atlantic Ocean for cyclogenesis processes. *Proceedings of the First International Electronic Conference on the Hydrological Cycle*, Sciforum Electronic Conference Series, Vol. 1, MDPI, 5 pp., <https://doi.org/10.3390/CHyCle-2017-04862>.
- Pérez-Alarcón, A., R. Sorí, J. C. Fernández-Alvarez, R. Nieto, and L. Gimeno, 2021a: Moisture sources for tropical cyclones genesis in the coast of West Africa through a Lagrangian approach. *Environ. Sci. Proc.*, **4**, 3, <https://doi.org/10.3390/ecas2020-08126>.
- , —, J. C. Fernández-Alvarez, R. Nieto, and L. Gimeno, 2021b: Comparative climatology of outer tropical cyclone size using radial wind profiles. *Wea. Climate Extremes*, **33**, 100366, <https://doi.org/10.1016/j.wace.2021.100366>.
- , J. C. Fernández-Alvarez, R. Sorí, R. Nieto, and L. Gimeno, 2021c: The combined effects of SST and the North Atlantic subtropical high-pressure system on the Atlantic basin tropical cyclone interannual variability. *Atmosphere*, **12**, 329, <https://doi.org/10.3390/atmos12030329>.
- Pottapinjara, V., M. S. Girishkumar, R. Murtugudde, K. Ashok, and M. Ravichandran, 2019: On the relation between the boreal spring position of the Atlantic intertropical convergence zone and Atlantic zonal mode. *J. Climate*, **32**, 4767–4781, <https://doi.org/10.1175/JCLI-D-18-0614.1>.
- Poveda, G., and O. Mesa, 1999: La corriente de chorro superficial del Oeste (“del Chocó”) y otras dos corrientes de chorro en Colombia: Climatología y variabilidad durante las fases del ENSO. *Rev. Acad. Colomb. Cien.*, **23**, 517–528.
- , and —, 2000: On the existence of Lloró (the rainiest locality on Earth): Enhanced ocean-land-atmosphere interaction by a low-level jet. *Geophys. Res. Lett.*, **27**, 1675–1678, <https://doi.org/10.1029/1999GL006091>.
- Prat, O. P., and B. R. Nelson, 2013: Precipitation contribution of tropical cyclones in the southeastern United States from 1998 to 2009 using TRMM satellite data. *J. Climate*, **26**, 1047–1062, <https://doi.org/10.1175/JCLI-D-11-00736.1>.
- Redelsperger, J. L., A. Diongue, A. Diedhiou, J. P. Ceron, M. Diop, J. F. Guerey, and J. P. Lafore, 2002: Multiscale description of a Sahelian synoptic weather system representative of the West African monsoon. *Quart. J. Roy. Meteor. Soc.*, **128**, 1229–1257, <https://doi.org/10.1256/003590002320373274>.
- , C. D. Thorncroft, A. Diedhiou, T. Lebel, D. J. Parker, and J. Polcher, 2006: African monsoon multidisciplinary analysis: An international research project and field campaign. *Bull. Amer. Meteor. Soc.*, **87**, 1739–1746, <https://doi.org/10.1175/BAMS-87-12-1739>.
- Ren, J., J. A. Zhang, J. L. Vigh, P. Zhu, H. Liu, X. Wang, and J. B. Wadler, 2020: An observational study of the symmetric boundary layer structure and tropical cyclone intensity. *Atmosphere*, **11**, 158, <https://doi.org/10.3390/atmos11020158>.
- Sodemann, H., 2020: Beyond turnover time: Constraining the lifetime distribution of water vapor from simple and complex

- approaches. *J. Atmos. Sci.*, **77**, 413–433, <https://doi.org/10.1175/JAS-D-18-0336.1>.
- , C. Schwierz, and H. Wernli, 2008: Interannual variability of Greenland winter precipitation sources: Lagrangian moisture diagnostic and North Atlantic Oscillation influence. *J. Geophys. Res.*, **113**, D03107, <https://doi.org/10.1029/2007JD008503>.
- Stohl, A., and P. A. James, 2004: Lagrangian analysis of the atmospheric branch of the global water cycle. Part I: Method description, validation, and demonstration for the August 2002 flooding in central Europe. *J. Hydrometeor.*, **5**, 656–678, [https://doi.org/10.1175/1525-7541\(2004\)005<0656:ALAOTA>2.0.CO;2](https://doi.org/10.1175/1525-7541(2004)005<0656:ALAOTA>2.0.CO;2).
- , C. Forster, A. Frank, P. Seibert, and G. Wotawa, 2005: Technical Note: The Lagrangian particle dispersion model FLEXPART version 6.2. *Atmos. Chem. Phys.*, **5**, 2461–2474, <https://doi.org/10.5194/acp-5-2461-2005>.
- van der Ent, R. J., and O. Tuinenburg, 2017: The residence time of water in the atmosphere revisited. *Hydrol. Earth Syst. Sci.*, **21**, 779–790, <https://doi.org/10.5194/hess-21-779-2017>.
- Wang, C., S.-K. Lee, and D. B. Enfield, 2007: Impact of the Atlantic Warm Pool on the summer climate of the Western Hemisphere. *J. Climate*, **20**, 5021–5040, <https://doi.org/10.1175/JCLI4304.1>.
- Wang, F., H. H. Franco-Penya, J. D. Kelleher, J. Pugh, and R. Ross, 2017: An analysis of the application of simplified silhouette to the evaluation of k-means clustering validity. *Machine Learning and Data Mining in Pattern Recognition*, P. Perner, Eds., Lecture Notes in Computer Science, Vol. 10358, Springer, 291–305.
- Willoughby, H. E., R. W. R. Darling, and M. Rahn, 2006: Parametric representation of the primary hurricane vortex. Part II: A new family of sectionally continuous profiles. *Mon. Wea. Rev.*, **134**, 1102–1120, <https://doi.org/10.1175/MWR3106.1>.
- Wu, L., H. Su, R. G. Fovell, T. J. Dunkerton, Z. Wang, and B. H. Kahn, 2015: Impact of environmental moisture on tropical cyclone intensification. *Atmos. Chem. Phys.*, **15**, 14041–14053, <https://doi.org/10.5194/acp-15-14041-2015>.
- Xu, G., T. J. Osborn, and A. J. Matthews, 2017: Moisture transport by Atlantic tropical cyclones onto the North American continent. *Climate Dyn.*, **48**, 3161–3182, <https://doi.org/10.1007/s00382-016-3257-6>.
- Yang, M., S. A. Braun, and D. Chen, 2011: Water budget of Typhoon Nari (2001). *Mon. Wea. Rev.*, **139**, 3809–3828, <https://doi.org/10.1175/MWR-D-10-05090.1>.
- Yoshida, R., Y. Miyamoto, H. Tomita, and Y. Kajikawa, 2017: The effect of water vapor on tropical cyclone genesis: A numerical experiment of a non-developing disturbance observed in PALAU 2010. *J. Meteor. Soc. Japan*, **95**, 35–47, <https://doi.org/10.2151/jmsj.2017-001>.
- Zhao, N., A. Manda, X. Guo, K. Kikuchi, T. Nasuno, M. Nakano, Y. Zhang, and B. Wang, 2021: A Lagrangian view of moisture transport related to the heavy rainfall of July 2020 in Japan: Importance of the moistening over the subtropical regions. *Geophys. Res. Lett.*, **48**, e2020GL091441, <https://doi.org/10.1029/2020GL091441>.

4.5 Moisture source identification for precipitation associated with tropical cyclone development over the Indian Ocean: a Lagrangian approach

Pérez-Alarcón, A., Fernández-Alvarez, J.C., Sorí, R., Nieto, R., Gimeno, L., 2022. Moisture source identification for precipitation associated with tropical cyclone development over the Indian Ocean: a Lagrangian approach. *Climate Dynamics*. doi: 10.1007/s00382-022-06429-4

Table 4.5: Summary of the impact and quality of the journal where the fourth paper that conformed to this thesis was published. The data correspond to the year 2021 (last year available at the date of preparation of this document) in the Web of Science (JCR). **IF:** Impact Factor

Journal	Description	Journal Metrics
Climate Dynamics	It publishes high-quality research on all aspects of the dynamics of the global climate system, including numerical modelling research on the structure and behaviour of the atmosphere	IF: 4.901, 5-year IF: 4.742 Ranking: 22 out of 108 (Q1) in Meteorology & Atmospheric Sciences



Moisture source identification for precipitation associated with tropical cyclone development over the Indian Ocean: a Lagrangian approach

Albenis Pérez-Alarcón^{1,2} · José C. Fernández-Alvarez^{1,2} · Rogert Sorri^{1,3} · Raquel Nieto¹ · Luis Gimeno¹

Received: 1 February 2022 / Accepted: 18 July 2022
© The Author(s) 2022

Abstract

In this study, we investigated the moisture sources for precipitation through a Lagrangian approach during the genesis, intensification, and dissipation phases of all tropical cyclones (TCs) that occurred over the two hemispheric sub-basins of the Indian Ocean (IO) from 1980 to 2018. In the North IO (NIO), TCs formed and reached their maximum intensity on both sides of the Indian Peninsula, to the east in the Bay of Bengal (BoB), and to the west in the Arabian Sea (AS). The oceanic areas where TCs occurred were their main moisture sources for precipitation associated with TCs. Additionally, for TCs over the BoB, continental sources from the Ganges River basin and the South China Sea also played a notable role; for TCs over the AS, the Somali Low-Level jet (along the African coast in a northerly direction) also acted as an essential moisture transport. In the South IO (SIO), the western, central, and eastern basins were identified as the preferred areas for the genesis and development of TCs. During TC activity, the central IO and the Wharton and Perth basins mostly supplied atmospheric moisture. The Mascarene High circulation was the main moisture transport mechanism for the precipitation of TCs formed in the SIO basin. In both basins, during their intensification process, TCs gained more moisture (even more intensely when reaching the hurricane category) than during the genesis or dissipation stages. Additionally, the modulation during monsoonal seasons of the moisture contribution to the TCs was more noticeable over the NIO basin than for the SIO. Overall, the moisture uptake for precipitation from the sources for TCs occurred slightly faster in the NIO basin than in the SIO basin.

Keywords Moisture uptake · Tropical cyclones · Lagrangian approach · Indian Ocean

1 Introduction

Tropical cyclones (TCs) are essential elements of the hydrological cycle in tropical and subtropical regions (Dominguez and Magaña 2018). However, the combined effects of extreme winds, precipitation, and storm surges cause significant economic losses and human death, especially in coastal regions (Boruff 2009). Therefore, the forecasting of

TC intensity and trajectory to reduce the negative effects of these storms has been of special interest to the international scientific community.

TCs are formed over the tropical and subtropical waters of different cyclogenetic basins: North Atlantic, Central and East Pacific, North-Western and South Pacific Ocean, North Indian Ocean (NIO), and South Indian Ocean (SIO). The warm waters of the oceans provide the energy source for TCs, and their intensification is led by the enhanced latent and sensible heat fluxes due to the evaporation and heat transfer from the surface of the warm oceans, moistening the TC boundary layer (Williams 2016).

The role of moisture in TC development is crucial. Wang et al. (2016) demonstrated that latent heating associated with the condensation of water vapour is an important source of potential energy for TC intensification, and Gray (1968) showed that the relatively moist layers near the mid-troposphere are a necessary factor for their genesis. Early findings of Gray (1977) suggested that when mid-level

✉ Albenis Pérez-Alarcón
albenis.perez.alarcon@uvigo.es

¹ Centro de Investigación Mariña, Universidade de Vigo, Environmental Physics Laboratory (EPhysLab), Campus As Lagoas s/n, 32004 Ourense, Spain

² Departamento de Meteorología, Instituto Superior de Tecnologías y Ciencias Aplicadas, Universidad de La Habana, 10400 La Habana, Cuba

³ Instituto Dom Luiz, Faculdade de Ciências da Universidade de Lisboa, 1749-016 Campo Grande, Portugal

relative humidity over the ocean is less than 60%, cumulus convection does not typically occur, and when relative humidity is less than 40%, cyclonic development is not possible. The intensity of storms in sheared environments is enhanced (suppressed) if there is an increasing (reducing) mid-tropospheric relative humidity (Emanuel et al. 2004). Moreover, a moistened environment is considered one of the most important factors for forecasting the intensity of TCs (Wu et al. 2015). Therefore, globally, identifying where the atmospheric moisture comes from to the TCs during their different life stages is necessary to improve the predictive power of numerical TC prediction models and to improve the understanding of the global hydrological cycle.

The focus of this study was the analysis of TCs that formed over the Indian Ocean (IO), namely the northern and southern basins, the site of most of the world's deadliest cyclones (Longshore 2009; Samson et al. 2014), mostly due to flash flooding caused by storm surges and heavy rainfall (Needham et al. 2015; Bousquet et al. 2021; Wahiduzzaman 2021). Therefore, knowing precisely the origin of the humidity that generates precipitation in TCs is crucial.

In addition to the more or less common characteristics that can facilitate or inhibit the development or maintenance of TCs, the IO is affected by one of the most prominent climatic systems worldwide, the monsoon. In fact, it is affected by different monsoonal regimes, and they modulate the occurrence and frequency of TCs in the basin. For instance, during the summer monsoon season over the IO and South Asia, the cyclonic vorticity to the north of the strong cross-equatorial low-level jet stream is a dynamic force for the genesis of depressions and cyclones north of the Bay of Bengal (BoB) (Muni 2009). Nevertheless, according to Li et al. (2013) and Yuan et al. (2019), TCs formed over the NIO basin exhibit a bimodal seasonal distribution caused by unfavourable environmental conditions during the monsoon season. Thus, the monsoonal system phases and their seasonally associated fluxes throughout the areas of the IO can play an important role, including moisture availability, in TC activity over the basin.

Various methods and approaches have been developed to identify and follow the atmospheric moisture that reaches or leaves a specific region. Eulerian (van der Ent et al. 2014), Lagrangian (Stohl and James 2005; Sodemann et al. 2008; Sprenger and Wernli 2015) and analytical (Martínez and Domínguez 2014; Ordóñez et al. 2012) models, and physical water vapour tracers using isotopes (Henderson-Sellers et al. 2002) are the most used (Gimeno et al. 2010, 2012, 2020). Lagrangian models are commonly used to study the water vapour budget of air parcels as they travel either forward or backward in time and space (Stohl and James 2005; Gimeno et al. 2010, 2012, 2020). Nevertheless, the moisture sources that supply the atmospheric humidity that generates TC precipitation during their genesis and intensification stages remain poorly studied in any basin. Using the Lagrangian FLEXible

PARTicle (FLEXPART) dispersion model (Stohl et al. 2005), Xu et al. (2017) investigated in the Pacific basin the physical processes that caused extreme precipitation in Japan during the landfall of Typhoon Fitow in 2013, and Pazos and Gimeno (2017) studied over the North Atlantic Ocean the climatological moisture sources during the genesis phase of 110 TCs formed in the eastern part of the basin; Pérez-Alarcón et al. (2021) extended the study to the whole basin and to further phases of TC development.

In this study, we aim to investigate the origin of the moisture that becomes in precipitation associated with TCs formed over the IO by using a Lagrangian approach. The analysis also attempts to show the differences by considering the different regions of occurrence for the three life phases of the TCs: during their genesis, lifetime maximum intensity (LMI), and dissipation.

1.1 Study area

The IO is an ocean surrounded by large landmasses at low latitudes and the Indonesian archipelago (Fig. 1), which favours the formation of the monsoon system and the reversal of ocean currents. According to Hermes et al. (2019), the IO's climate is unique. The sea surface temperature (SST) at low latitudes is commonly characterised by values higher than 28 °C, which leads to the maintenance of atmospheric deep convection and seasonal air–sea interactions (DeMott et al. 2015).

The atmospheric transport patterns over the northern IO are mainly modulated by the seasonally reversing monsoon winds (Tegtmeier et al. 2022) and the Somali Low-Level Jet (SLLJ) positioned on the northeastern African continent. This configuration is crucial for moisture and momentum transport in regional circulation towards the Indian Peninsula (IP) (Halpern and Woiceshyn 1999; Viswanadhapalli et al. 2020). Over the southwest IO, the moisture fluxes and the low-level convergence of circulations associated with the Angola thermal low (ATL, positioned over the Angola–Namibia border), the Mascarene High pressure system (MHPS, Manatsa et al. 2014) positioned over 25–35° S and 40–110° E, and the flow from the northeast monsoon region through the tropical IO results in the formation of the SIO Convergence Zone (SICZ) during the austral summer (Ninomiya 2008; Lazenby et al. 2016; Barimalala et al. 2018). Furthermore, the northern branch of the MHPS plays an important role in defining the trajectories of TCs formed in the western SIO (Xulu et al. 2020).

2 Materials and methods

2.1 Data

We used the best track TC archive of the Joint Typhoon Warning Centre (JTWC), which provides complete data

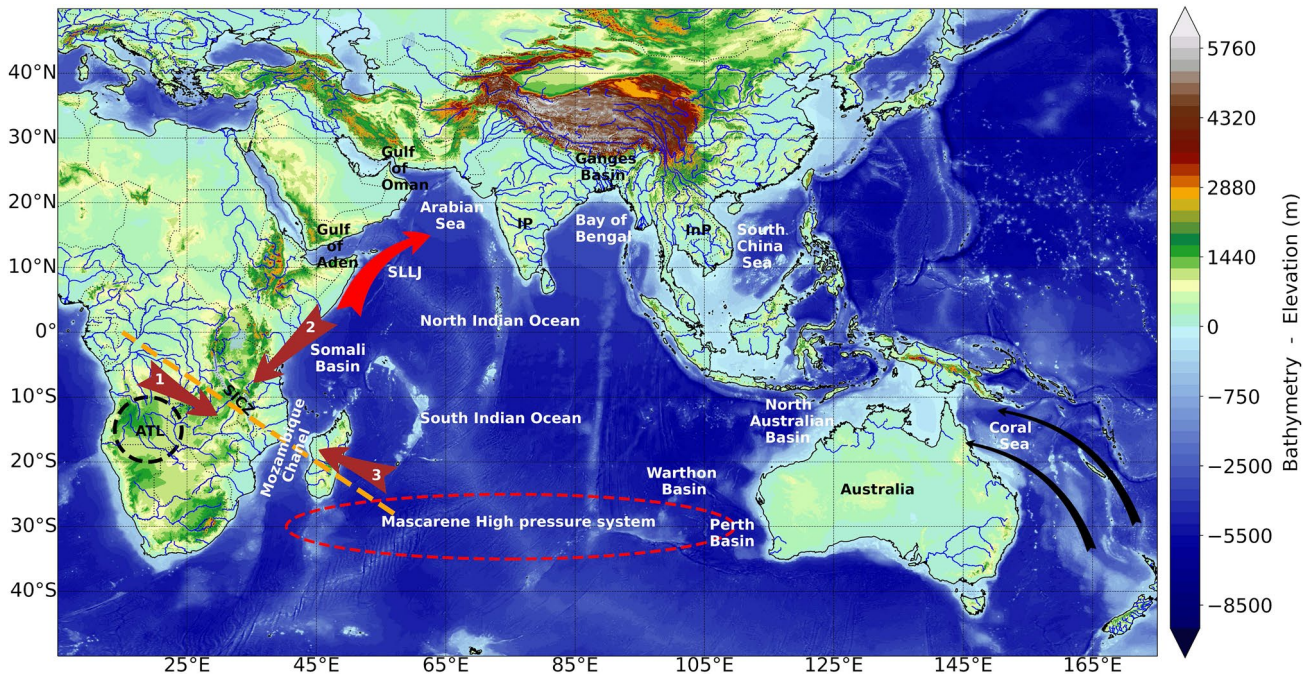


Fig. 1 Indian Ocean and surrounding landmasses. The red arrow represents the position of the Somali Low-Level Jet (SLLJ). The dashed orange line shows the mean location of the South Indian Ocean Convergence Zone (SICZ) during the austral summer. Brown arrows represent the major flows of moisture at low levels from: (1) the northern branch of the circulation of the Angola Thermal Low (ATL, black

dashed circle), (2) northeast monsoon region, (3) and northern branch of the Mascarene High pressure system (dashed red line). Black arrows represent the South-East trade winds at the east of Australia. IP denotes the Indian Peninsula, and InP denotes the Indochina Peninsula

on the systems formed over the NIO and SIO during their lifetime. The period available, from 1980 to 2018, is in the post-satellite era, for which TC records are considerably better than those in the pre-satellite era (Mohapatra et al. 2012). The best track dataset has a text format that contains the location, maximum winds, and minimum central pressure of all known tropical and subtropical cyclones every 6 h.

To compute the vertically integrated moisture flux (VIMF), we used the vertically integrated northward and eastward moisture flux every 6 h extracted from the European Centre for Medium-Range Weather Forecasts (ECMWF) ERA-Interim reanalysis (Dee et al. 2011). The ERA-Interim reanalysis is based on 4D-Var variational analysis in ECMWF's Integrated Forecast System from 1979 to 2019 with a spatial resolution of $1^\circ \times 1^\circ$ in latitude and longitude, and 61 vertical levels from the surface up to 0.1 hPa.

To determine the onset and offset of the monsoon system to investigate its relationship with variations in moisture sources during the phases of the TCs, we used daily precipitation data over the extended period of the study from the Multi-Source Weighted-Ensemble Precipitation (MSWEP) v2 dataset. This database incorporates a wide range of data from different sources (Beck et al. 2019).

2.2 Methodology

2.2.1 Cluster analysis

We objectively grouped TC genesis, lifetime maximum intensity (LMI), and dissipation locations in clusters using the K-means cluster technique (MacQueen 1967). The K-means algorithm divides N points in D dimensions into k clusters, where the addition of the variance within a cluster is minimised to ensure that the objects of each cluster are as close to each other as possible (Hartigan and Wong 1979). The optimal cluster number was determined by the maximum mean and minimum number of negative silhouette values. The silhouette value for each observation is a measure of the similarity of these observations within the same cluster when compared with observations in other clusters (Rousseeuw, 1987; Kaufman and Rousseeuw 2005). This clustering technique is one of the most used because of its simplicity, and it is used for clustering TCs in different basins (e.g. Nakamura et al. 2009; Corporal-Lodangco et al. 2014; Rahman et al. 2018; Pérez-Alarcón et al. 2022a).

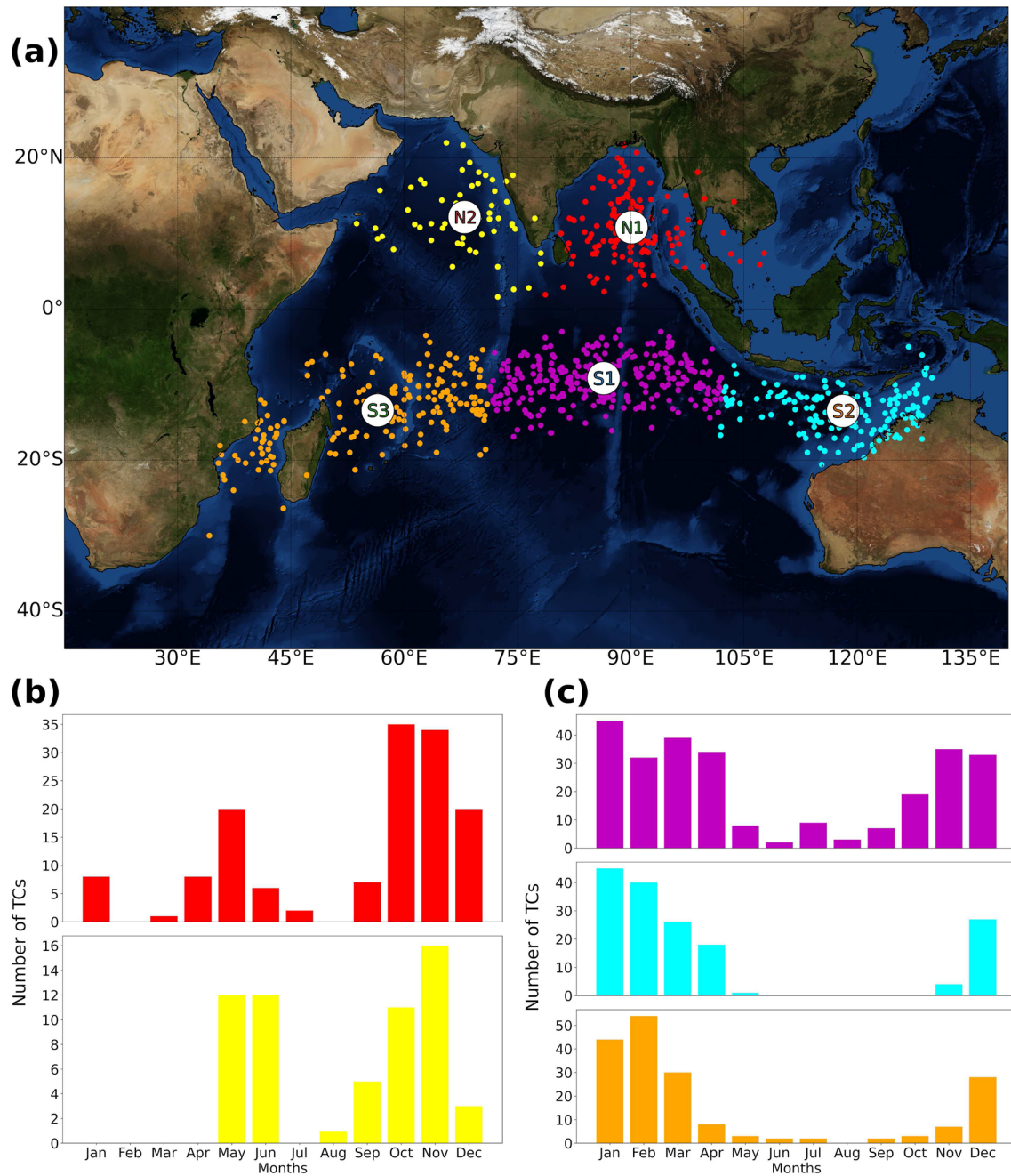


Fig. 2 **a** Genesis points of tropical cyclones (TCs) in the Indian Ocean from 1980 to 2018. Colours represent each cluster calculated by K-means for the North Indian Ocean (Nn, n=1, 2) and South

Indian Ocean (Sn, n=1, 2, 3). **b** Monthly frequency of TCs by cluster for the North Indian Ocean and **c** South Indian Ocean

2.2.2 Moisture sources diagnostic

To determine the origin of the precipitation that occurred during the genesis, the LMI, and the dissipation phases of TCs, we used the outputs from the Lagrangian model FLEXPART v9.0 (Stohl and James 2004, 2005). The model was forced using ERA-Interim reanalysis data (Dee et al. 2011) from the ECMWF at 6-h intervals with a 1° horizontal

resolution and 61 vertical levels covering the entire troposphere. FLEXPART was executed considering that the atmosphere was homogeneously divided into ~2.0 million parcels. It is worth noting that forcing the FLEXPART model with the ERA-5 reanalysis (Hersbach et al. 2020) at 0.25° horizontal resolution and 137 vertical levels or performing dynamic downscaling using the WRF (Skamarock et al. 2008) and FLEXPART-WRF (Brioude et al. 2013)

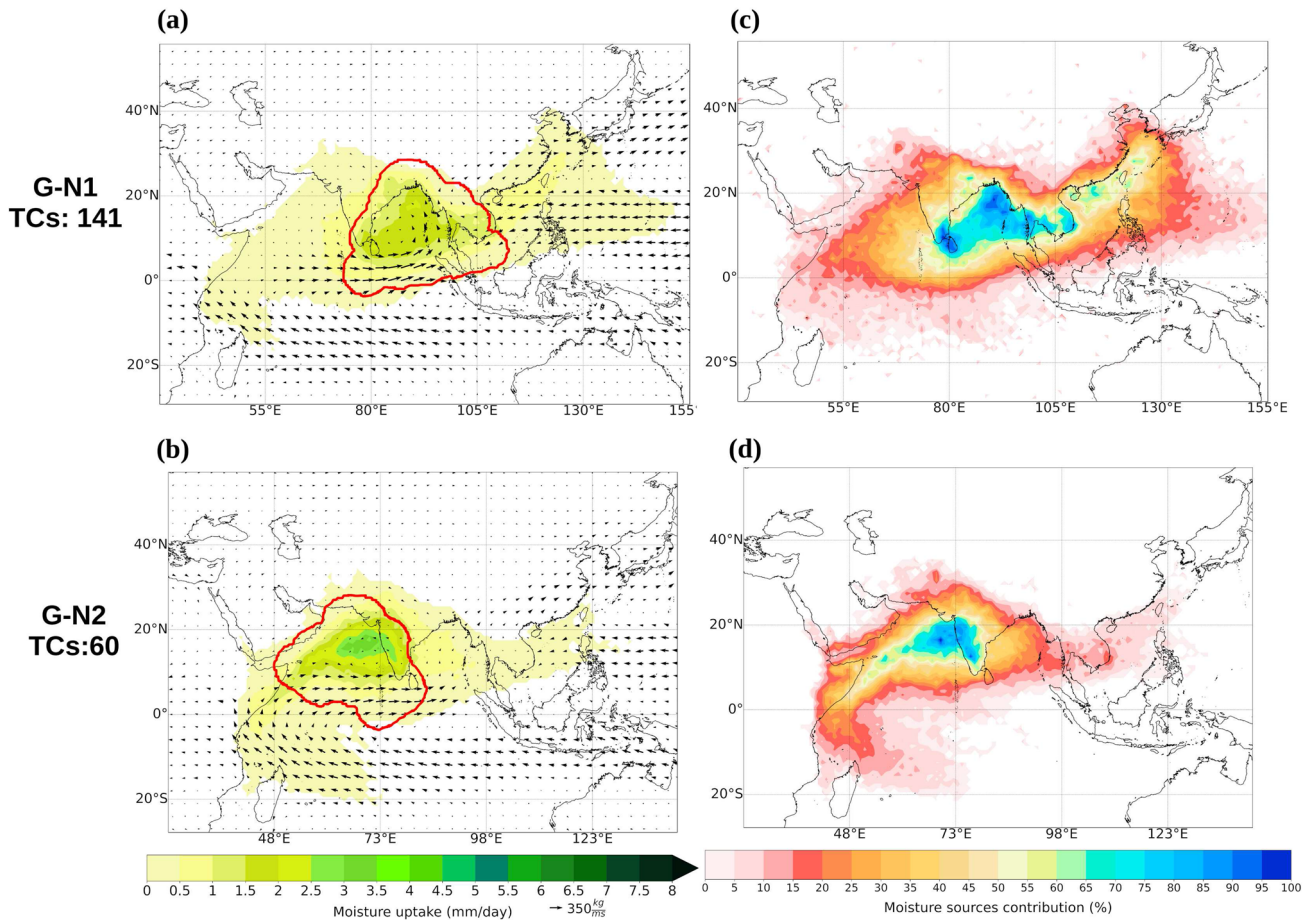


Fig. 3 **a, b** Composite of the moisture uptake (mm/day) pattern during the genesis phase of TCs and the vertically integrated moisture flux (VIMF) (arrows, kg/ms) for the North Indian Ocean. The red line

represents the area occupied by the size of all TCs (numbered on the left) within the cluster. **c, d** Composite of moisture sources contribution (%). Period of study: 1980–2018

models are not suitable for climatological long term studies due to the needed of high computing resources.

We focused on moisture sources for precipitation produced by TCs; thus, the trajectory of all precipitant parcels in the prior 6 h before arriving at the region of interest were followed backward in time up to 10 days. Several authors (Numaguti 1999; van der Ent and Tuinenburg 2017; Gimeno et al. 2021) have considered these 10 days as the average water vapour residence time in the atmosphere at a global scale. According to Läderach and Sodemann (2016), precipitant parcels were defined as those that achieved a decrease in specific humidity higher than 0.1 g/kg. Thus, for each parcel, the moisture variation ($e - p$) every 6 h was computed as

$$m \frac{dq}{dt} \approx m \left(\frac{\Delta q}{\Delta t} \right) = (e - p) \quad (1)$$

where e and p are the evaporation and precipitation from the environment, respectively, m is the mass of the parcel, and q is the specific humidity.

Therefore, by applying the methodology developed by Sodemann et al. (2008) for the identification of moisture sources, we identified regions where air masses gained moisture before the precipitation associated with each TC occurs and measured the moisture uptake (MU) during TC genesis, LMI, and dissipation phases. Further details of the moisture source diagnostic method are in Läderach and Sodemann (2016) and Pérez-Alarcón et al. (2022b). The region of interest around each TC, where the tracked atmospheric particles finally precipitated, was determined by the size of the TC. This target area was calculated as the region inside a circle delimited by the outer radius of the TC, which was computed as it was in Pérez-Alarcón et al. (2021, 2022c). After the individual MU for each TC was computed, a composite was performed to determine the total moisture uptake pattern for each genesis, LMI, and dissipation cluster.

Furthermore, a quantitative estimation of the moisture fractional contribution of each evaporative grid to the precipitation over the entire ocean basin was possible by using the moisture accounting method in Sodemann et al. (2008). The water

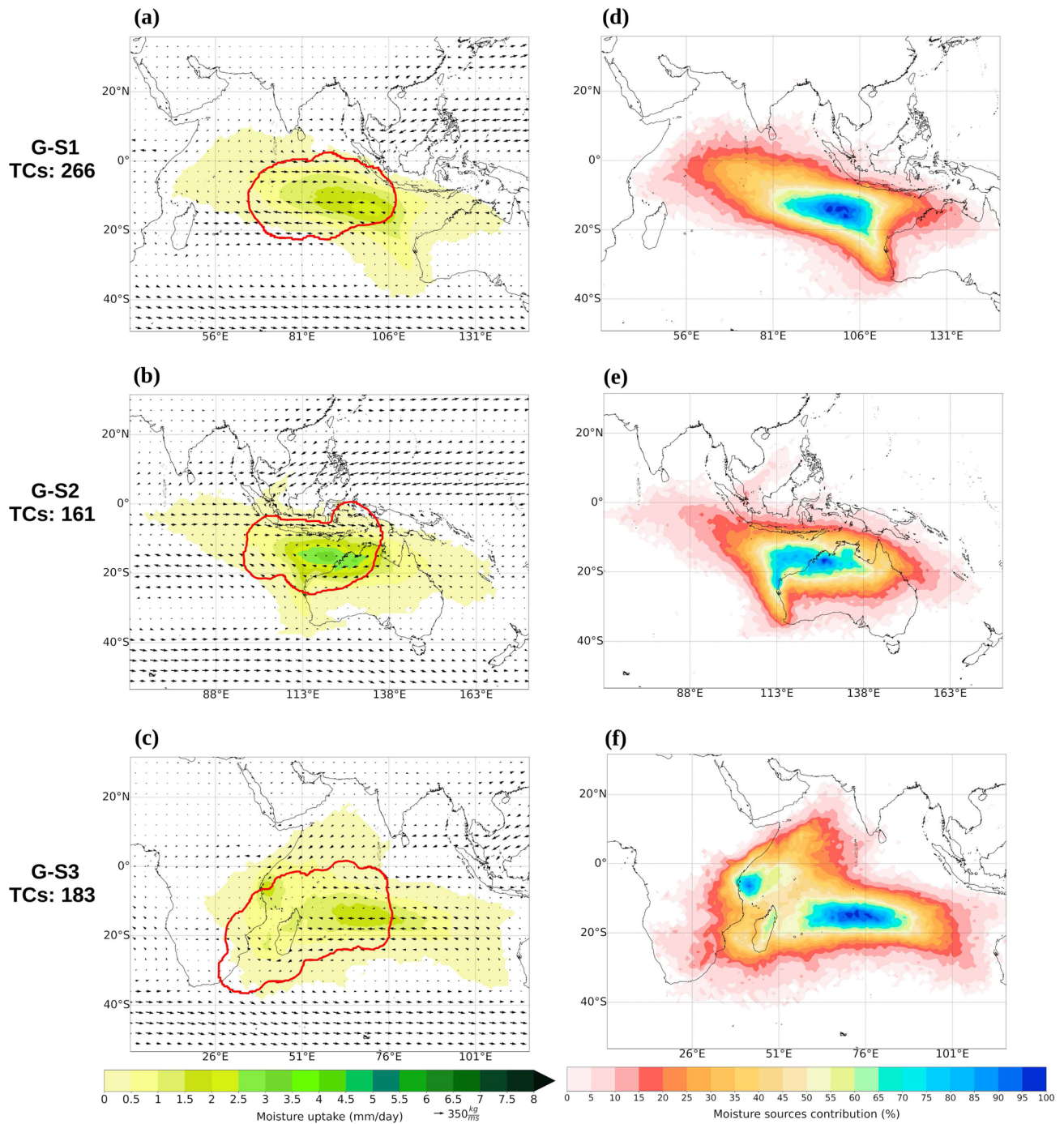


Fig. 4 a–c Composite of the moisture uptake (mm/day) pattern during the genesis phase of TCs and the vertically integrated moisture flux (VIMF) (arrows, kg/ms) for the South Indian Ocean. The red line

represents the area occupied by the size of all TCs (numbered on the left) within the cluster. **d–f** Composite of moisture sources contribution (%). Period of study: 1980–2018

vapour supplied by the moisture sources can be estimated by adding the individual fractional contributions over each grid cell. This methodology is similar to the Eulerian diagnostics of strong, large-scale ocean evaporation events (Aemisegger and Papritz 2018).

Moreover, the moisture source diagnostic method applied in this study permits an estimation of the time that an atmospheric parcel flows in the atmosphere before it precipitates, the known backward transit time, or water vapour residence time (WVRT) (Gimeno et al. 2021). The WVRT of each parcel

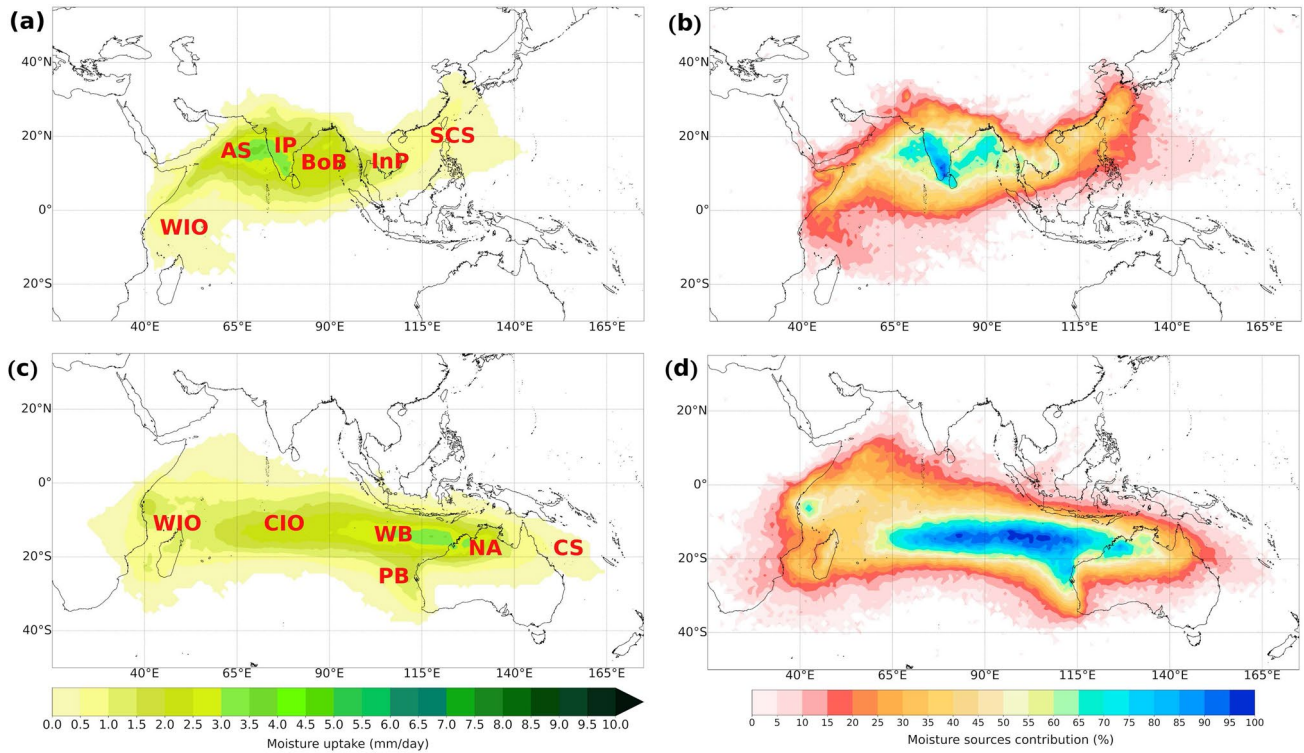


Fig. 5 Composite pattern of the moisture uptake (mm/day) for all TCs genesis locations for the **a** North Indian Ocean (NIO) and **c** South Indian Ocean (SIO); and moisture sources contribution composite for the **b** NIO and **d** SIO basins during the study period (1980–2018)

was estimated as the time between the far evaporation and precipitation within the TC limits, weighted by each evaporation location fractional contribution along the parcel trajectory. Therefore, by averaging the WVRT of all precipitant parcels over the target region, the Lagrangian mean residence time of water vapour (MWVRT) can be computed.

2.2.3 Determination of the monsoon onset and offset dates

To improve the understanding and elucidate the linkages between the monsoon systems and the extension and intensity of moisture sources for TC genesis, LMI, and the dissipation stages, we analysed the variability of moisture sources for the TCs during the pre-monsoon, monsoon, and post-monsoon phases.

To objectively determine the onset and offset dates throughout the year of the different monsoonal circulations over the study area (the Indian Summer Monsoon [ISM], the East Asian Summer monsoon [EASM], the Southeastern African Monsoon [SEAM], and the North Australia Monsoon [NAM]) we used the method in Noska and Misra (2016). This methodology was applied by Dunning et al. (2016) to study the onset and cessation of seasonal rainfall over Africa, and by Sorí et al. (2017) to investigate the atmospheric transport of moisture linked to monsoonal phases for the Indus, Ganges,

and Brahmaputra River basins. The methodology is based on computing the daily cumulative anomalies ($C'm$) of the average precipitation for an affected region throughout the year. The daily cumulative anomalies for day i of year m are computed as:

$$C'm(i) = \sum_{n=1}^i [D_m(n) - R_c] \quad (2)$$

where $D_m(n)$ is the daily rainfall for day n of year m , and R_c is the climatology of the annual mean of the precipitation for N days ($N = 365$ or 366) for M years:

$$R_c = \frac{1}{MN} \sum_{m=1}^M \sum_{n=1}^N D(m, n) \quad (3)$$

The $C'm$ for the ISM, EASM, SEAM, and NAM were calculated over the limited regions defined as (7° – 22° N, 73° – 90° E), (5° – 45° N, 90° – 125° E), (0° – 40° S, 25° – 50° E) and (10° – 22° S, 110° – 140° E), respectively.

Therefore, the onset is defined as the day after the $C'm$ reaches its absolute minimum, and the offset is defined as the day when the $C'm$ reaches its absolute maximum after the onset date. We assumed the pre-monsoon from 60 days before the onset and the post-monsoon until 60 days after the offset, in agreement with Kiguchi and Matsumoto (2005).

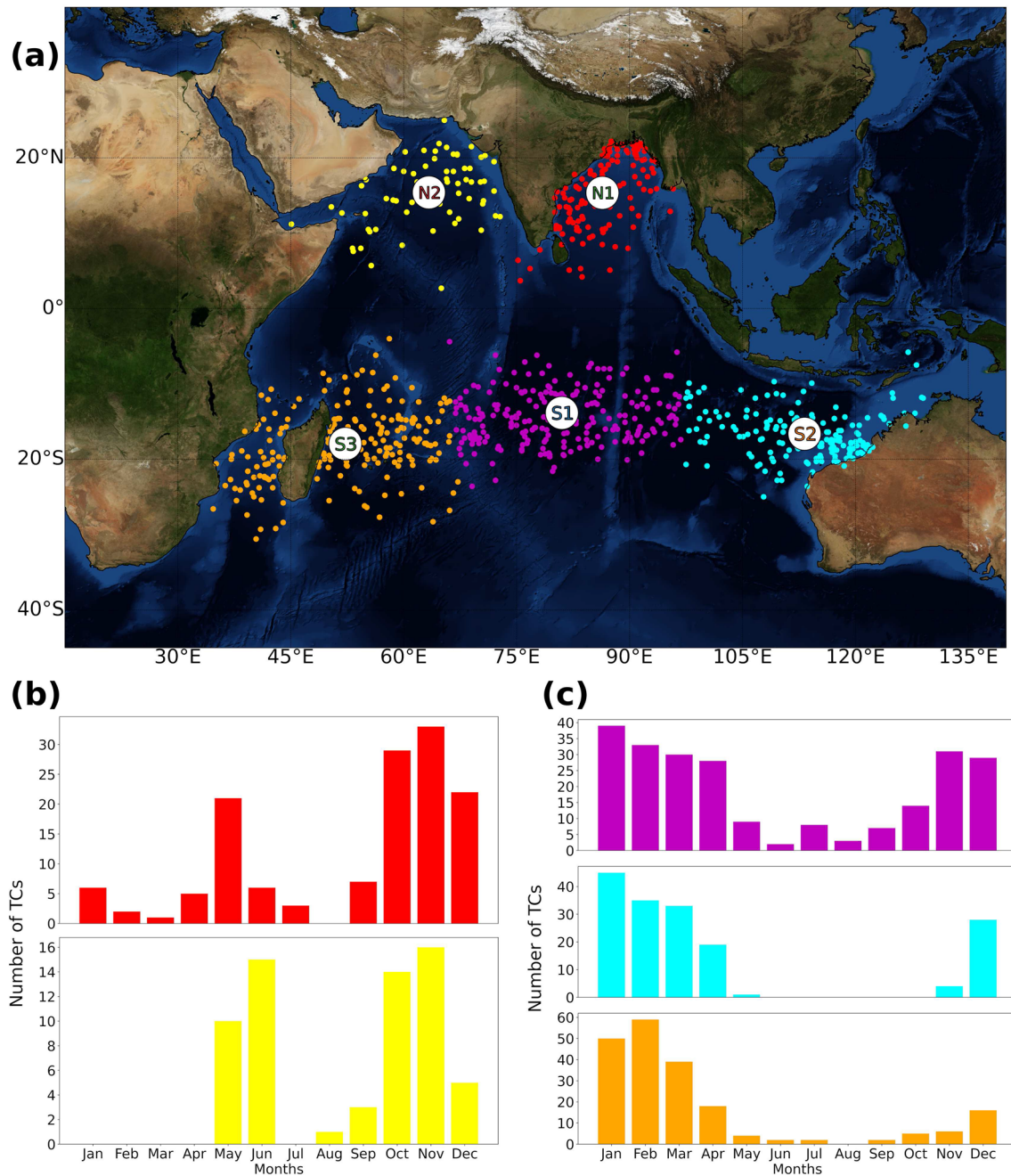


Fig. 6 a Tropical cyclones (TCs) lifetime maximum intensity (LMI) over the Indian Ocean from 1980 to 2018. Colours represent each cluster calculated by K-means for the North Indian Ocean (Nn, n=1,

2) and South Indian Ocean (Sn, n=1, 2, 3). Monthly frequency of TCs by cluster is also represented for the **b** North Indian Ocean and **c** for South Indian Ocean

3 Results and discussion

3.1 Origin of TCs' precipitation during the genesis phase

The K-means cluster analysis (Fig. 2a) clearly reveals five regions of TC genesis for the entire IO basin. For the NIO basin, the Bay of Bengal (G-N1) accounts for 70% of the

systems, and the Arabian Sea (G-N2) with the remaining 30% (Fig. 2a). These results agree with those of Bhatla et al. (2020), who also noted that TCs are uncommon in the Arabian Sea. In both regions, the TC activity in the NIO has a bimodal annual frequency distribution (Fig. 2b) with a marked maximum during October and November, and a secondary maximum in May and June, coinciding with the post- and pre-monsoon seasons, respectively (Yanase et al.

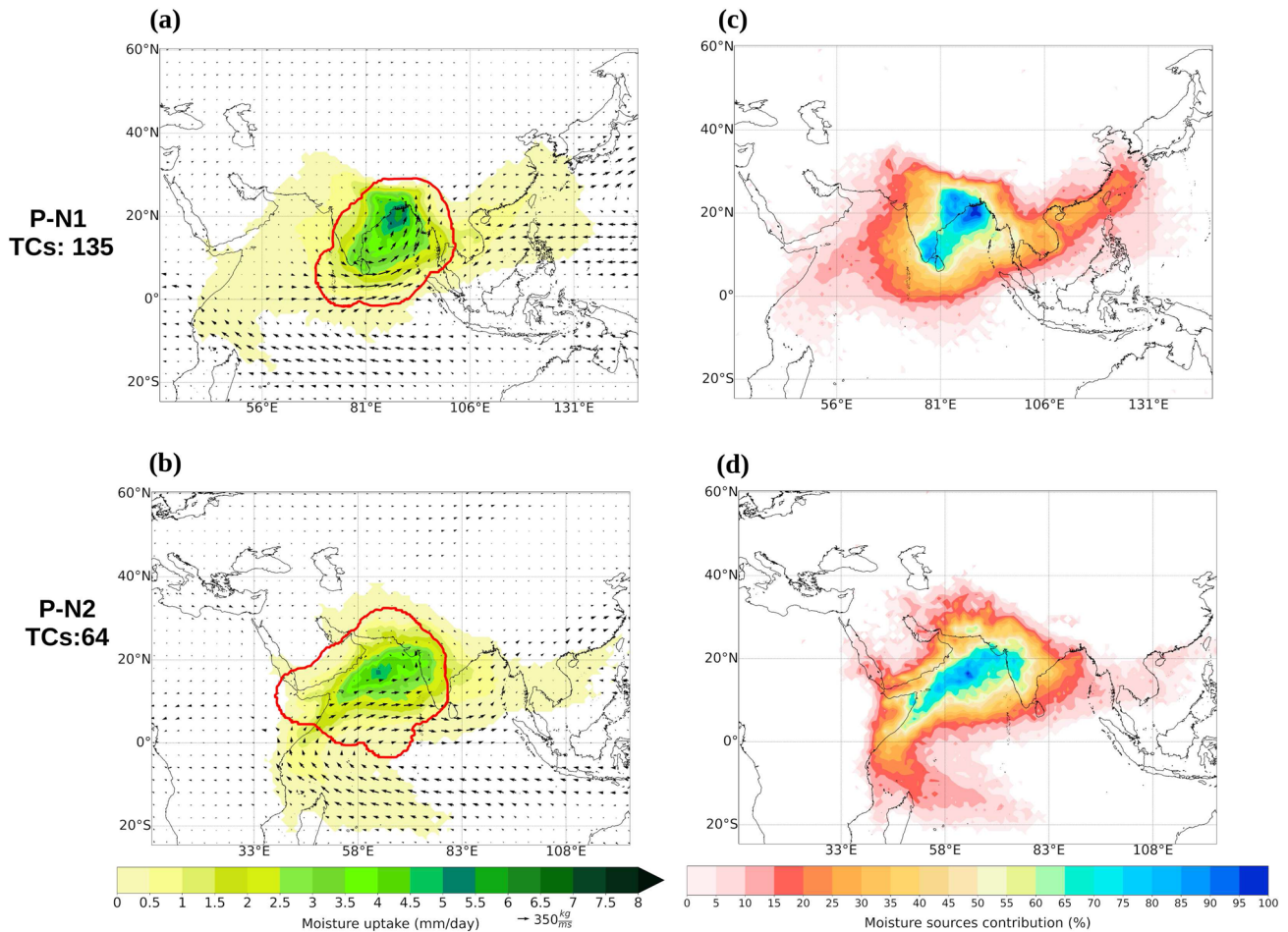


Fig. 7 **a, b** Composite of the moisture uptake (mm/day) pattern for the North Indian Ocean during TCs lifetime maximum intensity (LMI) phase and the vertically integrated moisture flux (VIMF)

(arrows, kg/ms). The red line represents the area occupied by the size of all TCs (numbered on the left) within the cluster. **c, d** Composite of moisture sources contribution (%). Period of study: 1980–2018

2012; Li et al. 2013). For the SIO basin, three regions of genesis were identified: the central tropical SIO (G-S1) with 43.6% of the events, northwest of Australia (G-S2, 26.4%), and the southwest IO (G-S3, 30%). Over the SIO basin, the highest TC frequency in each genesis cluster was observed in January and February (Fig. 2c), in agreement with Yuan et al. (2019).

The moisture uptake (MU) pattern over the NIO revealed that for the G-N1 region (Fig. 3a), the Bay of Bengal (BoB) was its main moisture source, contributing between ~50% and 70% of the atmospheric humidity (Fig. 3c), and the South China Sea (SCS) with a notable ~30–45%, and the Indian Peninsula (IP) with ~15–20%. The air masses reaching G-N2 gained moisture (Fig. 3b) mainly from the Arabian Sea (AS) and the southwestern portion of the IP, with a ~55–70% contribution (Fig. 3d), and the moisture contribution was lower from the SIO through the Somali Low-Level Jet (SLLJ) area of influence (~10–20%) and from the east African coast (~15–30%).

Over the SIO, the easterly trade winds blowing from the Mascarene High pressure system (MHPS) were the mainly mechanism of moisture transport from the Perth Basin (PB) and Wharton Basin (WB) to the G-S1 genesis cluster (Fig. 4a). The moisture contribution (Fig. 4d) from the WB ranged from 75 to 85%, and the PB supplied ~30–50%. For G-S2 (Fig. 4b, e), located over the North Australian Basin, the main moisture source was its region, supporting ~50–70%. The South-East trade winds transported moisture from the western Coral Sea (CS; ~10–25%), crossing north of Australia (Nieto et al. 2014). Additionally, the westerly winds linked to the Australian monsoon system during the warmer months in the South Hemisphere (Drosowsky 1996; Lisonbee et al. 2020) transported moisture (~5–25%) from the eastern tropical IO. Overall, these moisture transport patterns were supported by the VIMF field (Fig. 4b). For G-S3 (Fig. 4c, f), the MHPS also transported the majority of the atmospheric humidity (~65–90%) from the central

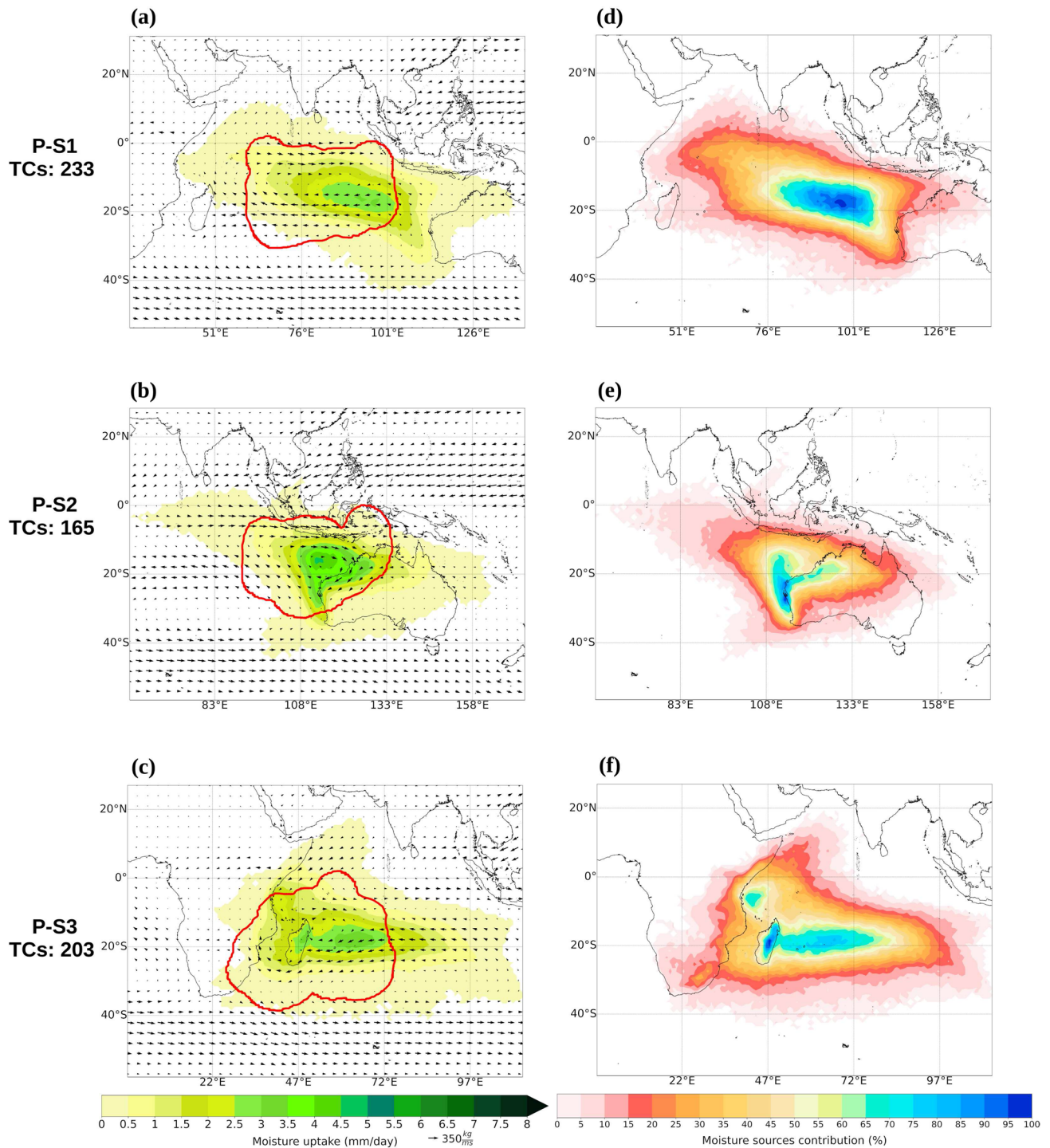


Fig. 8 a–c Composite of the moisture uptake (mm/day) pattern for the South Indian Ocean during TCs lifetime maximum intensity (LMI) phase and the vertically integrated moisture flux (VIMF)

(arrows, kg/ms). The red line represents the area occupied by the size of all TCs (numbered on the left) within the cluster. **d–f** Composite of moisture sources contribution (%). Period of study: 1980–2018

IO (CIO), and a secondary nucleus appeared over the Somali basin, exhibiting a moisture contribution of ~65%.

Several source regions contribute to moisture in various genesis areas; therefore, we analysed the total contribution

of moisture from each source to the cyclogenesis over both sub-basins. The total MU pattern of the precipitant parcels residing over the TC genesis regions over the IO is plotted in Fig. 5. The advection of oceanic moisture from the IO

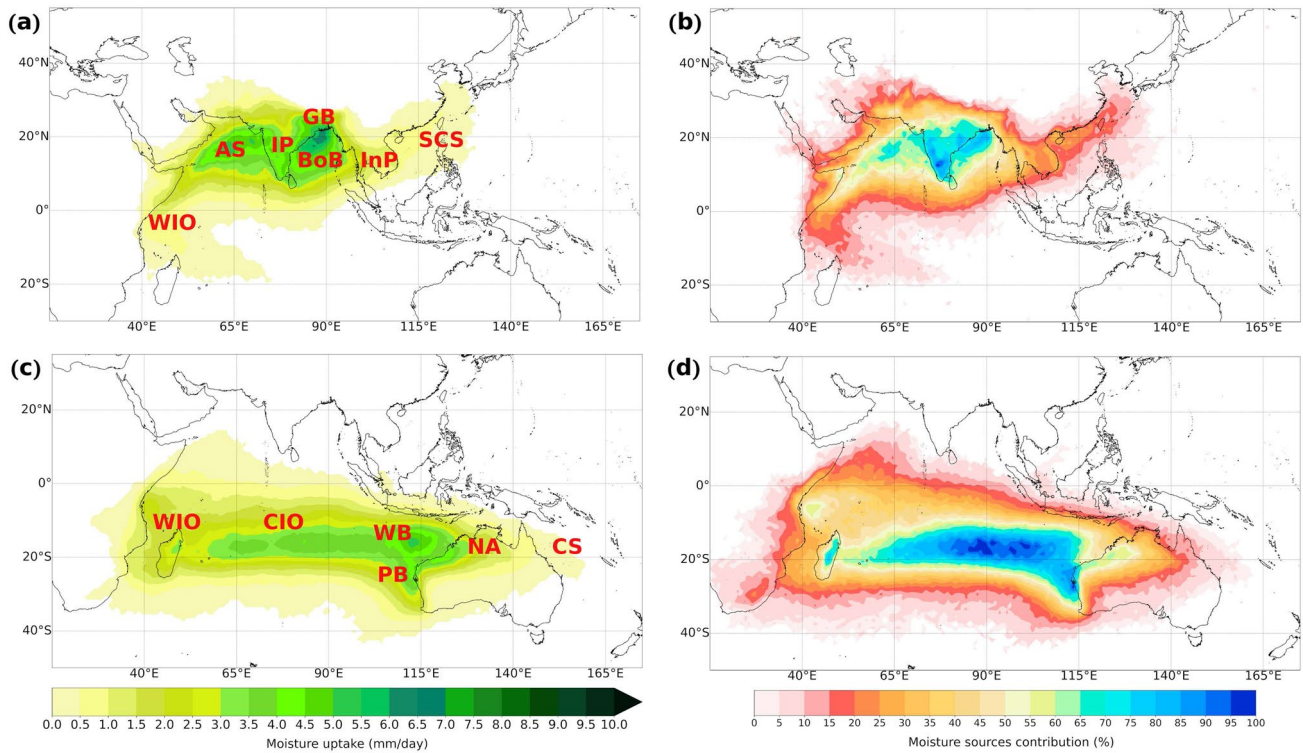


Fig. 9 The same as Fig. 5 but for the TCs lifetime maximum intensity

towards the TC genesis regions was higher than that from the subcontinental land. The oceanic and terrestrial sources in NIO contributed ~85.93% and ~14.07% of moisture, respectively, while the contributions from ocean and land regions accounted for ~80.29% and 19.71% in SIO, respectively. In summary, the results allowed the identification of six sources of moisture for cyclogenesis in the NIO basin (Fig. 5a): the Arabian Sea (AS), the Bay of Bengal (BoB), terrestrial moisture sources in the Indian (IP) and Indochina Peninsula (InP), the South China Sea (SCS), and the western IO (WIO) along the SLLJ jet. Overall, the IP, AS, and BoB contributed to the majority of the moisture (~70%), the moisture contributions from InP and SCS ranged from 20 to 30%, and the atmospheric humidity supported by the

WIO is less than 20% (Fig. 5b). Likewise, in the SIO basin (Fig. 5c), the moisture sources that supplied the atmospheric humidity during the genesis of TCs were the western IO (WIO), the central IO (CIO), the Wharton Basin (WB), the Perth Basin (PB), the Coral Sea (CS), and northern Australia (NA). As shown in Fig. 5d, the highest moisture contribution (~50–80%) was from CIO and WB, followed by NA (~40%) and WIO (~30%). Notably, the WIO exhibits nuclei with a maximum contribution of 60% over the Somali basin. Moreover, the moisture contribution from the CS was less than 10%.

From the different sources, the moisture lasted different times to become precipitation. The MWVRT for the whole sources over the NIO basin, calculated from the Lagrangian approach, during TCs genesis phases was 3.1 ± 0.5 days (variability indicated by one standard deviation), 3.2 ± 0.4 days for the Bay of Bengal (G-N1) cluster, and 2.9 ± 0.5 days for the cluster over the Arabian Sea (G-N2). For the whole SIO basin, the estimated MWVRT was higher than that in the NIO, at 3.3 ± 0.5 days. The central tropical SIO (G-S1) exhibited the highest values, 3.4 ± 0.5 days, followed by the western SIO (G-S3) and northeast Australia (G-S2), which showed 3.3 ± 0.5 days and 3.1 ± 0.5 days, respectively.

Table 1 Lagrangian mean water vapour residence time (MWVRT, in days) during the TCs lifetime maximum intensity (LMI), and for the TCs categorised by intensity: Tropical Storm (TS), Hurricanes (H, category 1 and 2 on the Saffir-Simpson scale), and Major Hurricane (MH, category 3+ on the Saffir-Simpson scale)

Basin	LMI	TS	H	MH
NIO	2.8 ± 0.5	3.0 ± 0.5	2.8 ± 0.5	2.7 ± 0.3
SIO	3.1 ± 0.5	3.2 ± 0.5	3.1 ± 0.4	3.1 ± 0.5

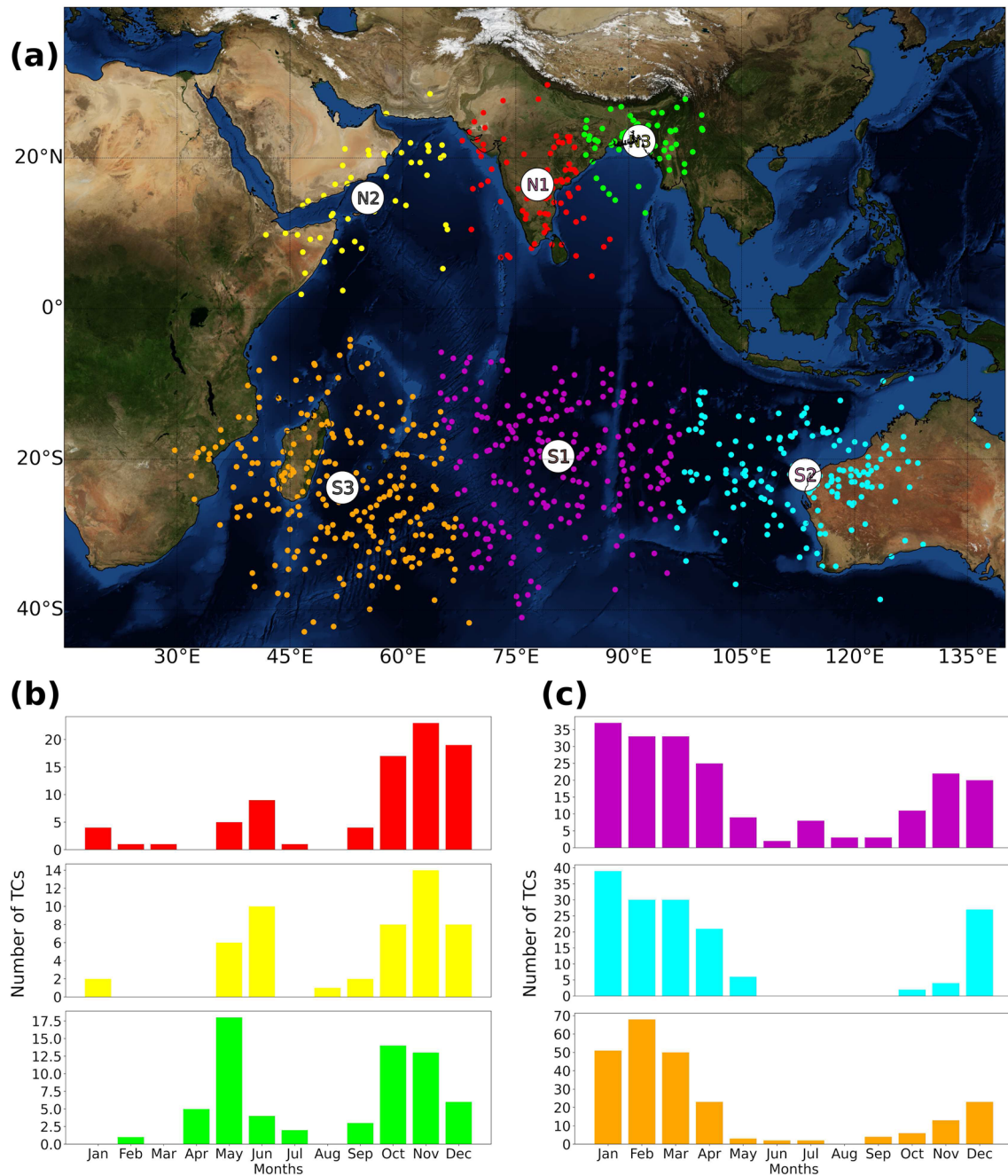


Fig. 10 a Dissipation points of tropical cyclones (TCs) formed over the Indian Ocean from 1980 to 2018. Colours represent each cluster calculated by K-means for the North Indian Ocean (Nn, $n = 1, 2$)

and South Indian Ocean (Sn, $n = 1, 2, 3$). The monthly frequency of TCs by cluster is also represented for the **b** North Indian Ocean and **c** South Indian Ocean

3.2 Origin of tropical cyclone precipitation in the lifetime maximum intensification phase

Cluster analysis (Fig. 6a) again revealed five regions in the IO basin where TCs reached the lifetime maximum intensity (LMI). For the NIO basin was the Bay of Bengal (P-N1) where 67.8% of the TCs showed their peak of intensification, and the Arabian Sea (P-N2) accounted the remaining 32.1%.

For the SIO basin was the central tropical South Indian Ocean (P-S1) where occurred 38.7% of the TCs during LMI, followed by the West Indian Ocean (P-S3, 33.7%), and the northwest of Australia (P-S2, 27.4%). For both basins, the monthly frequency showed a bimodal distribution, similar to that observed for genesis (Fig. 6b,c).

Figures 7a,b show that the evaporation of water over the BoB was the main region that supplied atmospheric

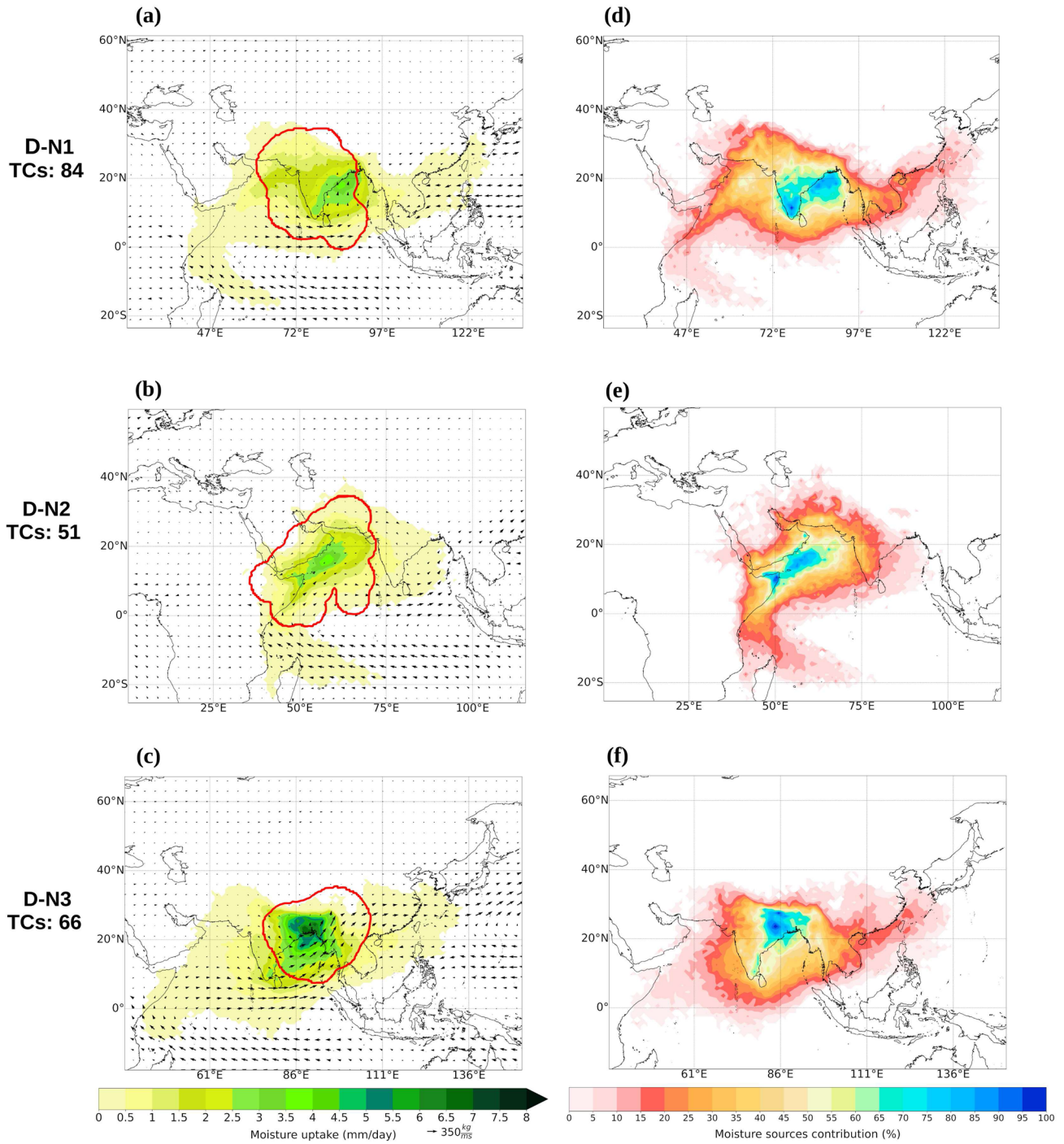


Fig. 11 a–c Composite of the moisture uptake (mm/day) pattern for the North Indian Ocean during the TCs dissipation phase and the vertically integrated moisture flux (VIMF) (arrows, kg/ms). The red line

represents the area occupied by the size of all TCs (numbered on the left) within the cluster. c–e Composite of moisture sources contribution (%). Period of study: 1980–2018

humidity (~60–75%) for the TCs in P-N1 during their LMI. In addition, P-N1 received, but in a smaller amount, moisture from the SCS (~25%), the IP (~15–25%), and from the AS (~5–10%), in Fig. 7b. The pattern changed for P-N2 (Fig. 7c), for which the AS supplied most of the moisture

(~60%), and not an inconsiderable amount arrives across the equator along the coast of East Africa and the Gulf of Aden (~25%) through the SLLJ (Fig. 7c), in agreement with Ordóñez et al. (2012).

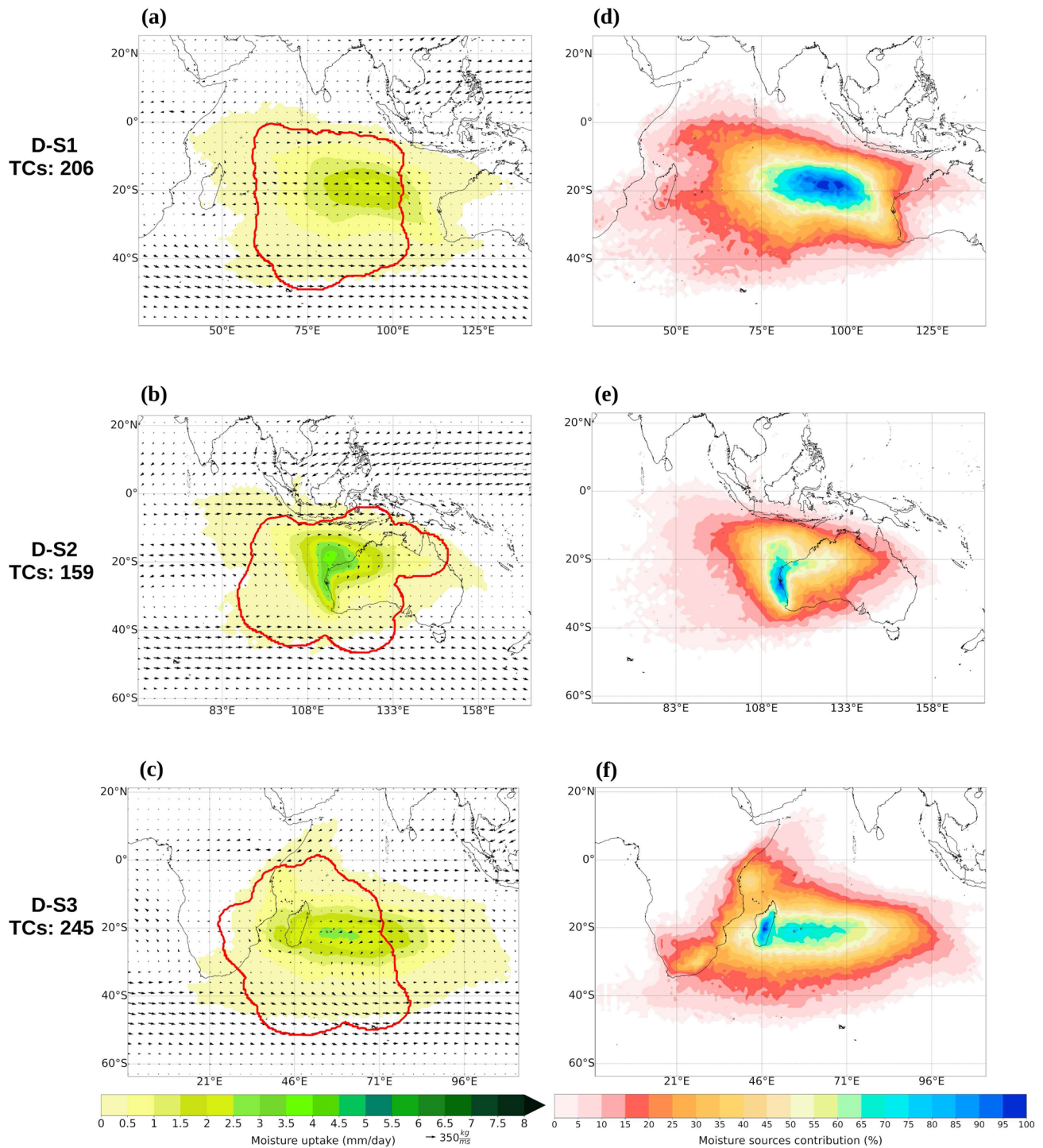


Fig. 12 a–c Composite of the moisture uptake (mm/day) pattern for the South Indian Ocean during the TCs dissipation phase and the vertically integrated moisture flux (VIMF) (arrows, kg/ms). The red line

represents the area occupied by the size of all TCs (numbered on the left) within the cluster. c–e Composite of moisture sources contribution (%). Period of study: 1980–2018

For the TC LMI phase over the SIO basin, the pattern of moisture uptake in each cluster was similar to that observed for TC genesis, but more intense (Fig. 8). The circulation pattern associated with the MHPS (see VIMF vectors,

Fig. 8a) transported moisture from the Wharton and Perth basins to P-S1 along its eastern branch, supplying approximately 50–70% of the moisture (Fig. 8d), and the northern branch towards the west supplied moisture from the central

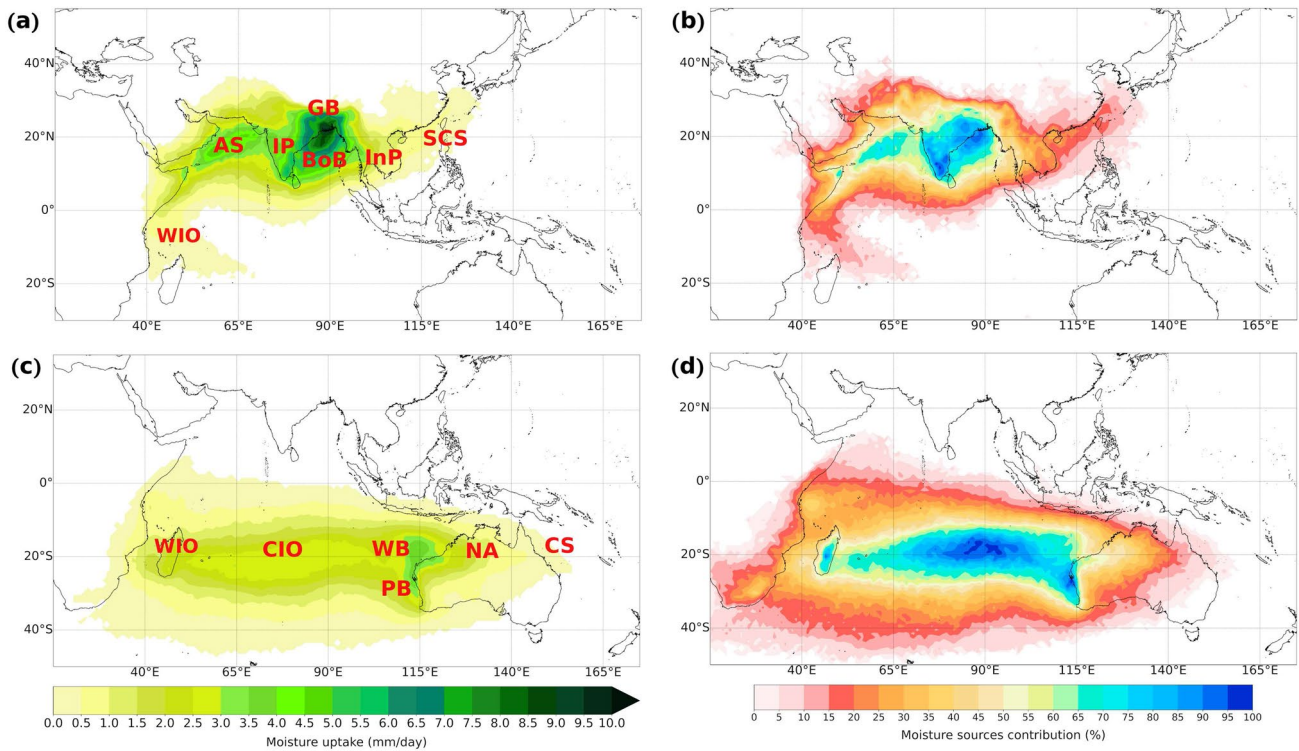


Fig. 13 The same as Fig. 5 but for the TCs dissipation phase

IO (~40–65%) to P-S3 (Fig. 8c, f). For P-S3, the flow from the northeast monsoon region from the northeastern coast of Africa and the Somali Basin also achieved ~20–40%. Furthermore, for P-S2 the importance of the moisture transported from inland northern Australia (~40–75%), and the winds related to the Australian monsoon, blowing from the northwest, also transported moisture (~5–25%) from the NOI towards P-S2 (Fig. 8b, e), complemented by the trade winds associated with high pressures around Australia from the Coral Sea (~5%), in agreement with Nieto et al. (2014).

Figure 9 summarises the moisture sources for the TCs during their LMI over the IO. Clearly, for the NIO basin, AS, BoB, Ganges basin (GB), and the IP were again the main moisture sources for this TC phase (Fig. 9a). The four supplied ~64% of the atmospheric humidity (Fig. 9b); the Indochina Peninsula (InP) and the South China Sea (SCS) provided ~27%; and the WIO, the remaining ~9%. Over the SIO basin (Fig. 9c), the unified area of the central IO, WB, and BP was the main moisture source for the TCs during the LMI phase, supplying most of the moisture (~63%), followed by the WIO (~22%) and northern Australia (NA) and western Coral Sea (CS) (~15%). Figure 9 also reveals that the moisture contributions from oceanic sources are notably higher than that from terrestrial sources during the LMI phase in both basins. Overall, the oceanic sources supplied ~84.33% (~78.19%) in the NIO (SIO) basin, while the terrestrial counterpart contributed ~15.67% (~21.81%).

The dynamic and thermodynamic processes leading to changes in TC intensity are a key factor in understanding TC development. Our findings revealed that intensity changes to hurricane category (NIO: 702.8 mm/day per TC, SIO: 765.1 mm/day per TC) required more atmospheric moisture than those to major hurricanes (NIO: 660.1 mm/day per TC, SIO: 705.4 mm/day per TC) or tropical storms (NIO: 575.8 mm/day per TC, SIO: 637.9 mm/day per TC) in the NIO and SIO basins. As a general feature, TCs during the LMI or intensity changes over the NIO gained less water vapour for precipitation than over the SIO. Additionally, like for LMI and genesis phases, the oceanic sources supplied the higher amount of moisture in both basins.

The MWVRT during TCs LMI and intensity changes (Table 1) was higher in the SIO (3.1 ± 0.5 days) than in the NIO (2.8 ± 0.5 days). On average, the moisture uptake that became precipitation during the tropical storm category (TS) exhibited higher MWVRT in both basins than during the hurricane category (H) and major hurricane category (MH).

3.3 Origin of tropical cyclone precipitation during the dissipation phase

The clusters for the TC dissipation phase over the NIO and SIO basins are shown in Fig. 10a. In this phase, three clusters appear in the NIO basin. The majority of TCs (41.7%) dissipated over the Indian Peninsula (D-N1, red),

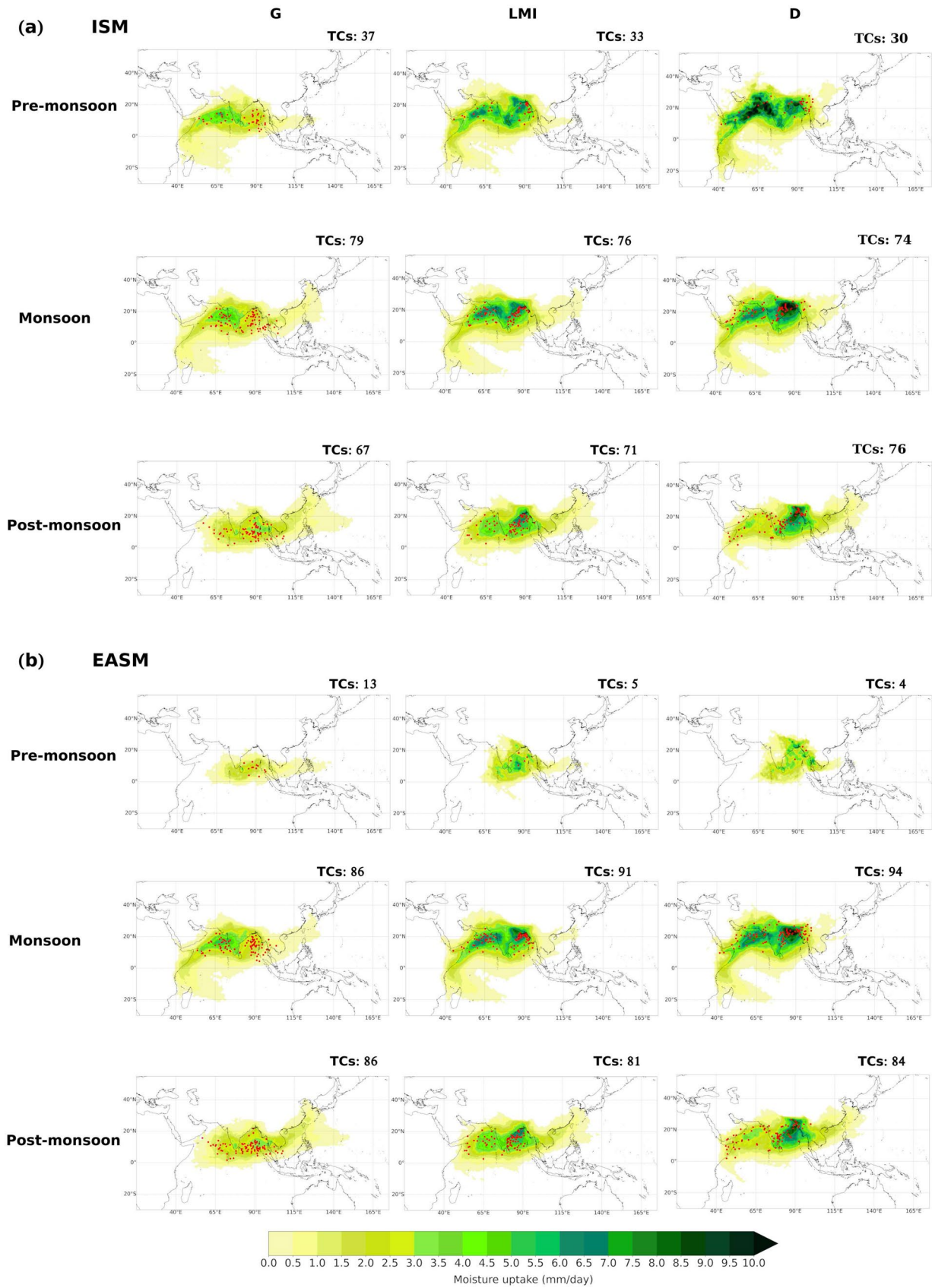


Fig. 14 Moisture uptake (greenish colour) for tropical cyclones (TCs) genesis, peak of maximum intensity, and dissipation over the NIO basin during the pre-monsoon, monsoon, and post-monsoon seasons for the **a** Indian Summer Monsoon (ISM) and **b** East Asian Summer Monsoon (EASM). Capital letters at the top indicate the TCs phases, genesis (G), lifetime maximum intensity (LMI), and dissipation (D). Red points indicate the TCs position in each stage. In the top right of each map is the number of TCs during each monsoon phase

the Arabian Sea accounted for 25.4% (D-N2, yellow), and the remaining 32.9% disappeared over the eastern coast of India and Bangladesh (D-N3, green). The SIO basin shows a cluster pattern for TC dissipation, similar to those for the genesis and LMI phases, although in this terminal phase, the TC positions within each cluster were more dispersed. One cluster was located in the central IO (D-S1, purple, 33.7%); one over the western coast of Australia (D-S2, cyan, 26%); and the third, which accounted for a higher number of TCs, appeared in the western IO (D-S3, orange, 40.1%).

The TC monthly distribution of each cluster revealed a high frequency of events from October to December in the NIO (Fig. 10b) and from December to April in the SIO (Fig. 10c). In both basins, the monthly distribution for TC dissipation showed a similar pattern to that observed for the prior life phases.

Over the NIO, the wind flux linked to the SLLJ appeared as the main mechanism of moisture transport from the western SIO and the eastern coast of Africa towards the D-N1 and D-N2 clusters, and the moisture uptake and VIMF patterns were more intense for D-N2 (Fig. 11a,b), supplying approximately 40–60% of moisture. For D-N1, the BoB and IP were the main moisture sources, supplying ~60–70% of moisture (Fig. 11d). Additionally, the moisture transported from the SCS was approximately 10% for D-N3 and D-N1. Furthermore, the inland GB exhibited the highest moisture supply (~65%) for D-N3 (Fig. 11c, f). According to Ying et al. (2005), the moisture supplied and the properties of the underlying surface have a significant effect on the TC rainfall distribution. Therefore, our results suggest that the moisture supplied is not only helpful in sustaining the TCs remnants at the dissipation stage over land but is also an essential condition for causing torrential rain.

In the SIO basin, the easterly winds linked to the northern branch of the MHPS transported much of the atmospheric moisture from the western coast of Australia and the Wharton Basin to D-S1 (Fig. 12a), contributing approximately 40–70% (Fig. 12b). For the D-S2 cluster, the Perth Basin, the north Australian basin, and the northwestern portion of mainland Australia supplied moisture in a range of ~45–70%, and the Australian monsoonal westerly winds transported the remaining amount (~5–20%) from the eastern IO (Fig. 12b,e). For D-S3, the central SIO through the easterly winds was the principal source (~40–65%), which

also received moisture from the eastern coast of Africa and the Somali basin (~20–35%), in Figs. 12c and f.

Similar to the TC genesis and LMI, Fig. 13 summarises the moisture sources and their contributions to the precipitation during the TC dissipation stage over the NIO and SIO basins. Figure 13a shows that the BoB, AS, GB, and IP were the main moisture sources in the NIO basin, providing ~60–80% (Fig. 13b). Additionally, the InP and the SCS along the coast of South China supplied ~20–30%, and the WIO provided the remaining ~10%. Similarly, from Fig. 13c, the WB, PB, and CIO were identified as the main sources of atmospheric humidity for the precipitation of TCs during the dissipation process in the SIO basin, supplying ~50–70% of moisture (Fig. 13d). Additionally, the moisture transported from the WIO was ~25–35% of the total amount, and the northwestern portion of Australia (NA) contributed ~5–10%. Overall, the oceanic (terrestrial) sources supplied ~81.83% (~18.17%) and ~83.17% (~16.82%) of moisture in NIO and SIO basins, respectively.

Regarding the MWVRT, no noticeable differences were found to the genesis and LMI stages. The MWVRT during the dissipation stage that formed over the NIO basin varied from 2.4 ± 0.5 (in D-N2) to 2.8 ± 0.5 (in D-N3) days; for the SIO basin, it was higher than for NIO, ranging from 2.7 ± 0.4 (in D-S2) to 3.1 ± 0.4 (in D-S1) days.

3.4 Relationship between monsoon systems and moisture sources

The region of the NIO basin is affected by the most important monsoon system, the Asian summer monsoon, which includes the Indian summer monsoon (ISM) and the East Asian Summer monsoon (EASM). The Asian summer monsoon ASM is considered a large-scale coupled ocean–atmosphere phenomenon and is associated with changes in atmospheric circulation patterns (Liu et al. 2019) over the region. Our findings revealed that on average, the ISM started on 01 June and ended on 26 October, the mean onset of EASM occurred on 02 May, and the offset was approximately on 16 October, in agreement with Noska and Misra (2016). Accordingly, 39.3% (42.8%) and 33.3% (42.8%) of TC genesis in the NIO occurred during the ISM (EASM) monsoon and post-monsoon seasons.

We also investigated the changes in the intensity and position of moisture sources for TCs over the NIO basin because of the different monsoon seasons (pre-monsoon, monsoon, and post-monsoon), as shown in Fig. 14 for the genesis, LMI, and dissipation phases, and in Figure S1 for the TS, H, and MH intensity categories. During the ISM pre-monsoon and monsoon seasons, the highest moisture contribution to TCs over the NIO basin was from the IP, AS, and WIO along the eastern coast of Africa. The moisture was mainly transported to the TC position by a strong

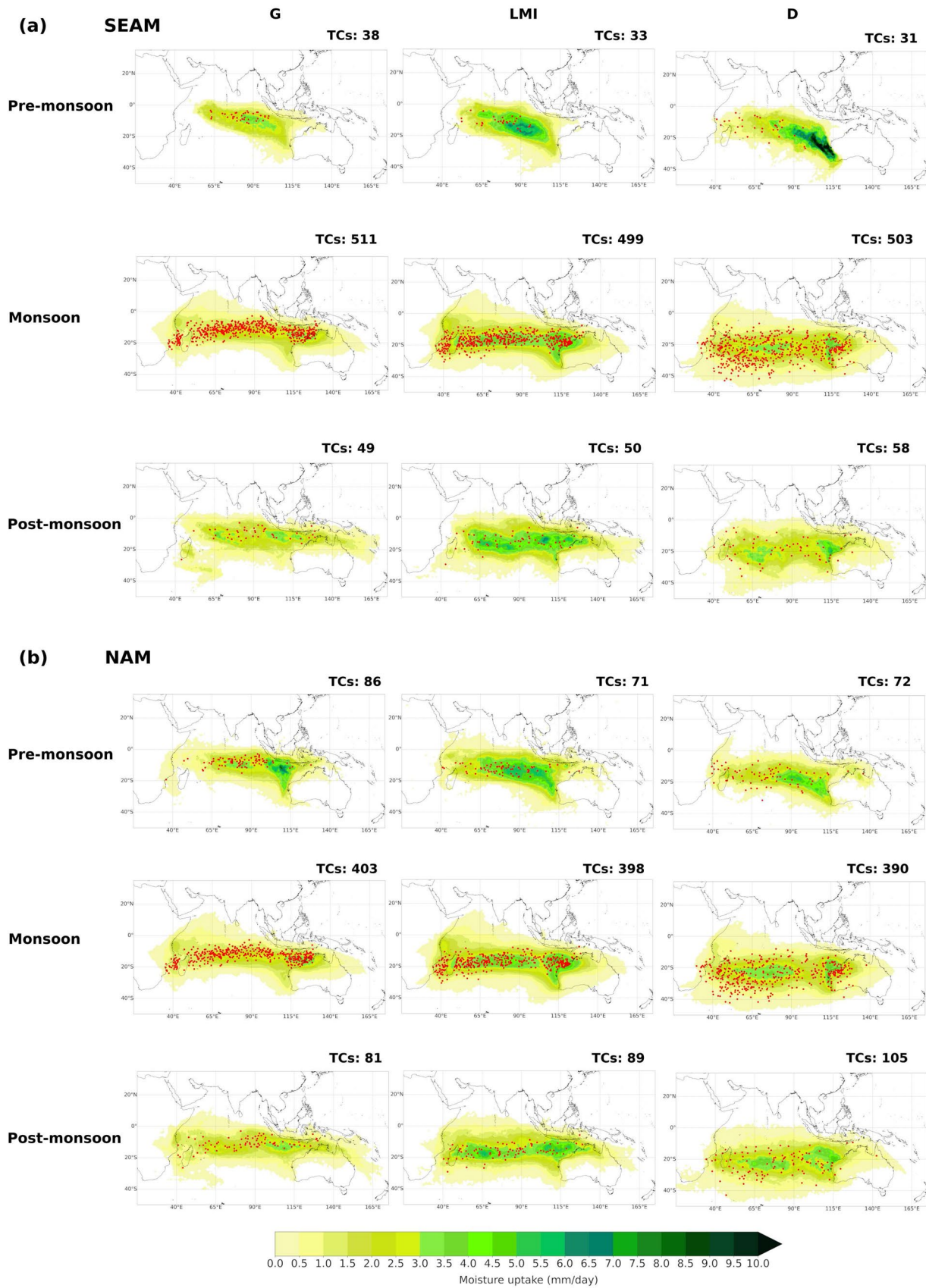


Fig. 15 Moisture uptake (greenish colour) for tropical cyclones (TCS) genesis, peak of maximum intensity and dissipation over the SIO basin during the pre-monsoon, monsoon and post-monsoon seasons for the **a** Southeastern African Monsoon (SEAM) and **b** North Australia Monsoon (NAM). Capital letters at the top indicate the TCs phases, genesis (G), lifetime maximum intensity (LMI), and dissipation (D). Red points indicate the TCs position in each stage. In the top right of each map is the number of TCs during each monsoon phase

cross-equatorial low-level jet stream (Joseph et al. 2006). Moreover, because the zonal branch of the Somali Jet forms during the boreal summer, moisture is advected eastward towards the ISM (Liebmann et al. 2012). That is, the ISM is associated with an increase in the precipitation, building up of vertically integrated humidity, strengthening of the low-level westerly wind over southwestern India and an increase in the kinetic energy (Krishnamurti 1985; Sahana et al. 2015). During the EASM pre-monsoon, the moisture gained by TCs was mainly from the southeastern AS, the IP, and the northern BoB. In general, a weak moisture contribution was observed from the BoB and the SCS. Nevertheless, during the post-monsoon season, the moisture uptake from the BoB and SCS was strengthened, and the moisture supplied from the AS and the Somali basin was lower than that of the pre-monsoon and monsoon seasons, being practically zero for TC genesis during the ISM pre-monsoon season. During all monsoon phases, the moisture sources supplied more moisture as the TCs became more intense, although the moisture gained by TCs during the dissipation phase was notably high.

The SIO basin is affected by the Southeastern African Monsoon (SEAM) and the North Australia Monsoon (NAM) occurring on both sides of the basin, in southeast Africa and the north Australia, respectively. According to our estimations, the SEAM started on approximately 08 November and ended on 16 April (as found by Kniveton et al. (2009), Shongwe et al. (2015) and Dunning et al. (2016)), and the NAM started on 13 December and ended on 25 March (in agreement with Suppiah (1992) and Pope et al. (2009)). Thus, 83.8% and 66.1% of the TCs generated in the SIO basin occurred during the SEAM and NAM monsoon seasons, respectively.

Figure 15 shows the intensity and position of moisture sources during the monsoon seasons for TC genesis, LMI, and dissipation phases over the SIO. Likewise, Figure S2 is similar to Fig. 15 but for the TS, H, and MH intensity categories. During the pre-monsoon period, the moisture supplied from the WB and PB was a more intense source during the NAM than during the SEAM and remained active throughout the TC season. During the SEAM and NAM monsoon seasons, the moisture contribution from the WIO and the northeastern coast of Africa was notable. The ISM reversal seasonal circulation (Funk et al. 2016) affects the moisture transport patterns in the region. Thus,

the southward movement of the continental tropical convergence zone and the subtropical anticyclone led to the winds blowing from the Indian subcontinent towards the IO in a northeasterly direction during the boreal winter, triggering the northeastern monsoon (Rajeevan et al. 2012), transporting moisture from the Arabian Sea along the east coast of Africa to the position of the TCs over the western basin of the SIO. In addition, during the post-monsoon season, the North Australia and the Coral Sea also contributed to atmospheric moisture for the precipitation associated with TC activity. In summary, TCs uptake more moisture during intensity changes than during the genesis or dissipation phases (Figs. 15 and S2).

Overall, the largest differences in the moisture uptake pattern during the monsoon phases (pre-monsoon, monsoon and post-monsoon) occurred over the NIO basin. This behaviour is probably caused by the intensity of the ISM and EASM compared to the SEAM and NAM. Note that the intensity of the former is notably higher than the latter (Liu et al. 2019). It is worth noting that experiments (e.g. Clemens and Prell 2003) with atmospheric global circulation models have revealed that the elevation of Himalaya-Tibet has significant effects on the intensity of the Asia Summer Monsoon.

Furthermore, according to Table 2, in general, the largest Lagrangian MWVRT observed in the NIO was during the post-monsoon season, and for the SIO basin, during the pre-monsoon season. Regardless of the monsoon season, in both basins, TCs exhibited the highest MWVRT during the genesis phase and the lowest during the dissipation stage, always having in all cases, as discussed, higher values in the SIO than in the NIO basin.

4 Conclusion and remarks

Tropical cyclones (TCs) are one of the most destructive weather phenomena that affect coastal countries in tropical regions, producing major impacts over significantly large areas. In this study, a Lagrangian approach was used to identify the origin of TC precipitation during the genesis, intensification, and dissipation stages over the Indian Ocean. We objectively separated the locations of TC genesis, lifetime maximum intensification, and dissipation stages into clusters in both the North Indian Ocean (NIO) and the South Indian Ocean (SIO) basins to determine the moisture sources and moisture transport mechanisms in these regions. The position and size of each TC formed in the NIO and SIO from 1980 to 2018 were extracted from the Joint Typhoon Warning Centre best track archives and the TCSize database, respectively.

A Lagrangian moisture source diagnostic method was applied to the backward trajectories of atmospheric parcels

Table 2 Lagrangian mean water vapour residence time (in days) during monsoon seasons for the TCs genesis (G), lifetime maximum intensity (LMI) intensity changes, and dissipation (D) in the North Indian Ocean (NIO) and South Indian Ocean (SIO) basins

Basin	G	LMI	TS	H	MH	D
NIO						
ISM						
Pre-	3.0±0.3	2.6±0.4	2.9±0.3	2.7±0.3	2.6±0.3	2.5±0.3
Mon	3.0±0.4	2.5±0.4	2.8±0.4	2.7±0.3	2.8±0.3	2.5±0.4
Post-	3.3±0.6	2.9±0.7	3.1±0.7	3.0±0.6	2.7±0.4	2.8±0.5
EASM						
Pre-	3.1±0.6	2.6±0.5	2.9±0.4	2.8±0.4	2.9±0.1	2.3±0.6
Mon	3.0±0.3	2.6±0.3	2.8±0.4	2.7±0.3	2.5±0.3	2.5±0.3
Post-	3.3±0.6	2.8±0.5	3.1±0.5	2.9±0.5	2.8±0.4	2.7±0.6
SIO						
SEAM						
Pre-	3.5±0.4	3.2±0.3	3.3±0.4	3.3±0.3	3.7±0.1	3.2±0.4
Mon	3.3±0.5	3.1±0.4	3.2±0.4	3.1±0.4	3.2±0.4	2.9±0.4
Post-	3.2±0.3	3.1±0.4	3.1±0.4	3.0±0.3	3.0±0.3	2.8±0.3
NAM						
Pre-	3.4±0.7	3.3±0.6	3.3±0.6	3.2±0.6	3.4±0.4	3.0±0.6
Mon	3.2±0.4	3.1±0.4	3.2±0.4	3.1±0.4	3.1±0.5	2.9±0.4
Post-	3.3±0.4	3.1±0.4	3.2±0.4	3.0±0.4	3.0±0.4	2.9±0.3

TS: Tropical Storm, H: Hurricanes (category 1 and 2 on the Saffir-Simpson scale) and MH: Major Hurricane (category 3+ on Saffir-Simpson scale). Pre-, Mon and Post- referred to Pre-monsoon, Monsoon and Post-monsoon seasons, respectively

ISM: Indian Summer Monsoon, EASM: East Asian Summer Monsoon, SEAM: Southeastern African Monsoon, NAM: North Australia Monsoon

residing over the area occupied by the TC outer radius to identify the moisture sources. The pathways of the parcels were obtained from the global outputs of the Lagrangian model FLEXPART, forced with the ERA-Interim reanalysis data.

This study revealed that in the NIO basin, the Bay of Bengal, the Arabian and South China Sea were the predominant oceanic moisture sources for TC activity, and continental areas such as the Indian Peninsula, the Ganges basin and the southern coast of China also contributed to the moisture supply for the genesis, intensification, and dissipation stages. We also found that the western Indian Ocean and the eastern coast of Africa were a notable moisture sources through the SLLJ for TCs that occurred over the Arabian Sea. Notably, for the TCs over the Bay of Bengal the most intense source of moisture was the Ganges River basin when the TCs were at their most intense phase.

For the cyclogenesis and development of TCs over the SIO basin, the central Indian Ocean, the Wharton and the Perth basins were identified as the main moisture sources that supply the precipitant atmospheric humidity throughout the easterly trade winds blowing out the Mascarene High pressure system. Moreover, the Western Indian Ocean, the northern Australian mainland, and the Coral Sea contributed to the moisture supply but with less intensity. The climatological pattern of moisture uptake revealed that during the intensification process, TCs

gained more moisture for precipitation than during the genesis and dissipation stages. Overall, the differences found in the moisture uptake pattern during the different phases of TCs development over the Indian Ocean were statistically significant at a 95% significance level. In summary, the oceanic (terrestrial) sources supplied ~86% (~14%) of moisture in the NIO basin and ~80% (~20%) in the SIO basin.

In both basins, TCs required more atmospheric humidity during intensity changes to hurricanes than to major hurricanes or tropical storms. This finding was also supported by computing the average of total specific humidity in the atmospheric column enclosed by the TC outer radius. Figure S3 reveals that the mean total specific humidity increased in both basins from genesis, reaching its maximum value for the hurricane category and then decreasing for the dissipation stage. Additionally, we compared the moisture uptake pattern of each TC phase with respect to the genesis phase by applying the statistical t-Student test. Furthermore, the moisture sources that supply atmospheric humidity for TC activity over the NIO basin were more heavily modulated by monsoon systems than those over the SIO.

The Lagrangian methodology used in this work allowed us to find that the time taken by the moisture for precipitation to reach the TCs differs for both basins, being faster for the NIO (from 2.6 to 3.1 days) than for the SIO (from 2.9 to 3.2 days). Overall, the highest time was during the

genesis phase and tropical storm intensity category, and the lowest was during the dissipation stage. Differences were also found in monsoonal episodes. On average, these times were higher during the post-monsoon season in the NIO and during the pre-monsoon season in the SIO. In general, the time values it takes for precipitant moisture to reach the TCs are lower than the climatological estimations by Läderach and Sodemann (2016) and Sodemann (2020) for the global tropics (4.5 to 5.8 days) for which they did not differentiate weather systems, including in their estimates for all days of the year and any weather situation, unlike our work.

Climate and meteorological dynamics are influenced by modes of climate variability, such as the Indian Ocean Dipole and El Niño-Southern Oscillation. They modulate TC activity and can also affect the moisture transport for the TCs. In further research, it will be necessary to focus our attention on the role of these modes in the variability of the intensity and extent of moisture sources for precipitation originating from TCs during their lifetime. In addition, the findings from this study will also be used as a reference in future works to identify changes in the intensity and position of moisture sources for precipitation associated with TCs over the Indian Ocean in the different climate scenarios projections.

Supplementary Information The online version contains supplementary material available at <https://doi.org/10.1007/s00382-022-06429-4>.

Acknowledgements A.P-A acknowledges a PhD grant from the University of Vigo. J.C.F-A and R.S thanks the Xunta de Galicia (Galician Regional Government) for support this study under the grants no. ED481A-2020/193 and ED481B 2019/070, respectively. The authors thanks to JTWC for the best track archive database and to Copernicus Climate Change Service for the ERA-Interim reanalysis. We acknowledge the partial support from the Xunta de Galicia under the Project ED431C 2021/44. This work has been also possible thanks to the computing resources and technical support provided by CESGA (Centro de Supercomputacion de Galicia). We acknowledge the funding for open access from the Universidade de Vigo/Consorcio Interuniversitario do Sistema Universitario de Galicia.

Author contributions Conceptualization: LG, RN, AP-A; Methodology: LG, RN, APA, RS; Formal analysis and investigation: AP-A, JCF-A, RS; Writing—original draft preparation: AP-A; Writing—review and editing: AP-A; RS, RN, LG, JCF-A; Supervision: LG, RN. All authors read and approved the final manuscript.

Funding Open Access funding provided thanks to the CRUE-CSIC agreement with Springer Nature. This research is supported by the LAGRIMA and SETESTRELO projects (grants no. RTI2018-095772-B-I00 and PID2021-122314OB-I00, respectively) funded by the Ministerio de Ciencia, Innovación y Universidades, Spain. Partial support was also obtained from the Xunta de Galicia, Consellería de Cultura, Educación e Universidade, under project ED431C 2021/44 “Programa de Consolidación e Estructuración de Unidades de Investigación Competitivas”.

Data availability The datasets used during the current study are available online. The best track archive database from the JTWC is

accessible at <https://www.metoc.navy.mil/jtwc/jtwc.html?best-tracks> and the the ERA-Interim reanalysis at <https://apps.ecmwf.int/datasets/data/interim-full-daily/levtype=sfc>. The Multi-Source Weighted-Ensemble Precipitation (MSWEP) v2 was obtained from <http://www.gloh2o.org/mswep/>, and the TCSIZE database was from <http://doi.org/10.17632/8997r89fbf.1>. The FLEXPART model source code is available at <https://www.flexpart.eu/downloads/6>.

Declarations

Conflict of interest The authors declare no conflict of interest.

Open Access This article is licensed under a Creative Commons Attribution 4.0 International License, which permits use, sharing, adaptation, distribution and reproduction in any medium or format, as long as you give appropriate credit to the original author(s) and the source, provide a link to the Creative Commons licence, and indicate if changes were made. The images or other third party material in this article are included in the article's Creative Commons licence, unless indicated otherwise in a credit line to the material. If material is not included in the article's Creative Commons licence and your intended use is not permitted by statutory regulation or exceeds the permitted use, you will need to obtain permission directly from the copyright holder. To view a copy of this licence, visit <http://creativecommons.org/licenses/by/4.0/>.

References

- Aemisegger F, Papritz L (2018) A climatology of strong large-scale ocean evaporation events. Part I: Identification, global distribution, and associated climate conditions. *J Clim* 31(18):7287–7312. <https://doi.org/10.1175/JCLI-D-17-0591.1>
- Barimalala R, Desbiolles F, Blamey RC, Reason C (2018) Madagascar influence on the South Indian Ocean Convergence Zone, the Mozambique Channel Trough and southern African rainfall. *Geophys Res Lett* 45(11):380–389. <https://doi.org/10.1029/2018GL079964>
- Beck HE, Wood EF, Pan M, Fisher CK, Miralles DG, van Dijk AIJM, McVicar TR, Adler RF (2019) MSWEP V2 Global 3-Hourly 0.1° Precipitation: Methodology and Quantitative Assessment. *Bull Am Meteorol Soc* 100:473–500. <https://doi.org/10.1175/BAMS-D-17-0138.1>
- Bhatla R, Raj R, Mall RK, Shivani (2020) Tropical Cyclones over the North Indian Ocean in changing climate. In: Srivastava PK, Singh SK, Mohanty UC, Murty T (eds) *Techniques for disaster risk management and mitigation*. Wiley Online Library, New Jersey. <https://doi.org/10.1002/9781119359203.ch5>
- Boruff BJ (2009) *Environmental hazards: assessing risk and reducing disasters*, 5th edition by Keith Smith and David N. Petley. *Geogr Res* 47:454–455. <https://doi.org/10.1111/j.1745-5871.2009.00611.x>
- Bousquet O, Barruol G, Cordier E, Barthe C, Bielli S, Calmer R, Rindraharisaona E, Roberts G, Tulet P, Amelie V, et al. (2021) Impact of tropical cyclones on inhabited areas of the swio basin at present and future horizons. part 1: overview and observing component of the research project RENOVRISK-CYCLONE. *Atmosphere* 12:544. <https://doi.org/10.3390/atmos12050544>
- Brioude J, Arnold D, Stohl A, Cassiani M, Morton D, Seibert P, Angevine W, Evan S, Dingwell A, Fast JD, Easter RC, Pissio I, Burkhardt J, Wotawa G (2013) The Lagrangian particle dispersion

- model FLEXPART-WRF version 3.1. *Geosci Model Dev* 6:1889–1904. <https://doi.org/10.5194/gmd-6-1889-2013>
- Clemens SC, Prell WL (2003) A 350,000 year summer-monsoon multiproxy stack from the Owen Ridge, Northern Arabian Sea. *Mar Geol* 201(1–3):35–51. [https://doi.org/10.1016/S0025-3227\(03\)00207-X](https://doi.org/10.1016/S0025-3227(03)00207-X)
- Corporal-Lodangco I-L, Richman MB, Leslie LM, Lamb PJ (2014) Cluster analysis of north atlantic tropical cyclones. *Proced Comput Sci* 36:293–300. <https://doi.org/10.1016/j.procs.2014.09.096>
- Dee DP et al (2011) The ERA-Interim reanalysis: configuration and performance of the data assimilation system. *Q J R Meteorol* 137:553–597. <https://doi.org/10.1002/qj.828>
- DeMott CA, Klingaman NP, Woolnough SJ (2015) Atmosphere-ocean coupled processes in the Madden-Julian oscillation. *Rev Geophys* 53:1099–1154. <https://doi.org/10.1002/2014RG000478>
- Dominguez C, Magaña V (2018) The role of tropical cyclones in precipitation over the tropical and subtropical North America. *Front Earth Sci* 6:19. <https://doi.org/10.3389/feart.2018.00019>
- Drosowsky W (1996) Variability of the Australian summer monsoon at Darwin: 1957–1992. *J Clim* 9(1):85–96. [https://doi.org/10.1175/1520-0442\(1996\)09<0092:CO>2](https://doi.org/10.1175/1520-0442(1996)09<0092:CO>2)
- Dunning CM, Black ECL, Allan RP (2016) The onset and cessation of seasonal rainfall over Africa. *J Geophys Res Atmos* 121:405–424. <https://doi.org/10.1002/2016JD025428>
- Emanuel K, De Autels C, Holloway C, Korty R (2004) Environmental control of tropical cyclone intensity. *J Atmos Sci* 61:843–858. [https://doi.org/10.1175/1520-0469\(2004\)061%3C0843:ECOTCI%3E2.0.CO;2](https://doi.org/10.1175/1520-0469(2004)061%3C0843:ECOTCI%3E2.0.CO;2)
- Funk C, Hoell A, Shukla S, Husak G, Michaelsen J (2016) The east African monsoon system: seasonal climatologies and recent variations. In: de Carvalho L, Jones C (eds) *The monsoons and climate change*. Springer, Cham. https://doi.org/10.1007/978-3-319-21650-8_8
- Gimeno L, Drumond A, Nieto R, Trigo RM, Stohl A (2010) On the origin of continental precipitation. *Geophys Res Lett* 37:L13804. <https://doi.org/10.1029/2010GL043712>
- Gimeno L, Stohl A, Trigo RM, Dominguez F, Yoshimura K, Yu L, Drumond A, Durán-Quesada AM, Nieto R (2012) Oceanic and terrestrial sources of continental precipitation. *Rev Geophys* 50:RG4003. <https://doi.org/10.1029/2012RG000389>
- Gimeno L, Vázquez M, Eiras-Barca J, Sorí R, Stojanovic M, Algarra I, Nieto R, Ramos AM, Durán-Quesada AM, Dominguez F (2020) Recent progress on the sources of continental precipitation as revealed by moisture transport analysis. *Earth-Sci Rev* 201:103070. <https://doi.org/10.1016/j.earscirev.2019.103070>
- Gimeno L, Eiras-Barca J, Durán-Quesada AM, Dominguez F, van der Ent R, Sodemann H, Sánchez-Murillo R, Nieto R, Kirchner JW (2021) The residence time of water vapour in the atmosphere. *Nat Rev Earth Environ* 2(8):558–569. <https://doi.org/10.1038/s43017-021-00181-9>
- Gray WM (1968) Global view of the origin of tropical disturbances and storms. *Mon Weather Rev* 96:669–700. [https://doi.org/10.1175/1520-0493\(1968\)096%3C0669:GVOTOO%3E2.0.CO;2](https://doi.org/10.1175/1520-0493(1968)096%3C0669:GVOTOO%3E2.0.CO;2)
- Gray WM (1977) Tropical cyclone genesis in the Western North Pacific. *J Meteorol Soc Jpn Ser II* 55:465–482. https://doi.org/10.2151/jmsj1965.55.5_465
- Halpern D, Woiceshyn PM (1999) Onset of the Somali Jet in the Arabian Sea during June 1997. *J Geophys Res* 104:18041–18046. <https://doi.org/10.1029/1999JC900141>
- Hartigan J, Wong M (1979) Algorithm AS 136: a K-means clustering algorithm. *J R Stat Soc Ser C Appl Stat* 28(1):100–108. <https://doi.org/10.2307/2346830>
- Henderson-Sellers A, McGuffie K, Zhang H (2002) Stable isotopes as validation tools for global climate model predictions of the impact of Amazonian deforestation. *J Clim* 15:2664–2677. [https://doi.org/10.1175/1520-0442\(2002\)015%3C2664:SIATVF%3E2.0.CO;2](https://doi.org/10.1175/1520-0442(2002)015%3C2664:SIATVF%3E2.0.CO;2)
- Hermes JC, Masumoto Y, Beal LM, Roxy MK, Vialard J, Andres M, Annamalai H et al (2019) A sustained ocean observing system in the Indian Ocean for climate related scientific knowledge and societal needs. *Front Mar Sci* 6:355. <https://doi.org/10.3389/fmars.2019.00355>
- Hersbach H, Bell B, Berrisford P, Hirahara S, Horányi A, Muñoz-Sabater J, Nicolas J, Peubey C et al (2020) The ERA5 global reanalysis. *Q J R Meteorol Soc* 146:1999–2049. <https://doi.org/10.1002/qj.3803>
- Joseph PV, Sooraj KP, Rajan CK (2006) The summer monsoon onset process over South Asia and an objective method for the date of monsoon onset over Kerala. *Int J Climatol* 26:1871–1893. <https://doi.org/10.1002/joc.1340>
- Kaufman L, Rousseeuw PJ (2005) *Finding groups in data: an introduction to cluster analysis*. Wiley Series in Probability and Statistics, New Jersey
- Kiguchi M, Matsumoto J (2005) The rainfall phenomena during the pre-monsoon period over the Indochina Peninsula in the GAME-IOP Year, 1998. *J Meteorol Soc Japan* 83(1):89–106. <https://doi.org/10.2151/jmsj.83.89>
- Kniveton DR, Layberry R, Williams CJR, Peck M (2009) Trends in the start of the wet season over Africa. *Int J Climatol* 29(9):1216–1225. <https://doi.org/10.1002/joc.1792>
- Krishnamurti TN (1985) Summer monsoon experiment: a review. *Mon Weather Rev* 113:1590–1626. [https://doi.org/10.1175/1520-0493\(1985\)113%3C1590:SMER%3E2.0.CO;2](https://doi.org/10.1175/1520-0493(1985)113%3C1590:SMER%3E2.0.CO;2)
- Läderach A, Sodemann H (2016) A revised picture of the atmospheric moisture residence time. *Geophys Res Lett* 43:924–933. <https://doi.org/10.1002/2015GL067449>
- Lazenby MJ, Todd MC, Wang Y (2016) Climate model simulation of the South Indian Ocean Convergence zone: mean state and variability. *Clim Res* 68(1):59–71. <https://doi.org/10.3354/cr01382>
- Li Z, Yu W, Li T, Murty VSN, Tangang F (2013) Bimodal character of cyclone climatology in the bay of Bengal modulated by monsoon seasonal cycle. *J Clim* 26:1033–1046. <https://doi.org/10.1175/JCLI-D-11-00627.1>
- Liebmann B, Bladé I, Kiladis GN, Carvalho LMV, Senay GB, Allured D, Leroux S, Funk C (2012) Seasonality of African precipitation from 1996 to 2009. *J Clim* 25(12):4304–4322. <https://doi.org/10.1175/JCLI-D-11-00157.1>
- Lisonbee J, Ribbe J, Wheeler M (2020) Defining the north Australian monsoon onset: a systematic review. *Prog Phys Geogr* 44(3):398–418. <https://doi.org/10.1177/0309133319881107>
- Liu Y, Liang P, Sun Y (2019) Basic features of the Asian summer monsoon system. *The Asian summer monsoon: characteristics, variability, teleconnections and projection*. Elsevier, Amsterdam, p 237
- Longshore D (2009) *Encyclopedia of Hurricanes, Typhoons, and Cyclones*. Infobase Publishing, New York, p 467
- MacQueen J (1967) Some methods for classification and analysis of multivariate observations. *Proceedings of fifth Berkeley symposium on mathematical statistics and probability*. University of California, Berkeley, pp 281–297
- Manatsa D, Morioka Y, Behera SK, Matarira CH, Yamagata T (2014) Impact of Mascarene High variability on the East African ‘short rains’. *Clim Dyn* 42:1259–1274. <https://doi.org/10.1007/s00382-013-1848-z>
- Martínez JA, Dominguez F (2014) Sources of atmospheric moisture for the La Plata River basin. *J Clim* 27:6737–6753. <https://doi.org/10.1175/JCLI-D-14-00022.1>
- Mohapatra M, Bandyopadhyay BK, Tyagi A (2012) Best track parameters of tropical cyclones over the North Indian Ocean: a review. *Nat Hazards* 63:1285–1317. <https://doi.org/10.1007/s11069-011-9935-0>

- Muni KK (2009) Intensifying tropical cyclones over the North Indian Ocean during summer monsoon-global warming. *Glob Planet Change* 65(1–2):12–16. <https://doi.org/10.1016/j.gloplacha.2008.10.007>
- Nakamura J, Lall U, Kushnir Y, Camargo SJ (2009) Classifying North Atlantic tropical cyclone tracks by mass moments. *J Clim* 22:5481–5494. <https://doi.org/10.1175/2009JCLI2828.1>
- Needham HF, Keim BD, Sathiaraj D (2015) A review of tropical cyclone-generated storm surges: global data sources, observations, and impacts. *Rev Geophys* 53:545–591. <https://doi.org/10.1002/2014RG000477>
- Nieto R, Castillo R, Drumond A (2014) The modulation of oceanic moisture transport by the hemispheric annular modes. *Front Earth Sci* 2:11. <https://doi.org/10.3389/feart.2014.00011>
- Ninomiya K (2008) Similarities and differences among the South Indian Ocean Convergence Zone, North American convergence zone, and other subtropical convergence zones simulated using an AGCM. *J Meteorol Soc Jpn Ser II* 86(1):141–165. <https://doi.org/10.2151/jmsj.86.141>
- Noska R, Misra V (2016) Characterizing the onset and demise of the Indian summer monsoon. *Geophys Res Lett* 43:4547–4554. <https://doi.org/10.1002/2016GL068409>
- Numaguti A (1999) Origin and recycling processes of precipitating water over the Eurasian continent: Experiments using an atmospheric general circulation model. *J Geophys Res* 104:1957–1972. <https://doi.org/10.1029/1998JD20002>
- Ordoñez P, Ribera P, Gallego D, Peña-Ortiz C (2012) Major moisture sources for Western and Southern India and their role on synoptic-scale rainfall events. *Hydrol Process* 26:3886–3895. <https://doi.org/10.1002/hyp.8455>
- Pazos M, Gimeno L (2017) Identification of moisture sources in the Atlantic Ocean for cyclogenesis processes. In: *Proceedings of the 1st International Electronic Conference on Hydrological Cycle (ChyCle-2017)*. Sciforum Electronic Conf Ser. <https://doi.org/10.3390/CHyCle-2017-04862>
- Pérez-Alarcón A, Sorí R, Fernández-Alvarez JC, Nieto R, Gimeno L (2021) Comparative climatology of outer tropical cyclone size using radial wind profiles. *Weather Clim Extrem* 33:100366. <https://doi.org/10.1016/j.wace.2021.100366>
- Pérez-Alarcón A, Sorí R, Fernández-Alvarez JC, Nieto R, Gimeno L (2022a) Where does the moisture for North Atlantic tropical cyclones come from? *J Hydrometeorol*. <https://doi.org/10.1175/JHM-D-21-0117.1>
- Pérez-Alarcón A, Coll-Hidalgo P, Fernández-Alvarez JC, Sorí R, Nieto R, Gimeno L (2022b) Moisture sources for precipitation associated with major hurricanes during 2017 in the North Atlantic basin. *J Geophys Res Atmos* 127:e2021JD035554. <https://doi.org/10.1029/2021JD035554>
- Pérez-Alarcón A, Sorí R, Fernández-Alvarez JC, Nieto R, Gimeno L (2022c) Dataset of outer tropical cyclone size from a radial wind profile. *Data BR* 40:107825. <https://doi.org/10.1016/j.dib.2022.107825>
- Pope M, Jakob C, Reeder MJ (2009) Regimes of the north Australian wet season. *J Clim* 22:6699–6715. <https://doi.org/10.1175/2009JCLI3057.1>
- Rahman M, Yang R, Di L (2018) Clustering Indian ocean tropical cyclone tracks by the standard deviational ellipse. *Climate* 6(2):39. <https://doi.org/10.3390/cli6020039>
- Rajeevan M, Unnikrishnan CK, Bhate J, Niranjan-Kumar K, Sreekala PP (2012) Northeast monsoon over India: variability and prediction. *Meteorol Appl* 19:226–236. <https://doi.org/10.1002/met.1322>
- Rousseeuw PJ (1987) Silhouettes: a graphical aid to the interpretation and validation of cluster analysis. *J Comput Appl Math* 20:53–65. [https://doi.org/10.1016/0377-0427\(87\)90125-7](https://doi.org/10.1016/0377-0427(87)90125-7)
- Sahana AS, Ghosh S, Ganguly A, Murtugudde R (2015) Shift in Indian summer monsoon onset during 1976/1977. *Environ Res Lett* 10(5):054006. <https://doi.org/10.1088/1748-9326/10/5/054006>
- Samson G, Masson S, Lengaigne M, Keerthi MG, Vialard J, Pous S, Madec G, Jourdain NC, Jullien S, Menkes C, Marchesiello P (2014) The NOW regional coupled model: application to the tropical Indian Ocean climate and tropical cyclone activity. *J Adv Model Earth Syst* 6:700–722. <https://doi.org/10.1002/2014M5000324>
- Shongwe ME, Lennard C, Liebmann B, Kalognomou EA, Ntsangwane L, Pinto I (2015) An evaluation of CORDEX regional climate models in simulating precipitation over southern Africa. *Atmos Sci Lett* 16(3):199–207. <https://doi.org/10.1002/asl2.538>
- Skamarock W, Klemp J, Dudhi J, Gill D, Barker D, Duda M, Huang X-Y, Wang W, Powers J (2008) A description of the advanced research WRF version 3. Tech Rep. <https://doi.org/10.5065/D6DZ069T>
- Sodemann H (2020) Beyond turnover time: constraining the lifetime distribution of water vapor from simple and complex approaches. *J Atmos Sci* 77(2):413–433. <https://doi.org/10.1175/JAS-D-18-0336.1>
- Sodemann H, Schwierz C, Wernli H (2008) Interannual variability of Greenland winter precipitation sources: Lagrangian moisture diagnostic and North Atlantic Oscillation influence. *J Geophys Res Atmos* 113:D03107. <https://doi.org/10.1029/2007JD008503>
- Sorí R, Nieto R, Drumond A, Vicente-Serrano SM, Gimeno L (2017) The atmospheric branch of the hydrological cycle over the Indus, Ganges, and Brahmaputra river basins. *Hydrol Earth Syst Sci* 21:6379–6399. <https://doi.org/10.5194/hess-21-6379-2017>
- Sprenger M, Wernli H (2015) The LAGRANTO Lagrangian analysis tool – version 2.0. *Geosci Model Dev* 8(8):2569–2586. <https://doi.org/10.5194/gmd-8-2569-2015>
- Stohl A, James PA (2004) Lagrangian analysis of the atmospheric branch of the global water cycle. Part I: method description, validation, and demonstration for the August 2002 flooding in Central Europe. *J Hydrometeorol* 5:656–678. [https://doi.org/10.1175/1525-7541\(2004\)005%3c0656:ALAOTA%3e2.0.CO;2](https://doi.org/10.1175/1525-7541(2004)005%3c0656:ALAOTA%3e2.0.CO;2)
- Stohl A, James PA (2005) A Lagrangian analysis of the atmospheric branch of the global water cycle: part II: earth's river catchments ocean basins, and moisture transports between them. *J Hydrometeorol* 6:961–984. <https://doi.org/10.1175/JHM470.1>
- Stohl A, Forster C, Frank A, Seibert P, Wotawa G (2005) Technical note: the Lagrangian particle dispersion model FLEXPART version 6.2. *Atmos Chem Phys* 5:2461–2474. <https://doi.org/10.5194/acp-5-2461-2005>
- Suppiah R (1992) The Australian summer monsoon: a review. *Prog Phys Geogr* 16(3):283–318. <https://doi.org/10.1177/030913339201600302>
- Tegtmeier S, Marandino C, Jia Y, Quack B, Mahajan AS (2022) Atmospheric gas-phase composition over the Indian Ocean. *Atmos Chem Phys* 22(10):6625–6676. <https://doi.org/10.5194/acp-22-6625-2022>
- Viswanadhapalli Y, Dasari HP, Dwivedi S, Madineni VR, Langodan S, Hoteit I (2020) Variability of monsoon low-level jet and associated rainfall over India. *Int J Climatol* 40:1067–1089. <https://doi.org/10.1002/joc.6256>
- van der Ent RJ, Tuinenburg OA (2017) The residence time of water in the atmosphere revisited. *Hydrol Earth Syst Sci* 21:779–790. <https://doi.org/10.5194/hess-21-779-2017>
- Van der Ent RJ, Wang-Erlandsson L, Keys PW, Savenije HHG (2014) Contrasting roles of interception and transpiration in the hydrological cycle—Part 2: moisture recycling. *Earth Syst Dyn* 5(2):471–489. <https://doi.org/10.5194/esd-5-471-2014>
- Wahiduzzaman M (2021) Major floods and tropical cyclones over Bangladesh: clustering from ENSO timescales. *Atmosphere* 12(6):692. <https://doi.org/10.3390/atmos12060692>

- Wang YP, Cui XP, Li XF, Zhang WL, Huang YJ (2016) Kinetic energy budget during the genesis period of tropical cyclone Dorian (2001) in the South China Sea. *Mon Weather Rev* 144:2831–2854. <https://doi.org/10.1175/MWR-D-15-0042.1>
- Williams GJ (2016) The inner core thermodynamics of the tropical cyclone boundary layer. *Meteorol Atmos Phys* 128:545–564. <https://doi.org/10.1007/s00703-016-0441-5>
- Wu L, Su H, Fovell RG, Dunkerton TJ, Wang Z, Kahn BH (2015) Impact of environmental moisture on tropical cyclone intensification. *Atmos Chem Phys* 15:14041–14053. <https://doi.org/10.5194/acp-15-14041-2015>
- Xu H, Zhai G, Li X (2017) Precipitation efficiency and water budget of Typhoon Fitow 787 (2013): a particle trajectory study. *J Hydrometeorol* 18(9):2331–2354. <https://doi.org/10.1175/JHM-D-16-0273.1>
- Xulu NG, Chikoore H, Bopape MJM, Nethengwe NS (2020). Climatology of the mascarene high and its influence on weather and climate over Southern Africa. *Climate* 8(7):86. <https://doi.org/10.3390/cli8070086>
- Yanase W, Satoh M, Taniguchi H, Fujinami H (2012) Seasonal and intraseasonal modulation of tropical cyclogenesis environment over the Bay of Bengal during the extended summer monsoon. *J Clim* 25:2914–2930. <https://doi.org/10.1175/JCLI-D-11-00208.1>
- Yuan J, Gao Y, Feng D, Yang Y (2019) The zonal dipole pattern of tropical cyclone genesis in the Indian Ocean influenced by the tropical Indo-Pacific Ocean sea surface temperature anomalies. *J Clim* 32(19):6533–6549. <https://doi.org/10.1175/JCLI-D-19-0042.1>

Publisher's Note Springer Nature remains neutral with regard to jurisdictional claims in published maps and institutional affiliations.

4.6 Moisture source for the precipitation of tropical cyclones over the Pacific Ocean through a Lagrangian approach

Pérez-Alarcón, A., Sorí, R., Fernández-Alvarez, J.C., Nieto, R., Gimeno, L., 2023. Moisture source for the precipitation of tropical cyclones over the Pacific Ocean through a Lagrangian approach. *Journal of Climate*, 36(4),1059–1083. doi:10.1175/JCLI-D-22-0287.1. ©American Meteorological Society. Used with permission.

Table 4.6: Summary of the impact and quality of the journal where the fifth paper that conform this thesis was published. The data correspond to the year 2021 (last year available at the date of preparation of this document) in the Web of Science (JCR). **IF:** Impact Factor

Journal	Description	Journal Metrics
Journal of Climate	It publishes research that advances , basic understanding of the dynamics and physics of the climate system on large spatial scales, including variability of the atmosphere, oceans, land surface, and cryosphere.	IF: 5.380, 5-year IF: 6.549 Ranking: 20 out of 108 (Q1) in Meteorology & Atmospheric Sciences

Moisture Source for the Precipitation of Tropical Cyclones over the Pacific Ocean through a Lagrangian Approach

ALBENIS PÉREZ-ALARCÓN^{a,b}, ROBERT SORÍ,^{a,c} JOSÉ C. FERNÁNDEZ-ALVAREZ,^{a,b} RAQUEL NIETO,^a
AND LUIS GIMENO^a

^a *Centro de Investigación Mariña, Environmental Physics Laboratory (EPhysLab), Campus As Lagoas s/n, Universidade de Vigo, Ourense, Spain*

^b *Departamento de Meteorología, Instituto Superior de Tecnologías y Ciencias Aplicadas, Universidad de La Habana, La Habana, Cuba*

^c *Instituto Dom Luiz, Faculdade de Ciências da Universidade de Lisboa, Campo Grande, Portugal*

(Manuscript received 22 April 2022, in final form 12 September 2022)

ABSTRACT: Tropical cyclones (TCs) are an important component of the hydrological cycle at tropical latitudes. In this study, we investigated the origin of precipitation associated with TCs formed from 1980 to 2018 over the Pacific Ocean in three subbasins: the western North Pacific Ocean (WNP), central and east Pacific Ocean (NEPAC), and South Pacific Ocean (SPO) basins. The analysis was performed throughout the TC lifetime during genesis, when they reached the lifetime maximum intensity (LMI), and the dissipation stage. The backward trajectories of all precipitant atmospheric parcels residing over the TC locations from the global outputs of the Lagrangian Flexible Particle (FLEXPART) dispersion model fed by the ERA-Interim dataset were used to identify moisture sources. The South and East China Seas and the western tropical North Pacific Ocean were identified as the principal moisture sources in the WNP basin, while the atmospheric moisture that precipitated mainly came from the eastern tropical North and South Pacific Ocean in the NEPAC basin, followed by the Caribbean Sea. Meanwhile, the Coral Sea, western tropical South Pacific Ocean, and northern Australia are the origins of the moisture in the SPO. The mean moisture uptake per TC was higher during the hurricane category than during any other stage in each basin.

KEYWORDS: Precipitation; Tropical cyclones; Water budget/balance

1. Introduction

The central and northeast Pacific Ocean (NEPAC), South Pacific Ocean (SPO), western North Pacific Ocean (WNP), North Atlantic Ocean, and north and south Indian Ocean basins are often the starting grounds for tropical cyclogenesis. According to Gao et al. (2020), the WNP is the most active basin for tropical cyclone (TC) activity, followed by the NEPAC basin (Zhao and Raga 2015).

Some studies have shown that the large-scale circulation established by the East Asian monsoon (EAM), which extends to the adjacent oceanic areas, controls when and where TCs form over the WNP basin (Elsberry 2004; Choi et al. 2016). Moreover, the eastward extending/westward retreating monsoon trough is closely related to TC formation in the WNP (Molinari and Vollaro 2013; Cao et al. 2014, 2016). The zonal orientation of the South Pacific convergence zone (SPCZ), defined by a monsoon-type convergence zone, favors cyclogenesis in the SPO basin. Meanwhile, the Australian monsoon enhances vorticity in the Coral Sea, which favors the genesis of TCs in this region because of the horizontal shear between the monsoon and trade winds (Vincent et al. 2011).

Huang et al. (2014) showed that atmospheric moisture transport is a key factor in TC genesis and maintenance modulating the latent heat distribution inside and outside the TC. The underlying ocean water vapor in the inner core area constitutes a very small portion of total vapor gained, while the net horizontal moisture flux convergence constitutes a large part of the net condensation within the inner core (Yang et al. 2011; Braun 2006; Fritz and Wang 2014; Fujiwara et al. 2017). Moreover, several modeling studies have suggested that the size of TCs is significantly reduced with decreasing atmospheric humidity (Hill and Lackmann 2009; Wu and Chen 2012). Rotunno and Emanuel (1987) found that although the intensity of TCs depends less on the environmental moisture content during genesis, it takes more time for a drier TC to develop to its final intensity. Moreover, Wu et al. (2015) found that modifications of environmental moisture have significant impacts on TCs when it leads to convective activity that deforms the quasi-Lagrangian boundary of the storm. Kudo et al. (2014) demonstrated that a significant proportion of total precipitable water around the TC center during its mature stage comes from external moisture sources rather than the underlying ocean. Through a Lagrangian diagnosis, Fujiwara et al. (2017) found positive feedback between TC intensity over the WNP basin and moisture transport from the Indian Ocean, China Sea, and Philippine Sea.

Other studies have focused on the relationship between heavy TC rainfall and moisture transport. The contribution of TCs to total rainfall quantities over land generally occurs when they make landfall, or during the dissipation stage over land or close to landmasses (Khouakhi et al. 2017). For

Supplemental information related to this paper is available at the Journals Online website: <https://doi.org/10.1175/JCLI-D-22-0287.s1>.

Corresponding author: Albenis Pérez-Alarcón, albenis.perez.alarcon@uvigo.es

DOI: 10.1175/JCLI-D-22-0287.1

© 2023 American Meteorological Society. For information regarding reuse of this content and general copyright information, consult the [AMS Copyright Policy](https://www.ametsoc.org/PUBSReuseLicenses) (www.ametsoc.org/PUBSReuseLicenses).

example, [Gao et al. \(2021\)](#) pointed out that atmospheric moisture shapes increased TC precipitation in southern China over the past four decades, and the findings of [Xu et al. \(2017\)](#) suggest that TCs are an important source of freshwater for the North American continent. Furthermore, the moisture transport performed by westward-moving TCs over the WNP basin is an important source of the water budget over the East Asia region when the East Asian summer monsoon diminishes ([Guo et al. 2017](#)). [Dominguez and Magaña \(2018\)](#) investigated the positive and negative impacts of TCs on summer rainfall over tropical and subtropical North America and found that regional precipitation may be below (above) normal when the NEPAC TC activity is below (above) normal. The results of [Jiang and Zipser \(2010\)](#) showed that the TC rainfall contributions were 3%–4%, 7%, and 11% in the SPO, NEPAC, and WNP, respectively. Furthermore, from the perspective of the water budget, [Wu et al. \(2013\)](#) analyzed three TCs that passed through the Taiwan Strait and found that the moisture flux convergence was dominant and contributed 70% of the moisture for TC precipitation.

While several studies have focused on the water budget of TCs, the identification of the origin of moisture for precipitation during the different phases of TCs along their tracks has been poorly studied. Several methodologies, such as analytical models, vapor tracers, and numerical models have been used to identify moisture sources in specific target regions ([Gimeno et al. 2012](#)). Analytical models provide simple paradigms to evaluate the vertically integrated balance of water vapor, and the vapor tracers are based on the concentrations of hydrogen and oxygen isotopes contained in water vapor and precipitation ([Goessling and Reick 2013](#)), whereas numerical models (Eulerian and Lagrangian) provide a more sophisticated analysis by considering many physical processes ([Winschall et al. 2014](#)). Lagrangian techniques are the most widely used because of their ability to determine long-term moisture sources ([Gimeno et al. 2012, 2020](#)). Additionally, they have been used to analyze the main atmospheric moisture sources of the cumulative effect of torrential rain events during the pre-flood season in South China ([Chu et al. 2017](#)).

The method proposed by [Stohl and James \(2004, 2005\)](#) has been widely used for the identification of moisture sources in climatological studies; however, recent studies ([Cloux et al. 2021](#); [Papritz et al. 2021](#)) have shown that for meteorological systems, the moisture sources are more local and better determined by discounting the precipitation along the air parcel trajectories before reaching the target region, as in [Sodemann et al. \(2008\)](#). This methodology was also used to identify the climatological moisture sources for the precipitation of each tropical cyclone that occurred in the North Atlantic Ocean ([Pérez-Alarcón et al. 2022a](#)) and in a particular case study covering the six major hurricanes in this basin during the 2017 TC season ([Pérez-Alarcón et al. 2022b](#)).

Following the same procedure as for the climatological study in the North Atlantic basin discussed above, this study aimed to investigate the origin of moisture that generated the precipitation of TCs formed over the Pacific Ocean during genesis, intensification, and dissipation phases through a Lagrangian approach, while separately analyzing the NEPAC,

WNP, and SPO basins. It is well known that oceans are the primary source of energy for the genesis and development of TCs (e.g., [Emanuel 2004](#)); commonly, the related cause-and-effect studies base the analysis on the role of surface winds on the ocean evaporation and the SST conditions. In this study, we aim to go further by jointly analyzing multiple parameters through modeling, that allows us to identify and characterize the ocean areas (moisture sources) that contribute to the evolution of precipitation during the genesis and development of TCs. For the Pacific basin, we found no previous studies that objectively determined the location and extent of the sources of moisture for precipitation associated with the development of the TCs, so the expected results could be relevant for understanding the dynamics of TC formation and development. Knowing the climatological TCs' moisture sources (oceanic and terrestrial) for precipitation could be also a novel key predictor for the seasonal prediction of TCs. We expect that our results support the forecast of rainfall associated with TCs, and in turn the potential negative (floods) and positive (drought amelioration) impacts on the continental hydrological cycle and associated socioeconomic effects. Identifying the regions where the humidity that produces the precipitation accompanying TCs and where it originated may help improve the seasonal prediction of TC activity and related rainfall. The seasonal prediction of TCs is controlled by several factors, including large-scale atmospheric circulation patterns, oceanic thermodynamic conditions, and climatic variability modes ([Chan et al. 2001](#); [Zhan et al. 2012](#)). Therefore, the knowledge about the specific climatological moisture sources for TCs' precipitation could contribute to improve seasonal forecasting of precipitation associated with these systems. That is, the analysis of the moisture availability over those regions identified as moisture sources could be a very useful indication of how active a TC season will be in terms of related rainfall. The remainder of the paper, and [section 2](#) specifically, describes the datasets and the [Sodemann et al. \(2008\)](#) methodology used to identify the moisture sources, while [section 3](#) presents the results and discussion. A summary, conclusions, and future plans for continuing this work are presented in [section 4](#).

2. Materials and methods

a. Data

The NEPAC TC data used in this study correspond to the post-season analysis dataset (best track, HURDAT2) from the National Hurricane Center, which includes position and intensity at 6-h intervals. The TC information developed over the WNP and SPO basins was extracted from the Joint Typhoon Warning Center best-track archive. One of the benefits of using data from these agencies is that they follow the same definition of maximum winds: the highest 1-min average at 10-m height over a smooth surface ([Harper et al. 2010](#); [Bhatia et al. 2019](#)). The TC genesis and dissipation locations are defined as the first and last records in the best-track database, respectively. The TC size was obtained from the TCSize database ([Pérez-Alarcón et al. 2022c](#)), in which

the TC outer radius was computed as the radius at which the tangential wind speed was $\leq 2 \text{ m s}^{-1}$ by applying the Willoughby et al. (2006) radial wind profile (Pérez-Alarcón et al. 2021a).

To identify the moisture sources for TCs, the parcel trajectories from the global output of the FLEXPART v9.0 (Stohl et al. 2005) model were used. The model was fed by the ERA-Interim datasets from the European Center for Medium-Range Weather Forecasts (ECMWF, Dee et al. 2011) at $1^\circ \times 1^\circ$ and 6-hourly spatial and temporal resolutions, respectively, and 61 vertical levels. The outputs of the Lagrangian Flexible Particle (FLEXPART) model forced with the ERA-Interim have been previously used for investigating the moisture sources for the precipitation of synoptic weather system such as tropical cyclones (e.g., Pérez-Alarcón et al. 2022a,b,d), extratropical cyclones (e.g., Gozzo et al. 2017; Coll-Hidalgo et al. 2022a), Mediterranean cyclones (Coll-Hidalgo et al. 2022b), and atmospheric rivers (e.g., Ramos et al. 2016). In our study, FLEXPART v9.0 represents the global atmosphere divided into approximately two million parcels with the same mass, and then moving these parcels over time through a three-dimensional wind field. As ERA-Interim does not resolve individual convective cells (Stohl and James 2004), FLEXPART simulations were performed using the convection scheme developed by Emanuel and Živković-Rothman (1999) to account for subgrid-scale convective transport. Further details of FLEXPART model can be found in Stohl et al. (2005) and Pisso et al. (2019). Sodemann (2020) noted that simulations without convection cause an underestimation of vertical transport and, therefore, deficiencies in the precipitation estimates over tropical and subtropical regions. FLEXPART internally interpolates the input data from ERA-Interim (at 0000, 0600, 1200, and 1800 UTC) to intermediate times (0300, 0900, 1500, and 2100 UTC); therefore, the model runs with a temporal resolution of 3 h, nearest to the internal movements in a TC. In addition, ERA-Interim was used to compute the vertical integrated moisture flux (VIMF) every 6 h.

Based on the high quality of TC records after the beginning of meteorological satellite era (Vecchi and Knutson 2008; Kossin et al. 2013; Bhatia et al. 2019) and the availability of ERA-Interim data, the study period was set from 1980 to 2018. Following the works of Hodges et al. (2017), we used in this study to follow the TCs along their trajectories the best track archives instead an objective method from ERA-Interim dataset. Hodges et al. (2017) found that $\sim 98\%$ of the TCs were detected in different reanalysis datasets, with a good agreement with best-track data concerning the mean separation from their position being less than $\sim 220 \text{ km}$, but with more deficiencies in the TC properties as intensity. Furthermore, missing storms were attributed to the lifetime threshold imposed on the tracking methods. Additionally, Pérez-Alarcón et al. (2022b) used TC positions from best track data and the FLEXPART model forced with ERA-Interim, showing that the Lagrangian diagnostic method (section 2b) is a suitable tool for identifying the origin and quantifying precipitation from TCs.

b. Methodology

1) CLUSTER ANALYSIS TECHNIQUE

To identify the regions where TC genesis, intensification, and dissipation occur frequently over the Pacific Ocean basins, we applied a cluster method. The *K*-means method (MacQueen 1967) was used, and is very useful for data analysis and mining (Morissette and Chartier 2013). This technique is based on the iterative relocation of data points between clusters. It is used to divide the cases or variables of a dataset into non-overlapping clusters based on the characteristics uncovered (Morissette and Chartier 2013). The *K*-means method was previously applied to identify TC genesis (Corporal-Lodango et al. 2014; Pérez-Alarcón et al. 2022a) and landfall (Pérez-Alarcón et al. 2021b) regions over the North Atlantic basin, to classify the TC tracks over the WNP basin (Yu et al. 2016) and to study the post-landfall tracks of landfalling tropical cyclones over China (Zhang et al. 2013).

2) IDENTIFICATION OF MOISTURE SOURCES FOR TC PRECIPITATION

The moisture content of an air parcel can be modified owing to gains or losses of specific humidity by evaporation (e) or precipitation (p), respectively, during its movement through the atmosphere (Stohl and James 2004, 2005), as described in Eq. (1):

$$m \frac{dq}{dt} \approx m \left(\frac{\Delta q}{\Delta t} \right) = (e - p), \quad (1)$$

where Δq represents the changes in the specific humidity (q) within time ($\Delta t = 6 \text{ h}$), maintaining a constant particle mass (m).

We are interested in identifying the origin of moisture resulting in precipitation during the three well-known stages (genesis, lifetime maximum intensification, and dissipation) of TCs. Therefore, only the precipitating parcels over the area enclosed by the outer radius of the TCs (our target region) were tracked backward. Following Läderach and Sodemann (2016), precipitating parcels were defined as those in which the specific humidity decreased more than 0.1 g kg^{-1} in a period of 6 h. The backward trajectories of the precipitating parcels were analyzed individually for up to 10 days to ensure the largest MWVRT for the best identification of the moisture sources. The 10-day period has been considered by several authors (Numaguti 1999; van der Ent and Tuinenburg 2017; Gimeno et al. 2021) as the mean water vapor residence time in the atmosphere.

To identify the sources of moisture for TCs activity, we used the WaterSip Lagrangian moisture source diagnostic method (Sodemann et al. 2008), which has been used successfully in several studies (Fremme and Sodeman 2019; Hu et al. 2021; Papritz et al. 2021; Xin et al. 2022; Pérez-Alarcón et al. 2022a,b,d, Coll-Hidalgo et al. 2022a,b). From the end to the starting point of a parcel's trajectory, the fractional contribution of the humidity increment to the parcel's moisture content is computed at each time step. If precipitation occurs

along the route, all previous moisture uptakes are assumed to have contributed according to their fractional contributions and are therefore discounted. As WaterSip discounts the precipitation in route from previous moisture uptakes, the trajectories of the air parcels that precipitated in the target region were shorter than 10 days. The WaterSip method also provides the contribution of each evaporation region to the final precipitation over the target region for each parcel. It should be noted that our study does not separate the moisture uptake from the planetary boundary layer or the free atmosphere.

The moisture uptake in the atmospheric column over each grid cell of $1^\circ \times 1^\circ$ (MU_A) was computed by adding the final moisture changes along the trajectories of all parcels that precipitated within the TC outer radius, following Eq. (2):

$$MU_A = \frac{m \sum_{i=1}^N \Delta q_i}{A}, \quad (2)$$

where Δq is the specific humidity changes within time ($\Delta t = 6$ h), A is the area of the grid cell, and N represents the number of moisture changes over A that contributed to the final precipitation in the target region (Sodemann et al. 2008; Pérez-Alarcón et al. 2022a). Then, by summing all MU_A values we estimated the total moisture uptake (MU) by TC. In summary, the MU is the integrated value of all moisture changes of all parcels that precipitated within the area delimited by the TC size. Therefore, the MU during each TC development phase (genesis, intensification, and dissipation) was computed by averaging the total moisture uptake of all TCs. Moreover, by averaging the fractional contribution over each $1^\circ \times 1^\circ$ cell, the percentage contribution of each moisture source to the precipitation event was calculated. Further details on how the moisture source contributions were computed can be found in Pérez-Alarcón et al. (2022b).

The moisture changes estimations using this Lagrangian tracking method could be influenced by the neglect of liquid water and ice in the atmosphere and the mixing of air parcels, or other processes like evaporation of precipitating hydrometeors, by numerical diffusion and numerical errors related to the trajectory calculation (Sodemann et al. 2008). Despite these shortcomings, the method has proved to be a useful tool for identifying the moisture sources for precipitating weather systems such as TCs (Pérez-Alarcón et al. 2022a,b,d), deep extratropical cyclones (Papritz et al. 2021; Coll-Hidalgo et al. 2022a), and Mediterranean cyclones (Coll-Hidalgo et al. 2022b).

3. Results and discussion

a. Climatological mean moisture sources during tropical cyclone genesis phase

During the study period, approximately 1167, 763, and 425 TCs were formed over the WNP, NEPAC, and SPO basins, representing 31.1%, 20.3%, and 11.2%, respectively, of all TCs that occurred during the study period globally. These statistics confirm that the WNP and NEPAC are the most active basins (Zhao and Raga 2015; Gao et al. 2020).

Cluster analysis (Fig. 1a) revealed that the spatial distribution of the genesis points is quite compact, and the TC genesis regions in the Pacific Ocean are restricted to a stretch band of 0° – 30° N for the WNP, 0° – 20° N for the NEPAC, and 0° – 20° S for the SPO. The WNP basin exhibits four genesis clusters: the first (G-W1, red, 40.1% of genesis) is located over the Philippine Sea, the second (G-W2, purple, 24.5%) is positioned over the South China Sea, the third (G-W3, yellow, 32.9%) over the Mariana Islands, and the last one (G-W4, lime green, 2.31%) appears over the central Pacific Ocean between the Marshall Islands and Hawaii, and is the least numerous cluster. Over the NEPAC basin four clusters were also detected: the first one is located over the Middle America Trench (G-N1, blue, 35.6%), the centroid of the second cluster (G-N2, green, 14.4%) is positioned approximately at 12° N, 128° W, the third NEPAC genesis cluster (G-N3, brown, 44.4%) is observed toward the southwest Pacific coast of Mexico, and the last (G-N4, pink, 5.5%) is located in the central Pacific Ocean south of the Hawaiian Islands. Figure 1a also shows the three genesis clusters identified over the SPO basin: the first (G-S1, black, 29.6%) is in northern Australia, the second (G-S2, orange, 28.2%) over the central South Pacific Ocean, and the third over the Coral Sea (G-S3, magenta, 42.1%).

The monthly frequency showed a similar pattern between the clusters in each basin; in the WNP (Fig. 1b) and NEPAC (Fig. 1c) basins, the highest frequency of genesis was observed in July, August, and September, although the N-G1 cluster exhibited its maximum in June; for the SPO, the highest TC activity was recorded from December to April (Fig. 1d).

For each genesis cluster in the WNP basin, Fig. 2 shows the mean moisture uptake (left column) and respective moisture source contributions (right column). As a general pattern revealed by the VIMF, the western North Pacific subtropical high (WNPSH) acted as the main mechanism for transporting atmospheric humidity toward the genesis regions, which agrees with the fact that the WNPSH is a key circulation system controlling TC activity over this region (Chen et al. 2020). The western tropical North Pacific Ocean (WTNPac) supplies up to 80% of moisture to G-W1 and approximately 50% to G-W3. Over the region by about $\sim 70\%$ – 80% of TCs formed occurred within the monsoon trough (Molinari and Vollaro 2013), a signal found here throughout the circulation of the South Asian monsoon transporting moisture from the Bay of Bengal that reached G-W2 ($\sim 20\%$ – 30%) and G-W1 ($\sim 5\%$). For G-W2 the remaining moisture was mainly from the East China Sea, which contributed approximately 40%–60% of the moisture precipitated during cyclogenesis in this cluster, from the South China Sea (SCS; $\sim 30\%$ – 50%), and from the Arafura Sea ($\sim 10\%$ – 20%). It worth noting that the retreat of the WNPSH from the SCS to the Philippine Sea and the western Pacific leads to the monsoon westerly winds penetrating from the Indian Ocean to the South China Sea, the Philippine Sea, and the western Pacific, as revealed the moisture transport pattern for the genesis in clusters G-W1 and G-W2 (see also Fig. S1 in the online supplemental material). In addition, the small cluster G-W4 mainly received moisture from the central tropical Pacific Ocean (CenPac).

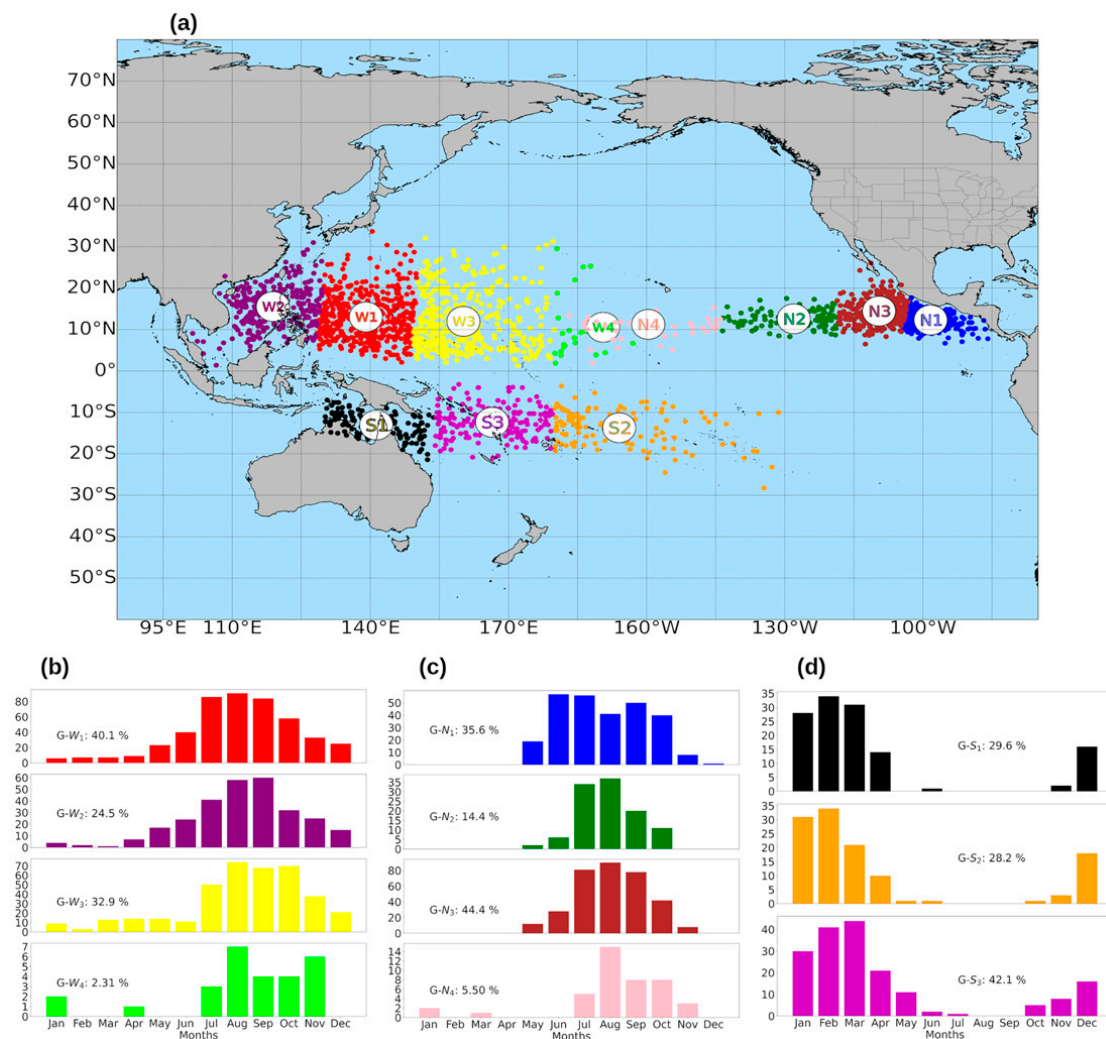


FIG. 1. (a) Tropical cyclone (TC) genesis locations in the Pacific Ocean from 1980 to 2018. Colors represent the TC genesis clusters ($n = 1, 2, 3, \dots$) calculated by k -means for the western North Pacific Ocean (WNP; red, purple, yellow, and lime green), the central and northeast Pacific Ocean (NEPAC; blue, green, brown, and pink), and the South Pacific Ocean (SPO; black, orange, and magenta). Monthly distribution by clusters is also represented for the (b) WNP, (c) NEPAC, and (d) SPO basins.

The moisture transport during TC cyclogenesis in the NEPAC basin (Fig. 3, left column) was modulated by the eastern branch of the North Pacific high (NPH), which is one of the principal centers of action in the Northern Hemisphere (Hordon 2005), and the South Pacific high (SPH), but also by the easterly winds from the Caribbean Sea, as shown by the climatological VIMF pattern for each cluster. These three drivers gave the global moisture source a concave hook shape on the right. The moisture branch from the Caribbean Sea supplied 30%–40% of the humidity for the genesis in G-N1, and contributed to G-N2 and G-N3, but covered a smaller area. From the Pacific Ocean, the G-N1, G-N2, and G-N3 clusters also received moisture from an elongated source over the eastern tropical South Pacific Ocean (ETSPac), eastern tropical North Pacific Ocean (ETNPac), and Pacific coast of Central America. The moisture uptake patterns over the Pacific during cyclogenesis showed a north–south division approximately at 10°N

latitude, which may be linked to the mean position of the intertropical convergence zone (ITCZ) during the summer season in the eastern Pacific Ocean (Hastenrath 2002; Marshall et al. 2014; Pottapinjara et al. 2019). The G-N2 exhibited a similar moisture contribution from both sides at 10°N, providing 40%–60% of the moisture that was precipitated in this cluster, but for G-N1 and G-N3, the moisture was supplied from a source south of 10°N which accounted for 20%–40%. The Central American coast mainly provided substantial moisture for G-N1 (60%–75%) and G-N2 (40%–60%) clusters. Note also the support of moisture from the Caribbean Sea (10%–30%) for G-N1 and from the ETNPac (35%–45%) for G-N2 (Fig. 3). The cluster N-G4 showed a less intense pattern of moisture uptake from the middle of the Pacific Basin.

In the SPO basin, the main moisture transport mechanism during TC genesis was due to wind convergence linked to the South Pacific convergence zone (SPCZ), which reaches its

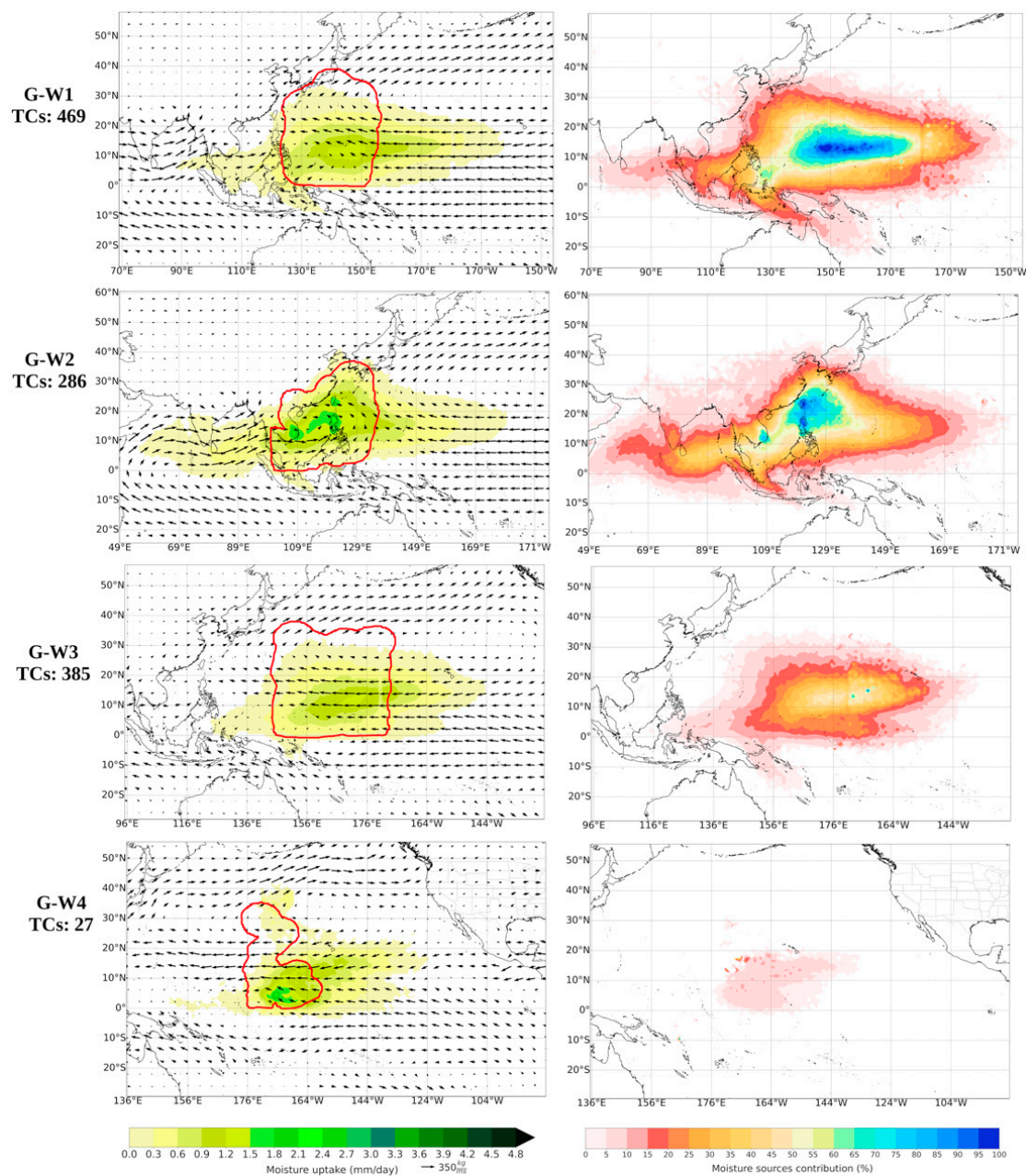


FIG. 2. (left) Mean moisture uptake (mm day^{-1}) and (right) moisture sources contribution (%) by tracking precipitating parcels over the area enclosed by the TC outer radius (target region) backward in time up to 10 days for each TC genesis cluster over the western North Pacific basin. The vertically integrated moisture flux (VIMF; $\text{kg m}^{-1} \text{s}^{-1}$; arrows) is also plotted. The red line represents the composite target region of all TCs (numbered on the left) within the cluster from 1980 to 2018.

maximum strength during the most active months of the TC season (December–February; Fahad et al. 2021) (Fig. 1d). Vincent et al. (2011) stated that the SPCZ location not only strongly constrains the hydrological cycle, but also favors the development of TCs in this basin. Nevertheless, our results revealed that the western branch of the SPH weakly contributed to the transport of moisture to clusters G-S2 and G-S3, as shown by the VIMF pattern in Fig. 4. The seas in northern Australia and the Coral Sea were the main moisture sources

for TCs formed in cluster G-S1, providing approximately 50%–70% of the humidity, whereas the northeastern mainland of Australia contributed 30%–40%, which can be linked to recycling processes. The Coral Sea also supported moisture (20%–40%) for TCs formed in G-S3, but TCs in this cluster mainly received atmospheric humidity (40%–55%) from the seas around New Caledonia Island. Additionally, most of the moisture (20%–60%) fell in G-S2 during the TCs formation.

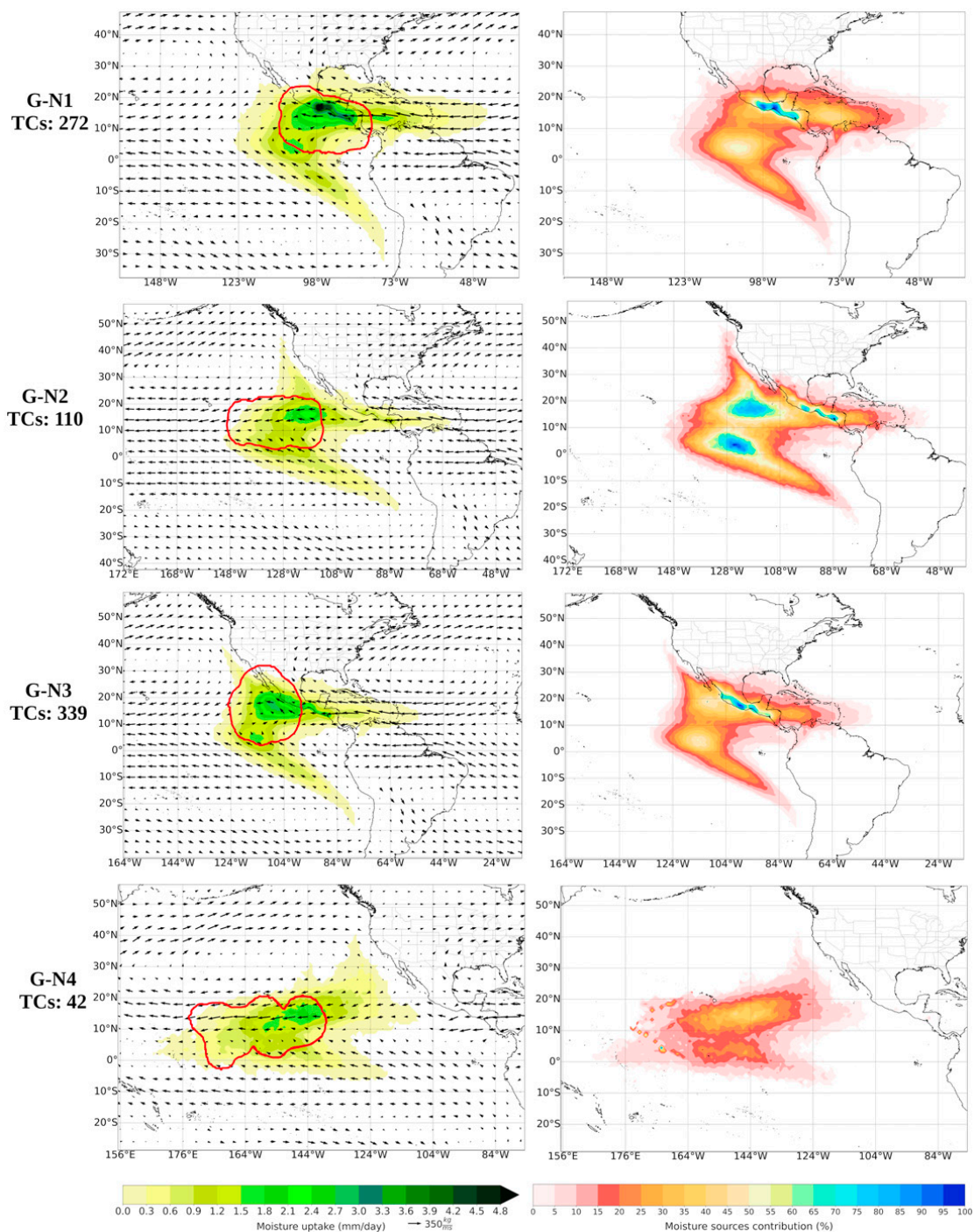


FIG. 3. As in Fig. 2, but for TCs over the central and northeast Pacific Ocean (NEPAC) basin.

Figure 5 summarizes the moisture sources and their contributions to precipitation associated with TCs during cyclogenesis in the Pacific Ocean. From Fig. 5a, the climatological moisture uptake pattern in the WNP basin zonally extended from the middle North Pacific to the Indian subcontinent. This moisture uptake pattern orientation coincides with the mean orientation and position of the summer western North Pacific monsoon trough, which provides favorable conditions for TC formation, namely high midtropospheric relative humidity,

weak vertical wind shear, and relative vorticity (Molinari and Vollaro 2013; Zong and Wu 2015; Feng and Wu 2021). Overall, the moisture was mainly supplied by the SCS (20%–30%) and the western tropical North Pacific Ocean (WTNPac; 50%–75%). Additionally, the moisture contribution from the remaining moisture sources (Arabian Sea, Bay of Bengal, Indian Peninsula, and southeastern Asia) was less than 20%. TCs over the NEPAC generally originated from the easterly waves, convectively coupled Kelvin waves, breakdown

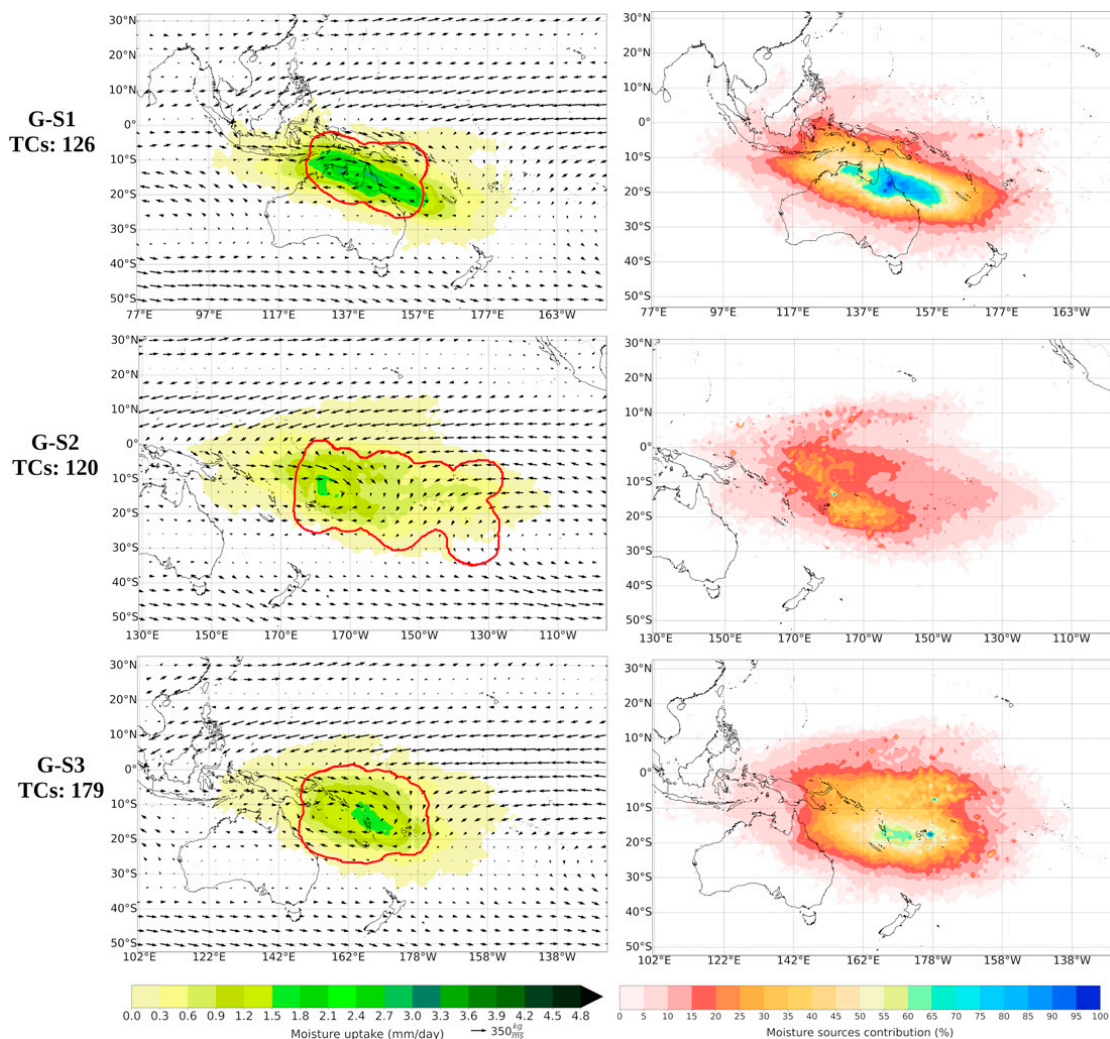


FIG. 4. As in Fig. 2, but for TCs over the South Pacific Ocean (SPO) basin.

of the ITCZ, and mesoscale convective systems, in which the lower-tropospheric cyclonic vorticity is maximized (Schreck et al. 2016; Fu et al. 2021). As noted above, the easterly wind in which the easterly wave is transported contributed to the moisture transport toward TCs genesis locations over the NEPAC basin. Additionally, the moisture uptake pattern exhibited a north–south division around 10°N , which coincides with the mean position of the ITCZ during the boreal summer (see Fig. 5b). Overall, the moisture sources for TCs in the NEPAC basin (Fig. 5b) were more intense north of 10°N , supplying 40%–55% of atmospheric humidity from the ETNPac and 20%–30% from the Caribbean Sea, although south of 10°N the ETSPac contributed up to 25%–40%. It is worth noting the meridional transport of water vapor from the South American coasts by the southeast trade winds to cyclogenesis regions in NEPAC, confirming interhemispheric moisture transport (Gallego et al. 2019). The genesis of TCs over SPO is highly favored by the SPCZ, which modulates large-scale environment factors for cyclonic activity (Vincent et al. 2011). The SPCZ extends from the west Pacific warm pool southeastward

toward French Polynesia (see Fig. 1 in Vincent et al. 2011). Note from Fig. 5c that the orientation of the moisture uptake pattern during the genesis over SPO followed the orientation of the SPCZ; however, it is less widespread than that observed in the WNP and NEPAC. The highest contribution of humidity (45%–65%) came from the main moisture source comprised of the Timor Sea, Arafura Sea, Coral Sea, and the north-eastern areas of Australia. The western tropical South Pacific Ocean (WTSPC), including the Salomon Sea, also provided 20%–30%, while the contribution from the most remote sources was less than 5%. For the three subbasins, the moisture uptake from ocean sources was predominant. Overall, the moisture uptake patterns during cyclogenesis were influenced by the mechanisms that modulated TC formation.

Our results showed that TCs that formed over the WNP, the most active basin of all (Gao et al. 2020), gained less moisture to generate precipitation during genesis than those formed in the NEPAC and SPO. The mean moisture uptake per TC was higher in the SPO (1347 mm day^{-1}) than in the NEPAC (1258 mm day^{-1}) and WNP (1118 mm day^{-1}) basins.

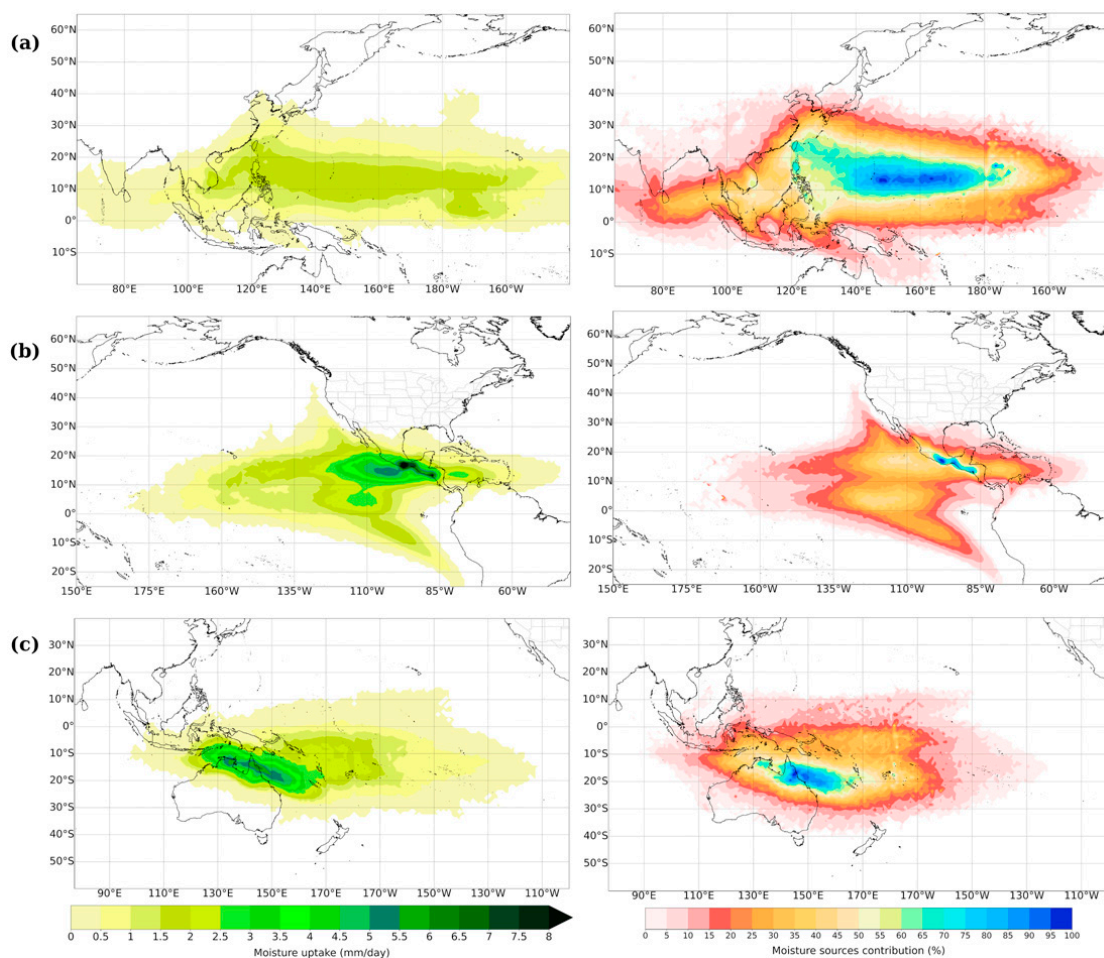


FIG. 5. (left) Climatological moisture uptake (mm day^{-1}) patterns and (right) the contribution of moisture sources (%) during the TC genesis over the (a) western North Pacific Ocean, (b) central and northeast Pacific Ocean, and (c) South Pacific Ocean basins from 1980 to 2018.

b. Climatological mean moisture sources during the tropical cyclone maximum intensity

Similar to the genesis phase, the clusters for the TCs lifetime maximum intensity (LMI) showed a zonal distribution in the band between 30°S and 45°N . Three LMI clusters were identified in each subbasin using *K*-means clustering. In the WNP basin (Figs. 6a,b), one cluster (P-W1; red) was located over the South China Sea (representing 26.3% of the TCs over this subbasin), while the East China Sea and western Philippine Sea were home to the second cluster (P-W2; purple), accounting for 48%. The last cluster (P-W3; yellow; 25.5%) covered a larger area from the central Philippine Sea to the central North Pacific Ocean, but exhibited greater dispersion in the TC LMI locations. In the NEPAC basin (Figs. 6a,c), TCs commonly reached the LMI close to the Central American coast, where the first cluster was located (P-N1; blue), and it was the NEPAC cluster that accounted for the majority of the TCs (57.1%). The second cluster (P-N2; green; 31.8%) appeared in the region of 10° – 20°N , 116° – 143°W , while the centroid of the third cluster (P-N3; brown; 10.9%) was just off the southern Hawaiian Islands and stretched to the date line. In the SPO

basin (Figs. 6a,d), the first LMI cluster (P-S1; black; 28.4%) was over the seas north of Australia and the western Coral Sea, the second cluster (P-S2; orange; 28.2%) extended from the eastern Fiji Islands toward the central South Pacific Ocean, and the third cluster (P-S3; magenta), accounting for 43.4% of the TCs, was located over the Melanesia Archipelago and surrounding seas. The monthly distribution was like that observed during the genesis phase for each basin.

During the TCs' LMI stage in the WNP basin, the western branch of the WNP SH was responsible for the moisture transport from the WNPac toward the three LMI clusters (like in the genesis stage), as indicated by the VIMF pattern (Fig. 7). However, the moisture contribution was less than 20%–30% for P-W1 and P-W2 but could be up to 30%–70% for P-W3 (Fig. 7). For P-W1, the Arabian Sea and Bay of Bengal, through the monsoonal wind circulation, contributed with a 5.25% moisture supply, the East and South China Seas contributed 40%–50% and 25%–35%, respectively, and the Philippine Sea contributed 15%–55%. For P-W2, the Bay of Bengal also supplied a small amount of moisture (10%–15%), with the East China Sea and Philippine Sea once again being the main

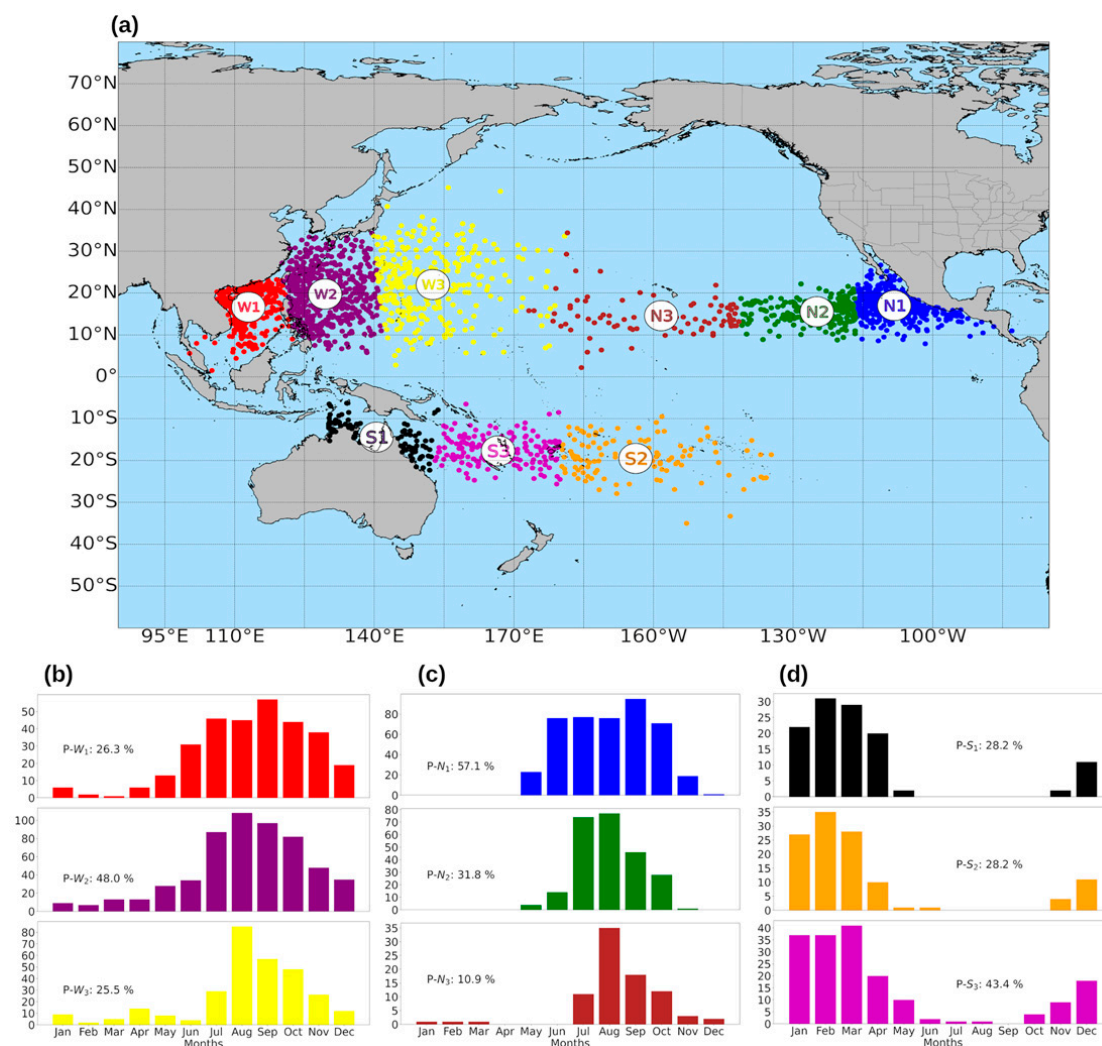


FIG. 6. (a) Tropical cyclone (TC) lifetime maximum intensity (LMI) locations in the Pacific Ocean from 1980 to 2018. Colors represent the TC LMI clusters ($n = 1, 2, 3 \dots$) calculated by k -means for the western North Pacific Ocean (WNP; red, purple, yellow, and lime green), the central and northeast Pacific Ocean (NEPAC; blue, green, brown, and pink), and the South Pacific Ocean (SPO; black, orange, and magenta). The monthly distribution by clusters is also represented for the (b) WNP, (c) NEPAC, and (d) SPO basins.

moisture reservoirs, supplying approximately 40%–70%. For P-W3, from the eastern Philippine Sea 30%–50% of the atmospheric moisture was transported, while the moisture contribution from the Celebes Sea was less than 20%. The contribution from terrestrial sources was less than 5%.

The trade winds originating from the eastern branch of the NPH and SPH were the main mechanism for moisture transport in the NEPAC basin during the TC lifetime maximum intensity (VIMF patterns in Fig. 8), like during the genesis phase. Westerly water vapor transport controlled by the easterly winds from the Caribbean Sea contributed with approximately 15% and 25% of precipitant moisture for P-N1 and P-N2, respectively. Nevertheless, the moisture gained by TCs over P-N1 mainly proceeded from the ETNPac, close to the Mexican coast (40%–60%) and along the southwestern U.S. coast (30%); besides, for P-N2, the moisture came mainly from the ETNPac (40%–75%) and the ETSPac

(30%–60%). Moreover, the landmasses of Central America also provided a nonnegligible amount of moisture to P-N1, which was slightly lower than P-N2. According to Amador (2008), the regional low-level jet structure, the Caribbean low-level jet, controlled by thermal gradients and topography, is a key factor that governs the distribution of moisture in Central America. From Fig. 8, we confirmed that P-N3 mainly received moisture from the central tropical Pacific Ocean (CTPac; 35%–55%), but remote sources over the Pacific coast of Central America and the southwestern U.S. coast also contributed, supplying 5%–10% of moisture.

Figure 9 shows the climatological moisture uptake patterns associated with each cluster during the TC LMI stage in the SPO basin. Compared with the genesis phase (Fig. 4), no notable differences were observed regarding the location and extent of moisture sources. However, the pattern of moisture uptake was more intense during the LMI (Fig. 9). The wind

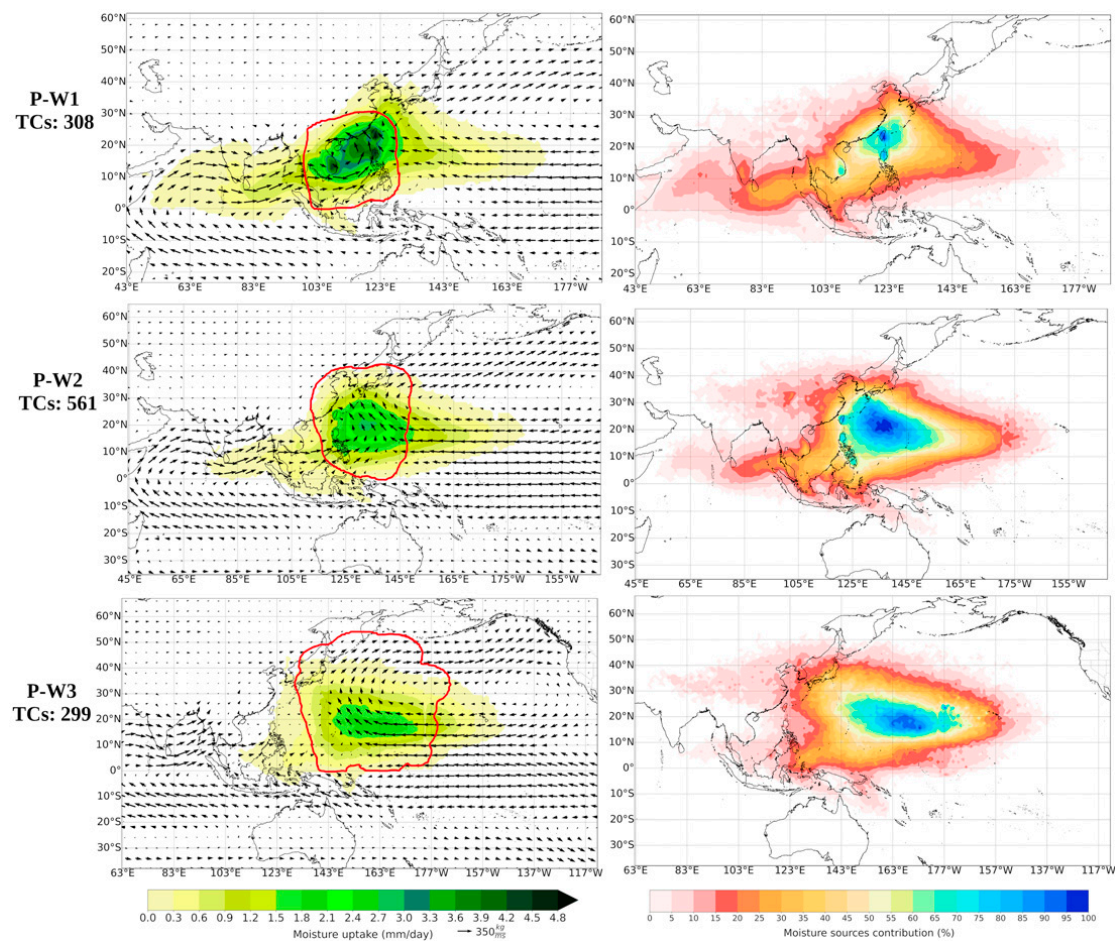


FIG. 7. (left) Mean moisture uptake (mm day^{-1}) and (right) moisture source contributions (%) by tracking precipitating parcels over the area enclosed by the TC outer radius (target region) backward in time up to 10 days for each TCs lifetime maximum intensity (LMI) cluster over the western North Pacific basin. The vertically integrated moisture flux (VIMF; kg m s^{-1} ; arrows) is also plotted. The red line represents the composite target region of all TCs (numbered on the left) within the cluster from 1980 to 2018.

fluxes that sustain the SPCZ were the main mechanisms for transporting atmospheric moisture to the LMI clusters. The VIMF pattern exhibited a cyclonic curvature in each cluster, probably linked to the Australian monsoon trough region, according to Vincent et al. (2011). The monsoon westerly winds transported moisture from the North Australian Basin to P-S1 (5%–20%) and P-S3 (5%–10%). The moisture that arrived at P-S1 commonly came from the Timor and Arafura Seas (20%–30%), Coral Sea (30%–60%), and mainland Australia (10%–60%), while the maximum contribution of atmospheric humidity for P-S3 was from the surrounding seas of the Melanesian Archipelago, accounting for more than 55% of all moisture accumulated to influence the precipitation in this cluster during the TCs LMI stage, making this area the most important source. The maximum contribution for P-S2 proceeded from the western tropical South Pacific Ocean (WTSPac; 40%–75%).

The entire overview of moisture sources that supply the precipitant moisture during the TC LMI stage over the WNP basin (Fig. 10a) showed that the major sources were located

over the East China Sea, South China Sea, and WTNPac, including the Philippine Sea. The moisture transported from these sources to TC locations accounted for 30%–60%, 20%–35%, and 30%–40%, respectively. The Bay of Bengal, southern Asia, and the central Pacific Ocean near the southwestern Hawaiian Islands also contributed, but by less than 15%–20%.

The location of the ITCZ divides the moisture sources for the TCs formed over the NEPAC basin into two well-defined asymmetric regions in the north (ETNPac) and south (ETSPac) at a latitude 10°N (Fig. 10b). Previous research findings (de Zoeke and Xie 2008) have indicated that the northwest–southeast slant of the Pacific coast of the American continent breaks the meridional symmetry of the eastern Pacific climate, causing more precipitation in the Northern Hemisphere. Indeed, the ETNPac was established as the main moisture source for the TC LMI phase in the NEPAC basin, contributing approximately 40%–70%. Meanwhile, the contributions originated from the Caribbean Sea and ETSPac moisture sources accounting for 10%–30% and 30%–50%.

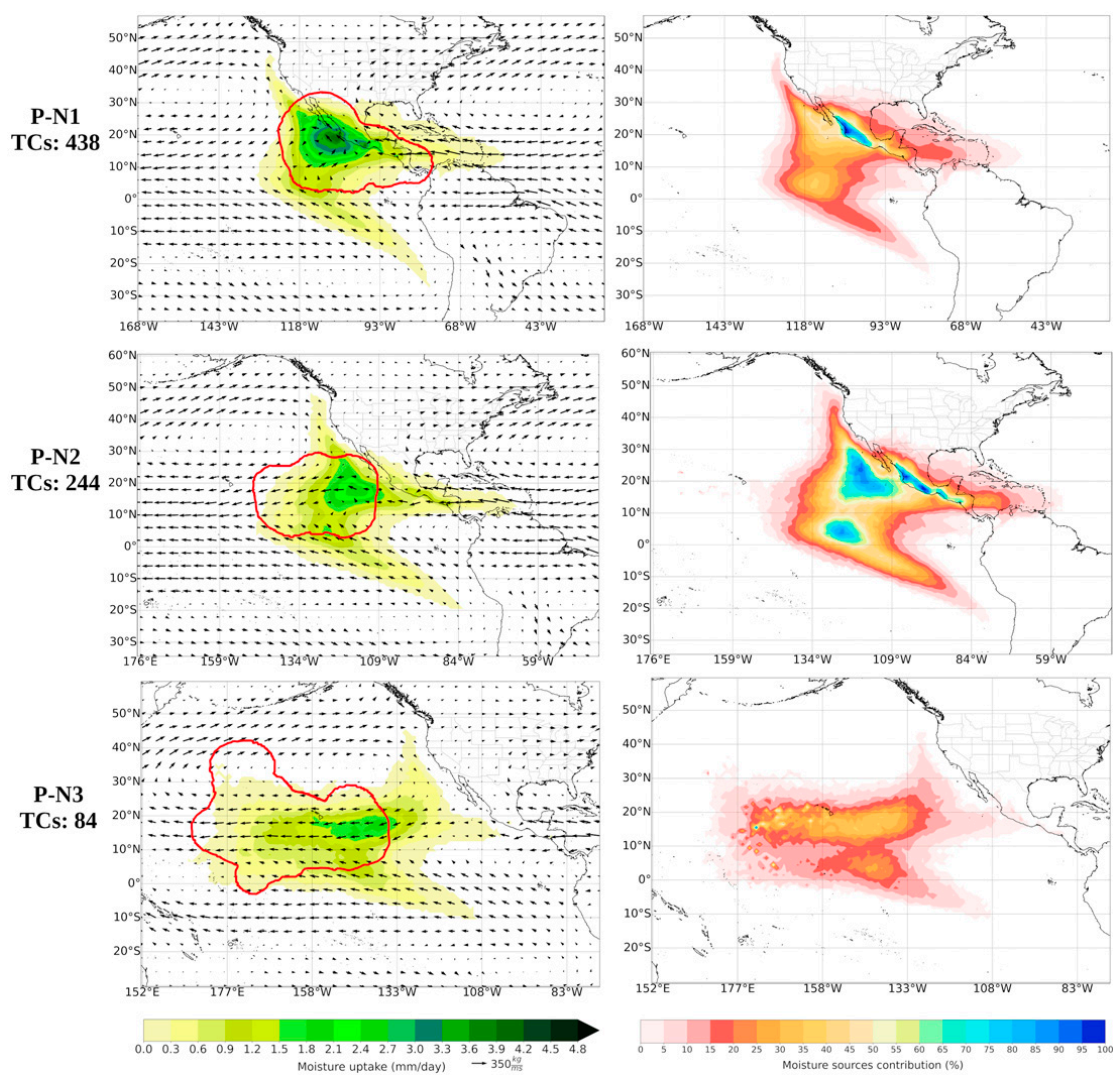


FIG. 8. As in Fig. 7, but for TCs over the central and northeast Pacific Ocean (NEPAC) basin.

TCs that formed over the SPO basin during the LMI stage generally gained moisture from the WTSPac source (Fig. 10c). The water vapor transported from the land area of northern Australia (20%–40%), the Coral Sea (30%–70%), and the seas surrounding the Melanesia Archipelago (50%–60%) played the largest role. The eastern Indian Ocean supplied less than 2%–5%.

On average, during the LMI stage, TCs over the WNP gained approximately 2225 mm day^{-1} of precipitant water vapor. A similar rate was found for the SPO basin (2193 mm day^{-1}) and was slightly lower for TCs formed in the NEPAC basin (1507 mm day^{-1}). It is worth noting that TCs in the NEPAC tended to gain less moisture during the LMI stage than during the genesis phase; this was not the case for TCs over the WNP and SPO, which gained more moisture during the LMI than during genesis.

Considering the different categories attained by the TCs, it was observed that the spatial pattern of moisture uptake was similar in each basin for tropical storms (TSs), hurricanes (Hs; category 1 and 2 on the Saffir–Simpson wind scale), and major

hurricanes (MHs; category 3+ on the Saffir–Simpson wind scale), as shown in Fig. 11. However, it was more intense during the H and MH intensity categories than during the TS category but tended to be more compact in the WNP and more elongated in the NEPAC. In the latter basin, the central Pacific Ocean appeared as an important source of moisture for precipitation associated with MHs. Moreover, the climatological moisture uptake patterns shown in Fig. 11 highlight the moisture contributions from WTNPac for the WNP, ETNPac, and ETSPac for NEPAC, and the Coral Sea for the SPO basin. Another feature of Fig. 11 is the poor contribution of atmospheric moisture from terrestrial sources, as previously observed for the genesis and LMI stages. It should be noted that the moisture flux pattern illustrated by the VIMF in Fig. 11 did not show noticeable differences between each intensity category in each basin. In the case of WNP, as discussed above for genesis and LMI phases, the moisture was mainly driven by easterly winds associated with the WNPSH wind circulation and the westerly wind from the Indian Ocean. For NEPAC, the convergence of the trade wind linked to the

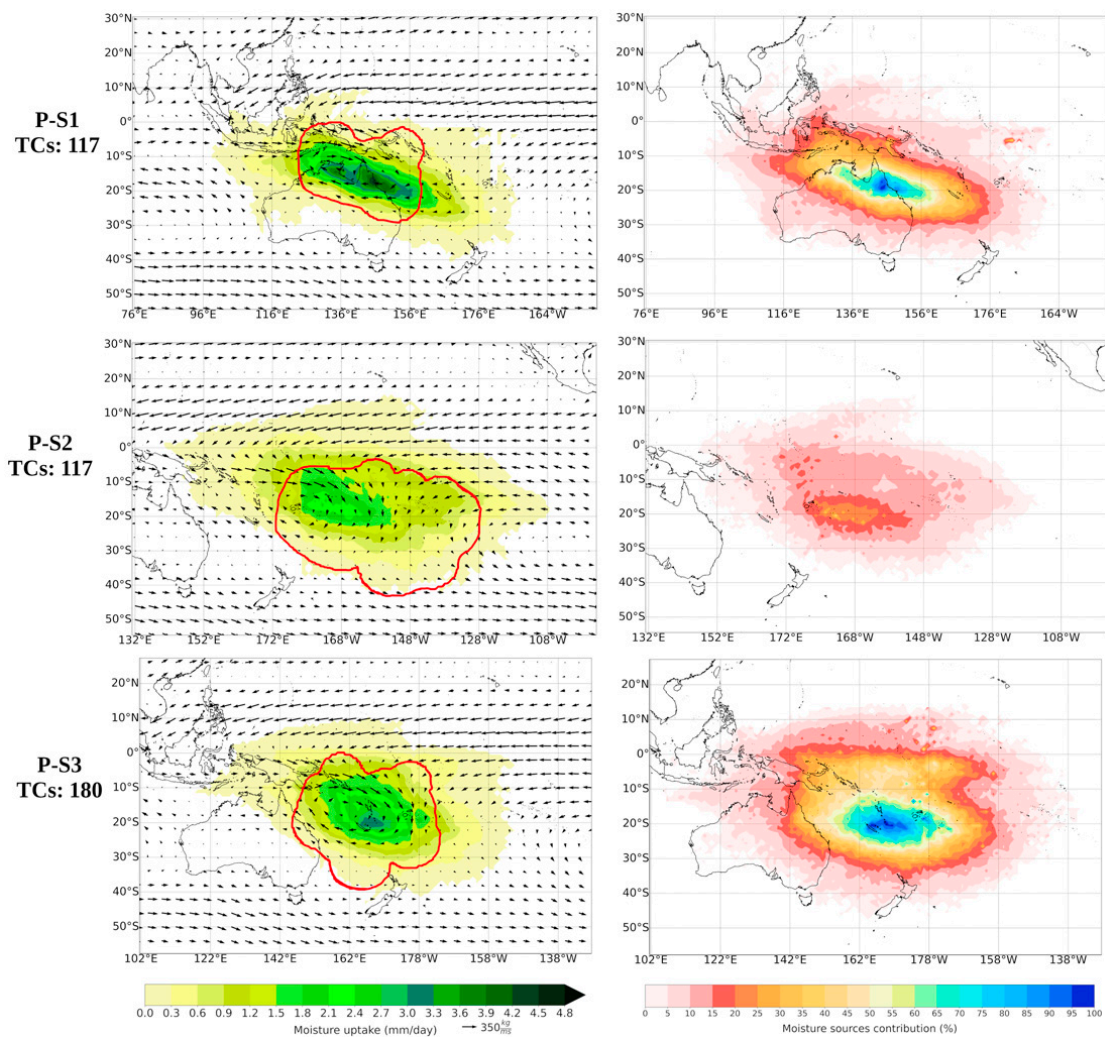


FIG. 9. As in Fig. 7, but for TCs over the South Pacific Ocean (SPO) basin.

NPH and SPH and the easterly wind from the Caribbean Sea acted as the main transport mechanisms for the atmospheric moisture that precipitated within the TC outer radius over NEPAC during the TS, H, and MH intensity categories. Furthermore, during the different TC intensities over the SPO basin, the wind convergence supporting the SPCZ was identified as the main moisture driver.

The intensity of the moisture sources was directly reflected in the mean moisture uptake amount per TC for any intensity category in each basin. Hurricanes exhibited the higher rate of moisture uptake in the three basins, contributing 1779 mm day^{-1} in the NEPAC, 2282 mm day^{-1} in the SPO, and 2308 mm day^{-1} in the WNP. In contrast, during the TS intensity category, the daily precipitant water vapor gained by TCs was less than 1900 mm day^{-1} per TC in any basin, falling below 1450 mm day^{-1} in the NEPAC. During the MH category, they gained by approximately 2100 mm day^{-1} per TC in the WNP and SPO, lower than 1600 mm day^{-1} per TC in the NEPAC. As a general pattern, moisture uptake was higher for hurricanes than for major hurricanes or tropical storms in any basin. This behavior can be explained by the fact

that the mean size of Hs in all basins was higher than the average size of TSs or MHs, as shown in Table S1 in the online supplemental material. The moisture uptake significantly ($p < 0.05$) correlated with the TC outer radius, with a Pearson's correlation coefficient of 0.47, 0.68, and 0.73 in NEPAC, SPO, and WNP, respectively. As noted above, the precipitation moisture uptake per TC during the LMI phase or intensity changes in the NEPAC were lower than those in the WNP and SPO.

c. Climatological mean moisture sources during the tropical cyclone dissipation phase

Figure 12a shows the regions (clusters) where TCs formed over the Pacific Ocean frequently dissipate. The first cluster in the WNP basin (D-W1; red; 22.1%) covered the band within 0° – 55°N , 150°E – 180° ; the second (D-W2; purple; 1.45%) was a small cluster over the Bering Sea; the third cluster (D-W3; yellow; 46.8%) was located over the South China Sea and southern China; and the last cluster (D-W4; lime green; 29.4%) extended from the Korean Peninsula to the Philippine Sea, including the East China Sea, Japan Sea, and Japan. Over the

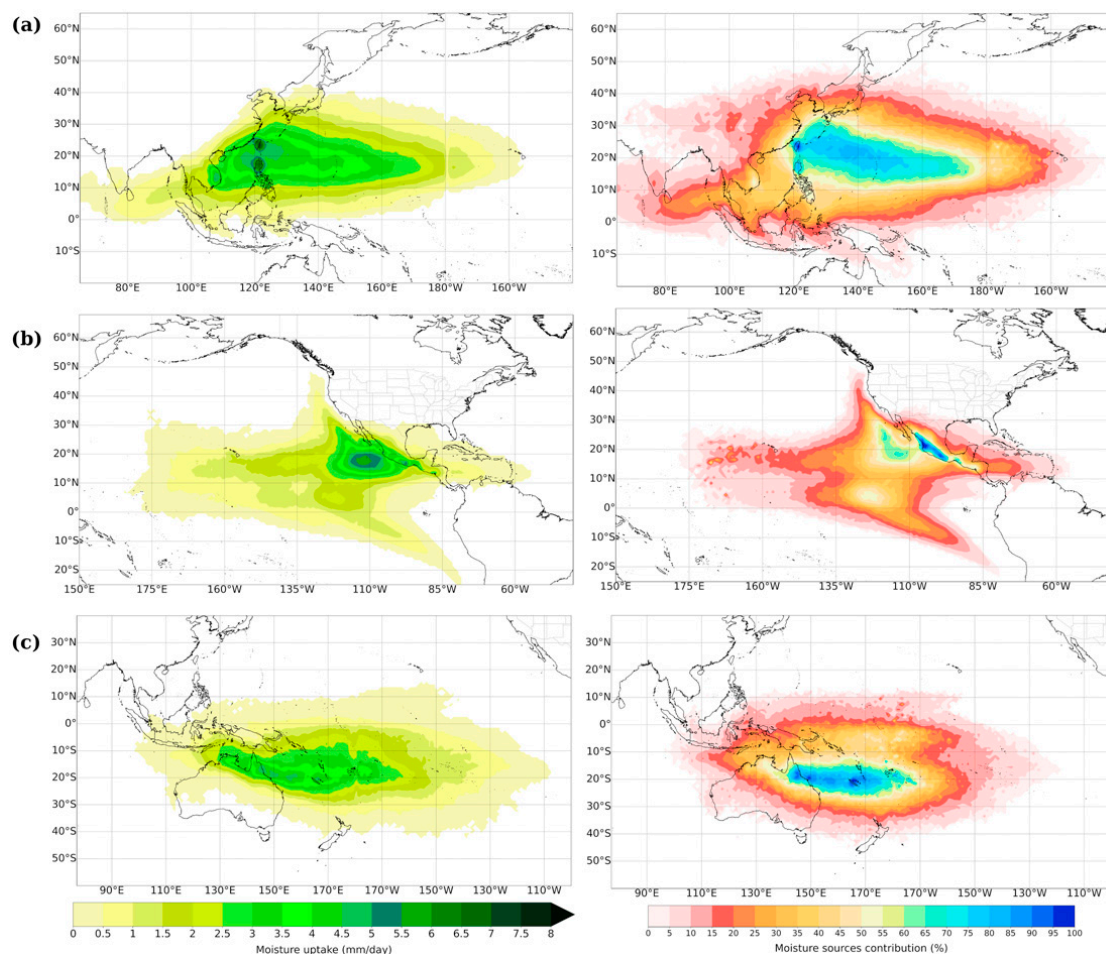


FIG. 10. (left) Climatological moisture uptake pattern (mm day^{-1}) and (right) the contribution of moisture sources (%) during the tropical cyclones lifetime maximum intensity over the (a) western North Pacific Ocean, (b) central and northeast Pacific Ocean, and (c) South Pacific Ocean basins.

NEPAC basin, four clusters were also identified: the first (D-N2; blue) was located striking the Mexican Pacific coast, accounting for 41.8% of TCs in their dissipation stage; the second (D-N2; green; 2.48%) was a small cluster over the western Pacific Ocean; the third (D-N3; brown; 38.8%) was limited to D-N1 in the eastern tropical North Pacific Ocean; and the fourth (D-N4; pink; 16.8%) was located over the Hawaiian Islands and surrounding seas. In the SPO basin, the first cluster was located over the western South Pacific Ocean (D-S1; black) where 25.8% of TCs dissipated, the second over the Coral Sea (D-S2; orange; 33.4%), followed by the third cluster over mainland Australia and the eastern Indian Ocean (D-S3; magenta; 27.0%) and the fourth over the central South Pacific Ocean (D-S4; light blue; 13.6%). Figure 8b shows that August, September, and October exhibited the highest monthly TC dissipation frequency in the WNP, although many TCs dissipated in D-W3 from July to November. Likewise, TCs that formed over the NEPAC commonly dissipated from July to September (Fig. 12c). Conversely, the highest dissipation frequency in SPO was observed from January to March (Fig. 12d). This monthly distribution agreed with that found for the genesis and LMI stages.

As shown in Fig. 13, the WNPSH controlled most of the moisture flux toward the dissipation clusters in the WNP basin. The cluster D-W1 mainly received substantial moisture from the North Pacific Ocean on the southern Japanese island providing 40%–70% of total moisture for the TC precipitation during the dissipation stage, followed by 20%–35% from the Japan Sea and eastern China. The contribution from remote sources was less than 10%. Similarly, the northern Pacific Ocean supplied moisture (30%–55%) to the small dissipation cluster D-W2 over the Bering Sea. This cluster also received moisture (5%–20%) from terrestrial sources in eastern China. The South and East China Seas acted as the principal reservoir of water vapor (40%–70%) for the TCs over W-D3, which also received 5%–30% from the Arabian Sea and the Bay of Bengal through the westerly winds linked to the South Asia monsoon. The cluster D-W4 not only gained moisture from the East China Sea and Japan Sea (35%–70%) but also from the South China Sea (5%–20%) and terrestrial sources over eastern China (15%–35%). In addition, the WTNPac supplied 5%–20% of precipitant moisture to W-D3 and W-D4.

The origin of the moisture that generated precipitation during the TC dissipation stage over the NEPAC basin is shown

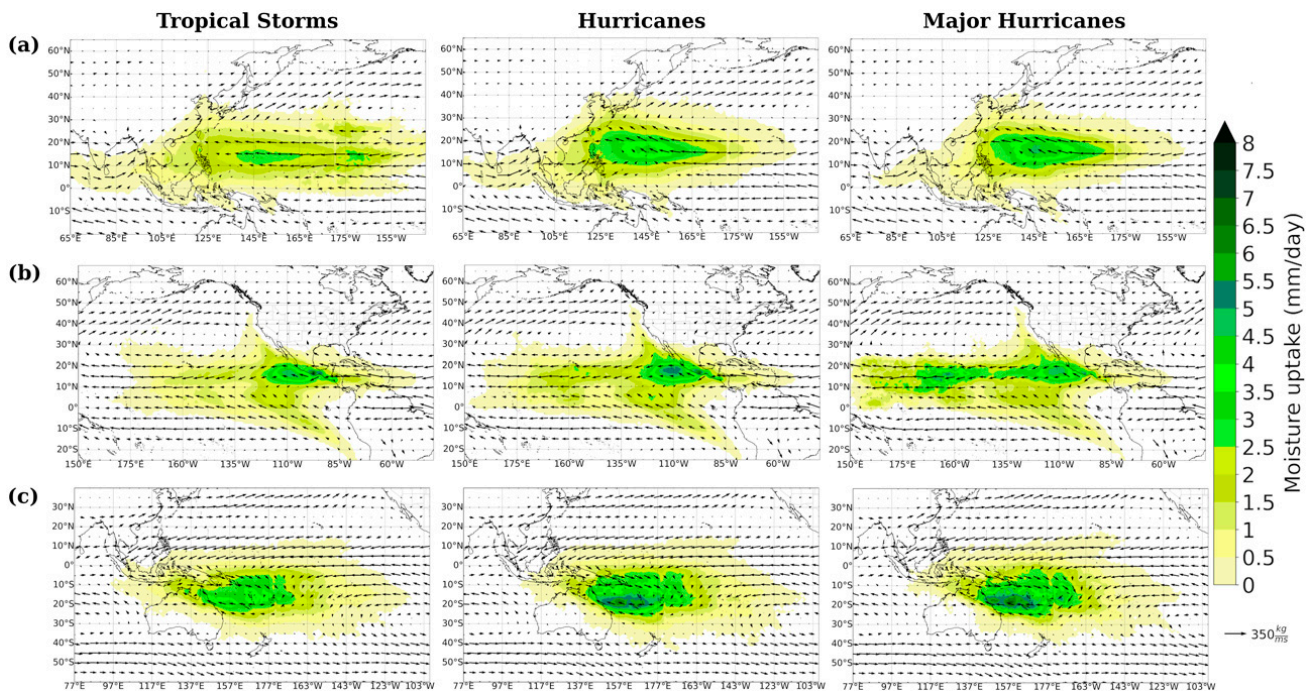


FIG. 11. Climatological moisture uptake (mm day^{-1}) pattern during the (left) tropical storm, (center) hurricane (category 1 and 2 on the Saffir–Simpson wind scale), and (right) major hurricane (category 3+ on the Saffir–Simpson wind scale) intensity categories of tropical cyclones formed over the (a) western North Pacific Ocean, (b) central and northeast Pacific Ocean, and (c) South Pacific Ocean basins. Arrows represent the climatological vertically integrated moisture flux (VIMF; $\text{kg m}^{-1} \text{s}^{-1}$; arrows) during each intensity category.

in Fig. 14. As in the other TC stages, the main moisture transport mechanism in the NEPAC was mainly controlled by the circulation of the NPH and SPH. The ETNPac was identified as the principal moisture source for D-N1 and D-N3, supplying 30%–60% and 30%–75%, respectively. Nevertheless, these clusters also received moisture from the Caribbean Sea and ETSPac, which was higher for D-N3 than for D-N1. The maximum contribution to D-N2 (20%–60%) came from small portions of the seas surrounding the Hawaiian Islands, while the western North Pacific Ocean (WNPac) provided 15%–30%. The dissipation cluster D-N4 took moisture from a wide moisture source extending from the date line to the western coast of the United States and from the equator to midlatitudes, with the highest moisture uptake (50%–70%) from the seas around the southern Hawaiian Islands.

The convergence of westerly and easterly winds that sustain the SPCZ was responsible for moisture transport toward the TC dissipation clusters over the SPO basin (Fig. 15). The cluster D-S1 received most of the moisture from the WTSPac (~20%–50%). This was a source that also contributed to the D-S2 (15%–35%), which was complemented with a large amount of precipitant moisture from the Coral Sea (40%–65%) and a weak contribution (less than 25%) from eastern Australia. Likewise, the Coral Sea and northern Australia acted as the main moisture sources for D-S3, contributing approximately 50%–70% of precipitant atmospheric moisture, and by the eastern Indian Ocean, which supplied 20%–40%. The moisture that precipitated over D-S4 mainly originated from the central South Pacific Ocean (CenSPac).

Figure 16 summarizes the findings discussed above related to the moisture sources for the precipitation associated with TCs formed over the Pacific Ocean during their dissipation phase. Overall, the moisture sources in the WNP were displaced to the north relative to the moisture sources for the genesis and LMI stages (see Figs. 5a and 10a), and the spatial pattern of moisture uptake was also broader. This displacement may be explained by the fact that TCs tend to move westward or northward in the WNP basin, and therefore the dissipation locations were found poleward regarding the genesis location (Camargo et al. 2007). Clearly, the East China Sea, the Japan Sea, and the WTNPac (the band in 10° – 40° N, 130° E– 170° W) were the principal sources (40%–70%) for the precipitated moisture during TC dissipation. This moisture was mainly transported by the western flank of the WNPSH. It is worth noting that, on average, the poor moisture contribution (less than 15%) from the Arabian Sea and the Bay of Bengal, while the terrestrial sources over eastern China, the Korean Peninsula, Japan, and Taiwan played an important role in moisture supply (20%–35%). Figure 16b shows an elongated westward moisture uptake pattern during the TC dissipation stage in the NEPAC basin. However, the highest moisture contribution (similar for genesis and LMI stages) was found in the ETNPac, including the Mexican Pacific coast, which both supplied approximately 45%–75% moisture. The contribution of moisture was also important (~35%) in the band stretching between 10° – 20° N and from 125° W to the date line. Overall, the moisture uptake was weak (less than 15%–20%) from the ETSPac, Caribbean Sea, and WNPac.

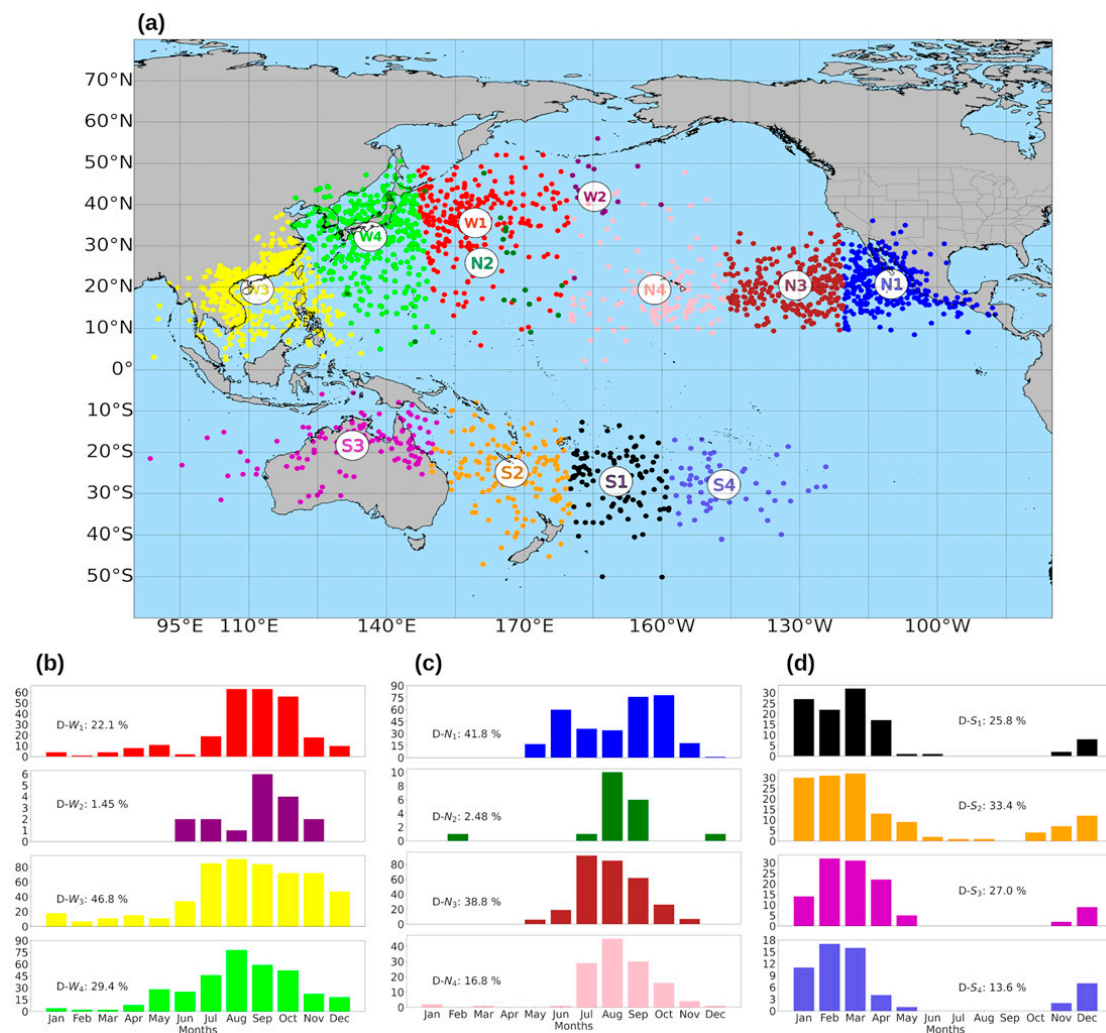


FIG. 12. (a) Tropical cyclones (TCs) dissipation locations in the Pacific Ocean from 1980 to 2018. Colors represent the TC dissipation clusters ($n = 1, 2, 3 \dots$) calculated by k -means for the western North Pacific Ocean (WNP; red, purple, yellow, and lime green), the central and northeast Pacific Ocean (NEPAC; blue, green, brown, and pink), and the South Pacific Ocean (SPO; black, orange, magenta, and light blue). The monthly distribution by clusters is also represented for the (b) WNP, (c) NEPAC, and (d) SPO basins.

Moreover, for the SPO basin, Fig. 16c reveals that the moisture uptake pattern extended more toward the central South Pacific Ocean during the dissipation phase than during the previous stages. Nevertheless, the WTSPac and the Coral Sea were the principal moisture sources for the precipitation caused by TCs during the dissipation stage, providing approximately 45%–70% of precipitant moisture, followed by northern Australia and CenSPac, which contributed 40%–50% and 20%–30%, respectively.

By quantifying the mean moisture uptake per TC that contributed to precipitation during the dissipation stage, we found that TCs that formed over the WNP gained more moisture (2197 mm day^{-1}) than those formed over the SPO (2051 mm day^{-1}) or NEPAC (997 mm day^{-1}). Moisture uptake in the dissipation stage was slightly lower than in the LMI phase. Although the northward poleward displacement increases the size of TCs (e.g., Kimball and Mulekar 2004;

Knaff et al. 2014; Pérez-Alarcón et al. 2021a) and this could imply an increase in moisture uptake due to their larger area, several TCs dissipated over land (Fig. 12a), and it is well known that terrain features influence the total TC-induced precipitation (e.g., Qiu et al. 2019) and that during the dissipation stage the weakening of the secondary circulation of TCs causes an overall reduction of the moisture flux inward the TCs.

4. Summary and conclusions

Tropical cyclones (TCs) play an important role in the atmospheric branch of the hydrological cycle, acting as a precipitant water vapor corridor from ocean to land. Several studies have focused on the water budget linked to TCs over the land surrounding the Pacific Ocean or on the contribution of TCs to total and extreme rainfall over East Asia (Jiang and Zipser 2010;

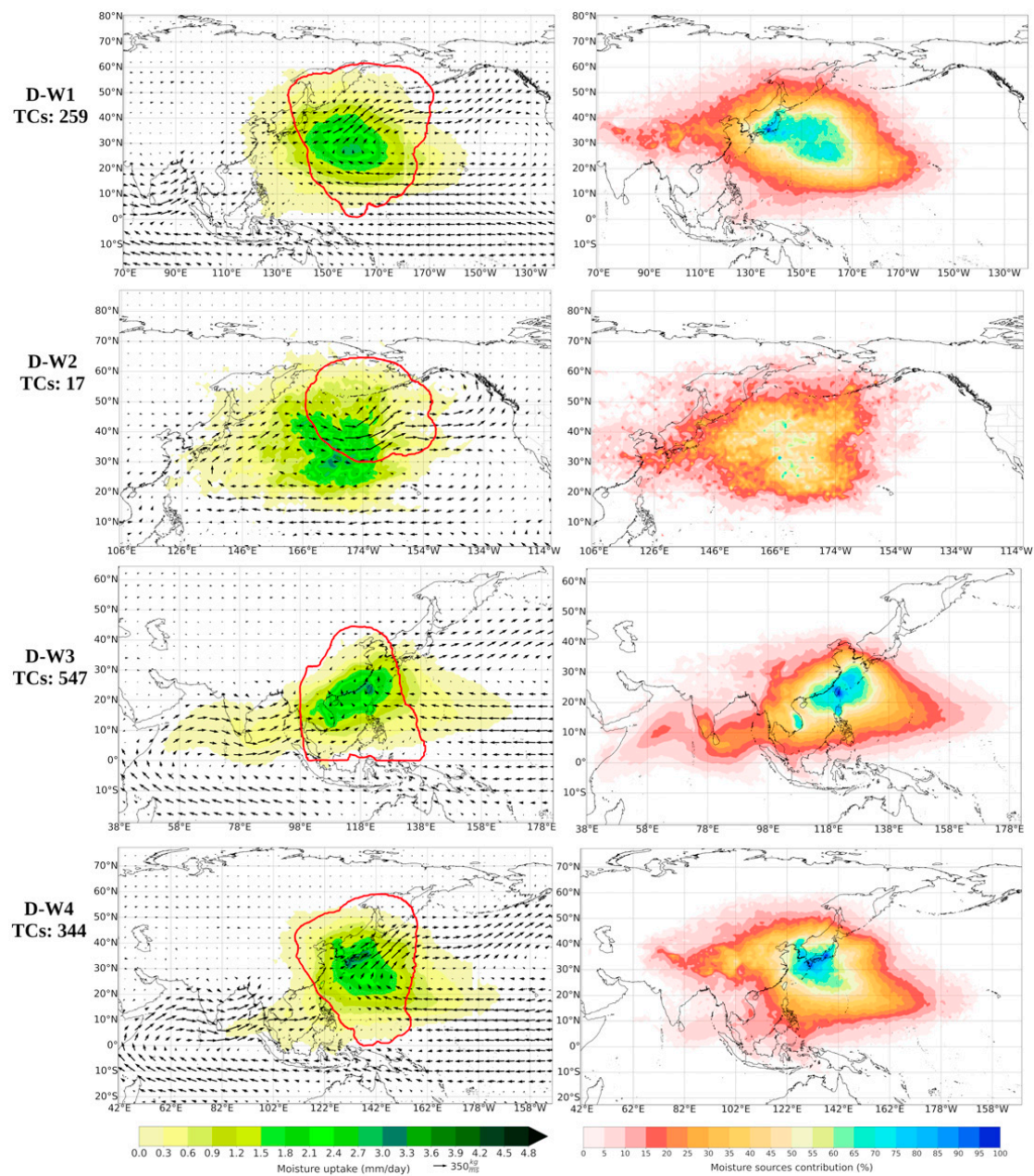


FIG. 13. (left) Mean moisture uptake (mm day^{-1}) and (right) moisture sources contribution (%) by tracking precipitating parcels over the area enclosed by the TC outer radius (target region) backward in time up to 10 days for each TC dissipation cluster over the western North Pacific basin. The vertically integrated moisture flux (VIMF; $\text{kg m}^{-1} \text{s}^{-1}$; arrows) is also plotted. The red line represents the composite target region of all TCs (numbered on the left) within the cluster from 1980 to 2018.

Guo et al. 2017), northern Australia (Ng et al. 2014), and tropical and subtropical North America (Xu et al. 2017; Dominguez and Magaña 2018). However, few studies have been conducted to identify the moisture sources for TC precipitation. Therefore, this study was motivated by the need to identify this lack concerning the moisture sources identification for the precipitation associated with TCs during the genesis, LMI, and dissipation phases over the Pacific Ocean, which is the site of $\sim 62\%$ of the world's TCs. The period analyzed was 1980–2018.

To identify the moisture sources, Lagrangian backward tracking of precipitant air parcels residing over each TC genesis, LMI, and dissipation location over the western North Pacific Ocean (WNP), central and east Pacific Ocean (NEPAC), and South Pacific Ocean (SPO) basins was performed. The trajectories were obtained from the global outputs of the FLEXPART model (Stohl et al. 2005) and WaterSip moisture source diagnostic method (Sodemann et al. 2008). In addition, to gain coherent insight into the relative importance of the identified

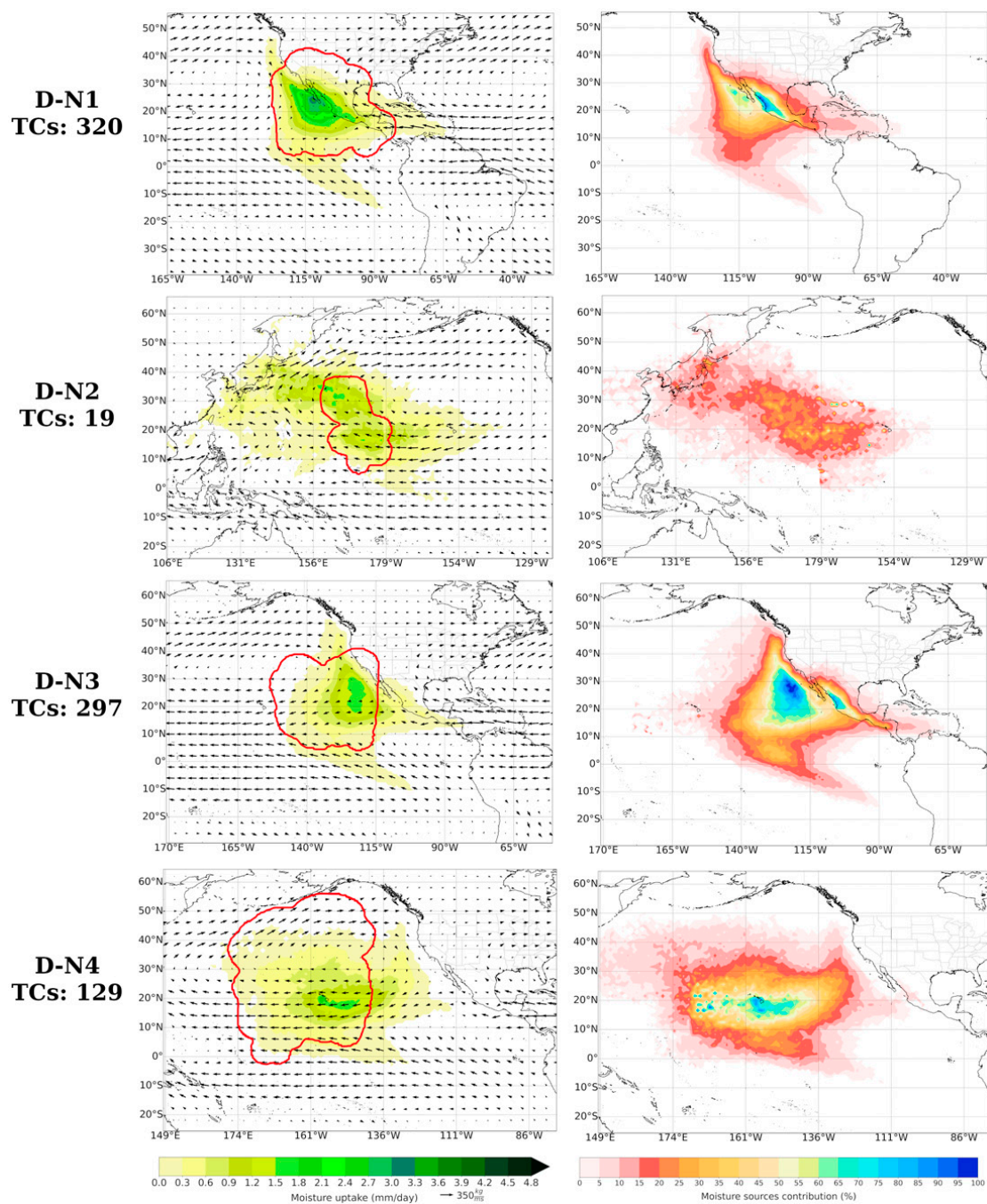


FIG. 14. As in Fig. 13, but for TCs over the central and northeast Pacific Ocean (NEPAC) basin.

moisture sources and moisture transport mechanisms, we separated the TC locations into clusters by applying the *K*-means technique.

Over the WNP, moisture was mainly transported by the circulation of the western North Pacific subtropical high (WNPSH) and westerly winds linked to the South Asian monsoon. The WNPSH conforms the western part of the North Pacific high (NPH); thus, seasonal variations of the mean position and extension of NPH modulate the moisture transport patterns (Fig. S1). During June–August, the NPH

center was located at $\sim 38^{\circ}\text{N}$, 148°W , and the anticyclonic ridge extended into the Philippine Sea. This large-scale circulation pattern favored the moisture transport by the westerly monsoon winds from the Bay of Bengal and southeastern Asia toward the China Sea and the western Philippine Sea. However, during September–November, the NPH retreats south-eastward ($\sim 35^{\circ}\text{N}$, 140°W), drastically reducing the moisture driven by the westerly winds. As previously noted, the moisture flux convergence depends on the positions of the monsoon trough and the ridge of the WNPSH (Guo et al. 2017).

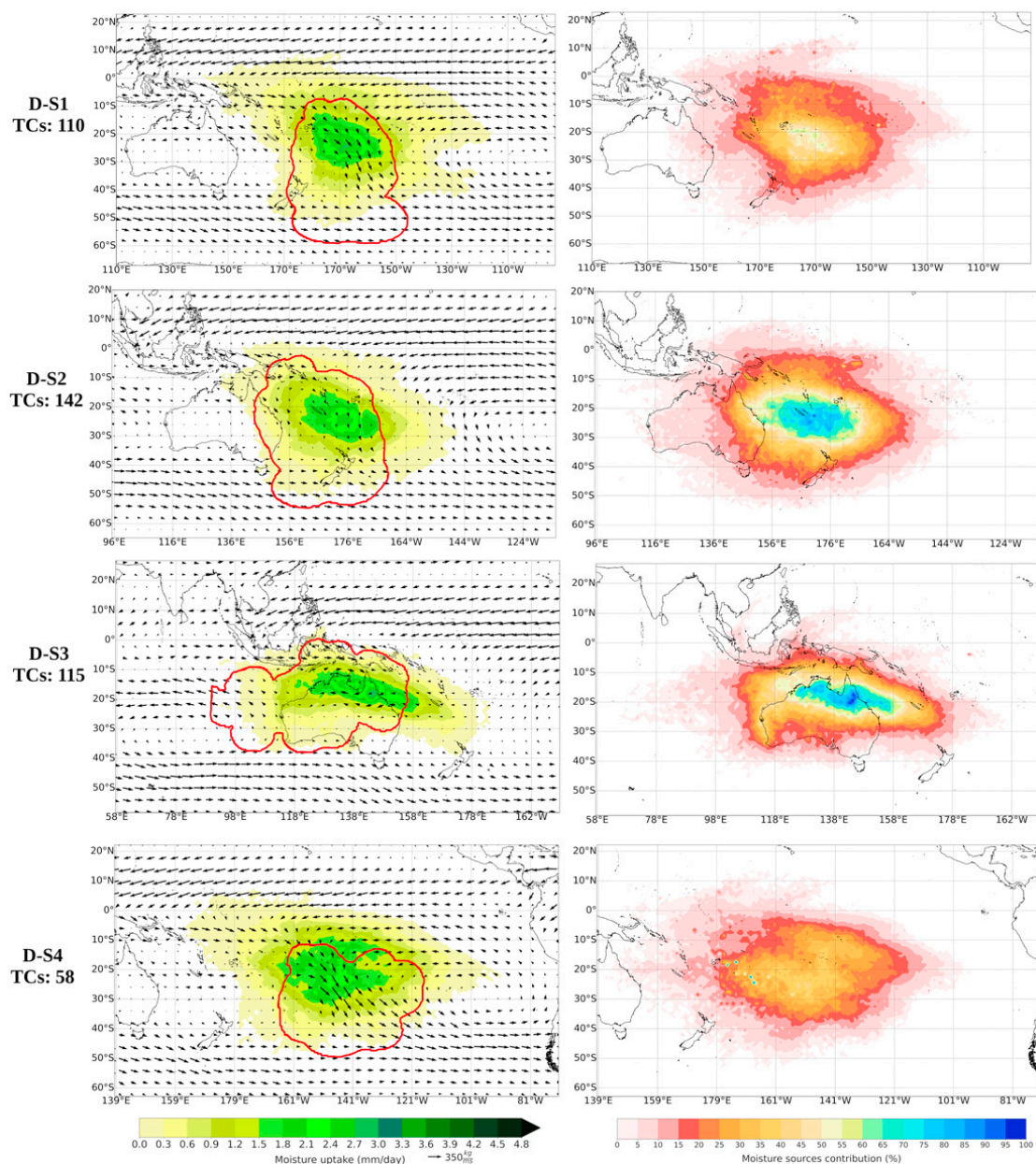


FIG. 15. As in Fig. 13, but for TCs over the South Pacific Ocean (SPO) basin.

Therefore, further studies are required to understand the linkages of seasonal variation of the NPH and moisture transport for TCs precipitation. As a general pattern, the moisture sources were elongated eastward during the genesis and LMI stages, with the WTNPac ($\sim 60\%$) and the South and East China Seas ($\sim 25\%$) being the regions of major moisture contribution, although the latter was crucial during the LMI stage, increasing the moisture supplied by up to 55%. During the dissipation stage, a northward shift of moisture sources was observed, with the WTNPac, East China Sea, and Japan Sea being the most important moisture sources, which supplied approximately 70% of total moisture amounts.

The moisture source pattern in the NEPAC basin exhibited a notable north–south division caused by the mean position of

the ITCZ during the summer months in the Northern Hemisphere. The combined circulation of the NPH and the South Pacific high (SPH) acted as the principal mechanism for transporting moisture, followed by easterly winds traveling across the tropical North Atlantic Ocean. No notable differences in the moisture uptake patterns during genesis or LMI caused by the seasonal variation of both NPH and SPH were found. Nevertheless, the weakening of NPH and the strengthening of SPH favored the moisture uptake during TCs dissipation in the boreal fall (September–November), as revealed in Fig. S2. The precipitant moisture gained by TCs in the NEPAC during genesis, the LMI, or dissipation stages mainly came from the eastern tropical North Pacific Ocean (ETNPac), accounting for approximately 65% of moisture; the eastern tropical

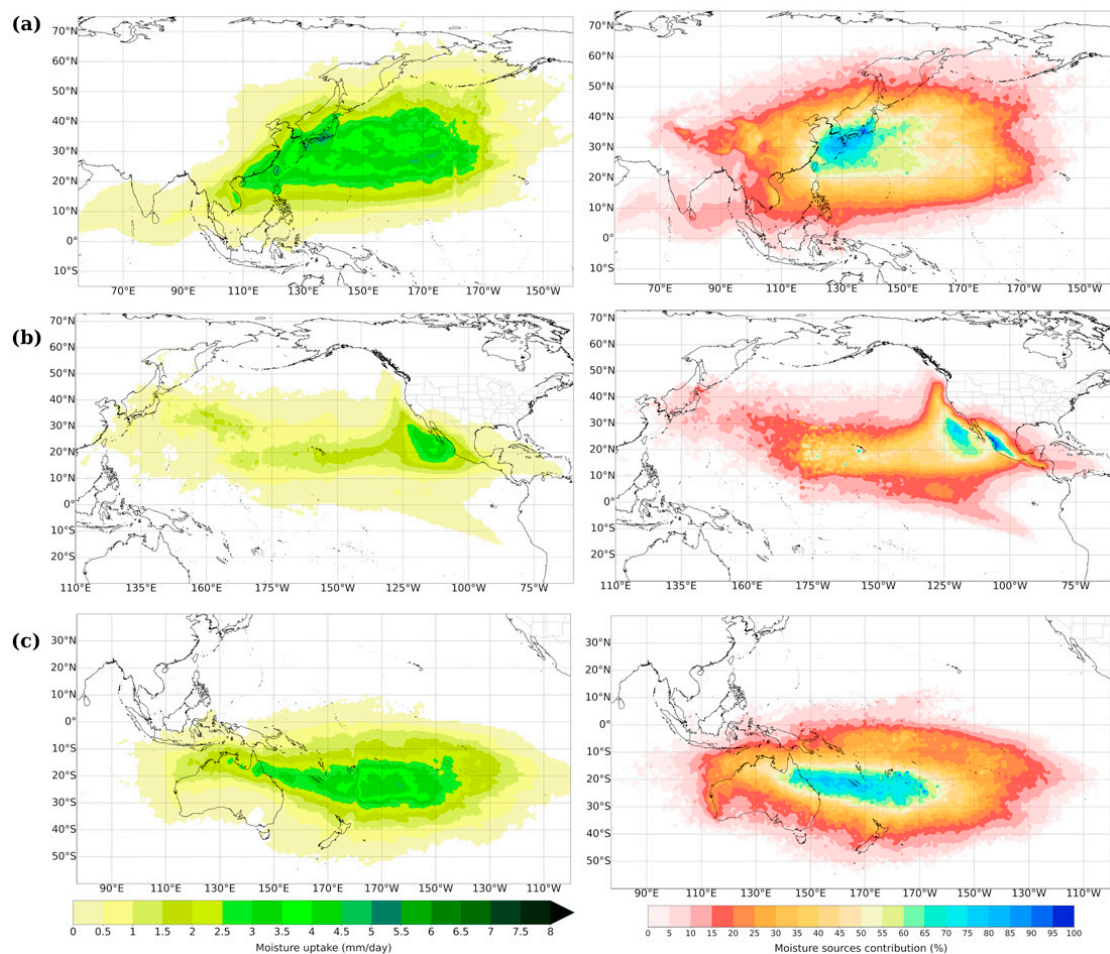


FIG. 16. (left) Climatological moisture uptake pattern (mm day^{-1}) and (right) the contribution of moisture sources (%) during the TC dissipation stage over the (a) western North Pacific Ocean, (b) central and northeast Pacific Ocean, and (c) South Pacific Ocean basins.

South Pacific Ocean (ETSPac), which supplied $\sim 20\%$; and the Caribbean Sea at $\sim 15\%$. The poor moisture contribution from the Caribbean Sea is influenced by the Central American isthmus. Fu et al. (2021) found that this mountainous region significantly interrupts the abundant moisture transport from the Caribbean Sea to the NEPAC, limiting deep convection over the open ocean area where TCs preferentially occurred. Part of water vapor from the Caribbean Sea transported by the easterly winds precipitated over the Atlantic landside of Central American mountains, reducing the total moisture that reaches the TCs over NEPAC. In addition, during the TC dissipation stage, the ETNPac moisture source extended westward to the date line.

Similarly, the convergence of westerly and easterly winds that form the South Pacific convergence zone (SPCZ) was identified as the main mechanism of precipitant moisture transport toward TC locations over the SPO basin. It is worth noting that the SPCZ is well defined during the austral summer and is less structured from May to October (e.g., Niznik et al. 2015; Harvey et al. 2019). This pattern is mainly caused by the seasonal changes of the SPH (e.g., Takahashi et al. 2007; see also Fig. S3); however, we did not discuss here its

impacts on the moisture sources for TCs precipitation over SPO. In summary, our findings reveal that the Coral Sea, the western tropical South Pacific Ocean (WTSPac), and northern Australia (NA) were the principal moisture sources, contributing 40%–50%, 20%–35%, and 20%–30%, respectively. However, during the dissipation stage, the moisture source patterns were slightly modified, as was observed for WNP and NEPAC. Hence, the highest moisture contribution came from the WTSPac (40%–55%) and not from the Coral Sea (20%–30%). The central South Pacific Ocean also contributed significant amounts of moisture (10%–15%).

Furthermore, the moisture contribution in these three basins during each TC stage was predominantly from moisture sources of maritime origin. The relatively low values of moisture uptake found in this work during the genesis phase do not contradict previous studies that found (e.g., Gray 1968; Yoshida et al. 2017; Fudeyasu et al. 2020), that TC formation requires substantial moisture availability in the atmosphere (e.g., Gray 1968; Yoshida et al. 2017; Fudeyasu et al. 2020). Note that here we present the origin of the moisture that finally precipitated during each phase of TC development, and the low values of moisture uptake during the genesis stage are

only related to low values of TC precipitation in this initial phase. Indeed, previous works (e.g., Wang and Hanks 2016; Ankur et al. 2020) pointed out that TC formation can be considered a process in which convection becomes stronger and better organized, and the rain rate increase as the storm intensifies. The percentage of the total moisture gained by the TCs that becomes into precipitation and how this relationship varies throughout its life cycle would be another interesting characterization to be study in future work. The reduction of the moisture uptake during the dissipation stage can be related to the TC propagation directions and their positions when dissipated, generally over land or at high latitudes, away from the genesis and LMI locations. It has been well documented (e.g., Tuleya 1994; Wang and Matyas 2022) that the interaction of TCs with the land surface affected the thermodynamics mechanism that controlled the maintenance of TCs. On the other hand, during the dissipation stage, the moisture flux inward is reduced due to the weakening or breaking of the secondary circulation of TCs.

Backward tracking of precipitant air masses over TC locations also revealed that TCs gained more moisture during the genesis phase in the SPO than in any basin, and WNP exhibited the highest mean moisture uptake per TC during the LMI and dissipation stages. Thus, TCs over the NEPAC basin showed the lowest moisture uptake. According to the intensity categories, the moisture uptake of hurricanes was, on average, higher than that of major hurricanes or tropical storms in the three basins. Indeed, the moisture uptake and the TC intensity significantly ($p < 0.05$) correlate with Pearson's correlation coefficients of 0.37, 0.41, and 0.46 in the NEPAC, SPO, and WNP, respectively. Following the results of Yu et al. (2017) and Feng and Shu (2018), it is worth noting that while stronger TCs have more averaged total precipitation and decaying TCs show a decrease in the total rainfall, the maximum total precipitation, maximum precipitation area, and maximum precipitation rate are not fully dependent on TC intensity.

Future studies will focus on the relationship between climatic modes and variability in moisture sources for the precipitation of TCs in the Pacific Ocean. Several authors (e.g., Kaplan and DeMaria 2003; Chen et al. 2018; Zhang et al. 2020) have addressed the notable differences between TCs undergoing rapid intensification (RI) processes and non-RI. Therefore, in ongoing works, we investigate the differences in the moisture sources for the precipitation of RI and non-RI TCs. Moreover, as noted above and as Figs. S1–S3 revealed, the seasonal variations of high pressure systems over the Pacific Ocean modulated the moisture transport patterns. Therefore, it is expected that also they influenced the interannual variability of moisture uptake, which will be further investigated in future studies.

Our findings reveal the climatological moisture sources for TCs in the Pacific Ocean under historical and present climates. The variation of the location and extension of these sources in future scenarios considering global warming could be used as parameters for anticipating possible changes in the TCs activity in the Pacific basin, which constitutes an added

value of our results to support future scientific research and policy-making plans for adaptation and mitigation.

Acknowledgments. A.P-A acknowledges the PhD grant from the University of Vigo. J.C.F-A and R.S acknowledge support from the Xunta de Galicia (Galician Regional Government) under Grants ED481A-2020/193 and ED481B 2019/070, respectively. This work has also been made possible thanks to the computing resources and technical support provided by the Centro de Supercomputación de Galicia (CESGA). The authors acknowledge the NHC and JTWC for freely providing the best track archive and the Copernicus Climate Change Service for the ERA-Interim database. This work was supported by the LAGRIMA and SETESTRELO projects (Grants RTI2018-095772-B-I00 and PID2021-122314OB-I00, respectively) funded by the Ministerio de Ciencia, Innovación y Universidades, Spain. Partial support was also obtained from the Xunta de Galicia under the Project ED431C 2021/44 [Programa de Consolidación e Estructuración de Unidades de Investigación Competitivas (Grupos de Referencia Competitiva) and Consellería de Cultura, Educación e Universidade].

Data availability statement. The sources of databases used in this study are as follows: the JTWC and HURDAT2 best track archives are from <https://www.metoc.navy.mil/jtwc/jtwc.html?best-tracks> and <https://www.nhc.noaa.gov/data/#hurdat>, respectively; ERA-Interim from <https://apps.ecmwf.int/datasets/data/interim-full-daily/levtype=sfc/>; and the TCSize database from <https://doi.org/10.17632/8997r89fbf.1>. The FLEXPART source code is available at <https://www.flexpart.eu/downloads/6>.

REFERENCES

- Amador, J. A., 2008: The Intra-Americas Sea low-level jet: Overview and future research. *Ann. N. Y. Acad. Sci.*, **1146**, 153–188, <https://doi.org/10.1196/annals.1446.012>.
- Ankur, K., N. K. R. Busireddy, K. K. Osuri, and D. Niyogi, 2020: On the relationship between intensity changes and rainfall distribution in tropical cyclones over the north Indian Ocean. *Int. J. Climatol.*, **40**, 2015–2025, <https://doi.org/10.1002/joc.6315>.
- Bhatia, K. T., G. A. Vecchi, T. R. Knutson, H. Murakami, J. Kossin, K. W. Dixon, and C. E. Whitlock, 2019: Recent increases in tropical cyclone intensification rates. *Nat. Commun.*, **10**, 635, <https://doi.org/10.1038/s41467-019-08471-z>.
- Braun, S. A., 2006: High-resolution simulation of Hurricane Bonnie (1998). Part II: Water budget. *J. Atmos. Sci.*, **63**, 43–64, <https://doi.org/10.1175/JAS3609.1>.
- Camargo, S. J., A. W. Robertson, S. J. Gaffney, P. Smyth, and M. Ghil, 2007: Cluster analysis of typhoon tracks. Part I: General properties. *J. Climate*, **20**, 3635–3653, <https://doi.org/10.1175/JCLI4188.1>.
- Cao, X., T. Li, M. Peng, W. Chen, and G. Chen, 2014: Effects of monsoon trough interannual variation on tropical cyclogenesis over the western North Pacific. *Geophys. Res. Lett.*, **41**, 4332–4339, <https://doi.org/10.1002/2014GL060307>.
- , G. Chen, T. Li, and F. Ren, 2016: Simulations of tropical cyclogenesis associated with different monsoon trough patterns

- over the western North Pacific. *Meteor. Atmos. Phys.*, **128**, 491–511, <https://doi.org/10.1007/s00703-015-0428-7>.
- Chan, J. C. L., J. E. Shi, and K. S. Liu, 2001: Improvements in the seasonal forecasting of tropical cyclone activity over the western North Pacific. *Wea. Forecasting*, **16**, 491–498, [https://doi.org/10.1175/1520-0434\(2001\)016<0491:IITSFO>2.0.CO;2](https://doi.org/10.1175/1520-0434(2001)016<0491:IITSFO>2.0.CO;2).
- Chen, X., Y. Wang, J. Fang, and M. Xue, 2018: A numerical study on rapid intensification of Typhoon Vicente (2012) in the South China Sea. Part II: Roles of inner-core processes. *J. Atmos. Sci.*, **75**, 235–255, <https://doi.org/10.1175/JAS-D-17-0129.1>.
- , T. Zhou, P. Wu, Z. Guo, and M. Wang, 2020: Emergent constraints on future projections of the western North Pacific subtropical high. *Nat. Commun.*, **11**, 2802, <https://doi.org/10.1038/s41467-020-16631-9>.
- Choi, K.-S., Y. Cha, H.-D. Kim, and S.-D. Kang, 2016: Possible relationship between East Asian summer monsoon and western North Pacific tropical cyclone genesis frequency. *Theor. Appl. Climatol.*, **124**, 81–90, <https://doi.org/10.1007/s00704-015-1383-4>.
- Chu, Q.-C., Q.-G. Wang, and G.-L. Feng, 2017: Determination of the major moisture sources of cumulative effect of torrential rain events during the pre-flood season over South China using a Lagrangian particle model. *J. Geophys. Res. Atmos.*, **122**, 8369–8382, <https://doi.org/10.1002/2016JD026426>.
- Cloux, S., D. Garaboa-Paz, D. Insua-Costa, G. Míguez-Macho, and V. Pérez-Muñuzuri, 2021: Extreme precipitation events in the Mediterranean area: Contrasting Lagrangian and Eulerian models for moisture sources identification. *Hydrol. Earth Syst. Sci.*, **25**, 6465–6477, <https://doi.org/10.5194/hess-25-6465-2021>.
- Coll-Hidalgo, P., A. Pérez-Alarcón, and L. Gimeno, 2022a: Origin of moisture for the precipitation produced by the exceptional winter storm formed over the Gulf of Mexico in March 1993. *Atmosphere*, **13**, 1154, <https://doi.org/10.3390/atmos13071154>.
- , —, and R. Nieto, 2022b: Moisture sources for the precipitation of tropical-like cyclones in the Mediterranean Sea: A case of study. *Atmosphere*, **13**, 1327, <https://doi.org/10.3390/atmos13081327>.
- Corporal-Lodangco, I. L., M. B. Richman, L. M. Leslie, and P. J. Lamb, 2014: Cluster analysis of North Atlantic tropical cyclones. *Procedia Comput. Sci.*, **36**, 293–300, <https://doi.org/10.1016/j.procs.2014.09.096>.
- Dee, D. P., and Coauthors, 2011: The ERA-Interim reanalysis: Configuration and performance of the data assimilation system. *Quart. J. Roy. Meteor. Soc.*, **137**, 553–597, <https://doi.org/10.1002/qj.828>.
- de Szoeké, S. P., and S. Xie, 2008: The tropical eastern Pacific seasonal cycle: Assessment of errors and mechanisms in IPCC AR4 coupled ocean–atmosphere general circulation models. *J. Climate*, **21**, 2573–2590, <https://doi.org/10.1175/2007JCLI1975.1>.
- Dominguez, C., and V. Magaña, 2018: The role of tropical cyclones in precipitation over the tropical and subtropical North America. *Front. Earth Sci.*, **6**, 19, <https://doi.org/10.3389/feart.2018.00019>.
- Elsberry, R. L., 2004: Monsoon-related tropical cyclones in East Asia. *East Asian Monsoon*, C.-P. Chang, Ed., World Scientific, 463–498, https://doi.org/10.1142/9789812701411_0013.
- Emanuel, K. A. 2004: Tropical cyclone energetics and structure. *Atmospheric Turbulence and Mesoscale Meteorology*, E. Fedorovich, R. Rotunno, and B. Stevens, Eds., Cambridge University Press, 165–192.
- , and M. Živković-Rothman, 1999: Development and evaluation of a convection scheme for use in climate models. *J. Atmos. Sci.*, **56**, 1766–1782, [https://doi.org/10.1175/1520-0469\(1999\)056<1766:DAEOAC>2.0.CO;2](https://doi.org/10.1175/1520-0469(1999)056<1766:DAEOAC>2.0.CO;2).
- Fahad, A. A., N. J. Burls, E. T. Swenson, and D. M. Straus, 2021: The influence of South Pacific convergence zone heating on the South Pacific subtropical anticyclone. *J. Climate*, **34**, 3787–3798, <https://doi.org/10.1175/JCLI-D-20-0509.1>.
- Feng, X., and S. Shu, 2018: How do weak tropical cyclones produce heavy rainfall when making landfall over China? *J. Geophys. Res. Atmos.*, **123**, 11 830–11 848, <https://doi.org/10.1029/2018JD029228>.
- , and L. Wu, 2021: Roles of interdecadal variability of the western North Pacific monsoon trough in shifting tropical cyclone formation. *Climate Dyn.*, **58**, 87–95, <https://doi.org/10.1007/s00382-021-05891-w>.
- Fremme, A., and H. Sodemann, 2019: The role of land and ocean evaporation on the variability of precipitation in the Yangtze River valley. *Hydrol. Earth Syst. Sci.*, **23**, 2525–2540, <https://doi.org/10.5194/hess-23-2525-2019>.
- Fritz, C., and Z. Wang, 2014: Water vapor budget in a developing tropical cyclone and its implication for tropical cyclone formation. *J. Atmos. Sci.*, **71**, 4321–4332, <https://doi.org/10.1175/JAS-D-13-0378.1>.
- Fu, D., P. Chang, C. M. Patricola, R. Saravanan, X. Liu, and H. E. Beck, 2021: Central American mountains inhibit eastern North Pacific seasonal tropical cyclone activity. *Nat. Commun.*, **12**, 4422, <https://doi.org/10.1038/s41467-021-24657-w>.
- Fudeyasu, H., R. Yoshida, M. Yamaguchi, H. Eito, C. Muroi, S. Nishimura, and Coauthors, 2020: Development conditions for tropical storms over the western North Pacific stratified by large-scale flow patterns. *J. Meteor. Soc. Japan*, **98**, 61–72, <https://doi.org/10.2151/jmsj.2020-004>.
- Fujiwara, K., R. Kawamura, H. Hirata, T. Kawano, M. Kato, and T. Shinoda, 2017: A positive feedback process between tropical cyclone intensity and the moisture conveyor belt assessed with Lagrangian diagnostics. *J. Geophys. Res. Atmos.*, **122**, 12 502–12 512, <https://doi.org/10.1002/2017JD027557>.
- Gallego, D., R. García-Herrera, F. D. P. Gómez-Delgado, P. Ordoñez-Pérez, and P. Ribera, 2019: Tracking the moisture transport from the Pacific towards central and northern South America since the late 19th century. *Earth Syst. Dyn.*, **10**, 319–331, <https://doi.org/10.5194/esd-10-319-2019>.
- Gao, S., L. Zhu, W. Zhang, and X. Shen, 2020: Western North Pacific tropical cyclone activity in 2018: A season of extremes. *Sci. Rep.*, **10**, 5610, <https://doi.org/10.1038/s41598-020-62632-5>.
- , J. Mao, W. Zhang, F. Zhang, and X. Shen, 2021: Atmospheric moisture shapes increasing tropical cyclone precipitation in southern China over the past four decades. *Environ. Res. Lett.*, **16**, 034004, <https://doi.org/10.1088/1748-9326/abd78a>.
- Gimeno, L., and Coauthors, 2012: Oceanic and terrestrial sources of continental precipitation. *Rev. Geophys.*, **50**, RG4003, <https://doi.org/10.1029/2012RG000389>.
- , and Coauthors, 2020: Recent progress on the sources of continental precipitation as revealed by moisture transport analysis. *Earth-Sci. Rev.*, **201**, 103070, <https://doi.org/10.1016/j.earscirev.2019.103070>.
- , and Coauthors, 2021: The residence time of water vapour in the atmosphere. *Nat. Rev. Earth Environ.*, **2**, 558–569, <https://doi.org/10.1038/s43017-021-00181-9>.
- Goessling, H. F., and C. H. Reick, 2013: On the “well-mixed” assumption and numerical 2-D tracing of atmospheric moisture.

- Atmos. Chem. Phys.*, **13**, 5567–5585, <https://doi.org/10.5194/acp-13-5567-2013>.
- Gozzo, L. F., R. P. da Rocha, L. Gimeno, and A. Drumond, 2017: Climatology and numerical case study of moisture sources associated with subtropical cyclogenesis over the southwestern Atlantic Ocean. *J. Geophys. Res. Atmos.*, **122**, 5636–5653, <https://doi.org/10.1002/2016JD025764>.
- Gray, W. M., 1968: Global view of the origin of tropical disturbances and storms. *Mon. Wea. Rev.*, **96**, 669–700, [https://doi.org/10.1175/1520-0493\(1968\)096<0669:GVOTOO>2.0.CO;2](https://doi.org/10.1175/1520-0493(1968)096<0669:GVOTOO>2.0.CO;2).
- Guo, L., N. P. Klingaman, P. L. Vidale, A. G. Turner, M.-E. Demory, and A. Cobb, 2017: Contribution of tropical cyclones to atmospheric moisture transport and rainfall over East Asia. *J. Climate*, **30**, 3853–3865, <https://doi.org/10.1175/JCLI-D-16-0308.1>.
- Harper, B. A., J. D. Kepert, and J. D. Ginger, 2010: Guidelines for converting between various wind averaging periods in tropical cyclone conditions. WMO/TD 1555, 54 pp., https://library.wmo.int/doc_num.php?explnum_id=290.
- Harvey, T., J. A. Renwick, A. M. Lorrey, and A. Ngari, 2019: The representation of the South Pacific convergence zone in the Twentieth Century Reanalysis. *Mon. Wea. Rev.*, **147**, 841–851, <https://doi.org/10.1175/MWR-D-18-0237.1>.
- Hastenrath, S., 2002: The intertropical convergence zone of the eastern Pacific revisited. *Int. J. Climatol.*, **22**, 347–356, <https://doi.org/10.1002/joc.739>.
- Hill, K. A., and G. M. Lackmann, 2009: Influence of environmental humidity on tropical cyclone size. *Mon. Wea. Rev.*, **137**, 3294–3315, <https://doi.org/10.1175/2009MWR2679.1>.
- Hodges, K., A. Cobb, and P. L. Vidale, 2017: How well are tropical cyclones represented in reanalysis datasets? *J. Climate*, **30**, 5243–5264, <https://doi.org/10.1175/JCLI-D-16-0557.1>.
- Hordon, R. M., 2005: Pacific (Hawaiian) high. *Encyclopedia of World Climatology*. J. E. Oliver, Ed., Springer, 562–563, https://doi.org/10.1007/1-4020-3266-8_156.
- Hu, Q., D. Jiang, X. Lang, and S. Yao, 2021: Moisture sources of summer precipitation over eastern China during 1979–2009: A Lagrangian transient simulation. *Int. J. Climatol.*, **41**, 1162–1178, <https://doi.org/10.1002/joc.6781>.
- Huang, H.-L., M.-J. Yang, and C.-H. Sui, 2014: Water budget and precipitation efficiency of Typhoon Morakot (2009). *J. Atmos. Sci.*, **71**, 112–129, <https://doi.org/10.1175/JAS-D-13-053.1>.
- Jiang, H., and E. J. Zipser, 2010: Contribution to the global precipitation from eight seasons of TRMM data: Regional, seasonal, and interannual variations. *J. Climate*, **23**, 1526–1543, <https://doi.org/10.1175/2009JCLI3303.1>.
- Kaplan, J., and M. DeMaria, 2003: Large-scale characteristics of rapidly intensifying tropical cyclones in the North Atlantic basin. *Wea. Forecasting*, **18**, 1093–1108, [https://doi.org/10.1175/1520-0434\(2003\)018<1093:LCORIT>2.0.CO;2](https://doi.org/10.1175/1520-0434(2003)018<1093:LCORIT>2.0.CO;2).
- Khouakhi, A., G. Villarini, and G. A. Vecchi, 2017: Contribution of tropical cyclones to rainfall at the global scale. *J. Climate*, **30**, 359–372, <https://doi.org/10.1175/JCLI-D-16-0298.1>.
- Kimball, S. K., and M. S. Mulekar, 2004: A 15-year climatology of North Atlantic tropical cyclones. Part I: Size parameters. *J. Climate*, **17**, 3555–3575, [https://doi.org/10.1175/1520-0442\(2004\)017<3555:AYCONA>2.0.CO;2](https://doi.org/10.1175/1520-0442(2004)017<3555:AYCONA>2.0.CO;2).
- Knaff, J. A., S. P. Longmore, and D. A. Molenar, 2014: An objective satellite-based tropical cyclone size climatology. *J. Climate*, **27**, 455–476, <https://doi.org/10.1175/JCLI-D-13-00096.1>.
- Kossin, J. P., T. L. Olander, and K. R. Knapp, 2013: Trend analysis with a new global record of tropical cyclone intensity. *J. Climate*, **26**, 9960–9976, <https://doi.org/10.1175/JCLI-D-13-00262.1>.
- Kudo, T., R. Kawamura, H. Hirata, K. Ichianagi, M. Tanoue, and K. Yoshimura, 2014: Large-scale vapor transport of remotely evaporated sea water by a Rossby wave response to typhoon forcing during the Baiu/Meiyu season as revealed by the JRA-55 reanalysis. *J. Geophys. Res. Atmos.*, **119**, 8825–8838, <https://doi.org/10.1002/2014JD021999>.
- Läderach, A., and H. Sodemann, 2016: A revised picture of the atmospheric moisture residence time. *Geophys. Res. Lett.*, **43**, 924–933, <https://doi.org/10.1002/2015GL067449>.
- MacQueen, J., 1967: Some methods for classification and analysis of multivariate observations. *Proc. Fifth Berkeley Symp. on Mathematical Statistics and Probability*, Berkeley, CA, University of California, 281–297, <http://www.cs.cmu.edu/~bhiksha/courses/mlsp.fall2010/class14/macqueen.pdf>.
- Marshall, J., A. Donohoe, D. Ferreira, and D. McGee, 2014: The ocean's role in setting the mean position of the inter-tropical convergence zone. *Climate Dyn.*, **42**, 1967–1979, <https://doi.org/10.1007/s00382-013-1767-z>.
- Molinari, J., and D. Vollaro, 2013: What percentage of western North Pacific tropical cyclones form within the monsoon trough? *Mon. Wea. Rev.*, **141**, 499–505, <https://doi.org/10.1175/MWR-D-12-00165.1>.
- Morissette, L., and S. Chartier, 2013: The *k*-means clustering technique: General considerations and implementation in *Mathematica*. *Tutorials Quant. Methods Psychol.*, **9**, 15–24, <https://doi.org/10.20982/tqmp.09.1.p015>.
- Ng, B., K. Walsh, and S. Lavender, 2014: The contribution of tropical cyclones to rainfall in northwest Australia. *Int. J. Climatol.*, **35**, 2689–2697, <https://doi.org/10.1002/joc.4148>.
- Niznik, M., B. R. Lintner, A. J. Matthews, and M. J. Widlansky, 2015: The role of tropical–extratropical interaction and synoptic variability in maintaining the South Pacific convergence zone in CMIP5 models. *J. Climate*, **28**, 3353–3374, <https://doi.org/10.1175/JCLI-D-14-00527.1>.
- Numaguti, A., 1999: Origin and recycling processes of precipitating water over the Eurasian continent: Experiments using an atmospheric general circulation model. *J. Geophys. Res.*, **104**, 1957–1972, <https://doi.org/10.1029/1998JD200026>.
- Papritz, L., F. Aemisegger, and H. Wernli, 2021: Sources and transport pathways of precipitating waters in cold-season deep North Atlantic cyclones. *J. Atmos. Sci.*, **78**, 3349–3368, <https://doi.org/10.1175/JAS-D-21-0105.1>.
- Pérez-Alarcón, A., R. Sorí, J. C. Fernández-Alvarez, R. Nieto, and L. Gimeno, 2021a: Comparative climatology of outer tropical cyclone size using radial wind profiles. *Wea. Climate Extremes*, **33**, 100366, <https://doi.org/10.1016/j.wace.2021.100366>.
- , J. C. Fernández-Alvarez, R. Sorí, R. Nieto, and L. Gimeno, 2021b: The combined effects of SST and the North Atlantic subtropical high-pressure system on the Atlantic basin tropical cyclone interannual variability. *Atmosphere*, **12**, 329, <https://doi.org/10.3390/atmos12030329>.
- , R. Sorí, J. C. Fernández-Alvarez, R. Nieto, and L. Gimeno, 2022a: Where does the moisture for North Atlantic tropical cyclones come from? *J. Hydrometeorol.*, **23**, 457–472, <https://doi.org/10.1175/JHM-D-21-0117.1>.
- , P. Coll-Hidalgo, J. C. Fernández-Alvarez, R. Sorí, R. Nieto, and L. Gimeno, 2022b: Moisture sources for precipitation associated with major hurricanes during 2017 in the North Atlantic basin. *J. Geophys. Res. Atmos.*, **127**, e2021JD035554, <https://doi.org/10.1029/2021JD035554>.

- , R. Sorí, J. C. Fernández-Alvarez, R. Nieto, and L. Gimeno, 2022c: Dataset of outer tropical cyclone size from a radial wind profile. *Data Brief*, **40**, 107825, <https://doi.org/10.1016/j.dib.2022.107825>.
- , J. C. Fernández-Alvarez, R. Sorí, R. Nieto, and L. Gimeno, 2022d: Moisture source identification for precipitation associated with tropical cyclone development over the Indian Ocean: A Lagrangian approach. *Climate Dyn.*, <https://doi.org/10.1007/s00382-022-06429-4>, in press.
- Pisso, I., and Coauthors, 2019: The Lagrangian particle dispersion model FLEXPART version 10.4. *Geosci. Model Dev.*, **12**, 4955–4997, <https://doi.org/10.5194/gmd-12-4955-2019>.
- Pottapinjara, V., M. S. Girishkumar, R. Murtugudde, K. Ashok, and M. Ravichandran, 2019: On the relation between the boreal spring position of the Atlantic intertropical convergence zone and Atlantic zonal mode. *J. Climate*, **32**, 4767–4781, <https://doi.org/10.1175/JCLI-D-18-0614.1>.
- Qiu, W., F. Ren, L. Wu, L. Chen, and C. Ding, 2019: Characteristics of tropical cyclone extreme precipitation and its preliminary causes in Southeast China. *Meteor. Atmos. Phys.*, **131**, 613–626, <https://doi.org/10.1007/s00703-018-0594-5>.
- Ramos, A. M., R. Nieto, R. Tomé, L. Gimeno, R. M. Trigo, M. L. R. Liberato, and D. A. Lavers, 2016: Atmospheric rivers moisture sources from a Lagrangian perspective. *Earth Syst. Dyn.*, **7**, 371–384, <https://doi.org/10.5194/esd-7-371-2016>.
- Rotunno, R., and K. Emanuel, 1987: An air–sea interaction theory for tropical cyclones. Part II: Evolutionary study using a non-hydrostatic axisymmetric numerical model. *J. Atmos. Sci.*, **44**, 542–561, [https://doi.org/10.1175/1520-0469\(1987\)044<0542:AAITFT>2.0.CO;2](https://doi.org/10.1175/1520-0469(1987)044<0542:AAITFT>2.0.CO;2).
- Schreck, C. J., III, 2016: Convectively coupled Kelvin waves and tropical cyclogenesis in a semi-Lagrangian framework. *Mon. Wea. Rev.*, **144**, 4131–4139, <https://doi.org/10.1175/MWR-D-16-0237.1>.
- Sodemann, H., 2020: Beyond turnover time: Constraining the lifetime distribution of water vapor from simple and complex approaches. *J. Atmos. Sci.*, **77**, 413–433, <https://doi.org/10.1175/JAS-D-18-0336.1>.
- , C. Schwierz, and H. Wernli, 2008: Interannual variability of Greenland winter precipitation sources: Lagrangian moisture diagnostic and North Atlantic oscillation influence. *J. Geophys. Res.*, **113**, D03107, <https://doi.org/10.1029/2007JD008503>.
- Stohl, A., and P. A. James, 2004: Lagrangian analysis of the atmospheric branch of the global water cycle. Part I: Method description, validation, and demonstration for the August 2002 flooding in central Europe. *J. Hydrometeorol.*, **5**, 656–678, [https://doi.org/10.1175/1525-7541\(2004\)005<0656:ALAOTA>2.0.CO;2](https://doi.org/10.1175/1525-7541(2004)005<0656:ALAOTA>2.0.CO;2).
- , and —, 2005: A Lagrangian analysis of the atmospheric branch of the global water cycle: Part II: Earth's river catchments ocean basins, and moisture transports between them. *J. Hydrometeorol.*, **6**, 961–984, <https://doi.org/10.1175/JHM470.1>.
- , C. Forster, A. Frank, P. Seibert, and G. Wotawa, 2005: Technical note: The Lagrangian particle dispersion model FLEXPART version 6.2. *Atmos. Chem. Phys.*, **5**, 2461–2474, <https://doi.org/10.5194/acp-5-2461-2005>.
- Takahashi, K., and D. S. Battisti, 2007: Processes controlling the mean tropical Pacific precipitation pattern. Part I: The Andes and the eastern Pacific ITCZ. *J. Climate*, **20**, 3434–3451, <https://doi.org/10.1175/JCLI4198.1>.
- Tuleya, R. E., 1994: Tropical storm development and decay: Sensitivity to surface boundary conditions. *Mon. Wea. Rev.*, **122**, 291–304, [https://doi.org/10.1175/1520-0493\(1994\)122<0291:TSDADS>2.0.CO;2](https://doi.org/10.1175/1520-0493(1994)122<0291:TSDADS>2.0.CO;2).
- van der Ent, R. J., and O. A. Tuinenburg, 2017: The residence time of water in the atmosphere revisited. *Hydrol. Earth Syst. Sci.*, **21**, 779–790, <https://doi.org/10.5194/hess-21-779-2017>.
- Vecchi, G. A., and T. R. Knutson, 2008: On estimates of historical North Atlantic tropical cyclone activity. *J. Climate*, **21**, 3580–3600, <https://doi.org/10.1175/2008JCLI2178.1>.
- Vincent, E. M., M. Lengaigne, C. E. Menkes, N. C. Jourdain, P. Marchesiello, and G. Madec, 2011: Interannual variability of the South Pacific convergence zone and implications for tropical cyclone genesis. *Climate Dyn.*, **36**, 1881–1896, <https://doi.org/10.1007/s00382-009-0716-3>.
- Wang, Y., and C. J. Matyas, 2022: Simulating the effects of land surface characteristics on planetary boundary layer parameters for a modeled landfalling tropical cyclone. *Atmosphere*, **13**, 138, <https://doi.org/10.3390/atmos13010138>.
- Wang, Z., and I. Hankes, 2016: Moisture and precipitation evolution during tropical cyclone formation as revealed by the SSM/I–SSMIS retrievals. *J. Atmos. Sci.*, **73**, 2773–2781, <https://doi.org/10.1175/JAS-D-15-0306.1>.
- Willoughby, H. E., R. W. R. Darling, and M. Rahn, 2006: Parametric representation of the primary hurricane vortex. Part II: A new family of sectionally continuous profiles. *Mon. Wea. Rev.*, **134**, 1102–1120, <https://doi.org/10.1175/MWR3106.1>.
- Winschall, A., S. Pfahl, H. Sodemann, and H. Wernli, 2014: Comparison of Eulerian and Lagrangian moisture source diagnostics—The flood event in eastern Europe in May 2010. *Atmos. Chem. Phys.*, **14**, 6605–6619, <https://doi.org/10.5194/acp-14-6605-2014>.
- Wu, L., H. Su, R. G. Fovell, T. J. Dunkerton, Z. Wang, and B. H. Kahn, 2015: Impact of environmental moisture on tropical cyclone intensification. *Atmos. Chem. Phys.*, **15**, 14041–14053, <https://doi.org/10.5194/acp-15-14041-2015>.
- Wu, W., and J.-L. Chen, 2012: Sensitivity of tropical cyclone precipitation to atmospheric moisture content: Case study of Bilis (2006). *Atmos. Oceanic Sci. Lett.*, **5**, 420–425, <https://doi.org/10.1080/16742834.2012.11447030>.
- , J. Chen, and R. Huang, 2013: Water budgets of tropical cyclones: Three case studies. *Adv. Atmos. Sci.*, **30**, 468–484, <https://doi.org/10.1007/s00376-012-2050-7>.
- Xin, F., D. Peng, R. Liu, and S. C. Liu, 2022: Moisture sources for the weather pattern classified extreme precipitation in the first rainy season over South China. *Int. J. Climatol.*, **42**, 6027–6041, <https://doi.org/10.1002/joc.7576>.
- Xu, G., T. J. Osborn, and A. J. Matthews, 2017: Moisture transport by Atlantic tropical cyclones onto the North American continent. *Climate Dyn.*, **48**, 3161–3182, <https://doi.org/10.1007/s00382-016-3257-6>.
- Yang, M.-J., S. A. Braun, and D. S. Chen, 2011: Water budget of Typhoon Nari (2001). *Mon. Wea. Rev.*, **139**, 3809–3828, <https://doi.org/10.1175/MWR-D-10-05090.1>.
- Yoshida, R., Y. Miyamoto, H. Tomita, and Y. Kajikawa, 2017: The effect of water vapor on tropical cyclone genesis: A numerical experiment of a non-developing disturbance observed in PALAU2010. *J. Meteor. Soc. Japan*, **95**, 35–47, <https://doi.org/10.2151/jmsj.2017-001>.
- Yu, J., Y. Zheng, Q. Wu, J. Lin, and Z. Gong, 2016: K-means clustering for classification of the northwestern Pacific tropical cyclone tracks. *J. Trop. Meteorol.*, **22**, 127–135, <https://doi.org/10.16555/j.1006-8775.2016.02.003>.
- Yu, Z., Y. Wang, H. Xu, N. Davidson, Y. Chen, Y. Chen, and H. Yu, 2017: On the relationship between intensity and rainfall

- distribution in tropical cyclones making landfall over China. *J. Appl. Meteor. Climatol.*, **56**, 2883–2901, <https://doi.org/10.1175/JAMC-D-16-0334.1>.
- Zhan, R., Y. Wang, and M. Ying, 2012: Seasonal forecasts of tropical cyclone activity over the western North Pacific: A review. *Trop. Cyclone Res. Rev.*, **3**, 307–324, <https://doi.org/10.6057/2012TCRR03.07>.
- Zhang, D., J. Zhang, L. Shi, and F. Yao, 2020: Interdecadal changes of characteristics of tropical cyclone rapid intensification over Western North Pacific. *IEEE Access*, **8**, 15 781–15 791, <https://doi.org/10.1109/ACCESS.2020.2965976>.
- Zhang, W., Y. Leung, and Y. Wang, 2013: Cluster analysis of post-landfall tracks of landfalling tropical cyclones over China. *Climate Dyn.*, **40**, 1237–1255, <https://doi.org/10.1007/s00382-012-1519-5>.
- Zhao, H., and G. B. Raga, 2015: On the distinct interannual variability of tropical cyclone activity over the eastern North Pacific. *Atmósfera*, **28**, 161–178, <https://doi.org/10.20937/ATM.2015.28.03.02>.
- Zong, H., and L. Wu, 2015: Synoptic-scale influences on tropical cyclone formation within the western North Pacific monsoon trough. *Mon. Wea. Rev.*, **143**, 3421–3433, <https://doi.org/10.1175/MWR-D-14-00321.1>.

4.7 Estimation of mean water vapour residence time during tropical cyclones using a Lagrangian approach

Pérez-Alarcón, A., Coll-Hidalgo, P., Fernández-Alvarez, J.C., Nieto, R., Gimeno, L., 2022. Estimation of mean water vapour residence time during tropical cyclones using a Lagrangian approach. *Tropical Cyclone Research and Review* 11(2), 76–87. doi: 10.1016/j.tcr.2022.08.001

Table 4.7: Summary of the impact and quality of the journal where the sixth paper that conformed to this thesis was published. The data correspond to the year 2021 (last year available at the date of preparation of this document) in the Web of Science (JCR). **IF:** Impact Factor

Journal	Description	Journal Metrics
Tropical Cyclone Research and Review	It is an international journal, focusing on tropical cyclone monitoring, forecasting, research and its associated hydrological effects and disaster risk reduction.	IF: -, 5-year IF: - Ranking: 79 out of 108 (Q3) in Meteorology & Atmospheric Sciences



ESCAP/WMO
Typhoon Committee

Available online at www.sciencedirect.com

ScienceDirect

Tropical Cyclone Research and Review 11 (2022) 76–87



www.keaipublishing.com/tcrr

Estimation of mean water vapour residence time during tropical cyclones using a Lagrangian approach

Albenis Pérez-Alarcón^{a,b,*}, Patricia Coll-Hidalgo^{a,c}, José C. Fernández-Alvarez^{a,b}, Raquel Nieto^a, Luis Gimeno^a

^aCentro de Investigación Mariña, Universidade de Vigo, Environmental Physics Laboratory (EPhysLab), Ourense, Spain

^bDepartamento de Meteorología, Instituto Superior de Tecnologías y Ciencias Aplicadas, Universidad de La Habana, La Habana, Cuba

^cDepartamento de Meteorología, Empresa Cubana de Navegación Aérea, La Habana, Cuba

Available online 13 August 2022

Abstract

Tropical cyclone (TC)-related rainfall mostly depends on the atmospheric moisture uptake from local and remote sources. In this study, the mean water vapour residence time (MWVRT) was computed for precipitation related to TCs in each basin and on a global scale by applying a Lagrangian moisture source diagnostic method. According to our results, the highest MWVRT was found for the TCs over the South Indian Ocean and South Pacific Ocean basins (~3.08 days), followed by the Western North Pacific Ocean, Central and East North Pacific Ocean, North Indian Ocean, and North Atlantic Ocean basins (which exhibited values of 2.98, 2.94, 2.85, and 2.72 days, respectively). We also found a statistically significant ($p < 0.05$) decrease in MWVRT, at a rate of ~2.4 h/decade in the North Indian Ocean and ~1.0 h/decade in the remaining basins. On average, the MWVRT decreased during the 24 h before TCs made landfall, and the atmospheric parcels precipitated faster after evaporation when TCs moved over land than over the ocean. Further research should focus on the relationship between global warming and MWVRT of atmospheric parcels that precipitate over TC positions.

© 2022 The Shanghai Typhoon Institute of China Meteorological Administration. Publishing services by Elsevier B.V. on behalf of KeAi Communication Co. Ltd. This is an open access article under the CC BY-NC-ND license (<http://creativecommons.org/licenses/by-nc-nd/4.0/>).

Keywords: Tropical cyclones; Water vapour residence time; Lagrangian approach; Tropical cyclones precipitation

1. Introduction

Heavy precipitation related to tropical cyclones (TCs), which commonly cause flash flooding, landslide events, and economic and life losses, is one of the most significant impacts of TCs in coastal regions of tropical and subtropical latitudes

(Rogers et al., 2009; Willoughby, 2012; Rappaport, 2014). Despite its negative effects, authors have shown the positive role of precipitation associated with TCs in attenuating drought episodes (e.g. Maxwell et al., 2012; Brun and Barros, 2014). Other research findings (Jiang and Zipser, 2010; Xu et al., 2017) have revealed that the contribution of TCs to annual rainfall totals ranged from 3% to 19%. More recently, Guzman and Jiang (2021) found an increasing trend of ~1.3% per year in the average TC rainfall rate.

In general, TC-related precipitation depends on atmospheric moisture availability (Guo et al., 2017; Xu et al., 2017) and moisture transport mechanisms (Schumacher and Galarneau, 2012). Studies have concluded that the moisture transported by these systems is crucial for the water budget over East Asia (Guo et al., 2017) or the North American continent (Xu et al., 2017). More recently, Pérez-Alarcón et al. (2021a, 2022a)

* Corresponding author. Centro de Investigación Mariña, Universidade de Vigo, Environmental Physics Laboratory (EPhysLab), Campus As Lagoas s/n, Ourense, 32004, Spain.

E-mail address: albenis.perez.alarcon@uvigo.es (A. Pérez-Alarcón).

Peer review under responsibility of Shanghai Typhoon Institute of China Meteorological Administration.



Production and hosting by Elsevier on behalf of KeAi

<https://doi.org/10.1016/j.tcrr.2022.08.001>

2225-6032/© 2022 The Shanghai Typhoon Institute of China Meteorological Administration. Publishing services by Elsevier B.V. on behalf of KeAi Communication Co. Ltd. This is an open access article under the CC BY-NC-ND license (<http://creativecommons.org/licenses/by-nc-nd/4.0/>).

measured the origin of moisture for TC-related precipitation during their lifetime along the North Atlantic basin.

Moisture transport mechanisms were strongly modulated by the mean water vapour residence time (MWVRT). This water vapour lifetime is defined as the time that moisture spends in the atmosphere between evaporation and precipitation (Läderach and Sodemann, 2016; Sodemann 2020). Because MWVRT cannot be calculated directly, indirect metrics have been developed to estimate it (Gimeno et al., 2021). One of these indirect metrics is based on the size of the atmospheric reservoir divided by the incoming or outgoing flux (Savenije, 2000); according to this method, MWVRT ranges from 8 to 10 days. Likewise, Trenberth (1998) found a global MWVRT of 8.9 days by applying local depletion times (the rate of water in the atmospheric column and precipitation). Moisture tracking models have been used to estimate it reaching different results. Bosilovich and Schubert (2002) and Yoshimura et al. (2004) have estimated that the MWVRT varies from 7.3 to 9.2 days, a range confirmed as reasonable by Van der Ent and Tuinenburg (2017), who found values of 8–10 days; however, theirs were lower those of Läderach and Sodemann (2016), with an MWVRT of 4–5 days. More recently, Sodemann (2020) concluded that the MWVRT distribution is highly skewed. These discrepancies in MWVRT estimations were mainly caused by the use of different definitions. Gimeno et al. (2021) reconciled these differences by framing MWVRT as a probability density function with a mean of 8–10 days and a median of 4–5 days.

Nevertheless, these studies have generally focused on a global scale and considered the worldwide mechanism of moisture transport and all the weather systems, which have several different lifetimes. This fact was revealed when a particular weather system is analysed separately from the others. For instance, for extratropical cyclones Papritz et al. (2021) found an MWVRT of ~2 days, and for TCs in the North Atlantic Pérez-Alarcón et al. (2022a) showed values from 2.6 to 2.9 days.

Gedzelman et al. (2003) linked the stable isotope ratios of rain and water vapour to the water budget of hurricanes. Based on all the aforementioned evidence, our aim in this study was to estimate the MWVRT for precipitant water vapour during the complete TC lifetime in each oceanic basin of the planet by applying a Lagrangian moisture source diagnostic method. Additionally, an MWVRT interbasin comparison was performed to advance the knowledge of TC climatology.

2. Materials and methods

2.1. Data

The TC historical records (best track archives) over the worldwide oceanic basins were provided by two United States' agencies: the National Hurricane Center (NHC) Atlantic hurricane database (HURDAT2) (Landsea and Franklin, 2013) for the North Atlantic (NATL) and North East Pacific (NEPAC) basins, and the Joint Typhoon Warning Center (JTWC) for the remaining basins. Both agencies guarantee the homogeneity of

the estimation methods of the TC parameters recorded in the best track records.

The TC size database (TCSize) developed by Pérez-Alarcón et al. (2021b, 2022b) was used to delimit the area inside a TC's outer radius, which is necessary to apply the Lagrangian moisture sources diagnostic method to compute the MWVRT. The study period was set from 1980 to 2018.

The ERA-Interim reanalysis dataset (Dee et al., 2011) from the European Center for Medium Range Weather Forecasting (ECMWF) at 61 vertical levels and 1°×1 horizontal grid spacing, was used as input data to run the FLEXPART model (Stohl et al., 2005). We used the trajectories of atmospheric parcels from a global FLEXPART experiment, in which the atmosphere was uniformly divided into ~2 million parcels of equal mass every 6 h, which moved with time through a three-dimensional wind field, to determine the moisture sources associated with TC-related precipitation and therefore the MWVRT. Similar experiments with different aims have been performed (Sori et al., 2017; Ciric et al., 2018; Nieto and Gimeno, 2019; Gimeno et al., 2020; Algarra et al., 2020, Pérez-Alarcón et al., 2022a, c).

2.2. Lagrangian MWVRT estimate

To compute the MWVRT of parcels that precipitated over the TC's location (defined by TCSize), we selected those in which the specific humidity decreased more than 0.1 g/kg in the 6 h before arrival at the target area (using the methodology of Läderach and Sodemann (2016)). To identify where air atmospheric parcels gain or lose moisture along their trajectories, we followed them backward in time for up to 10 days by applying the moisture source diagnostic method developed by Sodemann et al. (2008).

An atmospheric parcel can gain or lose a specific humidity (q) along its trajectory through evaporation (e) or precipitation (p), as defined by the Lagrangian water budget equation (Stohl and James, 2004; 2005):

$$(e - p) = m \left(\frac{dq}{dt} \right) \quad (1)$$

where m is the parcel mass. The used of the specific humidity in Eq. (1) allow to estimate the moisture changes in air parcel three dimensionally. The specific humidity change between time t and time t_{-6} is assigned to time t according to Eq. (2):

$$\Delta q(t) = q(x(t)) - q(x(t-6)) \quad (2)$$

where $x(t)$ denotes the parcel position at time t . Based on the objective selection criteria, a moisture uptake event was identified along a trajectory if a moisture increase occurred ($\Delta q > 0$), but the parcel can also undergo moisture loss ($\Delta q < 0$). Because of the precipitation *en route*, previous moisture uptake from evaporative locations contributed less and less to the precipitation over the target area (Sodemann et al., 2008). Notably, from the end to the start point, the precipitation *en route* was discounted from all previous

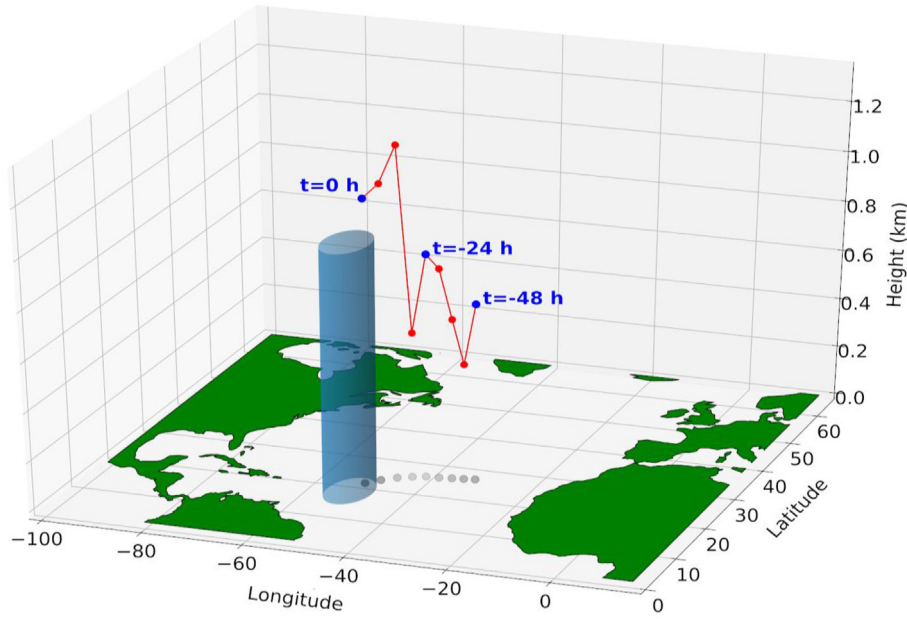


Fig. 1. Three-dimensional schematic representation of the atmospheric particle trajectory of 48 h. Red dots denote the particle position at each time step, grey dots represent the red dot projections over the surface, and the target area is indicated by the blue cylinder.

moisture uptakes in proportion to the precipitation amount, according to Eq. (3):

$$\Delta q'_j = \Delta q_j + \Delta q_i \frac{\Delta q_j}{\sum_{k=i_{end}}^{i-6} \Delta q_k} \quad \text{for all } j > i \quad (3)$$

where Δq_i and $\Delta q'_j$ denote the precipitation losses at a precipitation location and the new moisture contribution from previous evaporative locations at times $j > i$, respectively. The fractional contribution (f_c) of each evaporative location at each time step to the final precipitation over the target area can be defined as

$$f_c = \frac{\Delta q'_i}{Q} \quad (4)$$

where Q denotes the moisture content of the atmospheric parcel before its arrival at the target area. Therefore, the water vapour residence time (WVRT) of each parcel was estimated by weighting the effective moisture contribution of each evaporation event to the final precipitation (Läderach and Sodemann, 2016), according to Eq. (5). MWVRT can be computed by averaging the water vapour residence time (WVRT) of all precipitant parcels over the target area.

$$WVRT = \sum_{k=i_{end}}^{i_0} t_k \cdot f_{C_k} \quad (5)$$

Fig. 1 shows a three-dimensional schematic representation of the trajectory of an atmospheric parcel with a length of 48 h. The supplementary information in Läderach and Sodemann (2016) provides a further explanation for this method. As an example, in Fig. 1, we present a detailed description of the

Table 1

Moisture source diagnostic for the particle trajectory in Fig. 1, where q (g/kg) is the specific humidity of the atmospheric particle; Δq (g/kg) is the moisture change between sequential time steps, according to Eq. (2); $\Delta q'_j$ (g/kg) is the new moisture contribution of each evaporative location after the discount in proportion the precipitation amount *en route*, according to Eq. (3); and f_c is the fraction of moisture contribution to the final precipitation over the target area.

Time	-48 h	-42 h	-36 h	-30 h	-24 h	-18 h	-12 h	-6 h
q	0.2	4.5	12.1	8.7	10.2	6.4	9.8	12.2
Δq	-	+4.3	+7.6	-3.4	+1.5	-3.8	+3.4	+2.4
$\Delta q'_{-36h}$	-	3.1	5.4	0	-	-	-	-
$\Delta q'_{-24h}$	-	3.1	5.4	0	1.5	-	-	-
$\Delta q'_{-18h}$	-	1.9	3.4	0	0.9	0	-	-
$\Delta q'_{-12h}$	-	1.9	3.4	0	0.9	0	3.4	-
$\Delta q'_{-06h}$	-	1.9	3.4	0	0.9	0	3.4	2.4
f_c	-	0.158	0.283	0	0.075	0	0.283	0.200

WVRT estimation based on the trajectory of a parcel. Table 1 lists the specific humidity values at each time step and their time-step changes. At the starting point of the trajectory, $t = -48$ h, the atmospheric parcel had a specific humidity value of $q = 0.2$ g/kg. During the two next time steps, q increases from -48 h to -42 h by $+4.3$ g/kg, and from -42 h to -36 h by $+7.6$ g/kg. Subsequently, precipitation occurred *en route* from -36 h to -30 h, losing -3.4 g/kg. According to the aforementioned Läderach and Sodemann (2016) diagnostic method, all previous moisture uptakes ($4.3 + 7.6 = 11.9$ g/kg) contributed to this precipitation. Therefore, by applying Eq. (3), the new contribution to the final precipitation at $t = -42$ h was $4.3 - 3.4 \times (4.3/11.9) = 3.1$ g/kg. Similarly, for -36 h, 5.4 g/kg was obtained. The parcel again gained $+1.5$ g/kg from -30 h to -24 h, and lost -3.8 g/kg from -24 h to -18 h. Consequently, the new contribution to the final precipitation at $t = -42$ h was $3.1 - 3.8 \times (3.1/10) = 1.9$ g/kg; at $t = -36$ h,

3.4 g/kg; and at $t = -24$ h, 0.9 g/kg. Finally, from -18 h to -12 h and from -12 h to -06 h, the parcel gained 3.4 g/kg and 2.4 g/kg of moisture, respectively.

The last row in Table 1 lists the fractional contributions (Eq. (4)). The WVRT for the final precipitation over the target area was estimated using Eq. (5), resulting in 23.22 h or ~ 0.97 days.

3. Results and discussion

Fig. 2 reveals notable inter-basin differences in the probability density function (PDF) of TCs trajectories. While TCs over NATL most frequently straight moved toward the Caribbean Sea and the Gulf of Mexico or crossed bordering the north portion of the Antilles islands and the eastern coast of the United States (Fig. 2a), TCs over the NEPAC often described a north-westward track close to the Mexican coast (Fig. 2b). The Bay of Bengal and the Arabian Sea are the home for TCs formed over NIO (Fig. 3c), although they most probably crossed over the former. The PDF of TCs trajectories over SIO exhibited a quasi-zonal maximum in the band between 10° – 20° S of latitude and a secondary maximum over the North Australian basin (Fig. 2d), while a zonal pattern was also observed over the Coral Sea in the SPO basin (Fig. 2e). TCs over WNP mainly moved from the western North Pacific to the Philippine Sea and South China Sea (Fig. 2f). Based on the PDFs shown in Fig. 2, TCs in NATL moved over a larger area than in any other basin. Overall, during the study period, WNP

recorded approximately 31% of the annual global average of TCs, followed by NEPAC ($\sim 20\%$), SIO ($\sim 17\%$), NATL ($\sim 16\%$), SPO ($\sim 11\%$) and NIO ($\sim 5\%$).

The Lagrangian moisture source diagnostic method for the trajectories of precipitant parcels over the TC locations applied in this study yielded relevant information on the WVRT. Fig. 3 shows the MWVRT for each TC basin. The South Indian Ocean (SIO) and South Pacific Ocean (SPO) basins exhibited the highest MWVRT, with 3.08 ± 0.4 days (uncertainty given as one standard deviation), followed by the Western North Pacific Ocean (WNP) (2.98 ± 0.4 days), NEPAC (2.94 ± 0.4 days), North Indian Ocean (NIO) (2.85 ± 0.4 days), and NATL (2.72 ± 0.4 days). From a global perspective, the MWVRT of atmospheric parcels that became in precipitation over TC locations was estimated to be 2.96 ± 0.4 days.

The MWVRT found in this study is three times lower than the widely used MWVRT of 8–10 days (Trenberth, 1998; Bosilovich and Schubert, 2002; Van der Ent and Tuinenburg, 2017); however, it is closer to, but also lower than, the global estimation of 3.9 ± 0.8 days by Läderach and Sodemann (2016). These studies in the literature were performed for all weather systems on a global scale, not for specific systems such as TCs, as in our case. Additionally, the MWVRT estimate of Läderach and Sodemann (2016) only reported the lifetime of water vapour within the boundary layer. Nevertheless, the circulation associated with evaporating downdraft motion in tropical clouds, and thus in TC clouds (Gray, 2012), transports the colder and drier air from the upper levels to the surface,

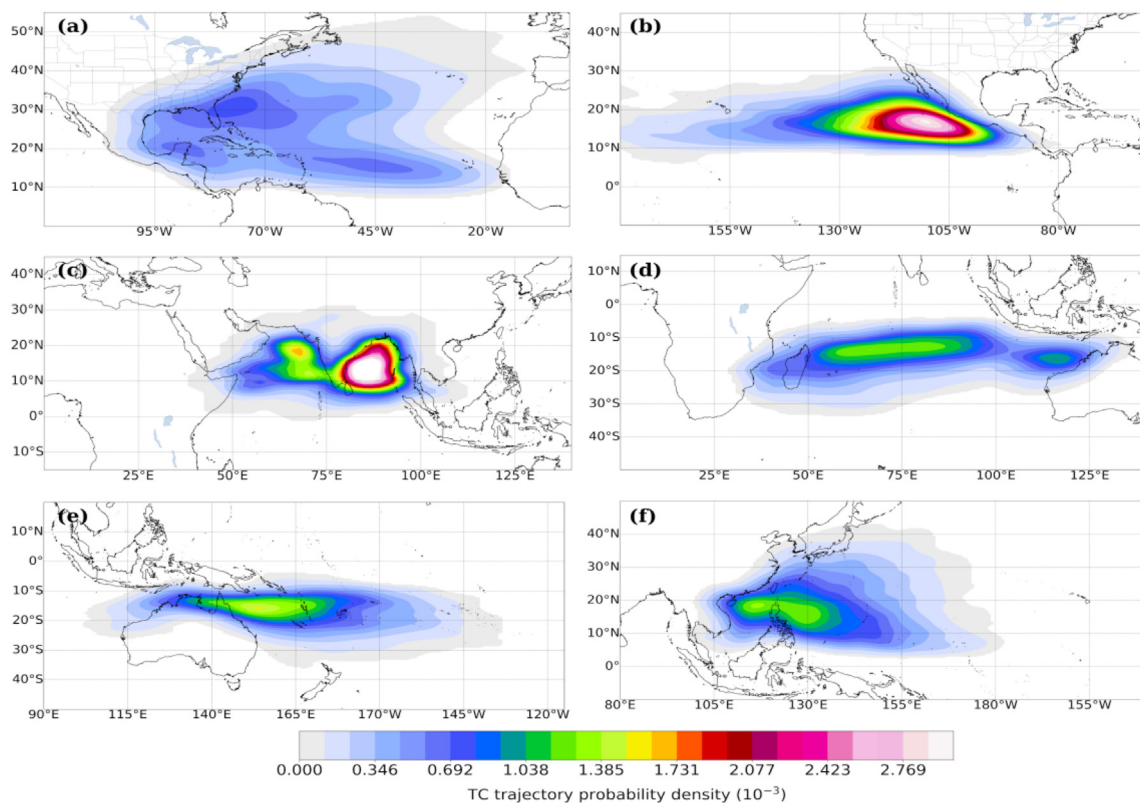


Fig. 2. Probability density of tropical cyclones trajectories over (a) North Atlantic Ocean, (b) Central and East North Pacific Ocean, (c) North Indian Ocean, (d) South Indian Ocean, (e) South Pacific Ocean, and (f) Western North Pacific basins.

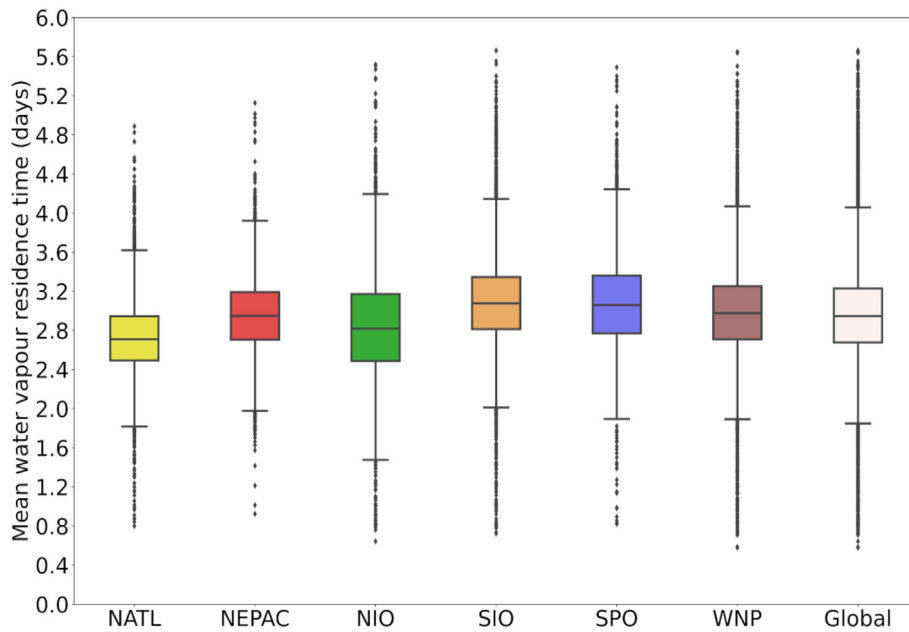


Fig. 3. Lagrangian estimate of mean water vapour residence time. NATL: North Atlantic Ocean, NEPAC: Central and East North Pacific Ocean, NIO: North Indian Ocean, SIO: South Indian Ocean, SPO: South Pacific Ocean, and WNP: Western North Pacific.

leading to a local decrease in MWVRT (Worden et al., 2007; Gimeno et al., 2021), which supports our results.

As the El Niño-Southern Oscillation (ENSO) influences the TC activity in each basin by changes in vertical wind shear, humidity, low-level vorticity, the strength and position of subtropical highs, sea surface temperature (SST) and upper ocean heat content and structure (e.g. Lin et al., 2020), we also computed the MWVRT during the warm (El Niño), cold (La Niña) and neutral phases of ENSO. However, we did not find notable differences in the MWVRT for the precipitation of TCs. Overall, the highest MWVRT values (higher than the mean values in each basin) were found during El Niño, while

an opposite pattern was detected during La Niña. Further studies will investigate the influence of climatic modes on the MWVRT during TCs.

Fig. 4 provides a global spatial view of MWVRT for TC-related precipitation. In all basins, the maximum MWVRT values appeared close to the equator, coinciding with the climatological mean position of the Inter-Tropical Convergence Zone (ITCZ, Lashkari et al., 2017; Byrne et al., 2018). This pattern can be directly linked to the upward vertical motion in the ITCZ, which induces generalised moisture convergence from the subtropical regions towards the ITCZ. The higher MWVRTs at low latitudes reflect the quasi-continuous

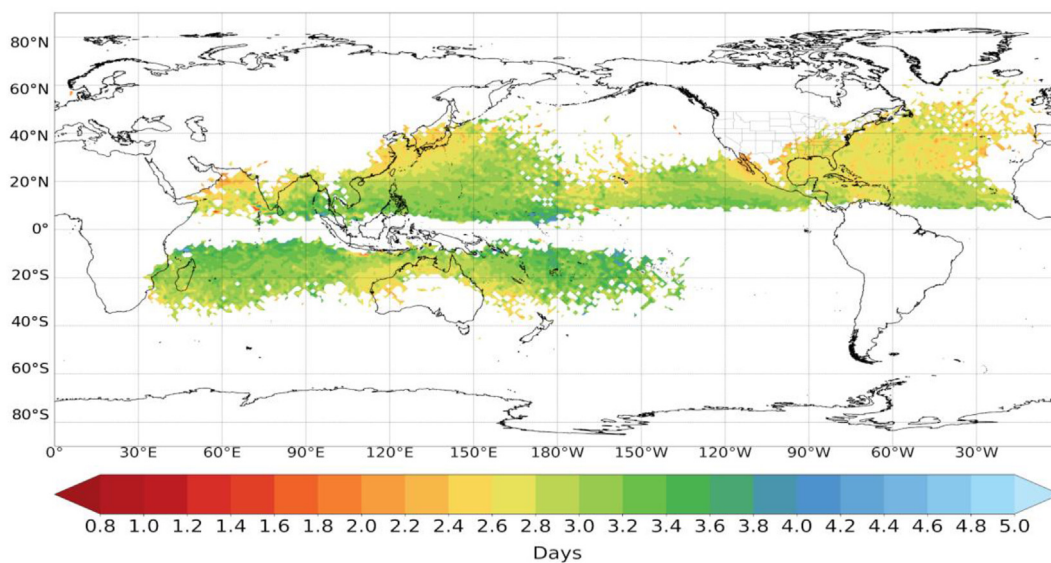


Fig. 4. Mean water vapour residence time (MWVRT) of atmospheric parcels that precipitate over the TC locations from 1980 to 2018. The MWVRT was estimated by applying a Lagrangian moisture source diagnostics method.

evaporation in the subtropics and the subsequent moisture transport driven by the trade winds towards the equator. This result agrees with findings in the literature (Läderach and Sodemann, 2016; Van der Ent and Tuinenburg, 2017; Gimeno et al., 2021).

Fig. 4 also reveals a gradual poleward decrease in MWVRT, which is most evident in the NATL basin. According to Van der Ent and Tuinenburg (2017), regions of low MWVRT coincide mostly with areas of low precipitation. This result can be confirmed by considering that the TC trajectories over the NATL are more dispersed than in the remaining basins (see Fig. 2) and therefore the spatial distribution of TC-related precipitation. The low MWVRT values in the Arabian Sea, Western Caribbean Sea, and surrounding the Gulf of California and the Lower California Peninsula are striking, confirming that regional and local processes influence the spatial distribution of MWVRT, in agreement with Tuinenburg and Van der Ent (2019) and Gimeno et al. (2021).

The spatial distribution of the MWVRT shown in Fig. 4 can also explain why the MWVRT in NIO and NATL show a slightly larger difference than in the remaining basins by comparing it with the global average. In the case of NATL, TCs can move poleward until high latitudes, crossing the subtropics, where the lowest MWVRT values were observed considering only TCs (Fig. 4) or all weather systems (Läderach and Sodemann, 2016; Van der Ent and Tuinenburg, 2017). These lowest values influenced the average time spent by the water vapour in the atmosphere from evaporation to the precipitation over the whole NATL. Conversely, the relatively lower MWVRT values over NIO can be related to the land-sea configuration of NIO, which confines TCs to the Bay of Bengal and the Arabian Sea. The moisture gained by TCs in NIO

mainly came from these local sources. Overall, the difference of the average MWVRT in each basin with the global mean could be explained by the heterogeneous distribution of TCs trajectories and evaporation, in agreement with Van der Ent and Tuinenburg (2017).

Several authors (e.g. Bulgin et al., 2020; Pérez-Alarcón et al., 2021c) have addressed the increase in SST in recent decades, and Knutson et al. (2020), using the Clausius–Clapeyron equation, demonstrated that a warmer SST under constant relative humidity conditions favoured higher availability of water vapour. Accordingly, an increase in global MWVRT (considering all weather systems) by 3–6%/°C has been projected (O’Gorman and Muller, 2010; Gimeno et al., 2021). However, by analysing the annual variation in MWVRT in each basin (Fig. 5), we found a statistically significant decrease ($p < 0.05$) in MWVRT at a rate of ~ 2.4 h/decade in NIO and ~ 1 h/decade in the remaining basins. These decreasing trends in the MWVRT of atmospheric parcels that precipitate in TCs could be related to the increasing trend in the average TC rain rate that has been found by Guzman and Jiang (2021) and Tu et al. (2021), caused by the increasing water vapour availability in the atmosphere with rising SST. As aforementioned, a downdraft motion during TC precipitation might decrease MWVRT, in agreement with Gimeno et al. (2021). By computing the Spearman correlation coefficient, while the MWVRT tends to decrease when the amount of precipitation within the TC outer radius increase in NATL and WNP, an opposite pattern was observed in the remaining basins. The correlation coefficients for NATL and WNP, although statistically significant at a 95% confidence level, are too small, being -0.05 and -0.07 , respectively. For the other basins, the Spearman correlation coefficients were 0.12, 0.14, 0.24, and

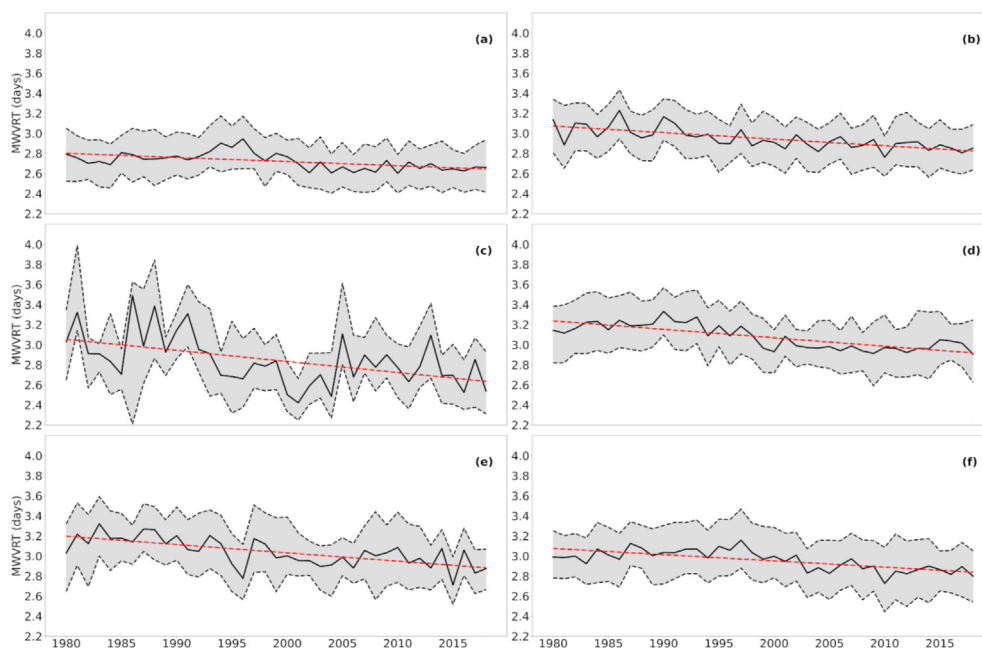


Fig. 5. Annual variation in mean water vapour residence time (MWVRT, solid black line) for precipitation of tropical cyclones in (a) North Atlantic Ocean, (b) Central and East North Pacific Ocean, (c) North Indian Ocean, (d) South Indian Ocean, (e) South Pacific Ocean, and (f) Western North Pacific basins. Red dashed lines represent the statistically significant (at a 95% significance level) trend line; the shaded grey area denotes the interquartile [q1–q3] range.

0.38 for SIO, SPO, NEPAC and NIO, respectively. This relationship is complex due to the several dynamic and thermodynamic processes involved in TCs precipitation. Additionally, the Lagrangian moisture tracking method applied in this work to estimate the MAVRT neglects the presence of liquid water and ice in the atmosphere, evaporation of hydrometeors and mixing of air parcels that can influence the total amount of precipitation (Sodemann et al., 2008).

We also hypothesized that the variability and spread of the MWVRT could be modulated by the same large-scale environmental parameters that modulated TC activity, such as sea surface temperature, 200–850-hPa vertical wind shear, low tropospheric moisture content, 200-hPa divergence and ocean heat content; however, we did not further investigate on how this modulation occurs. Future studies will further explore the variability of the MWVRT for TCs precipitation caused by large-scale environmental factors.

Furthermore, the highest MWVRT occurred in July (the second month of the official TC season) in the NATL basin, but no notable differences were from May to November. The lowest MWVRT was in January and December, but these

months are out of the TC season in NATL. For the remaining basins, the monthly MWVRT oscillated around the MWVRT estimated for the study period. Interestingly, we found an MWVRT of ~3.5 days in March for TCs over NEPAC, but it was an atypical value because March is out of TC season, and only one TC formed from 1980 to 2018. These results suggest that the seasonal variation of TCs did not modulate the MWVRT in each basin.

We also found that MWVRT had a significant ($p < 0.05$) inverse Spearman correlation with TC intensity in the SIO (−0.10), NATL (−0.16), NIO (−0.18), WNP (−0.25), and SPO (−0.05), but not in NEPAC. Accordingly, the fastest circulation of air in these basins suggests a short MWVRT, which is expected during the development of intense TCs. Therefore, the discussed decreasing trend in the MWVRT is also supported by the increase in TC intensity over the past four decades (Emanuel, 2005; Elsner et al., 2008; Wing et al., 2007; Holland and Bruyère, 2014; Wang et al., 2017; Bhatia et al., 2019; Kossin et al., 2013; 2020). Nevertheless, this finding must be cautiously interpreted because the sample size was smaller as TCs intensified. For example, the total entries during the H5

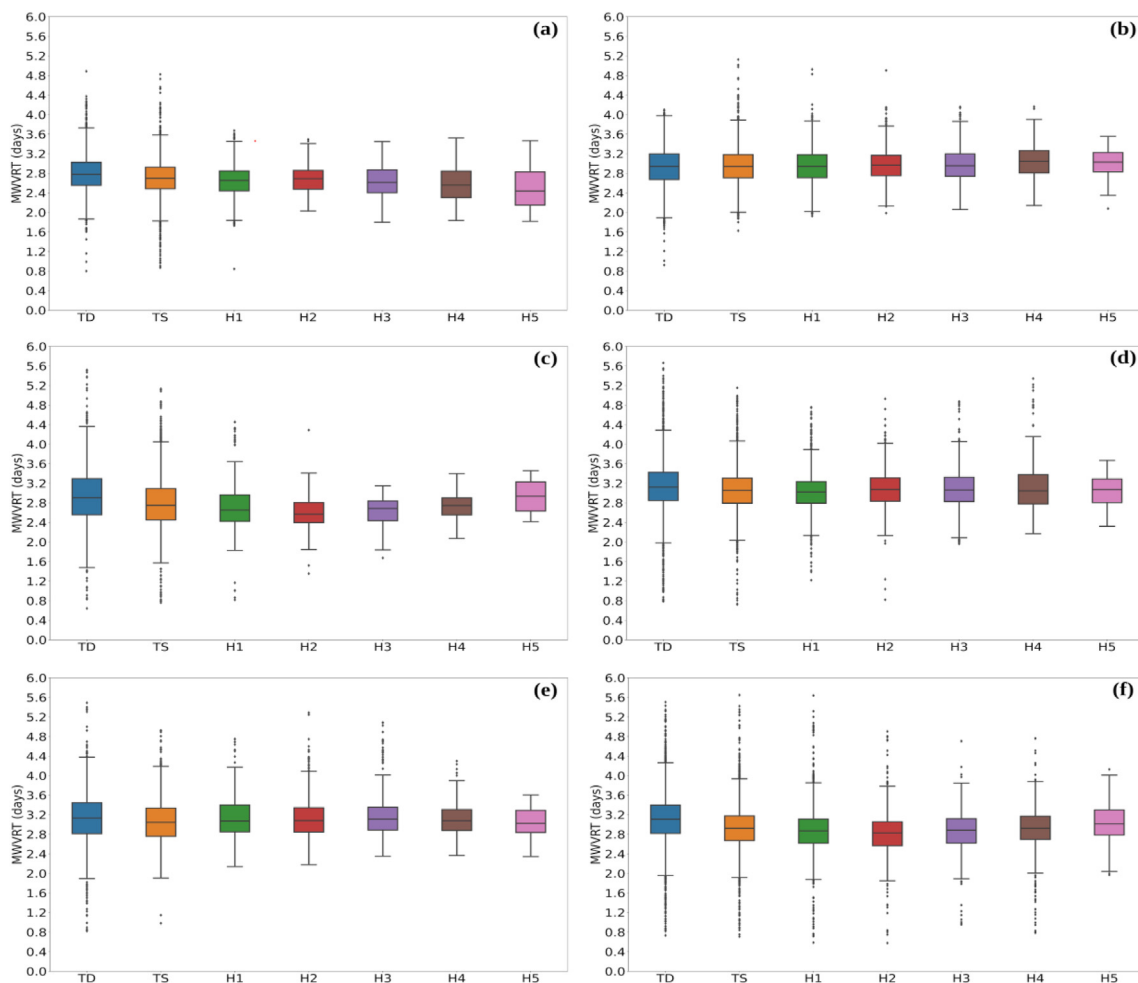


Fig. 6. Lagrangian estimate of mean water vapour residence time for each TC intensity category over (a) North Atlantic Ocean, (b) Central and East North Pacific Ocean, (c) North Indian Ocean, (d) South Indian Ocean, (e) South Pacific Ocean, and (f) Western North Pacific basins. TD: Tropical Depression, TS: Tropical Storm, H_N (N = 1, 2, 3, 4, 5): Hurricane categories on the Saffir-Simpson wind scale.

category represented from 0.2% (in NIO) to 1.2% (in WNP) of all 6-hourly TC records. Therefore, the MWVRT values for stronger TCs could be influenced by the sample size.

These results were partially confirmed by analysing the variations in MWVRT according to intensity categories. Fig. 6a shows a decrease in the MWVRT as TCs intensify in the NATL basin, ranging from $\sim 2.8 \pm 0.3$ days for tropical depressions (TDs) to $\sim 2.5 \pm 0.4$ days for Category 5 hurricanes (H5, on the scale Saffir-Simpson wind scale). In the NIO basin, the MWVRT also decreased from $\sim 2.9 \pm 0.6$ days for TDs to $\sim 2.6 \pm 0.3$ days for categories H2 and H3 (Fig. 5c). For the WNP, the results were similar to those of NIO, the MWVRT decreased from $\sim 3.1 \pm 0.5$ days for TDs to $\sim 2.8 \pm 0.4$ days for category H2, but few differences were found for category H5. In NEPAC, no changes in MWVRT were observed among the categories (Fig. 6b), confirming the weak relationship between TC intensity and MWVRT in this basin. Moreover, the intensity categories in the basins in the Southern Hemisphere did not exhibit significant differences in the MWVRT (Fig. 6d and e), which supported the lower Spearman coefficients between the MWVRT and TC intensity, as discussed in this study. Overall, the highest MWVRT was for TCs in the TD phase ($\sim 3.1 \pm 0.6$ days) and the lowest for category H2 ($\sim 2.8 \pm 0.4$ days).

Pérez-Alarcón et al. (2022c) have shown that remote moisture sources support less atmospheric humidity than those close to the area occupied by TC circulation (our target region), and this phenomenon has a signal in the MWVRT. The MWVRT showed a positive correlation ($p < 0.05$, Spearman test) with the radial distance between the weighted centroid of moisture sources and the boundary of the TCs in the SIO (0.15), NATL (0.22), SPO (0.28), NEPAC (0.35), and WNP (0.35) basins.

3.1. Changes in the Lagrangian MWVRT before TC landfall

Fig. 7a depicts the climatology of the TC tracks 24 h before the landfall. In general, 1320 trajectories were identified and distributed as follows: 79 in NEPAC, 108 in the SPO, 119 in the NIO, 142 in the SIO, 247 in the NATL, and 625 in the WNP. Notably, these values did not represent the total number of landfalling events recorded in each basin during the study period. We only considered landfalling events if the TC moved over the water in the previous 24 h (Rappaport et al., 2010; Liu et al., 2021; Zhu et al., 2021; Fudeyasu et al., 2014).

The MWVRTs in the 24 h before the TC's made landfall were estimated, being $\sim 2.7 \pm 0.3$ days in the NATL and

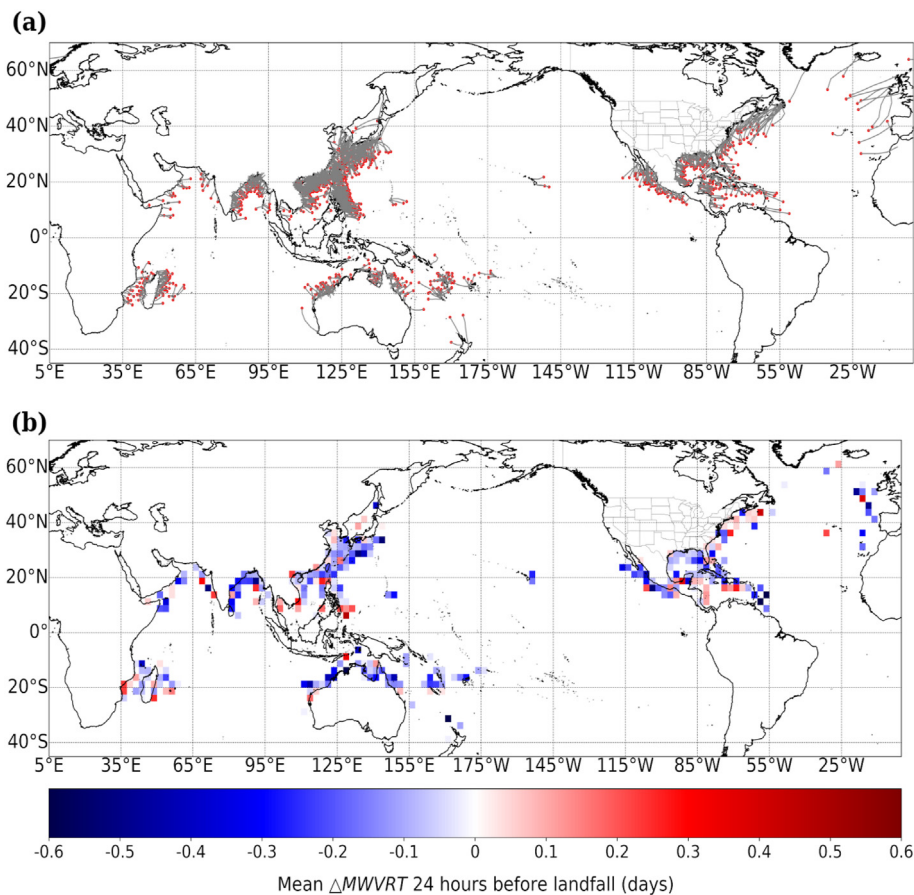


Fig. 7. (a) Tropical cyclone trajectories (grey solid lines) 24 h before landfall from 1980 to 2018 using HURDAT2 databases and Joint Typhon Warning Center best track archives. Red dots indicate the TC position 24 h before landfall. (b) Averaged differences of the MWVRT during the 24 h before the TC's landfall, calculated over a $2.5^\circ \times 2.5$ grid.

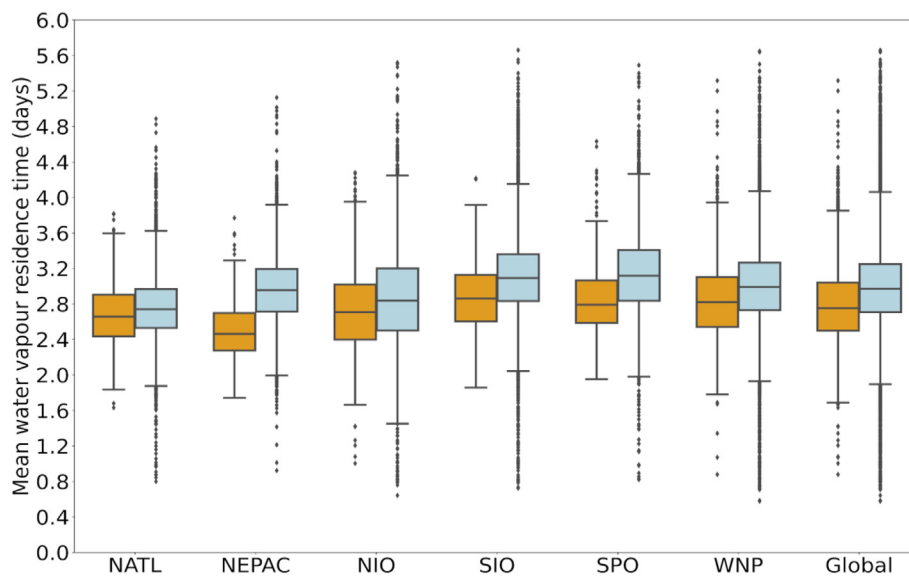


Fig. 8. Lagrangian estimate of mean water vapour residence time when TCs move over ocean (cyan boxes) and over land (orange boxes). NATL: North Atlantic Ocean, NEPAC: Central and East North Pacific Ocean, NIO: North Indian Ocean, SIO: South Indian Ocean, SPO: South Pacific Ocean, WNP: Western North Pacific.

NEPAC, $\sim 2.8 \pm 0.4$ days in the NIO and WNP, $\sim 2.9 \pm 0.4$ days in the SIO, and $\sim 3.0 \pm 0.4$ days in the SPO. Next, we determined if any change occurred along each trajectory: the difference between the MWVRT at landfall and 24 h before landfall was computed, and this value was assigned to the centroid of each 24 h track. Fig. 7b shows these differences averaged over a grid with 2.5×2.5 horizontal resolution. Positive (negative) values imply an increase (decrease) in the MWVRT of the atmospheric parcels 24 h before the landfall. In general, a decrease in the MWVRT is observed before a TC's landfall on a global scale, being more notable in the East China Sea, the western Bay of Bengal and the Arabian Sea, the eastern Pacific Ocean bordering the Mexican coast, the seas in northern Australia, and the seas surrounding Cuba, where the values fall between -0.2 and -0.5 days. Likewise, a slight decrease was observed in the Gulf of Mexico, varying from -0.1 to -0.2 days. Fig. 7b also reveals regions where the MWVRT before landfall increases: the Caribbean Sea, the East Coast of the United States, the southern Indochina Peninsula, and the coast of Africa in the Mozambique Channel.

On average, over each ocean basin (Fig. 8), the MWVRT decreased by 3.5% at TC landfall in the NATL basin, and 6.5% and 6.9% in the NIO and SIO, respectively. In the WNP and SPO basins were 9.4% and 9.8%. The reduction in NEPAC is notable: the MWVRT decreased 16.7% at TC landfall. The interaction of TC circulation with land influenced these changes. The general reduction is related to the effects of the orography, which is more evident in mountainous regions than in other areas, inducing changes in the steering flow, and cyclonic circulation tends to favour precipitation processes associated with spiral bands (Lin, 2007; Liu et al., 2016). The high percentage observed in the NEPAC basin may be directly related to the mountainous orography of Central America over TC landfall. Several authors (e.g. Tuleya et al., 1984; Andersen

and Shepherd, 2014; Zhu et al., 2021; Wang and Matyas, 2022) have highlighted the impact of the land surface on the dynamics and thermodynamics of TCs, such as the decrease in water vapour availability and low evaporation rate, reducing latent heat flux. During the interaction of the TC circulation with land, the evaporation rate drops dramatically compared with the evaporation rate over the ocean (e.g. Wang and Matyas, 2022), mainly caused by the decreased moisture and increased roughness length over land. Based on these previous findings, we hypothesized that the surface characteristics (e.g. vegetation, orography) influenced the MWVRT after the TCs made landfall. Therefore, studies in more depth than this are required to identify the factors and their linkages with a decrease in MWVRT.

4. Conclusion

The time spent from evaporation to precipitation, or mean water vapour residence time (MWVRT), is a fundamental characteristic of the atmospheric branch of the hydrological cycle. In this study, we applied a Lagrangian moisture source diagnostic method based on backward trajectories up to 10 days from the global outputs of the FLEXPART model to estimate the MWVRT of precipitant parcels during the lifetime of tropical cyclones (TCs) in each ocean basin.

The highest MWVRT was in the South Indian Ocean (SIO) and South Pacific Ocean (SPO) with $\sim 3.08 \pm 0.4$ days (uncertainty given as one standard deviation). TCs in the North Atlantic basin (NATL) exhibited the lowest value, 2.72 ± 0.4 days. In addition, the MWVRT for the Western North Pacific Ocean (WNP), Central and East Pacific Ocean (NEPAC), and North Indian Ocean (NIO) was estimated to be 2.98 ± 0.4 , 2.94 ± 0.4 , and 2.85 ± 0.4 , respectively. The analysis of all the basins demonstrated that the global MWVRT estimate for TC

precipitation was $\sim 2.96 \pm 0.4$ days, approximately two–three times lower than the classical estimate of 8–10 days, which considered all weather systems. Nevertheless, the spatial distribution of MWVRT provided a picture that agreed with other global studies, with MWVRT decreasing from the tropics to the subtropics. Therefore, the MWVRT spatial pattern reflected the temporal and spatial scales of moisture transport within the TC location.

Our study also revealed statistically significant decreasing trends in the MWVRT of ~ 2.4 h/decade in the NIO and a ~ 1.0 h/decade in the remaining basins, which could be related to the increase in TC intensity and precipitation rates over the last four decades. At global scale, the tropical depressions exhibited the highest MWVRT and Category 2 hurricanes on the Saffir-Simpson wind scale the lowest.

Additionally, we found that the MWVRT generally decreases between 0.2 and 0.5 days in the 24 h before the TCs made landfall, although we identified regions where the MWVRT increased, which was most significant in the Caribbean sea and the east coast of the United States. The MWVRT during this period ranged from 2.7 to 3.0 days. Moreover, the MWVRT decreases over the land by $\sim 3.5\%$ (in NATL) to 16.7% (in NEPAC) of its mean value over the ocean.

This work aimed to advance the knowledge of TC climatology in each basin and on a global scale based on MWVRT. Further research should conduct sensitivity studies to investigate the impact on the MWVRT estimates depending on the length of the backward trajectories and the threshold for considering the occurrence of precipitation. Furthermore, our results lead to new questions regarding how global warming affects the mean residence time of water vapour during TC precipitation. Therefore, further research should analyse the relationship between SST in a warmer climate and the MWVRT of atmospheric parcels that precipitate over TC locations.

Funding

This work was supported by the LAGRIMA and SETES-TRELO projects (grants no. RTI2018-095772-B-I00 and PID2021-122314OB-I00, respectively) funded by the Ministerio de Ciencia, Innovación y Universidades, Spain. Partial support was also obtained from the Xunta de Galicia under the Project ED431C2021/44 (Programa de Consolidación e Estructuración de Unidades de Investigación Competitivas (Grupos de Referencia Competitiva) and Consellería de Cultura, Educación e Universidade).

Acknowledgments

A.P.-A. acknowledges support from the UVigo PhD grants. J.C.F.-A. acknowledges support from the Xunta de Galicia (Galician Regional Government) under grant No. ED481A-2020/193. This work has also been supported by the computing resources and technical support provided by the Centro de Supercomputación de Galicia (CESGA).

Data Availability Statement

The datasets used in this study are freely available on the internet. The ERA-Interim reanalysis dataset was extracted from <https://apps.ecmwf.int/datasets/data/interim-full-daily/levtype=sfc/>, the HURDAT2 and the JWTC best track archives from <https://www.nhc.noaa.gov/data/#hurdat> and <https://www.metoc.navy.mil/jtwc/jtwc.html?best-tracks>. Moreover, the TCSize database was obtained from <http://doi.org/10.17632/8997r89fbf.1>. The FLEXPART model can be downloaded from <https://www.flexpart.eu/wiki/FpRoadmap>

References

- Algarra, I., Nieto, R., Ramos, A.M., Eiras-Barca, J., Trigo, R.M., Gimeno, L., 2020. Significant increase of global anomalous moisture uptake feeding landfalling Atmospheric Rivers. *Nat. Commun.* 11, 5082. <https://doi.org/10.1038/s41467-020-18876-w>.
- Andersen, T.K., Shepherd, J.M., 2014. A global spatiotemporal analysis of inland tropical cyclone maintenance or intensification. *Int. J. Climatol.* 34 (2), 391–402. <https://doi.org/10.1002/joc.3693>.
- Bhatia, K.T., Vecchi, G.A., Knutson, T.R., Murakami, H., Kossin, J., Dixon, K.W., Whitlock, C.E., 2019. Recent increases in tropical cyclone intensification rates. *Nat. Commun.* 10 (1). <https://doi.org/10.1038/s41467-019-08471-z>.
- Bosilovich, M.G., Schubert, S.D., 2002. Water vapor tracers as diagnostics of the regional hydrologic cycle. *J. Hydrometeorol.* 3, 149–165. [https://doi.org/10.1175/1525-7541\(2002\)003<0149:WVTADO>2.0.CO;2](https://doi.org/10.1175/1525-7541(2002)003<0149:WVTADO>2.0.CO;2).
- Brun, J., Barros, A.P., 2014. Mapping the role of tropical cyclones on the hydroclimate of the southeast United States: 2002–2011. *Int. J. Climatol.* 34 (2), 494–517. <https://doi.org/10.1002/joc.3703>.
- Bulgin, C.E., Merchant, C.J., Ferreira, D., 2020. Tendencies, variability and persistence of sea surface temperature anomalies. *Sci. Rep.* 10, 7986. <https://doi.org/10.1038/s41598-020-64785-9>.
- Byrne, M.P., Pendergrass, A.G., Rapp, A.D., Wodzicki, K.R., 2018. Response of the intertropical convergence zone to climate change: location, width, and strength. *Curr. Clim. Change Rep.* 4, 355–370. <https://doi.org/10.1007/s40641-018-0110-5>.
- Ciric, D., Nieto, R., Ramos, A.M., Drumond, A., Gimeno, L., 2018. Contribution of moisture from mediterranean sea to extreme precipitation events over danube river basin. *Water* 10, 1182. <https://doi.org/10.3390/w10091182>.
- Dee, D.P., Uppala, S.M., Simmons, A.J., Berrisford, P., Poli, P., Kobayashi, S., Andrae, U., Balmaseda, M.A., et al., 2011. The ERA-Interim reanalysis: configuration and performance of the data assimilation system. *Q. J. R. Meteorol. Soc.* 137, 553–597. <https://doi.org/10.1002/qj.828>.
- Elsner, J., Kossin, J., Jagger, T., 2008. The increasing intensity of the strongest tropical cyclones. *Nature* 455, 92–95. <https://doi.org/10.1038/nature07234>.
- Emanuel, K.A., 2005. Increasing destructiveness of tropical cyclones over the past 30 years. *Nature* 436, 686–688. <https://doi.org/10.1038/nature03906>.
- Fudeyasu, H., Hirose, S., Yoshioka, H., Kumazawa, R., Yamasaki, S., 2014. A global view of the landfall characteristics of tropical cyclones. *Trop. Cyclone Res. Rev.* 3 (3), 178–192. <https://doi.org/10.6057/2014TCRR03.04>.
- Gedzelman, S., Lawrence, J., Gamache, J., Black, M., Hindman, E., Black, R., Dunion, J., Willoughby, H., Zhang, X., 2003. Probing hurricanes with stable isotopes of rain and water vapor. *Mon. Wea. Rev.* 131 (6), 1112–1127. [https://doi.org/10.1175/1520-0493\(2003\)131<1112:PHWSIO>2.0.CO;2](https://doi.org/10.1175/1520-0493(2003)131<1112:PHWSIO>2.0.CO;2).
- Gimeno, L., Eiras-Barca, J., Durán-Quesada, A.M., Dominguez, F., van der Ent, R., Sodemann, H., Sánchez-Murillo, M., Nieto, R., Kirchner, J.W., 2021. The residence time of water vapour in the atmosphere. *Nat. Rev. Earth Environ.* 2 (8), 558–569. <https://doi.org/10.1038/s43017-021-00181-9>.

- Gimeno, L., Nieto, R., Sorí, R., 2020. The growing importance of oceanic moisture sources for continental precipitation. *Npj Clim. Atmos. Sci.* 3, 27. <https://doi.org/10.1038/s41612-020-00133-y>.
- Gray, W.M., 2012. Fundamental importance of convective downdrafts and mass recycling within the tropical cloud cluster and the typhoon-hurricane. *Trop. Cyclone Res. Rev.* 1 (1), 130–141. <https://doi.org/10.6057/2012TCRR01.14>.
- Guo, L., Klingaman, N.P., Vidale, P.L., Turner, A.G., Demory, M., Cobb, A., 2017. Contribution of tropical cyclones to atmospheric moisture transport and rainfall over East Asia. *J. Clim.* 30 (10), 3853–3865. <https://doi.org/10.1175/JCLI-D-16-0308.1>.
- Guzman, O., Jiang, H., 2021. Global increase in tropical cyclone rain rate. *Nat. Commun.* 12, 5344. <https://doi.org/10.1038/s41467-021-25685-2>.
- Holland, G., Bruyère, C.L., 2014. Recent intense hurricane response to global climate change. *Clim. Dyn.* 42, 617–627. <https://doi.org/10.1007/s00382-013-1713-0>.
- Jiang, H., Zipser, E.J., 2010. Contribution of tropical cyclones to the global precipitation from eight seasons of TRMM data: regional, seasonal, and interannual variations. *J. Clim.* 23, 1526–1543. <https://doi.org/10.1175/2009JCLI3303.1>.
- Knutson, T., Camargo, S.J., Chanm, J.C.L., Emanuel, K., Ho, C., Kossin, J., Mohapatra, M., Satoh, M., Sugi, M., Walsh, K., Wu, L., 2020. Tropical cyclones and climate change assessment: Part II: projected response to anthropogenic warming. *Bull. Am. Meteorol. Soc.* 101 (3), 303–322. <https://doi.org/10.1175/BAMS-D-18-0194.1>.
- Kossin, J.P., Olander, T.L., Knapp, K.R., 2013. Trend analysis with a new global record of tropical cyclone intensity. *J. Clim.* 26 (24), 9960–9976. <https://doi.org/10.1175/JCLI-D-13-00262.1>.
- Kossin, J.P., Knapp, K.R., Olander, T.L., Velden, C.S., 2020. Global increase in major tropical cyclone exceedance probability over the past four decades. *Proc. Natl. Acad. Sci. U.S.A.* 117 (22), 11975–11980. <https://doi.org/10.1073/pnas.1920849117>.
- Landsea, C.W., Franklin, J.L., 2013. Atlantic hurricane database uncertainty and presentation of a new database format. *Mon. Wea. Rev.* 141, 3576–3592. <https://doi.org/10.1175/mwr-d-12-00254.1>.
- Lashkari, H., Mohammadi, Z., Keikhosravi, G., 2017. Annual fluctuations and displacements of inter tropical convergence zone (ITCZ) within the range of Atlantic Ocean-India. *Open J. Ecol.* 7 (1), 12–33. <https://doi.org/10.4236/oje.2017.71002>.
- Läderach, A., Sodemann, H., 2016. A revised picture of the atmospheric moisture residence time. *Geophys. Res. Lett.* 43, 924–933. <https://doi.org/10.1002/2015GL067449>.
- Lin, Y.L., 2007. *Mesoscale Dynamics*, 630. Cambridge University Press, Cambridge. <https://doi.org/10.1017/cbo9780511619649>.
- Lin, I.-I., Camargo, S.J., Patricola, C.M., Boucharel, J., Chand, S., Klotzbach, P., Chan, J.C.L., Wang, B., Chang, P., Li, T., Jin, F.-F., 2020. ENSO and tropical cyclones. In: McPhaden, M.J., Santoso, A., Cai, W. (Eds.), *El Niño Southern Oscillation in a Changing Climate*. <https://doi.org/10.1002/9781119548164.ch17>.
- Liu, L., Lin, Y.L., Chen, S.H., 2016. Effects of landfall location and approach angle of an idealized tropical cyclone over a long mountain range. *Front. Earth Sci.* 14. <https://doi.org/10.3389/feart.2016.00014>.
- Liu, Q., Song, J., Klotzbach, P., 2021. Trends in western North Pacific tropical cyclone intensity change before landfall. *Front. Earth Sci.* 1025. <https://doi.org/10.3389/feart.2021.780353>.
- Maxwell, J.T., Soulé, P.T., Ortegren, J.T., Knapp, P., 2012. Drought-busting tropical cyclones in the southeastern Atlantic United States: 1950–2008. *Ann. Am. Assoc. Geogr.* 102 (2), 259–275. <https://doi.org/10.1080/00045608.2011.596377>.
- Nieto, R., Gimeno, L., 2019. A database of optimal integration times for Lagrangian studies of atmospheric moisture sources and sinks. *Sci. Data* 6, 1–10. <https://doi.org/10.1038/s41597-019-0068-8>.
- O’Gorman, P., Muller, C.J., 2010. How closely do changes in surface and column water vapor follow Clausius–Clapeyron scaling in climate change simulations? *Environ. Res. Lett.* 5. <https://doi.org/10.1088/1748-9326/5/2/025207>.
- Papritz, L., Aemisegger, F., Wernli, H., 2021. Sources and transport pathways of precipitating waters in cold-season deep North Atlantic cyclones. *J. Atmos. Sci.* 78 (10), 3349–3368. <https://doi.org/10.1175/JAS-D-21-0105.1>.
- Pérez-Alarcón, A., Sorí, R., Fernández-Alvarez, J.C., Nieto, R., Gimeno, L., 2021a. Moisture sources for tropical cyclones genesis in the coast of west Africa through a Lagrangian approach. *Environ. Sci. Proc.* 4, 3. <https://doi.org/10.3390/ecas2020-08126>.
- Pérez-Alarcón, A., Sorí, R., Fernández-Alvarez, J.C., Nieto, R., Gimeno, L., 2021b. Comparative climatology of outer tropical cyclone size using radial wind profiles. *Weather Clim. Extrem.* 33, 100366. <https://doi.org/10.1016/j.wace.2021.100366>.
- Pérez-Alarcón, A., Fernández-Alvarez, J.C., Sorí, R., Nieto, R., Gimeno, L., 2021c. The relationship of the sea surface temperature and climate variability modes with the North Atlantic tropical cyclones activity. *Rev. Cub. Met.* 27 (3). <http://rcm.insmet.cu/index.php/rcm/article/view/575/1145>.
- Pérez-Alarcón, A., Sorí, R., Fernández-Alvarez, J.C., Nieto, R., Gimeno, L., 2022a. Where does the moisture for North Atlantic tropical cyclones come from? *J. Hydrometeorol.* 23 (3), 457–472. <https://doi.org/10.1175/JHM-D-21-0117.1>.
- Pérez-Alarcón, A., Sorí, R., Fernández-Alvarez, J.C., Nieto, R., Gimeno, L., 2022b. Dataset of outer tropical cyclone size from a radial wind profile. *Data Br.* 40, 107825. <https://doi.org/10.1016/j.dib.2022.107825>.
- Rappaport, E.N., 2014. Fatalities in the United States from Atlantic tropical cyclones: new data and interpretation. *Bull. Am. Meteorol. Soc.* 95, 341–346. <https://doi.org/10.1175/BAMS-D-12-00074.1>.
- Rappaport, E.N., Franklin, J.L., Schumacher, A.B., DeMaria, M., Shay, L.K., Gibney, E.J., 2010. Tropical cyclone intensity change before US Gulf Coast landfall. *Weather Forecast* 25 (5), 1380–1396. <https://doi.org/10.1175/2010waf2222369.1>.
- Rogers, R., Marks, F., Marchok, T., 2009. Tropical cyclone rainfall. In: McDonnell, J.J. (Ed.), *Encyclopedia of Hydrological Sciences* Anderson MG. American Cancer Society. <https://doi.org/10.1002/0470848944.hsa030>.
- Savenije, H.H.G., 2000. Water scarcity indicators; the deception of the numbers. *Phys. Chem. Earth B* 25, 199–204. [https://doi.org/10.1016/S1464-1909\(00\)00004-6](https://doi.org/10.1016/S1464-1909(00)00004-6).
- Schumacher, R.S., Galareau, T.J., 2012. Moisture transport into midlatitudes ahead of recurring tropical cyclones and its relevance in two predecessor rain events. *Mon. Wea. Rev.* 140 (6), 1810–1827. <https://doi.org/10.1175/MWR-D-11-00307.1>.
- Sodemann, H., Schwierz, C., Wernli, H., 2008. Interannual variability of Greenland winter precipitation sources: Lagrangian moisture diagnostic and North Atlantic Oscillation influence. *J. Geophys. Res. Atmos.* 113, D03107. <https://doi.org/10.1029/2007JD008503>.
- Sodemann, H., 2020. Beyond turnover time: constraining the lifetime distribution of water vapor from simple and complex approaches. *J. Atmos. Sci.* 77 (2), 413–433. <https://doi.org/10.1175/JAS-D-18-0336.1>.
- Sorí, R., Nieto, R., Vicente-Serrano, S.M., Drumond, A., Gimeno, L., 2017. A Lagrangian perspective of the hydrological cycle in the Congo River basin. *Earth. Syst. Dyn.* 8, 653–675. <https://doi.org/10.5194/esd-8-653-2017>.
- Stohl, A., Forster, C., Frank, A., Seibert, P., Wotawa, G., 2005. Technical Note: the Lagrangian particle dispersion model FLEXPART version 6.2. *Atmos. Chem. Phys.* 5, 2461–2474. <https://doi.org/10.5194/acp-5-2461-2005>.
- Stohl, A., James, P.A., 2004. Lagrangian analysis of the atmospheric branch of the global water cycle. Part I: method description, validation, and demonstration for the august 2002 flooding in central europe. *J. Hydrometeorol.* 5, 656–678. [https://doi.org/10.1175/1525-7541\(2004\)005<0656:ALAOTA>2.0.CO;2](https://doi.org/10.1175/1525-7541(2004)005<0656:ALAOTA>2.0.CO;2).
- Stohl, A., James, P.A., 2005. A Lagrangian analysis of the atmospheric branch of the global water cycle: Part II: earth’s river catchments ocean basins, and moisture transports between them. *J. Hydrometeorol.* 6, 961–984. <https://doi.org/10.1175/JHM470.1>.
- Trenberth, K.E., 1998. Atmospheric moisture residence times and cycling: implications for rainfall rates and climate change. *Clim. Change* 39, 667–694. <https://doi.org/10.1023/A:1005319109110>.
- Tu, S., Xu, J., Chan, J.C., Huang, K., Xu, F., Chiu, L.S., 2021. Recent global decrease in the inner-core rain rate of tropical cyclones. *Nat. Commun.* 12 (1), 1–9. <https://doi.org/10.1038/s41467-021-22304-y>.
- Tuinenburg, O., Van der Ent, R., 2019. Land surface processes create patterns in atmospheric residence time of water. *J. Geophys. Res. Atmos.* 124, 583–600. <https://doi.org/10.1029/2018JD028871>.

- Tuleya, R.E., Bender, M.A., Kurihara, Y., 1984. A simulation study of the landfall of tropical cyclones. *Mon. Wea. Rev.* 112 (1), 124–136. [https://doi.org/10.1175/1520-0493\(1984\)112<0124:ASSOTL>2.0.CO;2](https://doi.org/10.1175/1520-0493(1984)112<0124:ASSOTL>2.0.CO;2).
- Van der Ent, R.J., Tuinenburg, O.A., 2017. The residence time of water in the atmosphere revisited. *Nat. Hazards Earth Syst. Sci.* 21, 779–790. <https://doi.org/10.5194/hess-21-779-2017>.
- Wang, C., Wang, X., Weisberg, R.H., Black, M.L., 2017. Variability of tropical cyclone rapid intensification in the North Atlantic and its relationship with climate variations. *Clim. Dyn.* 49, 3627–3645. <https://doi.org/10.1007/s00382-017-3537-9>.
- Wang, Y., Matyas, C.J., 2022. Simulating the effects of land surface characteristics on planetary boundary layer parameters for a modeled landfalling tropical cyclone. *Atmosphere* 13 (1), 138. <https://doi.org/10.3390/atmos13010138>.
- Worden, J., Noone, D., Bowman, K., 2007. Importance of rain evaporation and continental convection in the tropical water cycle. *Nature* 445, 528–532. <https://doi.org/10.1038/nature05508>.
- Willoughby, H.E., 2012. Distributions and trends of death and destruction from hurricanes in the United States, 1900–2008. *Nat. Hazards Rev.* 13, 57–64. [https://doi.org/10.1061/\(ASCE\)NH.1527-6996.0000046](https://doi.org/10.1061/(ASCE)NH.1527-6996.0000046).
- Wing, A.A., Sobel, A.H., Camargo, S.J., 2007. Relationship between the potential and actual intensities of tropical cyclones on interannual time scales. *Geophys. Res. Lett.* 34, L08810. <https://doi.org/10.1029/2006GL028581>.
- Xu, G., Osborn, T.J., Matthews, A.J., 2017. Moisture transport by Atlantic tropical cyclones onto the North American continent. *Clim. Dyn.* 48, 3161–3182. <https://doi.org/10.1007/s00382-016-3257-6>.
- Yoshimura, K., Oki, T., Ohte, N., Kanae, S., 2004. Colored moisture analysis estimates of variations in 1998 Asian monsoon water sources. *J. Meteorol. Soc. Japan* 82, 1315–1329. <https://doi.org/10.2151/jmsj.2004.1315>.
- Zhu, Y.J., Collins, J.M., Klotzbach, P.J., 2021. Nearshore hurricane intensity change and post-landfall dissipation along the United States Gulf and East coasts. *Geophys. Res. Lett.* 48 (17), e2021GL094680. <https://doi.org/10.1029/2021gl094680>.

4.8 Moisture sources for precipitation associated with major hurricanes during 2017 in the North Atlantic basin

Pérez-Alarcón, A., Coll-Hidalgo, P., Fernández-Alvarez, J.C., Sorí, R., Nieto, R., Gimeno, L., 2022. Moisture sources for precipitation associated with major hurricanes during 2017 in the North Atlantic basin. *J. of Geophysical Research: Atmospheres* 127(4), e2021JD035554. doi: 10.1029/2021JD035554.

Table 4.8: Summary of the impact and quality of the journal where the seventh paper that conformed to this thesis was published. The data correspond to the year 2021 (last year available at the date of preparation of this document) in the Web of Science (JCR). **IF:** Impact Factor

Journal	Description	Journal Metrics
Journal of Geophysical Research: Atmospheres	It publishes original research articles, that advance and improve the understanding of atmospheric properties of and processes, including the interaction of the atmosphere with other components of the Earth system.	IF: 5.217, 5-year IF: 5.302 Ranking: 28 out of 108 (Q2) in Meteorology & Atmospheric Sciences



RESEARCH ARTICLE

10.1029/2021JD035554

Special Section:

The Three Major Hurricanes of 2017: Harvey, Irma and Maria

Key Points:

- The tropical North Atlantic Ocean was the main moisture source for precipitation associated with major hurricanes in 2017
- The South Atlantic moisture source is not negligible, with contributions of ~14%–20%
- The highest moisture uptake generally occurred within approximately 3° to 5° of tropical cyclone trajectories

Supporting Information:

Supporting Information may be found in the online version of this article.

Correspondence to:

A. Pérez-Alarcón,
albenis.perez.alarcon@uvigo.es

Citation:

Pérez-Alarcón, A., Coll-Hidalgo, P., Fernández-Alvarez, J. C., Sorí, R., Nieto, R., & Gimeno, L. (2022). Moisture sources for precipitation associated with major hurricanes during 2017 in the North Atlantic basin. *Journal of Geophysical Research: Atmospheres*, 127, e2021JD035554. <https://doi.org/10.1029/2021JD035554>

Received 10 JUL 2021

Accepted 24 JAN 2022

Author Contributions:

Conceptualization: Albenis Pérez-Alarcón, José C. Fernández-Alvarez, Rogert Sorí, Raquel Nieto, Luis Gimeno
Data curation: Albenis Pérez-Alarcón, Rogert Sorí

Formal analysis: Albenis Pérez-Alarcón, Patricia Coll-Hidalgo, José C. Fernández-Alvarez, Rogert Sorí, Luis Gimeno

© 2022 The Authors.

This is an open access article under the terms of the [Creative Commons Attribution-NonCommercial License](#), which permits use, distribution and reproduction in any medium, provided the original work is properly cited and is not used for commercial purposes.

Moisture Sources for Precipitation Associated With Major Hurricanes During 2017 in the North Atlantic Basin

Albenis Pérez-Alarcón^{1,2} , Patricia Coll-Hidalgo^{1,3} , José C. Fernández-Alvarez^{1,2} , Rogert Sorí^{1,4} , Raquel Nieto¹ , and Luis Gimeno¹ 

¹Centro de Investigación Mariña, Universidade de Vigo, Environmental Physics Laboratory (EPhysLab), Ourense, Spain, ²Departamento de Meteorología, Instituto Superior de Tecnologías y Ciencias Aplicadas, Universidad de La Habana, La Habana, Cuba, ³Empresa Cubana de Navegación Aérea, La Habana, Cuba, ⁴Instituto Dom Luiz, Faculdade de Ciências da Universidade de Lisboa, Campo Grande, Portugal

Abstract The 2017 North Atlantic tropical cyclone season was among the most active in the last two decades, with 17 named storms, of which six reached the major hurricane (MH) intensity: Harvey, Irma, Jose, Lee, Maria, and Ophelia. In this study, the water vapor sources for precipitation for these six MHs were examined using a Lagrangian approach. The particle dispersion model, FLEXPART, was used to identify moisture sources. Overall, the North Atlantic Ocean, the Caribbean Sea, and the Gulf of Mexico were identified as the main moisture sources, supplying ~75%–85% of the atmospheric humidity gained by tropical cyclones, which resulted in precipitation associated with the MHs. However, the South Atlantic Ocean also contributed considerable humidity (~14%–20%), and the remaining ~1%–5% originated from the tropical eastern Pacific Ocean. The accumulated moisture uptake higher than the 90th percentile generally appeared within approximately 3° to 5° of the TC trajectory.

1. Introduction

Tropical cyclones (TCs) can produce intense rainfall, and with storm surges can cause coastal flooding with serious societal impacts. The most significant disasters (Blake & Zelinsky, 2018; Cangialosi et al., 2021; Knabb et al., 2005; Pasch et al., 2006) caused by TCs are produced by major hurricanes (MHs), which are defined as TCs with maximum sustained (1 min) surface winds higher than 178 km/hr at any time during their lifetimes (including hurricanes categories ≥ 3 on the Saffir-Simpson Wind Scale).

The 2017 North Atlantic TC season was extremely active (Wachnicka et al., 2020), with 17 named storms, 10 hurricanes, and six MHs (the median was 12, 7, and 2, respectively, in 1980–2019). This increased activity occurred during La Niña and the warm phase of the Atlantic Multidecadal Oscillation. Three of these MHs made landfall at least once in their lifetime, causing ecological and human tolls, mainly due to heavy rainfall. Hurricane Harvey affected the coast of Texas in the United States (US; Blake & Zelinsky, 2018). Hurricane Irma affected the northern coast of Cuba and the southeastern US (Cangialosi et al., 2021). Hurricane Maria impacted several Caribbean islands, such as the US Virgin Islands and Puerto Rico (Pasch et al., 2019).

Dynamics and thermodynamics are factors that play an essential role in TC genesis and development (Emanuel et al., 2004). Among other factors, TC formation requires moist layers in the mid-troposphere to enhance thunderstorm formation (Emanuel, 1987; Gray, 1968). Several studies (Braun et al., 2012; Emanuel et al., 2004; Ge et al., 2013; Kimball, 2006; Tao & Zhang, 2014; Wang et al., 2009) have investigated the role of atmospheric humidity in TC development. Theoretical and modeling studies (Emanuel et al., 2004; Ge et al., 2013; Kimball, 2006) have suggested that high environmental moisture may favor TC intensification, and Hill and Lackmann (2009) highlighted that environmental moisture is a key factor contributing to TC size. However, substantial moisture may also negatively affect TC strength by facilitating the formation of TC outer rain bands, which reduces the horizontal pressure gradient in a TC (Tao & Zhang, 2014; Wang et al., 2009; Ying & Zhang, 2012).

Studies (e.g., Braun, 2006) have revealed that a majority of condensation occurs in convective hot towers in the eyewall, whereas vapor deposition and aggregation are dominant outside the eyewall. In addition, the ocean source for water vapor in the inner core of TCs is a small portion of the horizontal vapor import, as shown by Yang et al. (2011) using Typhoon Nari (2001) simulations, with a 2 km horizontal fine grid resolution. Additionally, dry air intrusions weaken TCs by favoring convection-driven downdrafts and associated boundary layer

Funding acquisition: Raquel Nieto, Luis Gimeno

Investigation: Albenis Pérez-Alarcón, Patricia Coll-Hidalgo, Rogert Sorí, Raquel Nieto, Luis Gimeno

Methodology: Albenis Pérez-Alarcón, José C. Fernández-Alvarez, Rogert Sorí, Raquel Nieto, Luis Gimeno

Project Administration: Raquel Nieto, Luis Gimeno

Software: Albenis Pérez-Alarcón, José C. Fernández-Alvarez

Supervision: Raquel Nieto, Luis Gimeno

Validation: Albenis Pérez-Alarcón, Patricia Coll-Hidalgo

Visualization: Albenis Pérez-Alarcón

Writing – original draft: Albenis Pérez-Alarcón

Writing – review & editing: Albenis Pérez-Alarcón, Patricia Coll-Hidalgo, José C. Fernández-Alvarez, Rogert Sorí, Raquel Nieto, Luis Gimeno

cooling (Dunion & Velden, 2004; Ge et al., 2013), and idealized simulations (Braun et al., 2012) show that only dry air near the vortex center leads to asymmetric convection and delays the development of the storm. In a 6-km grid simulation of Hurricane Andrew (1992), Zhang et al. (2002) demonstrated that horizontal advection tended to transport drier air from the outer region into the core in the marine boundary air. Moreover, some studies have investigated other components of the water budget linked with TC genesis and intensification, such as precipitation (Alvey et al., 2015; Tao et al., 2017; Wu & Chen, 2012), surface evaporation (Gao et al., 2016, 2017; Jaimes et al., 2015), and moisture flux convergence (Gao et al., 2017; Makarieva et al., 2017; Yin et al., 2015).

Precipitation associated with TC extends far from their core, with a large amount of precipitation in the spiral bands. Wu and Chen (2012) conducted sensitivity experiments to investigate the impact of ambient moisture content on TC related precipitations. Their findings revealed that the decrease in precipitation was controlled by a decrease in available moisture and a reduction in TC size. Makarieva et al. (2017) studied how the water vapor budget of a TC is dependent on its motion and showed that TC precipitation could not be fully explained by local evaporation. Furthermore, Montgomery and Smith (2017) stated that TC precipitation is mainly a product of the secondary circulation transporting moisture inward; thus, most of the precipitation is expected to occur as the TC intensifies. Notably, surface evaporation is proportional to the 10 m wind speed and sea surface temperature (SST; Gao et al., 2016, 2017); therefore, TC precipitation increases with an increase in SST and an increase in atmospheric humidity (Hill & Lackmann, 2009; Lin et al., 2015; Matyas, 2010). Kim et al. (2021) used satellite precipitation and reanalysis data and confirmed that environmental flows, SST, and humidity influence the inner-core rainfall and rainfall area along the TC trajectory.

Several studies have used Eulerian approaches to compute the water budget associated with TCs (e.g., Chauvin et al., 2017; Fritz & Wang, 2013, 2014; Gao et al., 2017; Makarieva et al., 2017; Vannièrè et al., 2020; Wu et al., 2013); however, several methods can be applied to investigate the origin of atmospheric moisture (comparative review by Gimeno et al. (2012)). Lagrangian approaches have proven powerful tools for identifying moisture sources and studying anomalous atmospheric moisture transport in global and regional studies (Knippertz et al., 2013; Miralles et al., 2016; Nieto et al., 2014; Stohl & James, 2004, 2005; Vázquez et al., 2020), meteorological systems such as extra TCs (Cloux et al., 2021; Liberato et al., 2012), or low-level jets and atmospheric rivers (Algarra et al., 2019, 2020; Braz et al., 2021; Ramos et al., 2016, 2019). However, these techniques have rarely been used for TCs. For example, they were to analyze two individual TCs in the Pacific. Xu et al. (2017) used a Lagrangian flexible particle dispersion model (FLEXPART, Stohl et al., 2005, 2016) to investigate the physical processes responsible for the torrential rainfall that occurred along the northwestern Pacific coast of Japan during the landfall of Typhoon Fitow in 2013. Similarly, Yang et al. (2017) analyzed the moisture sources for Typhoon Nina (in 1975) by using the Lagrangian analysis tool LAGRANTO developed by Sprenger and Wernli (2015) fed by downscaled Weather Research and Forecasting (WRF) model simulations. Pazos and Gimeno (2017) and Pérez-Alarcón et al. (2021a), also using the FLEXPART model, accounted for the water budget associated with all the TCs whose origin is over the eastern part of the North Atlantic Ocean basin (near the West African coast); both studies differ in the period analyzed (1979–2012 and 1980–2018, respectively), and in the definition of the target regions. Pazos and Gimeno (2017) defined the target region as a fixed box between 8°–20°N and 15°–45°W, and the whole area was analyzed when a TC occurred. Pérez-Alarcón et al. (2021a) used only the area enclosed by each TC outer radius at the moment of genesis. However, both studies analyze the search for moisture sources associated with TCs, but not for the moisture that finally generates precipitation. Regarding this last goal, Sodemann et al. (2008) proposed an approach to identify the moisture sources by discounting proportionally to all previous moisture uptakes (MUs) the precipitation in route. This methodology was applied to identify sources and transport pathways of precipitating waters of weather systems at a synoptic scale, such as extratropical cyclones (e.g., Papritz et al., 2021), but never for TCs.

Climate modeling studies (Knutson et al., 2015; Patricola & Wehner, 2018; Scoccimarro et al., 2014; Yoshida et al., 2017) have reported increased TC rainfall due to global warming. A relevant common factor in these studies is the projected increase in atmospheric humidity, which leads to enhanced moisture convergence and thus increases the rainfall rate. In addition, Kossin et al. (2020) suggested a positive trend in TC intensity with a warming climate. Therefore, based on climate projections, studying the water budgets of MHs is necessary to improve the knowledge of the influence of atmospheric humidity on the development of intense TCs.

Despite the observational and modeling studies of TCs, deepening the understanding of the moisture transported to TCs that finally produces precipitation is necessary. Thus, in this study, by applying the Lagrangian

Table 1
Characteristics of the Six Major Hurricanes of the 2017 North Atlantic Tropical Cyclone Season Extracted From the HURDAT2 Database

TC name	Lifetime	V_{\max} (km/hr)	P_{\min} (hPa)
Harvey	17 August to 1 September	200	937
Irma	30 August to 12 September	290	914
Jose	4 to 25 September	250	938
Lee	14 to 30 September	190	962
Maria	16 September to 2 October	280	908
Ophelia	6 to 17 October	190	959

Note. V_{\max} , maximum wind speed; P_{\min} , minimum central pressure.

moisture source diagnostic method proposed by Sodemann et al. (2008), we investigated the moisture transport and sources that produced precipitation during the entire trajectories along their complete lifecycle of the six TCs that reached the MH category in the North Atlantic basin in 2017. In addition to improving the previous studies (e.g., Pazos & Gimeno, 2017; Pérez-Alarcón et al., 2021a), we assumed variable target regions defined by the outer radius of TCs in each position of each TC trajectory.

The remainder of this paper proceeds as follows. Section 2 describes the data set and the methodology used, namely the Lagrangian approach to computing the sources of moisture for TC. The results and discussion are presented in Section 3, and the conclusions are presented in Section 4.

2. Materials and Methods

2.1. Data

Data on MHs in 2017 were obtained from the Atlantic hurricane database (HURDAT2; Landsea & Franklin, 2013) available online at the US Hurricane Center (NHC) web page (<https://www.nhc.noaa.gov/data/#hurdat>). This data set is a reanalysis effort to extend and revise the NHC's North Atlantic hurricane database. Table 1 shows the features of the six MHs in the 2017 North Atlantic TC season. A brief description of the synoptic history of each MH is presented in Text S1 of Supporting Information.

Daily SST anomalies were extracted from the NOAA Daily Optimum Interpolation Sea Surface Temperature (OISST) data set v2.1 (Banzon et al., 2020), constructed by combining observations from different platforms (satellites, ships, and buoys) on a grid with $0.25^\circ \times 0.25^\circ$ horizontal resolution.

The precipitation rate from the Global Precipitation Measurement (GPM; Huffman et al., 2019) was used. In this data set, the precipitation was estimated from the relevant satellite passive microwave sensors comprising the GPM constellation, computed using the Goddard profiling algorithm (Kummerow et al., 2015; Randel et al., 2020), and merged into a grid of half-hourly $0.1^\circ \times 0.1^\circ$ horizontal resolution. Because the GPM precipitation data set has a higher horizontal resolution ($0.1^\circ \times 0.1^\circ$) than the other data sets used, we regridded the GPM data using the nearest neighbor method (Chen et al., 2010) to the MU grid resolution ($1^\circ \times 1^\circ$). In this study, we only considered the precipitation rate (R) related to TCs, which was defined as the R within the outer radius of the TC. The R calculation has been used in several studies (Guo et al., 2017; Jiang & Zipser, 2010; Larson et al., 2005; Prat & Nelson, 2013). The precipitation was computed for every 6 hr time step along the TC trajectories.

Furthermore, the integrated eastward and northward moisture fluxes, which were extracted from the European Centre for Medium-Range Weather Forecasts (ECMWF) ERA-5 reanalysis data set, were used to compute the vertically integrated moisture flux (VIMF). In addition, surface evaporation data used to calculate the local evaporation within the TC outer radius along the trajectory were derived from the ERA-5 reanalysis. ERA-5 combines model data and worldwide observations into a global consistent data set using the laws of physics. Data are available on a latitude-longitude grid with a 0.25° horizontal resolution (Hersbach et al., 2020).

2.2. Methodology

2.2.1. Lagrangian Identification of Moisture Sources for Precipitation

By neglecting the impact of mixing with adjacent air parcels and ignoring the presence of liquid water and ice in the atmosphere, moisture changes in an air parcel during a certain time interval ($dt = 6$ hr) are controlled by evaporation (e) and precipitation (p) along the atmospheric particle trajectory (Stohl & James, 2004, 2005) throughout its changes in the specific humidity (q):

$$m \frac{dq}{dt} \approx m \left(\frac{\Delta q}{\Delta t} \right) = (e - p) \quad (1)$$

where m represents the mass of the air parcel (a particle).

For identifying the source of the parcels that produce precipitation in TCs, parcels were individually followed backward in time up to 10 days, which is considered the mean residence time of water vapor in the atmosphere (Numaguti, 1999; van der Ent & Tuinenburg, 2017). According to Läderach and Sodemann (2016), we only considered those parcels in which the specific humidity decreased more than 0.1 g/kg in the 6 hr before arrival at our target regions.

Backward trajectories of precipitant parcels were extracted from the global outputs of the FLEXPART v9.0 model (Stohl et al., 2005, 2016). The model was forced with the ERA-Interim reanalysis data set (Dee et al., 2011) at a resolution of $1^\circ \times 1^\circ$ on the native ECMWF model levels. FLEXPART considers the atmosphere homogeneously divided into approximately 2 million uniformly distributed parcels, which are moved with 3D wind fields. Outputs are available every 6 hr at the initial grid resolution. According to Läderach and Sodemann (2016), the 6 hr-diagnostics preserve better than the 3 hr-diagnostics the consistency of the meteorological fields. Additionally, cycles of evaporation and precipitation within the TC occur quickly. However, outside TC circulation, evaporation and precipitation cycles occur at the time scale of typical tropical processes. Therefore, the 6 hr-diagnostics is suitable for our study because we are interested in the moisture changes of atmospheric parcels along their trajectories before reaching the TC circulation.

Our target regions were defined as the area enclosed by the outer radius of the best track position for each TC. Several authors (e.g., Kilroy & Smith, 2017; Lu et al., 2011; Wu et al., 2015) have used a radius of 34 kt (~ 17 m/s, R_{34kt}) as a metric for the TC size. However, by definition, R_{34kt} is available for TCs that reach the tropical storm wind force or higher. Likewise, the radius of the outermost closed isobar (ROCI) has been used as an estimation of the TC outer radius (e.g., Dean et al., 2009; Kimball & Mulekar, 2004; Wu et al., 2015). Nevertheless, as expected, values are missing for R_{34kt} and ROCI in the first and latest TC records. Recently, Pérez-Alarcón et al. (2021b) developed a new approach to estimate the TC outer radius by using the TC radial wind profile developed by Willoughby et al. (2006), which requires the maximum wind speed and TC position as input parameters. The outer radius was then defined as the radius at which the tangential wind speed estimated from the Willoughby et al. (2006) radial wind profile was equal to or less than 2 m/s. Pérez-Alarcón et al. (2021b) also demonstrated that this estimated outer radius fits well with the outer radius estimated from the ERA-5 reanalysis. Therefore, because we were interested in analyzing the moisture source for all TC positions along its trajectory, we computed the TC size by applying the method of Pérez-Alarcón et al. (2021b). Notably, the cloud pattern of TCs provides a large amount of precipitation in the spiral bands of the system once they appear; thus, reducing the radius of the system would induce the possible loss of areas with convection and intense precipitation that largely depend on the advected water vapor flux that feeds the TC. This fact would lead to underestimation and a less realistic identification of the sources of moisture associated with precipitation.

Although several studies (see Gimeno et al. (2020) and references therein) have used the water budget approach of Stohl and James (2004, 2005) to identify the origin of precipitation, one of the possible limitations of this method is that the precipitation in route between the sources and the target regions leads to a distorted picture of the source locations. Therefore, we followed the moisture source diagnostic method of Sodemann et al. (2008); see complete details in the cited paper. The moisture changes, based on the specific humidity (q) along each forward trajectory in time (from the end to the starting point of the backward trajectory), were assessed, and at a moisture loss location, all prior moisture contributions ($\Delta q > 0$) to the air parcel were discounted in proportion to the moisture loss amount. Hence, the precipitation of the target area is the weighted sum of the prior uptakes (Sodemann et al., 2008). Therefore, the MU of all particles resulting in precipitation along their trajectories was computed as the sum of the moisture contributions over a specific grid cell ($1^\circ \times 1^\circ$, in our study).

$$MU = \frac{m \sum_{k=1}^N \Delta q'_k}{A} \quad (2)$$

where m is the mass of the air parcel (assumed constant), N is the number of air parcels that crossed over a grid cell ($1^\circ \times 1^\circ$) of area A before arriving at the target region, and $\Delta q'$ is the final moisture change (see Equation (7) of Sodemann et al. (2008)) of each parcel over A .

In addition, over several days, an air parcel may undergo multiple cycles of evaporation and precipitation. Therefore, by applying the moisture source diagnostic method of Sodemann et al. (2008), we computed the moisture

contributions of each evaporation location to the final moisture content of each parcel before it precipitates over the target region. Next, to estimate the moisture contributions for the precipitation related to the TC at each position, we averaged all moisture contributions over each grid cell of $1^\circ \times 1^\circ$. Finally, to gain a total point of view of the relative contribution of moisture sources to the TC precipitation along its trajectory, the moisture contributions for all TC positions were summed and then relativized concerning the maximum of that sum. A detailed example of how moisture source contribution was computed is provided in Text S2 of Supporting Information.

It is worth noting that the moisture contributions from the moisture sources were first calculated every 6 hr for each position of the TC trajectory according to the HURDAT2 database, and then, the accumulated MU as the sum of all MUs along the TC trajectory. As a moisture source can supply atmospheric humidity for the precipitation associated with the TC at several TC positions, we focused our attention on the moisture contributions for the total precipitation of the TC during its lifetime by estimating the accumulated MU.

3. Results and Discussion

The 2017 North Atlantic TC season was very active in terms of TC recorded, it was characterized by a developing moderate La Niña and its associated conditions, and by positive SST anomalies over the North Atlantic Ocean (Murakami et al., 2018). The SST anomaly composite during the 2017 TC season was 1.5 standard deviations above normal in the Main Development Region of Atlantic tropical cyclones, a 10° – 20° N latitude belt stretching from North Africa to Central America (Gray et al., 1993). These factors were essential for TC intensification.

Murakami et al. (2018) also pointed out that five of the six TCs studied here (Harvey, Irma, Jose, Lee, and Maria) reached the MH intensity (green line over tracks in Figure 1) over warmer regions during their westward movement. Moreover, according to Stewart (2018), the rare and unusual strength of Ophelia (Figure 1f) was controlled by suitable environmental conditions for TC development. Positive SST anomalies along the trajectory of Ophelia contributed to the pronounced tropospheric lapse rates, supporting the development of vigorous deep convection (Stewart, 2018).

3.1. Spatial Distribution of Precipitation Rate

Precipitation within the outer radius of Hurricane Harvey (Figure 2a) during the first 6–7 days after genesis was small, with precipitation totals less than 45–80 mm. This may have been related to the weakening of Harvey into a tropical wave due to northerly wind shear during its movement through the Caribbean Sea (Blake & Zelinsky, 2018). Harvey reintensified over the Gulf of Mexico, and the accumulated precipitation ranged between 125 and 370 mm near the center (Figure 2a). After making landfall in Texas, the accumulated precipitation reached values higher than 620 mm. Previous studies (Emanuel, 2017) have reported that Harvey produced record levels of rainfall (\sim 1219 mm) in the Houston metropolitan area.

Figure 2b shows the accumulated precipitation along the Irma trajectory. Although Irma was already an MH 48 hr after genesis, the accumulated precipitation was less than 80 mm close to the TC center during that period. After the hurricane reached its maximum intensity near the northern islands of the Lesser Antilles Arc, the precipitation totals reached values higher than 200 mm along the northern coast of Cuba, the Straits of Florida, and the Florida Peninsula. The Institute of Meteorology of Cuba reported an accumulated rainfall of over 250 mm, with the maximum (585 mm) observed in Topes de Collantes, followed by a second record in Sancti Spiritus (490 mm). Over the Florida Peninsula, the accumulated rainfall ranged from 250 to 380 mm, and the storm-total rainfall was \sim 560 mm, measured from September 9 to 12 (Cangialosi et al., 2021).

Hurricanes Jose (Figure 2c) and Maria (Figure 2d) exhibited similar patterns in terms of accumulated precipitation. Heavy rainfall over land from Jose was limited to portions of extreme southeastern Massachusetts, which reported a storm-total rainfall of \sim 172 mm at Nantucket Memorial Airport (Berg, 2018). In the case of Maria, according to Pasch et al. (2019), Dominica experienced torrential rains with a maximum total rainfall of 580 mm, and Puerto Rico recorded values close to 965 mm. Maria also produced heavy rains in Guadeloupe and parts of the Dominican Republic, with a total rainfall of \sim 250–330 mm.

Hurricane Lee (Figure 2e) traveled over the North Atlantic Ocean without making landfall. Accumulated precipitation during most of its trajectory was less than 120 mm. However, some cores ranging from 175 to 290 mm were observed. The accumulated precipitation of Ophelia (Figure 2f) was less than 125 mm during its movement

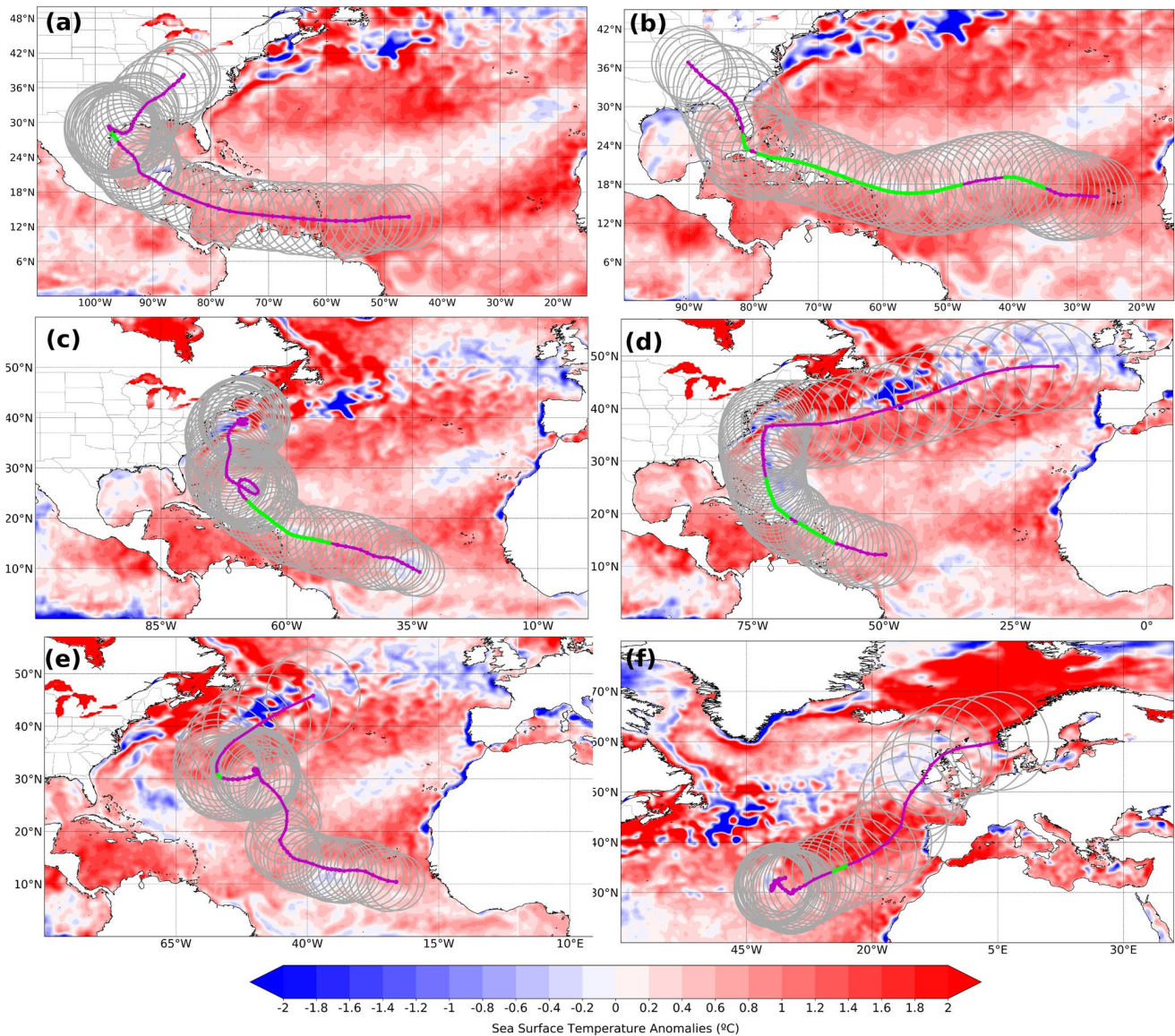


Figure 1. Composite of daily sea surface temperature anomalies (shaded) for each major hurricane (MH) lifetime in 2017: (a) Harvey, (b) Irma, (c) Jose, (d) Maria, (e) Lee and (f) Ophelia. The best track location of each tropical cyclone (TC) is plotted in purple, and the TC outer radius every 6 hr is in gray. The green line over each track represents the time interval at which TCs reached MH intensity.

to the northeast, although slightly higher precipitation totals were observed (150–200 mm), especially in the first days after its genesis. According to Stewart (2018), the remnants of Ophelia produced a total rainfall of less than 50 mm across Ireland and the United Kingdom.

3.2. Identification of the Moisture Sources for Major Hurricanes in 2017

The accumulated MU along the trajectory of each MH reveals the main global moisture sources that result in precipitation (Figure 3). Except for Ophelia, the moisture sources were located over a wide band along the North Atlantic from 10°N to 30°N and longitudinally across the entire basin, extending westward over continental areas into the Sahel. Two marked additional branches completed this field, one from the north along the European and African coasts and another from the South Atlantic Ocean. In addition, the pattern over the southeastern US suggested that a recycling process within the outer radius contributed moisture to maintain the MH over the continent in the case of Harvey and Irma (Figures 1a and 1b).

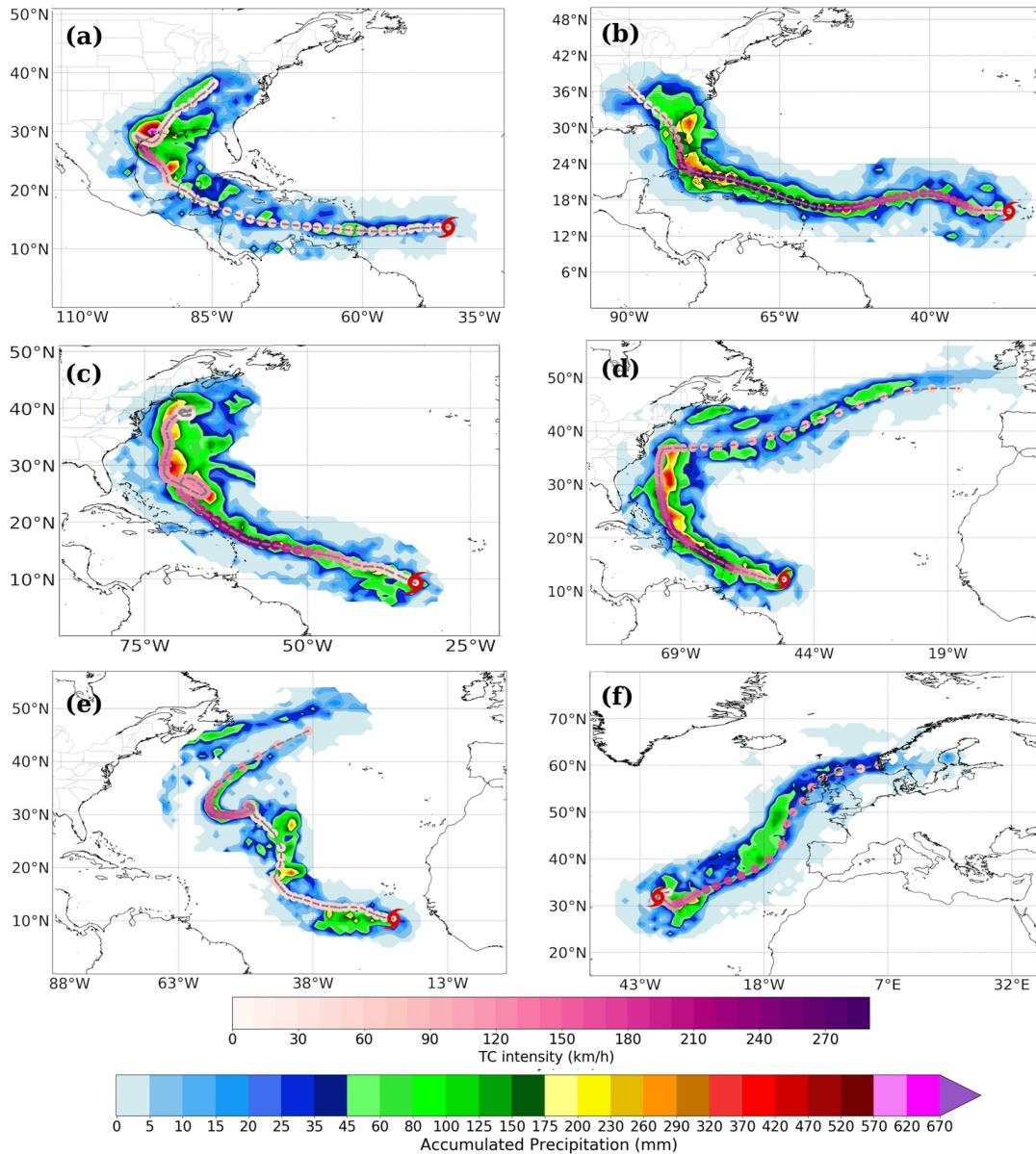


Figure 2. Accumulated precipitation (in mm) from Global Precipitation Measurement within the area enclosed by the tropical cyclone (TC) outer radius along the trajectory of each 2017 major hurricane (MH): (a) Harvey, (b) Irma, (c) Jose, (d) Maria, (e) Lee and (f) Ophelia. TC intensity is represented in shades of purples. The gray dashed line shows the TC trajectory. The red marker represents the genesis location. All plots are from the first to last record for each MH in the HURDAT2 database.

Figure 3 also reveals that the maximum MU was detected near their trajectories when the TCs reached maximum intensity, unlike the regions close to the TC genesis where the contribution from moisture sources is lower. Again, Ophelia did not match this behavior, with maximum MU during the initial days after genesis. Notably, Ophelia also differs from the other MHs in its non-tropical origin (Text S1 of Supporting Information and Stewart, 2018). According to Stewart (2018), Ophelia developed over marginal SSTs to TC intensification, but the mid-level temperatures being cooler than average favored deep convection.

Additionally, the VIMF fields plotted in Figure 3, accompanying the accumulated MU pattern, show that the moisture contribution from the North Atlantic basin was mainly due to the wind around the Bermuda-Azores High, and particularly intensified from the easterly winds along its southern branch and around it. The contribution

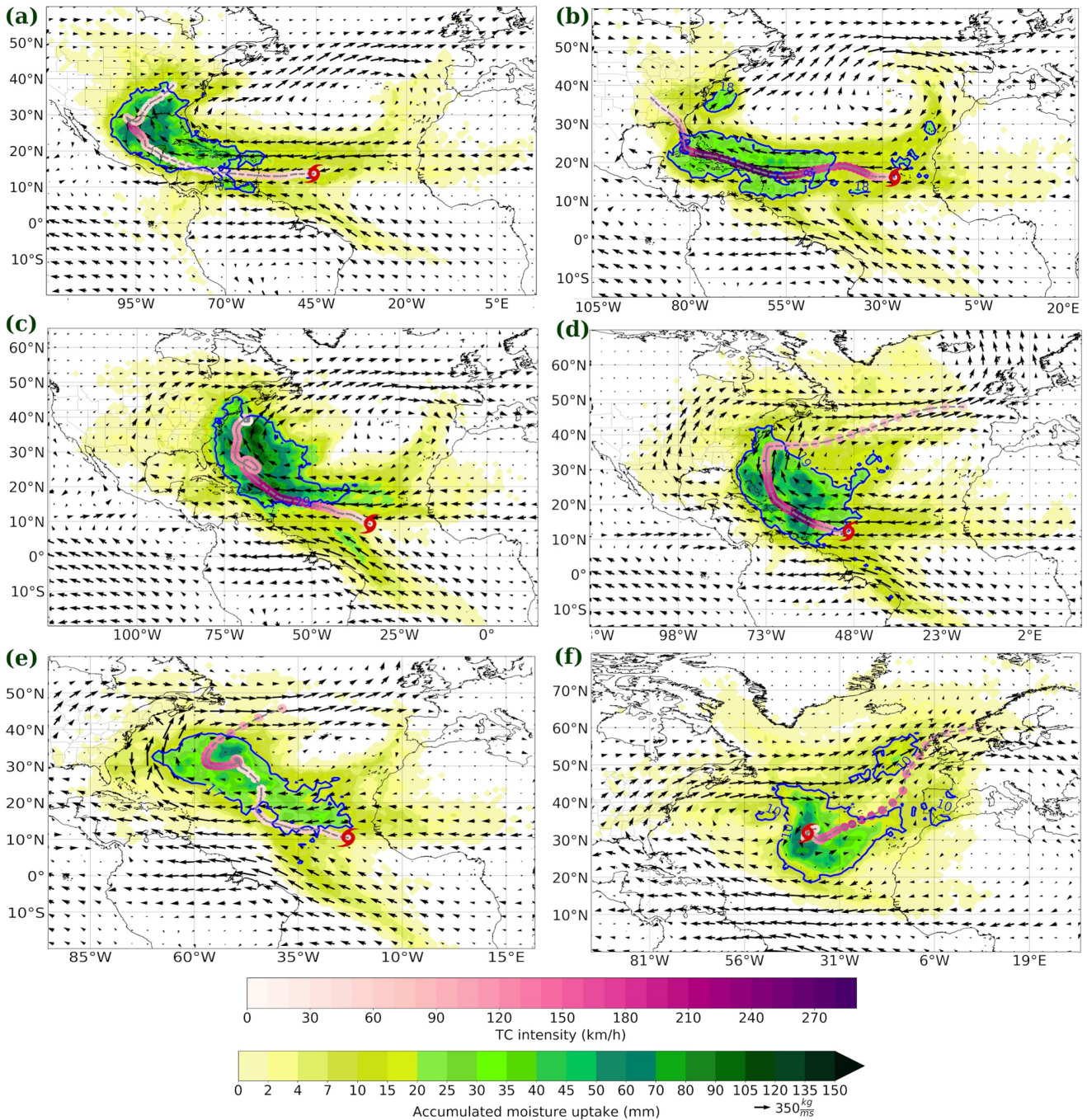


Figure 3. Accumulated moisture uptake (green colors, in mm) along the trajectory of each 2017 North Atlantic major hurricane (MH): (a) Harvey, (b) Irma, (c) Jose, (d) Lee, (e) Maria, and (f) Ophelia. The mean vertical integrated moisture flux (VIMF, kg/ms) from the ERA-5 reanalysis during the tropical cyclones (TCs) lifetime is represented as arrows. The red marker represents the tropical cyclone (TC) genesis location, the gray dashed line shows the trajectory, and the lifetime intensity of each TC is represented in shades of purples (data from HURDAT2 database). The blue line denoted the 90th percentile of the accumulated moisture.

from the South Atlantic Ocean occurred through the northwestward branch of the South Atlantic high-pressure system (SAHS).

Furthermore, of all the TCs studied, Jose exhibited the most intense MU throughout its lifetime, reaching 32,086 mm, which computes to the 90th percentile of the accumulated MU. Maria and Harvey totaled 24,760 and 20,706 mm, respectively, and Irma (12,902 mm) showed a lower uptake. The accumulated MU higher than the

90th percentile (blue contour in Figure 3) generally appeared within approximately 3° to 5° of the TC trajectory, but mostly occurred on the right side of the trajectory (which may be related to the anticlockwise circulation of TCs in the Northern Hemisphere). Previous research (Gao et al., 2017; Trenberth et al., 2007; Wang et al., 2015; Yang et al., 2011) has suggested that the ocean source for water vapor in the inner core is a small portion of the horizontal vapor input.

According to Makarieva et al. (2017), a TC first depletes available atmospheric moisture as it moves controlled by the large-scale flow in which it is embedded, while a moist flow proportional to the TC translation speed converges toward the TC position. This behavior could explain why along the trajectory of each TC, the areas of higher accumulated precipitation mostly coincide with areas of higher accumulated MU (Figures 2 and 3). Moreover, by comparing these patterns with the spatial distribution of accumulated evaporation from the ERA-5 reanalysis within the outer radius along the trajectory of each TC (Figure 4), the higher evaporation regions agree with the higher precipitation and MU areas. Nevertheless, as in the literature was suggested (e.g., Fritz & Wang, 2014; Huang et al., 2014; Makarieva et al., 2017; Yang et al., 2011), evaporation from local sources cannot fully explain TC precipitation. Indeed, the mean ratio between evaporation and precipitation within the outer radius along TC trajectory ranged from 0.43 (Maria) to 0.87 (Ophelia). We also found that this ratio decreased as the TCs intensified (not shown), which can be linked to the strengthening of the low-level convergence associated with the secondary circulation (Fritz & Wang, 2014). In other words, moisture was imported from the outer region (Figure 3).

As aforementioned, the tropical North Atlantic was the main moisture source for MHs that moved westward, but remarkable individual differences existed. The Gulf of Mexico is the most important moisture source for Harvey. The western North Atlantic contributed significantly to the moisture supply for Jose and Maria, and the central North Atlantic provided most of the moisture for Lee and Ophelia.

From Figure 5, the major part of moisture that originated the precipitation after the landfalling event of Harvey and Irma on Texas and Florida Peninsula, respectively, was of ocean origin. For Harvey (Figure 5a), the Gulf of Mexico and the Western Caribbean Sea were the main moisture sources. Nevertheless, the contribution of atmospheric humidity from the southern coast of the US suggested an important recycling process, while the contributions from distant sources were lesser extent. Similarly, for Irma (Figure 5b), the Caribbean Sea south of Cuba, the Straits of Florida, the seas at eastern Bahamas Archipelago, and the western North Atlantic Ocean close to the southeastern coast of US contributed more moisture to Irma's rainfall after landfalling on the Florida Peninsula than further away sources. Note that the MU of Harvey after landfalling was higher than Irma, which is in agreement with the highest accumulated precipitation generated by the former (see Figure 2).

3.3. Moisture Sources Contribution

The moisture contribution from each source region at each time step along the MH trajectories was quantitatively computed using the methodology of Sodemann et al. (2008). These values were added to each MH throughout its lifetime (Text S2 of Supporting Information). Figure 6 shows the percentage of the total SC. Our findings showed that the highest SC close to the trajectory occurred during the maximum intensification phase for the TCs, reaching values over 70% (blues). Based on Lagrangian analysis, for most TCs, the area within the outer radius contributed 35%–45% of the total moisture, while contributions from farther away were less than 30%. Figure 6 also reveals that the eastern tropical Pacific Ocean supplied 10%–20% of the moisture for Harvey. The moisture contribution from the South Atlantic Ocean (SATL) for all MHs accounted for 20%–30% of the total (except for Ophelia, which received no contribution). This result supports the findings of Pazos and Gimeno (2017) and Pérez-Alarcón et al. (2021a), who have identified the SATL as a moisture source during the TC genesis phase near the West African coast but did not quantify this value.

Furthermore, water vapor uptake from continental areas was not negligible. Moisture from the Sahel region accounted for 15%–30% for Irma and Lee but was lower for the remaining MHs (less than $\sim 10\%$). The moisture supplied from continental North America was notable for Harvey (40%–65%) and Irma ($\sim 30\%$) during landfall, and for Jose ($\sim 25\%$) and Maria ($\sim 25\%$) during their parallel movement along the coast. Because Lee occurred far from the eastern coast of North America, land moisture contribution was less than 10%.

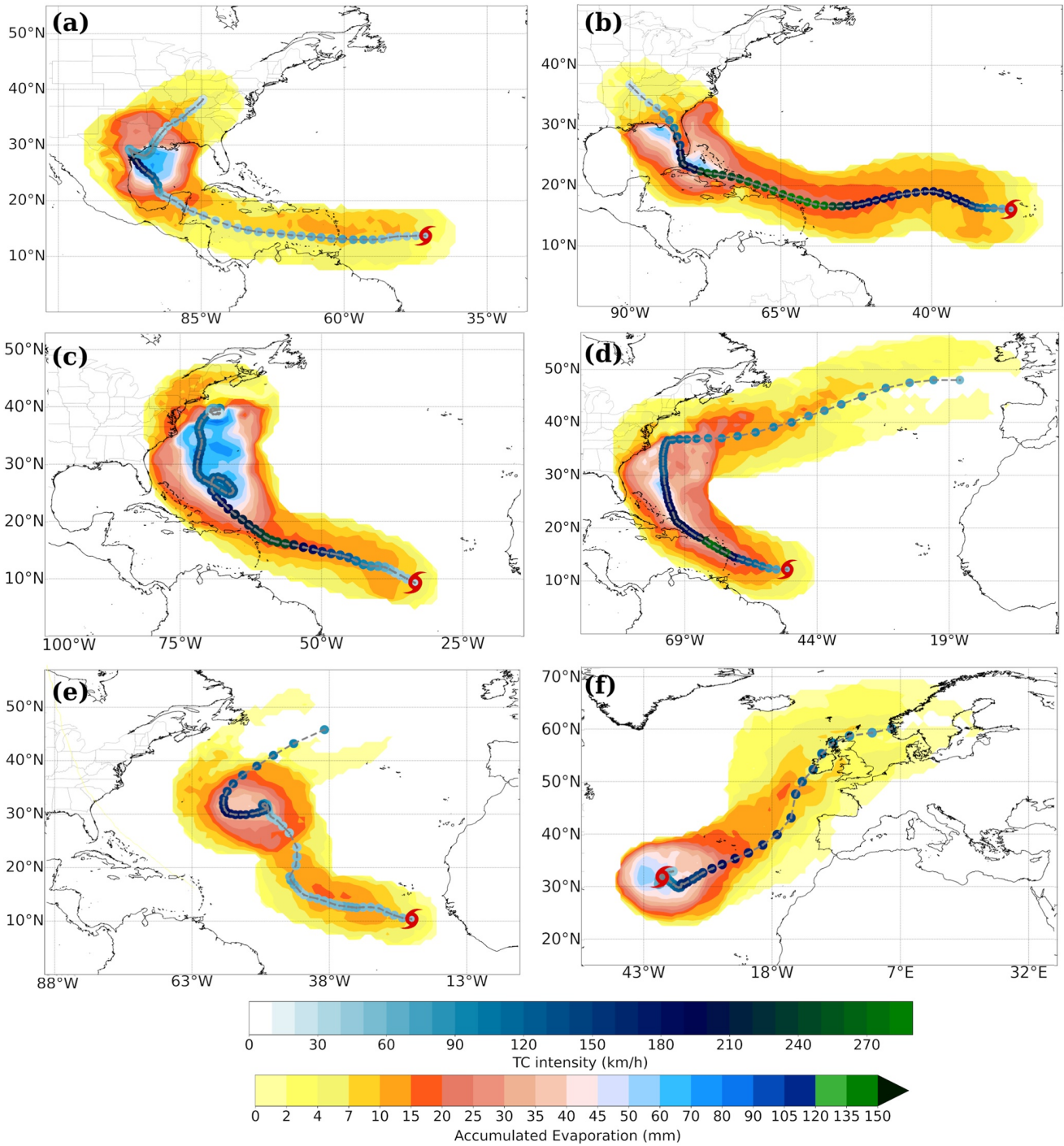


Figure 4. Accumulated evaporation from ERA-5 reanalysis within the area enclosed by the tropical cyclone (TC) outer radius for each 2017 major hurricane (MH): (a) Harvey, (b) Irma, (c) Jose, (d) Maria, (e) Lee, and (f) Ophelia. TC intensity along their trajectory is represented in blue-greens. The gray dashed line shows the TC trajectory. The red marker represents the genesis location. All plots are from the first to last record for each MH in the HURDAT2 database.

3.4. Assessment of the Lagrangian Moisture Source Uptake Diagnostic

The temporal evolution of MU and precipitation rate (R) during the lifetime of each MH indicates a close relationship between both quantities (Figure 7), as discussed. Both values were obtained using different methods. R was obtained from the GPM, and MU was obtained from the global outputs of the FLEXPART model

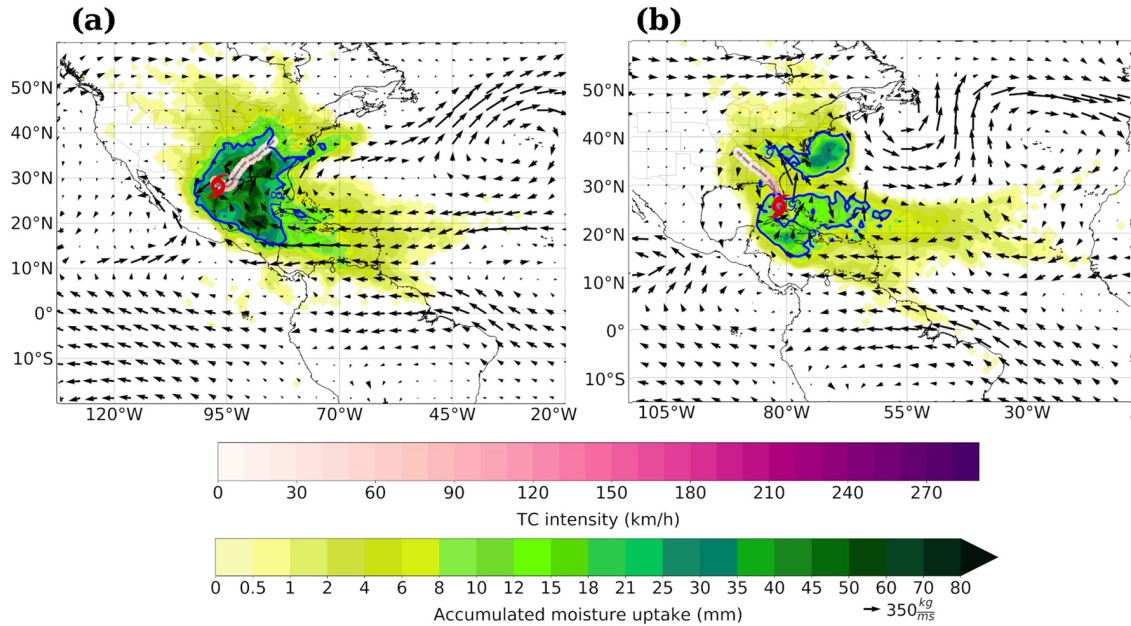


Figure 5. Accumulated moisture uptake (green colors, in mm) after landfalling (a) on Texas (Harvey) and (b) on Florida Peninsula (Irma). The mean vertical integrated moisture flux (VIMF, kg/ms) from the ERA-5 reanalysis after landfalling is represented as arrows. The red marker represents the tropical cyclone (TC) landfalling location, the gray dashed line shows the trajectory after the landfalling, and the lifetime intensity of each TC is represented in shades of purples (data from HURDAT2 database). The blue line denoted the 90th percentile of the accumulated moisture.

by applying the moisture source diagnostic developed by Sodemann et al. (2008). However, these values had a statistically significant Pearson correlation ($p < 0.05$) for all MH except for Maria. The highest Pearson correlation coefficients were found for Irma (0.83) and Harvey (0.66), followed by Ophelia (0.59). For Lee and Jose, the correlations were lower but similar (0.43 and 0.40, respectively). Wu and Chen (2012) demonstrated that the decrease in precipitation of TCs could be explained by a reduction in the ambient water vapor content. As expected, a simple inspection of Figure 7 confirms that the precipitation of these TCs was mainly driven by the moisture supply. These relationships confirm the ability of the moisture source diagnostic method (Sodemann et al., 2008) to quantify and identify the origins of the atmospheric humidity that caused precipitation along the trajectory of TCs, independent of the complex thermodynamic and dynamic processes involved in TCs.

Additionally, no consistent relationships were found between MU and total precipitation before and after maximum intensity. Differences observed between the temporal evolution of the precipitation rate (R) and the MU that originated the precipitation can be attributed to neglecting the Lagrangian approach for the complex processes that cause moisture changes, such as convection, turbulence, numerical diffusion, and rainwater evaporation (Sodemann et al., 2008).

4. Summary and Conclusions

The 2017 North Atlantic TC season was one of the most active in the last two decades since 2000, with 17 named storms and 10 hurricanes, six of which reached the category of a MH. The six MHs followed three pathways: two (MHs Harvey and Irma) moved in straightforwardly from the African coast to the Gulf of Mexico before recurving northward across the US coast, two (MHs Jose and Maria) recurved and bordered the US East Coast, and two (MHs Lee and Ophelia) recurved northward over the middle of the ocean and did not make landfall.

We analyzed the moisture sources that resulted in precipitation for the six 2017 MHs by using a Lagrangian approach. The particle dispersion model FLEXPART, along with the ERA-Interim reanalysis, was used to determine the moisture sources for each position of the best track of the MHs.

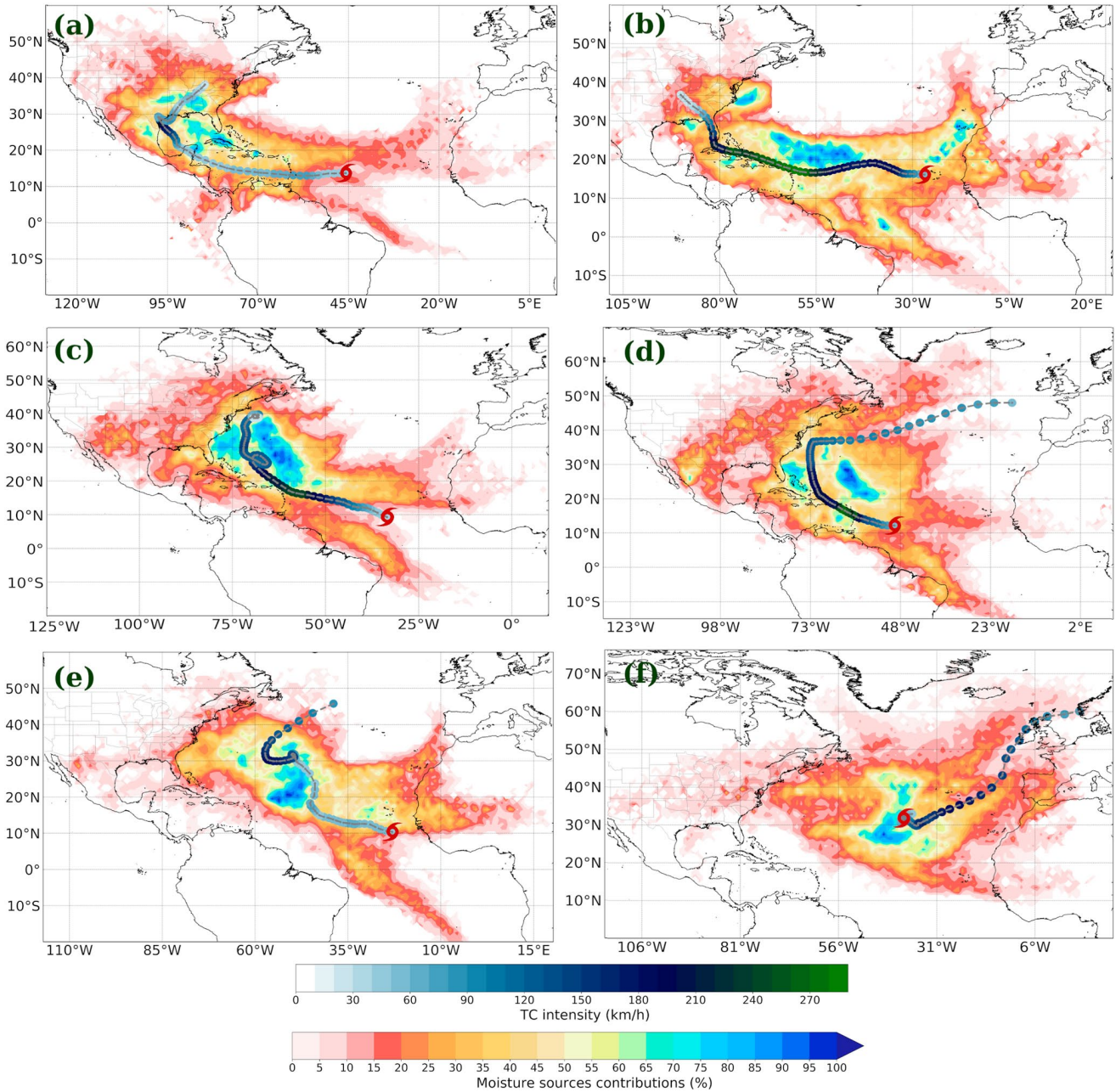


Figure 6. Moisture sources' contribution (in percent) during each 2017 major hurricane (MH) lifetime: (a) Harvey, (b) Irma, (c) Jose, (d) Maria, (e) Lee, and (f) Ophelia. The MH lifetime intensity is represented in blue-greens along the trajectory; the red marker represents the genesis location. All plots are from the first to last record of each MH in the HURDAT2 database.

The main moisture sources for Harvey and Irma were the tropical North Atlantic Ocean, the Caribbean Sea, and the Gulf of Mexico, providing approximately 85% of the total moisture. The western North Atlantic Ocean provided approximately 75%–80% for Jose and Maria. The central North Atlantic Ocean supplied similar amounts to Lee and Ophelia. In general, a higher MU was observed on the right side of the trajectory and during the maximum intensity phase of each TC. Additionally, on average, as a moisture source, the South Atlantic Ocean contributed ~14%–20%, and the tropical eastern Pacific Ocean contributed ~1%–5%. On average, higher MU occurred within approximately 3° to 5° of the TC trajectories.

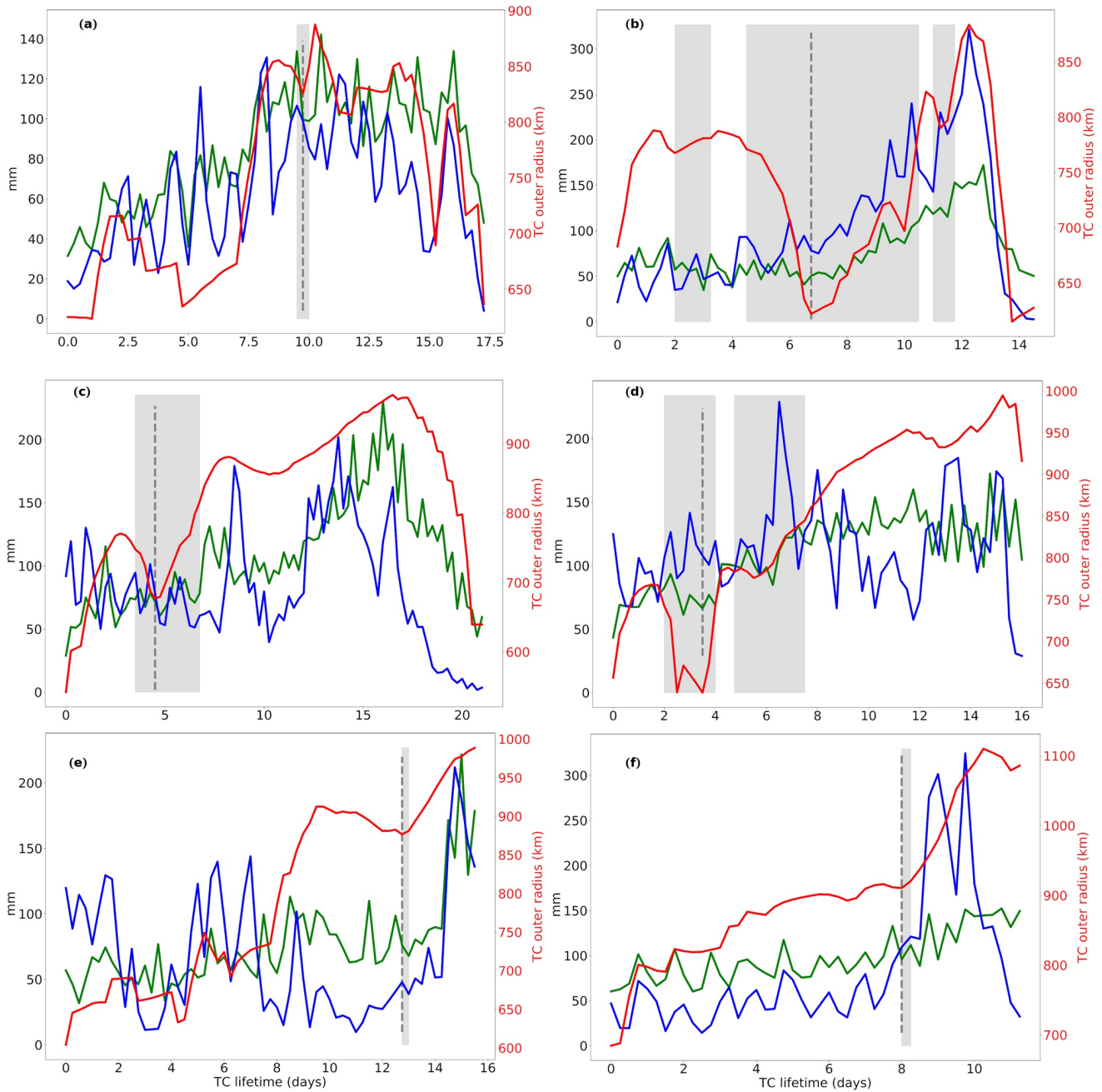


Figure 7. Temporal evolution (at 6 hr time steps) of total moisture uptake (green line, mm) from the Lagrangian approach, precipitation rate (blue line, mm) from Global Precipitation Measurement, and the TC outer radius (red line, km) during 2017 major hurricanes (MH) lifetimes: (a) Harvey, (b) Irma, (c) Jose, (d) Maria, (e) Lee, and (f) Ophelia. Total moisture uptake was calculated as the sum of all grid point values at each 6 hr time step. The vertical gray dashed line represents the time at which each TC reached the maximum intensity, and the gray shaded areas represent the time interval at which each TC was in the MH category.

Our results also reveal that the Lagrangian moisture precipitation source diagnostic method applied in this study is a suitable tool to provide useful information on the geographical position of these moisture sources and quantify precipitation from TCs. Nevertheless, this work analyzed six TCs and therefore does not provide a climatological view of the moisture sources of TC-related precipitation in this basin. In further research, a similar analysis should consider the total number of systems with different intensities over the Atlantic Ocean basin and focus on the contribution of TCs to the hydrological cycle over continents.

Data Availability Statement

The data sets used in this study are freely available on the internet. The Optimum Interpolation Sea Surface Temperature (OISST) data provided by the NOAA/NCDC were obtained from <https://www.ncdc.noaa.gov/oisst>, HURDAT2 database is accessible from <https://www.nhc.noaa.gov/data/#hurdat>, the ERA-5 reanalysis data set was extracted from <https://www.ecmwf.int/en/forecasts/datasets/reanalysis-datasets/era5>, and the GPM data set is available at <https://gpm.nasa.gov/data/directory>. The FLEXPART model can be downloaded from <https://www.flexpart.eu/wiki/FpRoadmap>.

Acknowledgments

A.P.-A. acknowledges support from the UVigo PhD grants. J.C.F.-A. and R.S. acknowledge support from the Xunta de Galicia (Galician Regional Government) under grants No. ED481A2020/193 and ED481B2019/070, respectively. We acknowledge the funding for open access from the Universidade de Vigo/Consortio Interuniversitario do Sistema Universitario de Galicia. This study received support from the LAGRIMA project (grant no. RTI2018-095772-B-I00) funded by the Ministerio de Ciencia, Innovación y Universidades, Spain and partial support from the Xunta de Galicia under the Project ED431C2021/44 (Programa de Consolidación e Estructuración de Unidades de Investigación Competitivas (Grupos de Referencia Competitiva) and Consellería de Cultura, Educación e Universidade). This work has also been supported by the computing resources and technical support provided by the Centro de Supercomputación de Galicia (CESGA). The authors also thank to Christopher W. Landsea and two anonymous reviewers for their comments and suggestions to improve the manuscript.

References

- Algarra, I., Eiras-Barca, J., Nieto, R., & Gimeno, L. (2019). Global climatology of nocturnal low-level jets and associated moisture sources and sinks. *Atmospheric Research*, 229, 39–59. <https://doi.org/10.1016/j.atmosres.2019.06.016>
- Algarra, I., Nieto, R., Ramos, A. M., Eiras-Barca, J., Trigo, R. M., & Gimeno, L. (2020). Significant increase of global anomalous moisture uptake feeding landfalling Atmospheric Rivers. *Nature Communications*, 11, 5082. <https://doi.org/10.1038/s41467-020-18876-w>
- Alvey, G. R., Zawislak, J., & Zipser, E. (2015). Precipitation properties observed during tropical cyclone intensity change. *Monthly Weather Review*, 143, 4476–4492. <https://doi.org/10.1175/MWR-D-15-0065.1>
- Banzon, V., Smith, T., Steele, M., Huang, B., & Zhang, H.-M. (2020). Improved estimation of proxy sea surface temperature in the Arctic. *Journal of Atmospheric and Oceanic Technology*, 37(2), 341–349. <https://doi.org/10.1175/JTECH-D-19-0177.1>
- Berg, R. (2018). *National hurricane center tropical cyclone report: Hurricane Jose*. National Weather Service: National Oceanic and Atmospheric Administration. Retrieved from https://www.nhc.noaa.gov/data/tcr/AL122017_Jose.pdf
- Blake, E. S., & Zelinsky, D. A. (2018). *National hurricane center tropical cyclone report: Hurricane Harvey*. National Weather Service: National Oceanic and Atmospheric Administration. Retrieved from https://www.nhc.noaa.gov/data/tcr/AL092017_Harvey.pdf
- Braun, S. A. (2006). High-resolution simulation of Hurricane Bonnie (1998). Part II: Water budget. *Journal of the Atmospheric Sciences*, 63, 43–64. <https://doi.org/10.1175/JAS3609.1>
- Braun, S. A., Sippel, J. A., & Nolan, D. S. (2012). The impact of dry mid-level air on hurricane intensity in idealized simulations with no mean flow. *Journal of the Atmospheric Sciences*, 69, 236–257. <https://doi.org/10.1175/JAS-D-10-05007.1>
- Braz, D. F., Ambrizzi, T., Porfírio da Rocha, R., Algarra, I., Nieto, R., & Gimeno, L. (2021). Assessing the moisture transports associated with nocturnal low-level jets in continental south America. *Frontiers in Environmental Science*, 9, 108. <https://doi.org/10.3389/fenvs.2021.657764>
- Cangialosi, J. P., Latto, A. S., & Berg, R. (2021). *National hurricane center tropical cyclone report: Hurricane Irma*. National Oceanic and Atmospheric Administration. Retrieved from https://www.nhc.noaa.gov/data/tcr/AL112017_Irma.pdf
- Chauvin, F., Douville, H., & Ribes, A. (2017). Atlantic tropical cyclones water budget in observations and CNRM-CM5 model. *Climate Dynamics*, 49, 4009–4021. <https://doi.org/10.1007/s00382-017-3559-3>
- Chen, D. L., Ou, T. H., Gong, L., Xu, C.-Y., Li, W. J., Ho, C.-H., & Qian, W. H. (2010). Spatial interpolation of daily precipitation in China: 1951–2005. *Advances in Atmospheric Sciences*, 27, 1221–1232. <https://doi.org/10.1007/s00376-010-9151-y>
- Cloux, S., Garaboa-Paz, D., Insua-Costa, D., Miguez-Macho, G., & Pérez-Muñuzuri, V. (2021). Extreme precipitation events in the Mediterranean area: Contrasting Lagrangian and Eulerian models for moisture sources identification. *Hydrology and Earth System Sciences*, 25, 6465–6477. <https://doi.org/10.5194/hess-25-6465-2021>
- Dean, L., Emanuel, K. A., & Chavas, D. R. (2009). On the size distribution of Atlantic tropical cyclones. *Geophysical Research Letters*, 36, L14803. <https://doi.org/10.1029/2009>
- Dee, D. P., Uppala, S. M., Simmons, S. J., Berrisford, P., Poli, P., Kobayashi, S., et al. (2011). The ERA-Interim reanalysis: Configuration and performance of the data assimilation system. *Quarterly Journal of the Royal Meteorological Society*, 137, 553–597. <https://doi.org/10.1002/qj.828>
- Dunion, J. P., & Velden, C. S. (2004). The impact of the Saharan air layer on Atlantic tropical cyclone activity. *Bulletin of the American Meteorological Society*, 85, 353–365. <https://doi.org/10.1175/BAMS-85-3-353>
- Emanuel, K., DesAutels, C., Holloway, C., & Korty, R. (2004). Environmental control of tropical cyclone intensity. *Journal of the Atmospheric Sciences*, 61, 843–858. [https://doi.org/10.1175/1520-0469\(2004\)061<0843:ECOTCI>2.0.CO;2](https://doi.org/10.1175/1520-0469(2004)061<0843:ECOTCI>2.0.CO;2)
- Emanuel, K. A. (1987). The dependence of hurricane intensity on climate. *Nature*, 326, 483–485.
- Emanuel, K. A. (2017). Assessing the present and future probability of Hurricane Harvey's rainfall. *Proceedings of the National Academy of Sciences*, 114(48), 12681–12684. <https://doi.org/10.1073/pnas.1716222114>
- Fritz, C., & Wang, Z. (2013). A numerical study of the impacts of dry air on tropical cyclone formation: A development case and a nondevelopment case. *Journal of the Atmospheric Sciences*, 70(1), 91–111. <https://doi.org/10.1175/JAS-D-12-018.1>
- Fritz, C., & Wang, Z. (2014). Water vapor budget in a developing tropical cyclone and its implication for tropical cyclone formation. *Journal of the Atmospheric Sciences*, 71(11), 4321–4332. <https://doi.org/10.1175/JAS-D-13-0378.1>
- Gao, S., Zhai, S., Chen, B., & Li, T. (2017). Water budget and intensity change of tropical cyclones over the western North Pacific. *Monthly Weather Review*, 145, 3009–3023. <https://doi.org/10.1175/MWR-D-17-0033.1>
- Gao, S., Zhang, W., Liu, J., Lin, I.-I., Chiu, L. S., & Cao, K. (2016). Improvement in typhoon intensity change classification by incorporating an ocean coupling potential intensity index into decision trees. *Weather and Forecasting*, 31, 95–106. <https://doi.org/10.1175/WAF-D-15-0062.1>
- Ge, X., Li, T., & Peng, M. (2013). Effects of vertical shears and midlevel dry air on tropical cyclone developments. *Journal of the Atmospheric Sciences*, 70, 3859–3875. <https://doi.org/10.1175/JAS-D-13-066.1>
- Gimeno, L., Stohl, A., Trigo, R. M., Dominguez, F., Yoshimura, K., Yu, L., et al. (2012). Oceanic and Terrestrial sources of continental precipitation. *Reviews of Geophysics*, 50, RG4003. <https://doi.org/10.1029/2012RG000389>
- Gimeno, L., Vázquez, M., Eiras-Barca, J., Sorí, R., Stojanovic, M., Algarra, I., et al. (2020). Recent progress on the sources of continental precipitation as revealed by moisture transport analysis. *Earth-Science Reviews*, 103070, 1–25. <https://doi.org/10.1016/j.earscirev.2019.103070>
- Gray, W. M. (1968). A global view of the origin of tropical disturbances and storms. *Monthly Weather Review*, 96, 669–700. [https://doi.org/10.1175/1520-0493\(1968\)096<0669:GVOTOO>2.0.CO;2](https://doi.org/10.1175/1520-0493(1968)096<0669:GVOTOO>2.0.CO;2)
- Gray, W. M., Landsea, C. W., Mielke, P. W., Jr., & Berry, K. J. (1993). Predicting Atlantic seasonal tropical cyclone activity by 1 August. *Weather and Forecasting*, 8, 73–86. [https://doi.org/10.1175/1520-0434\(1993\)008<0073:PABSTC>2.0.CO;2](https://doi.org/10.1175/1520-0434(1993)008<0073:PABSTC>2.0.CO;2)
- Guo, L., Klingaman, N. P., Vidale, P. L., Turner, A. G., Demory, M.-E., & Cobb, A. (2017). Contribution of tropical cyclones to atmospheric moisture transport and rainfall over East Asia. *Journal of Climate*, 30, 3853–3865. <https://doi.org/10.1175/jcli-d-16-0308.1>

- Hersbach, H., Bell, B., Berrisford, P., Hirahara, S., Horányi, A., Muñoz-Sabater, J., et al. (2020). The ERA5 global reanalysis. *Quarterly Journal of the Royal Meteorological Society*, *146*, 1999–2049. <https://doi.org/10.1002/qj.3803>
- Hill, K. A., & Lackmann, G. M. (2009). Influence of environmental humidity on tropical cyclone size. *Monthly Weather Review*, *137*, 3294–3315. <https://doi.org/10.1175/2009MWR2679.1>
- Huang, H., Yang, M., & Sui, C. (2014). Water budget and precipitation efficiency of typhoon Morakot (2009). *Journal of the Atmospheric Sciences*, *71*, 112–129. <https://doi.org/10.1175/JAS-D-13-053.1>
- Huffman, G., Stocker, E., Bolvin, D., Nelkin, E. & Tan, J. (2019). *GPM IMERG early precipitation L3 half hourly 0.1 degree x 0.1 degree V06, green-belt, MD, Goddard Earth Sciences Data and Information Services Center (GES DISC)*. <https://doi.org/10.5067/GPM/IMERG/3B-HH-E/06>
- Jaimes, B., Shay, L. K., & Uhlhorn, E. U. (2015). Enthalpy and momentum fluxes during Hurricane Earl relative to underlying ocean features. *Monthly Weather Review*, *143*, 111–131. <https://doi.org/10.1175/MWR-D-13-00277.1>
- Jiang, H., & Zipsper, E. J. (2010). Contribution of tropical cyclones to the global precipitation from eight seasons of TRMM data: Regional, seasonal, and interannual variations. *Journal of Climate*, *23*, 1526–1543. <https://doi.org/10.1175/2009JCLI3303.1>
- Kilroy, G., & Smith, R. K. (2017). The effects of initial vortex size on tropical cyclogenesis and intensification. *Quarterly Journal of the Royal Meteorological Society*, *143*, 2832–2845. <https://doi.org/10.1002/qj.3134>
- Kim, D., Ho, C., Murakami, H., & Park, D. R. (2021). Assessing the influence of large-scale environmental conditions on the rainfall structure of Atlantic tropical cyclones: An observational study. *Journal of Climate*, *34*(6), 2093–2106. <https://doi.org/10.1175/JCLI-D-20-0376.1>
- Kimball, S. K. (2006). A modeling study of hurricane landfall in a dry environment. *Monthly Weather Review*, *134*, 1901–1918. <https://doi.org/10.1175/MWR3155.1>
- Kimball, S. K., & Mulekar, M. S. (2004). A 15-year climatology of North Atlantic tropical cyclones. Part I: Size parameters. *Journal of Climate*, *17*, 3555–3575. [https://doi.org/10.1175/1520-0442\(2004\)017<3555:AYCONA>2.0.CO](https://doi.org/10.1175/1520-0442(2004)017<3555:AYCONA>2.0.CO)
- Knabb, R. D., Rhome, J. R., & Brown, D. P. (2005). *National hurricane center tropical cyclone report: Hurricane Katrina*. National Oceanic and Atmospheric Administration. Retrieved from https://www.nhc.noaa.gov/data/tcr/AL122005_Katrina.pdf
- Knippertz, P., Wernli, H., & Glaser, G. (2013). A global climatology of tropical moisture. *Journal of Climate*, *26*, 3031–3045. <https://doi.org/10.1175/JCLI-D-12-00401.1>
- Knutson, T. R., Sirutis, J. J., Zhao, M., Tuleya, R. E., Bender, M., Vecchi, G. A., et al. (2015). Global projections of intense tropical cyclone activity for the late twenty-first century from dynamical downscaling of CMIP5/RCP4.5 scenarios. *Journal of Climate*, *28*(18), 7203–7224. <https://doi.org/10.1175/JCLI-D-15-0129.1>
- Kossin, J. P., Knapp, K. R., Olander, L. T., & Velden, C. S. (2020). Global increase in major tropical cyclone exceedance probability over the past four decades. *Proceedings of the National Academy of Sciences*, *117*, 11975–11980. <https://doi.org/10.1073/pnas.1920849117>
- Kummerow, C. D., Randel, D. L., Kulie, M., Wang, N. Y., Ferraro, R., Munchak, J. S., & Petkovic, V. (2015). The evolution of the goddard profiling algorithm to a fully parametric scheme. *Journal of Atmospheric and Oceanic Technology*, *32*, 2265–2280. <https://doi.org/10.1175/JTECH-D-15-0039.1>
- Läderach, A., & Sodemann, H. (2016). A revised picture of the atmospheric moisture residence time. *Geophysical Research Letters*, *43*, 924–933. <https://doi.org/10.1002/2015GL067449>
- Landsea, C. W., & Franklin, J. L. (2013). Atlantic hurricane database uncertainty and presentation of a new database format. *Monthly Weather Review*, *141*, 3576–3592. <https://doi.org/10.1175/MWR-D-12-00254.1>
- Larson, J., Zhou, Y., & Higgins, R. W. (2005). Characteristics of landfalling tropical cyclones in the United States and Mexico: Climatology and interannual variability. *Journal of Climate*, *18*, 1247–1262. <https://doi.org/10.1175/JCLI3317.1>
- Liberato, M. L. R., Ramos, A. M., Trigo, R. M., Trigo, I. F., Durán-Quesada, A. M., Nieto, R., & Gimeno, L. (2012). Moisture sources and large-scale dynamics associated with a flash flood event. In J. Lin, D. Brunner, C. Gerbig, A. Stohl, A. Luhar, & P. Webley (Eds.), *Lagrangian modeling of the atmosphere*. American Geophysical Union. <https://doi.org/10.1029/2012GM001244>
- Lin, Y., Zhao, M., & Zhang, M. (2015). Tropical cyclone rainfall area controlled by relative sea surface temperature. *Nature Communications*, *6*, 6591. <https://doi.org/10.1038/ncomms7591>
- Lu, X., Yu, H., & Lei, X. (2011). Statistics for size and radial wind profile of tropical cyclones in the western North Pacific. *Acta Meteorologica Sinica*, *25*, 104–112. <https://doi.org/10.1007/s13351-011-0008-9>
- Makarieva, A. M., Gorshkov, V. G., Nefiodov, A. V., Chikunov, A. V., Sheil, D., Nobre, A. D., & Li, B. L. (2017). Fuel for cyclones: The water vapor budget of a hurricane as dependent on its movement. *Atmospheric Research*, *193*, 216–230. <https://doi.org/10.1016/j.atmosres.2017.04.006>
- Matyas, C. J. (2010). Associations between the size of hurricane rain fields at landfall and their surrounding environments. *Meteorology and Atmospheric Physics*, *106*, 135–148. <https://doi.org/10.1007/s00703-009-0056-1>
- Miralles, D. G., Nieto, R., McDowell, N. G., Dorigo, W., Verhoest, N. E. C., Liu, Y. L., et al. (2016). Contribution of water-limited ecoregions to their own supply of rainfall. *Environmental Research Letters*, *11*, 124007. <https://doi.org/10.1088/1748-9326/11/12/124007>
- Montgomery, M. T., & Smith, R. K. (2017). Recent developments in the fluid dynamics of tropical cyclones. *Annual Review of Fluid Mechanics*, *49*, 541–574. <https://doi.org/10.1146/annurev-fluid-010816-060022>
- Murakami, H., Levin, E., Delworth, T. L., Gudgel, R., & Hsu, P.-C. (2018). Dominant effect of relative tropical Atlantic warming on major hurricane occurrence. *Science*, *362*, 794–799. <https://doi.org/10.1126/science.aat6711>
- Nieto, R., Castillo, R., Drummond, A., & Gimeno, L. (2014). A catalog of moisture sources for continental climatic regions. *Water Resources Research*, *50*, 5325–5328. <https://doi.org/10.1002/2013WR013901>
- Numaguti, A. (1999). Origin and recycling processes of precipitating water over the Eurasian continent: Experiments using an atmospheric general circulation model. *Journal of Geophysical Research*, *104*, 1957–1972. <https://doi.org/10.1029/1998JD200026>
- Papritz, L., Aemisegger, F., & Wernli, H. (2021). Sources and transport pathways of precipitating waters in cold-season deep North Atlantic cyclones. *Journal of the Atmospheric Sciences*, *78*(10), 3349–3368. <https://doi.org/10.1175/JAS-D-21-0105.1>
- Pasch, R. J., Blake, E. S., Cobb, H. D., III., & Roberts, D. P. (2006). *National hurricane center tropical cyclone report: Hurricane Katrina*. National Oceanic and Atmospheric Administration. Retrieved from https://www.nhc.noaa.gov/data/tcr/AL252005_Wilma.pdf
- Pasch, R. J., Penny, A. B., & Berg, R. (2019). *National hurricane center tropical cyclone report: Hurricane Maria*. National Oceanic and Atmospheric Administration. Retrieved from https://www.nhc.noaa.gov/data/tcr/AL152017_Maria.pdf
- Patricola, C. M., & Wehner, M. F. (2018). Anthropogenic influences on major tropical cyclone events. *Nature*, *563*, 339–346. <https://doi.org/10.1038/s41586-018-0673-2>
- Pazos, M., & Gimeno, L. (2017). Identification of moisture sources in the Atlantic Ocean for cyclogenesis processes. *Proceedings of the 1st International Electronic Conference on Hydrological Cycle (ChyCle-2017)* (Vol. 1). Sciforum Electronic Conference Series. <https://doi.org/10.3390/chycle-2017-04862>

- Pérez-Alarcón, A., Sorí, R., Fernández-Alvarez, J. C., Nieto, R., & Gimeno, L. (2021a). Moisture sources for tropical cyclones genesis in the coast of West Africa through a Lagrangian approach. *Environmental Sciences Proceeding*, 4, 3. <https://doi.org/10.3390/ecas2020-08126>
- Pérez-Alarcón, A., Sorí, R., Fernández-Alvarez, J. C., Nieto, R., & Gimeno, L. (2021b). Comparative climatology of outer tropical cyclone size using radial wind profiles. *Weather and Climate Extremes*, 33, 100366. <https://doi.org/10.1016/j.wace.2021.100366>
- Prat, O. P., & Nelson, B. R. (2013). Mapping the world's tropical cyclone rainfall contribution over land using the TRMM Multi-satellite Precipitation Analysis. *Water Resources Research*, 49, 7236–7254. <https://doi.org/10.1002/wrcr.20527>
- Ramos, A. M., Blamey, R. C., Algarra, I., Nieto, R., Gimeno, L., Tomé, R., et al. (2019). From Amazonia to southern Africa: Atmospheric moisture transport through low-level jets and atmospheric rivers. *Annals of the New York Academy of Sciences*, 1436, 217–230. <https://doi.org/10.1111/nyas.13960>
- Ramos, A. M., Nieto, R., Tomé, R., Gimeno, L., Trigo, R. M., Liberato, M. L. R., & Lavers, D. A. (2016). Atmospheric rivers moisture sources from a Lagrangian perspective. *Earth System Dynamics*, 7, 371–384. <https://doi.org/10.5194/esd-7-371-2016>
- Randel, D., Kummerow, C., & Ringerud, S. (2020). The Goddard Profiling (GPROF) precipitation retrieval algorithm. In V. Levizzani, C. Kidd, D. Kirschbaum, C. Kummerow, K. Nakamura, & F. Turk (Eds.), *Satellite precipitation measurement* (pp. 141–152). Springer. https://doi.org/10.1007/978-3-030-24568-9_8
- Scoccimarro, E., Gualdi, S., Villarini, G., Vecchi, G. A., Zhao, M., Walsh, K., & Navarra, A. (2014). Intense precipitation events associated with landfalling tropical cyclones in response to a warmer climate and increased CO₂. *Journal of Climate*, 27(12), 4642–4654. <https://doi.org/10.1175/JCLI-D-14-00065.1>
- Sodemann, H., Schwierz, C., & Wernli, H. (2008). Interannual variability of Greenland winter precipitation sources: Lagrangian moisture diagnostic and north Atlantic oscillation influence. *Journal of Geophysical Research*, 113, D03107. <https://doi.org/10.1029/2007JD008503>
- Sprenger, M., & Wernli, H. (2015). The LAGRANTO Lagrangian analysis tool-Version 2.0. *Geoscientific Model Development*, 8, 2569–2586. <https://doi.org/10.5194/gmd-8-2569-2015>
- Stewart, S. R. (2018). *National hurricane center tropical cyclone report: Hurricane Ophelia*. National Oceanic and Atmospheric Administration. Retrieved from https://www.nhc.noaa.gov/data/tcr/AL172017_Ophelia.pdf
- Stohl, A., Forster, C., Frank, A., Seibert, P., & Wotawa, G. (2005). Technical note: The Lagrangian particle dispersion model FLEXPART version 6.2. *Atmospheric Chemistry and Physics*, 5, 2461–2474. <https://doi.org/10.5194/acp-5-2461-2005>
- Stohl, A., & James, P. A. (2004). Lagrangian analysis of the atmospheric branch of the global water cycle. Part I: Method description, validation, and demonstration for the August 2002 flooding in central Europe. *Journal of Hydrometeorology*, 5, 6562–6678. [https://doi.org/10.1175/1525-7541\(2004\)005<0656:alaota>2.0.co;2](https://doi.org/10.1175/1525-7541(2004)005<0656:alaota>2.0.co;2)
- Stohl, A., & James, P. A. (2005). Lagrangian analysis of the atmospheric branch of the global water cycle. Part II: Moisture transports between the Earth's ocean basins and river catchments. *Journal of Hydrometeorology*, 6, 961–984. <https://doi.org/10.1175/JHM470.1>
- Stohl, A., Sodemann, H., Eckhardt, S., Frank, A., Seibert, P., Wotawa, G., et al. (2016). The Lagrangian particle dispersion model FLEXPART version 9.3. Available online at <https://www.flexpart.eu/export/496c6079149f12fbb3e7ecf1f351470794679655/flexpart.git/doc/latex-manual/flexpart9.3.pdf>
- Tao, C., Jiang, H., & Zawislak, J. (2017). The relative importance of stratiform and convective rainfall in rapidly intensifying tropical cyclones. *Monthly Weather Review*, 145, 795–809. <https://doi.org/10.1175/MWR-D-16-0316.1>
- Tao, D., & Zhang, F. (2014). Effect of environmental shear, sea-surface temperature, and ambient moisture on the formation and predictability of tropical cyclones: An ensemble-mean perspective. *Journal of Advances in Modeling Earth Systems*, 6, 384–404. <https://doi.org/10.1002/2014MS000314>
- Trenberth, K. E., Davis, C. A., & Fasullo, F. (2007). Water and energy budgets of hurricanes: Case studies of Ivan and Katrina. *Journal of Geophysical Research*, 112, 3106. <https://doi.org/10.1029/2006JD008303>
- van der Ent, R. J., & Tuinenburg, O. (2017). A. The residence time of water in the atmosphere revisited. *Hydrology and Earth System Sciences*, 21, 779–790. <https://doi.org/10.5194/hess-21-779-2017>
- Vannière, B., Roberts, M., Vidale, P. L., Hodges, K., Demory, M., Caron, L., et al. (2020). The moisture budget of tropical cyclones in High-ResMIP models: Large-scale environmental balance and sensitivity to horizontal resolution. *Journal of Climate*, 33(19), 8457–8474. <https://doi.org/10.1175/JCLI-D-19-0999.1>
- Vázquez, M., Nieto, R., Liberato, M. L. R., & Gimeno, L. (2020). Atmospheric moisture sources associated with extreme precipitation during the peak precipitation month. *Weather and Climate Extremes*, 30, 100289. <https://doi.org/10.1016/j.wace.2020.100289>
- Wachnicka, A., Armitage, A. R., Zink, I., Browder, J., & Fourqurean, J. W. (2020). Major 2017 hurricanes and their cumulative impacts on coastal waters of the USA and the Caribbean. *Estuaries and Coasts*, 43, 941–942. <https://doi.org/10.1007/s12237-020-00702-7>
- Wang, C. C., Lin, B. X., Chen, C. T., & Lo, S. H. (2015). Quantifying the effects of long-term climate change on tropical cyclone rainfall using a cloud-resolving model: Examples of two landfall typhoons in Taiwan. *Journal of Climate*, 28, 66–85. <https://doi.org/10.1175/JCLI-D-14-00044.1>
- Wang, Z., Montgomery, M. T., & Dunkerton, T. J. A. (2009). Dynamically-based method for forecasting tropical cyclogenesis location in the Atlantic sector using global model products. *Geophysical Research Letters*, 36, L03801. <https://doi.org/10.1029/2008GL035586>
- Willoughby, H. E., Darling, R. W. R., & Rahn, M. (2006). Parametric representation of the primary hurricane vortex. Part II: A new family of sectionally continuous profiles. *Monthly Weather Review*, 134, 1102–1120. <https://doi.org/10.1175/MWR3106.1>
- Wu, L., Tian, W., Liu, Q., Cao, J., & Knaff, J. A. (2015). Implications of the observed relationship between tropical cyclone size and intensity over the western North Pacific. *Journal of Climate*, 28, 9501–9506. <https://doi.org/10.1175/JCLI-D-15-0628.1>
- Wu, W., Chen, J., & Huang, R. (2013). Water budgets of tropical cyclones: Three case studies. *Advances in Atmospheric Sciences*, 30, 468–484. <https://doi.org/10.1007/s00376-012-2050-7>
- Wu, W., & Chen, J.-L. (2012). Sensitivity of tropical cyclone precipitation to atmospheric moisture content: Case study of Bilis (2006). *Atmospheric and Oceanic Science Letters*, 5(5), 420–425. <https://doi.org/10.1080/16742834.2012.11447030>
- Xu, H., Zhai, G., & Li, X. (2017). Precipitation efficiency and water budget of typhoon Fitow (2013): A particle trajectory study. *Journal of Hydrometeorology*, 18(9), 2331–2354. <https://doi.org/10.1175/JHM-D-16-0273.1>
- Yang, L., Liu, M., Smith, J. A., & Tian, F. (2017). Typhoon Nina and the August 1975 flood over Central China. *Journal of Hydrometeorology*, 18(2), 451–472. <https://doi.org/10.1175/JHM-D-16-0152.1>
- Yang, M., Braun, S. S., & Chen, D. (2011). Water budget of typhoon Nari (2001). *Monthly Weather Review*, 139(12), 3809–3828. <https://doi.org/10.1175/MWR-D-10-05090.1>
- Yin, H., Wang, Y., & Zhong, W. (2015). A statistical analysis of moisture characteristics during the rapid intensification of tropical cyclones over the northwestern Pacific. *Climatic and Environmental Research*, 20, 433–442. <https://doi.org/10.3878/j.issn.1006-9585.2015.14210>
- Ying, Y., & Zhang, Q. (2012). A modeling study on tropical cyclone structural changes in response to ambient moisture variations. *Journal of the Meteorological Society of Japan*, 90, 755–770. <https://doi.org/10.2151/jmsj.2012-512>

- Yoshida, K., Sugi, M., Mizuta, R., Murakami, H., Ishii, M. (2017). Future changes in tropical cyclone activity in high-resolution large-ensemble simulations. *Geophysical Research Letters* 44, 9910–9917. <https://doi.org/10.1002/2017GL075058>
- Zhang, D.-L., Liu, Y., & Yau, M. K. (2002). A multiscale numerical study of Hurricane Andrew Part V: Inner-core thermodynamics. *Monthly Weather Review*, 130, 2745–2763. [https://doi.org/10.1175/1520-0493\(2002\)130<2745:AMNSOH>2.0.CO;2](https://doi.org/10.1175/1520-0493(2002)130<2745:AMNSOH>2.0.CO;2)

Summary and Conclusions

Tropical cyclones (TCs) are essential components of the hydrological cycle in tropical and subtropical latitudes and act as a bridge between oceanic evaporation and precipitation over continents. The general goal of this thesis was to identify the moisture sources for precipitation associated with TCs during their three well-known stages of development, that is, the genesis, lifetime maximum intensity (LMI), and dissipation, in each ocean basin of the planet, namely, the North Atlantic (NATL), Central and East North Pacific (NEPAC), Western North Pacific (WNP), North Indian Ocean (NIO), South Indian Ocean (SIO), and South Pacific Ocean (SPO), by applying a Lagrangian moisture source diagnostic method.

The information of each TC was extracted from the best-track archives from United States agencies: the National Hurricane Center for the NATL and NEPAC and the Joint Typhoon Warning Center for the remaining basins. To address the goal of this thesis, the trajectories of precipitant air parcels over each TC location at each stage were simulated using the Lagrangian FLEXible PARTicle dispersion (FLEXPART) model and followed backwards in time for up to 10 days, which is widely used in climate research as the mean water vapour residence time. Only air parcels that precipitated within the area delimited by the outer radius of TCs (the target region) were backtracked. The study period was set from 1980 to 2018 based on the high quality of TC records since the beginning of the meteorological satellite era. The FLEXPART model was fed by the European Centre for Medium-Range Weather Forecasts ERA-Interim reanalysis, and the outer radius of TCs were estimated based on a climatology analysis of TC size using five radial wind profiles.

5.1 Main results

The main findings derived from this thesis are listed below, following the sequence of articles presented in Chapter 4:

1. Climatology of outer radius of TCs based on radial wind profiles

The climatological study of the TCs outer radius estimated by using five radial wind profiles revealed notable interbasin differences.

- The radial wind profile developed by Willoughby et al. (2006) was determined as the profile that more accurately estimates the wind structure of TC and, therefore, the outer radius.
- The global mean outer radius of TCs was estimated as 748.71 km, and it ranged from 650 km to 850 km.
- The smallest TCs were found close to the Equator in each basin and the largest in extra-tropical latitudes.
- The estimation of the TCs outer radius based on the radial wind profile revealed that the largest TCs occurred in the NATL basin and the smallest occurred in the NIO.
- In all basins, TCs reached their greatest size when the maximum wind speed ranged between 20 and 40 m/s.

2. Origin of moisture for the TC precipitation over the NATL basin

Although the NATL basin was the host for only ~16% of global annual TCs, it exhibited a notable spatial distribution of TCs genesis, LMI and dissipation locations throughout the basin.

- The cluster analysis revealed seven regions where TCs generally formed (central North Atlantic, western Caribbean Sea, Lesser Antilles arc, region near the West Africa coast, central North Atlantic, western North Atlantic, and Gulf of Mexico), seven regions where they reached the LMI (Gulf of Mexico, western North Atlantic, central tropical North Atlantic, northeast area of the Lesser Antilles arc, north-central North Atlantic, and Caribbean Sea), and six regions where TCs often dissipate (Central America, including the southern coast of the United States, tropical North Atlantic Ocean, Eastern coast of United States, southeastern Terranova Island, northern North Atlantic ocean south of Greenland, and Western Europe).
- The main moisture source for TC precipitation during the genesis and LMI phases was the North Atlantic Ocean north of 10°N, with a special role for the tropical part of the source, Caribbean Sea and Gulf of Mexico. Meanwhile, the western North Atlantic mainly supplied moisture during the dissipation stage.
- The South Atlantic south of 10°N also supported substantial moisture, which was most notable during the genesis phase.
- TCs over the NATL basin during the genesis and LMI phases also received a weak moisture contribution from the eastern tropical North Pacific Ocean.
- The moisture sources for precipitation during the peak of maximum intensity of all TCs were more intense and widespread than for each intensity category individually.
- The circulation associated with the North Atlantic Subtropical High pressure system and easterly winds were identified as the main drivers of moisture toward the TC positions.

3. Origin of moisture for the TC precipitation over the Indian Ocean

The Indian Ocean was responsible for approximately 22% of global annual TCs, and the moisture source analysis was performed separately for the NIO and SIO basins. The spatial distribution of TCs in the NIO can be related to its land-sea configuration, which confines TCs to the Bay of Bengal and Arabian Sea, while TCs over the SIO basin were distributed from the eastern African coast to northwestern Australia.

North Indian Ocean (NIO) basin

- The Bay of Bengal and Arabian Sea were identified as the regions where the genesis and LMI of TCs frequently occurred over the NIO, while the Arabian Sea, Indian Peninsula, and eastern India and Bangladesh were the areas for TC dissipation.
- The moisture precipitated by TCs mainly came from the Arabian Sea, Bay of Bengal, and South China Sea.
- The terrestrial sources that also contributed notable moisture amounts for TC activity over the NIO included the Indian Peninsula, Ganges basin, and southern coast of China.
- The western Indian Ocean also acted as a weak moisture source for TCs positioned over the Arabian Sea.
- The Indian Summer Monsoon and East Asia Summer Monsoon highly modulated the intensity and extension of moisture sources for TC precipitation formed over the NIO basin.
- The Somali low-level acted as the main moisture driver for TCs over the Arabian Sea.

South Indian Ocean (SIO) basin

- The cluster analysis revealed that TCs over the SIO basin generally formed, intensified, and dissipated over the central South Indian Ocean, northwestern Australia, and southwestern Indian Ocean.
- The central Indian Ocean and Wharton and Perth basins were identified as the main moisture sources for TC-related precipitation in the SIO basin.
- A small intense contribution also came from the Western Indian Ocean, northern Australian mainland, and Coral Sea.
- The Southeastern African Monsoon and North Australian Monsoon did not strongly modulate the intensity and extension of moisture sources for TC activity over the SIO basin.
- The main drivers of moisture were the Mascarene High, the westerly winds associated with the North Australian Monsoon and the southeast trade winds.

4. Moisture source for TC precipitation over the Pacific Ocean

During the study period, the Pacific Ocean accounted for approximately 62% of the global annual average TCs, which were distributed as follow: 31% over the WNP, 20% over the NEPAC, and 11% over the SPO basin.

Western North Pacific Ocean (WNP) basin

- Four regions were identified for TC genesis (Philippine Sea, South China Sea, surrounding seas of Mariana Islands, and central Pacific Ocean between the Marshall Islands and Hawaii) and dissipation (band between 0–55°N and 150°–180°E, small cluster over the Bering Sea, South China Sea, and area from the Korean Peninsula to the Philippine Sea, including the East China Sea, and Japan Sea), and three regions were identified for the LMI phase (South China Sea, East China Sea to western Philippine Sea, and central Philippine Sea to the central North Pacific Ocean).
- For the genesis and LMI phases, the moisture sources were elongated eastward with the major contributions from the western tropical North Pacific Ocean, Philippine Sea, and China Sea.
- During the dissipation stage, the moisture sources shifted northward, and the highest moisture uptake was from the western tropical North Pacific Ocean, East China Seas, and Japan Sea.
- TCs also received a poor moisture support from the Bay of Bengal, the Arabian Sea and the central North Pacific Ocean.
- The moisture was mainly driven by the Western North Pacific Subtropical High and westerly winds linked to the South Asia Monsoon.

Central and East North Pacific Ocean (NEPAC) basin

- The genesis and dissipation in the NEPAC often occurred in four regions (Middle America Trench, centroid of the second region is positioned approximately at 12°N and 128°W, southwest Pacific coast of Mexico and central Pacific Ocean south of the Hawaiian Islands), while TCs reached the LMI in three regions. Likewise, TCs dissipated over the Mexican Pacific coast, western Pacific Ocean, eastern tropical North Pacific Ocean, and Hawaiian Islands and surrounding seas. The cluster analysis also revealed that the ocean area close to the Central America coast, the region limited by the box at 10° to 20°N and 116° to 143°W, and the southern Hawaiian Islands were the hosts for the LMI stage.
- The moisture uptake pattern showed a north-south division at 10°N, which coincided with the mean position of the Intertropical Convergence Zone during boreal summer.
- The precipitant moisture uptake by TCs in the NEPAC basin mainly came from the eastern tropical North Pacific Ocean, eastern tropical South Pacific Ocean, and Caribbean Sea.
- During the dissipation stage the moisture sources extended westward to the dateline.
- The combined circulation of the North Pacific High and the South Pacific High, and the easterly wind that crossed over the tropical North Atlantic Ocean were identified as the principal mechanisms of moisture transport toward TC positions.

South Pacific Ocean (SPO) basin

- The cluster analysis identified three regions for TC genesis (northern Australia, central South Pacific Ocean, and Coral Sea) and LMI (seas north of Australia and western Coral Sea, region extending from the Fiji Islands towards the central South Pacific Ocean, and the Melanesia Archipelago and surrounding seas), and four regions for TC dissipation (western South Pacific Ocean, Coral Sea, mainland Australia, eastern Indian Ocean, and central South Pacific Ocean) over the SPO basin.
- The Coral Sea, western tropical South Pacific Ocean, and northern Australia supplied the major amount of moisture for the TC precipitation.
- During the dissipation stage, the moisture sources shift eastward with the major contribution from the western tropical South Pacific Ocean.
- In all phases, the moisture contribution from the central South Pacific Ocean was weak.
- Moisture was mainly transported by the convergence of westerly and easterly winds that form the South Pacific Convergence Zone.

5. Mean water vapour residence time for the TC precipitation

The mean water vapour residence time (MWVRT) for the TC precipitation provides a picture of the moisture uptake from local and remote sources and new insights for understanding the interbasin differences in TC activity.

- The MWVRT for TCs ranged from 2.72 to 3.08 days. The smallest MWVRT was found over the NATL basin, and the highest value was observed over the SIO and SPO.
- The MWVRT for TCs including all basins was estimated in $\sim 2.96 \pm 0.4$ days, which is approximately two to three times lower than the classical estimate of 8 to 10 days for the whole atmosphere.
- The spatial pattern of the MWVRT distribution agreed with other global studies, showing a poleward decreasing. This behaviour was more notable over the NATL basin.
- A statistically significant decreasing trends in the MWVRT of ~ 2.4 hours/decade in the NIO and ~ 1.0 hour/decade in the remaining basins were found.
- By intensity category, the tropical depression exhibited the highest MWVRT and the Category 2 hurricane on the Saffir-Simpson wind scale exhibited the lowest.
- The MWVRT generally decreased in the 24-hour period before TCs made landfall, and it was lower when TCs moved over land than over the ocean.

6. Case study: Six major hurricanes formed over the NATL basin in 2017

The 2017 North Atlantic TC season was active with 17 named storms, of which six reached the major hurricane category showing higher rainfall amounts along their trajectories. Furthermore, the different pathways followed by the six MHs illustrate the variability of moisture sources for TC precipitation according to their tracks.

- Higher moisture uptake was observed on the right side of the trajectory and during the maximum intensity phase of each TC.
- Higher moisture uptake generally occurred within approximately 3° to 5° of the TCs trajectories.
- The major moisture sources for each major hurricane varied according to its track. For Harvey and Irma, that impacted the southern coast of United States, the tropical North Atlantic Ocean, the Caribbean Sea, and the Gulf of Mexico provided substantial moisture for their precipitation. For Jose and Maria, that moved parallel to the eastern coast of United States after recurving, the moisture mainly came from the western North Atlantic Ocean. Finally, for Lee and Ophelia that moved over the open waters of the central NATL, the central North Atlantic Ocean was the principal moisture source.
- The precipitation of each TC estimated using the Lagrangian moisture source diagnostic method agreed with the observed precipitation.
- The local evaporation could not explain the total TC precipitation, therefore, substantial moisture was mainly imported throughout the secondary circulation from the outer region.

5.2 General conclusions

From the results listed above, the following general and common conclusions for all oceanic basins can be drawn:

1. The Lagrangian moisture source diagnostic method is able for identifying the origin of moisture for the precipitation associated with TCs and to quantify that precipitation, independently of the complexity of thermodynamic and dynamic processes involved in TCs.
2. TCs gained more moisture from sources located close to their positions than from remote sources.
3. The spatial distribution of the moisture sources revealed interbasin differences. For NATL and NEPAC basins was notable the north-south division at 10°N , coinciding with the average location of the Intertropical Convergence Zone during the summer season in the North Hemisphere. For WNP and SPO, the region with highest moisture contribution agrees with the mean position during the TC season of the monsoon trough and the South Pacific Convergence Zone, respectively. For NIO the nuclei of the highest moisture supply appeared over the Bay of Bengal and the Arabian Sea, which are the regions for TC activity in this basin, while the moisture sources in the SIO are westward extended, following the circulation of the northern branch of the Mascarene High. In addition, the moisture sources shifted northward in NATL and WNP during the dissipation stages due to TCs tend to decay in high latitudes in this basins.
4. In all basins, during the hurricane category (Category 1 and 2 on the Saffir-Simpson wind scale) TCs gained more moisture than in any other stage.
5. The highest moisture uptake per TC during the hurricane category was intrinsically related to the largest TC size in this phase.

6. The MWVRT for TCs did not exhibit large differences between the basins, reaching the highest values at low latitudes and decreasing poleward. Likewise, it was lower over land than over the ocean.
7. The decadal decreasing trend in the MWVRT for TCs could be related to the increase in TC intensity and precipitation rates over the last four decades.
8. The study of the individual cases of TCs showed that the moisture contribution from local evaporation did not explain the TC-related precipitation totals and highlighted the role of secondary circulation of TCs in the moisture transport from external sources. Likewise, this analysis confirmed that TC precipitation from the Lagrangian approach fit with the precipitation observations from satellite.

The developed TC size database could also be useful for different risk analyses, that is, mapping potential storm surge impacts on the global population, ecosystems, and economies. Meanwhile, the climatological moisture sources could be used as key predictors for seasonal forecasts of TC activity. Furthermore, based on the projected increase in the low-level water vapour content in the atmosphere under global warming, the results from this thesis could be used as a reference to identify and project the changes in moisture sources for TC precipitation in a warmer climate, which constitutes an added value of these results to support future scientific research and policy-making plans for adaptation and mitigation.

5.3 Future works

TC activity is widely modulated by climatic variability modes, such as the El Niño-Southern Oscillation (ENSO), North Atlantic Oscillation (NAO), Pacific Decadal Oscillation (PDO), and Indian Ocean Dipole (IOD). The ENSO is considered one of the most important climate modes, and it influences the frequency, location, and intensity of TCs by causing changes in atmospheric and oceanic conditions (Zheng et al., 2015; Lin et al., 2020). For example, TC activity decreases in the NATL basin, and TCs tend to form closer to the dateline over the NEPAC and WNP basins during El Niño years (the warm phase of the ENSO) (Lin et al., 2020). During La Niña years (cold phase of the ENSO), moisture transport increased in the NIO basin, favouring TC development, although Li et al. (2016) found no notable differences in TC frequency over the NIO during both phases of ENSO. The ENSO caused year-to-year variability in the number of TCs in the Southern Hemisphere basins (Magee et al., 2017) by enhancing (suppressing) TC activity over the SPO basin east of 170°E during El Niño (La Niña) years and a similar behaviour east of 75°E over the SIO basin (Lin et al., 2020). The NAO modulated the TC tracks over the NATL basin by influencing the strength and position of the North Atlantic Subtropical high-pressure system (NASH) (Colbert and Soden, 2012). The negative phase of the PDO caused anomalous easterly steering flows, which favoured TCs making landfall on the eastern Chinese coast (Yang et al., 2018; Lee et al., 2021). The IOD not only influences TC activity over the Indian Ocean but also TC genesis over the South China Sea (Wang et al., 2019b). Climate variability modes can also modulate the rainfall contribution of TCs over the continents. Aryal et al. (2018) noted that ENSO and NAO are related to the associated heavy rainfall of TCs, and Khouakhi et al. (2017) found that the TC-induced extreme rainfall over the US increased during

La Niña years. Therefore, **the relationship between climatic modes and the intensity and extent of moisture sources for TC precipitation must be better understood.**

Additionally, TC activity over the NIO and WNP is highly related to the monsoon season (Wu et al., 2012; Choi et al., 2016; Zhao et al., 2019; Dhavale et al., 2022). In the NIO, TCs exhibit a bimodal annual distribution, with a maximum during the post-monsoon season and a secondary maximum during the pre-monsoon season (Yanase et al., 2012; Li et al., 2013), while approximately 70-80% of tropical cyclogenesis over the WNP basin occurs in the WNP monsoon trough (WNPMT) (Molinari and Vollaro, 2013; Choi et al., 2016; Wang and Wu, 2018). In the paper focused on Indian Ocean basins (Pérez-Alarcón et al., 2022c), changes in the position and intensity of moisture sources for the precipitation produced by TCs formed over the NIO and SIO during the monsoon seasons were discussed; however, the influence of monsoon strength on moisture sources was not investigated. Likewise, the interannual variability of the position of the WNPMT regulates the TC genesis location and TC frequency over the WNP (Zhao et al., 2019), and consequently, the moisture flux converges toward TC positions (Guo et al., 2017). In addition, a recent study by Kelly et al. (2018) found that a strong Indian Summer Monsoon (ISM) provoked a significant enhancement of the NASH, causing a westward shift of NATL TCs trajectories and increasing landfall probability. Therefore, **changes in moisture sources for TC precipitation caused by monsoon systems should be investigated in future studies.**

This thesis also noted that the moisture sources for precipitation produced by TCs were generally located close to TC positions, as revealed by the moisture source analysis for the six TCs that reached Category 3+ on the Saffir-Simpson wind scale in the NATL in the 2017 season. The wind circulation associated with subtropical high-pressure systems acts as the principal moisture driver. TC trajectories are highly modulated both by the large-scale steering flow linked to the strength and position of subtropical high-pressure systems and by interactions between the steering flow and storm dynamics (for example, Kossin and Camargo, 2009; Kossin et al., 2010; Colbert and Soden, 2012; Ramsay et al., 2012; Wang et al., 2019a). In particular, during the analysis of moisture sources for the precipitation of the six major hurricanes formed over the NATL during the 2017 TC season (Pérez-Alarcón et al., 2022b), the highest moisture uptake generally occurred within 3-5° of the TC trajectory. The variability of the intensity and position of the subtropical high in each basin governs the variability of the TC trajectories (for example, Colbert and Soden, 2012; Torn et al., 2018; Sainsbury et al., 2022). Therefore, **in future studies, the influence of seasonal variations in these high-pressure systems on the interannual variability of moisture uptake will be examined.**

Investigating atmospheric moisture transport is a crucial step in the study of extreme precipitation events (for example, Chu et al., 2017; Ordoñez et al., 2019; Vázquez et al., 2020), and TCs play an important role in onshore moisture transport (Schumacher and Galarneau Jr, 2012; Xu et al., 2017). TCs are fuelled by heat and moisture fluxes from the warm sea surface (for example, Emanuel et al., 2004). Therefore, the presence of a TC at a specific location induces anomalous moisture fluxes toward the region influenced by TC circulation. Understanding anomalous moisture fluxes for precipitation associated with TCs can improve the predictability of regional rainfall extremes and reveal the response of the global hydrological cycle to climate warming. **Future research should aim to determine the anomalous moisture uptake of TCs on a global scale and the observed changes.**

Generally, the intensity of TCs rapidly decays after landfall because of the reduction in moisture supply by the ocean and increase in land surface friction (Chen et al., 2010; Andersen and Shepherd, 2014; Zhu et al., 2021; Wang and Matyas, 2022). During the interaction of TC circulation with inland heterogeneities, that is, soil type, land cover, vegetation type, and topography, the evaporation rate dramatically decreased compared with that over the ocean, thereby reducing the latent heat flux (Yoo et al., 2020; Wang and Matyas, 2022). Nonetheless, observational studies have found that some TCs maintain intensity or reintensify after landfall due to fluxes of moisture and energy derived from anomalously wet soils in a phenomenon referred to as the “brown ocean” effect (Evans et al., 2011; Andersen et al., 2013; Andersen and Shepherd, 2014; Nair et al., 2019; Yoo et al., 2020; Brauer et al., 2021; Wakefield et al., 2021). Therefore, **the anomalous moisture supplied from terrestrial sources after the landfalling of TCs will be studied in a future work** .

Previous studies (for example, Kaplan and DeMaria, 2003; Kaplan et al., 2010; Chen and Wang, 2018; Zhang et al., 2020) have also noted noticeable differences between TCs that underwent slow and rapid intensification processes (SI and RI, respectively). RI mainly occurs under high tropospheric humidity and oceanic heat content, low vertical wind shear, and large upper-tropospheric divergence; however, these conditions have also been found during the SI process. Therefore, convective-scale processes are important for TCs undergoing RI (Tao and Jiang, 2015; Tao et al., 2017). During RI, convective bursts favour warming of the TC core (for example, Kieper and Jiang, 2012). Recently, Vinodhkumar et al. (2022) found an increment in heavy rainfall in the inner core region of RI-TCs 12 hours before RI onset, and Tan et al. (2022) reported that RI processes tend to increase extreme precipitation over land. Based on these previous findings, **future studies will examine the differences in moisture sources for the precipitation of RI and SI TCs**.

TCs can also undergo an extratropical transition (ET) during their poleward movement, that is, approximately 40-50% of TCs over the NATL basin undergo ET (Evans et al., 2017; Bieli et al., 2019a,b). During ET, the warm core of the storm is replaced with a cold core, a frontal structure develops (Hart and Evans, 2001; Bieli et al., 2019a), the size increases (Evans and Hart, 2008), the intensity of precipitation decreases, the spatial range of precipitation tends to be wider (Harr et al., 2008), and the precipitation pattern notably expands in the area (Jones et al., 2003). Additionally, while heavy precipitation in TCs often occurs on both sides of the trajectory, it generally occurs on the left side of the track after ET in the Northern Hemisphere (Evans et al., 2017; Keller et al., 2019). Based on these structural changes of TCs during ET, **future work will aim to identify the changes in the moisture sources for the precipitation associated with TCs before and after undergoing ET**.

Future projections of TC activity are subject to uncertainties in climate projections, such as climate forcing scenario, model dynamics, physics, and resolution (for example, Bacmeister et al., 2014; Reed et al., 2015; Roberts et al., 2018; Vecchi et al., 2019). Despite these constraints, several studies have addressed the increase in the frequency (Camargo, 2013; Murakami et al., 2014; Bacmeister et al., 2018; Wehner et al., 2018) and intensity (Emanuel et al., 2008; Balaguru et al., 2016; Bhatia et al., 2018; Pérez-Alarcón et al., 2021a) of TCs under global warming. The current relentless increase in global mean surface temperature is closely associated with an increase in atmospheric water vapour content of approximately $\sim 6\text{-}7\%/K$ at a constant relative humidity (Held and Soden, 2006; O’Gorman and

Muller, 2010; Allan, 2012; Bao et al., 2017; Gimeno et al., 2021). Recently, several studies (Bacmeister et al., 2018; Liu et al., 2019a; Knutson et al., 2020) addressed a global increase of approximately 14% in TC precipitation rates. Indeed, observational and modelling studies suggest that the strong dependence of saturated vapour pressure on temperature based on the Clausius-Clapeyron relationship will result in increased evaporation and precipitation, thus leading to an intensification of the water cycle (Gimeno et al., 2015). Therefore, an increase in moisture uptake by TCs is expected owing to the higher moisture availability. Therefore, **future studies will investigate the impact of climate change on moisture sources for the TC precipitation by applying dynamic downscaling using the Weather Research and Forecasting model to reduce the effects of horizontal resolution.**



Supplementary Material

In this section is presented the supplementary material linked to each article that makes the main part of this thesis. All material related with published articles is available online by each journal.

Comparative climatology of outer tropical cyclone size using radial wind profiles

Albenis Pérez-Alarcón^{a,b,*}, Rogert Sorí^{a,c}, José C. Fernández-Alvarez^{a,b}, Raquel Nieto^a and Luis Gimeno^a

^aCentro de Investigación Mariña, Universidade de Vigo, Environmental Physics Laboratory (EPhysLab), Campus As Lagoas s/n, Ourense, 32004, Spain

^bDepartamento de Meteorología, Instituto Superior de Tecnologías y Ciencias Aplicadas, Universidad de La Habana, 10400 La Habana, Cuba

^cInstituto Dom Luiz, Faculdade de Ciências da Universidade de Lisboa, 1749-016 Campo Grande, Portugal

Introduction

This Supplementary Information provides Figures and Tables that support the statistical analysis presented in the manuscript.

- r_m : Tropical cyclones (TCs) radius of maximum wind speed
- r_{34} : radial distance from the centre where the TCs sustained winds of 34 kt (approximately 17 ms^{-1}) are observed on the surface
- r_{50} : radial distance from the centre where the TCs sustained winds of 50 kt (approximately 26 ms^{-1}) are observed on the surface
- r_{64} : radial distance from the centre where the TCs sustained winds of 64 kt (approximately 33 ms^{-1}) are observed on the surface
- r_{100} : radial distance from the centre where the TCs sustained winds of 100 kt (approximately 51 ms^{-1}) are observed on the surface
- H80: Radial wind profile of Holland (1980)
- D87: Radial wind profile of DeMaria (1987)
- W06: Radial wind profile of Willoughby et al. (2006)
- E11: Radial wind profile of Emanuel and Rotunno (2011)
- F13: Radial wind profile of Frisius and Scgönemann (2013)
- C16: TC outer radius estimated from Chavas et al. (2016)
- ERA-5: TC outer radius estimated from the ERA-5 reanalysis
- NHC: National Hurricane Center
- JTWC: Joint Typhoon Warning Center
- NATL: North Atlantic basin
- NEPAC: Central and East Pacific basin
- WNP: Western North Pacific basin
- NIO: North Indian Ocean basin
- SIO: Southern Indian Ocean basin
- SPO: Southern Pacific Ocean basin
- TD: Tropical Depressions
- TS: Tropical Storms
- H: Hurricanes (Category 1 and 2 on the Saffir-Simpson wind scale, $33 < V_{max} < 49 \text{ ms}^{-1}$)
- MH: Major Hurricanes (Category 3+ on the Saffir-Simpson wind scale, $V_{max} \geq 49 \text{ ms}^{-1}$)
- Trop: TC in tropical zone ($|latitude| \leq 30^\circ$)
- HTrop: Hurricane in tropical areas ($|latitude| \leq 30^\circ$ and $V_{max} \geq 33 \text{ ms}^{-1}$)
- Extrop: TC in extratropical zone ($|latitude| > 30^\circ$)

*Corresponding author

 albenis.perez.alarcon@uvigo.es (A. Pérez-Alarcón)

ORCID(s): 0000-0002-9454-2331 (A. Pérez-Alarcón); 0000-0001-6699-4595 (R. Sorí); 0000-0003-3409-6138 (J.C. Fernández-Alvarez); 0000-0002-8984-0959 (R. Nieto); 0000-0002-0778-3605 (L. Gimeno)

Supplementary Information

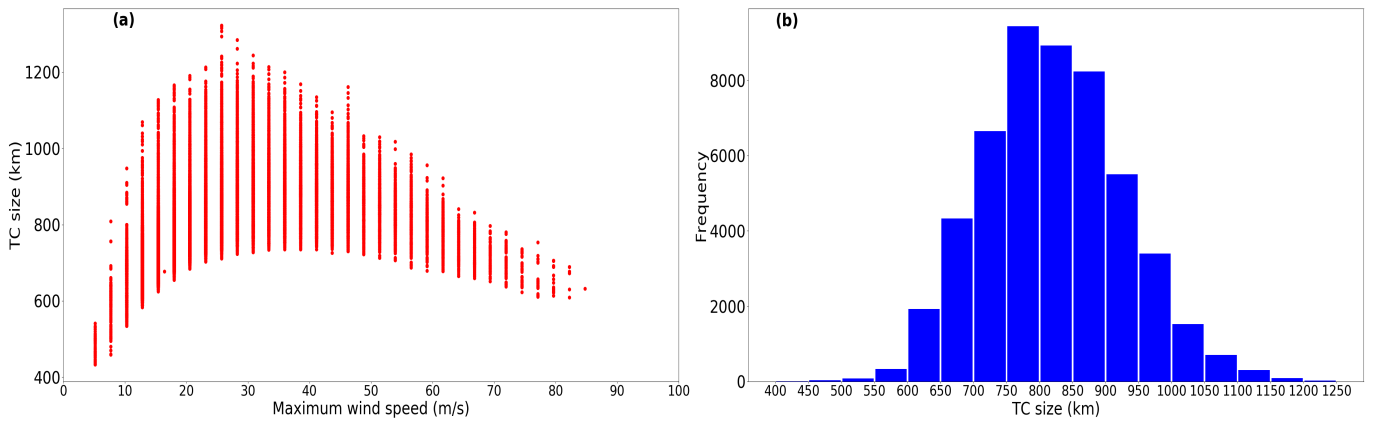


Figure S1: NATL TC size estimated from W06 (a) Distribution relative to maximum wind speed. (b) Frequency. Period 1851-2020

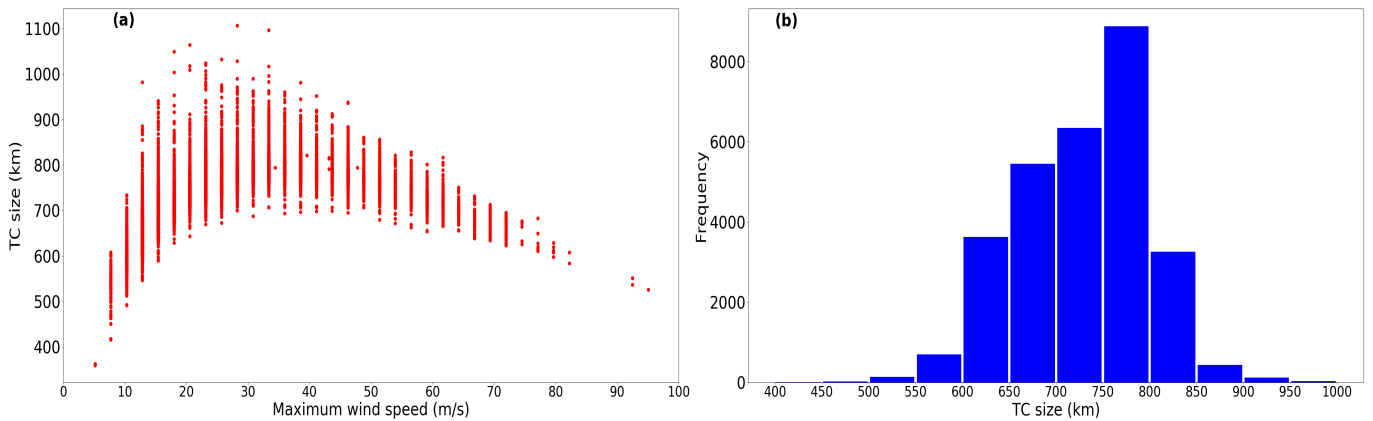


Figure S2: NEPAC TC size estimated using W06 (a) Distribution relative to maximum wind speed. (b) Frequency. Period 1949-2020

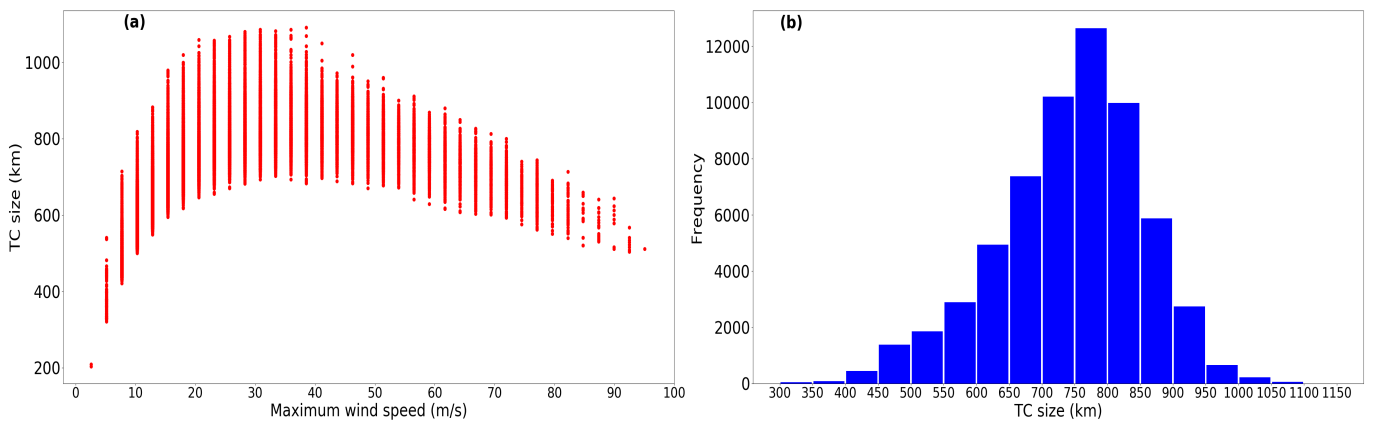


Figure S3: WNP TCs size estimated using W06 (a) Distribution relative to maximum wind speed. (b) Frequency. Period 1945-2019

Supplementary Information

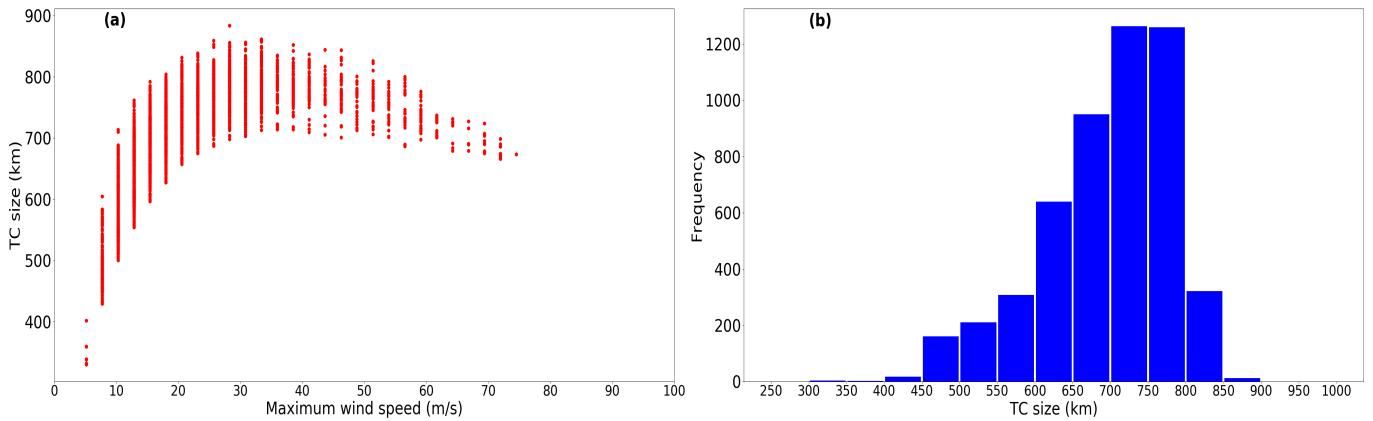


Figure S4: NIO TCs size estimated using W06 (a) Distribution relative to maximum wind speed. (b) Frequency. Period 1945-2019

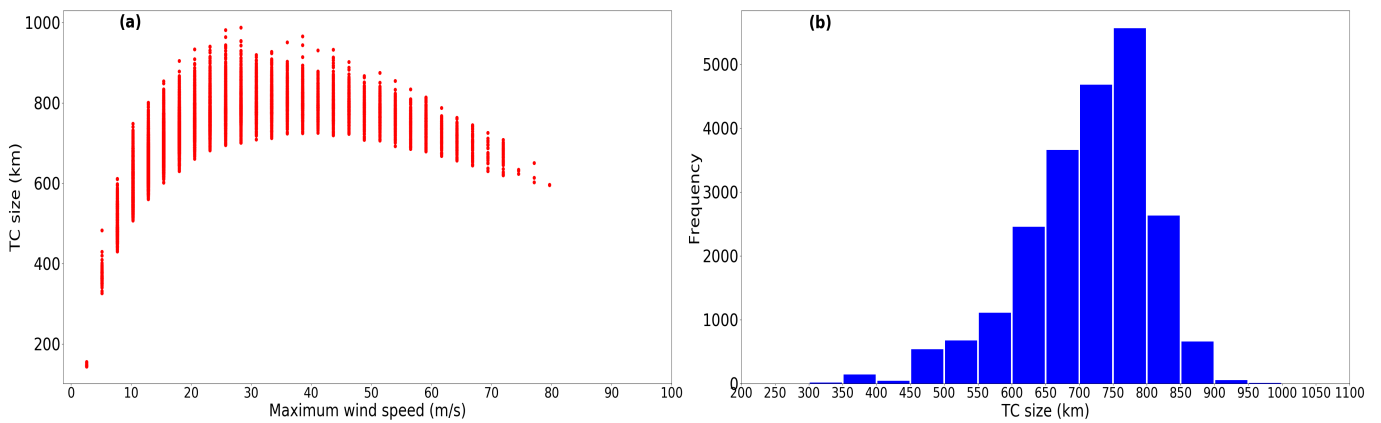


Figure S5: SIO TCs size estimated using W06 (a) Distribution relative to maximum wind speed. (b) Frequency. Period 1945-2019

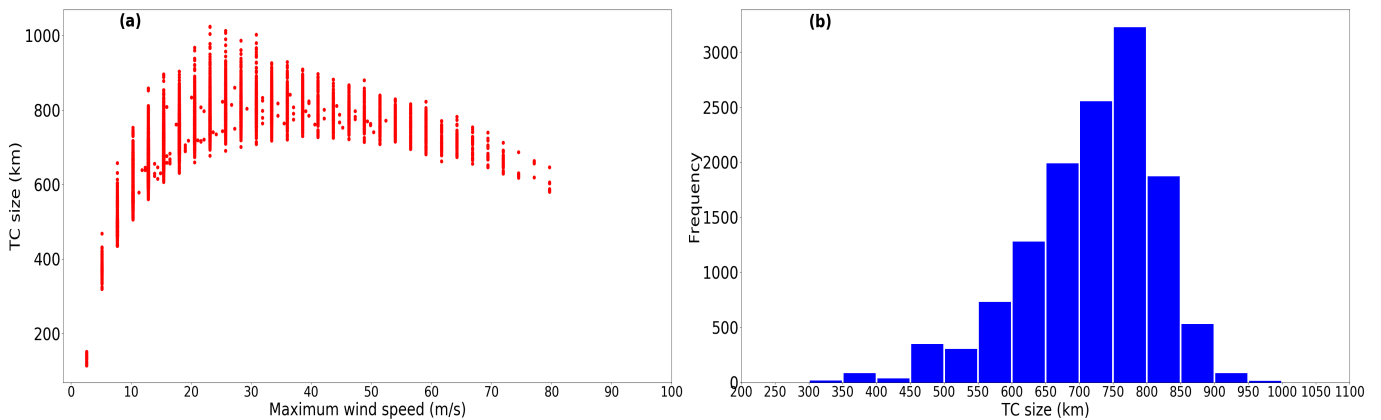


Figure S6: SPO TCs size estimated using W06 (a) Distribution relative to maximum wind speed. (b) Frequency. Period 1945-2019

Supplementary Information

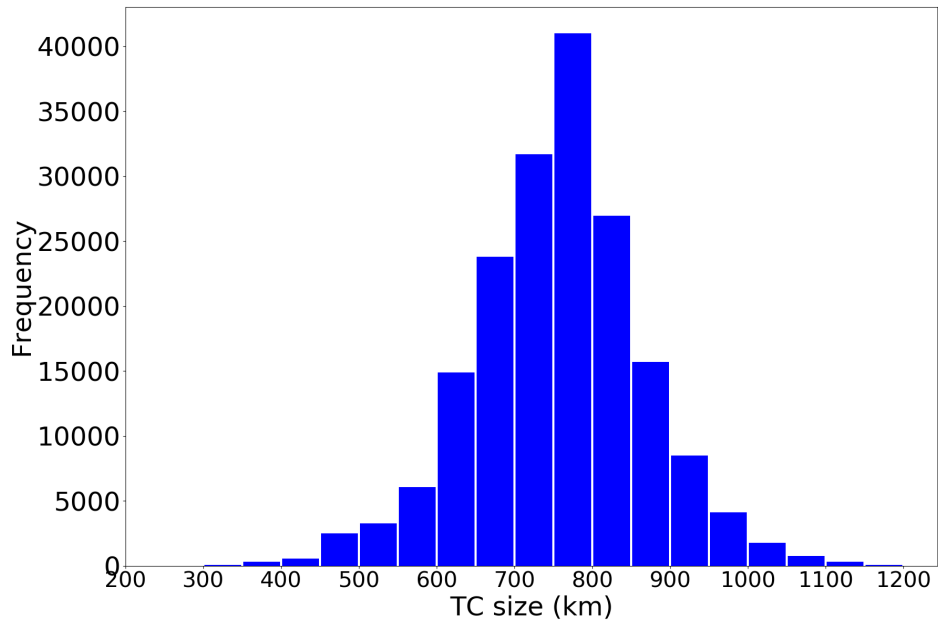


Figure S7: Frequency of TCs size estimated by W06 at global scale

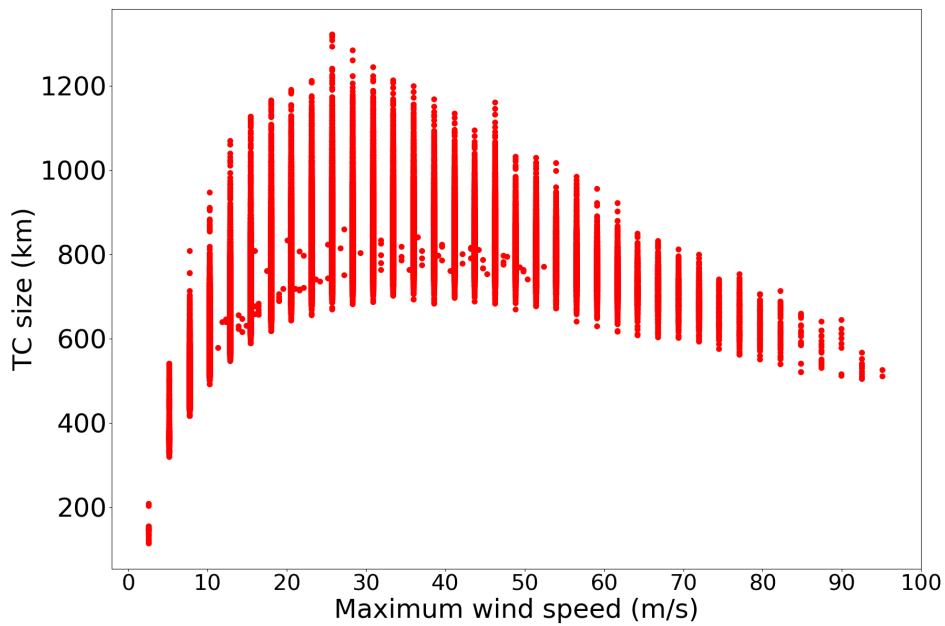


Figure S8: Relationships between TC size estimated by W06 and mean maximum wind speed

Supplementary Information

Table S1

NATL statistics for r_m , r_{34} , r_{50} , r_{64} and r_{100} (in km): including the mean, mean absolute error (MAE) and BIAS. Note that was used the same r_m in all radial wind profiles. It is remarkable that the r_m is operationally estimated by NHC, but not quality controlled after TC season and r_{100} is not recorded.

Class		Mean						MAE					BIAS				
		NHC	H80	D87	W06	E11	F13	H80	D87	W06	E11	F13	H80	D87	W06	E11	F13
TS	r_m	87.6	50.1	50.1	50.1	50.1	50.1	44.5	44.5	44.5	44.5	44.5	-37.1	-37.1	-37.1	-37.1	-37.1
	r_{34}	195.1	93.8	113.4	133.2	91.9	49.3	107.1	95.4	89.1	109.2	161.3	-103.4	-84.2	-66.1	-104.6	-161.2
	r_{50}	94.4	71.6	87.1	85.7	73.4	46.3	40.2	38.4	37.7	40.3	49.2	-25.1	-11.2	-13.4	-24.6	-46.3
H	r_m	47.2	40.1	40.1	40.1	40.1	40.1	19.2	19.2	19.2	19.2	19.2	-6.0	-6.0	-6.0	-6.0	-6.0
	r_{34}	275.8	144.8	159.6	249.7	136.7	110.9	140.1	129.1	96.5	146.3	201.1	-133.1	-117.4	-30.2	-140.1	-200.7
	r_{50}	133.6	93.1	113.42	142.8	96.4	70.9	56.5	51.5	52.1	55.8	67.9	-42.8	-22.3	5.17	-38.4	-71.6
	r_{64}	69.4	64.8	78.1	79.2	67.9	39.9	30.1	33.1	33.4	31.0	35.9	-6.5	5.8	6.2	-3.5	-31.1
MH	r_m	29.5	29.2	29.2	29.2	29.2	29.2	8.5	8.5	8.5	8.5	8.5	-1.8	-1.8	-1.8	-1.8	-1.8
	r_{34}	291.3	153.3	145.4	266.7	147.1	129.5	145.1	155.2	68.0	147.5	214.1	-144.1	-154.2	-36.1	-146.7	-210.3
	r_{50}	150.8	101.9	113.3	175.6	107.8	85.5	57.8	53.3	42.1	53.2	116.4	-52.4	-43.1	18.1	-45.2	-122.6
	r_{64}	86.7	76.9	91.9	120.9	84.2	29.5	28.1	27.4	39.2	26.8	59.5	-12.1	0.94	31.0	-4.6	-59.1
	r_{100}	-	41.8	50.2	46.1	45.5	44.1	-	-	-	-	-	-	-	-	-	-
Trop	r_m	76.1	44.5	44.5	44.5	44.5	44.5	38.9	38.9	38.9	38.9	38.9	-32.1	-32.1	-32.1	-32.1	-32.1
	r_{34}	209.7	106.6	119.9	167.1	106.3	40.6	111.4	103.7	81.5	111.2	181.1	-107.4	-94.1	-52.8	-107.2	-176.4
	r_{50}	109.4	83.1	98.9	124.2	88.4	36.5	44.6	41.9	39.1	42.7	79.4	-32.8	-18.5	7.1	-27.4	-77.8
	r_{64}	78.7	63.3	76.1	83.4	68.3	33.9	25.0	27.3	31.5	25.3	43.4	-4.8	7.38	18.8	0.71	-41.7
	r_{100}	-	41.8	49.5	45.8	44.9	43.2	-	-	-	-	-	-	-	-	-	-
HTrop	r_m	33.4	34.4	34.4	34.4	34.4	34.4	11.7	11.7	11.7	11.7	11.7	0.26	0.26	0.26	0.26	0.26
	r_{34}	259.9	136.3	143.6	236.6	134.5	97.5	127.1	126.4	73.1	129.6	226.7	-123.7	-119.4	-23.5	-124.1	-220.1
	r_{50}	127.7	88.5	104.9	139.2	94.5	34.6	49.3	45.6	41.9	46.6	94.7	-38.1	-24.2	13.9	-32.4	-94.1
	r_{64}	68.7	63.3	76.1	83.4	68.3	33.9	25.0	27.3	31.5	25.3	43.4	-4.8	7.38	18.8	0.71	-41.7
	r_{100}	-	41.8	49.5	45.8	44.9	43.2	-	-	-	-	-	-	-	-	-	-
ExTrop	r_m	85.6	55.5	55.5	55.5	55.5	55.5	39.4	39.4	39.4	39.4	39.4	-29.1	-29.1	-29.1	-29.1	-29.1
	r_{34}	261.4	138.5	158.3	224.1	125.1	51.2	140.8	126.5	105.4	149.2	228.1	-132.4	-112.5	-58.4	-144.8	-227.2
	r_{50}	146.1	101.5	122.9	154.4	101.2	47.5	68.5	61.8	61.0	98.8	104.1	-55.3	-34.6	-8.4	-54.3	-103.1
	r_{64}	87.8	75.1	90.4	96.8	77.1	44.5	39.8	40.9	43.3	40.0	47.0	-16.1	-2.5	1.0	-14.1	-42.2
	r_{100}	-	46.9	55.4	48.6	49.7	45.1	-	-	-	-	-	-	-	-	-	-
Full basin	r_m	79.0	47.7	47.7	47.7	47.7	47.7	39.0	39.0	39.0	39.0	39.0	-31.1	-31.1	-31.1	-31.1	-31.1
	r_{34}	225.1	116.6	132.1	185.1	112.2	44.1	119.1	110.2	88.8	122.2	195.4	-155.1	-99.6	-54.1	-118.7	-190.4
	r_{50}	120.7	89.4	107.2	134.6	92.8	40.2	52.0	48.0	45.8	50.7	86.9	-39.4	-23.7	2.3	-35.6	-86.5
	r_{64}	84.5	67.3	81.2	88.1	71.4	37.4	29.5	31.4	35.1	29.8	44.4	-8.3	-4.4	13.4	-3.8	-41.3
	r_{100}	-	41.8	50.2	46.1	45.5	44.1	-	-	-	-	-	-	-	-	-	-

Supplementary Information

Table S2

NATL statistics for TC outer radius from 1851 to 2020: including the mean (μ), median, standard deviation (σ), coefficient of variation (CV), 25th percentile (P_{25}), 75th percentile (P_{75}), 95th percentile (P_{95}) and the 95% confidence interval (CI). N represents the total data analysed and the outer radius is given in km .

Class	Wind profile	N	μ	Median	σ	CV	P_{25}	P_{75}	P_{95}	CI
TD	H80	11637	631.57	620.00	107.5	0.1703	563.00	701.00	818.00	629.61, 633.52
	D87	11637	399.74	392.00	55.69	0.1393	353.50	440.50	494.00	398.73, 400.75
	W06	11637	701.35	697.50	64.38	0.0918	657.50	747.00	806.50	700.18, 702.52
	E11	11637	208.87	208.00	20.05	0.0959	195.00	221.00	243.00	208.51, 209.24
	F13	11637	194.35	193.50	25.99	0.1337	178.50	212.00	236.00	193.88, 194.83
TS	H80	20008	962.21	939.50	191.2	0.1987	819.50	1084.5	1313.0	959.56, 964.86
	D87	20008	434.00	428.50	62.32	0.1436	382.00	476.00	545.50	433.13, 434.86
	W06	20008	821.21	816.50	73.15	0.0890	764.50	872.00	947.50	820.19, 822.22
	E11	20008	252.12	250.50	20.92	0.0829	237.50	264.00	290.50	251.83, 252.41
	F13	20008	242.66	241.00	24.08	0.0992	225.00	257.50	286.00	242.33, 243.00
H	H80	12007	1319.3	1311.0	189.7	0.1438	1171.5	1450.0	1644.0	1315.9, 1322.7
	D87	12007	418.07	413.50	62.09	0.1485	369.50	459.00	527.00	416.96, 419.18
	W06	12007	876.80	876.50	69.65	0.0794	822.00	927.00	992.50	875.55, 878.05
	E11	12007	287.06	282.50	18.03	0.0628	274.50	295.50	324.50	286.74, 287.39
	F13	12007	281.54	277.00	19.93	0.0708	267.00	292.00	322.00	281.18, 281.90
MH	H80	3195	1368.2	1362.5	139.4	0.1019	1259.5	1455.5	1609.0	1363.4, 1373.1
	D87	3195	334.33	333.00	46.65	0.1395	301.50	365.50	412.50	332.71, 335.94
	W06	3195	800.93	802.50	66.87	0.0835	755.00	847.00	906.65	798.61, 803.25
	E11	3195	305.28	300.50	16.26	0.0532	293.00	314.50	337.15	304.72, 305.85
	F13	3195	302.64	298.50	17.08	0.0564	290.00	312.50	335.50	302.05, 303.23
Trop	H80	32913	914.07	888.50	269.6	0.2950	681.50	1138.5	1370.5	911.15, 916.98
	D87	32913	383.38	381.50	42.82	0.1117	353.00	416.50	453.00	382.92, 383.84
	W06	32913	768.11	774.00	73.98	0.0963	717.50	826.00	877.50	767.31, 768.91
	E11	32913	258.28	258.00	37.76	0.1462	229.00	288.50	318.50	257.87, 258.68
	F13	32913	250.71	251.00	41.54	0.1656	219.00	284.00	316.00	250.27, 251.16
HTrop	H80	9989	1234.9	1238.0	126.4	0.1024	1144.0	1332.5	1432.0	1232.5, 1237.4
	D87	9989	363.39	364.50	43.61	0.1200	334.50	395.00	432.50	362.53, 364.24
	W06	9989	818.42	822.50	50.75	0.0620	785.00	859.00	890.00	817.43, 819.42
	E11	9989	299.21	296.50	18.14	0.0606	286.50	310.00	333.50	298.86, 299.57
	F13	9989	295.50	293.00	19.35	0.0654	282.00	307.00	331.00	295.12, 295.88
ExTrop	H80	13934	1200.4	1241.5	320.4	0.2669	957.00	1465.5	1649.0	1195.1, 1205.8
	D87	13934	488.37	484.00	46.10	0.0944	462.00	513.00	568.50	487.60, 489.13
	W06	13934	889.77	905.50	82.57	0.0928	850.00	942.50	999.00	888.40, 891.14
	E11	13934	243.77	248.50	32.24	0.1322	219.00	270.00	284.00	243.23, 244.30
	F13	13934	230.55	238.00	38.81	0.1683	203.50	262.50	279.00	229.91, 231.19

Supplementary Information

Table S3

NATL statistics for TC outer radius from 1980 to 2020: including the mean (μ), median, standard deviation (σ), coefficient of variation (CV), 25th percentile (P_{25}), 75th percentile (P_{75}), 95th percentile (P_{95}), the 95% confidence interval (CI) and the mean absolute error (MAE) respect to TC size from ERA-5 reanalysis. N represents the total data analysed and the outer radius is given in *km*. The lower MAE is marked in bold text. WP: Wind Profile

Class	WP	N	μ	Median	σ	CV	P_{25}	P_{75}	P_{95}	CI	MAE
TD	H80	5580	623.00	610.0	112.9	0.1813	551.5	696.5	819.0	620.03, 625.96	169.1
	D87	5580	396.82	386.0	56.50	0.1423	349.5	439.0	496.5	395.33, 398.30	366.2
	W06	5580	695.79	690.0	68.26	0.0981	652.0	745.5	808.5	694.00, 697.59	112.9
	E11	5580	208.36	208.5	22.14	0.1062	194.0	222.0	243.5	207.78, 208.94	552.8
	F13	5580	193.64	194.0	28.76	0.1485	177.5	213.0	236.5	192.88, 194.39	557.5
	ERA-5	5580	761.06	766.87	120.0	0.1576	696.90	835.39	946.5	757.91, 764.21	-
TS	H80	6747	958.07	933.5	197.2	0.2058	809.0	1085.0	1322.0	953.36, 962.77	193.1
	D87	6747	434.51	429.0	65.92	0.1517	378.0	479.5	552.34	432.93, 436.08	383.1
	W06	6747	820.05	816.5	76.73	0.0935	759.0	874.0	953.5	818.21, 821.88	95.77
	E11	6747	252.24	251.0	21.26	0.0843	237.5	264.0	291.5	251.73, 252.75	563.4
	F13	6747	242.67	241.5	24.63	0.1015	225.0	257.5	287.5	242.08, 243.26	572.9
	ERA-5	6747	815.11	828.47	122.2	0.1499	752.74	899.50	988.01	812.20, 818.03	-
H	H80	3155	1315.9	1316.5	185.2	0.1407	1171.5	1451.5	1619.5	1309.5, 1322.4	460.5
	D87	3155	422.05	420.0	62.72	0.1486	372.0	465.0	529.64	419.86, 424.24	436.5
	W06	3155	879.07	885.0	69.27	0.0788	823.0	931.5	986.50	876.65, 881.49	95.96
	E11	3155	285.71	281.0	18.87	0.0660	271.5	294.5	326.0	285.05, 286.37	570.8
	F13	3155	279.96	275.0	20.89	0.0746	264.5	290.5	323.5	279.23, 280.69	576.5
	ERA-5	3155	855.81	872.01	120.3	0.1406	797.26	932.32	1016.4	851.61, 860.02	-
MH	H80	1126	1321.9	1306.0	126.4	0.0956	1224.6	1405.8	1543.6	1314.5, 1329.3	460.6
	D87	1126	315.60	312.75	45.38	0.1437	282.0	343.5	394.75	312.95, 318.26	545.8
	W06	1126	773.47	771.5	67.26	0.0869	726.0	819.5	885.0	769.54, 777.40	122.1
	E11	1126	311.30	308.0	17.96	0.0577	297.0	323.5	345.37	310.25, 312.35	555.1
	F13	1126	309.04	306.0	18.71	0.0605	294.5	322.0	344.0	307.94, 310.13	552.3
	ERA-5	1126	861.34	874.78	106.7	0.1239	795.21	934.68	1015.0	855.10, 867.59	-
Trop	H80	11615	857.69	804.5	269.4	0.3141	628.75	1073.7	1339.0	852.79, 862.59	214.2
	D87	11615	378.28	375.5	45.41	0.1200	347.5	412.5	452.5	377.45, 379.11	420.1
	W06	11615	749.54	752.5	77.55	0.1034	692.5	808.75	872.5	748.13, 750.95	106.5
	E11	11615	253.08	250.0	39.47	0.1559	221.5	283.5	320.5	252.36, 253.80	544.1
	F13	11615	245.09	242.5	43.45	0.1772	211.0	278.5	318.5	244.30, 245.88	552.1
	ERA-5	11615	796.90	806.41	126.2	0.1584	726.22	884.26	982.19	794.60, 799.19	-
HTrop	H80	2801	1228.6	1230.5	125.2	0.1019	1143.0	1318.5	1428.0	1224.0, 1233.3	379.1
	D87	2801	352.59	355.5	50.49	0.1431	319.0	388.5	434.0	350.72, 354.46	498.1
	W06	2801	804.70	809.0	59.20	0.0735	766.5	851.5	890.0	802.50, 806.89	102.9
	E11	2801	302.45	299.0	20.10	0.0664	288.5	315.5	339.0	301.70, 303.19	547.9
	F13	2801	298.99	296.0	21.43	0.0717	284.0	313.5	337.5	298.19, 299.78	551.3
	ERA-5	2801	850.04	862.95	113.2	0.1331	785.07	928.03	1003.3	845.85, 854.24	-
ExTrop	H80	4993	1125.3	1156.5	328.7	0.2921	856.0	1406.5	1597.1	1116.2, 1134.4	346.5
	D87	4993	488.50	484.0	46.88	0.0959	462.0	514.5	571.19	487.20, 489.80	348.7
	W06	4993	871.99	896.5	94.38	0.1082	819.5	935.5	990.0	869.37, 874.61	96.04
	E11	4993	235.72	239.5	34.69	0.1471	207.0	264.5	282.0	234.76, 236.68	598.2
	F13	4993	220.78	227.5	42.11	0.1907	189.0	255.0	276.5	219.61, 221.95	613.1
	ERA-5	4993	833.22	844.23	121.0	0.1452	766.28	908.77	1009.6	829.86, 836.58	-
Full basin	H80	16608	938.15	891.5	313.5	0.3342	671.0	1191.5	1480.5	933.38, 942.92	253.9
	D87	16608	411.42	404.0	68.24	0.1658	358.5	459.0	531.5	410.38, 412.46	398.6
	W06	16608	786.35	783.0	100.1	0.1274	712.0	860.12	952.5	784.83, 787.88	103.4
	E11	16608	247.86	247.0	38.92	0.1570	219.0	275.0	313.5	247.27, 248.45	560.4
	F13	16608	237.78	238.0	44.47	0.1870	206.0	268.5	311.0	237.10, 238.46	570.4
	ERA-5	16608	807.82	817.48	125.7	0.1557	738.18	896.84	991.35	805.91, 809.73	-

Supplementary Information

Table S4

NEPAC statistics for r_m , r_{34} , r_{50} , r_{64} and r_{100} (in km): including the mean, mean absolute error (MAE) and BIAS. Note that was used the same r_m in all radial wind profiles. It is remarkable that the r_m is operationally estimated by NHC, but not quality controlled after TC season and r_{100} is not recorded.

Class		Mean						MAE					BIAS				
		NHC	H80	D87	W06	E11	F13	H80	D87	W06	E11	F13	H80	D87	W06	E11	F13
TS	r_m	61.8	43.9	43.9	43.9	43.9	43.9	23.8	23.8	23.8	23.8	23.8	-17.4	-17.4	-17.4	-17.4	-17.4
	r_{34}	132.1	79.8	96.7	107.5	82.6	43.1	56.5	47.2	47.1	55.0	97.4	-52.1	-36.5	-25.1	-50.3	-97.3
	r_{50}	63.3	59.6	72.2	66.2	66.3	39.9	21.2	23.5	21.4	21.6	28.6	-8.0	-4.5	-1.3	-4.5	-27.1
H	r_m	32.6	34.3	34.3	34.3	34.3	34.3	8.9	8.9	8.9	8.9	8.9	-1.4	-1.4	-1.4	-1.4	-1.4
	r_{34}	181.1	120.9	133.8	209.1	124.8	34.5	64.5	56.3	54.5	62.0	146.2	-59.6	-47.2	28.3	-55.3	-146.2
	r_{50}	86.6	77.6	94.8	144.0	84.6	46.2	22.6	24.4	35.7	22.4	52.3	-8.8	-8.1	-28.0	-1.8	-52.3
	r_{64}	43.3	53.8	64.8	62.5	58.1	40.8	15.6	24.0	23.3	18.8	15.1	-10.5	21.4	20.0	-14.8	-12.2
MH	r_m	30.2	25.3	25.3	25.3	25.3	25.3	8.2	8.2	8.2	8.2	8.2	-5.2	-5.2	-5.2	-5.2	-5.2
	r_{34}	212.1	133.5	126.2	233.4	138.3	45.5	81.3	88.7	55.9	77.3	160.1	-78.3	-86.4	-21.1	-73.9	-166.7
	r_{50}	109.8	88.8	98.4	150.9	98.3	35.5	29.6	28.4	47.6	27.6	84.6	-20.1	-11.7	41.6	-11.4	-74.3
	r_{64}	61.7	66.9	80.0	103.6	75.6	25.9	18.7	25.6	43.4	22.7	36.6	5.4	18.1	42.6	14.0	-36.0
	r_{100}	-	37.2	45.1	41.5	41.1	28.6	-	-	-	-	-	-	-	-	-	-
Trop	r_m	59.8	42.9	42.9	42.9	42.9	42.9	24.4	24.4	24.4	24.4	24.4	-18.2	-18.2	-18.2	-18.2	-18.2
	r_{34}	152.4	97.1	110.2	149.7	100.5	48.1	60.4	53.7	49.5	58.3	123.1	-56.3	-44.7	-6.2	-53.7	-118.2
	r_{50}	81.9	75.7	90.3	110.6	82.5	43.5	23.4	24.7	34.3	22.9	53.2	-10.2	2.9	23.9	-4.1	-52.8
	r_{64}	69.5	57.1	68.7	73.1	62.6	48.2	16.7	24.6	30.1	20.2	23.5	-8.81	20.3	27.6	14.6	-21.3
	r_{100}	-	37.2	45.1	41.5	41.1	28.6	-	-	-	-	-	-	-	-	-	-
HTrop	r_m	31.8	31.9	31.9	31.9	31.9	31.9	8.7	8.7	8.7	8.7	8.7	-0.8	-0.8	-0.8	-0.8	-0.8
	r_{34}	191.1	123.9	131.5	214.9	128.2	52.3	69.9	67.0	54.9	66.8	149.2	-65.4	-60.2	-26.0	-61.4	-141.1
	r_{50}	94.3	80.3	95.6	123.4	88.1	41.5	24.9	25.7	39.7	24.1	58.1	-12.3	1.48	32.6	-4.9	-56.5
	r_{64}	49.5	57.1	68.7	73.1	62.6	38.2	16.7	24.6	30.1	20.2	23.5	-8.8	20.3	27.6	14.6	-21.3
	r_{100}	-	37.2	45.1	41.5	41.1	28.6	-	-	-	-	-	-	-	-	-	-
Full basin	r_m	59.9	43.2	43.2	43.2	43.2	43.2	24.4	24.4	24.4	24.4	24.4	-18.1	-18.1	-18.1	-18.1	-18.1
	r_{34}	153.9	97.4	110.6	150.2	100.7	68.2	61.5	54.5	50.0	59.5	115.1	-57.1	-45.3	-6.8	-54.2	-115.4
	r_{50}	82.6	75.8	90.5	110.7	82.6	63.5	23.9	25.1	34.6	23.4	43.5	-11.2	2.34	23.1	-4.8	-43.5
	r_{64}	69.5	57.2	68.7	73.1	62.6	37.4	21.6	28.6	35.4	26.1	29.6	8.8	20.3	27.5	14.6	-21.8
	r_{100}	-	37.2	45.1	41.5	41.1	28.6	-	-	-	-	-	-	-	-	-	-

Supplementary Information

Table S5

NEPAC statistics for TC outer radius from 1949 to 2020: including the mean (μ), median, standard deviation (σ), coefficient of variation (CV), 25th percentile (P_{25}), 75th percentile (P_{75}), 95th percentile (P_{95}) and the 95% confidence interval (CI). N represents the total data analysed and the outer radius is given in *km*.

Class	Wind profile	<i>N</i>	μ	Median	σ	CV	P_{25}	P_{75}	P_{95}	CI
TD	H80	10472	558.64	563.00	74.22	0.1328	507.50	603.50	680.00	557.22, 560.06
	D87	10472	356.98	352.00	32.20	0.0902	335.00	374.50	416.00	356.37, 357.60
	W06	10472	655.38	657.00	46.34	0.0707	626.50	683.50	730.00	654.49, 656.26
	E11	10472	216.91	217.50	21.30	0.0982	203.50	230.50	249.00	216.50, 217.32
	F13	10472	206.54	207.50	24.57	0.1189	191.00	223.00	243.00	206.07, 207.01
TS	H80	11450	824.32	821.00	112.2	0.1362	742.50	896.00	1010.5	822.27, 826.38
	D87	11450	377.46	373.00	30.17	0.0799	357.50	392.00	430.00	376.90, 378.01
	W06	11450	758.40	757.00	41.78	0.0550	731.50	783.50	826.50	757.63, 759.16
	E11	11450	266.77	265.00	21.79	0.0817	251.50	280.00	305.00	266.37, 267.17
	F13	11450	260.36	259.00	23.54	0.0904	244.00	275.00	301.00	259.92, 260.79
H	H80	5582	1104.3	1100.5	85.72	0.0776	1045.6	1154.0	1247.0	1102.1, 1106.6
	D87	5582	352.17	349.50	27.92	0.0792	333.00	367.00	399.50	351.44, 352.90
	W06	5582	794.93	791.50	32.52	0.0409	773.00	811.50	851.50	794.07, 795.78
	E11	5582	309.71	308.50	18.35	0.0592	297.50	321.00	339.00	309.23, 310.19
	F13	5582	306.30	305.50	19.22	0.0627	293.50	318.50	337.00	305.80, 306.81
MH	H80	1931	1191.4	1188.0	56.25	0.0472	1154.5	1223.5	1291.0	1188.8, 1193.9
	D87	1931	289.64	290.50	24.52	0.0846	274.50	305.50	327.25	288.54, 290.73
	W06	1931	731.81	734.50	38.54	0.0526	710.00	756.50	788.50	730.09, 733.53
	E11	1931	331.96	330.50	15.46	0.0465	322.50	340.50	358.00	331.27, 332.65
	F13	1931	330.25	328.50	15.77	0.0477	320.50	339.00	357.00	329.54, 330.95
Trop	H80	29033	804.65	785.50	237.0	0.2945	594.00	1007.0	1196.5	801.92, 807.38
	D87	29033	357.99	358.00	34.26	0.0957	338.50	379.00	413.00	357.60, 358.39
	W06	29033	725.45	737.00	67.94	0.0936	674.00	777.00	821.50	724.67, 726.23
	E11	29033	261.98	259.50	43.60	0.1664	227.50	296.50	332.50	261.48, 262.48
	F13	29033	255.17	253.00	47.02	0.1842	218.50	292.50	330.50	254.63, 255.71
HTrop	H80	7454	1124.6	1126.0	84.69	0.0753	1065.5	1182.0	1258.0	1122.7, 1126.5
	D87	7454	335.07	338.50	36.75	0.1096	312.50	359.50	391.50	334.23, 335.90
	W06	7454	777.55	780.50	42.06	0.0541	756.00	804.00	841.50	776.60, 778.51
	E11	7454	315.78	315.50	19.83	0.0628	301.50	328.00	348.50	315.33, 316.24
	F13	7454	312.85	312.50	20.77	0.0664	298.00	326.00	347.00	312.38, 313.32

Supplementary Information

Table S6

NEPAC statistics for TC outer radius from 1980 to 2020: including the mean (μ), median, standard deviation (σ), coefficient of variation (CV), 25th percentile (P_{25}), 75th percentile (P_{75}), 95th percentile (P_{95}), the 95% confidence interval (CI) and the mean absolute error (MAE) respect to TC size from ERA-5 reanalysis. N represents the total data analysed and the outer radius is given in *km*. The lower MAE is marked in bold text. WP: Wind Profile

Class	WP	N	μ	Median	σ	CV	P_{25}	P_{75}	P_{95}	CI	MAE
TD	H80	8751	558.12	564.0	76.89	0.1377	505.0	605.5	682.5	556.51, 559.73	218.8
	D87	8751	356.58	352.0	32.14	0.0901	335.0	374.5	414.5	355.90, 357.25	399.8
	W06	8751	654.74	657.0	47.92	0.0731	625.5	683.5	730.5	653.74, 655.75	145.2
	E11	8751	216.90	217.5	22.04	0.1016	203.5	231.5	249.0	216.44, 217.36	534.9
	F13	8751	206.53	208.0	25.35	0.1227	191.0	223.5	243.0	205.99, 207.06	545.2
	ERA-5	8751	751.31	772.5	143.1	0.1905	687.31	844.2	935.5	748.31, 754.31	-
TS	H80	7793	819.30	810.0	118.9	0.1451	725.0	900.5	1017.0	816.66, 821.94	126.1
	D87	7793	375.62	370.5	30.02	0.0799	355.5	390.0	427.19	374.95, 376.29	425.9
	W06	7793	755.51	753.0	42.84	0.0567	725.5	782.0	825.5	754.56, 756.46	106.5
	E11	7793	267.25	265.5	23.69	0.0886	249.5	282.5	308.0	266.72, 267.78	532.6
	F13	7793	260.87	259.5	25.52	0.0978	242.0	277.5	304.5	260.31, 261.44	538.9
	ERA-5	7793	799.27	816.07	127.0	0.1589	737.29	885.05	972.01	796.45, 802.09	-
H	H80	3637	1104.1	1101.5	88.50	0.0801	1042.0	1159.0	1250.6	1101.2, 1106.9	271.7
	D87	3637	350.66	348.0	28.42	0.0810	331.0	366.5	399.5	349.74, 351.59	483.3
	W06	3637	793.21	789.5	32.61	0.0411	771.5	810.5	850.09	792.15, 794.27	98.17
	E11	3637	310.48	309.5	19.54	0.0629	297.0	322.0	342.0	309.85, 311.12	523.1
	F13	3637	307.11	306.5	20.43	0.0665	293.5	319.5	339.5	306.45, 307.78	526.5
	ERA-5	3637	833.34	848.43	114.5	0.1374	779.44	904.72	989.24	829.62, 837.07	-
MH	H80	1639	1188.9	1186.5	53.51	0.0450	1154.0	1222.5	1282.5	1186.3, 1191.5	339.1
	D87	1639	288.23	289.5	24.66	0.0855	272.0	304.5	325.5	287.03, 289.42	561.6
	W06	1639	729.54	733.0	38.85	0.0532	706.5	755.0	785.0	727.66, 731.42	144.1
	E11	1639	332.61	331.0	15.52	0.0466	323.0	341.0	359.5	331.85, 333.36	517.3
	F13	1639	330.93	329.0	15.81	0.0478	321.0	340.0	358.04	330.16, 331.69	519.0
	ERA-5	1639	849.84	860.2	113.9	0.1340	784.96	924.08	1017.5	844.32, 855.37	-
Trop	H80	21550	787.68	736.5	241.9	0.3072	584.0	992.0	1198.5	784.44, 790.91	202.9
	D87	21550	355.78	356.0	35.01	0.0984	336.0	377.5	411.5	355.31, 356.25	436.5
	W06	21550	718.07	724.5	68.77	0.0957	668.0	771.0	818.0	717.15, 718.99	123.8
	E11	21550	259.65	254.0	45.33	0.1745	224.0	296.0	334.0	259.04, 260.25	530.3
	F13	21550	252.64	247.5	48.91	0.1936	215.5	292.0	332.0	251.99, 253.29	537.2
	ERA-5	21550	789.45	807.68	35.4	0.1716	724.52	878.87	972.70	787.64, 791.26	-
HTrop	H80	5240	1128.8	1137.5	86.54	0.0766	1068.5	1188.5	1261.0	1126.5, 1131.2	291.1
	D87	5240	330.40	333.5	38.43	0.1163	304.5	357.5	389.5	329.35, 331.44	508.3
	W06	5240	772.45	776.0	44.08	0.0570	749.0	801.0	839.0	771.26, 773.65	112.4
	E11	5240	317.68	317.5	20.75	0.0653	303.0	330.12	351.0	317.11, 318.24	520.9
	F13	5240	314.86	315.0	21.72	0.0690	299.5	328.5	349.5	314.27, 315.45	523.7
	ERA-5	5240	838.45	851.66	113.9	0.1359	781.27	910.01	1002.2	835.36, 841.54	-
Full basin	H80	21820	789.79	739.0	243.3	0.3081	584.5	995.0	1201.0	786.56, 793.02	203.6
	D87	21820	357.26	356.5	37.44	0.1048	336.0	378.5	416.5	356.76, 357.76	435.2
	W06	21820	719.43	725.5	70.18	0.0975	668.5	772.5	821.0	718.50, 720.36	123.4
	E11	21820	259.17	253.5	45.40	0.1751	224.0	295.5	334.0	258.57, 259.77	530.8
	F13	21820	252.05	246.5	49.09	0.1947	215.0	291.0	332.0	251.39, 252.70	537.9
	ERA-5	21820	789.51	807.7	135.4	0.1716	724.46	879.2	972.63	787.72, 791.31	-

Supplementary Information

Table S7

WNP statistics for r_m , r_{34} , r_{50} , r_{64} and r_{100} (in km): including the mean, mean absolute error (MAE) and BIAS. Note that was used the same r_m in all radial wind profiles. It is remarkable that the r_m is operationally estimated by NHC, but not quality controlled after TC season and r_{100} is not recorded.

Class		Mean						MAE					BIAS				
		JTWC	H80	D87	W06	E11	F13	H80	D87	W06	E11	F13	H80	D87	W06	E11	F13
TS	r_m	65.9	49.6	49.6	49.6	49.6	49.6	18.9	18.9	18.9	18.9	18.9	-6.7	-6.7	-6.7	-6.7	-6.7
	r_{34}	184.4	92.5	11.7	126.5	92.8	58.4	81.8	72.4	70.0	82.7	121.1	-72.1	-48.3	-39.6	-72.4	-121.4
	r_{50}	84.7	67.9	82.4	77.4	70.8	54.7	37.7	43.3	38.0	39.0	35.8	-4.6	11.7	2.1	-1.6	-25.1
H	r_m	38.5	37.9	37.9	37.9	37.9	37.9	13.8	13.8	13.8	13.8	13.8	5.3	5.3	5.3	5.3	5.3
	r_{34}	251.4	135.5	149.2	227.4	134.5	58.2	97.4	87.0	60.5	100.0	201.2	-92.1	-77.3	-9.5	-96.3	-201.3
	r_{50}	117.1	81.1	106.1	127.7	92.8	48.3	39.0	41.6	46.0	39.8	69.1	-14.1	7.2	23.1	-8.7	-68.5
	r_{64}	64.3	60.4	72.7	71.2	64.5	41.2	25.7	35.3	32.4	28.8	27.2	10.1	26.5	22.3	15.4	-22.3
MH	r_m	29.6	27.5	27.5	27.5	27.5	27.5	10.8	10.8	10.8	10.8	10.8	3.8	3.8	3.8	3.8	3.8
	r_{34}	288.6	152.6	140.9	249.9	151.8	57.9	104.1	118.1	61.3	110.2	243.2	-101.1	-116.5	-21.5	-107.4	-246.3
	r_{50}	148.4	101.7	110.7	166.1	110.1	45.5	40.4	39.6	49.9	39.6	109.2	-22.1	-12.3	32.5	-14.2	-108.3
	r_{64}	83.9	76.9	90.7	116.6	85.7	36.9	25.7	34.4	48.1	30.5	46.2	11.2	27.8	45.8	20.9	-43.1
	r_{100}	-	43.8	53.4	49.3	48.5	31.2	-	-	-	-	-	-	-	-	-	-
Trop	r_m	60.6	46.3	46.3	46.3	46.3	46.3	17.2	17.2	17.2	17.2	17.2	-1.1	-1.1	-1.1	-1.1	-1.1
	r_{34}	224.7	114.7	125.5	176.3	115.9	59.4	86.9	83.5	62.7	89.1	172.5	-80.2	-68.4	-23.7	-81.3	-172.1
	r_{50}	118.5	86.2	100.8	126.4	92.7	46.7	37.9	40.6	44.8	38.3	79.8	-13.1	3.3	23.3	-6.9	-72.5
	r_{64}	73.2	65.9	78.7	87.4	72.1	42.6	25.6	35.0	39.5	29.7	38.2	-11.2	27.8	33.6	18.8	-35.2
	r_{100}	-	43.7	53.3	49.9	48.4	30.1	-	-	-	-	-	-	-	-	-	-
HTrop	r_m	34.6	33.3	33.3	33.3	33.3	33.3	12.5	12.5	12.5	12.5	12.5	4.8	4.8	4.8	4.8	4.8
	r_{34}	264.7	140.1	143.7	232.1	140.5	53.5	97.5	97.9	59.8	101.1	212.3	-93.1	-91.4	-14.2	-97.1	-211.3
	r_{50}	129.4	91.4	106.3	139.8	98.6	43.5	38.6	40.3	46.8	38.8	84.9	-16.2	0.14	27.4	-9.5	-81.2
	r_{64}	73.2	65.9	78.7	87.4	72.1	42.6	25.6	35.0	39.5	29.7	38.2	-11.2	27.8	33.6	18.8	-35.2
	r_{100}	-	43.7	53.3	49.9	48.4	30.1	-	-	-	-	-	-	-	-	-	-
ExTrop	r_m	60.7	58.6	58.6	58.6	58.6	58.6	20.2	20.2	20.2	20.2	20.2	-5.3	-5.3	-5.3	-5.3	-5.3
	r_{34}	255.4	128.4	149.8	202.9	117.5	69.1	130.1	115.1	86.0	139.4	201.3	-127.1	-108.3	-51.2	-137.4	-20.3
	r_{50}	126.9	94.1	114.2	136.7	94.5	66.8	52.6	48.4	54.7	52.1	82.2	-33.2	-14.5	-8.84	-32.1	-77.2
	r_{64}	72.4	69.3	82.4	85.1	71.5	62.1	26.7	32.6	39.3	27.3	35.7	1.13	16.6	23.4	4.4	-29.1
	r_{100}	-	48.8	58.8	53.9	52.4	34.1	-	-	-	-	-	-	-	-	-	-
Full basin	r_m	60.6	47.6	47.6	47.6	47.6	47.6	17.4	17.4	17.4	17.4	17.4	-1.5	-1.5	-1.5	-1.5	-1.5
	r_{34}	227.9	116.5	128.6	179.7	116.2	64.2	91.6	86.9	65.1	94.4	177.2	-85.2	-72.1	-26.3	-87.1	-177.2
	r_{50}	119.3	86.9	102.3	127.5	92.9	56.8	39.2	41.3	45.6	39.6	76.4	-15.2	1.8	22.0	-9.2	-77.1
	r_{64}	73.1	66.3	79.1	87.2	71.9	51.2	25.7	34.9	39.5	29.5	38.1	10.6	27.1	32.9	17.9	-31.4
	r_{100}	-	43.8	53.4	49.9	48.5	31.2	-	-	-	-	-	-	-	-	-	-

Supplementary Information

Table S8

WNP statistics for TC outer radius from 1945 to 2019: including the mean (μ), median, standard deviation (σ), coefficient of variation (CV), 25th percentile (P_{25}), 75th percentile (P_{75}), 95th percentile (P_{95}) and the 95% confidence interval (CI). N represents the total data analysed and the outer radii are given in km .

Class	Wind profile	N	μ	Median	σ	CV	P_{25}	P_{75}	P_{95}	CI
TD	H80	20760	580.07	554.50	183.1	0.3156	445.00	709.50	901.00	577.57, 582.56
	D87	20760	392.13	357.50	102.6	0.2618	312.50	483.12	581.50	390.73, 393.53
	W06	20760	632.28	639.50	91.87	0.1453	576.00	693.00	773.50	631.03, 633.53
	E11	20760	230.97	220.00	51.48	0.2229	198.50	252.00	334.50	230.27, 231.67
	F13	20760	217.47	209.00	52.49	0.2413	184.00	240.00	318.50	216.76, 218.19
TS	H80	20907	951.00	946.00	198.5	0.2088	796.50	1096.0	1286.5	948.31, 953.69
	D87	20907	429.91	412.00	76.45	0.1778	365.50	498.50	553.50	428.87, 430.94
	W06	20907	794.95	786.00	74.13	0.0932	742.00	839.00	931.00	793.94, 795.95
	E11	20907	275.91	266.00	43.67	0.1582	246.50	293.50	359.50	275.32, 276.50
	F13	20907	267.37	258.50	45.76	0.1711	237.00	287.50	353.00	266.75, 267.99
H	H80	12985	1235.6	1227.5	179.4	0.1452	1087.0	1370.0	1531.0	1232.5, 1238.7
	D87	12986	390.83	383.00	55.96	0.1431	346.50	435.50	478.00	389.86, 391.79
	W06	12986	827.00	822.00	57.25	0.0692	786.00	866.00	923.50	826.01, 827.98
	E11	12986	311.44	302.00	38.64	0.1240	286.00	326.50	386.00	310.78, 312.10
	F13	12986	307.08	298.50	39.52	0.1287	281.00	323.50	382.00	306.40, 307.76
MH	H80	7058	1359.2	1302.5	207.8	0.1529	1199.5	1550.5	1758.6	1354.4, 1364.1
	D87	7058	319.36	313.00	54.97	0.1721	278.00	363.87	409.00	318.08, 320.64
	W06	7058	748.51	751.50	63.94	0.0854	707.50	793.00	849.00	747.02, 750.01
	E11	7058	337.20	325.00	41.34	0.1226	308.50	354.00	418.00	336.24, 338.17
	F13	7058	335.10	323.50	41.53	0.1239	306.50	352.00	415.57	334.13, 336.07
Trop	H80	55029	906.41	901.00	342.7	0.3781	630.50	1156.0	1487.5	903.54, 909.27
	D87	55031	383.64	367.50	81.60	0.2127	327.00	427.50	532.50	382.95, 384.32
	W06	55031	724.10	742.00	101.5	0.1402	664.00	799.00	862.00	723.25, 724.95
	E11	55031	279.66	281.00	59.58	0.2130	237.50	314.50	380.00	279.17, 280.16
	F13	55031	271.87	274.00	62.50	0.2298	227.50	310.00	374.50	271.35, 272.39
HTrop	H80	18339	1264.6	1239.5	199.3	0.1576	1115.5	1378.0	1628.0	1261.7, 1267.5
	D87	18339	357.20	355.50	60.44	0.1692	315.75	399.50	455.00	356.33, 358.08
	W06	18339	787.93	793.00	61.53	0.0781	750.50	832.00	880.00	787.04, 788.82
	E11	18339	324.81	314.50	40.68	0.1252	297.50	341.00	404.50	324.23, 325.40
	F13	18339	321.56	311.50	41.28	0.1283	294.00	338.50	401.50	320.96, 322.16
ExTrop	H80	6680	1150.2	1174.5	270.3	0.2350	961.00	1358.0	1535.0	1143.7, 1156.7
	D87	6680	500.92	493.50	55.87	0.1115	467.50	531.50	605.02	499.58, 502.26
	W06	6680	886.33	902.50	77.16	0.0870	854.50	928.00	992.02	884.48, 888.18
	E11	6680	239.16	240.50	29.98	0.1253	219.00	263.00	282.50	238.45, 239.88
	F13	6680	224.00	228.00	37.35	0.1667	199.00	253.00	277.50	223.10, 224.90

Supplementary Information

Table S9

WNP statistics for TC outer radius from 1980 to 2019: including the mean (μ), median, standard deviation (σ), coefficient of variation (CV), 25th percentile (P_{25}), 75th percentile (P_{75}), 95th percentile (P_{95}), the 95% confidence interval (CI) and the mean absolute error (MAE) respect to TC size from ERA-5 reanalysis. N represents the total data analysed and the outer radius is given in *km*. The lower MAE is marked in bold text. WP: Wind Profile

Class	WP	N	μ	Median	σ	CV	P_{25}	P_{75}	P_{95}	CI	MAE
TD	H80	15256	589.02	557.0	197.4	0.3352	427.5	784.0	901.0	585.89, 592.15	238.7
	D87	15256	403.34	366.0	111.5	0.2764	308.5	523.5	588.0	401.57, 405.11	374.3
	W06	15256	626.13	634.7	93.29	0.1489	561.0	692.5	767.5	624.65, 627.61	176.9
	E11	15256	236.53	223.0	56.30	0.2380	198.5	263.0	346.5	235.64, 237.42	536.1
	F13	15256	222.48	211.5	56.58	0.2543	185.0	248.0	331.0	221.58, 223.38	550.0
	ERA-5	15256	771.29	785.75	138.8	0.1800	703.55	860.5	966.4	769.09, 773.49	-
TS	H80	11596	979.22	981.5	196.5	0.2007	826.5	1130.5	1290.5	975.65, 982.80	209.5
	D87	11596	445.10	461.0	75.39	0.1693	375.0	512.0	544.0	443.72, 446.47	396.1
	W06	11596	793.89	788.0	68.38	0.0861	746.0	835.5	917.5	792.65, 795.14	112.2
	E11	11596	284.61	272.5	50.09	0.1760	250.5	306.0	381.0	283.70, 285.52	554.1
	F13	11596	275.79	265.0	51.68	0.1873	240.5	298.5	373.5	274.84, 276.73	562.8
	ERA-5	11596	837.09	850.52	127.2	0.1519	775.0	908.83	1020.0	834.77, 839.41	-
H	H80	6765	1290.0	1314.5	183.1	0.1419	1134.5	1429.0	1535.0	1285.6, 1294.4	413.1
	D87	6766	407.18	419.5	56.24	0.1381	358.0	455.0	478.0	405.84, 408.52	473.3
	W06	6766	832.13	829.0	54.28	0.0652	792.5	869.5	922.5	830.84, 833.42	102.1
	E11	6766	318.42	307.0	45.25	0.1421	287.5	337.0	405.5	317.35, 319.50	561.4
	F13	6766	313.81	303.0	45.97	0.1464	282.5	333.5	401.5	312.72, 314.91	566.5
	ERA-5	6765	878.89	897.5	110.1	0.1253	821.99	945.74	1041.3	876.27, 881.52	-
MH	H80	3762	1450.2	1476.0	226.8	0.1564	1238.0	1628.0	1792.5	1443.0, 1457.5	546.1
	D87	3762	339.85	347.0	56.70	0.1668	291.62	389.0	420.5	338.04, 341.67	564.8
	W06	3762	754.56	755.5	59.71	0.0791	715.12	797.0	849.5	752.65, 756.46	163.4
	E11	3762	349.73	336.5	47.41	0.1355	315.0	375.37	436.0	348.21, 351.24	554.9
	F13	3762	347.44	334.5	47.55	0.1368	312.5	373.0	434.0	345.92, 348.96	557.2
	ERA-5	3762	904.32	900.0	101.3	0.1120	855.15	969.75	1058.1	901.08, 907.55	-
Trop	H80	33927	902.91	893.0	374.1	0.4144	593.5	1172.0	1574.0	898.92, 906.89	288.7
	D87	33927	402.03	384.5	92.00	0.2288	330.5	482.5	560.0	401.05, 403.01	424.9
	W06	33927	713.23	732.5	108.7	0.1524	645.5	796.0	861.0	712.07, 714.38	146.8
	E11	33927	281.66	280.5	66.01	0.2343	233.5	321.0	396.5	280.96, 282.36	542.5
	F13	33927	272.68	272.0	68.76	0.2521	221.5	315.0	391.5	271.94, 273.41	551.4
	ERA-5	33927	822.82	839.3	137.7	0.1673	751.27	902.42	1021.5	821.36, 824.29	-
HTrop	H80	9630	1340.1	1327.5	220.5	0.1645	1165.0	1510.0	1739.4	1335.7, 1344.5	251.1
	D87	9630	376.38	376.5	62.94	0.1672	331.0	428.0	468.5	375.12, 377.63	515.3
	W06	9630	793.58	798.5	59.31	0.0747	756.0	838.0	882.27	792.40, 794.77	126.6
	E11	9630	334.80	323.0	47.29	0.1412	301.5	355.0	424.0	333.86, 335.75	556.5
	F13	9630	331.31	320.0	47.81	0.1443	298.0	352.0	421.5	330.36, 332.27	559.9
	ERA-5	9630	890.50	900.0	106.7	0.1198	835.78	955.87	1050.5	888.37, 892.63	-
ExTrop	H80	3453	1127.0	1150.5	269.7	0.2393	909.5	1341.5	1521.1	1118.0, 1136.0	325.9
	D87	3453	494.81	489.5	49.46	0.0999	463.5	521.5	588.0	493.16, 496.46	351.4
	W06	3453	877.32	898.0	75.05	0.0855	840.5	922.0	971.69	874.82, 879.83	94.18
	E11	3453	238.38	239.5	30.38	0.1274	218.5	263.0	283.0	237.36, 239.39	604.2
	F13	3453	223.41	227.0	37.47	0.1677	196.5	253.0	277.5	222.16, 224.66	619.0
	ERA-5	3453	841.69	851.4	116.9	0.1389	780.31	911.09	1011.3	837.79, 845.59	-
Full basin	H80	37380	923.61	901.0	371.5	0.4022	625.5	1202.5	1568.0	919.84, 927.38	292.9
	D87	37380	410.60	396.0	92.89	0.2262	336.0	489.5	560.0	409.66, 411.54	418.1
	W06	37380	728.39	744.5	116.2	0.1595	656.5	811.0	896.5	727.21, 729.56	141.9
	E11	37380	277.66	274.0	64.79	0.2333	230.0	316.0	392.5	277.00, 278.32	548.2
	F13	37380	268.12	264.5	68.00	0.2536	218.0	310.0	387.5	267.44, 268.81	557.6
	ERA-5	37380	824.57	840.7	136.0	0.1649	754.15	903.33	1020.9	823.19, 825.95	-

Supplementary Information

Table S10

NIO statistics for r_m , r_{34} , r_{50} , r_{64} and r_{100} (in km): including the mean, mean absolute error (MAE) and BIAS. Note that was used the same r_m in all radial wind profiles. It is remarkable that the r_m is operationally estimated by NHC, but not quality controlled after TC season and r_{100} is not recorded.

Class		Mean						MAE					BIAS				
		JTWC	H80	D87	W06	E11	F13	H80	D87	W06	E11	F13	H80	D87	W06	E11	F13
TS	r_m	60.6	50.4	50.4	50.4	50.4	50.4	16.5	16.5	16.5	16.5	16.5	0.28	0.28	0.28	0.28	0.28
	r_{34}	144.6	86.6	104.1	106.2	89.7	68.5	48.4	45.1	47.7	47.6	79.6	-36.1	-13.2	-16.5	-32.4	-79.4
	r_{50}	64.8	64.4	77.7	68.3	68.5	53.2	25.4	35.0	26.0	27.5	25.1	-8.8	24.4	10.6	13.0	-11.1
H	r_m	34.8	36.7	36.7	36.7	36.7	36.7	12.9	12.9	12.9	12.9	12.9	6.4	6.4	6.4	6.4	6.4
	r_{34}	191.4	127.9	141.9	206.1	133.3	56.9	61.3	53.1	50.4	57.7	142.1	-47.1	-31.2	23.9	-43.1	-143.2
	r_{50}	90.4	81.8	100.1	113.0	89.6	47.9	27.5	35.8	39.0	30.0	47.1	1.63	22.0	30.6	9.7	-46.4
	r_{64}	51.1	56.1	67.1	62.7	60.5	38.8	21.5	31.8	26.7	25.2	19.5	15.4	29.8	23.2	21.0	-11.1
MH	r_m	22.1	26.3	26.3	26.3	26.3	26.3	8.4	8.4	8.4	8.4	8.4	4.6	4.6	4.6	4.6	4.6
	r_{34}	219.9	140.9	132.2	238.9	144.4	46.5	81.1	90.6	37.9	77.7	183.1	-74.2	-84.1	20.2	-71.5	-181.5
	r_{50}	118.8	93.7	103.4	156.2	103.3	41.2	31.5	28.2	42.3	26.9	84.9	-22.2	-12.3	39.4	-12.4	-87.8
	r_{64}	70.2	70.8	84.3	108.2	79.7	35.5	20.6	25.7	40.9	23.2	43.9	2.81	16.2	40.4	11.9	-37.2
	r_{100}	-	39.1	47.2	43.5	43.1	27.5	-	-	-	-	-	-	-	-	-	-
Trop	r_m	61.9	53.5	53.5	53.5	53.5	53.5	16.3	16.3	16.3	16.3	16.3	1.4	1.4	1.4	1.4	1.4
	r_{34}	162.1	97.5	112.6	132.7	101.1	64.5	54.5	51.6	47.2	52.9	108.2	-42.1	-24.5	-4.2	-39.4	-107.2
	r_{50}	89.1	77.6	92.4	104.3	84.3	57.5	28.0	33.6	36.3	28.5	33.9	-2.5	13.7	27.4	4.9	-31.8
	r_{100}	-	39.1	47.2	43.5	43.1	27.5	-	-	-	-	-	-	-	-	-	-
HTrop	r_m	30.3	33.8	33.8	33.8	33.8	33.8	11.3	11.3	11.3	11.3	11.3	5.8	5.8	5.8	5.8	5.8
	r_{34}	201.3	131.5	139.2	215.4	136.4	34.1	68.2	66.1	46.1	64.7	151.2	-57.8	-50.4	22.6	-53.6	-154.6
	r_{50}	100.5	85.2	100.9	125.2	93.4	48.9	28.9	33.1	40.2	28.9	64.9	-6.8	9.6	33.8	1.84	-57.8
	r_{64}	59.1	60.3	71.9	75.9	65.9	56.4	21.1	29.3	32.5	24.4	15.1	10.2	24.2	30.3	17.3	-13.4
	r_{100}	-	39.1	47.2	43.5	43.1	27.5	-	-	-	-	-	-	-	-	-	-
Full basin	r_m	61.9	53.5	53.5	53.5	53.5	53.5	16.3	16.3	16.3	16.3	16.3	1.4	1.4	1.4	1.4	1.4
	r_{34}	162.1	97.5	112.6	132.7	101.1	64.1	54.5	51.6	47.2	52.9	111.4	-42.1	-24.3	-4.2	-39.4	-110.8
	r_{50}	89.2	77.6	92.4	104.3	84.3	57.5	28.0	33.6	36.3	28.5	43.9	-2.5	13.7	27.4	-4.9	-47.2
	r_{64}	59.1	66.3	71.9	75.9	65.9	56.4	21.1	29.3	32.5	24.4	15.1	10.2	24.2	30.3	17.3	-13.4
	r_{100}	-	39.1	47.2	43.5	43.1	27.5	-	-	-	-	-	-	-	-	-	-

Supplementary Information

Table S11

NIO statistics for TC outer radius from 1945 to 2019: including the mean (μ), median, standard deviation (σ), coefficient of variation (CV), 25th percentile (P_{25}), 75th percentile (P_{75}), 95th percentile (P_{95}) and the 95% confidence interval (CI). N represent the total data analysed and the outer radius are given in *km*.

Class	Wind profile	N	μ	Median	σ	CV	P_{25}	P_{75}	P_{95}	CI
TD	H80	2588	628.36	570.50	209.3	0.3331	470.50	819.50	929.50	620.28, 636.43
	D87	2588	417.94	363.00	119.4	0.2858	316.00	549.50	590.00	413.34, 422.55
	W06	2588	632.55	644.00	76.35	0.1207	591.37	691.50	734.00	629.61, 635.50
	E11	2588	258.33	240.00	68.87	0.2665	212.50	294.50	390.50	255.68, 260.99
	F13	2588	245.51	229.50	68.31	0.2782	202.50	277.50	378.32	242.88, 248.15
TS	H80	2125	916.26	913.00	193.5	0.2112	752.00	1072.0	1214.5	908.03, 924.50
	D87	2125	429.01	395.50	84.12	0.1960	356.50	517.00	539.50	425.43, 432.59
	W06	2125	750.88	753.50	41.80	0.0556	721.50	779.00	815.00	749.10, 752.66
	E11	2125	309.35	295.00	61.49	0.1987	266.00	343.00	408.20	306.73, 311.96
	F13	2125	301.98	288.50	61.58	0.2039	259.00	335.50	401.30	299.35, 304.60
H	H80	488	1168.6	1168.2	158.2	0.1354	1042.3	1268.0	1478.4	1154.5, 1182.7
	D87	488	375.61	366.50	52.03	0.1385	333.00	418.50	467.30	370.98, 380.24
	W06	488	784.50	784.50	30.51	0.0388	764.00	804.00	834.82	781.79, 787.22
	E11	488	343.75	332.00	46.69	0.1358	313.00	364.50	414.30	339.59, 347.91
	F13	488	340.23	329.50	46.83	0.1376	309.00	360.62	410.82	336.07, 344.40
MH	H80	192	1256.7	1281.0	109.8	0.0873	1206.1	1301.5	1422.5	1241.0, 1272.4
	D87	192	302.15	306.25	37.89	0.1254	279.12	320.50	361.00	296.74, 307.56
	W06	192	736.31	732.00	36.98	0.0502	712.37	765.75	798.22	731.03, 741.59
	E11	192	337.36	333.00	27.46	0.0814	317.50	355.25	381.50	333.44, 341.28
	F13	192	335.53	331.50	27.42	0.0817	315.75	353.62	379.45	331.62, 339.45
Trop	H80	5393	813.06	819.50	278.4	0.3424	579.50	1004.5	1272.0	805.63, 820.50
	D87	5393	414.35	376.50	102.9	0.2485	330.50	523.50	577.00	411.60, 417.10
	W06	5393	696.62	712.50	86.62	0.1243	647.00	762.50	809.00	694.31, 698.93
	E11	5393	288.98	282.00	70.42	0.2436	238.00	331.00	401.40	287.10, 290.86
	F13	5393	279.54	271.50	71.82	0.2569	228.50	324.50	393.20	277.62, 281.45
HTrop	H80	680	1193.5	1219.5	151.5	0.1269	1073.8	1284.0	1469.3	1182.1, 1204.9
	D87	680	354.87	342.75	58.67	0.1653	317.00	394.00	448.00	350.45, 359.29
	W06	680	770.90	773.75	39.05	0.0506	747.50	796.50	831.50	767.95, 773.84
	E11	680	341.95	332.50	42.26	0.1235	314.00	362.50	407.02	338.76, 345.13
	F13	680	338.91	330.00	42.31	0.1248	311.00	358.50	403.55	335.72, 342.10

Supplementary Information

Table S12

NIO statistics for TC outer radius from 1980 to 2019: including the mean (μ), median, standard deviation (σ), coefficient of variation (CV), 25th percentile (P_{25}), 75th percentile (P_{75}), 95th percentile (P_{95}), the 95% confidence interval (CI) and the mean absolute error (MAE) respect to TC size from ERA-5 reanalysis. N represents the total data analysed and the outer radius is given in *km*. The lower MAE is marked in bold text. WP: Wind Profile

Class	WP	N	μ	Median	σ	CV	P_{25}	P_{75}	P_{95}	CI	MAE
TD	H80	2458	635.02	578.75	211.8	0.3335	473.0	846.0	929.5	626.64, 643.40	185.9
	D87	2458	422.50	369.0	120.7	0.2857	316.5	549.5	590.0	417.72, 427.27	254.4
	W06	2458	633.41	645.5	77.14	0.1217	592.5	693.0	735.0	630.35, 636.46	97.2
	E11	2458	260.47	243.0	69.80	0.2679	213.5	297.0	393.0	257.71, 263.24	409.9
	F13	2458	247.45	231.0	69.30	0.2800	203.5	279.5	379.5	244.71, 250.19	422.8
	ERA-5	2458	668.97	674.5	108.3	0.1619	610.4	735.4	836.5	664.68, 673.25	-
TS	H80	1827	935.92	981.0	197.1	0.2106	766.0	1089.0	1214.5	926.87, 944.97	260.1
	D87	1827	439.70	451.0	85.50	0.1944	359.0	517.0	556.14	435.78, 443.63	267.5
	W06	1827	752.36	755.5	42.15	0.0560	723.5	781.0	816.5	750.42, 754.29	92.1
	E11	1827	314.67	300.5	63.46	0.2016	269.5	350.0	414.34	311.76, 317.58	391.3
	F13	1827	307.03	294.0	63.58	0.2070	262.5	342.0	406.5	304.11, 309.95	398.9
	ERA-5	1827	704.80	707.6	97.38	0.1381	652.41	766.95	862.3	700.33, 709.27	-
H	H80	376	1208.7	1219.5	155.0	0.1282	1089.0	1277.5	1523.0	1192.9, 1224.4	489.2
	D87	376	388.50	389.5	50.97	0.1312	346.37	431.0	476.0	383.32, 393.68	331.4
	W06	376	790.01	789.5	28.19	0.0356	771.87	807.0	838.37	787.15, 792.87	93.4
	E11	376	347.86	338.25	50.05	0.1438	313.5	367.12	425.62	342.78, 352.94	371.9
	F13	376	344.14	335.0	50.15	0.1457	309.87	362.62	421.0	339.05, 349.23	375.7
	ERA-5	376	719.48	724.7	87.76	0.1219	666.44	777.48	867.09	710.57, 728.40	-
MH	H80	176	1270.3	1283.2	103.8	0.0817	1222.5	1302.3	1422.5	1254.8, 1285.8	542.8
	D87	176	304.13	307.5	38.87	0.1278	282.0	323.0	362.25	298.33, 309.93	423.4
	W06	176	738.32	736.25	37.67	0.0510	713.62	767.75	798.5	732.70, 743.94	73.3
	E11	176	335.44	330.5	27.48	0.0819	316.0	351.25	382.62	331.33, 339.54	392.1
	F13	176	333.57	328.75	27.39	0.0821	314.0	349.12	381.0	329.48, 337.66	393.9
	ERA-5	176	727.53	723.11	81.74	0.1123	678.54	780.81	863.41	715.34, 739.73	-
Trop	H80	4837	816.39	819.5	285.1	0.3492	571.5	1004.5	1277.5	808.35, 824.43	250.8
	D87	4837	422.04	386.0	105.5	0.2500	331.5	526.5	582.5	419.07, 425.02	271.5
	W06	4837	694.33	709.5	88.02	0.1267	643.5	761.5	809.0	691.85, 696.81	94.1
	E11	4837	290.46	284.0	72.30	0.2489	237.5	334.5	404.59	288.43, 292.50	399.2
	F13	4837	280.60	272.5	73.68	0.2625	227.5	326.5	397.5	278.53, 282.68	409.04
	ERA-5	4837	688.56	694.3	103.9	0.1510	632.36	753.5	851.33	685.63, 691.49	-
HTrop	H80	552	1228.3	1244.5	143.6	0.1169	1145.1	1296.0	1501.7	1216.3, 1240.3	506.31
	D87	552	361.60	354.75	61.62	0.1704	320.0	409.0	451.22	356.44, 366.75	360.7
	W06	552	773.53	778.0	39.67	0.0512	749.5	798.12	833.5	770.21, 776.85	87.5
	E11	552	343.90	334.3	44.50	0.1294	314.0	364.12	413.0	340.17, 347.62	379.4
	F13	552	340.77	332.3	44.46	0.1304	311.5	360.5	408.89	337.05, 344.49	381.5
	ERA-5	552	722.05	723.58	85.97	0.1190	668.29	779.56	867.21	714.86, 729.24	-
Full basin	H80	4837	816.39	819.5	285.1	0.3492	571.5	1004.5	1277.5	808.35, 824.43	250.8
	D87	4837	422.04	386.0	105.5	0.2500	331.5	526.5	582.5	419.07, 425.02	271.5
	W06	4837	694.33	709.5	88.02	0.1267	643.5	761.5	809.0	691.85, 696.81	91.2
	E11	4837	290.46	284.0	72.30	0.2489	237.5	334.5	404.59	288.43, 292.50	399.3
	F13	4837	280.60	272.5	73.68	0.2625	227.5	326.5	397.5	278.53, 282.68	409.1
	ERA-5	4837	688.56	694.36	103.9	0.1510	632.36	753.49	851.33	685.63, 691.49	-

Supplementary Information

Table S13

SIO statistics for r_m , r_{34} , r_{50} , r_{64} and r_{100} (in km): including the mean, mean absolute error (MAE) and BIAS. Note that was used the same r_m in all radial wind profiles. It is remarkable that the r_m is operationally estimated by NHC, but not quality controlled after TC season and r_{100} is not recorded.

Class		Mean						MAE					BIAS				
		JTWC	H80	D87	W06	E11	F13	H80	D87	W06	E11	F13	H80	D87	W06	E11	F13
TS	r_m	61.2	48.9	48.9	48.9	48.9	48.9	15.1	15.1	15.1	15.1	15.1	-4.1	-4.1	-4.1	-4.1	-4.1
	r_{34}	162.9	82.2	103.5	110.4	87.8	67.2	66.3	58.1	57.7	71.7	94.5	-58.1	-36.4	-30.1	-65.4	-96.4
	r_{50}	72.2	65.2	78.8	70.2	58.4	53.9	27.3	33.8	28.3	24.1	26.1	3.3	18.9	8.24	-2.6	-25.7
H	r_m	35.2	36.8	36.8	36.8	36.8	36.8	10.4	10.4	10.4	10.4	10.4	6.0	6.0	6.0	6.0	6.0
	r_{34}	219.5	130.4	143.8	214.4	127.9	57.1	77.1	66.7	51.7	81.6	159.4	-72.1	-57.6	5.54	-77.2	-161.1
	r_{50}	99.8	83.6	101.9	118.8	85.8	45.1	28.0	33.9	40.4	29.1	46.3	-5.0	15.3	24.8	16.3	-45.2
	r_{64}	54.7	57.7	69.3	66.3	62.9	38.2	20.8	32.6	28.6	22.4	19.6	14.3	29.6	24.8	16.3	-15.1
MH	r_m	28.3	28.4	28.4	28.4	28.4	28.4	10.2	10.2	10.2	10.2	10.2	3.1	3.1	3.1	3.1	3.1
	r_{34}	240.9	149.9	141.7	242.4	149.7	68.6	77.5	85.9	50.1	80.3	199.4	-73.5	-83.4	9.97	-76.4	-198.2
	r_{50}	118.5	99.7	110.6	158.7	106.9	55.5	28.3	29.7	52.6	29.2	76.4	-6.7	5.41	47.9	0.25	-79.2
	r_{64}	66.6	75.2	89.9	109.8	82.3	46.9	23.5	36.0	50.1	28.7	34.8	18.0	34.5	49.8	25.3	-27.8
	r_{100}	-	41.8	50.5	44.6	43.7	29.4	-	-	-	-	-	-	-	-	-	-
Trop	r_m	57.7	48.1	48.1	48.1	48.1	48.1	14.5	14.5	14.5	14.5	14.5	-0.5	-0.5	-0.5	-0.5	-0.5
	r_{34}	188.8	104.1	117.5	150.7	109.3	71.2	69.3	63.3	53.7	75.0	133.2	-62.4	-47.9	-12.1	-70.7	-141.2
	r_{50}	96.9	82.1	97.4	114.4	83.8	56.9	27.9	32.7	40.7	28.0	49.1	-3.3	13.5	28.8	-2.2	-49.4
	r_{64}	59.7	63.2	75.7	79.8	70.2	49.1	21.9	34.0	37.6	25.2	25.8	15.9	31.6	35.3	20.3	-23.4
	r_{100}	-	41.8	50.5	44.6	43.7	29.4	-	-	-	-	-	-	-	-	-	-
HTrop	r_m	32.6	34.1	34.1	34.1	34.1	34.1	10.3	10.3	10.3	10.3	10.3	4.9	4.9	4.9	4.9	4.9
	r_{34}	227.7	136.3	143.1	222.9	134.7	64.4	77.1	73.6	51.0	80.9	169.2	-72.3	-66.4	7.3	-76.5	-179.1
	r_{50}	106.7	88.6	104.5	131.1	92.4	53.5	28.0	32.3	45.0	29.1	59.0	-5.6	11.7	35.7	-2.1	-58.4
	r_{64}	59.7	63.2	75.7	79.8	70.2	53.3	21.9	34.0	37.6	25.2	26.3	15.9	31.6	35.3	20.3	-23.4
	r_{100}	-	41.8	50.5	44.6	43.7	29.4	-	-	-	-	-	-	-	-	-	-
Full basin	r_m	58.1	50.1	50.1	50.1	50.1	50.1	14.7	14.7	14.7	14.7	14.7	-0.8	-0.8	-0.8	-0.8	-0.8
	r_{34}	189.9	104.2	117.7	150.8	109.1	71.6	70.9	64.7	55.0	73.6	138.4	-64.5	-49.3	-14.1	-71.2	-139.1
	r_{50}	97.3	82.1	97.4	114.4	83.8	66.3	27.9	32.7	40.8	28.0	51.0	-3.4	13.5	28.7	-2.3	-47.2
	r_{64}	59.7	63.2	75.7	79.8	70.2	53.3	21.9	34.0	37.6	25.2	26.3	15.9	31.6	35.3	20.3	-23.4
	r_{100}	-	41.8	50.5	44.6	43.7	29.4	-	-	-	-	-	-	-	-	-	-

Supplementary Information

Table S14

SIO statistics for TC outer radius from 1945 to 2019: including the mean (μ), median, standard deviation (σ), coefficient of variation (CV), 25th percentile (P_{25}), 75th percentile (P_{75}), 95th percentile (P_{95}) and the 95% confidence interval (CI). N represents the total data analysed and the outer radii are given in km .

Class	Wind profile	N	μ	Median	σ	CV	P_{25}	P_{75}	P_{95}	CI
TD	H80	9693	601.55	568.50	184.1	0.3062	472.00	768.00	869.50	597.88, 605.21
	D87	9693	399.91	358.00	102.2	0.2556	320.00	506.50	576.00	397.88, 401.95
	W06	9693	633.26	647.50	82.89	0.1308	595.50	688.50	742.00	631.61, 634.91
	E11	9693	213.77	209.00	54.00	0.2526	181.00	242.00	311.50	212.70, 214.85
	F13	9693	227.33	220.00	52.93	0.2328	194.50	255.00	324.70	226.27, 228.38
TS	H80	8383	903.94	921.50	168.6	0.1865	767.50	1019.0	1187.0	900.33, 907.55
	D87	8383	418.84	403.50	64.56	0.1541	361.50	477.00	506.00	417.46, 420.22
	W06	8383	764.73	763.00	49.07	0.0641	730.50	795.00	853.00	763.68, 765.78
	E11	8383	271.15	264.00	44.81	0.1652	240.00	295.00	356.00	270.19, 272.11
	F13	8383	278.87	271.00	43.57	0.1562	248.00	301.00	363.00	277.93, 279.80
H	H80	3230	1189.8	1178.0	149.1	0.1253	1071.6	1307.5	1430.0	1184.6, 1194.9
	D87	3230	377.86	372.00	45.79	0.1211	340.00	414.00	447.00	376.28, 379.44
	W06	3230	799.73	797.00	34.45	0.0430	776.50	820.50	861.50	798.54, 800.91
	E11	3230	318.08	311.50	34.05	0.1070	294.50	336.50	382.27	316.91, 319.26
	F13	3230	321.90	315.00	33.64	0.1045	298.12	340.37	385.77	320.74, 323.06
MH	H80	1452	1337.7	1369.2	161.8	0.1210	1191.0	1472.0	1598.5	1329.4, 1346.1
	D87	1452	324.98	324.00	43.45	0.1336	289.00	361.00	388.50	322.74, 327.22
	W06	1452	744.33	748.00	41.06	0.0551	717.50	774.00	805.50	742.21, 746.44
	E11	1452	348.89	341.50	35.58	0.1019	322.50	368.00	414.00	347.06, 350.73
	F13	1452	350.96	343.25	35.52	0.1012	324.00	370.50	416.72	349.13, 352.79
Trop	H80	22427	841.32	825.00	298.3	0.3546	604.50	1050.0	1379.5	837.42, 845.23
	D87	22427	397.69	373.50	83.27	0.2093	335.50	471.50	544.50	396.60, 398.782
	W06	22427	710.47	726.00	93.38	0.1314	658.00	778.00	831.50	709.25, 711.70
	E11	22427	259.29	257.50	64.34	0.2481	213.50	304.00	365.50	258.45, 260.13
	F13	22427	268.46	266.50	61.04	0.2273	224.50	310.00	370.85	267.66, 269.26
HTrop	H80	4659	1234.9	1225.0	167.7	0.1358	1105.0	1366.5	1535.0	1230.1, 1239.7
	D87	4659	361.02	357.00	51.00	0.1412	325.75	398.50	447.00	359.56, 362.49
	W06	4659	781.90	785.50	43.82	0.0560	756.50	809.50	851.50	780.64, 783.16
	E11	4659	327.98	322.00	37.12	0.1132	302.00	350.00	395.50	326.91, 329.05
	F13	4659	331.24	325.00	36.58	0.1104	305.50	352.50	398.50	330.19, 332.29
ExTrop	H80	331	984.10	992.00	210.2	0.2136	853.75	1120.5	1334.0	961.33, 1006.8
	D87	331	486.11	483.00	34.56	0.0711	467.50	505.25	544.50	482.36, 489.85
	W06	331	842.96	858.00	68.76	0.0815	806.00	887.50	930.25	835.51, 850.40
	E11	331	193.32	197.50	38.05	0.1968	168.50	220.25	251.00	189.20, 197.44
	F13	331	210.98	213.00	30.65	0.1453	188.75	232.25	259.25	207.66, 214.30

Supplementary Information

Table S15

SIO statistics for TC outer radius from 1980 to 2019: including the mean (μ), median, standard deviation (σ), coefficient of variation (CV), 25th percentile (P_{25}), 75th percentile (P_{75}), 95th percentile (P_{95}), the 95% confidence interval (CI) and the mean absolute error (MAE) respect to TC size from ERA-5 reanalysis. N represents the total data analysed and the outer radius is given in *km*. The lower MAE is marked in bold text. WP: Wind Profile

Class	WP	N	μ	Median	σ	CV	P_{25}	P_{75}	P_{95}	CI	MAE
TD	H80	7789	631.45	601.5	178.4	0.2825	494.0	768.0	869.5	627.48, 635.41	197.1
	D87	7789	414.89	372.5	103.0	0.2484	325.0	514.0	576.0	412.60, 417.18	340.2
	W06	7789	644.73	654.5	71.16	0.1103	609.0	694.5	746.2	643.15, 646.32	153.4
	E11	7789	223.40	215.5	51.11	0.2288	190.5	251.0	317.5	222.27, 224.54	523.1
	F13	7789	237.01	227.0	50.30	0.2122	203.5	265.0	330.1	235.89, 238.13	509.7
	ERA-5	7789	744.01	760.6	151.6	0.2038	668.4	858.4	935.0	740.64, 747.37	-
TS	H80	7466	911.06	921.5	168.2	0.1847	777.0	1040.5	1187.0	907.24, 914.87	189.4
	D87	7466	421.89	412.5	64.86	0.1537	363.0	489.0	506.0	420.42, 423.36	376.5
	W06	7466	766.16	765.0	49.36	0.0644	732.0	796.0	856.5	765.04, 767.28	115.3
	E11	7466	272.04	265.0	45.34	0.1666	240.5	296.0	358.0	271.01, 273.07	521.5
	F13	7466	279.84	272.0	44.07	0.1574	248.5	302.0	365.0	278.84, 280.84	513.8
	ERA-5	7466	790.52	820.1	143.3	0.1813	724.7	900.0	949.7	787.26, 793.77	-
H	H80	2918	1194.3	1188.2	150.7	0.1262	1073.1	1307.5	1430.0	1188.9, 1199.8	368.9
	D87	2918	379.60	376.0	45.96	0.1210	342.0	421.37	447.0	377.93, 381.26	448.7
	W06	2918	800.73	798.0	34.78	0.0434	778.0	822.0	862.0	799.47, 801.99	97.6
	E11	2918	318.22	311.0	34.70	0.1090	293.5	338.0	382.5	316.96, 319.48	509.4
	F13	2918	322.07	314.7	34.28	0.1064	298.0	342.0	386.0	320.83, 323.32	505.5
	ERA-5	2918	825.82	859.6	115.2	0.1395	766.2	900.0	957.25	821.64, 830.01	-
MH	H80	1326	1341.8	1383.0	163.7	0.1219	1194.1	1472.0	1607.5	1333.0, 1350.6	502.1
	D87	1326	326.52	324.25	43.62	0.1335	291.0	368.5	390.0	324.17, 328.87	513.8
	W06	1326	745.64	750.0	40.58	0.0544	718.6	775.0	805.5	743.45, 747.83	121.6
	E11	1326	348.91	341.5	35.77	0.1025	322.5	367.3	417.7	346.98, 350.84	491.5
	F13	1326	351.00	343.0	35.73	0.1018	324.0	369.5	419.4	349.08, 352.93	489
	ERA-5	1326	839.79	871.1	97.90	0.1165	781.1	900.0	965.2	834.52, 845.07	-
Trop	H80	19202	868.99	869.5	288.9	0.3324	655.5	1076.5	1391.5	864.90, 873.07	240.9
	D87	19202	405.00	381.0	83.34	0.2057	339.5	489.0	544.5	403.82, 406.18	382.9
	W06	19202	719.43	733.0	84.50	0.1174	668.5	781.5	834.5	718.23, 720.62	128.7
	E11	19202	265.80	263.0	60.64	0.2281	220.5	307.5	368.0	264.94, 266.65	516.7
	F13	19202	265.80	263.0	60.64	0.2281	220.5	307.5	368.0	264.94, 266.65	507.9
	ERA-5	19202	780.06	804.39	144.2	0.1849	709.24	900.0	946.2	778.02, 782.10	-
HTrop	H80	4223	1239.8	1225.0	169.3	0.1366	1108.5	1373.0	1548.5	1234.6, 1244.9	409.9
	D87	4223	362.58	360.0	51.22	0.1412	326.5	398.5	447.0	361.03, 364.12	469.3
	W06	4223	782.87	786.5	43.85	0.0560	757.5	810.5	852.5	781.55, 784.20	105.3
	E11	4223	328.15	322.5	37.58	0.1145	301.5	350.5	396.4	327.02, 329.29	503.3
	F13	4223	331.44	325.0	37.03	0.1117	305.0	353.0	399.4	330.32, 332.56	500.1
	ERA-5	4223	830.09	861.8	110.2	0.1327	771.36	900.0	958.7	826.77, 833.42	-
ExTrop	H80	297	1005.0	992.0	193.7	0.1927	869.5	1122.0	1333.3	982.89, 1027.2	233.7
	D87	297	488.80	486.0	32.63	0.0667	469.5	506.5	546.3	485.07, 492.54	333.3
	W06	297	851.10	865.5	59.02	0.0693	817.5	889.0	930.5	844.35, 857.86	104.4
	E11	297	197.10	202.0	35.07	0.1779	172.0	221.5	251.0	193.09, 201.11	616.8
	F13	297	214.22	216.5	27.65	0.1290	193.0	233.5	259.1	211.06, 217.39	599.7
	ERA-5	297	851.16	900.0	158.6	0.1861	790.1	954.8	1042.3	833.36, 870.46	-
Full basin	H80	19499	871.06	869.5	288.1	0.3308	658.5	1076.5	1391.5	867.01, 875.10	240.8
	D87	19499	406.28	382.0	83.43	0.2053	340.5	489.0	544.5	405.11, 407.45	382.1
	W06	19499	721.44	734.5	85.70	0.1188	670.0	783.5	839.5	720.23, 722.64	128.3
	E11	19499	264.75	261.5	60.91	0.2300	219.0	306.5	368.0	263.89, 265.60	518.2
	F13	19499	273.89	271.0	57.67	0.2105	230.5	312.5	372.5	273.08, 274.70	509.3
	ERA-5	19499	780.57	805.3	144.2	0.1848	709.5	900.0	946.7	778.55, 782.60	-

Supplementary Information

Table S16

SPO statistics for r_m , r_{34} , r_{50} , r_{64} and r_{100} (in km): including the mean, mean absolute error (MAE) and BIAS. Note that was used the same r_m in all radial wind profiles. It is remarkable that the r_m is operationally estimated by NHC, but not quality controlled after TC season and r_{100} is not recorded.

Class		Mean						MAE					BIAS				
		JTWC	H80	D87	W06	E11	F13	H80	D87	W06	E11	F13	H80	D87	W06	E11	F13
TS	r_m	63.3	49.8	49.8	49.8	49.8	49.8	16.5	16.5	16.5	16.5	16.5	-2.3	-2.3	-2.3	-2.3	-2.3
	r_{34}	172.2	87.9	105.8	113.5	87.1	68.2	73.8	68.9	71.2	72.2	106.3	-59.3	-35.4	-32.7	-61.8	-109.6
	r_{50}	69.5	66.1	79.9	72.3	58.2	51.3	33.8	42.1	34.5	27.1	29.2	7.8	23.7	11.7	-4.5	-16.3
H	r_m	34.4	37.2	37.2	37.2	37.2	37.2	13.2	13.2	13.2	13.2	13.2	8.2	8.2	8.2	8.2	8.2
	r_{34}	216.6	131.3	144.9	215.7	128.1	67.5	76.5	70.9	59.4	81.5	163.4	-65.1	-50.4	11.8	-72.1	-167.2
	r_{50}	99.6	84.2	102.6	119.5	85.9	55.3	33.1	38.9	43.9	34.3	58.6	-3.1	17.8	30.1	-2.3	-55.3
	r_{64}	54.5	58.1	69.5	66.5	62.8	36.1	24.0	34.6	31.2	25.0	20.2	15.5	30.9	25.7	17.7	-13.2
MH	r_m	28.2	27.8	27.8	27.8	27.8	27.8	9.2	9.2	9.2	9.2	9.2	2.1	2.1	2.1	2.1	2.1
	r_{34}	246.6	148.1	139.4	241.6	147.9	58.4	87.7	97.9	50.1	89.5	204.6	-84.5	-95.2	2.22	-86.1	-211.3
	r_{50}	116.2	98.4	108.9	158.2	105.7	47.6	27.0	28.3	52.4	28.1	85.7	-7.9	2.85	49.0	-0.8	-81.4
	r_{64}	64.8	98.4	108.9	158.2	81.3	35.1	23.2	33.8	51.7	28.3	34.6	17.1	32.3	51.3	24.4	-34.2
	r_{100}	-	41.8	50.7	45.7	44.1	30.1	-	-	-	-	-	-	-	-	-	-
Trop	r_m	59.7	50.8	50.8	50.8	50.8	50.8	15.9	15.9	15.9	15.9	15.9	1.8	1.8	1.8	1.8	1.8
	r_{34}	195.9	103.5	117.8	149.2	107.1	62.4	75.6	73.3	63.7	76.8	141.2	-64.1	-48.5	-12.6	-68.4	-140.8
	r_{50}	95.8	81.7	97.1	113.4	82.9	57.3	31.4	36.6	43.9	31.0	55.2	-1.5	15.4	31.4	-0.4	-51.3
	r_{64}	61.7	62.6	74.9	78.7	69.2	53.2	23.7	34.3	39.7	26.4	24.7	16.2	31.5	36.3	20.6	-21.1
	r_{100}	-	41.8	50.7	45.7	44.1	30.1	-	-	-	-	-	-	-	-	-	-
HTrop	r_m	32.2	34.5	34.5	34.5	34.5	34.5	11.8	11.8	11.8	11.8	11.8	6.1	6.1	6.1	6.1	6.1
	r_{34}	227.5	135.9	143.3	111.8	133.7	64.8	80.4	80.7	55.9	84.2	181.2	-72.1	-66.4	8.5	-77.2	-183.5
	r_{50}	105.4	88.2	104.3	130.3	91.5	54.6	30.8	35.0	46.9	31.9	58.6	-4.6	12.6	37.1	-1.5	-61.5
	r_{64}	61.7	62.6	74.9	78.7	69.2	43.3	23.7	34.3	39.7	26.4	24.7	16.2	31.5	36.3	20.6	-21.1
	r_{100}	-	41.8	50.7	45.7	44.1	30.1	-	-	-	-	-	-	-	-	-	-
Full basin	r_m	59.8	51.2	51.2	51.2	51.2	51.2	16.0	16.0	16.0	16.0	16.0	1.7	1.7	1.7	1.7	1.7
	r_{34}	196.9	103.7	118.1	149.4	106.7	62.8	76.8	74.2	64.4	78.4	141.5	-65.4	-49.7	-14.3	-69.2	-143.8
	r_{50}	90.1	81.7	97.2	113.3	82.8	56.7	31.6	36.7	44.0	31.1	59.4	-1.9	15.1	31.0	-0.5	-55.2
	r_{64}	61.7	62.6	74.9	78.7	69.2	43.3	23.7	34.3	39.7	26.4	24.7	16.2	31.5	36.3	20.6	-21.1
	r_{100}	-	41.8	50.7	45.7	44.1	30.1	-	-	-	-	-	-	-	-	-	-

Supplementary Information

Table S17

SPO statistics for TC outer radius from 1945 to 2019: including the mean (μ), median, standard deviation (σ), coefficient of variation (CV), 25th percentile (P_{25}), 75th percentile (P_{75}), 95th percentile (P_{95}) and the 95% confidence interval (CI). N represents the total data analysed and the outer radii are given in km .

Class	Wind profile	N	μ	Median	σ	CV	P_{25}	P_{75}	P_{95}	CI
TD	H80	5734	605.96	563.00	213.9	0.3530	461.00	778.25	952.00	600.42, 611.50
	D87	5734	403.99	352.50	121.9	0.3018	321.00	539.37	602.00	400.84, 407.15
	W06	5734	635.89	651.50	92.65	0.1457	591.75	696.50	757.00	633.49, 638.29
	E11	5734	204.11	202.00	51.25	0.2511	174.50	229.50	296.00	202.79, 205.44
	F13	5734	218.93	213.50	51.44	0.2349	188.50	242.50	314.00	217.60, 220.27
TS	H80	5138	919.74	905.00	185.7	0.2019	763.50	1059.0	1249.5	914.66, 924.82
	D87	5138	425.90	399.50	74.14	0.1740	364.50	492.50	550.50	423.87, 427.93
	W06	5138	774.52	773.50	52.68	0.0680	737.00	807.50	864.00	773.08, 775.96
	E11	5138	262.88	256.00	42.29	0.1608	234.00	283.00	344.50	261.72, 264.04
	F13	5138	271.30	263.50	41.31	0.1523	243.00	289.50	352.50	270.17, 272.43
H	H80	1806	1198.6	1174.5	157.0	0.1310	1076.0	1316.5	1445.0	1191.3, 1205.8
	D87	1806	381.58	373.50	50.55	0.1324	340.50	424.00	464.37	379.24, 383.91
	W06	1806	803.33	799.75	36.70	0.0456	776.62	826.50	868.87	801.64, 805.03
	E11	1806	316.16	310.00	35.56	0.1124	291.50	333.87	388.37	314.52, 317.80
	F13	1806	320.10	313.00	35.15	0.1098	295.50	337.37	391.75	318.48, 321.72
MH	H80	702	1320.8	1297.2	148.8	0.1126	1183.7	1469.0	1522.5	1309.8, 1331.8
	D87	702	319.48	312.50	42.18	0.1320	289.50	356.50	383.50	316.35, 322.61
	W06	702	741.62	747.00	46.11	0.0621	714.50	773.50	811.45	738.20, 745.04
	E11	702	344.74	336.50	32.34	0.0938	321.50	362.87	414.00	342.34, 347.14
	F13	702	346.76	338.25	32.22	0.0929	323.50	365.00	415.47	344.37, 349.15
Trop	H80	12985	840.17	847.50	305.7	0.3639	587.50	1071.0	1360.0	834.91, 845.43
	D87	12985	402.11	371.50	97.44	0.2423	337.00	455.00	600.00	400.43, 403.79
	W06	12985	713.50	732.50	98.98	0.1387	660.00	784.00	839.40	711.80, 715.20
	E11	12985	251.16	247.50	63.29	0.2520	207.50	294.50	357.00	250.08, 252.25
	F13	12985	261.08	258.00	60.41	0.2313	219.00	302.00	363.50	260.04, 262.12
HTrop	H80	2494	1232.3	1211.0	164.4	0.1334	1107.0	1353.0	1504.0	1225.8, 1238.7
	D87	2494	363.67	356.50	55.52	0.1526	323.62	403.75	456.50	361.49, 365.85
	W06	2494	785.35	786.50	47.49	0.0604	759.00	817.00	860.00	783.49, 787.22
	E11	2494	324.55	319.00	36.71	0.1131	300.00	343.00	396.17	323.11, 326.00
	F13	2494	327.93	322.00	36.14	0.1102	303.62	345.50	399.00	326.51, 329.35
ExTrop	H80	395	968.53	960.00	227.9	0.2353	796.75	1146.0	1352.8	945.95, 991.11
	D87	395	498.09	491.00	48.07	0.0965	470.75	518.00	590.15	493.33, 502.85
	W06	395	841.38	853.50	79.90	0.0949	791.75	896.75	952.50	833.46, 849.29
	E11	395	184.02	187.50	40.19	0.2184	160.25	214.50	242.00	180.03, 188.00
	F13	395	204.25	205.50	32.11	0.1572	185.00	228.00	251.50	201.07, 207.43

Supplementary Information

Table S18

SPO statistics for TC outer radius from 1980 to 2019: including the mean (μ), median, standard deviation (σ), coefficient of variation (CV), 25th percentile (P_{25}), 75th percentile (P_{75}), 95th percentile (P_{95}), the 95% confidence interval (CI) and the mean absolute error (MAE) respect to TC size from ERA-5 reanalysis. N represents the total data analysed and the outer radius is given in *km*. The lower MAE is marked in bold text. WP: Wind Profile

Class	WP	N	μ	Median	σ	CV	P_{25}	P_{75}	P_{95}	CI	MAE
TD	H80	4283	651.25	589.5	214.4	0.3293	493.5	858.5	952.0	644.82, 657.68	211.7
	D87	4283	428.24	364.0	127.6	0.2980	326.0	563.0	644.0	424.42, 432.07	317.9
	W06	4283	652.07	659.0	75.15	0.1152	612.5	705.3	759.5	649.82, 654.32	143.2
	E11	4283	216.14	208.5	47.65	0.2204	185.5	238.5	305.9	214.71, 217.57	514.8
	F13	4283	231.39	221.0	48.84	0.2110	198.0	257.0	325.0	229.93, 232.86	499.9
	ERA-5	4283	728.17	749.2	158.4	0.2176	656.66	841.4	918.6	723.40, 732.94	-
TS	H80	4339	941.04	939.0	186.9	0.1986	784.5	1071.0	1249.5	935.48, 946.61	208.1
	D87	4339	433.31	409.0	76.41	0.1763	366.5	507.0	550.5	431.04, 435.59	370.4
	W06	4339	777.82	776.5	52.02	0.0668	741.5	810.0	866.5	776.27, 779.37	109.3
	E11	4339	266.41	259.5	43.25	0.1623	237.0	288.0	349.0	265.12, 267.70	528.8
	F13	4339	274.97	267.0	42.37	0.1541	245.5	295.5	357.0	273.71, 276.23	520.5
	ERA-5	4339	791.54	820.7	145.9	0.1843	731.2	900.0	943.8	787.18, 795.90	-
H	H80	1636	1211.3	1192.0	157.1	0.1297	1085.3	1345.8	1445.0	1203.7, 1218.9	375.5
	D87	1636	384.64	379.0	51.35	0.1335	341.37	424.0	469.0	382.15, 387.14	453.5
	W06	1636	804.66	801.5	36.71	0.0456	777.5	828.0	869.62	802.87, 806.44	98.6
	E11	1636	317.39	311.5	36.24	0.1141	292.0	335.0	390.0	315.63, 319.15	519.5
	F13	1636	321.38	314.8	35.84	0.1115	296.37	338.5	394.5	319.64, 323.11	515.5
	ERA-5	1636	836.07	899.7	115.6	0.1382	786.28	900.0	958.1	830.46, 841.68	-
MH	H80	680	1325.3	1308.5	148.7	0.1122	1187.2	1469.0	1522.5	1314.1, 1336.5	477.9
	D87	680	320.17	313.5	42.60	0.1330	289.0	356.5	383.5	316.96, 323.38	528.4
	W06	680	741.52	747.25	46.66	0.0629	713.5	774.12	811.5	738.00, 745.04	134.8
	E11	680	345.27	337.0	32.61	0.0944	321.5	363.75	415.1	342.81, 347.72	502.8
	F13	680	347.29	339.0	32.48	0.0935	323.5	365.62	417.0	344.85, 349.74	500.8
	ERA-5	680	847.40	900.0	104.2	0.1230	807.1	900.0	955.5	839.54, 855.26	-
Trop	H80	10646	888.01	912.5	297.1	0.3345	645.5	1111.5	1393.0	882.37, 893.66	250.8
	D87	10646	414.53	379.0	100.4	0.2422	341.5	492.5	602.0	412.63, 416.44	373.8
	W06	10646	726.67	741.5	85.77	0.1180	676.0	789.0	842.5	725.04, 728.30	122.7
	E11	10646	261.02	256.5	59.65	0.2285	216.0	303.0	363.5	259.89, 262.15	517.8
	F13	10646	270.88	267.0	56.97	0.2103	228.5	310.0	368.8	269.80, 271.96	508.2
	ERA-5	10646	776.18	803.8	150.9	0.1944	705.43	900.0	941.4	773.30, 779.06	-
HTrop	H80	2302	1244.3	1227.5	163.5	0.1314	1117.5	1375.5	1507.0	1237.6, 1250.9	405.1
	D87	2302	365.15	356.5	56.79	0.1555	324.0	405.5	456.5	362.83, 367.47	474.1
	W06	2302	785.35	786.5	48.32	0.0615	759.0	817.37	861.5	783.38, 787.33	109.3
	E11	2302	326.01	320.5	37.12	0.1138	301.0	345.0	398.5	324.49, 327.53	514.1
	F13	2302	329.40	323.5	36.56	0.1110	304.5	347.5	401.5	327.90, 330.89	510.8
	ERA-5	2302	839.38	900.0	112.2	0.1337	790.9	900.0	957.2	834.79, 843.97	-
ExTrop	H80	292	1033.1	1019.2	197.3	0.1910	893.37	1172.5	1376.1	1010.3, 1055.9	244.9
	D87	292	507.47	494.5	46.01	0.0906	475.25	528.75	601.17	502.16, 512.78	359.4
	W06	292	863.86	870.75	60.88	0.0704	823.37	905.0	960.72	856.84, 870.89	122.2
	E11	292	194.84	198.25	33.83	0.1736	172.0	220.5	247.72	190.94, 198.75	658.2
	F13	292	213.41	214.75	26.49	0.1241	196.62	233.62	255.95	210.36, 216.47	639.7
	ERA-5	292	852.16	900.0	158.6	0.1861	790.05	954.85	1042.3	833.86, 870.46	-
Full basin	H80	10938	891.89	912.5	295.8	0.3316	652.5	1114.5	1389.1	886.34, 897.43	251.3
	D87	10938	417.02	382.5	100.4	0.2409	342.5	494.5	602.0	415.13, 418.90	372.2
	W06	10938	730.34	744.5	88.03	0.1205	678.5	792.0	851.0	728.69, 731.99	122.5
	E11	10938	259.25	254.5	60.06	0.2316	214.0	301.5	362.5	258.13, 260.38	520.3
	F13	10938	269.34	265.0	57.12	0.2120	226.5	309.0	368.07	268.27, 270.41	510.5
	ERA-5	10938	776.98	805.3	150.9	0.1942	706.0	900.0	942.03	774.15, 779.82	-

Supplementary Information

Table S19

Global statistics for TC outer radius: including the mean (μ), median, standard deviation (σ), coefficient of variation (CV), 25th percentile (P_{25}), 75th percentile (P_{75}), 95th percentile (P_{95}) and the 95% confidence interval (CI). N represents the total data analysed and the outer radii are given in *km*.

Class	Wind profile	<i>N</i>	μ	Median	σ	CV	P_{25}	P_{75}	P_{95}	CI
TD	H80	60884	594.14	576.5	163.6	0.2755	490.0	688.5	901.0	592.83, 595.44]
	D87	60884	390.99	362.0	91.16	0.2331	328.5	444.0	563.0	390.27, 391.72
	W06	60884	649.96	657.5	82.96	0.1276	609.5	700.5	773.5	649.30, 650.62
	E11	60884	220.22	213.5	46.16	0.2096	195.0	236.5	307.5	219.86, 220.59
	F13	60884	214.07	207.5	47.18	0.2204	186.5	232.0	304.5	213.70, 214.45
TS	H80	68011	923.72	904.0	186.1	0.2015	782.5	1040.5	1258.5	922.33, 925.12
	D87	68011	420.58	401.0	68.12	0.1619	365.5	475.0	537.5	420.07, 421.10
	W06	68011	789.88	779.0	68.74	0.0870	741.5	829.0	921.0	789.36, 790.39
	E11	68011	266.85	259.5	38.01	0.1424	243.0	282.0	338.0	266.56, 267.13
	F13	68011	261.71	254.5	39.99	0.1528	235.5	279.0	337.0	261.41, 262.01
H	H80	36099	1236.3	1211.0	183.2	0.1482	1090.5	1364.5	1560.0	1234.4, 1238.1
	D87	36099	392.08	381.0	58.14	0.1482	346.5	434.5	495.0	391.48, 392.68
	W06	36099	834.40	820.5	64.73	0.0775	786.5	875.5	957.5	833.74, 835.07
	E11	36099	304.33	298.0	32.56	0.1070	281.5	318.5	364.5	304.00, 304.67
	F13	36099	300.89	295.5	34.14	0.1134	277.0	316.5	364.0	300.54, 301.24
MH	H80	14530	1333.5	1289.5	181.3	0.1359	1193.5	1447.0	1693.0	1330.6, 1336.5
	D87	14530	319.04	312.5	49.93	0.1565	283.0	356.5	407.5	318.23, 319.85
	W06	14530	756.91	755.0	63.50	0.0839	716.62	796.5	863.0	755.87, 757.94
	E11	14530	331.02	323.5	36.24	0.1094	306.0	344.5	403.0	330.43, 331.61
	F13	14530	329.47	322.0	36.82	0.1117	304.0	344.0	402.0	328.87, 330.07
Trop	H80	157782	871.39	853.5	302.3	0.3470	626.0	1097.5	1379.5	869.89, 872.88
	D87	157782	383.43	369.0	72.52	0.1891	337.5	416.0	532.5	383.07, 383.79
	W06	157782	729.78	744.0	91.24	0.1250	675.5	794.0	858.5	729.33, 730.23
	E11	157782	267.03	265.5	55.63	0.2083	227.5	302.5	357.0	266.75, 267.30
	F13	157782	263.27	262.0	56.74	0.2155	222.0	300.0	355.5	262.99, 263.55
HTrop	H80	43615	1227.8	1204.5	170.1	0.1385	1104.5	1329.0	1557.0	1226.2, 1229.3
	D87	43615	355.58	353.5	52.95	0.1489	321.5	390.0	447.0	355.08, 356.07
	W06	43615	792.08	794.0	55.36	0.0699	760.0	830.0	880.0	791.56, 792.60
	E11	43615	318.00	311.0	34.84	0.1095	295.0	332.0	385.5	317.67, 318.32
	F13	43615	315.77	309.0	35.69	0.1130	292.0	330.5	384.5	315.44, 316.11
ExTrop	H80	21742	1173.3	1198.5	306.8	0.2614	942.5	1419.5	1620.0	1169.2, 1177.4
	D87	21742	492.16	486.0	49.47	0.1005	463.5	517.0	580.5	491.50, 492.81
	W06	21742	886.08	902.5	81.65	0.0921	848.0	936.0	995.5	885.00, 887.17
	E11	21742	240.12	245.5	33.44	0.1392	218.5	267.5	283.5	239.67, 240.56
	F13	21742	227.32	233.0	38.56	0.1696	201.0	259.0	278.0	226.81, 227.84
All TC stages	H80	179524	907.93	888.5	318.5	0.3508	652.0	1143.0	1450.5	906.46, 909.40
	D87	179524	396.60	378.5	78.59	0.1981	342.5	446.5	543.5	396.23, 396.96
	W06	179524	748.71	756.5	103.5	0.1383	686.0	813.0	913.0	748.23, 749.19
	E11	179524	263.77	262.0	54.15	0.2053	226.5	297.5	352.5	263.52, 264.02
	F13	179524	258.92	257.0	56.10	0.2166	219.0	294.5	351.0	258.66, 259.18
	C16	578	909.4	881.0	248.5	0.27	740.7	1054.4	-	-

Supplementary Information

Table S20

Mean outer radius (*km*) estimated using each radial wind profile in each basin.

Class	Wind profile	NATL	NEPAC	WNP	NIO	SIO	SPO	Global
TD	H80	631.57	558.64	580.07	628.36	601.55	605.96	594.14
	D87	399.77	356.98	392.13	417.94	399.91	403.99	390.99
	W06	701.35	655.38	632.28	632.55	633.26	635.89	649.96
	E11	208.87	216.98	230.97	258.33	213.77	204.11	220.22
	F13	194.35	206.54	217.47	245.51	227.33	218.93	214.07
	ROCI	266.28	273.96	297.94	309.12	306.66	305.72	296.42
	ERA-5	761.06	751.31	771.29	668.97	744.01	728.17	751.35
TS	H80	962.21	824.32	951.00	916.26	903.94	919.74	923.72
	D87	434.00	377.46	429.91	429.01	418.84	425.90	420.58
	W06	821.21	758.40	794.95	750.88	764.73	774.52	789.88
	E11	252.12	266.77	275.91	309.35	271.15	262.88	266.85
	F13	242.66	260.36	267.37	301.98	278.87	271.30	261.71
	ROCI	337.33	318.24	337.02	309.45	321.95	324.34	327.78
	ERA-5	815.11	799.27	837.07	704.8	790.52	791.54	806.17
H	H80	1319.3	1104.3	1235.6	1168.6	1189.8	1198.6	1236.3
	D87	418.07	352.17	390.83	375.61	377.86	381.58	392.08
	W06	876.80	794.93	827.00	384.50	799.73	803.33	834.40
	E11	287.06	309.71	311.44	343.75	318.08	316.16	304.33
	F13	281.54	306.30	307.08	340.23	321.90	320.10	300.89
	ROCI	409.17	355.55	366.80	337.32	345.63	343.09	363.20
	ERA-5	855.81	833.34	864.62	719.48	825.82	836.07	850.59
MH	H80	1368.2	1191.4	1359.2	1256.7	1337.7	1320.8	1333.5
	D87	334.33	289.64	319.36	302.15	324.98	319.48	319.04
	W06	800.93	731.81	748.51	736.31	744.33	741.62	756.91
	E11	305.28	331.96	337.20	337.36	348.89	344.74	331.02
	F13	302.64	330.25	335.10	335.53	350.96	346.76	329.47
	ROCI	385.23	389.54	386.91	348.81	345.10	340.28	373.85
	ERA-5	861.34	849.84	904.32	727.53	839.79	847.40	870.67
Trop	H80	914.07	804.65	906.41	813.06	841.32	840.17	871.39
	D87	383.38	357.99	383.64	414.35	397.69	402.11	383.43
	W06	768.11	725.45	724.10	696.62	710.47	713.50	729.78
	E11	258.28	261.98	279.66	288.98	259.29	251.16	267.03
	F13	250.71	255.17	271.87	279.54	268.46	261.08	263.27
	ROCI	323.24	322.06	335.27	314.69	322.70	322.73	326.92
	ERA-5	796.90	785.45	822.82	688.75	780.06	776.18	793.48
HTrop	H80	1234.9	1124.6	1254.6	1193.5	1234.9	1232.3	1227.8
	D87	363.39	335.07	357.20	354.87	361.02	363.67	355.58
	W06	818.42	777.55	787.93	770.90	781.90	785.35	792.08
	E11	299.21	315.78	324.81	341.95	327.97	324.55	318.00
	F13	295.50	312.85	321.56	338.91	331.24	327.93	315.77
	ROCI	379.29	367.11	375.37	341.77	345.29	342.01	363.71
	ERA-5	850.04	838.45	890.50	722.05	830.09	839.38	856.08
ExTrop	H80	1200.4	-	1150.2	-	984.10	958.63	1173.3
	D87	488.37	-	500.92	-	486.11	498.09	492.16
	W06	889.77	-	886.33	-	842.96	841.38	886.08
	E11	243.77	-	239.16	-	193.32	184.02	240.12
	F13	230.55	-	224.05	-	210.98	204.25	227.32
	ROCI	384.69	-	346.79	-	379.38	359.23	366.55
	ERA-5	833.22	-	841.69	-	813.87	806.09	833.78

References

- Chavas, D.R., Lin, N., Dong, W., Lin, Y., 2016. Observed tropical cyclone size revisited. *J. Clim.* 29, 2923–2939. doi:10.1175/JCLI-D-15-0731.1.
- DeMaria, M., 1987. Tropical cyclone track prediction with a barotropic spectral model. *Mon. Weather Rev.* 115, 2346–2357. doi:10.1175/1520-0493(1987)115,2346:TCTPWA.2.0.CO;2.
- Emanuel, K., Rotunno, R., 2011. Self-stratification of tropical cyclone outflow. Part I: Implications for storm structure. *J. Atmos. Sci.* 68, 8223–2249. doi:10.1175/JAS-D-10-05024.1.
- Frisius, T., Scgönemann, D., 2013. The impact of gradient wind imbalance on potential intensity of tropical cyclones in an unbalanced slab boundary layer model. *J. Atmos. Sci.* 70, 1874–1890. doi:10.1175/JAS-D-12-0160.1.
- Holland, G.J., 1980. An analytic model of the wind and pressure profiles in hurricanes. *Mon. Weather Rev.* 108, 1212–1218. doi:10.1175/1520-0493(1980)108,1212:AAMOTW.2.0.CO;2.
- Willoughby, H.E., Darling, R.W.R., Rahn, M., 2006. Parametric representation of the primary hurricane vortex. Part II: A new family of sectionally continuous profiles. *Mon. Weather Rev.* 134, 1102–1120. doi:10.1175/MWR3106.1.

Supplementary Information

Moisture source identification for precipitation associated with tropical cyclone development over the Indian Ocean: a Lagrangian approach

Albenis Pérez-Alarcón^{1,2}, José C. Fernández-Alvarez^{1,2}, Rogert Sorí^{1,3}, Raquel Nieto¹, Luis Gimeno¹

¹ Centro de Investigación Mariña, Universidade de Vigo, Environmental Physics Laboratory (EPhysLab), Campus As Lagoas s/n, Ourense, 32004, Spain.

² Departamento de Meteorología, Instituto Superior de Tecnologías y Ciencias Aplicadas, Universidad de La Habana, 10400 La Habana, Cuba.

³ Instituto Dom Luiz, Faculdade de Ciências da Universidade de Lisboa, 1749-016 Campo Grande, Portugal.

Corresponding author: Albenis Pérez-Alarcón (albenis.perez.alarcon@uvigo.es)

Introduction

This Supporting Information provides additional Figures to support the findings discussed in the manuscript.

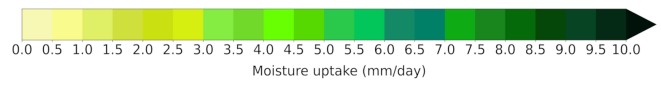
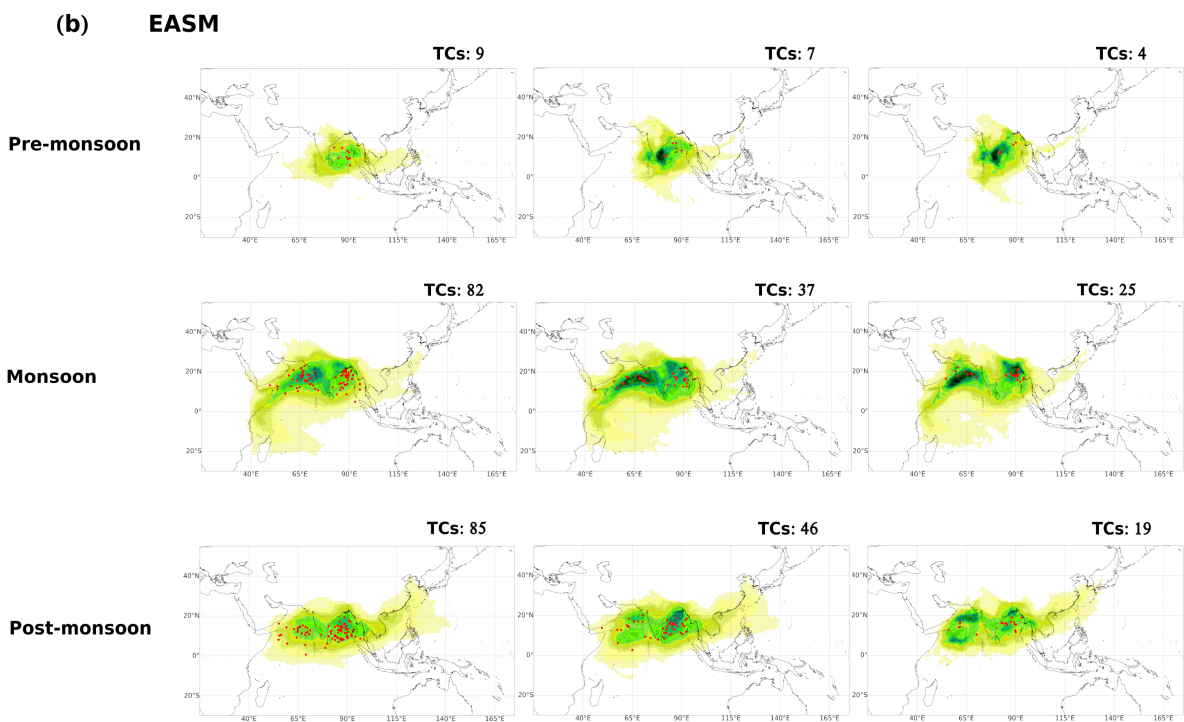
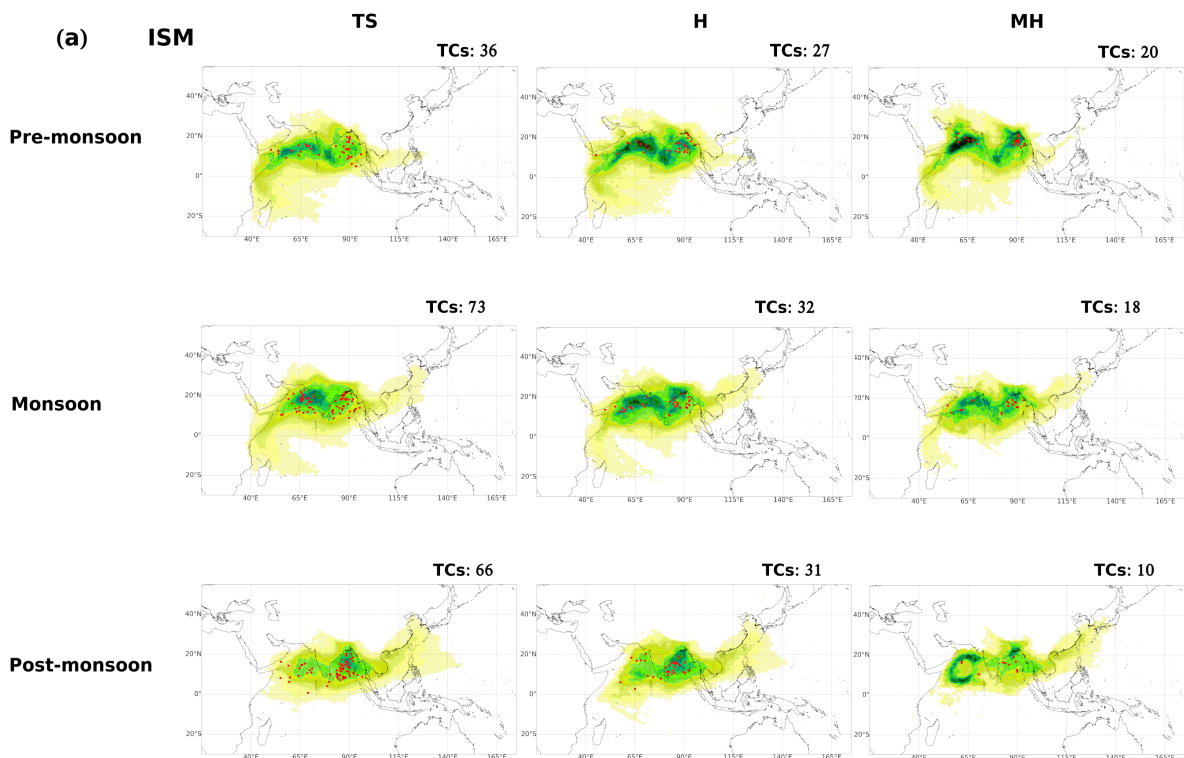


Fig. S1 Moisture uptake (greenish color) for tropical cyclones during tropical storms (TS), Hurricanes (H, category 1 and 2 on the Saffir-Simpson scale) and Major Hurricanes (MH, category 3+ on Saffir-Simpson scale) over the NIO basin during the pre-monsoon, monsoon and post-monsoon seasons for the **(a)** Indian Summer Monsoon (ISM) and **(b)** East Asian Summer Monsoon (EASM). Red points indicate the TCs position in each stage. In the top right of each map appears the number of TCs during each monsoon phase

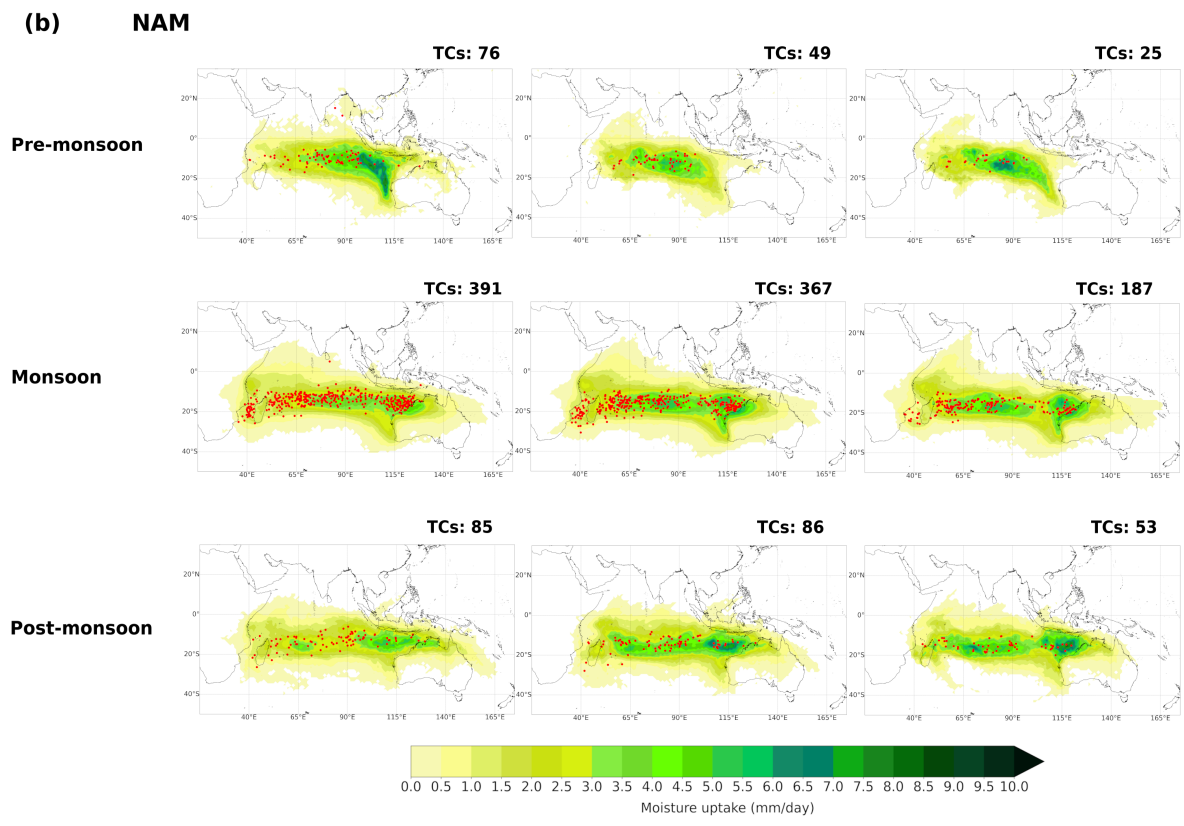
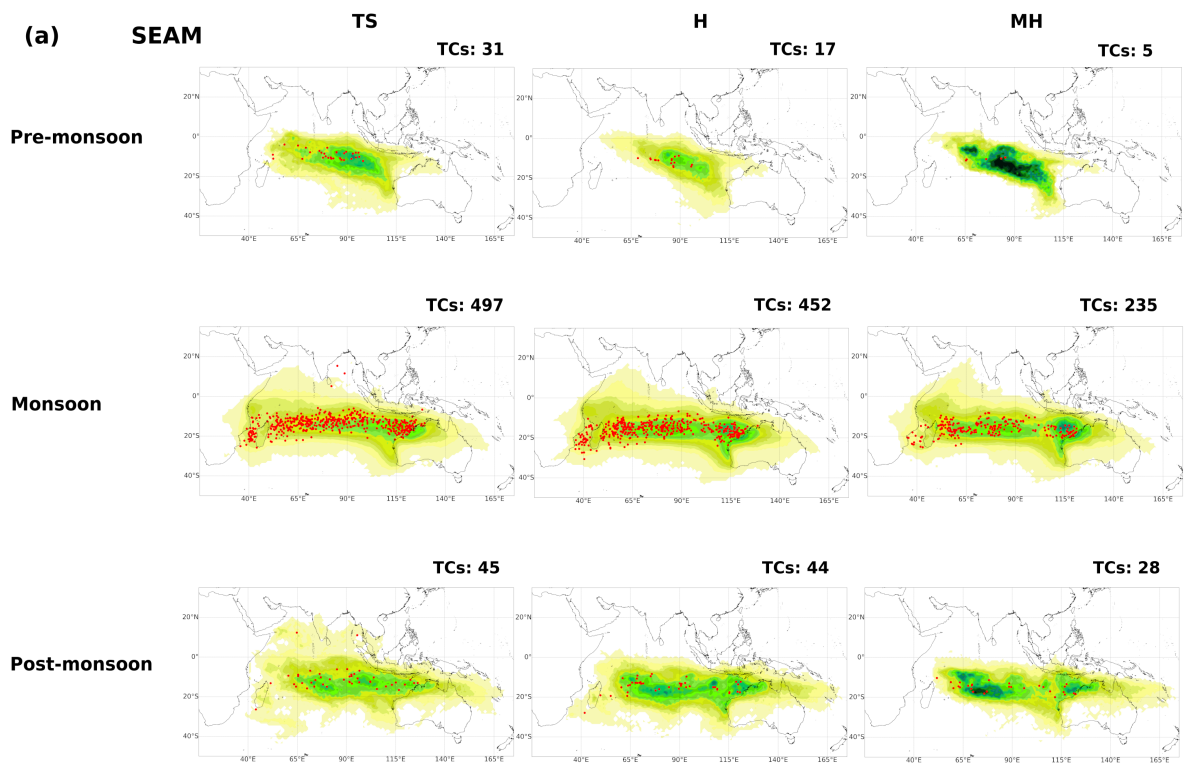


Fig. S2 Moisture uptake (greenish color) for tropical cyclones during tropical storms (TS), Hurricanes (H, category 1 and 2 on the Saffir-Simpson scale) and Major Hurricanes (MH, category 3+ on Saffir-Simpson scale) over the SIO basin during the pre-monsoon, monsoon and post-monsoon seasons for the **(a)** Southeastern African Monsoon (SEAM) and **(b)** North Australia Monsoon (NAM). Red points indicate the TCs position in each stage. In the top right of each map appears the number of TCs during each monsoon phase

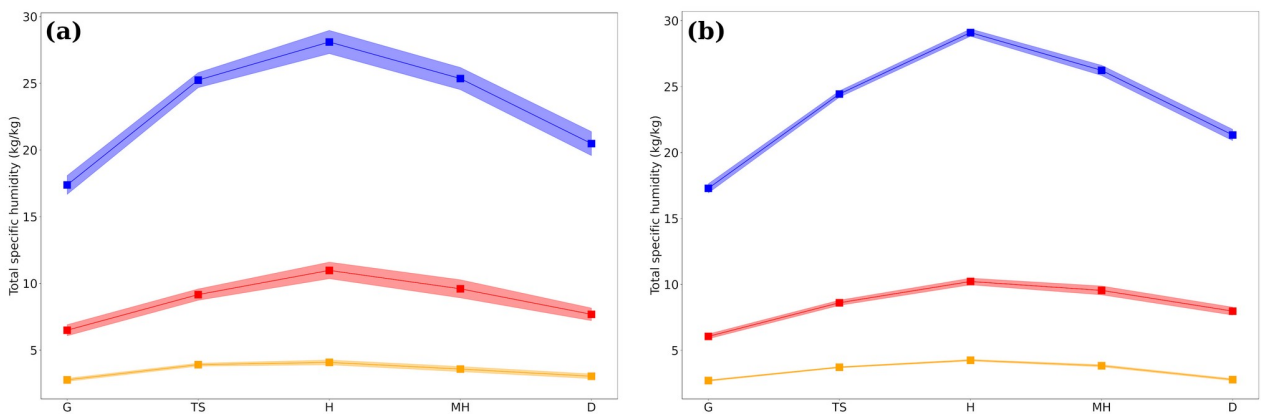


Fig. S3 Average total specific humidity in the atmospheric column (blue) and the mid-troposphere (700-500 hPa) (orange) enclosed by the outer radius of tropical cyclones (TCs), and the average total specific humidity computed using the Lagrangian diagnostic method (red) over the TCs area for **(a)** North Indian Ocean and **(b)** South Indian Ocean. The shaded areas denote the 95% confidence interval. G: Genesis, LMI: Lifetime Maximum Intensity, D: Dissipation, TS: Tropical Storm, H: Hurricanes (category 1 and 2 hurricanes on the Saffir-Simpson scale) and MH: Major Hurricanes (category 3+ hurricanes on Saffir-Simpson scale)

Supporting Information

Moisture Source for the Precipitation of Tropical Cyclones Over the Pacific Ocean Through a Lagrangian Approach

Albenis Pérez-Alarcón ^{a,b}, Rogert Sorí ^{a,c}, José C. Fernández-Alvarez ^{a,b}, Raquel Nieto^a, Luis Gimeno^a

^a *Centro de Investigación Mariña, Universidade de Vigo, Environmental Physics Laboratory (EPhysLab), Campus As Lagoas s/n, Ourense, 32004, Spain.*

^b *Departamento de Meteorología, Instituto Superior de Tecnologías y Ciencias Aplicadas, Universidad de La Habana, 10400 La Habana, Cuba.*

^c *Instituto Dom Luiz, Faculdade de Ciências da Universidade de Lisboa, 1749-016 Campo Grande, Portugal.*

Corresponding author: Albenis Pérez-Alarcón, albenis.perez.alarcon@uvigo.es

Introduction

This Supporting Information contains Figures and Tables that support the results discussed in the manuscript.

Table S1. Average outer radius (km) of tropical cyclones over the Western North Pacific (WNP), Central and East Pacific (NEPAC) and South Pacific Ocean (SPO) basins during the tropical storm (TS), hurricane (H, category 1 and 2 on the Saffir – Simpson wind scale) and major hurricanes (MH, Category 3+) intensity categories.

Intensity Category	WNP	NEPAC	SPO
TS	732	703	727
H	804	774	788
MH	750	727	741

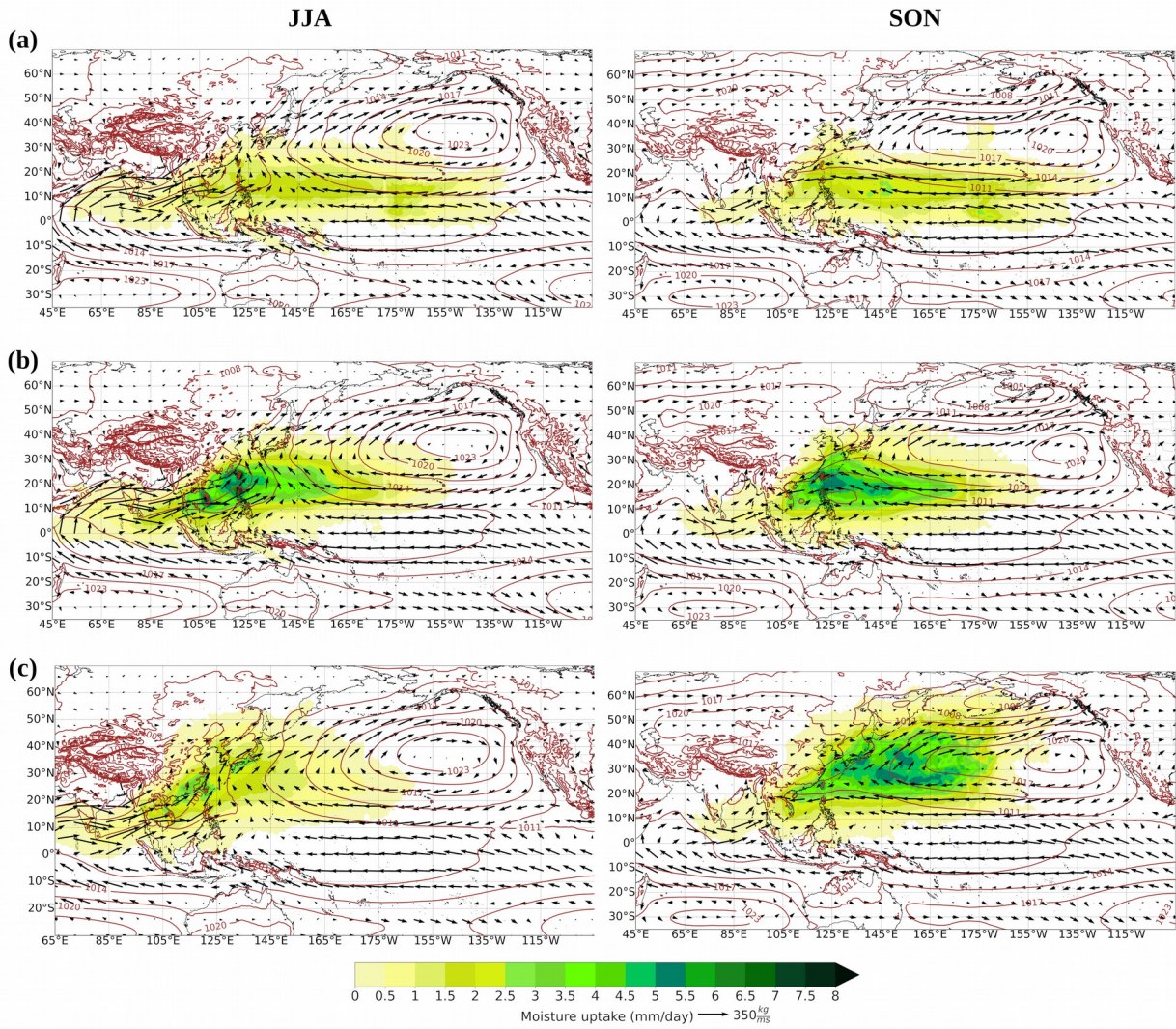


Fig. S1. Climatological moisture uptake (mm/d) patterns on June-July-August (JJA) and September-October-November (SON) during the TC (a) genesis, (b) lifetime maximum intensity and (c) dissipation stages over the Western North Pacific Ocean basin. The vertically integrated moisture flux (VIMF, kg/ms) and the mean sea level pressure (hPa) are represented by arrows and contours, respectively.

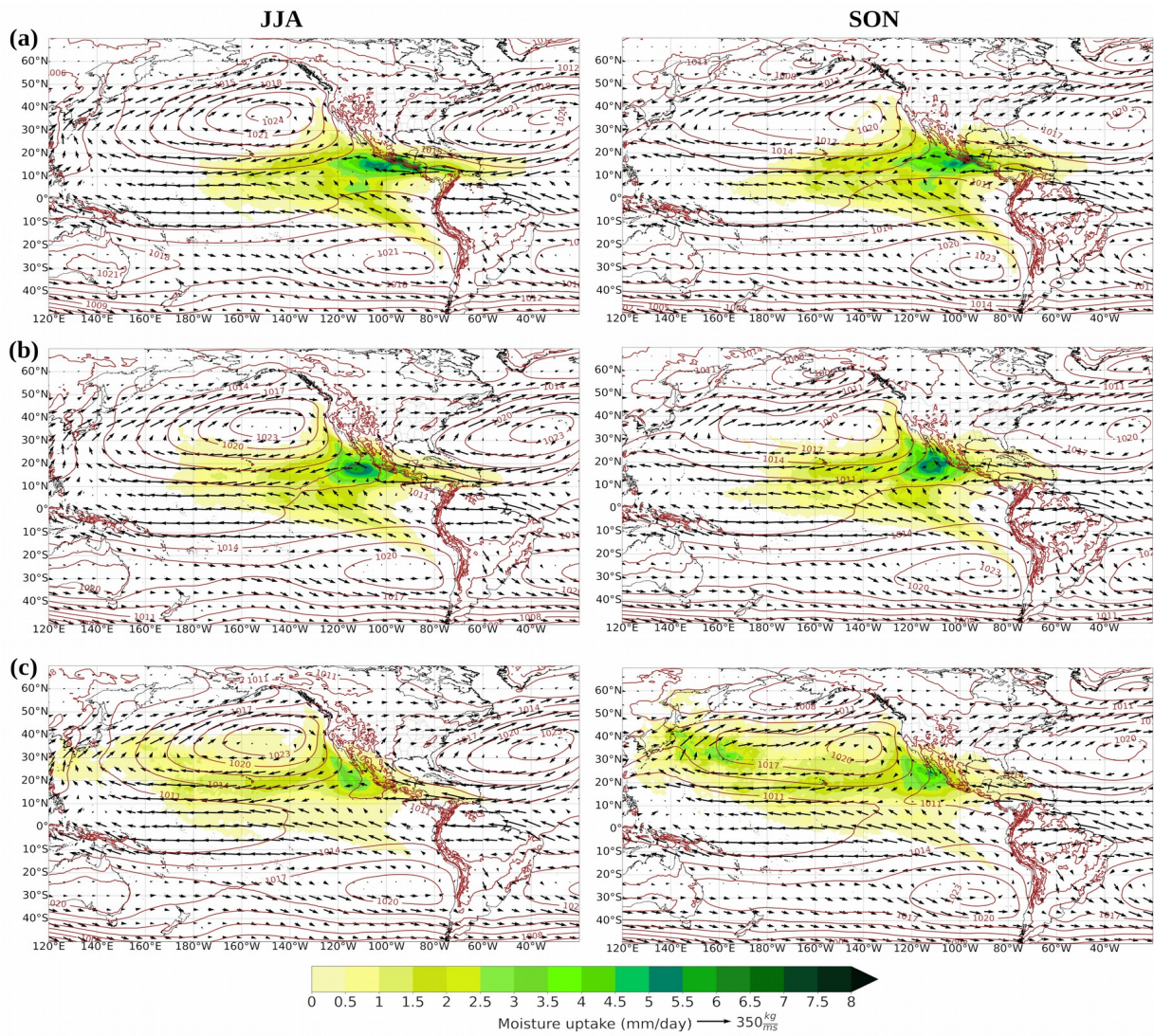


Fig. S2. Climatological moisture uptake (mm/d) patterns on June-July-August (JJA) and September-October-November (SON) during the TC (a) genesis, (b) lifetime maximum intensity and (c) dissipation stages over the Central and East North Pacific Ocean basin. The vertically integrated moisture flux (VIMF, kg/ms) and the mean sea level pressure (hPa) are represented by arrows and contours, respectively.

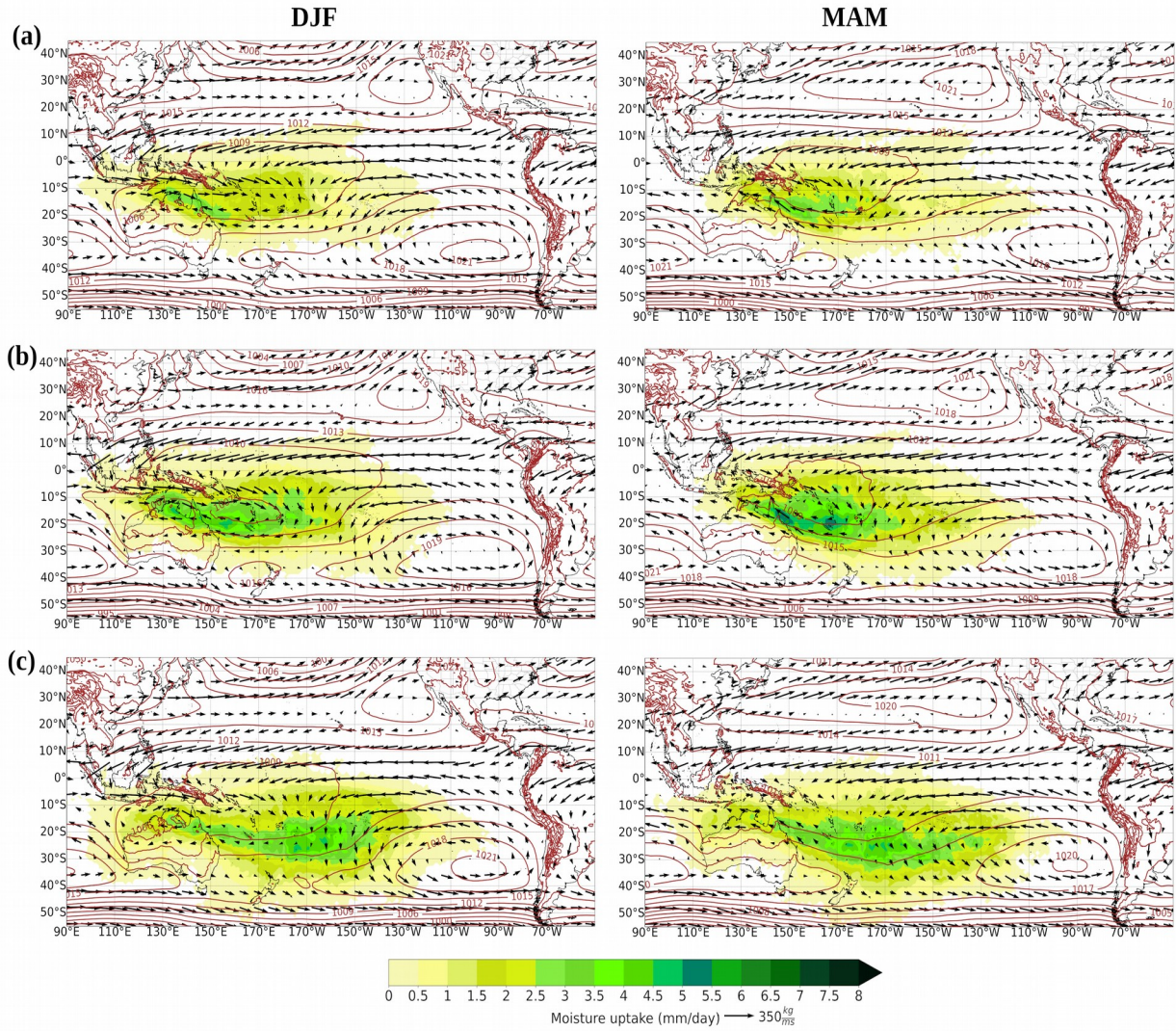


Fig. S3. Climatological moisture uptake (mm/d) patterns on December-January-February (DJF) and March-April-May (MAM) during the TC (a) genesis, (b) lifetime maximum intensity and (c) dissipation stages over the South Pacific Ocean basin. The vertically integrated moisture flux (VIMF, kg/ms) and the mean sea level pressure (hPa) are represented by arrows and contours, respectively.

Moisture sources for precipitation associated with major hurricanes during 2017 in the North Atlantic basin

Albenis Pérez-Alarcón^{1,2}, Patricia Coll-Hidalgo^{1,3}, José C. Fernández-Alvarez^{1,2}, Rogert Sorí^{1,4}, Raquel Nieto¹, Luis Gimeno¹

¹Centro de Investigación Mariña, Universidade de Vigo, Environmental Physics Laboratory (EPhysLab), Campus As Lagoas s/n, Ourense, 32004, Spain. ²Departamento de Meteorología, Instituto Superior de Tecnologías y Ciencias Aplicadas, Universidad de La Habana, 10400 La Habana, Cuba. ³Empresa Cubana de Navegación Aérea, 10800 La Habana, Cuba. ⁴Instituto Dom Luiz, Faculdade de Ciências da Universidade de Lisboa, 1749-016 Campo Grande, Portugal.

Contents of this file

Text S1 to S2
Figures S1 to S4

Introduction

This Supporting Information briefly describes the synoptic history of the 2017 major hurricanes formed in the North Atlantic basin and provides a detailed example of the procedure to compute the moisture source contribution for the precipitation associated with the 2017 North Atlantic major hurricanes along their trajectories.

Text S1. Brief synoptic history of 2017 North Atlantic major hurricanes

Hurricane Harvey

According to Blake and Zelinsky (2018), Hurricane Harvey formed from a tropical wave that moved off the coast of West Africa on 17 August at 0600 UTC. The increasing northerly wind shear led to Harvey degenerating into a tropical wave after reaching the tropical storm category. This tropical wave moved quickly over the Caribbean Sea in the westward and northwestward directions. On 23 August at 1200 UTC, after crossing over the Yucatán

Peninsula, Harvey reorganised over the warm waters of Campeche Bay, becoming a tropical depression that rapidly intensified into a Category 4 hurricane on the Saffir-Simpson Wind Scale at its maximum intensity, with a 200 km/h sustained wind speed and a central pressure of 937 hPa, before making landfall near Rockport, Texas, US, on 26 August 2017. After making landfall, the steady northwestward motion of Harvey stopped because it became embedded in light steering currents between a mid-tropospheric high and another high over the northern Gulf of Mexico.

Hurricane Irma

Hurricane Irma originated on 30 August at 0000 UTC from a tropical wave that travelled from the west coast of Africa (Cangialosi et al., 2021). During its west-northwestward movement, Irma underwent multiple cycles of rapid intensification, supported by favourable environmental conditions such as low-level wind shear, high moisture in the lower troposphere, and warm sea surface temperatures (SST). The high-pressure system in the north of Irma led to a change in its trajectory west-southwestward from 1 to 4 September, but this south-west movement over higher SSTs favoured its intensification. Later, erosion of the western side of the mid-level ridge on 4 September caused Irma to turn west-northwestward. When Irma moved east-southeast of Barbuda on 5 September at 1800 UTC, this hurricane reached its maximum intensity with a maximum wind of 290 km/h and a central pressure of 914 hPa. Irma continued its trajectory west-northwestward over the seas north of the Greater Antilles Arc until it made landfall again at Cayo Romano Cuba on 9 September at 0300 UTC as a Category 5 hurricane. The interaction of Irma's circulation with the Cuban keys caused it to weaken significantly to a Category 2 hurricane. Finally, Irma reintensified moving over the Florida Straits before landfall at the Florida Keys on 10 September.

Hurricane Jose

Hurricane Jose was formed on 4 September at 0600 UTC. Similar to Harvey and Irma, it originated from a tropical wave that departed from Africa. A mid-tropospheric ridge north of Jose controlled its movement westward to west-northwestward across the tropical Atlantic Ocean. Environmentally favourable conditions such as warm SSTs and low vertical wind shear caused Jose to undergo a rapid intensification process from 6 September at 0600 UTC to 8 September 1800 UTC (Berg, 2018). At this time, Jose reached its peak of intensification, with a 250 km/h maximum sustained wind and a minimum central pressure of 937 hPa. According to Berg (2018), the cyclonic circulation related to Hurricane Irma and a mid-latitude closed low on 12 September trapped Jose for approximately five days. The slow movement of Jose and the influence of northerly shear, drier mid-level air, and a self-induced oceanic cold wake weakened Jose. Nevertheless, by 17 September, Jose strengthened as a hurricane, but afterward, a strong wind shear and cold waters caused Jose to weaken into a tropical storm.

Hurricane Maria

Pasch et al. (2019) showed that Hurricane Maria originated on 16 September at 1200 UTC from a tropical wave that moved from the west coast of Africa. The hurricane strengthened into a tropical storm when it bordered

the south branch of the mid-level high-pressure area over the North Atlantic Ocean. Weak vertical shear and warm SST caused Maria to intensify rapidly, but it weakened after the interaction with the mountains of Dominica and then strengthened again, peaking in intensity with 280 km/h maximum sustained winds and 908 hPa minimum central pressure. Maria also made landfall in Puerto Rico on 20 September at 1050 UTC, this phenomenon weakened it slightly, but it intensified again as it moved towards the northwest. Nevertheless, by 22 September, a moderate southwesterly vertical shear limited any additional intensification. Maria also underwent an extratropical transition by 30 September at 1800 UTC.

Hurricane Lee

According to Blake (2018), Lee was a long-lived TC formed on 14 September at 1800 UTC from a strong tropical wave that moved off the coast of West Africa. After the genesis, the intensification of Lee was limited by a moderate northerly shear and the presence of dry air in the mid-levels of the atmosphere. Nevertheless, on 19 September, the interaction of Lee with a mid-tropospheric trough led to the favouring of deep convection. According to Blake (2018) by 20 September, Lee moved rapidly northeastward because Lee's low-level centre opened up into a trough. The persistent deep convection around the TC centre led to Lee rapidly intensifying into a hurricane on 24 September. After several eyewall replacement processes, Lee reached its maximum intensity on 27 September at 1200 UTC, with a maximum sustained wind speed of 190 km/h and a minimum central pressure of 962 hPa. Twelve hours after peak intensity, Lee started to weaken, gradually turn, and move northeastward.

Hurricane Ophelia

Hurricane Ophelia is of non-tropical origin (Stewart, 2018). Ophelia originated on 6 October from a vigorous mid-to upper-level trough amplified over the central subtropical Atlantic Ocean. On 8 October, Ophelia acquired subtropical characteristics, but the entrainment of dry mid-level air limited the development of deep convection. By 11 October at 1800 UTC, favourable environmental conditions, such as low vertical wind shear, led to Ophelia reaching the hurricane category. Continuous cycles of intensification caused Ophelia to achieve on 14 October at 1200 UTC its maximum intensity, a sustained wind speed of 190 km/h, and a central pressure of 959 hPa. Despite the relatively cold SSTs, the tropospheric colder-than-normal conditions supported the deep convection (Stewart, 2018). Nevertheless, the interaction with a strong upper-level trough and jet stream caused the extratropical transition to be completed on 16 October.

Text S2. Detailed example of the moisture sources contributions estimate

We now present a detailed example of how the moisture contributions were computed by considering more than one parcel that precipitated over a target region. Figure S1a shows a schematic of the trajectories of four particles that precipitate over a target region (red circle) and the moisture contribution (in percentage) at each time step (6h in this case) along the entire individual trajectory to the final moisture content. Notably, the sum of

all contributions along each parcel trajectory is 100 % at the final point (orange dot).

To represent the total contribution from the four trajectories in a gridded plot, we averaged all contributions higher than zero in each grid. We considered in this example, and for simplicity, grid cells of $5^{\circ} \times 5^{\circ}$ (blue boxes in Figure S1a). Therefore, the moisture contribution to the final precipitation over the target region by each grid is shown in Figure S1b.

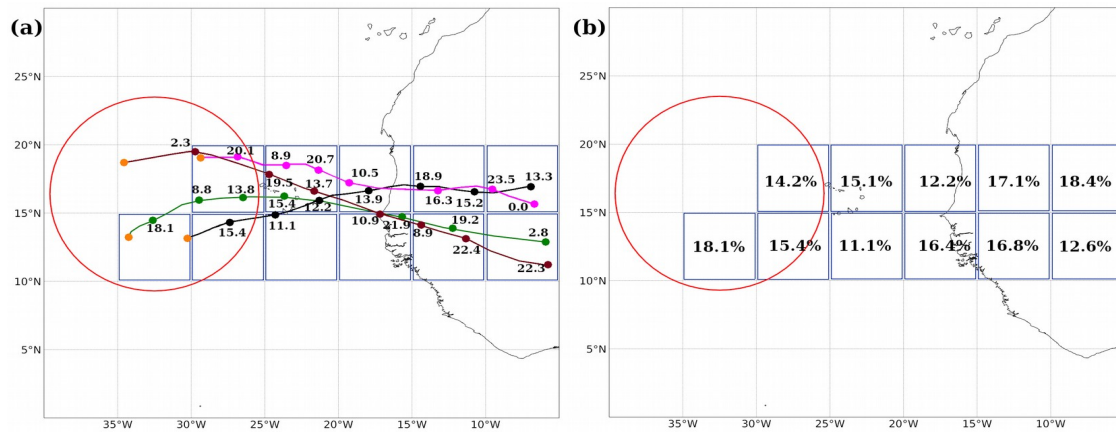


Figure S1. (a) Schematic of the trajectory of four particles that precipitated over the target region (red circle). Orange dots indicate regions where precipitation occurs; the remaining coloured dots indicate evaporation locations. Numbers indicate the contribution (in percentage) of each evaporation location to the final precipitation along each parcel trajectory. (b) Moisture contributions as an average of all contributions higher than zero in grid cells of $5^{\circ} \times 5^{\circ}$ (blue boxes).

To overview the computation of these moisture contributions to precipitation, we briefly analysed a real case. Figure S2a illustrates the trajectories of the 1812 precipitant particles identified over the area enclosed by the outer radius (788 km, black circle) of Hurricane Irma on 31 August at 0600 UTC. The outer radius was estimated by applying the methodology proposed by Pérez-Alarcón et al. (2021). The parcels travelled east-westward, crossing over Africa, and from the North and South Atlantic Ocean.

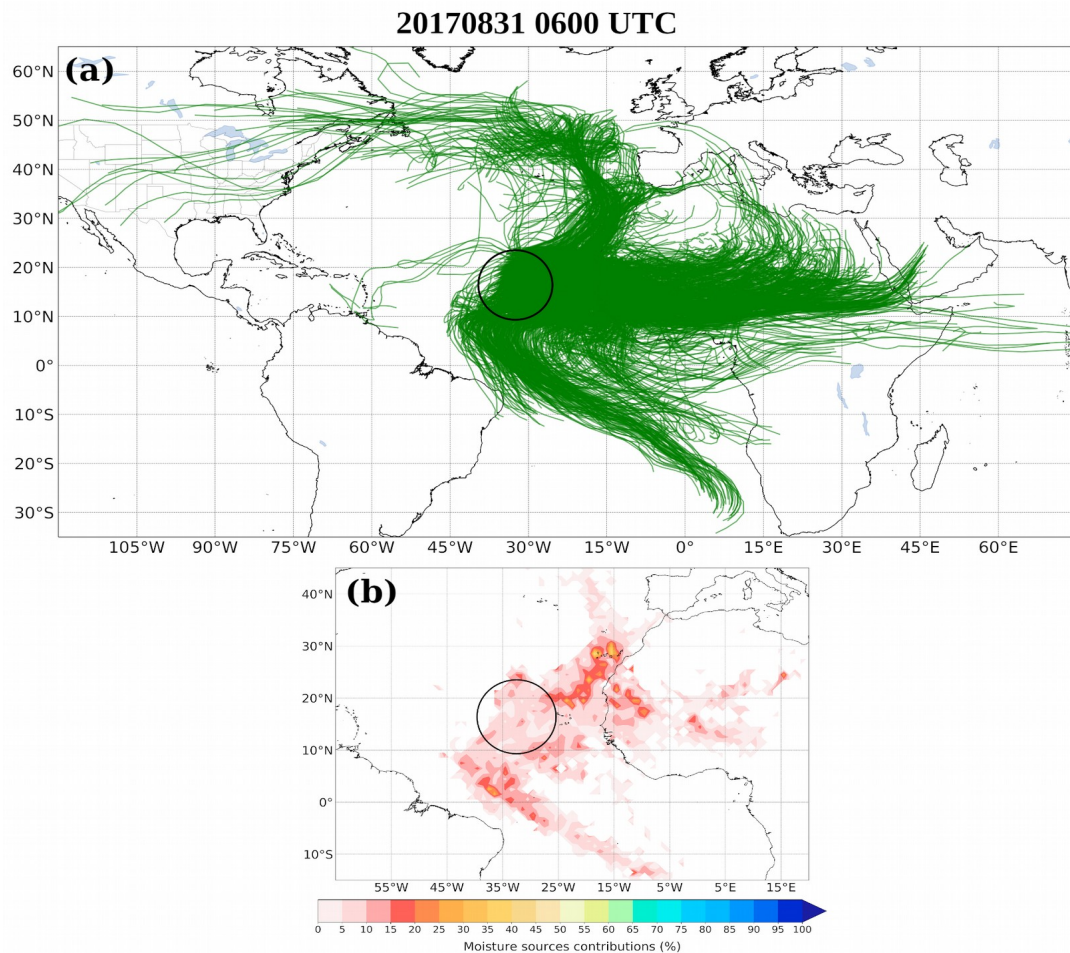


Figure S2. Figure S2. (a) Trajectory of all precipitant particles over the area enclosed by the outer radius (black circle) of Hurricane Irma on 31 August at 0600 UTC. (b) Moisture sources' contributions (%). The outer radius was estimated via the methodology proposed by Pérez-Alarcón et al. (2021)

The moisture contributions (Figure S2b) were computed by applying the aforementioned procedure. Notably, despite the lengthening of some parcels' trajectories, the moisture contributions occurred from sources relatively close to the target region. Sodemann et al. (2008) proposed that far away evaporative sources contribute less and less to the precipitation over the target region due to the precipitation en route.

Similarly, the moisture contributions along the complete lifetime of Hurricane Irma every 6 h were computed. As an example, Figure S3 shows the moisture contributions for precipitation inside the outer radius along 1 day of the hurricane movement, from 31 August at 0600 UTC to 1 September 0000 UTC.

Therefore, to estimate the total moisture source contribution (MSC) for the precipitation associated with a tropical cyclone (TC) during its entire lifetime, we added the moisture contribution (MC) of all TC positions. Figure S4a shows the sum of all moisture contributions along the Hurricane Irma trajectory

(dates from the HURDAT2 database) from 30 August at 0000 UTC (genesis time) to 13 September at 1200 UTC (dissipation time). The final values were notably higher than 100%.

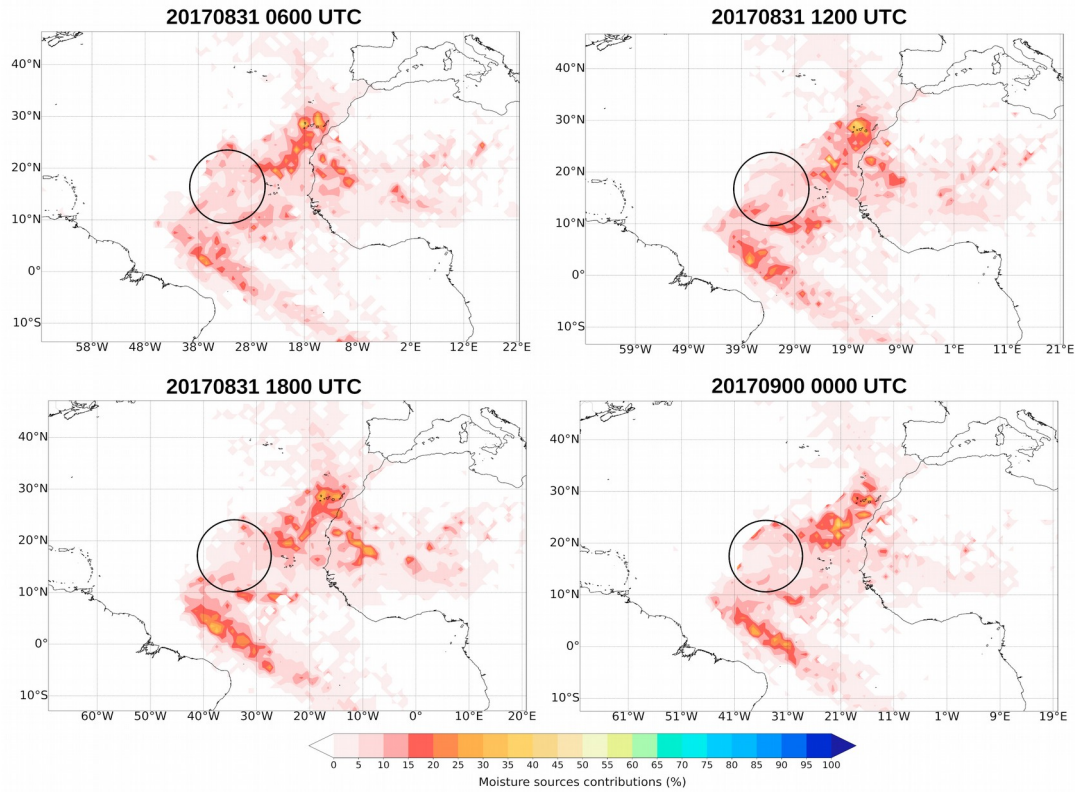


Figure S3. Moisture sources contributions' (%) for several portions of Hurricane Irma. The black circle represents the target region. The outer radius was estimated by applying the methodology proposed by Pérez-Alarcón et al. (2021).

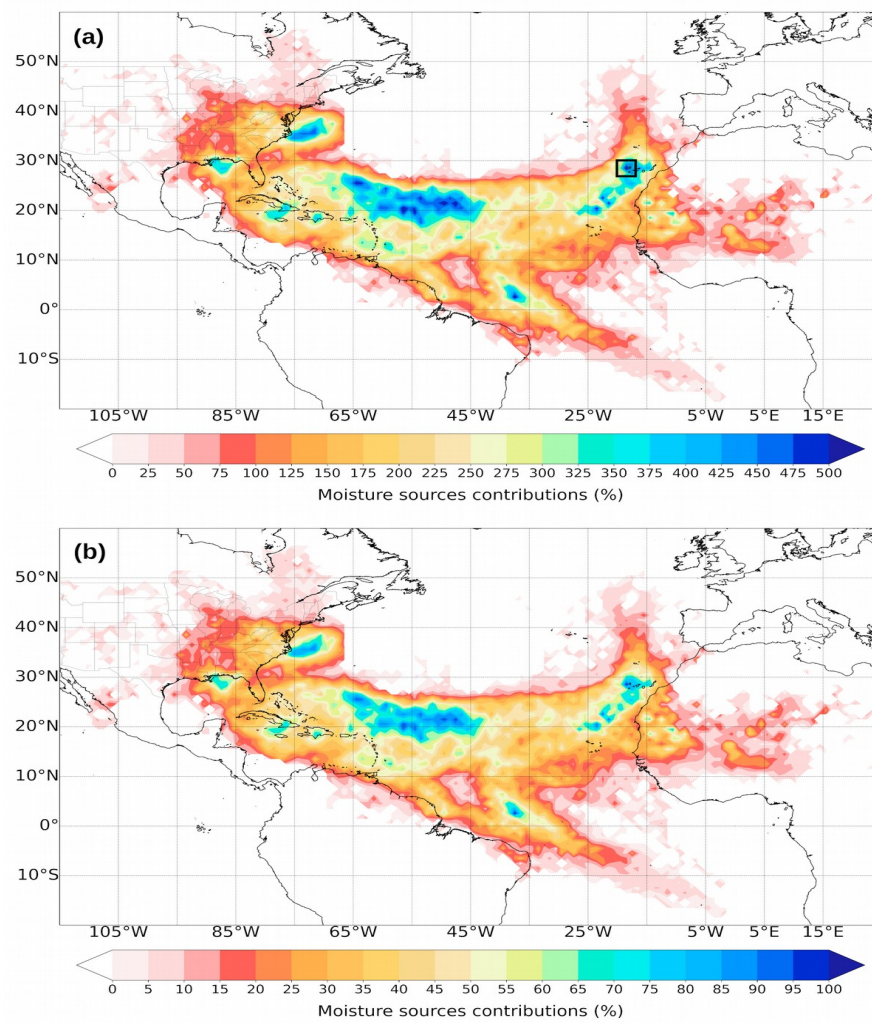


Figure S4. (a) Sum of moisture contributions of each position every 6 hours of the Hurricane Irma trajectory. The black box denotes the location of the maximum value of that sum. (b) Moisture sources' contributions (%) after applying equation S1.

Next, we relativised the values of all contributions concerning the maximum of that sum, using equation (S1):

$$MSC = \frac{\sum_{n=0}^N MC_n}{\max \left\{ \sum_{n=0}^N MC_n \right\}} \cdot 100 \quad (S1)$$

where N represents the number of time steps of the TC.

That is, the moisture contribution values at each grid point of the pattern shown in Figure S4a were divided by the maximum value of all grid points

(black box in Figure S4a). The result represents the moisture source contribution for the precipitation associated with Hurricane Irma during its lifetime (Figure S4b).

References

- Berg, R., (2018), National Hurricane Center Tropical Cyclone Report: Hurricane Jose. National Weather Service: National Oceanic and Atmospheric Administration.
https://www.nhc.noaa.gov/data/tcr/AL122017_Jose.pdf
- Blake, E. S. (2018), National Hurricane Center Tropical Cyclone Report: Hurricane Lee. National Weather Service: National Oceanic and Atmospheric Administration.
https://www.nhc.noaa.gov/data/tcr/AL142017_Lee.pdf
- Blake, E. S., & Zelinsky, D. A. (2018), National Hurricane Center Tropical Cyclone Report: Hurricane Harvey. National Weather Service: National Oceanic and Atmospheric Administration.
https://www.nhc.noaa.gov/data/tcr/AL092017_Harvey.pdf
- Cangialosi, J. P., Latto, A. S., & Berg, R. (2021), National Hurricane Center Tropical Cyclone Report: Hurricane Irma. National Oceanic and Atmospheric Administration,
https://www.nhc.noaa.gov/data/tcr/AL112017_Irma.pdf
- Läderach, A., & Sodemann, H. (2016), A revised picture of the atmospheric moisture residence time. *Geophysical Research Letters*, 43, 924– 933.
<https://doi.org/10.1002/2015GL067449>.
- Pasch, R. J., Penny, A. B., & Berg, R. (2019), National Hurricane Center Tropical Cyclone Report: Hurricane Maria. National Oceanic and Atmospheric Administration,
https://www.nhc.noaa.gov/data/tcr/AL152017_Maria.pdf
- Pérez-Alarcón, A., Sorí, R., Fernández-Alvarez, J. C., Nieto, R., & Gimeno, L. (2021), Comparative climatology of outer tropical cyclone size using radial wind profiles. *Weather and Climate Extremes*, 33, 100366.
<https://doi.org/10.1016/j.wace.2021.100366>
- Sodemann, H., Schwierz, C., & Wernli, H. (2008), Interannual variability of Greenland winter precipitation sources: Lagrangian moisture diagnostic and North Atlantic Oscillation influence, *Journal of Geophysical Research*, 113, D03107. <https://doi.org/10.1029/2007JD008503>
- Stewart, S. R. (2018), National Hurricane Center Tropical Cyclone Report: Hurricane Ophelia. National Oceanic and Atmospheric Administration,
https://www.nhc.noaa.gov/data/tcr/AL172017_Ophelia.pdf

References

- Algarra, I., Eiras-Barca, J., Miguez-Macho, G., Nieto, R., Gimeno, L., 2019a. On the assessment of the moisture transport by the great plains low-level jet. *Earth System Dynamics* 10, 107–119. doi:10.5194/esd-10-107-2019.
- Algarra, I., Eiras-Barca, J., Nieto, R., Gimeno, L., 2019b. Global climatology of nocturnal low-level jets and associated moisture sources and sinks. *Atmospheric Research* 229, 39–59. doi:10.1016/j.atmosres.2019.06.016.
- Algarra, I., Nieto, R., Ramos, A.M., Eiras-Barca, J., Trigo, R.M., Gimeno, L., 2020. Significant increase of global anomalous moisture uptake feeding landfalling atmospheric rivers. *Nature communications* 11, 1–7. doi:10.1038/s41467-020-18876-w.
- Allan, R.P., 2012. The role of water vapour in Earth's energy flows. *Surveys in geophysics* 33, 557–564. doi:10.1007/s10712-011-9157-8.
- Allan, R.P., Barlow, M., Byrne, M.P., Cherchi, A., Douville, H., Fowler, H.J., Gan, T.Y., Pendergrass, A.G., Rosenfeld, D., Swann, A.L., et al., 2020. Advances in understanding large-scale responses of the water cycle to climate change. *Annals of the New York Academy of Sciences* 1472, 49–75. doi:10.1111/nyas.14337.
- Allen, S.T., Keim, R.F., Barnard, H.R., McDonnell, J.J., Renée Brooks, J., 2017. The role of stable isotopes in understanding rainfall interception processes: a review. *WIREs Water* 4, e1187. doi:10.1002/wat2.1187.
- Andersen, T.K., Radcliffe, D.E., Shepherd, J.M., 2013. Quantifying surface energy fluxes in the vicinity of inland-tracking tropical cyclones. *Journal of applied meteorology and climatology* 52, 2797–2808. doi:10.1175/JAMC-D-13-035.1.
- Andersen, T.K., Shepherd, J.M., 2014. A global spatiotemporal analysis of inland tropical cyclone maintenance or intensification. *International Journal of Climatology* 34, 391–402. doi:10.1002/joc.3693.
- Anthes, R., 1982. Tropical cyclones: Their evolution, structure and effects. *American meteorological society*, 208 pp., and dp baumhefner, 1984: A diagram depicting forecast skill and predictability. *Bulletin of the American Meteorological Society*, 65–701.
- Aryal, Y.N., Villarini, G., Zhang, W., Vecchi, G.A., 2018. Long term changes in flooding and heavy rainfall associated with North Atlantic tropical cyclones: Roles of the North Atlantic Oscillation

- and El Niño-Southern Oscillation. *Journal of Hydrology* 559, 698–710. doi:10.1016/j.jhydrol.2018.02.072.
- Bacmeister, J.T., Reed, K.A., Hannay, C., Lawrence, P., Bates, S., Truesdale, J.E., Rosenbloom, N., Levy, M., 2018. Projected changes in tropical cyclone activity under future warming scenarios using a high-resolution climate model. *Climatic Change* 146, 547–560. doi:10.1007/s10584-016-1750-x.
- Bacmeister, J.T., Wehner, M.F., Neale, R.B., Gettelman, A., Hannay, C., Lauritzen, P.H., Caron, J.M., Truesdale, J.E., 2014. Exploratory high-resolution climate simulations using the Community Atmosphere Model (CAM). *Journal of Climate* 27, 3073–3099. doi:10.1175/JCLI-D-13-00387.1.
- Balaguru, K., Foltz, G.R., Leung, L.R., Emanuel, K.A., 2016. Global warming-induced upper-ocean freshening and the intensification of super typhoons. *Nature communications* 7, 1–8. doi:10.1038/ncomms13670.
- Banzon, V., Smith, T.M., Steele, M., Huang, B., Zhang, H.M., 2020. Improved estimation of proxy sea surface temperature in the arctic. *Journal of Atmospheric and Oceanic Technology* 37, 341–349. doi:10.1175/JTECH-D-19-0177.1.
- Bao, J., Sherwood, S.C., Alexander, L.V., Evans, J.P., 2017. Future increases in extreme precipitation exceed observed scaling rates. *Nature Climate Change* 7, 128–132. doi:10.1038/nclimate3201.
- Baumgartner, A., Reichel, E., 1975. *The World Water Balance*. Elsevier, Amsterdam.
- Beck, H.E., van Dijk, A.I.J.M., Levizzani, V., Schellekens, J., Miralles, D.G., Martens, B., de Roo, A., 2017. MSWEP: 3-hourly 0.25 global gridded precipitation (1979–2015) by merging gauge, satellite, and reanalysis data. *Hydrology and Earth System Sciences* 21, 589–615. doi:10.5194/hess-21-589-2017.
- Beck, H.E., Wood, E.F., Pan, M., Fisher, C.K., Miralles, D.G., Van Dijk, A.I., McVicar, T.R., Adler, R.F., 2019. MSWEP V2 global 3-hourly 0.1 precipitation: methodology and quantitative assessment. *Bulletin of the American Meteorological Society* 100, 473–500. doi:10.1175/BAMS-D-17-0138.1.
- Belyadi, H., Haghghat, A., 2021. Chapter 4 - unsupervised machine learning: clustering algorithms, in: Belyadi, H., Haghghat, A. (Eds.), *Machine Learning Guide for Oil and Gas Using Python*. Gulf Professional Publishing, pp. 125–168. doi:10.1016/B978-0-12-821929-4.00002-0.
- Bhatia, K., Vecchi, G., Murakami, H., Underwood, S., Kossin, J., 2018. Projected response of tropical cyclone intensity and intensification in a global climate model. *Journal of Climate* 31, 8281–8303. doi:10.1175/JCLI-D-17-0898.1.
- Bhatia, K.T., Vecchi, G.A., Knutson, T.R., Murakami, H., Kossin, J., Dixon, K.W., Whitlock, C.E., 2019. Recent increases in tropical cyclone intensification rates. *Nature communications* 10, 1–9. doi:10.1038/s41467-019-08471-z.
- Bieli, M., Camargo, S.J., Sobel, A.H., Evans, J.L., Hall, T., 2019a. A global climatology of extratropical transition. Part I: Characteristics across basins. *Journal of Climate* 32, 3557–3582. doi:10.1175/JCLI-D-17-0518.1.

- Bieli, M., Camargo, S.J., Sobel, A.H., Evans, J.L., Hall, T., 2019b. A global climatology of extratropical transition. Part II: Statistical performance of the cyclone phase space. *Journal of Climate* 32, 3583–3597. doi:10.1175/JCLI-D-18-0052.1.
- Brauer, N.S., Basara, J.B., Kirstetter, P.E., Wakefield, R.A., Homeyer, C.R., Yoo, J., Shepherd, M., Santanello Jr, J.A., 2021. The inland maintenance and reintensification of Tropical Storm Bill (2015). Part II: Precipitation microphysics. *Journal of Hydrometeorology* 22, 2695–2711. doi:10.1175/JHM-D-20-0151.1.
- Braun, S.A., 2006. High-resolution simulation of hurricane bonnie (1998). part ii: water budget. *Journal of the atmospheric sciences* 63, 43–64. doi:10.1175/JAS3609.1.
- Brun, J., Barros, A.P., 2014. Mapping the role of tropical cyclones on the hydroclimate of the southeast united states: 2002–2011. *International journal of climatology* 34, 494–517. doi:10.1002/joc.3703.
- Camargo, S.J., 2013. Global and regional aspects of tropical cyclone activity in the cmip5 models. *Journal of Climate* 26, 9880–9902. doi:10.1175/JCLI-D-12-00549.1.
- Cangialosi, J.P., Latta, A.S., Berg, R., 2021. National Hurricane center tropical cyclone report: Hurricane Irma. National Hurricane Center , 1–111URL: <https://www.nhc.noaa.gov/data/tcr/AL112017>.
- Chavas, D.R., Emanuel, K., 2014. Equilibrium tropical cyclone size in an idealized state of axisymmetric radiative–convective equilibrium. *Journal of the Atmospheric Sciences* 71, 1663–1680. doi:10.1175/JAS-D-13-0155.1.
- Chen, L., Li, Y., Cheng, Z., 2010. An overview of research and forecasting on rainfall associated with landfalling tropical cyclones. *Advances in Atmospheric Sciences* 27, 967–976. doi:10.1007/s00376-010-8171-y.
- Chen, L., Wang, L., 2018. Recent advance in earth observation big data for hydrology. *Big Earth Data* 2, 86–107. doi:10.1080/20964471.2018.1435072.
- Choi, J.W., Kim, B.J., Zhang, R., Park, K.J., Kim, J.Y., Cha, Y., Nam, J.C., 2016. Possible relation of the western north pacific monsoon to the tropical cyclone activity over western north pacific. *International Journal of Climatology* 36, 3334–3345. doi:10.1002/joc.4558.
- Chu, J.H., Sampson, C., Levine, A., Fukada, E., 2002. The Joint Typhoon Warning Center tropical cyclone best-tracks, 1945–2000. Naval Research Laboratory. URL: https://www.usno.navy.mil/NOOC/nmfc-ph/RSS/jtwc/best_tracks/TC_bt_report.html.
- Chu, Q.c., Wang, Q.g., Feng, G.l., 2017. Determination of the major moisture sources of cumulative effect of torrential rain events during the pre-flood season over South China using a Lagrangian particle model. *Journal of Geophysical Research: Atmospheres* 122, 8369–8382. doi:10.1002/2016JD026426.
- Ciric, D., Nieto, R., Ramos, A.M., Drumond, A., Gimeno, L., 2018. Contribution of moisture from mediterranean sea to extreme precipitation events over danube river basin. *Water* 10. doi:10.3390/w10091182.

- Cloux, S., Garaboa-Paz, D., Insua-Costa, D., Miguez-Macho, G., Pérez-Muñuzuri, V., 2021. Extreme precipitation events in the mediterranean area: contrasting lagrangian and eulerian models for moisture sources identification. *Hydrology and Earth System Sciences Discussions* 2021, 1–20. doi:10.5194/hess-25-6465-2021.
- Cocks, S.B., Gray, W.M., 2002. Variability of the outer wind profiles of western north pacific typhoons: Classifications and techniques for analysis and forecasting. *Monthly weather review* 130, 1989–2005. doi:10.1175/1520-0493(2002)130<1989:VOTOWP>2.0.CO;2.
- Colbert, A.J., Soden, B.J., 2012. Climatological variations in North Atlantic tropical cyclone tracks. *Journal of climate* 25, 657–673. doi:10.1175/JCLI-D-11-00034.1.
- Coll-Hidalgo, P., Pérez-Alarcón, A., 2021. Climatología de los ciclones tropicales que tocaron tierra en cuba entre 1980 y 2019. *Revista Cubana de Meteorología* 27, e06. URL: <https://rcm.insmet.cu/index.php/rcm/article/view/585>.
- Corporal-Lodangco, I.L., Richman, M.B., Leslie, L.M., Lamb, P.J., 2014. Cluster analysis of north atlantic tropical cyclones. *Procedia Computer Science* 36, 293–300. doi:10.1016/j.procs.2014.09.096.
- Dean, L., Emanuel, K.A., Chavas, D., 2009. On the size distribution of atlantic tropical cyclones. *Geophysical Research Letters* 36. doi:10.1029/2009GL039051.
- Dee, D.P., Uppala, S.M., Simmons, A.J., Berrisford, P., Poli, P., Kobayashi, S., Andrae, U., Balmaseda, M.A., Balsamo, G., Bauer, P., Bechtold, P., Beljaars, A.C.M., van de Berg, L., Bidlot, J., Bormann, N., Delsol, C., Dragani, R., Fuentes, M., Geer, A.J., Haimberger, L., Healy, S.B., Hersbach, H., Hólm, E.V., Isaksen, I., Kållberg, P., Köhler, M., Matricardi, M., McNally, A.P., Monge-Sanz, B.M., Morcrette, J.J., Park, B.K., Peubey, C., de Rosnay, P., Tavolato, C., Thépaut, J.N., Vitart, F., 2011. The era-interim reanalysis: configuration and performance of the data assimilation system. *Quarterly Journal of the Royal Meteorological Society* 137, 553–597. doi:10.1002/qj.828.
- DeMaria, M., 1987. Tropical cyclone track prediction with a barotropic spectral model. *Mon. Wea. Rev.* 115, 2346–2357. doi:10.1175/1520-0493(1987)115,2346:TCTPWA.2.0.CO;2.
- Deppermann, C.E., 1947. Notes on the origin and structure of philippine typhoons. *Bulletin of the American Meteorological Society*, 399–404.
- Dhavale, S., Mujumdar, M., Roxy, M.K., Singh, V.K., 2022. Tropical cyclones over the arabian sea during the monsoon onset phase. *International Journal of Climatology* 42, 2996–3006. doi:10.1002/joc.7403.
- Dirmeyer, P.A., Brubaker, K.L., 1999. Contrasting evaporative moisture sources during the drought of 1988 and the flood of 1993. *Journal of Geophysical Research: Atmospheres* 104, 19383–19397. doi:10.1029/1999JD900222.
- Dominguez, C., Magaña, V., 2018. The role of tropical cyclones in precipitation over the tropical and subtropical north america. *Frontiers in Earth Science* 6. doi:10.3389/feart.2018.00019.

- Drumond, A., Gimeno, L., Garcia-Herrera, R., Nieto, R., 2014. Changes in the contribution of moisture from the mediterranean basin to the continental precipitation from 1980 onwards: a lagrangian analysis. *Journal of the Black Sea / Mediterranean Environment* , 66–69.
- Emanuel, K., 2017. Assessing the present and future probability of hurricane harvey’s rainfall. *Proceedings of the National Academy of Sciences* 114, 12681–12684. doi:10.1073/pnas.1716222114.
- Emanuel, K., 2021. Atlantic tropical cyclones downscaled from climate reanalyses show increasing activity over past 150 years. *Nature communications* 12, 1–8. doi:10.1038/s41467-021-27364-8.
- Emanuel, K., DesAutels, C., Holloway, C., Korty, R., 2004. Environmental control of tropical cyclone intensity. *Journal of the atmospheric sciences* 61, 843–858. doi:10.1175/1520-0469(2004)061<0843:ECOTCI>2.0.CO;2.
- Emanuel, K., Rotunno, R., 2011. Self-stratification of tropical cyclone outflow. Part I: Implications for storm structure. *J. Atmos. Sci.* 68, 82236–2249. doi:10.1175/JAS-D-10-05024.1.
- Emanuel, K., Sundararajan, R., Williams, J., 2008. Hurricanes and global warming: Results from downscaling IPCC AR4 simulations. *Bulletin of the American Meteorological Society* 89, 347–368. doi:10.1175/BAMS-89-3-347.
- Emanuel, K.A., 1987. The dependence of hurricane intensity on climate. *Nature* 326, 483–485. doi:10.1038/326483a0.
- Evans, C., Hart, R.E., 2008. Analysis of the wind field evolution associated with the extratropical transition of Bonnie (1998). *Monthly weather review* 136, 2047–2065. doi:10.1175/2007MWR2051.1.
- Evans, C., Schumacher, R.S., Galarneau, T.J., 2011. Sensitivity in the overland reintensification of Tropical Cyclone Erin (2007) to near-surface soil moisture characteristics. *Monthly Weather Review* 139, 3848–3870. doi:10.1175/2011MWR3593.1.
- Evans, C., Wood, K.M., Aberson, S.D., Archambault, H.M., Milrad, S.M., Bosart, L.F., Corbosiero, K.L., Davis, C.A., Dias Pinto, J.R., Doyle, J., et al., 2017. The extratropical transition of tropical cyclones. Part I: Cyclone evolution and direct impacts. *Monthly Weather Review* 145, 4317–4344. doi:10.1175/MWR-D-17-0027.1.
- Fernández-Alvarez, J.C., Sorí, R., Pérez-Alarcón, A., Nieto, R., Gimeno, L., 2020. The role of tropical cyclones on the total precipitation in cuba during the hurricane season from 1980 to 2016. *Atmosphere* 11, 1156. doi:10.3390/atmos11111156.
- Findell, K.L., Keys, P.W., van der Ent, R.J., Lintner, B.R., Berg, A., Krasting, J.P., 2019. Rising temperatures increase importance of oceanic evaporation as a source for continental precipitation. *Journal of Climate* 32. doi:10.1175/JCLI-D-19-0145.1.
- Franco-Díaz, A., Klingaman, N.P., Vidale, P.L., Guo, L., Demory, M.E., 2019. The contribution of tropical cyclones to the atmospheric branch of middle america’s hydrological cycle using observed and reanalysis tracks. *Climate Dynamics* 53, 6145–6158. doi:10.1007/s00382-019-04920-z.
- Frank, W.M., Young, G.S., 2007. The interannual variability of tropical cyclones. *Monthly Weather Review* 135, 3587–3598. doi:10.1175/MWR3435.1.

- Frisius, T., Segönemann, D., Jonathan, V., 2013. The impact of gradient wind imbalance on potential intensity of tropical cyclones in an unbalanced slab boundary layer model. *J. Atmos. Sci.* 70, 1874–1890. doi:10.1175/JAS-D-12-0160.1.
- Fritz, C., Wang, Z., 2014. Water vapor budget in a developing tropical cyclone and its implication for tropical cyclone formation. *Journal of the Atmospheric Sciences* 71, 4321–4332. doi:10.1175/JAS-D-13-0378.1.
- Fujiwara, K., Kawamura, R., Hirata, H., Kawano, T., Kato, M., Shinoda, T., 2017. A positive feedback process between tropical cyclone intensity and the moisture conveyor belt assessed with lagrangian diagnostics. *Journal of Geophysical Research: Atmospheres* 122, 12–502. doi:10.1002/2017JD027557.
- Ge, X., Li, T., Peng, M., 2013. Effects of vertical shears and midlevel dry air on tropical cyclone developments. *Journal of the atmospheric sciences* 70, 3859–3875. doi:10.1175/JAS-D-13-066.1.
- Gedzelman, S., Lawrence, J., Gamache, J., Black, M., Hindman, E., Black, R., Dunion, J., Willoughby, H., Zhang, X., 2003. Probing hurricanes with stable isotopes of rain and water vapor. *Monthly Weather Review* 131, 1112–1127. doi:10.1175/1520-0493(2003)131<1112:PHWSIO>2.0.CO;2.
- Gimeno, L., 2013. Grand challenges in atmospheric science. *Frontiers in Earth Science* 1, 1. doi:10.3389/feart.2013.00001.
- Gimeno, L., 2014. Oceanic sources of continental precipitation. *Water Resources Research* 50, 3647–3649. doi:10.1002/2014WR015477.
- Gimeno, L., Dominguez, F., Nieto, R., Trigo, R., Drumond, A., Reason, C.J., Taschetto, A.S., Ramos, A.M., Kumar, R., Marengo, J., 2016. Major mechanisms of atmospheric moisture transport and their role in extreme precipitation events. *Annual Review of Environment and Resources* 41, 117–141. doi:10.1146/annurev-environ-110615-085558.
- Gimeno, L., Drumond, A., Nieto, R., Trigo, R.M., Stohl, A., 2010. On the origin of continental precipitation. *Geophysical Research Letters* 37. doi:10.1029/2010GL043712.
- Gimeno, L., Eiras-Barca, J., Durán-Quesada, A.M., Dominguez, F., van der Ent, R., Sodemann, H., Sánchez-Murillo, R., Nieto, R., Kirchner, J.W., 2021. The residence time of water vapour in the atmosphere. *Nature Reviews Earth & Environment* 2, 558–569. doi:10.1038/s43017-021-00181-9.
- Gimeno, L., Stohl, A., Trigo, R.M., Dominguez, F., Yoshimura, K., Yu, L., Drumond, A., Durán-Quesada, A.M., Nieto, R., 2012. Oceanic and terrestrial sources of continental precipitation. *Reviews of Geophysics* 50. doi:10.1029/2012RG000389.
- Gimeno, L., Vázquez, M., Eiras-Barca, J., Sorí, R., Stojanovic, M., Algarra, I., Nieto, R., Ramos, A.M., Durán-Quesada, A.M., Dominguez, F., 2020. Recent progress on the sources of continental precipitation as revealed by moisture transport analysis. *Earth-Science Reviews* 201, 103070. doi:10.1016/j.earscirev.2019.103070.
- Gimeno, L., Vázquez, M., Nieto, R., Trigo, R.M., 2015. Atmospheric moisture transport: the bridge between ocean evaporation and arctic ice melting. *Earth System Dynamics* 6, 583–589. doi:10.5194/esd-6-583-2015.

- Giorgi, F., Raffaele, F., Coppola, E., 2019. The response of precipitation characteristics to global warming from climate projections. *Earth System Dynamics* 10, 73–89. doi:10.5194/esd-10-73-2019.
- Gray, W.M., 1968. Global view of the origin of tropical disturbances and storms. *Monthly Weather Review* 96, 669–700. doi:10.1175/1520-0493(1968)096<0669:GVOT00>2.0.CO;2.
- Gray, W.M., 1998. The formation of tropical cyclones. *Meteorology and atmospheric physics* 67, 37–69. doi:10.1007/BF01277501.
- Guo, L., Klingaman, N.P., Vidale, P.L., Turner, A.G., Demory, M.E., Cobb, A., 2017. Contribution of tropical cyclones to atmospheric moisture transport and rainfall over east asia. *Journal of Climate* 30, 3853–3865. doi:10.1175/JCLI-D-16-0308.1.
- Harr, P.A., Anwender, D., Jones, S.C., 2008. Predictability associated with the downstream impacts of the extratropical transition of tropical cyclones: Methodology and a case study of Typhoon Nabi (2005). *Monthly Weather Review* 136, 3205–3225. doi:10.1175/1520-0493(2008)136<3205:ETOTCO>2.0.CO;2.
- Hart, R.E., Evans, J.L., 2001. A climatology of the extratropical transition of Atlantic tropical cyclones. *Journal of Climate* 14, 546–564. doi:10.1175/1520-0442(2001)014<0546:ACOTET>2.0.CO;2.
- Held, I.M., Soden, B.J., 2006. Robust responses of the hydrological cycle to global warming. *Journal of climate* 19, 5686–5699. doi:10.1175/JCLI3990.1.
- Hendricks, E., Montgomery, M., Davis, C., 2004. On the role of “vortical” hot towers in hurricane formation. *Journal of Atmospheric Sciences* 61, 1209–1232. doi:10.1175/1520-0469(2004)061<1209:TROVHT>2.0.CO;2.
- Hersbach, H., Bell, B., Berrisford, P., Hirahara, S., Horányi, A., Muñoz-Sabater, J., Nicolas, J., Peubey, C., Radu, R., Schepers, D., et al., 2020. The ERA5 global reanalysis. *Quarterly Journal of the Royal Meteorological Society* 146, 1999–2049. doi:10.1002/qj.3803.
- Holland, G.J., 1980. An analytic model of the wind and pressure profiles in hurricanes. *Mon. Wea. Rev.* 108, 1212–1218. doi:10.1175/1520-0493(1980)108,1212:AAMOTW.2.0.CO;2.
- Holland, G.J., Belanger, J.I., Fritz, A., 2010. A revised model for radial profiles of hurricane winds. *Monthly weather review* 138, 4393–4401. doi:10.1175/2010MWR3317.1.
- Huang, B., Liu, C., Freeman, E., Graham, G., Smith, T., Zhang, H.M., 2021. Assessment and intercomparison of NOAA daily optimum interpolation sea surface temperature (DOISST) version 2.1. *Journal of Climate* 34, 7421–7441. doi:10.1175/JCLI-D-20-0166.1.
- Huang, H.L., Yang, M.J., Sui, C.H., 2014. Water budget and precipitation efficiency of typhoon morakot (2009). *Journal of the Atmospheric Sciences* 71, 112–129. doi:10.1175/JAS-D-13-053.1.
- Huffman, G.J., Stocker, E.F., Bolvin, D.T., Nelkin, E.J., Tan, J., 2019. GPM IMERG final precipitation L3 half hourly 0.1 degree x 0.1 degree V06. Goddard Earth Sciences Data and Information Services Center (GES DISC): Greenbelt, MD, USA doi:10.5067/GPM/IMERG/3B-HH-E/06.

- Jain, A.K., 2010. Data clustering: 50 years beyond k-means. *Pattern recognition letters* 31, 651–666. doi:10.1016/j.patrec.2009.09.011.
- Jain, A.K., Dubes, R.C., 1988. *Algorithms for clustering data*. Prentice-Hall, Inc.
- Jaiswal, N., Ha, D.T.T., Kishtawal, C., 2019. Estimation of size of tropical cyclones in the north indian ocean using oceansat-2 scatterometer high-resolution wind products. *Theoretical and Applied Climatology* 136, 45–53. doi:10.1007/s00704-018-2464-y.
- Jones, S.C., Harr, P.A., Abraham, J., Bosart, L.F., Bowyer, P.J., Evans, J.L., Hanley, D.E., Hanstrum, B.N., Hart, R.E., Lalaurette, F., et al., 2003. The extratropical transition of tropical cyclones: Forecast challenges, current understanding, and future directions. *Weather and forecasting* 18, 1052–1092. doi:10.1175/1520-0434(2003)018<1052:TETOTC>2.0.CO;2.
- Jouzel, J., Delaygue, G., Landais, A., Masson-Delmotte, V., Risi, C., Vimeux, F., 2013. Water isotopes as tools to document oceanic sources of precipitation. *Water Resources Research* 49, 7469–7486. doi:10.1002/2013WR013508.
- Kaplan, J., DeMaria, M., 2003. Large-scale characteristics of rapidly intensifying tropical cyclones in the North Atlantic basin. *Weather and forecasting* 18, 1093–1108. doi:10.1175/1520-0434(2003)018<1093:LCORIT>2.0.CO;2.
- Kaplan, J., DeMaria, M., Knaff, J.A., 2010. A revised tropical cyclone rapid intensification index for the atlantic and eastern north pacific basins. *Wea. Forecasting* 25, 220–241. doi:10.1175/2009WAF2222280.1.
- Keller, J.H., Grams, C.M., Riemer, M., Archambault, H.M., Bosart, L., Doyle, J.D., Evans, J.L., Galarneau, T.J., Griffin, K., Harr, P.A., et al., 2019. The extratropical transition of tropical cyclones. Part II: Interaction with the midlatitude flow, downstream impacts, and implications for predictability. *Monthly Weather Review* 147, 1077–1106. doi:10.1175/MWR-D-17-0329.1.
- Kelly, P., Leung, L.R., Balaguru, K., Xu, W., Mapes, B., Soden, B., 2018. Shape of atlantic tropical cyclone tracks and the indian monsoon. *Geophysical research letters* 45, 10–746. doi:10.1029/2018GL080098.
- Keune, J., Schumacher, D., Miralles, D., 2022. A unified framework to estimate the origins of atmospheric moisture and heat using lagrangian models. *Geoscientific Model Development* 15, 1875–1898. doi:10.5194/gmd-15-1875-2022.
- Keys, P.W., Wang-Erlandsson, L., Gordon, L.J., 2016. Revealing invisible water: Moisture recycling as an ecosystem service. *PLOS ONE* 11, 1–16. doi:10.1371/journal.pone.0151993.
- Khouakhi, A., Villarini, G., Vecchi, G.A., 2017. Contribution of tropical cyclones to rainfall at the global scale. *Journal of Climate* 30, 359–372. doi:10.1175/JCLI-D-16-0298.1.
- Kieper, M.E., Jiang, H., 2012. Predicting tropical cyclone rapid intensification using the 37 ghz ring pattern identified from passive microwave measurements. *Geophysical Research Letters* 39. doi:10.1029/2012GL052115.

- Kilroy, G., Smith, R.K., 2017. The effects of initial vortex size on tropical cyclogenesis and intensification. *Quarterly Journal of the Royal Meteorological Society* 143, 2832–2845. doi:10.1002/qj.3134.
- Kim, H.K., Seo, K.H., 2016. Cluster analysis of tropical cyclone tracks over the western north pacific using a self-organizing map. *Journal of Climate* 29, 3731–3751. doi:10.1175/JCLI-D-15-0380.1.
- Kimball, S.K., 2006. A modeling study of hurricane landfall in a dry environment. *Monthly weather review* 134, 1901–1918. doi:10.1175/MWR3155.1.
- Knaff, J.A., Longmore, S.P., Molenaar, D.A., 2014. An objective satellite-based tropical cyclone size climatology. *Journal of Climate* 27, 455–476. doi:10.1175/JCLI-D-13-00096.1.
- Knapp, K.R., Diamond, H.J., Kossin, J.P., Kruk, M.C., Schreck, C.J., 2018. International Best Track Archive for Climate Stewardship (IBTrACS) Project, Version 4. NOAA National Centers for Environmental Information. doi:10.25921/82ty-9e16.
- Knapp, K.R., Kruk, M.C., Levinson, D.H., Diamond, H.J., Neumann, C.J., 2010. The International Best Track Archive for Climate Stewardship (IBTrACS): Unifying Tropical Cyclone Data. *Bulletin of the American Meteorological Society* 91, 363 – 376. doi:10.1175/2009BAMS2755.1.
- Knutson, T., Camargo, S.J., Chan, J.C., Emanuel, K., Ho, C.H., Kossin, J., Mohapatra, M., Satoh, M., Sugi, M., Walsh, K., et al., 2020. Tropical cyclones and climate change assessment: Part II: Projected response to anthropogenic warming. *Bulletin of the American Meteorological Society* 101, E303–E322. doi:10.1175/BAMS-D-18-0194.1.
- Kossin, J.P., 2018. A global slowdown of tropical-cyclone translation speed. *Nature* 558, 104–107. doi:10.1038/s41586-018-0158-3.
- Kossin, J.P., Camargo, S.J., 2009. Hurricane track variability and secular potential intensity trends. *Climatic Change* 97, 329–337. doi:10.1007/s10584-009-9748-2.
- Kossin, J.P., Camargo, S.J., Sitkowski, M., 2010. Climate modulation of North Atlantic hurricane tracks. *Journal of Climate* 23, 3057–3076. doi:10.1175/2010JCLI3497.1.
- Kossin, J.P., Olander, T.L., Knapp, K.R., 2013. Trend analysis with a new global record of tropical cyclone intensity. *Journal of Climate* 26, 9960–9976. doi:10.1175/JCLI-D-13-00262.1.
- Kowaleski, A.M., Evans, J.L., 2016. A Reformulation of Tropical Cyclone Potential Intensity Theory Incorporating Energy Production along a Radial Trajectory. *Mon. Wea. Rev.* 144, 3569–3578. doi:10.1175/MWR-D-15-0383.1.
- Krishna, K.M., 2009. Intensifying tropical cyclones over the north indian ocean during summer monsoon—global warming. *Global and Planetary Change* 65, 12–16. doi:10.1016/j.gloplacha.2008.10.007.
- Kudo, T., Kawamura, R., Hirata, H., Ichiyanagi, K., Tanoue, M., Yoshimura, K., 2014. Large-scale vapor transport of remotely evaporated seawater by a rossby wave response to typhoon forcing during the baiu/meiyu season as revealed by the jra-55 reanalysis. *Journal of Geophysical Research: Atmospheres* 119, 8825–8838. doi:10.1002/2014JD021999.

- Läderach, A., Sodemann, H., 2016. A revised picture of the atmospheric moisture residence time. *Geophysical Research Letters* 43, 924–933. doi:10.1002/2015GL067449.
- Landsea, C.W., Franklin, J.L., 2013. Atlantic hurricane database uncertainty and presentation of a new database format. *Monthly Weather Review* 141, 3576–3592. doi:10.1175/MWR-D-12-00254.1.
- Lee, M., Kim, T., Cha, D.H., Min, S.K., Park, D.S.R., Yeh, S.W., Chan, J.C., 2021. How Does Pacific Decadal Oscillation Affect Tropical Cyclone Activity Over Far East Asia? *Geophysical Research Letters* 48, e2021GL096267. doi:10.1029/2021GL096267.
- Li, Z., Li, T., Yu, W., Li, K., Liu, Y., 2016. What controls the interannual variation of tropical cyclone genesis frequency over Bay of Bengal in the post-monsoon peak season? *Atmospheric Science Letters* 17, 148–154. doi:10.1002/asl.636.
- Li, Z., Yu, W., Li, T., Murty, V., Tangang, F., 2013. Bimodal character of cyclone climatology in the bay of bengal modulated by monsoon seasonal cycle. *Journal of Climate* 26, 1033–1046. doi:10.1175/JCLI-D-11-00627.1.
- Liberato, M.L., Ramos, A.M., Trigo, R.M., Trigo, I.F., Durán-Quesada, A.M., Nieto, R., Gimeno, L., 2012. Moisture sources and large-scale dynamics associated with a flash flood event. *Lagrangian modeling of the atmosphere* 200, 111–126. doi:10.1029/2012GM001244.
- Lin, I.I., Camargo, S.J., Patricola, C.M., Boucharel, J., Chand, S., Klotzbach, P., Chan, J.C., Wang, B., Chang, P., Li, T., Jin, F.F., 2020. ENSO and tropical cyclones, in: *El Niño Southern Oscillation in a Changing Climate*. Wiley Online Library, pp. 377–408. doi:https://doi.org/10.1002/9781119548164.ch17.
- Liu, M., Vecchi, G.A., Smith, J.A., Knutson, T.R., 2019a. Causes of large projected increases in hurricane precipitation rates with global warming. *npj Climate and Atmospheric Science* 2, 1–5. doi:10.1038/s41612-019-0095-3.
- Liu, Y., Liang, P., Sun, Y., 2019b. The Asian summer monsoon: characteristics, variability, teleconnections and projection. Elsevier. doi:10.1016/C2017-0-04074-0.
- Lu, X., Yu, H., Lei, X., 2011. Statistics for size and radial wind profile of tropical cyclones in the western north pacific. *Acta meteorologica sinica* 25, 104–112. doi:10.1007/s13351-011-0008-9.
- MacQueen, J., et al., 1967. Some methods for classification and analysis of multivariate observations, in: *Proceedings of the fifth Berkeley symposium on mathematical statistics and probability*, Oakland, CA, USA. pp. 281–297.
- Magee, A.D., Verdon-Kidd, D.C., Diamond, H.J., Kiem, A.S., 2017. Influence of ENSO, ENSO Modoki, and the IPO on tropical cyclogenesis: a spatial analysis of the southwest Pacific region. *International Journal of Climatology* 37, 1118–1137. doi:10.1002/joc.5070.
- Makarieva, A.M., Gorshkov, V.G., Nefiodov, A.V., Chikunov, A.V., Sheil, D., Nobre, A.D., Li, B.L., 2017. Fuel for cyclones: The water vapor budget of a hurricane as dependent on its movement. *Atmospheric Research* 193, 216–230. doi:10.1016/j.atmosres.2017.04.006.

- Malkus, J.S., Riehl, H., 1960. On the dynamics and energy transformations in steady-state hurricanes. *Tellus* 12, 1–20. doi:10.3402/tellusa.v12i1.9351.
- Matyas, C.J., 2010. Associations between the size of hurricane rain fields at landfall and their surrounding environments. *Meteorology and atmospheric physics* 106, 135–148. doi:10.1007/s00703-009-0056-1.
- Maxwell, J.T., Soulé, P.T., Ortegren, J.T., Knapp, P.A., 2012. Drought-busting tropical cyclones in the southeastern atlantic united states: 1950–2008. *Annals of the Association of American Geographers* 102, 259–275. doi:10.1080/00045608.2011.596377.
- Misra, V., Bhardwaj, A., Mishra, A., 2018. Local onset and demise of the indian summer monsoon. *Climate Dynamics* 51, 1609–1622. doi:10.1007/s00382-017-3924-2.
- Molinari, J., Vollaro, D., 2013. What percentage of western north pacific tropical cyclones form within the monsoon trough? *Monthly Weather Review* 141, 499–505. doi:10.1175/MWR-D-12-00165.1.
- Montgomery, M., Nicholls, M., Cram, T., Saunders, A., 2006. A vortical hot tower route to tropical cyclogenesis. *Journal of the atmospheric sciences* 63, 355–386. doi:10.1175/JAS3604.1.
- Montgomery, M.T., Farrell, B.F., 1993. Tropical cyclone formation. *Journal of Atmospheric Sciences* 50, 285–310. doi:10.1175/1520-0469(1993)050<0285:TCF>2.0.CO;2.
- Montgomery, M.T., Smith, R.K., 2017. Recent developments in the fluid dynamics of tropical cyclones. *Annual Review of Fluid Mechanics* 49, 541–574. doi:10.1146/annurev-fluid-010816-060022.
- Murakami, H., Hsu, P.C., Arakawa, O., Li, T., 2014. Influence of model biases on projected future changes in tropical cyclone frequency of occurrence. *Journal of Climate* 27, 2159–2181. doi:10.1175/JCLI-D-13-00436.1.
- Nair, U.S., Rappin, E., Foshee, E., Smith, W., Pielke, R.A., Mahmood, R., Case, J.L., Blankenship, C.B., Shepherd, M., Santanello, J.A., et al., 2019. Influence of land cover and soil moisture based brown ocean effect on an extreme rainfall event from a Louisiana Gulf Coast tropical system. *Scientific reports* 9, 1–10. doi:10.1038/s41598-019-53031-6.
- Nieto, R., Ciric, D., Vázquez, M., Liberato, M.L., Gimeno, L., 2019. Contribution of the main moisture sources to precipitation during extreme peak precipitation months. *Advances in Water Resources* 131, 103385. doi:10.1016/j.advwatres.2019.103385.
- Nishikawa, H., 2020. A face-area-weighted ‘centroid’ formula for finite-volume method that improves skewness and convergence on triangular grids. *Journal of Computational Physics* 401, 109001. doi:10.1016/j.jcp.2019.109001.
- Noska, R., Misra, V., 2016. Characterizing the onset and demise of the indian summer monsoon. *Geophysical Research Letters* 43, 4547–4554. doi:10.1002/2016GL068409.
- Numaguti, A., 1999. Origin and recycling processes of precipitating water over the eurasian continent: Experiments using an atmospheric general circulation model. *Journal of Geophysical Research: Atmospheres* 104, 1957–1972. doi:10.1029/1998JD200026.

- Ordoñez, P., Nieto, R., Gimeno, L., Ribera, P., Gallego, D., Ochoa-Moya, C.A., Quintanar, A.I., 2019. Climatological moisture sources for the Western North American Monsoon through a Lagrangian approach: their influence on precipitation intensity. *Earth System Dynamics* 10, 59–72. doi:10.5194/esd-10-59-2019.
- O’Gorman, P., Muller, C.J., 2010. How closely do changes in surface and column water vapor follow clausius–clapeyron scaling in climate change simulations? *Environmental Research Letters* 5, 025207. doi:10.1088/1748-9326/5/2/025207.
- Palazzi, E., Provenzale, A., 2016. Water in the climate system, in: *The Fluid Dynamics of Climate*. CISM International Centre for Mechanical Sciences. Springer, Viena. volume 564, pp. 161–182.
- Pazos, M., Gimeno, L., 2017. Identification of moisture sources in the atlantic ocean for cyclogenesis processes, in: *1st International Electronic Conference on Hydrological Cycle (ChyCle-2017)*. Sciforum Electronic Conference Series, pp. 1–5. doi:10.3390/CHyCle-2017-04862.
- Peixoto, J.P., Oort, A.H., 1992. *Physics of climate*. Springer Verlag, New York Press, New York, USA.
- Pérez-Alarcón, A., Coll-Hidalgo, P., Fernández-Alvarez, J.C., Nieto, R., Gimeno, L., 2022a. Estimation of mean water vapour residence time during tropical cyclones using a Lagrangian approach. *Tropical Cyclone Research and Review* 11, 76–87. doi:10.1016/j.tcrr.2022.08.001.
- Pérez-Alarcón, A., Coll-Hidalgo, P., Fernández-Alvarez, J.C., Sorí, R., Nieto, R., Gimeno, L., 2022b. Moisture sources for precipitation associated with major hurricanes during 2017 in the north atlantic basin. *Journal of Geophysical Research: Atmospheres* 127, e2021JD035554. doi:10.1029/2021JD035554.
- Pérez-Alarcón, A., Fernández-Alvarez, J., Díaz-Rodríguez, O., 2021a. Hurricane maximum potential intensity and global warming. *Revista Cubana de Física* 38, 77–85.
- Pérez-Alarcón, A., Fernández-Alvarez, J.C., Sorí, R., Nieto, R., Gimeno, L., 2021b. The combined effects of sst and the north atlantic subtropical high-pressure system on the atlantic basin tropical cyclone interannual variability. *Atmosphere* 12, 329. doi:10.3390/atmos12030329.
- Pérez-Alarcón, A., Fernández-Alvarez, J.C., Sorí, R., Nieto, R., Gimeno, L., 2022c. Moisture source identification for precipitation associated with tropical cyclone development over the Indian Ocean: a Lagrangian approach. *Climate Dynamics* 2022, 1–24. doi:10.1007/s00382-022-06429-4.
- Pérez-Alarcón, A., Sorí, R., Fernández-Alvarez, J.C., Nieto, R., Gimeno, L., 2021c. Comparative climatology of outer tropical cyclone size using radial wind profiles. *Weather and Climate Extremes* 33, 100366. doi:10.1016/j.wace.2021.100366.
- Pérez-Alarcón, A., Sorí, R., Fernández-Alvarez, J.C., Nieto, R., Gimeno, L., 2022d. Dataset of outer tropical cyclone size from a radial wind profile. *Data in Brief* 40, 107825. doi:10.1016/j.dib.2022.107825.
- Pérez-Alarcón, A., Sorí, R., Fernández-Alvarez, J.C., Nieto, R., Gimeno, L., 2022e. Where does the moisture for north atlantic tropical cyclones come from? *Journal of Hydrometeorology* 23,

- 457–472. doi:10.1175/JHM-D-21-0117.1. ©American Meteorological Society. Used with permission.
- Pérez-Alarcón, A., Sorí, R., Fernández-Alvarez, J.C., Nieto, R., Gimeno, L., 2023. Moisture Source for the Precipitation of Tropical Cyclones Over the Pacific Ocean Through a Lagrangian Approach. *Journal of Climate* 36, 1059–1083. doi:10.1175/JCLI-D-22-0287.1. ©American Meteorological Society. Used with permission.
- Pisso, I., Sollum, E., Grythe, H., Kristiansen, N., Cassiani, M., Eckhardt, S., Arnold, D., Morton, D., Thompson, R., 2019. Groot zwaaftink, 590 cd. Evangeliou, N., Sodemann, H., Haimberger, L., Henne, S., Brunner, D., Burkhardt, JF, Fouilloux, A., Brioude, J., Philipp, A., Seibert, P., and Stohl, A.: The Lagrangian particle dispersion model FLEXPART version 10, 4955–4997. doi:10.5194/gmd-12-4955-2019.
- Prat, O.P., Nelson, B.R., 2016. On the link between tropical cyclones and daily rainfall extremes derived from global satellite observations. *Journal of Climate* 29, 6127–6135. doi:10.1175/JCLI-D-16-0289.1.
- Rahman, M., Yang, R., Di, L., et al., 2018. Clustering indian ocean tropical cyclone tracks by the standard deviational ellipse. *Climate* 6, 39. doi:10.3390/cli6020039.
- Ramos, A.M., Nieto, R., Tomé, R., Gimeno, L., Trigo, R.M., Liberato, M.L.R., Lavers, D.A., 2016. Atmospheric rivers moisture sources from a lagrangian perspective. *Earth System Dynamics* 7, 371–384. doi:10.5194/esd-7-371-2016.
- Ramsay, H., 2017. The global climatology of tropical cyclones, in: *Oxford Research Encyclopedia of Natural Hazard Science*, pp. 1–37. doi:10.1093/acrefore/9780199389407.013.79.
- Ramsay, H.A., Camargo, S.J., Kim, D., 2012. Cluster analysis of tropical cyclone tracks in the Southern Hemisphere. *Climate dynamics* 39, 897–917. doi:10.1007/s00382-011-1225-8.
- Reed, K., Bacmeister, J., Rosenbloom, N., Wehner, M., Bates, S., Lauritzen, P., Truesdale, J., Hannay, C., 2015. Impact of the dynamical core on the direct simulation of tropical cyclones in a high-resolution global model. *Geophysical Research Letters* 42, 3603–3608. doi:10.1002/2015GL063974.
- Ren, D., Lynch, M., Leslie, L.M., Lemarshall, J., 2014. Sensitivity of tropical cyclone tracks and intensity to ocean surface temperature: Four cases in four different basins. *Tellus A: Dynamic Meteorology and Oceanography* 66, 24212. doi:10.3402/tellusa.v66.24212.
- Roberts, M., Vidale, P., Senior, C., Hewitt, H., Bates, C., Berthou, S., Chang, P., Christensen, H., Danilov, S., Demory, M.E., et al., 2018. The benefits of global high resolution for climate simulation: process understanding and the enabling of stakeholder decisions at the regional scale. *Bulletin of the American Meteorological Society* 99, 2341–2359. doi:10.1175/BAMS-D-15-00320.1.
- Sainsbury, E.M., Schiemann, R.K., Hodges, K.I., Baker, A.J., Shaffrey, L.C., Bhatia, K.T., 2022. hat Governs the Interannual Variability of Recurring North Atlantic Tropical Cyclones? *Journal of Climate* 35, 3627–3641. doi:10.1175/JCLI-D-21-0712.1.

- Schloemer, R., 1954. Analysis and synthesis of hurricane wind patterns over lake okechobee. Hydrometeorological Rep., Department of Commerce and U.S. Army Corps of Engineers, U.S. Weather Bureau 31, 1–49.
- Schreck III, C.J., Knapp, K.R., Kossin, J.P., 2014. The impact of best track discrepancies on global tropical cyclone climatologies using ibtracs. *Monthly Weather Review* 142, 3881–3899. doi:10.1175/MWR-D-14-00021.1.
- Schumacher, R.S., Galarneau Jr, T.J., 2012. Moisture transport into midlatitudes ahead of recurving tropical cyclones and its relevance in two predecessor rain events. *Monthly weather review* 140, 1810–1827. doi:10.1175/MWR-D-11-00307.1.
- Shan, K., Yu, X., 2020. Interdecadal variability of tropical cyclone genesis frequency in western north pacific and south pacific ocean basins. *Environmental Research Letters* 15, 064030. doi:10.1088/1748-9326/ab8093.
- Shi, X., Durran, D.R., 2015. Estimating the response of extreme precipitation over midlatitude mountains to global warming. *Journal of Climate* 28, 4246–4262. doi:10.1175/JCLI-D-14-00750.1.
- Sinnott, R., H.Duan, Y.Sun, 2016. Chapter 15 - A Case Study in Big Data Analytics: Exploring Twitter Sentiment Analysis and the Weather, in: Buyya, R., Calheiros, R.N., Dastjerdi, A.V. (Eds.), *Big Data*. Morgan Kaufmann, pp. 357–388. doi:10.1016/B978-0-12-805394-2.00015-5.
- Smith, R.K., Montgomery, M.T., 2016. Understanding hurricanes. *Weather* 71, 219–223. doi:10.1002/wea.2776.
- Sodemann, H., 2020. Beyond turnover time: constraining the lifetime distribution of water vapor from simple and complex approaches. *Journal of the Atmospheric Sciences* 77, 413–433. doi:10.1175/JAS-D-18-0336.1.
- Sodemann, H., Schwierz, C., Wernli, H., 2008. Interannual variability of greenland winter precipitation sources: Lagrangian moisture diagnostic and north atlantic oscillation influence. *Journal of Geophysical Research: Atmospheres* 113. doi:10.1029/2007JD008503.
- Sorí, R., Nieto, R., Liberato, M.L., Gimeno, L., 2021. Oceanic versus terrestrial origin of el niño southern oscillation-associated continental precipitation anomalies. *Annals of the New York Academy of Sciences* 1504, 202–214. doi:10.1111/nyas.14665.
- Sorí, R., Nieto, R., Vicente-Serrano, S., Drumond, A., Gimeno, L., 2017. Une perspective lagrangienne du cycle hydrologique dans le bassin du fleuve congo. *Earth System Dynamics* 8, 653–675. doi:10.5194/esd-8-653-2017.
- Stewart, S., 2018. National hurricane center tropical cyclone report: Hurricane ophelia. National Hurricane Center doi:<https://www.nhc.noaa.gov/data/tcr/AL172017>.
- Stohl, A., Forster, C., Frank, A., Seibert, P., Wotawa, G., 2005. Technical note: The Lagrangian particle dispersion model FLEXPART version 6.2. *Atmospheric Chemistry and Physics* 5, 2461–2474. doi:10.5194/acp-5-2461-2005.

- Stohl, A., Hittenberger, M., Wotawa, G., 1998. Validation of the lagrangian particle dispersion model flexpart against large-scale tracer experiment data. *Atmospheric Environment* 32, 4245–4264. doi:10.1016/S1352-2310(98)00184-8.
- Stohl, A., James, P., 2004. A lagrangian analysis of the atmospheric branch of the global water cycle. part i: Method description, validation, and demonstration for the august 2002 flooding in central europe. *Journal of Hydrometeorology* 5, 656–678. doi:10.1175/1525-7541(2004)005<0656:ALAOA>2.0.CO;2.
- Stohl, A., James, P., 2005. A lagrangian analysis of the atmospheric branch of the global water cycle. part 2: Earth's river catchments, ocean basins, and moisture transports between them. *J. Hydrometeorol* 6, 961–984. doi:10.1175/JHM470.1.
- Stohl, A., Thomson, D.J., 1999. A density correction for lagrangian particle dispersion models. *Boundary-Layer Meteorology* 90, 155–167. doi:10.1023/A:1001741110696.
- Sun, B., Wang, H., 2014. Moisture sources of semiarid grassland in china using the lagrangian particle model flexpart. *Journal of Climate* 27, 2457–2474. doi:10.1175/JCLI-D-13-00517.1.
- Tan, C., Fang, W., 2018. Mapping the Wind Hazard of Global Tropical Cyclones with Parametric Wind Field Models by Considering the Effects of Local Factors. *Int. J. Disaster Risk Sci.* 9, 86–99. doi:10.1007/s13753-018-0161-1.
- Tan, X., Liu, Y., Wu, X., Liu, B., Chen, X., 2022. Examinations on global changes in the total and spatial extent of tropical cyclone precipitation relating to rapid intensification. *Science of The Total Environment* 853, 158555. doi:10.1016/j.scitotenv.2022.158555.
- Tao, C., Jiang, H., 2015. Distributions of shallow to very deep precipitation–convection in rapidly intensifying tropical cyclones. *Journal of Climate* 28, 8791–8824. doi:10.1175/JCLI-D-14-00448.1.
- Tao, C., Jiang, H., Zawislak, J., 2017. The relative importance of stratiform and convective rainfall in rapidly intensifying tropical cyclones. *Monthly Weather Review* 145, 795–809. doi:10.1175/MWR-D-16-0316.1.
- Tao, D., Zhang, F., 2014. Effect of environmental shear, sea-surface temperature, and ambient moisture on the formation and predictability of tropical cyclones: An ensemble-mean perspective. *Journal of Advances in Modeling Earth Systems* 6, 384–404.
- Torn, R.D., Elles, T.J., Papin, P.P., Davis, C.A., 2018. Tropical cyclone track sensitivity in deformation steering flow. *Monthly Weather Review* 146, 3183–3201. doi:10.1175/MWR-D-18-0153.1.
- Trenberth, K.E., 1998. Atmospheric moisture residence times and cycling: Implications for rainfall rates and climate change. *Climatic change* 39, 667–694. doi:10.1023/A:1005319109110.
- VanDerEnt, R., Wang-Erlandsson, L., Keys, P.W., Savenije, H., 2014. Contrasting roles of interception and transpiration in the hydrological cycle–Part 2: Moisture recycling. *Earth System Dynamics* 5, 471–489. doi:10.5194/esd-5-471-2014.
- VanDerEnt, R.J., Savenije, H.H., Schaeffli, B., Steele-Dunne, S.C., 2010. Origin and fate of atmospheric moisture over continents. *Water Resources Research* 46. doi:10.1029/2010WR009127.

- VanDerEnt, R.J., Savenije, H.H.G., 2011. Length and time scales of atmospheric moisture recycling. *Atmospheric Chemistry and Physics* 11, 1853–1863. doi:10.5194/acp-11-1853-2011.
- VanDerEnt, R.J., Tuinenburg, O.A., 2017. The residence time of water in the atmosphere revisited. *Hydrology and Earth System Sciences* 21, 779–790. doi:10.5194/hess-21-779-2017.
- Vázquez, M., Nieto, R., Liberato, M.L., Gimeno, L., 2020. Atmospheric moisture sources associated with extreme precipitation during the peak precipitation month. *Weather and Climate Extremes* 30, 100289. doi:10.1016/j.wace.2020.100289.
- Vecchi, G.A., Delworth, T.L., Murakami, H., Underwood, S.D., Wittenberg, A.T., Zeng, F., Zhang, W., Baldwin, J.W., Bhatia, K.T., Cooke, W., et al., 2019. Tropical cyclone sensitivities to CO₂ doubling: Roles of atmospheric resolution, synoptic variability and background climate changes. *Climate Dynamics* 53, 5999–6033. doi:10.1007/s00382-019-04913-y.
- Vecchi, G.A., Knutson, T.R., 2008. On estimates of historical north atlantic tropical cyclone activity. *Journal of Climate* 21, 3580–3600. doi:10.1175/2008JCLI2178.1.
- Vinodhkumar, B., Busireddy, N.K.R., Ankur, K., Nadimpalli, R., Osuri, K.K., 2022. On occurrence of rapid intensification and rainfall changes in tropical cyclones over the north indian ocean. *International Journal of Climatology* 42, 714–726. doi:10.1002/joc.7268.
- Vogl, S., 2009. Tropical Cyclone Boundary-Layer Models. Ph.D. thesis. Ludwig-Maximilians-Universität München: Faculty of Physics. doi:10.5282/edoc.10274.
- Wakefield, R.A., Basara, J.B., Shepherd, J.M., Brauer, N., Furtado, J.C., Santanello Jr, J.A., Edwards, R., 2021. The inland maintenance and reintensification of Tropical Storm Bill (2015). Part I: Contributions of the brown ocean effect. *Journal of Hydrometeorology* 22, 2675–2693. doi:10.1175/JHM-D-20-0150.1.
- Walsh, K.J., Camargo, S.J., Vecchi, G.A., Daloz, A.S., Elsner, J., Emanuel, K., Horn, M., Lim, Y.K., Roberts, M., Patricola, C., et al., 2015. Hurricanes and climate: The us clivar working group on hurricanes. *Bulletin of the American Meteorological Society* 96, 997–1017. doi:10.1175/BAMS-D-13-00242.1.
- Wang, C., Wu, L., 2018. Projection of north pacific tropical upper-tropospheric trough in cmi5 models: implications for changes in tropical cyclone formation locations. *Journal of Climate* 31, 761–774. doi:10.1175/JCLI-D-17-0292.1.
- Wang, Q., Li, J., Li, Y., Xue, J., Zhao, S., Xu, Y., Wang, Y., Zhang, Y., Dong, D., Zhang, J., 2019a. Modulation of tropical cyclone tracks over the western North Pacific by intra-seasonal Indo-western Pacific convection oscillation during the boreal extended summer. *Climate Dynamics* 52, 913–927. doi:10.1007/s00382-018-4264-6.
- Wang, T., Lu, X., Yang, S., 2019b. Impact of south Indian Ocean Dipole on tropical cyclone genesis over the South China Sea. *International Journal of Climatology* 39, 101–111. doi:10.1002/joc.5785.
- Wang, Y., Matyas, C.J., 2022. Simulating the Effects of Land Surface Characteristics on Planetary Boundary Layer Parameters for a Modeled Landfalling Tropical Cyclone. *Atmosphere* 13, 138. doi:10.3390/atmos13010138.

- Wang, Z., 2014. Characteristics of convective processes and vertical vorticity from the tropical wave to tropical cyclone stage in a high-resolution numerical model simulation of tropical cyclone fay (2008). *Journal of the Atmospheric Sciences* 71, 896–915. doi:10.1175/JAS-D-13-0256.1.
- Wang, Z., 2015. Tropical cyclones and hurricanes: Tropical cyclogenesis, in: *Encyclopedia of Atmospheric Sciences: Second Edition*. Elsevier Inc., pp. 57–64. doi:10.1016/B978-0-12-382225-3.00506-5.
- Wang, Z., Montgomery, M.T., Dunkerton, T.J., 2009. A dynamically-based method for forecasting tropical cyclogenesis location in the atlantic sector using global model products. *Geophysical Research Letters* 36. doi:10.1029/2008GL035586.
- Wehner, M.F., Reed, K.A., Loring, B., Stone, D., Krishnan, H., 2018. Changes in tropical cyclones under stabilized 1.5 and 2.0 C global warming scenarios as simulated by the Community Atmospheric Model under the HAPPI protocols. *Earth System Dynamics* 9, 187–195. doi:10.5194/esd-9-187-2018.
- Wei, W., Ji-Long, C., 2012. Sensitivity of tropical cyclone precipitation to atmospheric moisture content: case study of bilis (2006). *Atmospheric and Oceanic Science Letters* 5, 420–425. doi:10.1080/16742834.2012.11447030.
- Willoughby, H.E., 1990. Gradient balance in tropical cyclones. *Journal of the Atmospheric Sciences* 47, 265–274. doi:10.1175/1520-0469(1990)047<0265:GBITC>2.0.CO;2.
- Willoughby, H.E., Darling, R.W.R., Rahn, M., 2006. Parametric representation of the primary hurricane vortex. Part II: A new family of sectionally continuous profiles. *Mon. Wea. Rev.* 134, 1102–1120. doi:10.1175/MWR3106.1.
- WMO, 2012. *International Glossary of Hydrology*. Technical Report WMO-No. 385. World Meteorological Organization. URL: https://library.wmo.int/doc_num.php?explnum_id=8209.
- Wohl, E., Barros, A., Brunsell, N., Chappell, N., Coe, M., Giambelluca, T., Goldsmith, S., Harmon, R., Hendrickx, J., Juvik, J., McDonnell, J., Ogden, F., 2012. The hydrology of the humid tropics. *Nature Climate Change* 2, 655–662.
- Wood, V.T., White, L.W., 2011. A new parametric model of vortex tangential-wind profiles: Development, testing, and verification. *Journal of the Atmospheric Sciences* 68, 990–1006. doi:10.1175/2011JAS3588.1.
- Wood, V.T., White, L.W., Willoughby, H.E., Jorgensen, D.P., 2013. A new parametric tropical cyclone tangential wind profile model. *Monthly weather review* 141, 1884–1909. doi:10.1175/MWR-D-12-00115.1.
- Wu, L., Tian, W., Liu, Q., Cao, J., Knaff, J.A., 2015. Implications of the observed relationship between tropical cyclone size and intensity over the western north pacific. *Journal of Climate* 28, 9501–9506. doi:10.1175/JCLI-D-15-0628.1.
- Wu, L., Wen, Z., Huang, R., Wu, R., 2012. Possible linkage between the monsoon trough variability and the tropical cyclone activity over the western north pacific. *Monthly Weather Review* 140, 140–150. doi:10.1175/MWR-D-11-00078.1.

- Xu, G., Osborn, T.J., Matthews, A.J., 2017. Moisture transport by atlantic tropical cyclones onto the north american continent. *Climate Dynamics* 48, 3161–3182. doi:10.1007/s00382-016-3257-6.
- Yanase, W., Satoh, M., Taniguchi, H., Fujinami, H., 2012. Seasonal and intraseasonal modulation of tropical cyclogenesis environment over the bay of bengal during the extended summer monsoon. *Journal of Climate* 25, 2914–2930. doi:10.1175/JCLI-D-11-00208.1.
- Yang, L., Chen, S., Wang, C., Wang, D., Wang, X., 2018. Potential impact of the Pacific Decadal Oscillation and sea surface temperature in the tropical Indian Ocean–Western Pacific on the variability of typhoon landfall on the China coast. *Climate Dynamics* 51, 2695–2705. doi:10.1007/s00382-017-4037-7.
- Ye, T., ZHOU, W., Wong, W., 2022. Detecting the interdecadal changes of western north pacific tropical cyclone genesis based on clustering analysis using phash+ kmeans. *Frontiers in Earth Science* , 1432doi:10.3389/feart.2021.825835.
- Ying, Y., Zhang, Q., 2012. A modeling study on tropical cyclone structural changes in response to ambient moisture variations. *Journal of the Meteorological Society of Japan. Ser. II* 90, 755–770. doi:10.2151/jmsj.2012-512.
- Yoo, J., Santanello, J.A., Shepherd, M., Kumar, S., Lawston, P., Thomas, A.M., 2020. Quantification of the land surface and brown ocean influence on tropical cyclone intensification over land. *Journal of Hydrometeorology* 21, 1171–1192. doi:10.1175/JHM-D-19-0214.1.
- Yoshida, R., Miyamoto, Y., Tomita, H., Kajikawa, Y., 2017. The effect of water vapor on tropical cyclone genesis: A numerical experiment of a non-developing disturbance observed in PALAU2010. *Journal of the Meteorological Society of Japan. Ser. II* doi:10.2151/jmsj.2017-001.
- Yu, J.H., Zheng, Y.Q., Wu, Q.S., Lin, J.G., Gong, Z.B., 2016. K-means clustering for classification of the northwestern pacific tropical cyclone tracks. *J. Trop. Meteor* 22, 127–135. doi:10.16555/j.1006-8775.2016.02.003.
- Zhang, D., Zhang, J., Shi, L., Yao, F., 2020. Interdecadal changes of characteristics of tropical cyclone rapid intensification over western north pacific. *IEEE access* 8, 15781–15791. doi:10.1109/ACCESS.2020.2965976.
- Zhao, H., Chen, S., Klotzbach, P.J., 2019. Recent strengthening of the relationship between the western north pacific monsoon and western north pacific tropical cyclone activity during the boreal summer. *Journal of Climate* 32, 8283 – 8299. doi:10.1175/JCLI-D-19-0016.1.
- Zhao, J., Zhan, R., Wang, Y., Xu, H., 2018. Contribution of the interdecadal Pacific oscillation to the recent abrupt decrease in tropical cyclone genesis frequency over the western North Pacific since 1998. *Journal of climate* 31, 8211–8224. doi:10.1175/JCLI-D-18-0202.1.
- Zheng, Z.W., Lin, I.I., Wang, B., Huang, H.C., Chen, C.H., 2015. A long neglected damper in the el niño—typhoon relationship: A ‘gaia-like’ process. *Scientific reports* 5, 1–7. doi:10.1038/srep11103.
- Zhu, Y.J., Collins, J.M., Klotzbach, P.J., 2021. Nearshore hurricane intensity change and post-landfall dissipation along the united states gulf and east coasts. *Geophysical Research Letters* 48, e2021GL094680. doi:10.1029/2021gl094680.



Universida_{de}Vigo